

**DEVELOPMENT OF EXPERIMENTAL TECHNIQUES
AND CFD SIMULATIONS OF MULTIPHASE
DISPERSIONS**

**A
THESIS SUBMITTED
TO THE
UNIVERSITY OF MUMBAI
FOR THE
Ph. D. (Tech.) DEGREE
IN
CHEMICAL ENGINEERING**

**SUBMITTED BY
MAYUR J. SATHE**

**UNDER THE GUIDANCE OF
PROFESSOR J. B. JOSHI
AND UNDER CO-GUIDANCE OF
DR. B. D. KULKARNI**

**INSTITUTE OF CHEMICAL TECHNOLOGY,
MATUNGA, MUMBAI-400 019.**

NOVEMBER 2010

**STATEMENT TO BE INCORPORATED BY THE CANDIDATE
IN THE THESIS AS REQUIRED UNDER ORDINANCE O.770 FOR THE
Ph.D. DEGREE**

STATEMENT BY THE CANDIDATE

As required by the University Ordinance O.770, I wish to state that the work embodied in this thesis titled “**DEVELOPMENT OF EXPERIMENTAL TECHNIQUES AND CFD SIMULATIONS OF MULTIPHASE DISPERSIONS**” forms my own contribution to the research work carried out under the guidance of **Professor Jyeshtharaj B. Joshi** at the Institute of Chemical Technology and under the co-guidance of **Dr. Bhaskar D. Kulkarni** at National Chemical Laboratory. This work has not been submitted for any other degree of this or other university. Wherever references have been made to previous work of other, these have been clearly indicated as such and included in the bibliography.



Sathé Mayur Jayantkumar
(Research Scholar)

Certified by



Professor Jyeshtharaj B. Joshi
Research Supervisor,
Department of Chemical Engineering,
Institute of Chemical Technology,
Mumbai 400 019

Date: 25, November, 2010.
Place: Mumbai.



Dr. Bhaskar D. Kulkarni
Research Co-Supervisor,
Chemical Engineering and Process
Development Division,
National Chemical Laboratory,
Pune 411 008

Date: 25, November, 2010.
Place: Mumbai.

CERTIFICATE

The research work described in this thesis has been carried out by **Sathe Mayur Jayantkumar** under our supervision. We certify that this is his bonafide work. The work described is original and has not been submitted for any other degree of this or any other university. Further that he was a regular student and has worked under our guidance as a full time student at Institute of Chemical Technology until the submission of the thesis to the University of Mumbai.



Professor Jyeshtharaj B. Joshi
(Research Supervisor)



Dr. Bhaskar D. Kulkarni
(Co- Research Supervisor)

Date: 25 November, 2010.

Place: Mumbai.

List of Publications

Based on the work reported in the thesis, the following papers have been published/forwarded for publication/ in preparation:

1. Deshmukh, S. S., **Sathe, M. J.**, Joshi, J. B. and Koganti, S. B., 2009. Residence Time Distribution and Flow Patterns in the Single Phase, Annular Region of Annular Centrifugal Extractor. *Industrial and Engineering Chemistry Research*, 48 (1), 37–46. (I.F. 1.895, 4 Citations)
2. Deshpande, S. S., **Sathe, M. J.** and Joshi, J. B., 2009. Evaluation of Energy Dissipation Rate Using Particle Image Velocimetry. *Industrial and Engineering Chemistry Research*, 48 (10), 5046–5057. (I.F. 1.895, 1 Citation)
3. Tabib, M. V., **Sathe, M. J.**, Deshpande, S. S. and Joshi, J. B., 2009. A Hybridized Snapshot Proper Orthogonal Decomposition-Discrete Wavelet Transform Technique for the Analysis of Flow Structures and Their Time Evolution. *Chemical Engineering Science*, 64 (21), 4319-4340. (I.F. 1.884, 1 Citation)
4. **Sathe, M. J.**, Deshmukh, S. S., Joshi, J. B. and Koganti, S. B., 2010. Computational fluid dynamics simulation and experimental investigation: Study of two-phase liquid-liquid flow in a vertical Taylor-couette contactor. *Industrial and Engineering Chemistry Research*, 49 (1), 14-28.
5. **Sathe, M. J.**, Thaker, I. H., Strand, T. E. and Joshi, J. B., 2010. Advanced PIV/LIF and Shadowgraphy System to Visualize Flow Structure in Two-Phase Bubbly Flows. *Chemical Engineering Science*, 65 (8), 2431-2442. (I.F. 2.316, 2 Citations)
6. Ganguli, A.A., **Sathe, M.J.**, Pandit, A.B., Joshi, J.B. and Vijayan, P.K., 2010. Hydrodynamics and heat transfer characteristics of passive decay heat removal systems: CFD simulations and experimental measurements. *Chemical Engineering Science*, 65 (11), 3457-3473.
7. Mathpati, C. S., **Sathe, M. J.** and Joshi, J. B., 2010. Reply to “Comments on ‘Dynamics of Flow Structures and Transport Phenomena—Part I: Experimental and Numerical Techniques for Identification and Energy Content of Flow Structures’ ”. *Industrial and Engineering Chemistry Research*, 49 (9), 4471–4473.
8. Dahikar, S. K., **Sathe, M. J.** and Joshi, J. B., 2010. Investigation of flow and temperature patterns in direct contact condensation using PIV, PLIF and CFD. *Chemical Engineering Science*, 65 (16), 4606–4620.
9. **Sathe, M. J.**, Mathpati, C. S. and Joshi, J. B. Investigation of flow structures and transport phenomena in bubble columns using particle image velocimetry and miniature pressure sensors. *Forwarded for publication in GLS-10 special issue of Chemical Engineering Science, 2010.*
10. Gandhi, M. S., **Sathe, M. J.**, Vijayan, P.K. and Joshi, J. B. Two phase natural convection: CFD Simulations and PIV measurement. *Forwarded for publication in GLS-10 special issue of Chemical Engineering Science, 2010.*
11. **Sathe, M. J.**, Joshi, J. B., Doroodchi, E., Roberts, R. H. and Evans, G. M.. Effect of Free Stream Turbulence and Surfactant Concentration on Bubble Rise Characteristics. *In preparation, 2010.*
12. **Sathe, M. J.**, Ghatge, S. V. and Joshi, J. B.. Characterization of turbulence in homogeneous and heterogeneous dispersed flows. *In preparation, 2010.*
13. Sathe, M. J., Ekambara, K. and Joshi J. B. Characterization of flow structures in bubble column using LES data. *In preparation, 2010.*



Dedicated to

Lotus feet of Shree Krishna

ACKNOWLEDGEMENT

Acknowledgement

I met wonderful people in these 5 years immediately after completing my BE from M S University. My experiences started from ordering food from menu for first time in restaurants- and new experiences have become almost a daily routine since then. I take this opportunity to thank everyone who taught me the necessary skills for every endeavor and helped me to get through my PhD. I thank my parents, my wife, Girija, and my in laws, especially Dr. S. N Sahasrabudhe for outstanding support during this support. At times, I have not even been able to call them for 3-4 days; however, their motivation and positive feeling filled me with energy.

I thank god for giving me opportunity to come to LDA lab under the guidance of two stalwarts: Professor J. B. Joshi and Dr. B D Kulkarni. They opened my eyes and gave a unique scientific perspective, to learn everything to deepest and to aim for the best. I have found that my thinking and learning abilities have grown up tremendously under their influence. A unique thing about Professor Joshi is that he trusts in younger generations- I stand in testimony that he let us use most advanced flow visualization equipment with freedom at par with the best organizations in the world. He assured me since very beginning of the work by quoting that I should not worry; If the success occurs, it goes to my students, if the failure comes it is mine! Rarely one would experience such generosity and tenderness from person of such eminence. He always ensured that we are always burdened with work to the maximum extent, but without letting us know he was always monitoring continuously that no student of his bends under this burdon, and supported openly or secretly to make us strong to make us dream big and do big, for our lives (At least for next 50 year, as he says it!). He not only guided me for chemical engineering, he mentored with all aspects of life to bring out complete transformation in me. I am indeed indebted for all the teachings, sir.

I thank Dr. B D Kulkarni for his guidance during the CSIR fellowship at NCL. His talks were brief, to the very points and with feeble sentences he was able to clarify any intriguing topic, not only mathematical. His modesty and pleasant smile gives one a hope, and every time I had conversation with him it charged me with positive energy to work hard for months. It was not without his support that I was able to manage completion of this thesis. I thank Dr. V. Ravikumar for helping me understand intricate details of wavelet transforms. I regret that I was not able to work for a long duration at a stretch at NCL. However, god has been generous to me with opportunities, and I bag for one opportunity to work with him on longer project soon.

I thank Professor A. B. Pandit for teaching me multiphase contactors. I also thank him for renting me his house after my marriage. I thank our Head of Department, Professor V. G. Gaikar, for providing me a opportunity of CSIR fellowship and his support during the tenure of PhD. I thank Professor G.D.Yadav, as former head of department and now Director of ICT. I acknowledge his support as warden of hostel 5 as well. I thank Professor Doraiswamy Ramkrishna for his guidance during PhD. I thank Professor Geoffrey Evans for the opportunity of collaborative work with University of Newcastle, Australia. He is always filled with energy- he inspired me to do more in life in every aspect. I thank Dr. P K Vijayan form BARC for guidance during the work on flow measurements in passive decay system model. I would also like to thank Dr. Amol kulkarni with his constant help throughout tenure of Phd with understanding of bubble columns.

I thank people from workshop, Shri Budhavale, Shri Bagul, Shri Vale and Shri Mayekar for their help with experimental setups. I thank Dr Paralkar for his help with electronics.

I still clearly remember how fascinated I was to read the plaque reading 'LASER DOPPLER ANEMOMETRY LABORATORY' while I first came here. Thanks to my lab mates, I still share the same fascination about this place while I enter the lab every day. They made this a great place to be, and to work, to learn. My mates, I am short of time writing this acknowledgement and hence request you to forgive any errors/omissions. I will follow chronological order to ease out sequencing ;) However, it might deviate slightly from chronology for I am writing in hurry.

Dr Swarnendu Roy (BABA) was a enchanting, flamboyant personality. His shouting, quotes, and the names given to me – Hingorani, chanchu still stay with me. Dr. Manish bhole, a rock solid calm and quiet fellow with deep knowledge and scarcity of talk (till he was in free mood) INSPIRED. I thank Dr. T Kumaresan, Dr. Sreepriya Vedantam, Dr. Mahesh Dhotre for being supportive in initial periods of PhD. Dr. Sagar Deshpande (Galgale) and Dr. Sagar Gulawani (Gullu) was a pair of 'DONS of PIV section'. Their help and support has been invaluable right from teaching with teaching PIV, to handling accounts and importing equipment. I thank Dr Indraneel Chatterjee (Neel) for help with computers, and management skills. Dr. B N Murthy was a cheerful grand personality, very cool (he still is very cool :P). He helped me with CFD, He had been a nice personal assistant to JBJ and he taught me the skills required to do that. Dr. Sandesh Deshmukh(Sandy) plays it cool. He taught me riding bike on roads of Mumbai. I cherish the times of experiments writing papers with him. Together, we won biggest cash reward of 500 Rs. From JBJ (and with the caution that we will receive same fine if we take more than couple of minutes to answer his question next time!).Dr. Arjit Ganguli (dada) was extremely supportive and inspirational. I take this opportunity to formally thank him. He has been a very good friend, and has been at all the times of need. Dr. Balaji kadam was like a rock, an empirical rock rather ;) He always got through the toughest times, and inspired us to do so. Dr Prakash Chavan (Badak) was the best body builder of the lab. He was always cheerful, and filled the atmosphere with joy and laughs in lab. Dr. Mandar Tabib, my bubble column senior was expert in mathematical techniques and was gifted with presentation skills. Dr. Sachin Dahikar (Nagpuri) was a most cheerful person (and silent worker from within). We had many good times, with Marine drive and Fafda-jalebi at 5 am. Dr. Ankit Gandhi was my roommate. We cherished many good times, in lab and dinners, and Kingfisher strong (I thank Vijay Mallya for that, too!). Dr. Sachin Mathpati (Mathya) has been a wonderful friend. His amazing habits of hard work, and extremely supportive character to everyone around is inspiring. I sincerely thank Dr. Naren for his help with NCL work. Without him, I would not have got fellowship for single month. I always counted on him for every small matter related to NCL. Dr Vishwanath Dalvi with his large frame and magnanimous personality has been inspirational and helpful.

I still feel that I am a junior by looking at the energy and abilities of juniors at the laboratory. They helped, they taught, and they gave me good times to cherish. I thank you all. Prashant Gupta was brilliant, hard working guy who silently 'dugged' through his way to masters ;). Shrikant Badgandi (Buddy) was cheerful, and we still have good times (as he is in my hometown, baroda now). Nilesh Ingle (Nilu) was full of laughter. I hope I see him soon in NY. Chinmay Rane (Masiha) has that signature smile, and fire in belly (I mean it :P) I hope that fire

part extinguishes soon. I thank him for help with many things, including LES chapter of this thesis. Mayur Gandhi, the next PIV man and my gujju partner in lab (we used to secretly bet that he is mix of Mayur sathe and Ankit Gandhi.. only time will tell how he turns out!). Tushar Tamhane (Tushki) the poet cum engineer; I cherish working with him on PDPA, spirit articles and wonderful times together. Omkar Gadgil (Pant) is my koknastha ethics teacher. Name any surname and he can tell gotra; An absorber of comments and complements and extreme hard worker. He gave Tushar, me and Swapnil personal names; I say for all three of us, we are thankful. Varsha (Chuchu, for she loves mice!) has been extremely supportive. Zoheb khan (Zobekenobe) is a cool dude. Together, Varsha and zobes gave me wonderful times with their knowledge of best food joints around and eloquent English. Dinesh (Rajni) is very hard worker (everyone in advanced center has to be!) and wonderful rider with his R15. Bhasker Patil (Vahana) is awesome (he must be smiling.. gaalatalya gaalat). Ram Patil (Rampo) is cheerful. He has become sharp and little zeherila; I thank him for all the help. Shyam sumanta Das (Shyamu) is my roommate. I thank him for all the great time, the books, the Puri trip, and giving me shelter in last days of PhD. He and Dada have been extremely supportive during the course of PhD. Yogesh shinde (mama) is the cooker specialist.

I thank Swapnil Ghatage for help with compiling all the chapters of the thesis. Without Swapnil, Chinmay, MayurG and Bhasker it was not possible for me to put together thesis in such a short interval of time. Together, Rampo, mama, shyamu, gadgil, swapnil, and bhasker have been very good company during thesis writing time.

I take this opportunity to thank Girija, my wife. She has been the most beautiful thing that happened to my life. She is very far from me right now, almost poles apart; and she is still ready to support me all the activities even if that means going to Australia (even far) for further work for quite some time. It was not without her help and support that I am able to finish this work in time.

I acknowledge CSIR for JRF fellowship for the tenure of July 2005 to June 2010. I thank Professor J. B. Joshi for fellowship support from July-December 2010.

I sincerely apologize to everyone whom I could not mention in this acknowledgement. You have always been helpful, and I cherished good time I had with all of you.

Mayur Sathe

Mumbai

24/11/2010

TABLE OF CONTENTS

TABLE OF CONTENTS

1. INTRODUCTION	1
1.1. Introduction	1
Notations	12
References	12
2. MEASUREMENT TECHNIQUES FOR MULTIPHASE DISPERSIONS	13
2.1. Hot Film Anemometry	13
2.1.1. Previous Work	13
2.1.2. Equipment	13
2.1.2.1. Principles of HFA	13
2.1.2.2. Probes and accessories	15
2.1.2.3. Probe mounting and cabling	16
2.1.2.4. Data acquisition system	17
2.1.2.5. CTA module	18
2.1.2.6. CCA module	20
2.1.3. Data Analysis	22
2.1.3.1. Measurement accuracy	22
2.1.3.2. Velocity calculation	23
2.1.3.3. Eddy identification strategy	25
2.2. Laser Doppler Anemometry	27
2.2.1. Previous Work	28
2.2.2. Equipment	28
2.2.2.1. Characteristics of LDA	28
2.2.2.2. Principles	30

2.2.2.3. The Fringe model	34
2.1.2.1. Frequency shift	37
2.2.2.2. Signals	40
2.2.2.3. Seeding	42
2.2.2.4. Signal processing	44
2.2.3. LDA Data Analysis	48
2.2.3.1. Interpolation of LDA data	49
2.2.3.2. Denoising the time series	55
2.2.3.3. Gas velocity estimation using LIM	56
2.2.3.4. Bubble size estimation	60
2.3. Particle Image Velocimetry (PIV)	63
2.3.1. Literature Review	63
2.3.2. Experimental	64
2.3.2.1. Principle of PIV	64
2.3.2.2. Laser and optics	66
2.3.2.3. Synchronizer system	69
2.3.2.4. CCD sensor details	72
2.3.2.5. Image capture	73
2.3.2.6. Stereoscopic technique	73
2.3.2.7. Scheimpflug stereoscopic arrangement	75
2.3.3. Data Processing of PIV	77
2.3.3.1. Image evaluation methods for PIV	77
2.3.3.2. Image shifting	78
2.3.3.3. Processing of PIV vector field	80
2.3.3.4. Stereo PIV: mapping function generation	83

2.3.3.5. Guidelines	84
2.3.3.6. Rules of thumb for autocorrelation PIV analysis:	86
2.3.3.7. PIV image processing to estimate bubble size	86
2.4. Shadow Imaging	88
2.4.1. Previous Work	88
2.4.2. Equipment	89
2.4.3. Data Processing of Shadow Images	92
2.4.3.1. High speed photography	92
2.4.3.2. Image processing for estimation of bubble size distribution	93
2.5. Planar Laser Induced Fluorescence (PLIF)	95
2.5.1. Literature Review	95
2.5.2. Equipment	96
2.5.2.1. Principle of PLIF	96
2.5.2.2. Experimental set-up	99
2.5.2.3. PLIF calibration	100
2.5.3. Processing of PLIF Images	101
2.6. Miniature Pressure Sensor Arrays	102
2.6.1. Previous Work	102
2.6.2. Equipment	103
2.6.2.1. Pressure measurement	103
2.6.2.2. Rectangular bubble column	104
2.6.2.3. Cylindrical bubble column	104
2.6.2.4. Pressure sensors	105
2.6.2.5. Signal conditioner	107
2.6.2.6. Analog to digital conversion:	107

2.6.3. Data Processing	108
2.6.3.1. Accuracy and resolution of pressure measurement	108
2.6.3.2. Noise analysis and data acquisition	109
2.6.3.3. Bubble size estimation	112
2.6.3.4. Spectral analysis of pressure time series	114
2.6.3.5. Power spectral density	115
2.6.3.6. Coherence	117
2.6.3.7. Liquid velocity estimation	121
Notations	122
References	127
3. ESTIMATION OF DESIGN PARAMETERS	132
3.1. Residence Time distribution in Annular Centrifugal Extractors	132
3.1.1. Introduction	132
3.1.2. Previous Work	132
3.1.3. Experimental	134
3.1.3.1. Geometrical details and operating conditions	135
3.1.3.2. Measurement principle	137
3.1.3.3. Probe calibration and data acquisition	139
3.1.4. Mathematical Modeling	140
3.1.4.1. Model formulation for species transport	140
3.1.4.2. Data analysis	141
3.1.4.3. Numerical simulation	142
3.1.5. Results and Discussion	143
3.1.5.1. RTD experiments	143

3.1.5.2. CFD predictions of RTD	145
3.1.5.2.1. Convective Transport	149
3.1.5.2.2. Turbulent transport	150
3.1.5.2.3. Relation between the number of vortices and number of tanks in series	152
3.1.5.3. Effect of aspect ratio	153
3.1.5.4. Reduction in back-mixing by providing internals	156
3.1.6. Conclusions	159
3.2. Estimation of Turbulent Energy Dissipation Rate in Jet loop Reactor	160
3.2.1 Introduction	160
3.2.2 Previous Work	161
3.2.3 Experimental	165
3.2.3.1 Particle Image Velocimetry	165
3.2.3.2 Laser Doppler Velocimetry (LDV)	167
3.2.3.3 Hot Film Anemometer (HFA)	168
3.2.3.4 Need for Multiple Measurement Technique	169
3.2.3.5 Processing Method	174
3.2.3.5.1 PIV data processing	174
3.2.3.5.2 LDV/HFA data processing	174
3.2.4 CFD Simulations	174
3.2.4.1 Model formulation and boundary conditions	174
3.2.4.2 Turbulent models and method of solutions	175
3.2.4.2.1 LES Model	175
3.2.5 Results and Discussion	176
3.2.5.1 Flow Characteristics: Comparison of PIV results with LDV	176

Measurement	
3.2.5.2 Estimation of Turbulent Energy Dissipation Rate per unit	179
Mass (ϵ)	
3.2.5.2.1 Method of Third Order Structure Function using PIV	180
Data	
3.2.5.2.2 Energy Spectrum using LDV/HFA Data	181
3.2.5.2.3 Optimization algorithm	182
3.2.5.2.4 Results of ϵ	186
3.2.5.3 CFD Simulations	196
3.2.5.3.1 Mean Velocity Profiles	197
3.2.5.3.2 ϵ Profiles	199
3.2.5.4 Application of the Methodology for Design of Reactor	201
3.2.6 Conclusions	201
Notations	203
References	207
4. EFFECT OF TURBULENCE ON BUBBLE RISE CHARACTERISTICS	212
4.1. Introduction	212
4.2. Literature Review	214
4.3. Experimental methods	222
4.3.2. Turbulence Generator	222
4.3.1. Bubble Generator	224
4.3.3. Measurement Principle	225
4.3.4. The Measurement System	227
4.3.5. Outline of the Experiments	228

4.4. Data Processing	231
4.4.1. Image Processing	232
4.4.2. PIV Processing	234
4.4.3. Particle Response Time and Stokes Number	236
4.5. Results and Discussion	248
4.6. Conclusions	249
Notations	250
References	
5. CHARACTERIZATION OF TURBULENCE IN HOMOGENEOUS AND HETEROGENEOUS DISPERSED FLOWS	252
5.1. Introduction	252
5.1.1. Characterization of Turbulence of Interest to Present Work	253
5.1.2. Profiles of Dispersed Phase Hold-up, Continuous Phase Velocity and Turbulent Kinetic Energy	254
5.1.3. Particle/Bubble Slip Velocity as a Function of Void Fraction	255
5.1.4. Statistics of Dispersed Phase Slip Velocity and Continuous Phase Velocity: Bubble Rise Velocity Fluctuations	256
5.1.5. Wake Attenuation and Wake Interactions	257
5.1.6. Spectral Slope for Continuous Phase Energy Spectrum in Inertial and Near Dissipation Subrange	258
5.2. Experiments and Methods	262
5.2.1. Fluidized Bed and Bubble Column	262
5.2.2. Particle Image Velocimetry and Shadowgraphy	267
5.2.3. Miniature Pressure Sensors	269

5.3. Data Processing	271
5.3.1. Image Processing to Generate Bubble/Particle mask	271
5.3.2. PDF of Liquid Velocity and Structure Functions	272
5.3.3. Evaluation of Energy Spectrum	274
5.4. Results and Discussion	276
5.4.1. Turbulence Inside Fluidized Bed and In the Decay Region Downstream of Fluidized Bed	276
5.4.2 PDF of Liquid Velocity in Fluidized Bed	280
5.4.3. Structure Functions of Liquid Velocity in Fluidized Bed	282
5.4.4. Integral Length Scale, RMS Velocity and the Decay Law for Flow Downstream the Fluidized Bed	286
5.4.5. Flow Pattern in Bubble Column	290
5.4.6. Structure Functions and Energy Spectra in Bubble Column	294
5.4.7. Bubble Size Distribution	300
5.4.8. Bubble Rise Velocity	305
5.4.9. Energy Spectrum of Turbulence in Dispersed Flows	309
5.5. Conclusions	320
Notations	321
References	322
6. LARGE EDDY SIMULATION OF BUBBLE COLUMN REACTORS	324
6.1. Introduction	324
6.2. Literature review	325
6.3. Equipment	327
6.4 Details of Simulation	328

6.5. Equations for Large eddy simulation	329
6.5.1. Euler--Euler description of the flow field	331
6.5.2. LES of turbulence	332
6.5.3. Dynamic procedure	333
6.5.4. One-equation model	335
6.5.5. Interface force modelling	335
6.5.5.1. Drag force	336
6.5.5.2. Lift force	336
6.5.5.3. Virtual mass force	337
6.5.5.4. Turbulent dispersion force	337
6.5.5.5. Bubble induced turbulence	338
6.6. 3D Gaussian Filtering	339
6.7. Results and discussion:	340
6.7.1. Cylindrical bubble column	340
6.7.2. Rectangular bubble column	341
6.7.3. Volume visualization with 3D filtering	345
6.8. Conclusions	347
Notations	347
References	350
7. INVESTIGATION OF FLOW STRUCTURES AND TRANSPORT PHENOMENA IN BUBBLE COLUMNS USING PARTICLE IMAGE VELOCIMETRY AND MINIATURE PRESSURE SENSORS	352
7.1. Introduction	352
7.1.1. Bubble Column as a Building Block of Understanding of	352

Transport Phenomena in Multiphase Contactors	
7.1.2. General Nature of Flow Pattern in Bubble columns	353
7.1.3. Evaluation of Mass Transfer Coefficient using Flow Information	354
7.1.4. Approaches to use Flow Information to Derive Transport Characteristics: Heuristics and Analytical Approaches	355
7.1.5. ‘Wish List’ for Desired Flow Parameters in Order to Clearly Understand Transport Phenomena	363
7.2. State of the Art on Estimation of Mass Transfer Coefficient in Bubble Column	364
7.3. Experimental Techniques	365
7.3.1. Bubble Column and Sparger Details	365
7.3.2. LDA Measurements	367
7.3.3. Pressure Sensor: Description, Mounting and Calibration	368
7.3.4. PIV Measurements	369
7.4. Data Processing	371
7.4.1. Stochastic Estimation	371
7.4.2. Image Processing	375
7.4.3. Discrete Wavelet Transform	377
7.4.4. Eddy Identification Methodologies (EIM)	378
7.4.4.1. Eddy identification method based on zero crossings (EIM-ZC)	379
7.4.4.2. Eddy identification method based on continuous wavelet transform (EIM-CWT)	380
7.4.4.3. Relative merits of EIM-ZC and EIM-CWT	383
7.4.5. Methodology for Evaluation of Flow Structures Characteristics	384

and the Estimation of Mass Transfer Coefficient	
7.5. Results and Discussion	385
7.5.1. MLSE of Pressure Fluctuation Signals	385
7.5.2. Discrete Wavelet transform	387
7.5.3. Properties of Flow Structures Evaluated from Pressure Fluctuation Signals	391
7.5.4. Evaluation of mass transfer coefficient	406
7.6. Conclusions	407
Notations	408
References	410
SCOPE FOR FUTURE WORK	414
SYNOPSIS	416

Chapter 1

INTRODUCTION

1.1. Introduction

Reaction engineering of multiphase systems is a ubiquitous feature of chemical engineering as it addresses a basic need; the transformation of nonrenewable or renewable resources into fuels, chemicals, food, pharmaceuticals and new materials. It is the chemical transformations including biochemical, electrochemical, biological reactions that change the structure and property of molecules to generate the desired products. The choice of reaction chemistry, catalyst, operating conditions and the selection of reactor type and contacting pattern determine the volumetric productivity, yield and selectivity of the process. An overwhelming percentage of reaction systems (over 95%) in practice are multiphase in nature. Quantifying reactor performance demands understanding of: a) mechanistic description of kinetic rates, b) transport kinetic interaction and c) reactor flow pattern and contacting. Therefore, understanding the physics of multiphase flows is of prime importance as far as efficient design and debottlenecking of the reactor is concerned. This can have a profound positive impact on the overall economics of the process.

The subject of multiphase flow has become increasingly important in a wide variety of engineering systems. These kind of flows can also be observed in a number of biological systems and natural phenomena. Some of the important applications are listed in Table 1.1 (Ishii & Hibiki, 2006). The underlying principle of all the systems listed here can be explained by the same physical laws of transport of mass, momentum and energy. Multiphase flows can be classified according to the state of the different phases or components and therefore refer to gas-solid flows or liquid-solid flows or gas-liquid flows or bubbly flows and so on. Further, two phase flows can be classified according to the geometry of the interfaces into three main classes, namely separated flow,

DEVELOPMENT OF EXPERIMENTAL TECHNIQUES AND CFD SIMULATIONS OF MULTIPHASE DISPERSIONS

transitional or mixed flow and dispersed flow, and a detailed classification appears in Table 1.1.

Table 1.1. Classification of two phase flow (Ishii, 1975)

Class	Typical regimes	Configuration	Example
Separated flows	Film flow	Liquid film in gas, gas film in liquid	Film condensation, film boiling
	Annular flow	Liquid core and gas film, gas core and liquid film	Film boiling boilers
	Jet flow	Liquid jet in gas, gas jet in liquid	Atomization, jet condenser
Mixed or Transitional flow	Cap, Slug or Churn-turbulent flow	Gas pocket in liquid	Sodium boiling in forced convection
	Bubbly annular flow	Gas bubbles in liquid film with gas core	Evaporation with wall nucleation
	Droplet annular flow	Gas core with droplets and liquid film	Steam generator
	Bubbly droplet annular flow	Gas core with droplets and liquid film with gas bubbles	Boiling nuclear reactor channel
Dispersed flow	Bubbly flow	Gas bubbles in liquid	Chemical reactor
	Droplet flow	Liquid droplets in gas	Spray cooling
	Particulate flow	Solid particle in gas or liquid	Transportation of powder

In general, reactor performance is governed by reaction specific and reactor specific phenomena. While the reaction specific phenomena depend on physical properties, stoichiometry, thermodynamics, kinetics etc., the reactor specific phenomena are largely dependent on operating conditions, physical properties of contacted materials, reactor type, and its geometric dimensions. For sound design of reactors, values of large number of design parameters, such as fractional phase holdups, pressure drop, dispersion coefficients (the extent of axial mixing) of all the compounds, heat and mass transfer coefficients and the rate-controlling steps, are needed. A large number of correlations are available for the fractional phase holdup, axial dispersion coefficient, pressure drop,

DEVELOPMENT OF EXPERIMENTAL TECHNIQUES AND CFD SIMULATIONS OF MULTIPHASE DISPERSIONS

mass transfer coefficient and heat transfer coefficient. With the help of these correlations, the model equations for a particular reactor, which are often complex, can be solved analytically using few assumptions. For instance, in the case of bubble columns, the liquid phase can be assumed to be backmixed, and the flow of the gas phase can be assumed to be plug flow in nature. With these assumptions, the model equation for bubble column can be solved analytically to get the volume of reactor for a specific requirement.

However, this design procedure is largely empirical in nature. The fundamental reason for empiricism is the complexity of fluid dynamics in the process equipment. Hence, much effort is expended in understanding the physics of turbulent flows. Most of the industrial equipment are operated under the turbulent conditions, wherein the motion of compendium of eddies (flow structures) of different length and time scales contribute towards mixing, momentum transfer, heat transfer, and mass transfer. Hence, a proper understanding of the mechanism related to the formation and the role of these turbulent flow structures in determining transport phenomena can bring about a significant improvement in the scale-up and design procedures.

There are almost 400 different types of reactors and multiphase contactors in practice which are designed by modifications in a few conventional hardware configurations (straight and coiled pipes, jets and venturies, ejectors, packed columns (with random or structured packings), falling and agitated film contactors, staged column contactors, bubble columns, fluidized beds, stirred tanks, etc.). Once such modifications are successful, they are reproduced as such for other production facilities of the same chemical or scaled-up or down depending upon the requirements.

By following the aforesaid procedure, the design may prove unreliable (and/or expensive) due to the lack of understanding of transport phenomena. This is mainly

because, as mentioned above, the present status of the design is still closer to an art rather than the desired status of science. Thus in practice, all these plants are always over-designed for given production rate. Such empirical practices lead to high capital and operating costs, long start up times, and expensive ways of solving plant problems. Further, such apparent overdesigns have resulted into underdesigns in several commercial operations. In addition, the selectivity levels may be low and lead to by-products, which in turn adds a burden on the environment. The overdesign also means energy intensive operation. Hence it was thought desirable to classify these reactors, then look into their design consideration and implement the knowledge of flow structures to optimize these reactors.

1.1. Reactor Classification on the Basis of Energy Input

For various applications, energy is required and there are various ways by which energy can be supplied to the equipment. In fact, all the equipment can be conveniently classified (Joshi and Doraiswamy, 2008) on the basis of the mode of energy supply: (1) pressure energy (2) potential energy (3) kinetic energy (Table 1.2).

The Class-1 equipment are also called column type equipment. Under this category, there is a variety of multiphase contactors. The gas-liquid contactors include bubble columns, packed bubble columns, internal loops and external loop airlift reactors, sectionalized bubble columns, plate columns, etc. Solid-fluid (liquid or gas) contactors include the static mixers, fixed beds, expanded beds, fluidized beds, transport reactors or contactors, etc. For instance, fixed bed geometry is used in unit operations such as ion exchange, adsorptive and chromatographic separations, drying and in catalytic reactors. The liquid-liquid contactors include spray columns, packed extraction columns, plate extraction columns, static mixers, etc. Similar equipment are widely used in liquid-gas, gas-liquid-solid, gas-liquid-liquid, gas-liquid-liquid-solid contactors.

Table 1.2: Reactor Classification on the basis of Energy Input

Class – 1	Class - 2	Class - 3
bubble columns	Falling film reactor/ evaporator	Stirred Reactors (single and multi-impeller)
packed bubble columns	Packed column with random and structure packing	Gas inducing reactor
Internal loop air lift reactors	Agitated film dryer/ evaporator/reactor	Surface aerators
External loop airlift reactors	Trickle bed reactors	Rotating disc contactor
sectionalized bubble columns	Trickling filters in waste water treatment	Annular centrifugal extractors
plate columns	Condensers	Asymmetric rotating disc contactor
Pipeline and coil reactors	Rotating disc contactors	Jet loop reactors
static mixers	Rotating basket (of packing) contactors	Mixer – settler
fixed bed reactor	Disk and donut contactors	Plunging jet reactors
expanded bed reactor	Solar water/air heaters	Scheibel columns
fluidized bed reactor	Wetted wall reactors	Centrifuges
Ion exchange column/ chromatographic separators	Wetted sphere reactors	Higee contactors
Dryers	Spinning disc contactors	
spray columns		
plate extraction columns		
Circulating fluidized bed		

In all these multiphase contactors, the dispersed phase consists of bubbles or drops or particles or two or all three of them. The continuous phase is either liquid or gas. The governing and the characteristic features of the dispersed phase is its size distribution and velocity distribution and these two features have a major impact on the performance of these equipment. The other governing parameters include the column diameter, the column height, the sparger design and the design of internals. Further, in Class-1 equipment, the energy is supplied through the introduction of phases. For instance, in the case of bubble columns and gas fluidized beds, the gas is supplied against the static pressure of multiphase dispersion and energy input rate is given by the following equation,

$$E_i = Q_G \rho_D H_D g \quad (1.1)$$

E_i is the pressure energy and Class-1 equipment, therefore, are classified under pressure energy. For the energy balance of different type of equipment type of Class-1 equipment, reader may refer Joshi (1980, 1983, 2001) and Joshi and co-workers (Pandit and Joshi, 1984; Ranade and Joshi, 1987; Joshi et al., 1988; Joshi et al., 1990a; Joshi et al., 1990b; Joshi et al., 2001).

In class-2 equipment, the energy supplied is in the form of potential energy associated with liquid. For instance, in the conventional packed column (used for either distillation or absorption), the liquid is pumped up to the top of the column and distributed over the packing. If the gas is introduced at the bottom, the gas phase has the pressure energy, however, it is usually negligible as compared with the potential energy of the liquid. Even if the gas and liquid phases flow co-current downwards, the major contribution to the energy is by the liquid phase. Since the liquid flows in the form of a film, these equipment (Class-2) may also be termed as film contactors. Other equipment in this category include trickle bed reactors and falling film reactors/ evaporators. In

DEVELOPMENT OF EXPERIMENTAL TECHNIQUES AND CFD SIMULATIONS OF MULTIPHASE DISPERSIONS

packed columns, a variety of packing shapes (and of course sizes and material of construction) are used in practice which include the Raschig rings (in old installations), berl saddles, partition rings, intelox saddles, pall rings, hipack rings, structured packings, etc. Equally important is the uniformity of liquid distribution, liquid redistribution and packing supports.

The Class-3 equipment includes stirred tank reactors. In this case, the mode of energy supply is through the impeller rotation. The flow leaving the impeller has kinetic energy in the form of mean or/and turbulent. The energy is used for a variety of objectives such as blending, heat transfer, liquid-liquid dispersions, gas-liquid dispersions, solid-liquid dispersions and higher order dispersions.

Stirred reactors, in which one or more impellers are used to generate, desired flow and mixing are among the most widely used reactors in chemical and allied industries. Stirred reactors offer unmatched flexibility and control over various transport processes occurring within the reactor. The performance of a stirred reactor can be optimized by appropriately adjusting the reactor hardware and the operating parameters. Parameters like vessel diameter aspect ratio design, number, type, location and size of impellers, degree of baffling, etc., provide effective handles to control the performance of stirred reactors. However, the availability of such a large number of parameters also makes the job of selecting suitable configuration of the stirred reactor quite difficult.

Stirred tank reactors are extensively used in the chemical process and allied industries to carry out mixing, heat transfer, solid suspension and large number of dispersion applications such as solid-liquid, gas-liquid, liquid-liquid, gas-liquid-solid, gas-liquid-liquid-solid, etc. These equipment are most sought after because of their reliability and flexibility towards the process requirements. In the stirred reactor, the primary mode of energy supply is through the impeller. The flow leaving the impeller

receives mean and turbulent kinetic energy resulting from the impeller motion. The introduction of a second/third phase (in multiphase contacting) may also introduce additional energy. The different impeller designs develop different flow patterns and local degree of turbulence in the vessel. The impeller designs are mainly categorized as open type and closed type impellers. The open type impeller designs are generally classified into two categories, (i) radial flow impellers, and (ii) axial flow impellers. Rushton turbine, straight blade turbines, curved blade turbines, etc. belong to the radial flow category. These impellers generally produce high shear and in turn high turbulence. Axial flow impellers can be operated in either the 'up-pumping' mode or 'down-pumping' mode. Marine propellers, pitched blade turbines, hydrofoil impellers, etc. fall under this category. These impellers provide more convection than turbulence as compared with radial flow impellers.

If the understanding of transport phenomena is improved to some extent, and the energy can be made to dissipate at the desired locations, then the energy input can be brought down by at least 5-10 times. All the equipment mentioned above are generally operated in turbulent regime (except high viscosity such as production and processing of polymers) to achieve the high rates of heat, mass and momentum transfer. The turbulent flows contain flow structures of a wide range of length and time scales which control the transport processes. The length scales of these structures can range from column dimensions (highest) to Kolmogorov scales (lowest). However, not all the scales of turbulence contribute equivalently to transport rates and mixing. Hence, it is important to understand the basic mechanism of participation of different scales of motions with the rates of different transport processes. The present empirical design practices do not consider these basic mechanisms and conceals detailed local information about the relationship between the turbulence and the equipment performance. The theme of the

work presented in this thesis is to understand the flow structure-reactor performance relationship for reliable designs. However, the deduction of flow structures for a particular geometry of reactor and the energy input itself is a very demanding task, and is a first step towards understanding the effect of flow structures on transport phenomena i.e. momentum, heat and mass transfer at different locations in a reactor. The major reason for lack of such knowledge is the limitations of conventional flow measurement techniques and data processing algorithms. Therefore, the current work aims at development of novel experimental techniques and data processing (of both CFD and EFD) to quantify the local flow in multiphase dispersions, to extract as much information as possible.

The structure of thesis is as follows: chapter 2 describes the experimental techniques in detail. The measurement techniques described include Hot Film Anemometry (HFA), Laser Doppler Anemometry (LDA), Particle Image Velocimetry (PIV), Shadow Imaging, Planer Laser Induced Fluorescence (PLIF) and Miniature Pressure Sensors. The operating principle, hardware and data processing for each technique to obtain the desired flow parameters are described. Several tips and tricks regarding individual technique are also described, to maximize the potential of each measurement technique.

Chapter 3 shows the example of extraction of design parameters from the experimental fluid dynamics (EFD) data. Two cases have been considered: estimation of residence time distribution in the annular region of an annular centrifugal extractor and the estimation of energy dissipation rate in a jet loop reactor. Annular Centrifugal Extractors (ACE) are example of miniaturization of process equipment by energy input optimization. The two fluids are mixed in the annular region between two concentric cylinders, with inner cylinder rotating and outer cylinder stationary. The flow in annulus

is turbulent Taylor–Couette flow. The fluid then enters the hollow inner cylinder where the two fluids are separated by centrifugal action. A very high energy dissipation rate in the annulus ensure high mass transfer coefficient and hence results in small contacting volume. The residence time distribution in annular region is important parameter which affects the volume of contactor required while performing reactive extraction. In this subsection, the methodology to obtain residence time distribution using flow pattern from EFD and CFD. The suitable change in geometry of annulus is also suggested to improve the performance of ACE from completely backmixed to plug flow with small extent of dispersion.

In the second subsection, the estimation method of energy dissipation rate using PIV and HFA is described. The estimation of local energy dissipation rate is very important from the reactor design point of view; since it describes the energy required to operate the reactor. The estimation of energy dissipation rate based on novel methodology of fitting the model 3D energy spectrum to the turbulent energy spectrum calculated from HFA, and the structure function methodology applied to PIV data are described. The results are compared with those obtained from large eddy simulations (LES) for jet loop reactor.

Chapter 4 describes the measurement of bubble rise characteristics in grid generated turbulence, with different surfactant concentration. A combined stereo PIV-shadowgraphy technique is used to measure the bubble rise velocity, bubble shape and the liquid phase velocity simultaneously. The effect of grid oscillation frequency, bubble size and surfactant concentration has been observed. Two surfactants, Isopropyl alcohol and Methyl Isobutyl Carbinol are employed.

The characterization of turbulence in liquid-solid and gas-liquid dispersions is described in Chapter 5. Complete description of turbulence in dispersed flows is essential

to understand its impact on phase interaction parameters like drag and lift force. Two geometries, a solid-liquid fluidized bed and rectangular bubble column are considered. The fluidized bed is an example of homogeneous turbulence, while the bubble column is an example of heterogeneous turbulence. Decaying turbulence downstream of fluidized bed is also considered. Different parameters, like PDF, structure functions and energy spectra are described for each of these flows. The similarity between turbulence generated by grid and the fluidized bed is brought out. It has been observed that the turbulence in liquid phase is not only ‘pseudo turbulence’ generated by interaction between sinuous paths of dispersed particles; true turbulence is also present.

LES simulations and 3D data processing is described in chapter 6. The geometry considered in rectangular bubble column, for which PIV/PFS measurements are available from current work. The superficial gas velocity of 20 mm/s is considered. The simulations are performed for bubble column with two spargers: single point and five point sparger. The volume data from LES is processed with 3D Gaussian filter bank to reveal the flow structures with different scales.

Chapter 7 describes the identification of flow structures in bubble column, and use of this information with theories of mass transfer to predict mass transfer coefficient in 2D and 3D bubble column. The pressure fluctuation signals and PIV data is used for analysis. MLSE is applied to evaluate the velocity profiles from multiple pressure sensor measurements. The velocity time series (and spatial series from PIV) are subjected to eddy isolation methodology based on zero crossings and continuous wavelet transforms. The resultant eddy age and length scale distributions are described, along with the prediction of mass transfer coefficient.

Notations

- E_i Energy input
- Q_G Inlet gas flow rate
- ρ_D Average density of dispersion
- H_D Height of dispersion
- g gravitational acceleration.

References

- Ishii, M., Hibiki, T., 2006. Thermo-fluid dynamics of two phase flow. Springer, NewYork.
- Joshi J. B., Dinkar M., Deshpande N. S., Phanikumar D.V., 2001. Hydrodynamic Stability of Multiphase Reactors. *Advances in Chemical Engineering* 26, 1-130.
- Joshi J.B., 1980. Axial Mixing in Multiphase Contactors-A Unified Correlation. *Transactions of Institution of Chemical Engineers (U.K.)*. 58, 155-165.
- Joshi J.B., 1983. Solid-Liquid-Fluidised Beds- Some Design Aspects. *Transactions of Institution of Chemical Engineers (U.K.)-A: Chemical Engineering Research and Design* 61,143-161.
- Joshi J.B., Doraiswamy L.K., 2008. *Chemical Reaction Engineering*, Albrights Handbook of Chemical Engineering, Taylor and Francis.
- Joshi J.B., Patil T.A., Ranade V.V., 1990a. Measurement of Hydrodynamic Parameters in Multiphase Sparged Reactors. *Reviews in Chemical Engineering* 6, 74-227.
- Joshi J.B., Ranade V.V., Gharat V.V., Lele S.S., 1990b. Sparged Loop Reactors. *Canadian Journal of Chemical Engineering* 68, 705-741.
- Joshi J.B., Shertukde P.V., Godbole S.P., 1988. Modeling of Three Phase Sparged Catalytic Reactors. *Reviews in Chemical Engineering* 6, 71-155.
- Joshi, J. B., 2001. Computational Flow Modeling and Design of Bubble Column Reactors. *Chemical Engineering Science* 56, 5893-5933.
- Pandit A.B., Joshi J.B., 1984. Three Phase Sparged Reactors- Some Design Aspects. *Reviews in Chemical Engineering* 2, 1-84.
- Ranade V.V., Joshi J.B., 1987. Transport Phenomena in MultiPhase Systems: Momemntum mass and heat transfer in bubble column Reactors. *Proceedings of Symposium on Transfer Process in Multiphase Systems, BHU, Varanasi*, 113-196.

Chapter 2

MEASUREMENT TECHNIQUES FOR MULTIPHASE DISPERSIONS

2.1. Hot Film Anemometry

HFA is based on convective heat transfer from a heated wire or film element placed in a fluid flow. Any change in the fluid flow condition that affects the heat transfer from the heated element will be detected virtually instantaneously by a constant temperature/constant current HFA system. HFA can therefore be used to provide information related to for example, the velocity and temperature of the flow, concentration changes in gas mixtures and phase change in multi-phase flows.

2.1.1. Previous Work

Many researchers have employed hot film anemometry for studies related with gas-liquid flows (Lance and Bataille, 1991; Martinez Mercado et al., 2010, Rensen et al., 2005; Riboux et al., 2009). In this technique, an optical fibre is attached close to the hot-film probe so that when a bubble impinges onto the sensor it also interacts with the optical fibre. Its working principle is based on the different index of refraction of light by gas and liquid. . The hot-film probe does not provide by itself means for a successful identification between the phases. Thus many parametric and nonparametric signal processing algorithms have been used to separate the information on both phases, i.e. thresholding (Bruun 1995) or pattern recognition methods (Luther et al. 2005).

Rensen et al. (2005) calculated probability distribution functions, structure functions (with and without the extended self-similarity (ESS) method), and spectra of the water velocity time series using HFA.

2.1.2. Equipment

2.1.2.1. Principles of HFA

Consider a film probe immersed in a fluid flow. Assume that the film, heated by an electrical current input, is in thermal equilibrium with its environment.

The electrical power input is equal to the power lost to convective heat transfer,

$$I^2 R_{film} = h A_{film} (T_{film} - T_f) \quad (2.1)$$

where I is the input current, R_{film} is the resistance of the film, T_{film} and T_f are the temperatures of the film and fluid respectively, A_{film} is the projected film surface area, and h is the heat transfer coefficient of the film. The film resistance R_{film} is also a function of temperature according to,

$$R_{film} = R_{film}[1 + a(T_{film} - T_{Ref})] \quad (2.2)$$

where a is the thermal coefficient of resistance and R_{Ref} is the resistance at the reference temperature T_{Ref} . The heat transfer coefficient h is a function of fluid velocity v_f according to King's law,

$$h = a + b.v_f^c \quad (2.3)$$

where a , b , and c are coefficients obtained from calibration ($c \sim 0.5$). Combining the above three equations allows us to eliminate the heat transfer coefficient h ,

$$a + b.v_f^c = \frac{I^2 R_W}{A_W (T_W - T_f)} = \frac{I^2 R_{Ref} [1 + a(T_W - T_{Ref})]}{A_W (T_W - T_f)} \quad (2.4)$$

Solving above equation we get the equation for the liquid velocity as:

$$v_f = \left\{ \left[\frac{I^2 R_{Ref} [1 + a(T_W - T_{Ref})]}{A_W (T_W - T_f)} - a \right] / b \right\}^{1/c} \quad (2.5)$$

2.1.2.2. Probes and accessories

Probes are primarily selected on basis of (1) Fluid medium, (2) Number of velocity, (3) components to be measured (1D, 2D or 3D), (4) Expected velocity range, (5) Quantity to be measured (velocity, wall shear stress etc.), (6) Required spatial resolution, (7) Turbulence intensity and fluctuation frequency in the flow, (8) Temperature variations, (9) Contamination risk, (10) Available space around the measuring point (free flow, boundary layer flows, confined flows). Anemometer probes are available with four types of sensors: miniature wires (Figure 2.1A), gold-plated wires (Figure 2.1B), fibre-film (Figure 2.1C) or film-sensors (Figure 2.1D). Wires are normally 5 μm in diameter and 1.2 mm long suspended between two needle-shaped prongs. Gold-plated wires have the same active length but are copper- and gold-plated at the ends to a total length of 3 mm long in order to minimize prong interference.

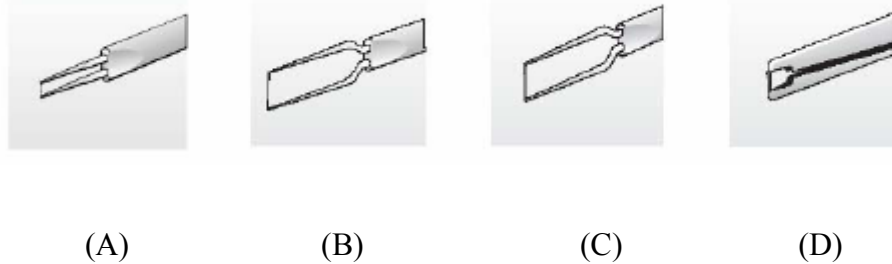


Figure 2.1. (Source: Dantec Dynamics Operation Manual).

Fibre-sensors are quartz-fibers, normally 70 μm in diameter and with 1.2 mm active length, covered by a nickel thin-film, which again is protected by a quartz coating. Fibre-sensors are mounted on prongs in the same arrays as are wires. Film sensors consist of nickel thin-films deposited on the tip of aerodynamically shaped bodies, wedges or cones.

Probes are available in one-, two- and three-dimensional versions as single- (Figure 2.2A), dual (Figure 2.2B) and triple (Figure 2.2C) sensor probes referring to the number of sensors. Since the sensors (wires or fibre-films) respond to both magnitude and direction of the velocity vector, information about both can be obtained, only when two or more sensors are placed under different angles to the flow vector. Split-fibre and triple-split fibre probes are special designs, where two or three thin-film sensors are placed in parallel on the surface of a quartz cylinder. They may supplement X probes in two-dimensional flows, when the flow vector exceeds an angle of $\pm 45^\circ$.

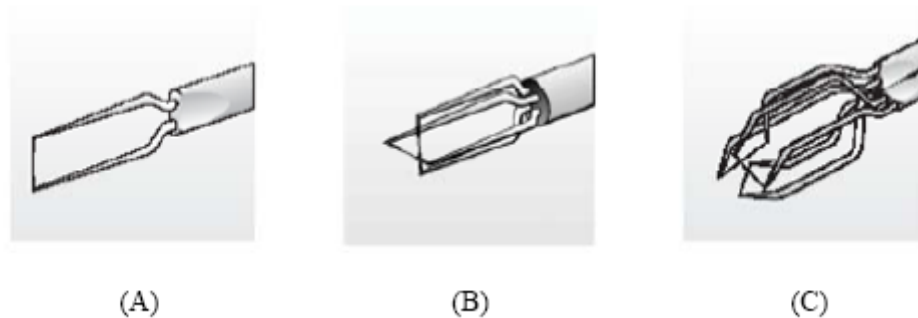


Figure 2.2. (Source: Dantec Dynamics Operation Manual).

2.1.2.3. Probe mounting and cabling

Probe mounting and orientation: The probe is mounted in the flow with the wire/film perpendicular to the flow and the prongs parallel with the flow. Straight probes are mounted with the probe axis parallel with the dominant velocity direction. It is recommended that the probe coordinate system ($x_1; x_2; x_3$) coincides with the laboratory coordinate system ($u_1; u_2; u_3$). The probe is mounted in a probe support, which is equipped with a cable and BNC connector, one for each sensor on the probe.

Film probes are equipped with fixed cables and need no supports. Probe bodies and the probe support are designed so that their outer surfaces are electrically insulated

from the electrical circuitry of the probe/anemometer circuit. They can therefore be mounted directly to any metal part of the test rig without the risk of ground loops.

Cabling: The distance between the probe and the anemometer should be kept as small as possible. The standard cable length is 4 m probe cable plus 1 m support cable, and this combination should be used if at all possible in order to obtain maximum bandwidth and in order to avoid picking up more noise than need be.

Liquid grounding: Film probes mounted in liquids may be damaged, if a voltage difference between the sensor film and the liquid builds up by electric charges in the flowing medium. If such charge build up occurs, the insulating quartz coating may break down and the thin-film will be etched away due to electrolysis. The liquid must therefore be grounded to the anemometer's signal ground as close to the probe as possible.

2.1.2.4. Data acquisition system

The measuring equipment constitutes a measuring chain. It consists typically of a probe with probe support and cabling, a CTA/CCA anemometer, a signal conditioner, an A/D converter, and a computer (Figure 2.3). Very often dedicated application software for CTA/CCA set-up, data acquisition and data analysis is part of the anemometer. A traverse system may be added for probe traverse, when profiles have to be investigated. A dedicated probe calibrator is also used.

Signal conditioner

Most CTA anemometers have built-in Signal Conditioners for high-pass and low pass filtering and for amplification of the CTA signal. High-pass filter removes the DC-part of the signal. When low frequency fluctuations have to be removed from the signal prior to spectral analysis high pass filter is utilized. Low pass filter removes electronic

noise from the signal and prevents folding back of spectra (aliasing). The filter is as steep as possible.

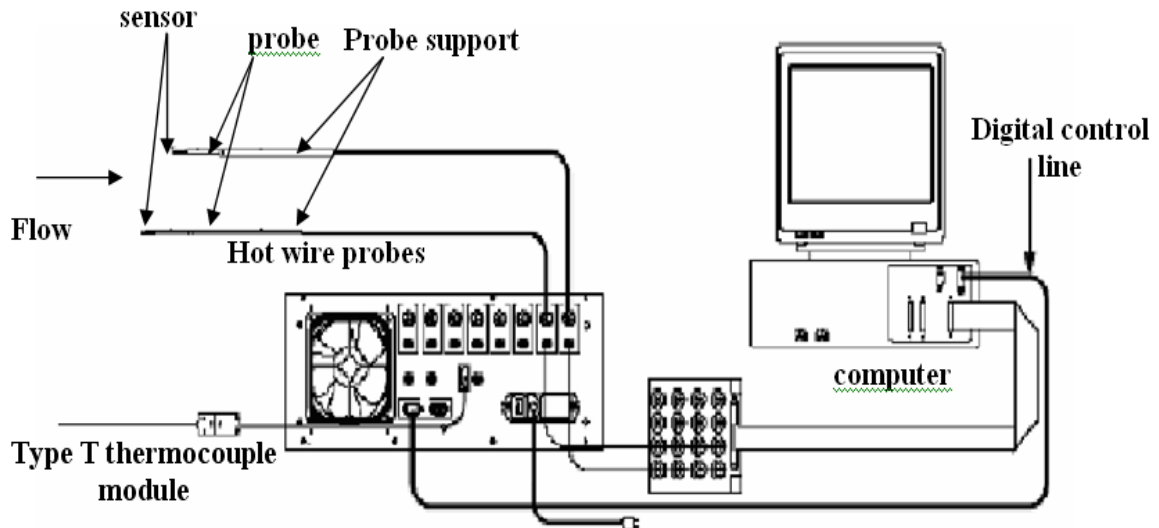


Figure 2.3 Flow diagram of HFA setup (Source: Dantec Dynamics Operation Manual)

A/D board

The CTA signal is acquired via an A/D converter board and saved as data-series in a computer. A/D board is used to select the number of channels required for the experiments plus additional channels (e.g. temperature). The suitable input range (0-10 Volts) is can be selected based on anemometers and applications. The board with 100 kHz sampling rate covers most low-to-medium velocity applications (< 100 m/s). The sampling rate should be minimum two times the maximum frequency in the flow. The sampling rate reduced by the number of channels. The board is also provided with external triggering which is needed to start the data acquisition by an event related to the flow.

2.1.2.5. CTA module

There are two main modes of operating a hot-wire probe: Constant Temperature and Constant Current. The constant-temperature anemometers are more widely used than

constant-current anemometers due to their reduced sensitivity to flow variations. Noting that the wire must be heated up high enough (above the fluid temperature) to be effective, if the flow were to suddenly slow down, the wire might burn out in a constant-current anemometer. Conversely, if the flow were to suddenly speed up, the wire may be cooled completely resulting in a constant-current unit being unable to register quality data.

Constant-Temperature: In this mode of operation, the probe temperature varies with the variation in the flow. For a hot-wire anemometer powered by an adjustable current to maintain a constant temperature, T_{film} and R_{film} are constants (Figure 2.4). The fluid velocity is a function of input current and flow temperature,

$$a + b.v_f^c = \frac{I^2 R_{film}}{A_{film}(T_{film} - T_f)} = f(I, T_f) \quad (2.6)$$

Furthermore, the temperature of the flow T_f can be measured. The fluid velocity is then reduced to a function of input current only.

Advantages:

1. Good signal-to-noise(SNR) ratio.
2. Useful for flow temperature (fluctuation) measurements.
3. Heating the sensor only marginally over ambient makes it insensitive to velocity fluctuations, but still sensitive to ambient temperature changes.
4. Linear temperature-voltage response.

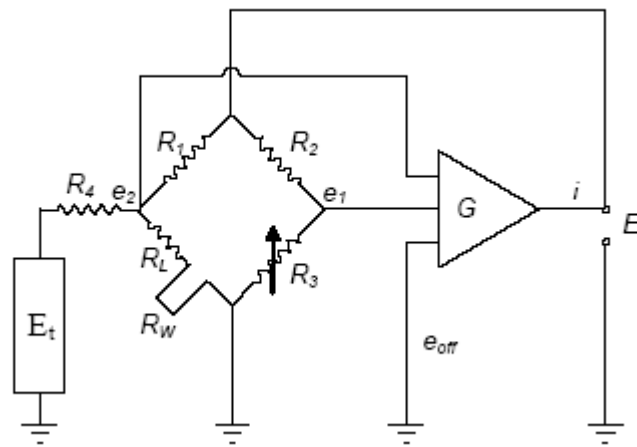


Figure 2.4 Circuit diagram for the constant temperature mode of operation (Source: Dantec Dynamics Operation Manual)

Disadvantages:

1. Low frequency response due to thermal inertia of sensor; thinner wires help but are more susceptible to breakage.
2. Large velocity fluctuations can cause burn out.
3. Relatively low sensitivity to velocity changes in normal range (> 1.5 m/s)
4. Compensation circuits (for thermal inertia of sensor) must be adjusted for each sensor and velocity range.

2.1.2.6. CCA module

Constant-Current: In this mode of operation, the probe resistance (and thereby its temperature) is kept constant by varying the current. For a HFA powered by a constant current I , the velocity of flow is a function of the temperatures of the film and the fluid,

$$a + b.v_f^c = \frac{I^2 R_{Ref} [1 + a(T_{film} - T_{Ref})]}{A_{film}(T_{film} - T_f)} = g(I, T_f) \quad (2.7)$$

DEVELOPMENT OF EXPERIMENTAL TECHNIQUES AND CFD SIMULATIONS OF MULTIPHASE DISPERSIONS

If the flow temperature is measured independently, the fluid velocity can be reduced to a function of wire temperature T_{film} alone. In turn, the film temperature is related to the measured film resistance R_{film} . Therefore, the fluid velocity can be related to the film resistance (Figure 2.5). In CTA-mode the sensor is not required to change temperature, thus there is no problem of thermal inertia as in CCA.

Advantages:

1. Large bandwidth|the limiting frequency is governed by the electronics (± 150 khz)
2. Very sensitive to velocity fluctuations

Disadvantages:

1. Requires stable feedback electronics.

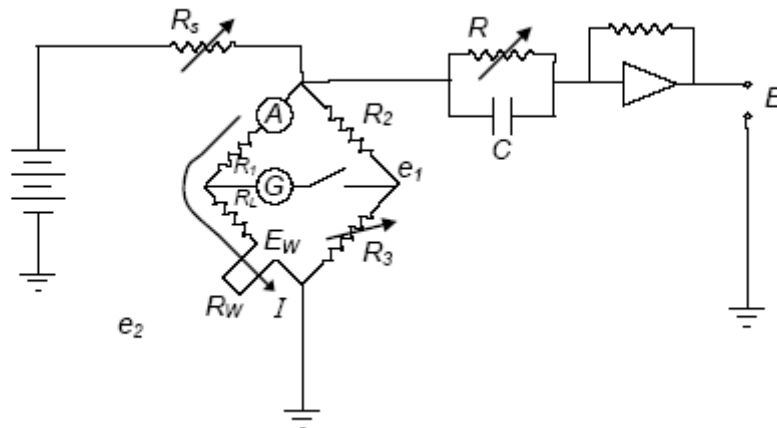


Figure 2.5 Flow diagram for the constant current mode of operation (Source: Dantec Dynamics Operation Manual)

2.1.3. Data Analysis

2.1.3.1. Measurement accuracy

A calibration of probes is most important aspect in the flow measurements using HFA system. It plays a vital role for the accuracy and the speed, with which an experiment can be carried out. Calibration establishes a relation between the CTA output and the flow velocity. It is performed by exposing the probe to a set of known velocities, U , and then record the voltages, E . A curve fit through the points (E , U) represents the transfer function to be used when converting data records from voltages into velocities. It is important to keep track of the temperature during calibration. If it varies from calibration to measurement, it may be necessary to correct the CTA data records for temperature variations. The calibration of HFA probe has been done by simultaneously measuring the velocities from LDV and corresponding voltages from HFA in the liquid-liquid (Homogeneous) jet. The cylindrical tank of I.D. 0.3 m and height 0.6 m with nozzle of I.D. 0.02 m has been used. The nozzle is inserted vertically downward with submergence of 50 mm from top. The total liquid height was 0.5 m. The position of the probe is so adjusted that the intersection point of LDV and cross section of probe film has same location. Further, the simultaneous measurements have been carried out to measure the average flow velocity using LDV and its corresponding voltage using HFA. Since the application of HFA is in the experiments where there is a sharp variation in the temperature, calibration curve needs to be adjusted by applying the temperature correction. Thus the calibration experiments have been done at various temperatures (32°C, 35°C, 38°C, 40°C, 42°C, 45°C, 48°C, 50°C, 52°C, 55°C) and at various flow rates of 2000 lph, 1800 lph, 1500 lph, 1200 lph, 1000 lph, 800 lph, 500 lph, 400 lph, 300 lph, 250 lph. The variation in the flowrate is in the range of 0 - 3.2 m/s. Figure 2.6A and 2.6B

show the plot of calibration curves with a velocity, temperature and voltage as a calibration axis.

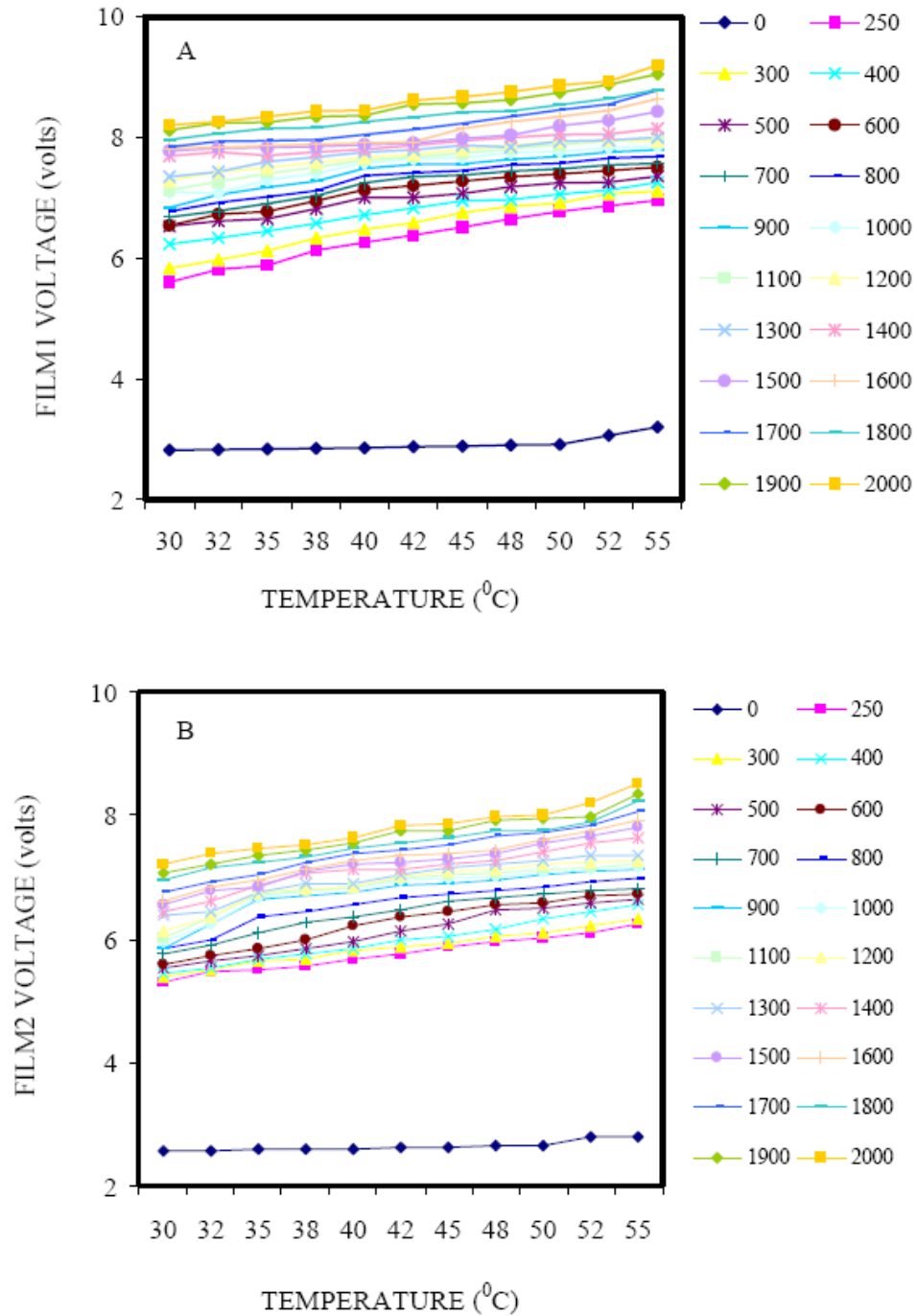


Figure 2.6: Calibration curves for both the films (A) for film 1 (B) for film 2

2.1.3.2. *Velocity calculation*

The voltage data obtained from the HFA is subjected to In-House code, where voltage-time series has been converted into velocity-time series using calibration curve. For dual probe with X-type the decomposition into velocity components for U and V has been done from the calibrated velocities of two films U_{cal1} and U_{cal2} obtained from their respective film voltages E_1 and E_2 respectively. The calibrated velocities together with the yaw coefficients k_1 and k_2 are used to calculate the velocity components U and V in the probe coordinate system. The yaw coefficients for the two sensors are manufacturer's default values. The velocities U_1 and U_2 in the wire-coordinate system defined by the sensors can be calculated as:

$$k_1^2 U_1^2 + U_2^2 = \frac{1}{2}(1+k_1^2)U_{cal1}^2 \quad (2.8)$$

$$U_1^2 + k_2^2 U_2^2 = \frac{1}{2}(1+k_2^2)U_{cal2}^2 \quad (2.9)$$

which gives:

$$U_1 = \frac{\sqrt{2}}{2} \sqrt{(1+k_2^2)U_{cal2}^2 - k_2^2 U_{cal1}^2} \quad (2.10)$$

$$U_2 = \frac{\sqrt{2}}{2} \sqrt{(1+k_1^2)U_{cal1}^2 - k_1^2 U_{cal2}^2} \quad (2.11)$$

Thus U and V can be obtained as

$$U = \frac{\sqrt{2}}{2} U_1 + \frac{\sqrt{2}}{2} U_2 \quad (2.12)$$

$$V = \frac{\sqrt{2}}{2} U_1 - \frac{\sqrt{2}}{2} U_2 \quad (2.13)$$

The velocity-time series after decomposition has been subjected to eddy identification strategy to study the turbulence characteristics of the flow. The eddy identification strategy determines number of eddies, characteristic eddy energy and diffusivity coefficient. Applying analogies of heat and mass transfer theories, the average heat transfer coefficient has been identified.

2.1.3.3. Eddy identification strategy

In this strategy, it is hypothesized that eddies are a group of fluid elements, which have the same hydrodynamic properties restricted to its spatial location at a particular instant. For the identification of eddies, Luk and Lee (1986) approach is adopted. Instantaneous velocity-time data at various spatial locations is subjected to the analysis and following assumptions are made while processing the data. Whenever a single eddy is passing through the measurement point, it maintains its existence till it passes completely. In other words, no breakage of an eddy takes place while it is present at the measurement point. Very large eddies (generally of the order of the inner cylinder diameter) may contain smaller eddies. However every eddy has its own characteristic velocity, life and size and is not affected by its location in the large size eddies. In other words, after isolation of an individual eddy, the large eddy motion has no net effect on the local characteristics of the small eddies. Eddies of same size need not have the same life (time taken by it to cross the measurement point) as it is decided by the surrounding net liquid motion and the eddy shapes. Individual eddy has no effect on the characteristic parameters (viz. size, life, dissipation nature, etc.) of the neighboring eddies in the time scale.

For these eddies, the characteristics/dynamics can be understood by analyzing the instantaneous velocity-time data properly. Whenever an eddy passes through the

measurement point, because of the local turbulence the velocity fluctuates about a mean value (Figure 2.7A).

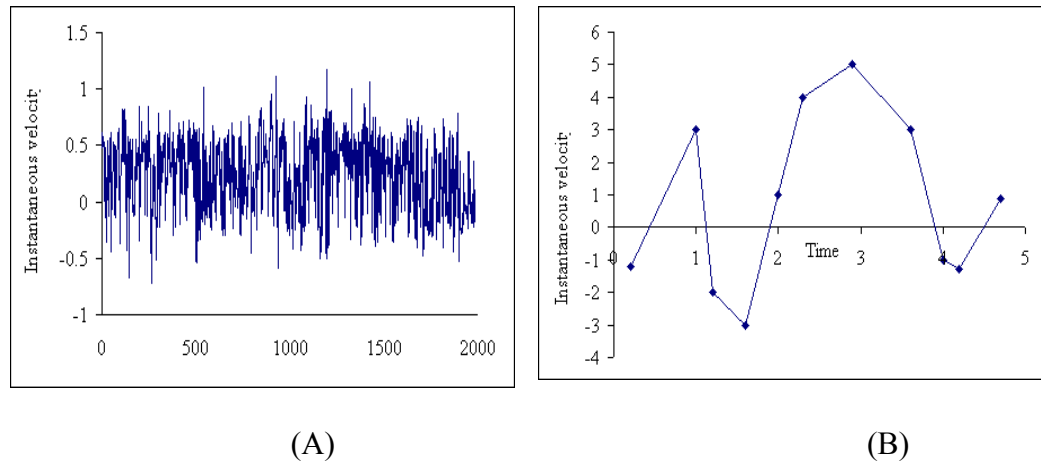


Figure 2.7. Eddy identification strategy (A) Time series (B) Eddy isolation using fluctuating component (enlarged view)

Subtracting the mean value, we get the fluctuating part of the velocity. Fluctuating velocity has positive and negative values and it crosses the time axis at many locations. As mentioned earlier, after subtracting the mean value, the fluctuating part changes from positive to negative or vice versa and it indicates that all the fluid elements that are accounted during the measurement have the same averaged kinetic properties. This can be considered as the existence of an eddy. Therefore, in the plot of fluctuating velocity (u_i') versus time (Figure 2.7B) as the velocity vector crosses the time axis, one eddy ends and the other eddy enters the volume of measurement. It has been proposed that the time gap (Δt) between the two successive crossings represents one eddy. Thus, different eddies show different time gaps (Δt_1 , Δt_2 , Δt_3 , Δt_4 , and Δt_5) which are taken as the eddy life.

For the estimation of characteristic eddy energy, each eddy was divided into ' n ' segments and the eddy energy was calculated using the following equation

$$E_i = \frac{\sum_{i=1}^n \frac{1}{2} u_i^2}{\sum_i i} \quad (2.14)$$

where, u_i is the average velocity of i^{th} segment.

The characteristic eddy velocity was then estimated from the eddy energy as

$$u_i = \sqrt{2E_i} \quad (2.15)$$

Eddy length scale (l_e) was calculated from the eddy lifetime (Δt_i) and characteristic eddy velocity (u_i).

$$l_e = u_i \Delta t_i \quad (2.16)$$

Based on local values of length scale and eddy time, the estimation of the gas-liquid and solid-liquid heat transfer coefficient is calculated using the theories of heat and mass transfer. For above calculations, a MATLAB code was developed. The details of heat and mass transfer theories have been given in chapter 7 in section 7.5.4.

2.2. Laser Doppler Anemometry

Laser Doppler Velocimetry (LDV), also called laser Doppler anemometry (LDA), measures the velocity of a moving object by illuminating it using laser light and measuring the Doppler shift of the light scattered by the moving object. The application of the technique to measure fluid velocity relies on collecting and processing the light scattered by objects such as small particles or bubbles that are assumed to be moving with the flow. The non-invasive nature of the technique and its ability to make accurate velocity measurements with good spatial resolution have led to the widespread use of LDV in industrial applications and fluid mechanics research. Measurements of highly

turbulent flows, flows around stationary as well as moving solid objects as in rotating machinery, very high or very low velocity flows, flows at high temperatures and in other hostile environments, and flows in small spaces are all achieved with LDV. The technique is also used to measure the motion of surfaces. Many details of the technique including some of the early developments of the hardware are provided in the book by Durst et al. (1981).

2.2.1. Previous Work

In recent years, several attempts have been made at extending the use of laser-Doppler anemometry (LDA) to bubbly flows (Ohba et al. 1977; Theofanous & Sullivan, 1982; Lance and Bataille 1991; Kulkarni et al., 2001). LDA gives point velocity components. LDA is used for the calibration of the other flow measuring devices including HFA. But it cannot be used to determine the length scales of the liquid agitation. This cannot be obtained by LDA since it requires simultaneous measurements of the liquid velocity in various locations. Also, whatever the experimental technique, this can hardly be achieved inside the bubble swarm where the bubbles cause any measured signal to be discontinuous. Using laser-Doppler anemometry (LDA), the data rate that can be obtained in the bulk of bubbly flow is still sufficient to estimate energy spectra. LDA has successfully been used very close to the boundaries of bubbly flow, (Mudde et al. 1997).

2.2.2. Equipment

2.2.2.1. Characteristics of LDA

A schematic of LDA is shown in Figure 2.8. Laser Doppler anemometers offer unique advantages in comparison with other fluid flow instrumentation:

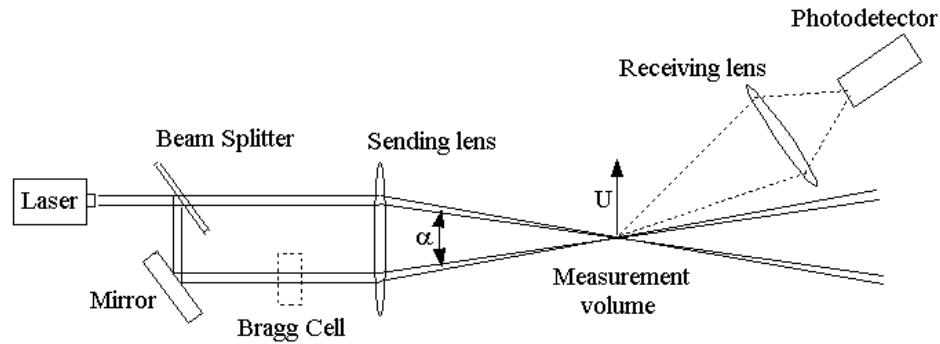


Figure 2.8. Schematic of LDA.

Non-contact optical measurement: Laser anemometers probe the flow with focused laser beams and can sense the velocity without disturbing the flow in the measuring volume. The only necessary conditions are a transparent medium with a suitable concentration of tracer particles (or seeding) and optical access to the flow through windows, or via a submerged optical probe. In the latter case the submerged probe will of course to some extent disturb the flow, but since the measurement take place some distance away from the probe itself, this disturbance can normally be ignored.

No calibration - no drift: The laser anemometer has a unique intrinsic response to fluid velocity - absolute linearity. The measurement is based on the stability and linearity of optical electromagnetic waves, which for most practical purposes can be considered unaffected by other physical parameters such as temperature and pressure.

Well-defined directional response: The quantity measured by the laser Doppler method is the projection of the velocity vector on the measuring direction defined by the optical system (a true cosine response). The angular response is thus unambiguously defined.

High spatial and temporal resolution: The optics of the laser anemometer is able to define a very small measuring volume and thus provides good spatial resolution and allows local measurement of Eulerian velocity. The small measuring volume in combination with fast signal processing electronics also permits high bandwidth, time-resolved measurements of fluctuating velocities, providing excellent temporal resolution.

Usually the temporal resolution is limited by the concentration of seeding rather than the measuring equipment itself.

Multi-component bi-directional measurements: Combinations of laser anemometer systems with component separation based on color, polarization or frequency shift allow one-, two- or three component LDA systems to be put together based on common optical modules. Acousto-optical frequency shift allows measurement of reversing flow velocities.

These properties of laser anemometers certainly constitute a very attractive description of a measuring instrument. The optimization of the performance of a system with respect to certain parameters may influence other performance characteristics negatively. As a matter of fact, some of the compromise decisions which have to be made when selecting and setting up a laser anemometer system can be traced back to the famous uncertainty principle of wave theory, which describes the impossibility of attaining complete information of both spatial and temporal location of a wave train simultaneously.

2.2.2.2. Principles

Laser beam: The special properties of the gas laser, making it so well suited for the measurement of many mechanical properties, are the spatial and temporal coherence. At all cross sections along the laser beam, the intensity has a Gaussian distribution, and the width of the beam is usually defined by the edge-intensity being $1/e^2=13\%$ of the core-intensity. At one point the cross section attains its smallest value, and the laser beam is uniquely described by the size and position of this so-called beam waist.

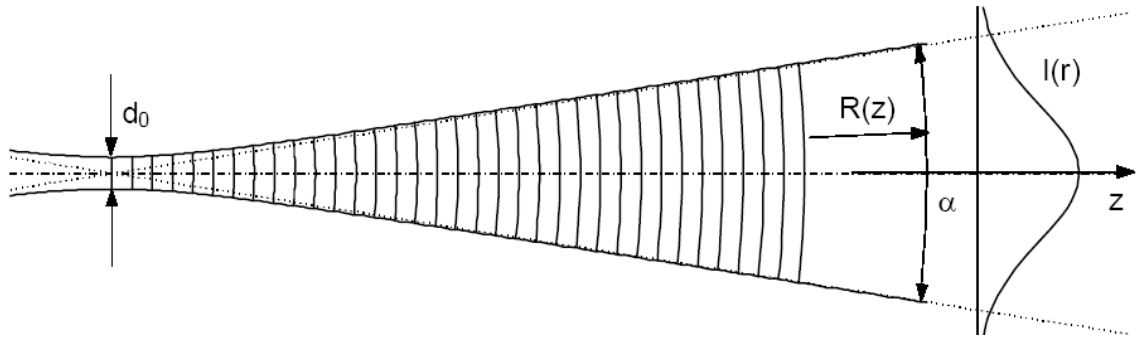


Figure 2.9. Laser beam with Gaussian intensity distribution

With a known wavelength λ of the laser light, the laser beam is uniquely described by the size d_0 and position of the beam waist as shown in Figure 2.9. With z describing the distance from the beam waist, the following formulae apply:

$$\text{Beam divergence: } \alpha = \frac{4\lambda}{\pi d_0} \quad (2.17)$$

$$\text{Beam diameter: } d(z) = d_0 \sqrt{1 + \left(\frac{4\lambda z}{\pi d_0^2}\right)^2} \rightarrow \alpha z, z \rightarrow \infty \quad (2.2) \text{ Wave front radius:}$$

$$R(z) = z \left[1 + \left(\frac{\pi d_0^2}{4\lambda z}\right)^2 \right] \quad (2.18)$$

$$\begin{aligned} R(z) &\rightarrow \infty, z \rightarrow 0 \\ R(z) &\rightarrow z, z \rightarrow \infty \end{aligned} \quad (2.19)$$

Doppler effect: As indicated by the name Laser Doppler Anemometry, the Doppler effect plays an important role in LDA, since the technique is based on Doppler shift of the light reflected (and/or refracted) from a moving seeding particle.

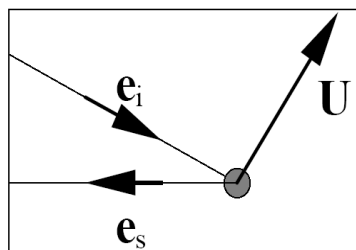


Figure 2.10. Light scattering from a moving seeding particle.

The principle is illustrated in Figure 2.10 above, where the vector U represent the particle velocity, and the unit vectors e_i and e_s describe the direction of incoming and scattered light respectively. According to the Lorenz-Mie scattering theory, the light is scattered in all directions at once, but we consider only the light reflected in the direction of the receiver. The incoming light has the velocity c and the frequency f_i , but due to the particle movement, the seeding particle “sees” a different frequency f_p , which is scattered towards the receiver. From the receiver’s point of view, the seeding particle act as a moving transmitter and the movement introduce additional Doppler-shift in the frequency of the light reaching the receiver. Using Doppler-theory, the frequency of the light reaching the receiver can be calculated as:

$$f_s = f_i \frac{1 - e_i(U/c)}{1 - e_s(U/c)} \quad (2.20)$$

Even for supersonic flows the seeding particle velocity $|U|$ is much lower than the speed of light, meaning that $|U/c| \ll 1$. Taking advantage of this, the above expression can be linearized to:

$$f_s \cong f_i \left[1 + \frac{U}{c} (e_s - e_i) \right] = f_i + \frac{f_i}{c} U (e_s - e_i) = f_i + \Delta f \quad (2.21)$$

With the particle velocity U being the only unknown parameter, in principle the particle velocity can be determined from measurements of the Doppler shift Δf .

Intersecting beams: In practice this frequency change can only be measured directly for very high particle velocities (Fabry - Perot interferometer). More commonly the light scattered from two intersecting laser beams is mixed as illustrated in Figure 2.11.

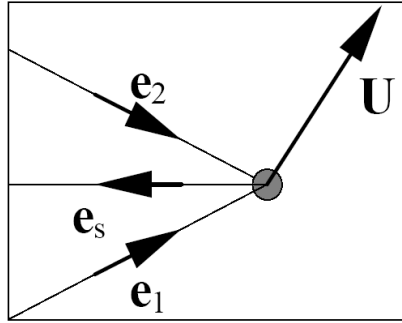


Figure 2.11. Scattering of two incoming laser beams.

In this way both incoming laser beams are scattered towards the receiver, but with slightly different frequencies due to the different angles of the two laser beams.

$$\begin{aligned} f_{s,1} &= f_1 \left[1 + \frac{U}{c} (e_s - e_1) \right] \\ f_{s,2} &= f_2 \left[1 + \frac{U}{c} (e_s - e_2) \right] \end{aligned} \quad (2.22)$$

Doppler frequency: When two wave trains of slightly different frequency are superimposed, we get the well-known phenomenon of a beat frequency due to the two waves intermittently interfering with each other constructively and destructively. The beat frequency correspond to the difference between the two wave-frequencies, and since the two incoming waves originate from the same laser, they also have the same frequency, $f_1=f_2=f_I$, where subscript I refer to incident light:

$$f_D = f_{s,2} - f_{s,1} = f_I \left[\frac{U}{c} (e_1 - e_2) \right] \quad (2.23)$$

$$f_D = \frac{f_I}{c} [|e_1 - e_2| |U| \cos \phi] = \frac{2 \sin(\theta/2)}{\lambda} u_x \quad (2.24)$$

Where θ is the angle between the incoming laser beams and ϕ is the angle between the velocity vector U and the direction of measurement. The unit vector e_s has dropped out of the calculation, implying that the position of the receiver has no direct influence on

the frequency measured. (According to the Lorenz-Mie light scattering theory, the position of the receiver will however have considerable influence on signal strength). The beat-frequency, also called the Doppler-frequency f_D , is much lower than the frequency of the light itself, and it can be measured as fluctuations in the intensity of the light reflected from the seeding particle. As shown in Eq. (2.24), the Doppler-frequency is directly proportional to the x-component of the particle velocity, and the velocity can thus be calculated directly from f_D :

$$u_x = \frac{\lambda}{2 \sin(\theta/2)} f_D \quad (2.25)$$

2.2.2.3. *The Fringe model*

While there are several ways to describe a dual-beam system the description based on a fringe model is, perhaps the easiest. For simplicity, the diameter and the intensity of both the beams are assumed to be the same. After they pass through the transmitting lens, the diameter of each beam continuously decreases to a minimum value (waist) at the focal point of the lens, and then increases again. Thus, the beam waists cross at the focal point of the lens. When the two laser beams intersect, the wave fronts in the beams interfere with one another creating a fringe pattern (Durst and Stevenson, 1976). In this pattern, assuming equal intensity beams and other needed quality of the beams, the light intensity varies from zero (dark fringe) to a maximum (bright fringe) and the fringes are equally spaced. The particles in the flow passing through the intersection region (measuring region) scatter light in all directions and are the signal source for velocity measurements. A receiver system, including a receiving lens (to collimate the scattered light collected), a focusing lens and a receiver, is used to collect the scattered light.

Interference fringes: When two coherent laser beams intersect, they will interfere in the volume of intersection. If the beams intersect in their respective beam waists, the wave fronts are approximately plane, and consequently the interference produce parallel planes of light and darkness as shown in Figure 2.12.

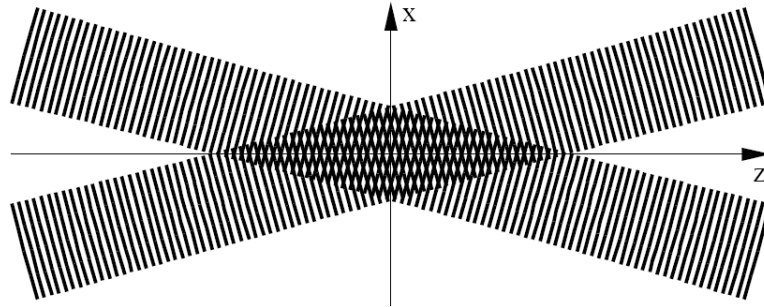


Figure 2.12. Fringes form where two coherent laser beams cross.

The interference planes are known as fringes, and the distance δ_f between them depend on the wavelength and the angle between the incident beams:

$$\delta_f = \frac{\lambda}{2 \sin(\theta/2)} \quad (2.26)$$

The fringes are oriented normal to the x-axis, so the intensity of light reflected from a particle moving through the measuring volume will vary with a frequency proportional to the x-component u_x of the particle velocity:

$$f_D = \frac{u_x}{\delta_f} = \frac{2 \sin(\theta/2)}{\lambda} u_x \quad (2.27)$$

Beam alignment: If the two laser beams do not intersect in the beam waists but elsewhere in the beams, the wave fronts will be curved rather than plane, and as a result the fringe spacing will not be constant but depend on the position within the intersection volume. As a consequence the measured Doppler frequency will also depend on the particle position, and as such it will no longer be directly proportional to particle velocity. If the beams are badly misaligned, you will probably not be able to get results at all, but if the

beams are just slightly misaligned, the errors will be small, and you may not be aware of them.

Measuring volume: Measurements take place in the intersection between the two incident laser beams, and the measuring volume is defined as the volume within which the modulation depth is higher than e^{-2} times the peak core value. Due to the Gaussian intensity distribution in the beams the measuring volume is an ellipsoid as indicated in Figure 2.13.

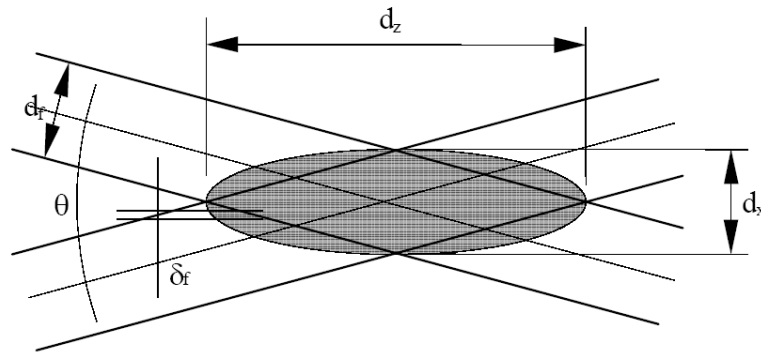


Figure 2.13. Measuring volume

The size of the measuring volume can be calculated from the beam waist diameter d_f of the focused laser beams and the angle θ between them:

$$d_x = \frac{d_f}{\cos(\theta/2)}, d_y = d_f, d_z = \frac{d_f}{\sin(\theta/2)} \quad (2.28)$$

where d_x is the height, d_y the width and d_z the length of the measuring volume. Since beam intersection angles are usually small, d_x and d_y are often almost equal, and are sometimes referred to as the diameter of the measuring volume. A very small seeding particle in the outskirts of the measuring volume may not reflect sufficient light to be detected. On the other hand a very large seeding particle may reflect so much light, that it is detected even if technically it is slightly outside the measuring volume as defined above. Other parameters such as system gain and threshold level influence the

measurements similarly. From the height d_x of the measuring volume and the fringe spacing δ_f , the total number of fringes can be calculated:

$$N_f = \frac{2d_f}{\lambda} \tan(\theta/2) \quad (2.29)$$

This number of fringes applies for a seeding particle moving straight through the center of the measuring volume along the x-axis. If the particle passes through the outskirts of the measuring volume, it will pass fewer fringes, and consequently there will be fewer periods in the recorded signal from which to estimate the Doppler frequency. Sufficiently high number of fringes in the measuring volume are to be ensured. The key issue here is the number of periods produced in the oscillating intensity of reflected light. Older LDA-processors often require a minimum of 8 periods to validate the burst, while modern processors can estimate particle velocity from as little as one period. The accuracy will however improve with more periods. Frequency shift will cause the fringe pattern to “roll” through the measuring volume, increasing or decreasing the number of fringes passed by a seeding particle. If the fringes move towards the movement of the seeding particle, the effective number of fringe-passings will increase, and if the fringes move away from the particle, it will decrease, corresponding to an increase or decrease in the number of periods in the recorded signal.

2.2.2.1. Frequency shift

A drawback of the LDA-technique described so far is that negative velocities $u_x < 0$ according to the Eq. (2.27), will produce negative frequencies $f_D < 0$, but the receiver cannot distinguish between positive and negative frequencies, and as such, there will be a directional ambiguity in the measured velocities.

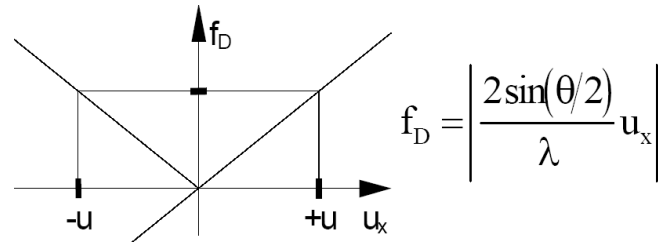


Figure 2.14. Directional ambiguity without frequency shift.

Directional ambiguity without frequency shift: To handle this problem, a Bragg cell is introduced in the path of one of the laser beams. The Bragg cell shown in Figure 2.15 is a slab of glass. On one side an electro-mechanical transducer driven by an oscillator produces an acoustic wave propagating through the slab generating a periodic moving pattern of high and low density. The opposite side of the slab is shaped to minimize reflection of the acoustic wave and is attached to a material absorbing the acoustic energy.

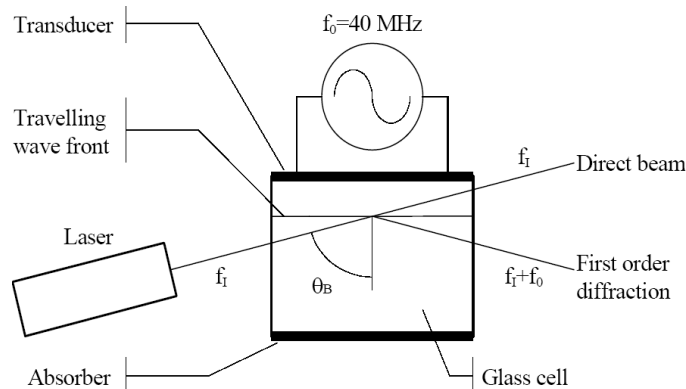


Figure 2.15. Bragg cell.

The incident light beam hits a series of traveling wave fronts which act as a thick diffraction grating. Interference of the light scattered by each acoustic wave front causes intensity maxima to be emitted in a series of directions. By adjusting the acoustic signal intensity and the tilt angle θ_B of the Bragg cell, the intensity balance between the direct beam and the first order of diffraction can be adjusted. In modern LDA-equipment this is exploited, using the Bragg cell itself as beam splitter. Not only does this eliminate the need for a separate beam splitter, but it also improves the overall efficiency of the light

transmitting optics, since more than 90% of the lasing energy can be made to reach the measuring volume, effectively increasing signal strength. The Bragg cell adds a fixed frequency shift f_0 to the diffracted beam, and including this in the Eq. (2.27) yields:

$$f_D \cong f_0 + \frac{2 \sin(\theta/2)}{\lambda} u_x \quad (2.30)$$

As long as the particle velocity does not introduce a negative frequency shift numerically larger than f_0 , the Bragg cell will thus ensure a measurable positive Doppler frequency f_D .

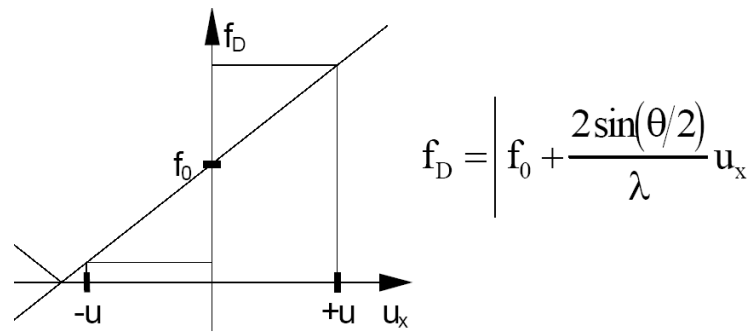


Figure 2.16. Resolving directional ambiguity using frequency shift.

In other words the frequency shift f_0 allows measurement of velocities down to the following without any directional ambiguity:

$$u_x > -\frac{\lambda f_0}{2 \sin(\theta/2)} \quad (2.31)$$

Introducing a fixed frequency shift f_0 in one of the beams will cause the fringe pattern itself to roll along the x-axis with constant velocity. This means that even a stationary particle will scatter light with an intensity pulsating at a frequency equal to f_0 . A seeding particle moving towards the fringes will produce a Doppler burst of higher frequency, while particles moving in the same direction as the fringes will produce a lower frequency. The lower velocity limit in Eq. (2.31) correspond to a seeding particle moving with exactly the same speed as the fringes. The key issue here is the number of fringes crossed by the seeding particle while it is in the measuring volume. If t_R is the particle's

residence time within the measuring volume, and f_D is the measurable Doppler frequency the fringe count N_f is simply calculated as:

$$N_f = f_D \cdot t_R \quad (2.32)$$

Fringe tilt: In principle the frequency shift will also tilt the fringes slightly, so they are no longer exactly normal to the x-axis, but in practice this can be ignored, since the typical frequency shift of 40 Mhz is several orders of magnitude smaller than the frequency of light. This means that the difference in wavelength between the shifted and the unshifted beam will also be several orders of magnitude smaller than the laser wavelength itself, and consequently the tilt angle of the fringes get negligible.

2.2.2.2. Signals

The primary result of a laser anemometer measurement is a current pulse from the photodetector. This current contains the frequency information relating to the velocity to be measured. The photocurrent also contains noise. The primary source of noise is the photodetection shot noise, which is a fundamental property of the detection process. The interaction between the optical field and the photo-sensitive material is a quantum process, which unavoidably impresses a certain amount of fluctuation on the mean photocurrent. In addition there is mean photocurrent and shot noise from undesired light reaching the photodetector. Much of the design effort for the optical system is aimed at reducing the amount of unwanted reflected laser light or ambient light reaching the detector. Further noise sources are secondary electron noise from the photomultiplier dynode chain and preamplifier thermal noise in the signal processor. A laser anemometer is most advantageously operated under such circumstances that the shot noise in the signal is the predominant noise source. This shot noise limited performance can be obtained by proper selection of laser power, seeding particle size and optical system

parameters. In addition, noise should be minimized by selecting only the minimum bandwidth needed for measuring the desired velocity range by setting low-pass and high-pass filters in the signal processor input. Very important for the quality of the signal, and the performance of the signal processor, is the number of seeding particles present simultaneously in the measuring volume. If on average much less than one particle is present in the volume, we speak of a burst type Doppler signal. A typical Doppler burst signal is shown in Figure 2.17 and Figure 2.18 shows the filtered signal which is actually input to the signal processor. The DC-part which was removed by the high-pass filter is known as the Doppler Pedestal, and it is often used as a trigger-signal, which starts sampling of an assumed burst signal. The envelope of the Doppler modulated current reflects the Gaussian intensity distribution in the measuring volume.

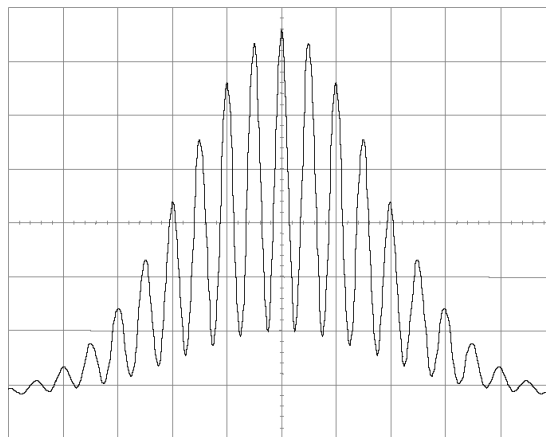


Figure 2.17. Doppler burst.

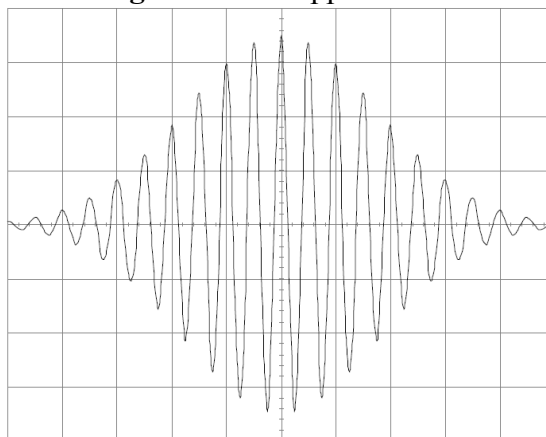


Figure 2.18. Filtered signal with the DC-component removed

If more particles are present in the measuring volume simultaneously, we speak of a multi-particle signal. The detector current is the sum of the current bursts from each individual particle within the illuminated region. Since the particles are located randomly in space, the individual current contributions are added with random phases, and the resulting Doppler signal envelope and phase will fluctuate. Most LDA-processors are designed for single-particle bursts, and with a multi-particle signal, they will normally estimate the velocity as a weighted average of the particles within the measuring volume. You should be aware however, that the random phase fluctuations of the multi-particle LDA signal add a phase noise to the detected Doppler frequency, which is very difficult to remove.

2.2.2.3. Seeding

In LDA it is not actually the velocity of the flow that is measured, but the velocity of particles suspended in the flow. In this respect these seeding particles can be considered to be the actual velocity probes, and seeding considerations are thus important in LDA. The particles must be small enough to track the flow accurately, yet large enough to scatter sufficient light for the photodetector to be able to detect the Doppler frequency. Ideally, the particles should also be neutrally buoyant in the fluid, that is they should have approximately the same density as the fluid itself, but in many experiments this is a secondary consideration. Durst et al. (1981) state the following desired properties of seeding particles: Particles whose motion is used to represent that of a fluid should be:

- Able to follow the flow.
- Good light scatterers.
- Conveniently generated.
- Cheap.

- Non-toxic, non-corrosive, non-abrasive.
- Non-volatile, or slow to evaporate.
- Chemically inactive.
- Clean.

Seeding as flow field tracers: In general the motion of particles suspended in a fluid is affected by

- Particle shape.
- Particle size.
- Relative density of particle and fluid.
- Concentration of particles in the fluid.
- Body forces.

The shape of the seeding particles affect the drag exerted on the particle by the surrounding fluid, and the size of the particles along with their relative density influence their response to velocity changes of the surrounding fluid. The concentration of particles affects particle motion through interaction between different particles. In practice the concentrations used are normally so low, that particle interaction can be neglected. Also body forces, such as gravity, can normally be ignored, except in very slow flows, where buoyancy of the seeding particles may be an issue. Also in experiments including for example electrostatic fields, body forces may be of importance, but in such cases, they will probably be part of the experiment, and as such they cannot really be considered a disturbance.

The choice of seeding depends on a number of parameters. Primarily the seeding material should be chosen considering the flow that is to be measured, and the laser available. In general seeding particles should be chosen as large as possible in order to scatter the most light, but the particle size is limited, since too large particles will not

track the flow properly. In general the maximum allowable particle size decrease with increasing flow velocity, turbulence and velocity gradients. Ideally the seeding material should also be chosen, so the seeding particles are neutrally buoyant in the carrying fluid, but in many flows this is a secondary consideration. Finally it should be considered how the flow is seeded. Water flows are often implemented using water in a closed circuit, and here commercial seeding particles such as latex beads or pine pollen can easily be added. Air flows on the other hand are often not recirculated, and thus require the seeding to be generated at the inlet and disposed of at the outlet. The natural concentration of very small particles is often much greater than that of particles in the useful range. In some cases, most often when measuring in liquids, this causes an undesirable shot noise level due to the incoherent signals from the many small particles. In general, it is strongly recommended, whenever possible, to control the size and concentration of the seeding particles by filtering the fluid and subsequently adding seeding particles of known size.

2.2.2.4. Signal processing

Figure 2.19 shows the output of a photo detector as a function of time. The sudden increase in the amplitude of the signal indicates the passage of the particle through the measuring volume and the subsequent increase in the scattered light intensity. Because of the sudden increase in amplitude the signal is often referred to as a signal burst. The impact of the Gaussian light intensity distribution in the measuring region can be seen from the presence of the pedestal component (Figure 2.19B) of the signal. In a properly designed optical system, the maximum frequency associated with the pedestal component is orders of magnitude lower than the Doppler frequency. Contributions due to reflections, stray light, and electronic noise appear as high-

frequency noise. Generally, both pedestal and high-frequency noises are filtered out using band pass filters. The resulting cyclic signal has zero mean and varying amplitude.

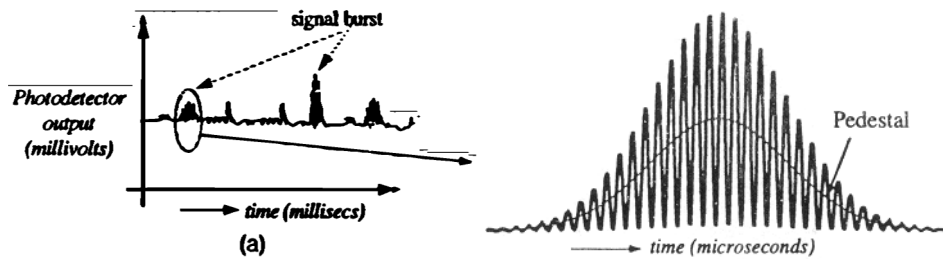


Figure 2.19. Nature of the signal burst (A) Time history. (B) Doppler burst

The primary task of the signal processor is to extract the frequency information from the burst signal, generated by a particle passing through the measuring volume, and provide an analog or digital output proportional to the frequency of the signal. It should be noted that the burst signals are generally noisy, may only have a few cycles, have amplitudes varying within a burst arrive at random times, have peak amplitude of one burst different from that of the next, and can be over 100 MHz in frequency. Hence, adapting existing or finding new frequency measuring techniques suitable to these signal characteristics, is key to making accurate velocity measurements. Since burst signals exist only when the particle passes through the measuring volume, the processing approach can benefit from having a provision to separate or distinguish the signal burst from the background noise.

A variety of techniques has been used for processing Doppler signals. Signal processors have been based on spectrum analysis, frequency tracking, photon correlation, frequency counting, Fourier transform, and autocorrelation principles. All but the first three are designed to make measurements on individual frequency bursts. The evolution of the signal processing techniques shows the improvement in their ability to handle

more difficult measuring situations (generally meaning noisier signals), give more accurate measurements, and provide increased processing speed.

The traditional instrument to measure signal frequency is a spectrum analyzer. A traditional spectrum analyzer gives a time-averaged spectrum of the input signal. Hence, the information obtained from this type of signal processor will be the mean velocity and an indication of the turbulence (spectral width). The need to measure individual particle velocities and obtain the time history and other properties of the flow have eliminated the use of spectrum analyzers (Adrian, 1983).

The "tracker" can be thought of as a fixed bandwidth filter that "tracked" the Doppler frequency as the fluid velocity changed. This technique worked quite well at modest velocities and where the concentration of scattering centers was high enough to provide an essentially continuous signal, so that the velocity variation in the flow could be "tracked" However, too frequently these conditions could not be met in the flows of most interest (Adrian, 1983).

In most measuring situations, after the appropriate low-pass filter, the scattered light level is high enough that the individual photon pulses "pile up" to create a continuous photo detector output (Adrian, 1983; Mayo, 1978). When the scattered light level is very low, the photo detector output would reveal the presence of the individual photon pulses. By correlating the actual photon pulses from a wide-bandwidth photo detector, the photon correlator was designed to work in situations where the attainable signal intensity was very low [low SNR (signal to noise ratio)]. However, as normally used it could not provide the velocity of individual particles but only the averaged quantities such as mean and turbulence intensity.

The "counter" type processor was developed next, and basically measured the time for a certain number of cycles (typically 8) of the Doppler signal. This measured the velocity of individual particles and worked very well on signals with a good SNR. But it depended on the careful setting of amplifier gain and, especially, threshold levels to discriminate between background noise and burst signals. Even then, erroneous output could occur with noisy input signals. While these erroneous readings were often so far from the true value that they can be easily rejected, it did make counters difficult to use reliably on signals with poor SNR. Even so, counters were the processors of choice for many years and excellent measurements have been obtained by them (Karlsson and Johansson, 1998).

Although counter processors provide good velocity measurements, the reliance on user skill, difficulty in handling low SNR signals, possibility of getting erroneous measurements, the inclination to ignore signals from small particles, and the desire to make measurements close to surfaces and in complex flows led to the need for a better signal processor. Recent developments in high-speed digital signal processing now permit the use of these techniques to extract the frequency from individual Doppler bursts fast enough to actually follow the flow when the seeding concentration is adequate. By digitizing the incoming signal and using the Fourier transform (Ibrahim et al., 1990) or autocorrelation algorithms, these new digital processors can work with lower SNR signals (than counters), while generally avoiding erroneous data outputs. While instruments using these techniques are certainly not new, standard instruments were not designed to make rapid individual measurements on the noisy, short-duration burst signals with varying amplitudes that are typical of Doppler bursts.

Besides optimizing the sample rate, the burst detector information is also used to focus on and process the middle portion of the burst where the SNR is maximum. These

optimization schemes, followed by digital signal processing, provide an accurate digital output that is proportional to the signal frequency and hence the fluid velocity.

2.2.3. LDA Data Analysis

In turbulent two-phase flows as in a bubble column, the passage of the bubbles at a particular location is a discontinuous process and occurs intermittently. Intermittency is related to turbulence and its study is therefore of importance. It particularly helps in identifying events when gradients in variables (e.g., velocity) become large, which in turn causes flow properties to change. For the bubble column, it may be visualized that the passage of bubbles through a location in the column results in bursts of energy termed as singularities.

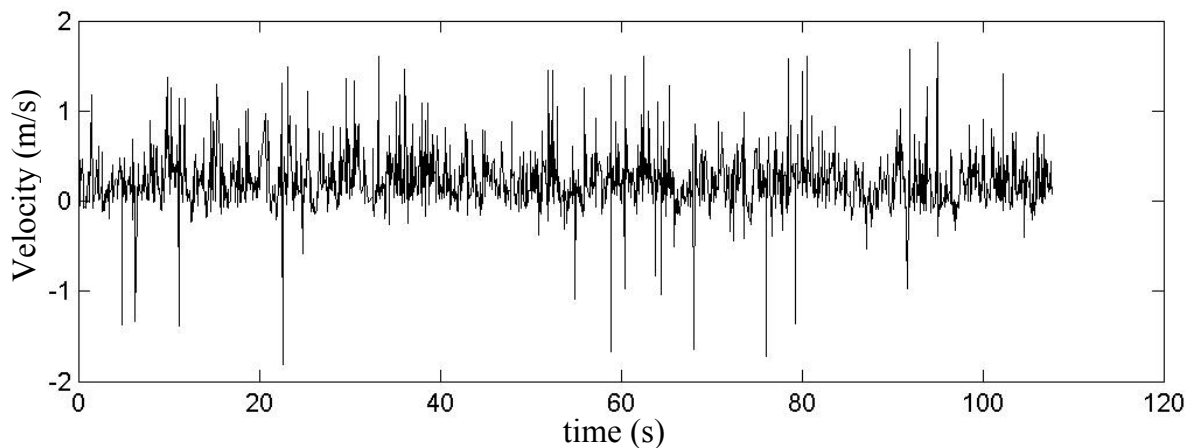


Figure 2.20. Velocity-time data available from LDA (At H/D =2.2, centerline)

It seems possible not only to identify these singularities but also when they occur from the properties of the scale wise wavelet transformed reconstruction $[x_j(i)]$, by evaluating a quantity termed as the local intermittency measure (LIM). The LIM has been used earlier in studies related to characterizing intermittency in turbulent systems and is seen to provide valuable insight about the system behavior. In the present work, we show how the LIM may be effectively used to study the intermittent features in the

bubble column. The velocity at any location in turbulent flow exhibits intermittent spikes whose amplitude depends on the changing magnitude of velocity in the vicinity of the measurement volume. For bubble columns, the interest is to identify the sharp gradients in velocity, which arise due to passage of bubbles. We identify these events by calculating the $LIM_j(i)$ over all wavelet scales ($j=0; 2; \dots; p - 1$) given by:

$$LIM_j(i) = \frac{|\hat{x}_j(i)|^2}{\langle |\hat{x}_j(i)|^2 \rangle}, \quad i = 1, 2, 3, \dots, N \quad (2.33)$$

representing the deviation in local energy distribution for a scale j and time index i from the average ($\langle \rangle$) in time for the particular scale j . Thus, a graphical representation of $LIM_j(i)$ is a good indicator of the local intermittency in time because its magnitude effectively represents the local energy changes that occur in each scale. In the present study, an analysis of the $LIM_j(i)$ is seen to effectively detect bubble passage from local velocity measurements for the multi-phase bubble column. Figure 2.20 shows the sample time series from LDA. Figure 2.21 and 2.22 show the scalewise reconstruction using wavelet transform and the LIM plots for the same time series shown in Figure 2.20.

2.2.3.1. Interpolation of LDA data

Since the data obtained from LDA are not equispaced in time, interpolation of the time series was done using Piecewise Cubic Polynomials. The time interval for interpolation was calculated as:

$$\Delta t_{int} = \frac{1}{m} \times \left\{ \frac{t(n)}{n} \right\} \quad (2.34)$$

where n = number of elements in time series, and m is a factor dependent on fraction of the average time interval desired, e.g. $m=2$ will set time interval for interpolation to half

of $\frac{t(n)}{n}$, hence number of elements in interpolated series will be double the number of

elements in original series.

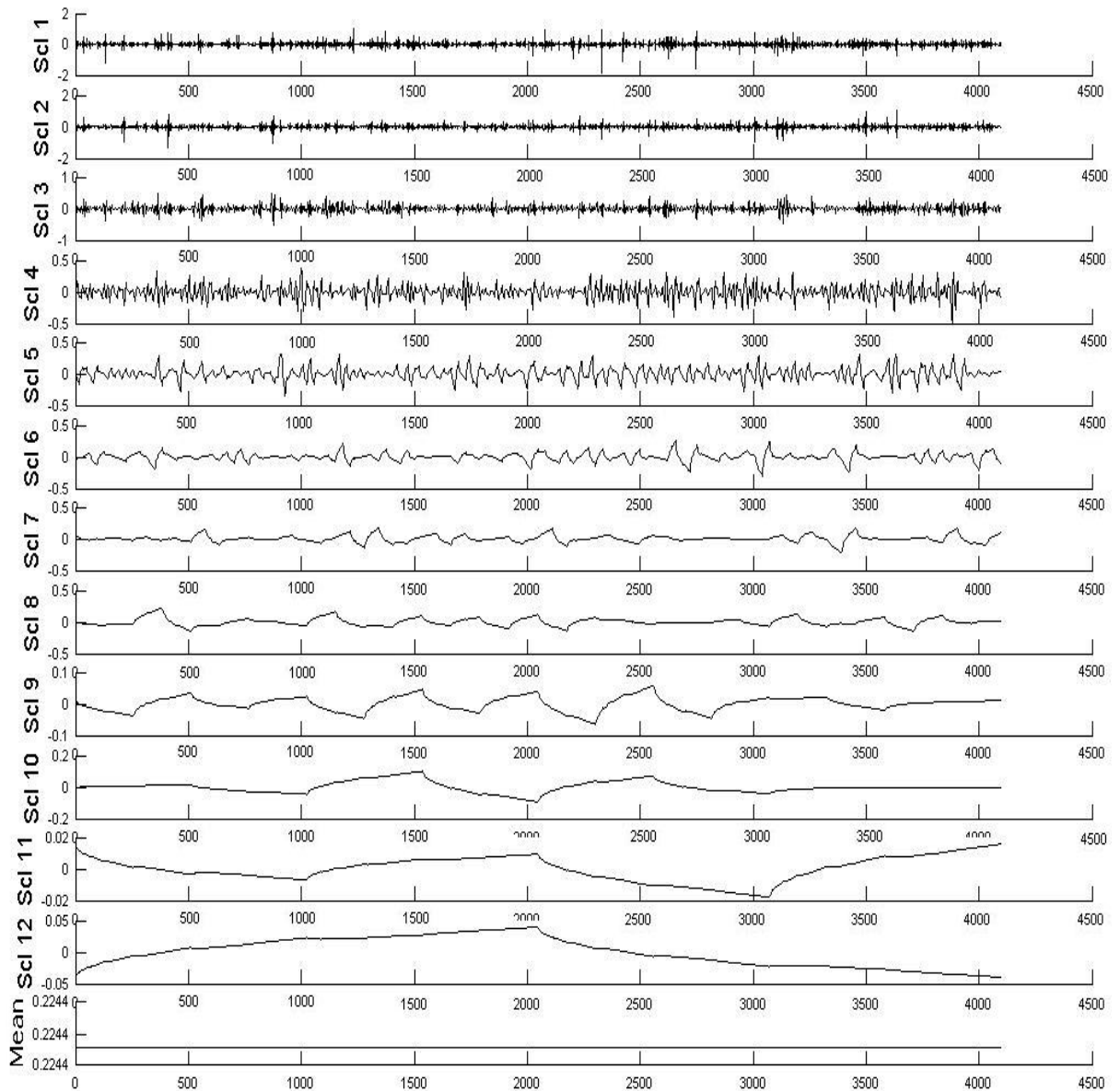


Figure 2.21. Scale wise decomposition obtained from wavelet transform

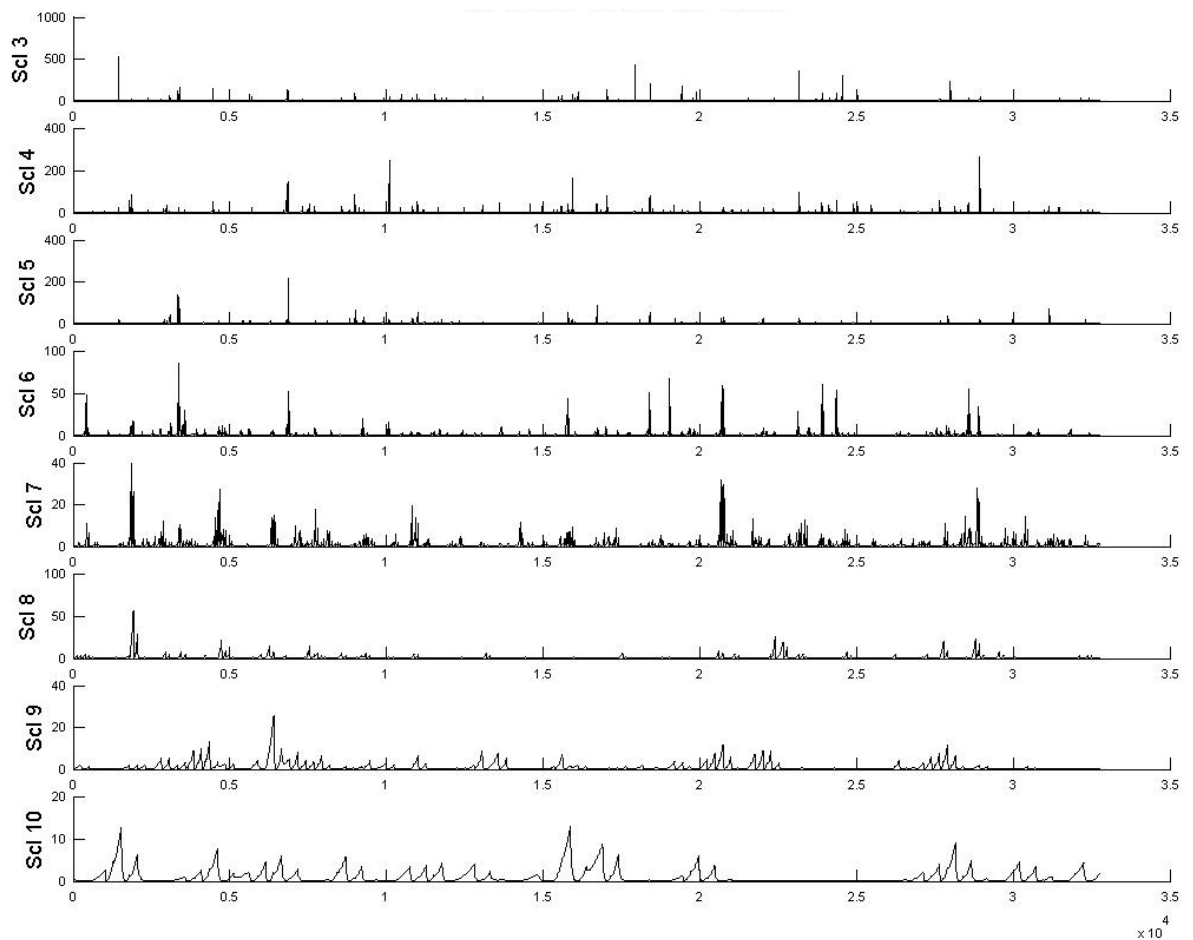


Figure 2.22. LIM of velocity time series

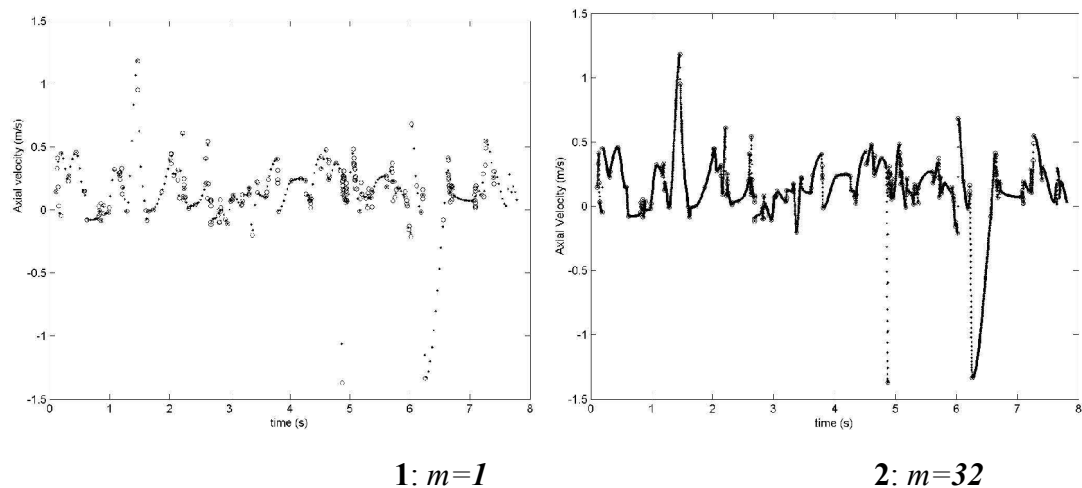


Figure 2.23. Interpolated LDA velocity time series with different intervals

Effect of interpolation on power spectra

The interpolated LDA data series are displayed in Figure 2.23. In order to observe the effect of interpolation of the time series, wavelet power spectrum of the interpolated velocity series was constructed.

Power for j^{th} scale is calculated from wavelet coefficients $c_w(i,j)$ as:

$$P(j) = \sum_{i=1}^n c_w(i,j)^2$$

Scale j can be related to corresponding frequency as:

$$F_a = \frac{\Delta t_{int} \cdot F_c}{j}$$

Where: Δt_{int} represents the time interval between successive points in time series and F_c is the center frequency corresponding to the particular wavelet chosen.

Based on above equations, the power spectra for wavelet transform of original signal (unequispaced i.e. without interpolation) and interpolated series is plotted in Figure 2.24.

Wavelet transform of interpolated data

We require the scalewise reconstruction from wavelet transform at unequispaced time data. One way to overcome this difficulty is to follow the following steps:

1. Interpolate the velocity time series to generate equispaced data
2. Take wavelet transform of the equispaced data
3. Interpolate scale wise reconstructed signal to generate unequispaced scale wise information
4. Reconstruct the velocity signal from unequispaced scale wise data
5. Compare the two series for the errors in the reconstructed series

Figure 2.25 to 2.28 show the outcome of above procedure.

DEVELOPMENT OF EXPERIMENTAL TECHNIQUES AND CFD SIMULATIONS OF MULTIPHASE DISPERSIONS

Energy lost from the signal in above procedure is plotted in Figure 2.29, and listed below:

Interp. factor	1	2	4	8	16	32	64	128
Dt	0.026242	0.013121	0.006561	0.00328	0.00164	0.00082	0.00041	0.000205
ori_energy	464.4526	464.4526	464.4526	464.4526	464.4526	464.4526	464.4526	464.4526
est_enr	418.486	430.7968	457.0485	455.7218	457.9069	460.3196	462.7321	464.123
Err	45.96665	33.65578	7.404066	8.7308	6.545752	4.133046	1.720529	0.329579
%	9.896951	7.246332	1.594149	1.879804	1.409348	0.889875	0.370442	0.070961

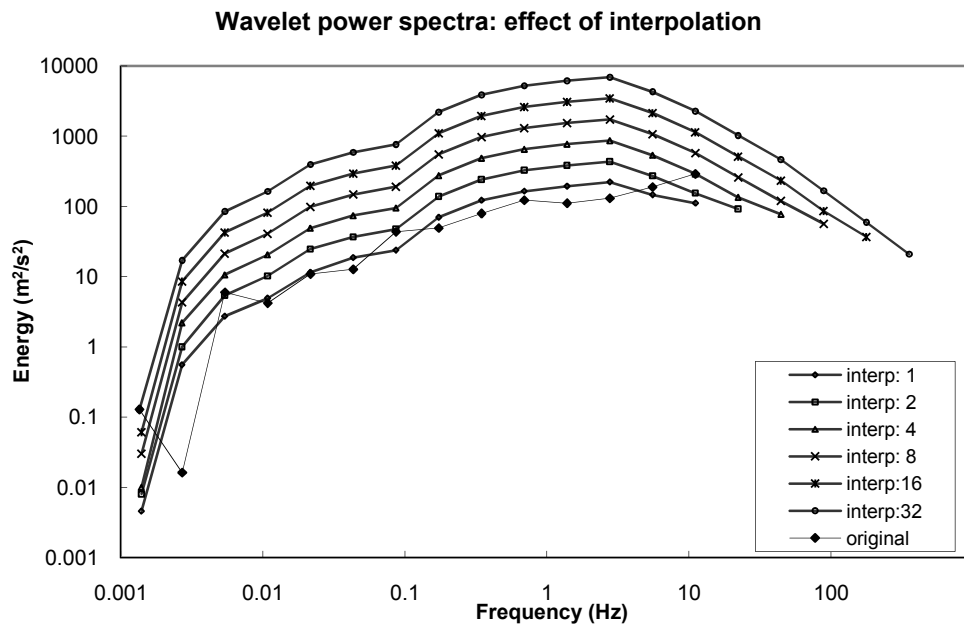


Figure 2.24. Wavelet power spectrum for interpolated velocity series

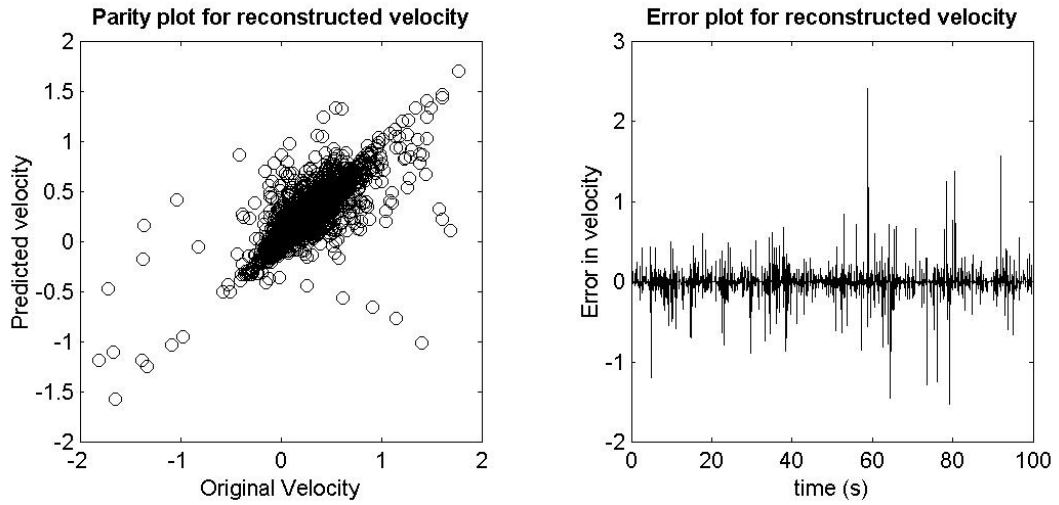


Figure 2.25. Error in reconstruction for interpolation with $\Delta t = 0.02624$ s

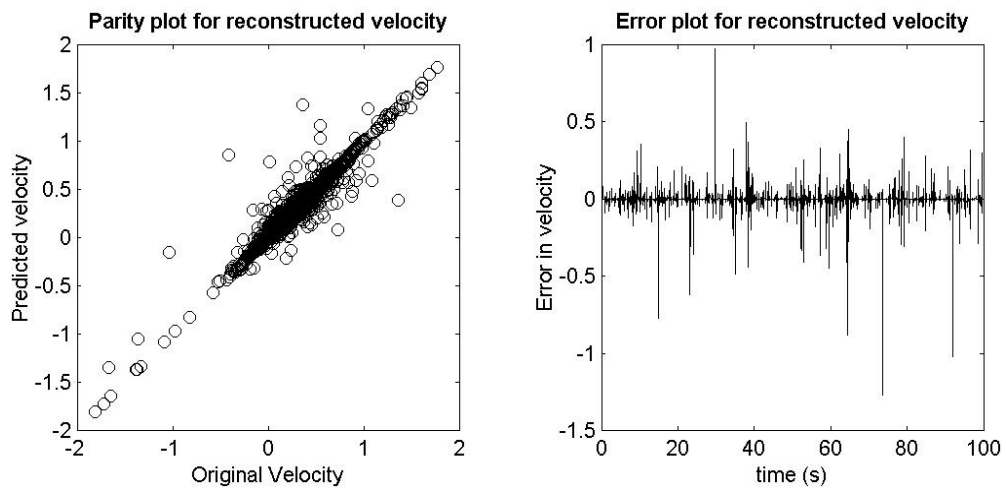


Figure 2.26. Error in reconstruction for interpolation with $\Delta t = 0.00328$ s

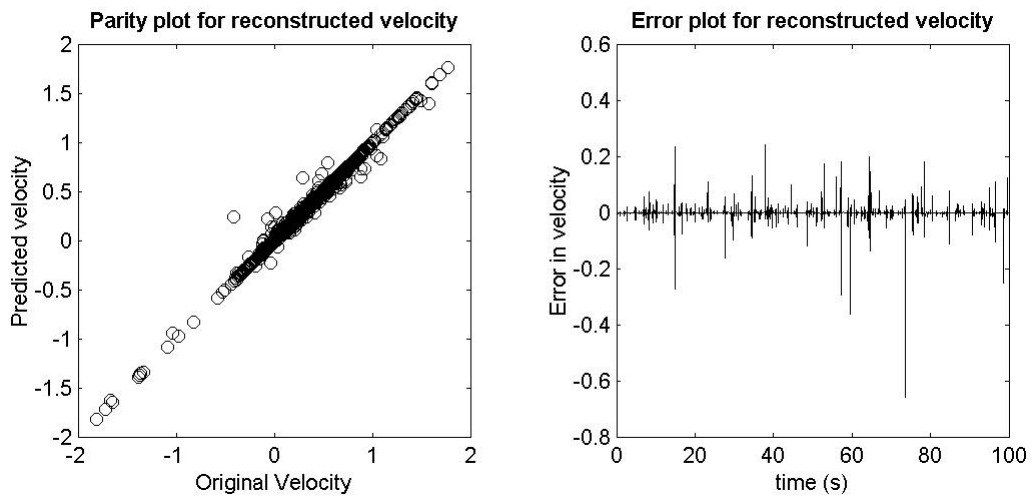


Figure 2.27. Error in reconstruction for interpolation with $\Delta t = 0.00082$ s

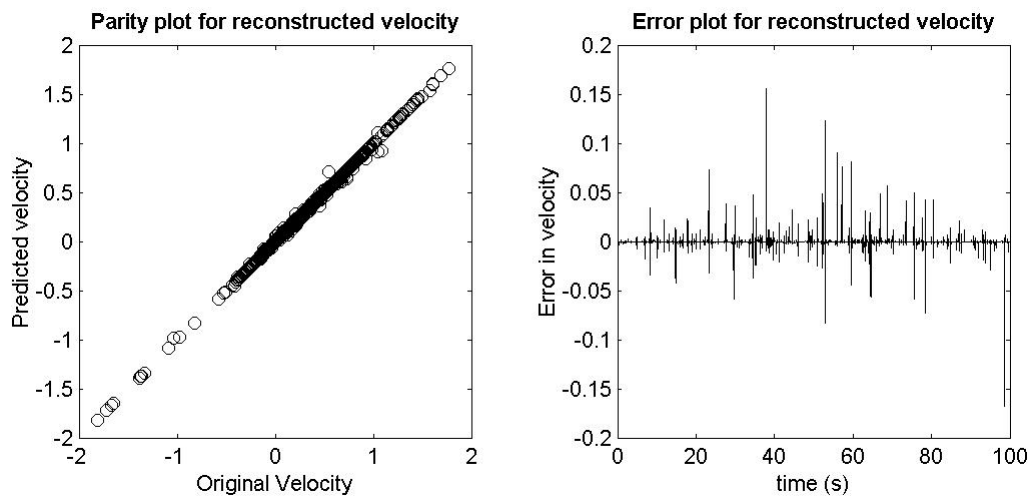


Figure 2.28. Error in reconstruction for interpolation with $\Delta t = 0.00041$ s

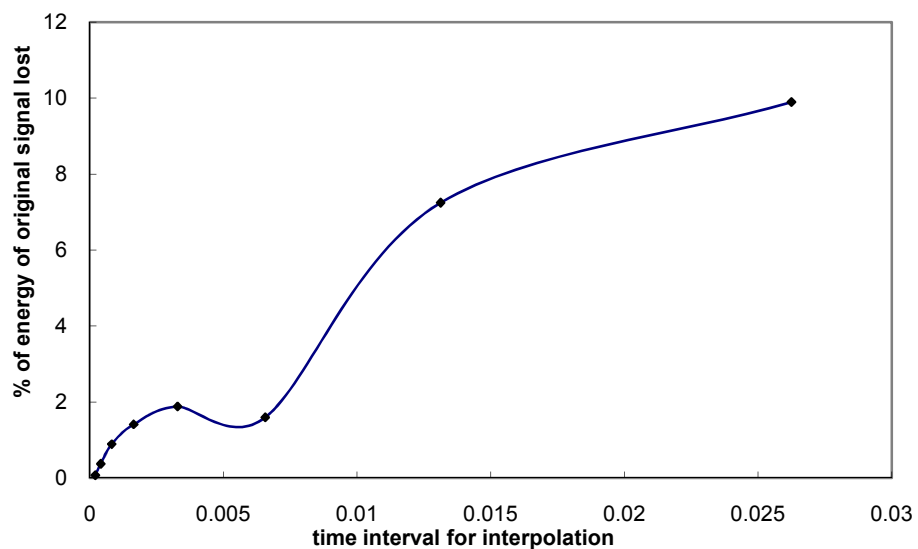


Figure 2.29. Energy lost from the signal in interpolation procedure

2.2.3.2. Denoising the time series

A wavelet based denoising algorithm suggested by Roy et. al. (1999) is employed for denoising. This method is better suited to chaotic signals than soft or hard thresholding the wavelet coefficients.

The Algorithm is as follows:

1. The time series data is differentiated to get the derivative time series.

2. The derivative time series is subjected to wavelet transform, and the wavelet power spectrum is plotted from the scalewise coefficients obtained.
3. The minima in the power spectrum is the marker, indicating the scalewise coefficients up to this particular scale are to be set to zero.
4. The derivative series is reconstructed from the wavelet coefficients.
5. The reconstructed series is integrated to generate the denoised time series.

Figure 2.30 illustrates this sequence.

For the signal demonstrated, the energy contained in noise was found to be 0.975 %. The denoised signal overlapped on original signal and the noise separated are displayed in Figs. 2.31 and 2.32 respectively.

2.2.3.3. Gas velocity estimation using LIM

Processing of denoised time series to obtain gas holdup(isolation of gas points)

The procedure to obtain gas holdup is as follows:

1. Wavelet transform of denoised time series is taken to obtain scalewise reconstruction.
2. LIM (Local Intermittancy Measure) Values for j^{th} scale and i^{th} elements are :

$$LIM_j(i) = \frac{|x_j(i)|^2}{\langle |x_j(i)|^2 \rangle}, \text{ where } \langle |x_j(i)|^2 \rangle \text{ denotes the mean of squared values.}$$

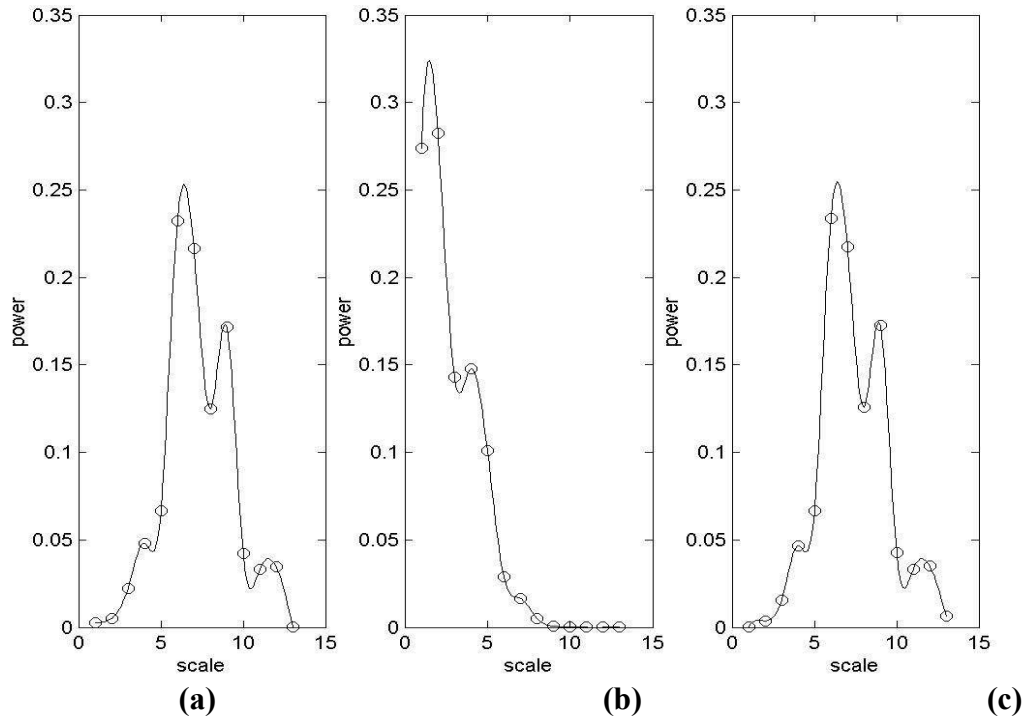


Figure 2.30. Wavelet power spectra for denoising of velocity – time data for (a) original series (b) differentiated series (c) denoised series

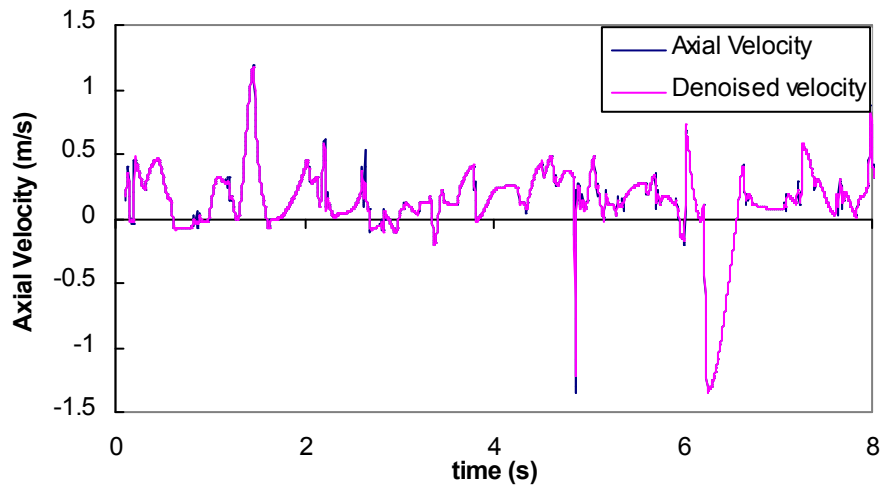


Figure 2.31. The denoised series superimposed over original time series

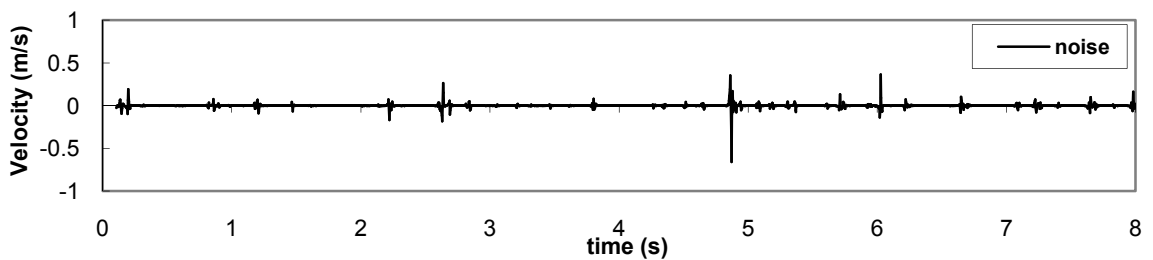


Figure 2.32. The noise separated by wavelet denoising

3. It is considered that a time gap larger than a threshold value Δt_{thr} followed by LIM value larger than a threshold value LIM_{thr} indicates the passage of bubble through the measurement volume, at all other times the measurement volume is considered in liquid.
4. The time series is analysed for occurrences of all such events, to get t_g , the time for which the measurement volume was in gas.
5. t_g divided by total time for measurement gives the local gas holdup, ϵ_g .
6. The area averaged gas holdup can be calculated by using:

$$\bar{\epsilon}_g = \frac{\int_0^R \epsilon_g(r) \cdot (2\pi r) dr}{\int_0^R (2\pi r) dr} \approx \frac{\sum_{i=1}^n \epsilon_g(r_i) \cdot (2\pi r_i) \cdot \Delta r_i}{\sum_{i=1}^n (2\pi r_i) \cdot \Delta r_i} \quad (2.35)$$

Where: n=16 corresponds to number of radial locations.

7. Steps (4) to (6) are performed for particular threshold values, and the area averaged holdup is compared with the experimentally measured value. If the holdup values do not match, then new thresholds are chosen and the three steps repeated till we get experimentally measured area averaged gas holdup.

Based on the above procedure, the following holdup profiles were obtained for Δt_{thr} value of 0.05 and LIM_{thr} values of 1.9, 1.7 and 1.4. The area averaged gas hold-up value of 0.0524 (5.24%), $\bar{\epsilon}_g = 0.0582$ (5.82%) and $\bar{\epsilon}_g = 0.0689$ (6.89%) respectively. This value is most nearer to the experimental value of 6.5 %. The gas hold-up profiles for these cases are depicted in figures 2.33 to 2.35.

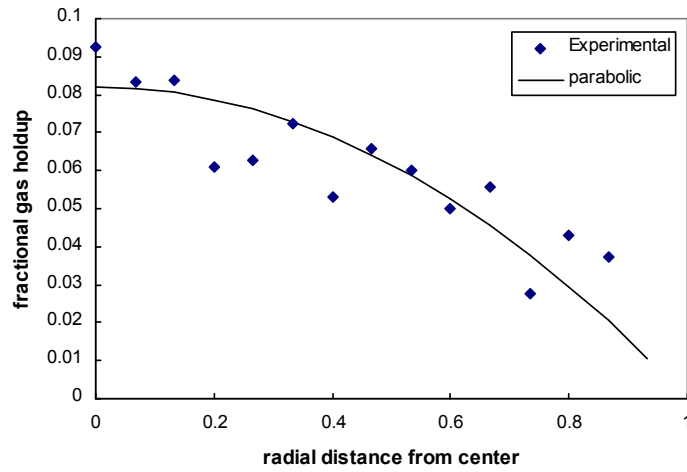


Figure 2.33. Hold-up profile, computed with $\Delta t_{thr} = 0.05$ s and LIMthr = 1.9
 $\bar{\epsilon}_g = 0.0524$ (5.24%).

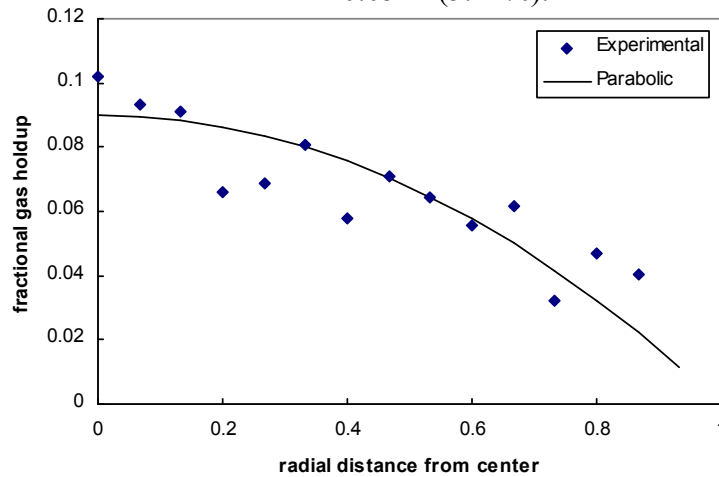


Figure 2.34. Hold-up profile, computed with $\Delta t_{thr} = 0.05$ s and LIMthr = 1.7
 $\bar{\epsilon}_g = 0.0582$ (5.82%).

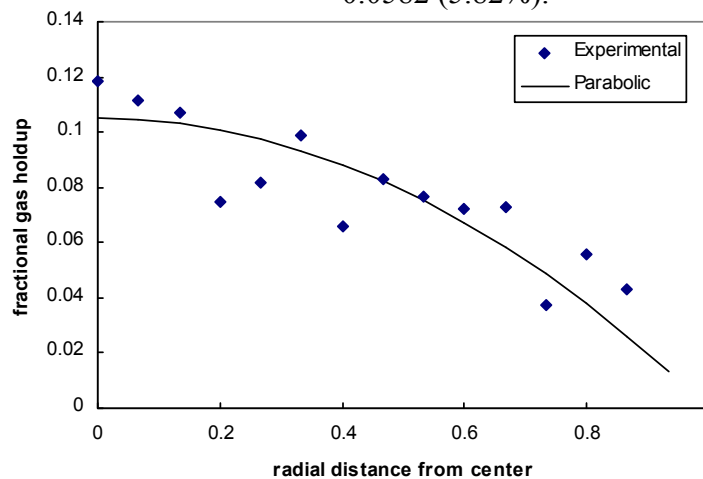


Figure 2.35. Hold-up profile, computed with $\Delta t_{thr} = 0.05$ s and LIMthr = 1.4
 $\bar{\epsilon}_g = 0.0689$ (6.89%).

Calculation of liquid velocity profile

It is considered that the gas carries a small volume of liquid with it while rising through the liquid phase. Thus, the velocity immediately following the time gap identified as bubble passage is considered as bubble rise velocity. As these particular points represent the liquid velocity is equal to that of the gas phase, these points are isolated from the time series.

The average of all other points gives the mean liquid velocity at that particular location in the column. The liquid velocity profile thus obtained is shown in Figure 2.36. The area averaged liquid velocity must be zero in order to satisfy the material balance of liquid in the bubble column. The area averaged liquid velocity is calculated as 0.001255 m/s.

2.2.3.4. Bubble size estimation

Data processing considering slip velocity criteria

If the bubbles are identified only on the basis of time gap threshold and LIM threshold, negative slip velocities and slip velocities predicting bubble diameter much higher than observed values are encountered. To eliminate this possibility, a slip velocity threshold value was introduced as an additional criterion to identify bubble passage.

The following threshold values satisfy the liquid phase material balance, gas phase material balance and area averaged gas holdup:

Δt_{thr} : 0.0008 s, LIM_{thr} : 0.8, **Slip velocity (bounds)**: $0 < V_s < 0.434$.

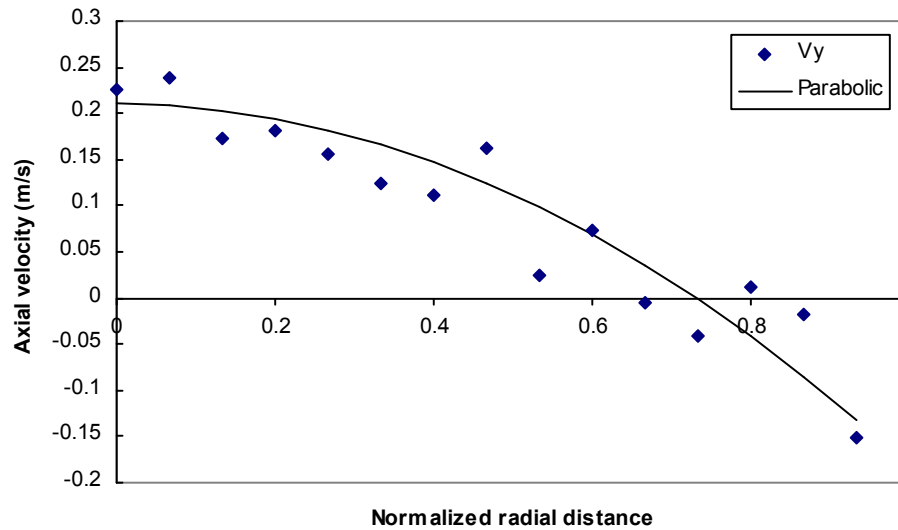


Figure 2.36. Average liquid velocity profile after separation of gas-velocity points, Area averaged value = 0.010539 m/.

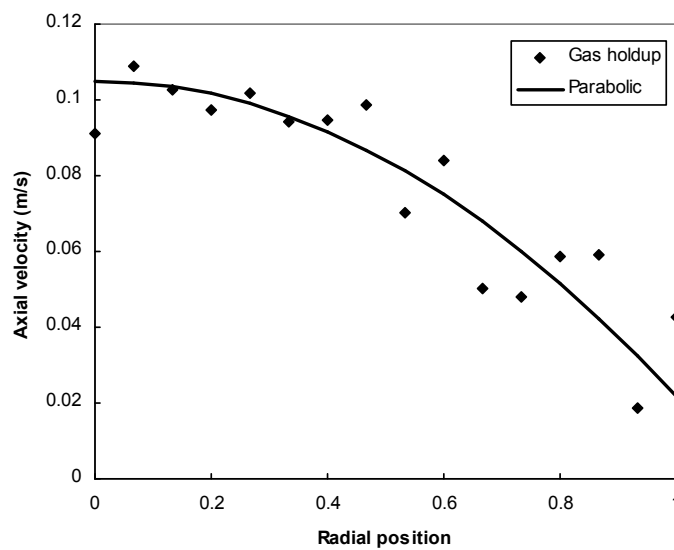


Figure 2.37: Fractional gas holdup profile: Area averaged value = 0.062226

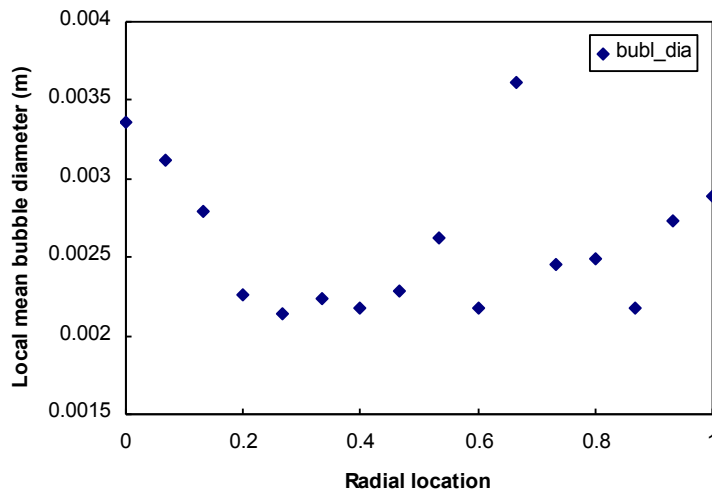


Figure 2.38. Local mean bubble diameter profile: area averaged value: 0.0028858 m

The material balance criteria checked are as follows:

- 1) Liquid phase material balance: The area averaged liquid velocity should be zero, since liquid is in batch mode, i.e. there is no net flow of liquid out of the column.

$$\text{Area averaged liquid velocity} = \langle V_L \rangle = \frac{\sum_{r=0}^R V_L \cdot r \cdot \Delta r}{\sum_{r=0}^R r \cdot \Delta r} = 0.010539 \text{ m/s (4\% of } V_{\text{center}}).$$

- 2) Gas phase material balance: The area averaged gas velocity should match to that of the gas superficial velocity, since that represents the net rate of escape of gas through the bubble column cross section.

$$\text{Area averaged gas velocity} = \frac{\sum_{r=0}^R V_{R, \text{gas}} \cdot \epsilon_G \cdot r \cdot \Delta r}{\sum_{r=0}^R r \cdot \Delta r} = 0.022318 \text{ m/s (} V_G = 0.02 \text{ m/s)}$$

2.3. Particle Image Velocimetry (PIV)

Particle Image Velocimetry (PIV), in effect “Quantitative flow visualization” is an extension of visualization techniques, where velocity vectors are measured simultaneously at thousands of points with accuracy and resolution approaching LDA technique. While LDA provides the time history of flow at the measurement location, PIV measures at many points at one instant of time. In LDA, the measurement volume size determines the spatial resolution, the maximum image displacement gives a measure of spatial resolution in PIV.

2.3.1. Literature Review

Over the period of last 15 years, PIV technique has developed significantly for single and multiphase flows. Lui et al. (1994), Webster and Longmire (1997), Nishimura et al. (2000) and Webster et al. (2001) studied the planar variation of velocity using PIV data for liquid jets. Haut et al. (2003) investigated instantaneous and time-averaged velocity fields experimentally by using PIV in the annular region in horizontal corotating cylinders, for the wavy vortex flow and the turbulent Taylor vortex flow. Deshmukh et al. (2008) carried out PIV measurements in annular region of annular centrifugal extractors. Van Wissen et al. (2004, 2005) have measured the detailed flow pattern of steam condensation jet using PIV. Dahikar et al. (2010) carried out PIV/PLIF study for simultaneous measurement of temperature and velocity.

Chen and Fan (1992) reported a PIV system with continuous 4W Ar ion laser applied on a refractive index matched 3 phase fluidized bed. After identifying each particle as a seeding particle, suspended solid particle or a bubble, the velocity was calculated using particle tracking. Delnoij et al. (1999) proposed the ensemble correlation PIV for bubbly flow based on the single-frame double-exposure technique

along with image shifting to overcome directional ambiguity. Masking technique for removal of bubbles from PIV images was implemented by Lindken and Merzkirch (1999). Deen et al. (1999) applied the Laser Induced Fluorescence (LIF)- PIV technique to the analysis of the hydrodynamics in a locally aerated square bubble column. Bröder and Sommerfeld (2002) extend this method to simultaneous measurements of the velocity field of both phases in a laboratory scale, cylindrical bubble column operated at a relatively high void fraction.

2.3.2. Experimental

2.3.2.1. Principle of PIV

The experimental set-up of a PIV system typically consists of several subsystems. In most applications tracer particles have to be added to the flow. These particles are illuminated in a plane of the flow at least twice within a short interval of time. The light scattered by the particles has to be recorded either on a single frame or on a sequence of frames. The displacement of the particle images between the light pulses has to be determined through evaluation of PIV recordings. Figure 2.39 describes a set-up for PIV recording.

Small tracer particles are added to the flow. A plane (light sheet) within the flow is illuminated twice by means of a laser (the time delay between pulses depending on the mean velocity and the magnification at imaging). It is assumed that the tracer particles move with local flow velocity between the two illuminations.

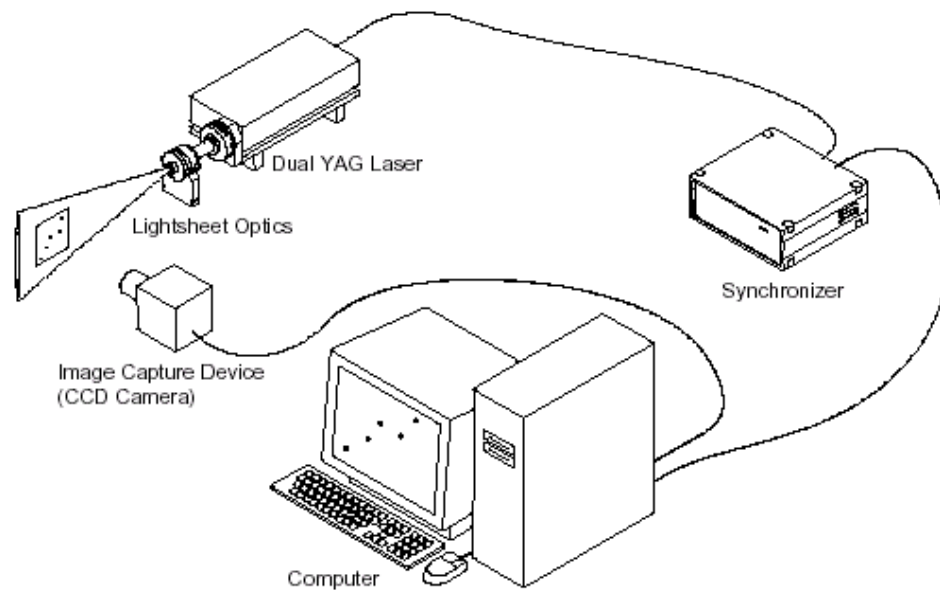


Figure 2.39. PIV system overview

The light scattered by the tracer particles is recorded with a high quality lens either on a single photographic negative or on two separate frames on a special cross correlation CCD sensor. After development, the photographic PIV recording is digitized by means of a scanner. The output of the CCD sensor is stored in real time in the memory of a computer directly.

For evaluation, the digital PIV recording is divided in small sub-areas called “interrogation areas”. The local displacement vector for the images of the tracer particles of the first and second illumination is determined for each interrogation area by means of statistical methods (auto- and cross- correlation). It is assumed that all particles within one interrogation area have moved homogeneously between two illuminations. The projection of the vector of the local flow velocity into the plane of the light sheet (2-component velocity vector) is calculated taking into account the time delay between the two illuminations and the magnification at imaging. The process of interrogation is repeated for all interrogation areas of PIV recordings.

2.3.2.2. Laser and optics

Argon lasers are continuous wave lasers and are pulsed using mechanical choppers or Bragg cell based (optical) modulation. The pulse duration is variable. Pulse duration refers to the time that the light sheet illuminates a plane in the flow field. Pulse separation on the other hand is the time between two laser pulses and is set based on the velocity of the particles and the desired spatial resolution. Higher energy per pulse is required for flows with smaller particles and larger areas. Repetition rate refers to the number of pulse repetitions per second. With high energy per pulse and minimal jitter pulsed Nd:YAG lasers are ideal for a large number of applications. Ruby lasers are not as common as pulsed YAG lasers, primarily because they cannot keep up with the frame rate of the modern high resolution CCD cameras. Cu-vapor lasers with their high repetition rate are ideal for high speed imaging which is generally of lower resolution than what is preferred by the fluid dynamic researcher. The energy per pulse of a Cu-vapor laser limits it to relatively lower flow velocity with large particles or smaller field of view PIV measurements.

The dual Nd:YAG laser is the preferred light source for most PIV experiments. This integrated laser houses two separate laser heads whose pulses are combined with built-in beam combination optics to produce a coaxial pulse train. The very short pulse duration is fast enough to “freeze” even particle images in supersonic flow without image streaking. The high pulse energy illuminates small particles for either air or water flows.

Lower power (10 to 100 mJ) Nd:YAG lasers are now available for water flow experiments or small air flow experiments. These small Nd:YAG lasers are able to deliver much higher energy than even a 10 Watt argon laser. Dual Nd:YAG lasers can

come with variable pulse repetition rate from 10-30 Hz. A dual YAG laser with 15 Hz repetition rate per laser works well with special 30 Hz cross correlation camera, when two images are captured on separate frames. This would give 15 velocity fields per second.

Nd:YAG lasers use two trigger signals in generating a pulse of light. The first trigger fires a flash lamp. Photons from the flash lamp are absorbed by the Nd:YAG rod where this energy is stored. The second trigger opens the Q-Switch releasing the stored energy as a laser pulse. The light discharge from the flash lamp takes some time to reach maximum brightness when the Q-Switch is opened. By setting the Q-switch delay time, the pulse energy is selected. This allows a minimum energy pulse to be used for alignment and setup, and a high energy pulse to be used for the experiment. The Synchronizer and Laser pulse software set the laser pulse energy by setting the Q-Switch delay time. The pulse energy can also be set (on some laser models) by setting the flash lamp voltage. Adjusting the pulse energy with Q-Switch delay is recommended because it keeps the laser at the operating temperature it was tuned for. This maintains the best beam quality.

The articulating laser light delivery arm consists of a series of rotating knuckles, specially coated mirrors, and aluminum tubes which form a fully enclosed, infinitely adjustable light sheet delivery system. The overall length of the arm is 1.8 meters and the aperture can be positioned anywhere in the sphere whose radius is equal to this distance. The articulating arm safely handles upto 500mJ/ pulse. To form a light sheet from the incident laser beams, sets of spherical and cylindrical lenses are employed. Sets of each type of lens are included with the system (200, 500, and 1000 mm focal length spherical lenses and -15, -25, -50, -100, and -200 mm focal length cylindrical lenses). These optics mount directly to the aperture of the laser, which eliminates the need for an optical rail

mount and keeps the system compact and easy to use, or to the optional articulating light arm. The lenses can be used in series to match just about any light sheet dimension requirements.

Laser light sheet optics are used to control the dimensions of the illuminated area. A cylindrical lens controls the light sheet height. A spherical lens is used to control the light sheet thickness. The schematic of the light sheet optics is shown in the Figure 2.40.

The top view shows the thickness of the light sheet. The cylindrical lens has no effect on the light sheet thickness. The spherical lens forms a waist in the light sheet at its focal point. The bottom view shows the light sheet height. The beam diverges in the vertical

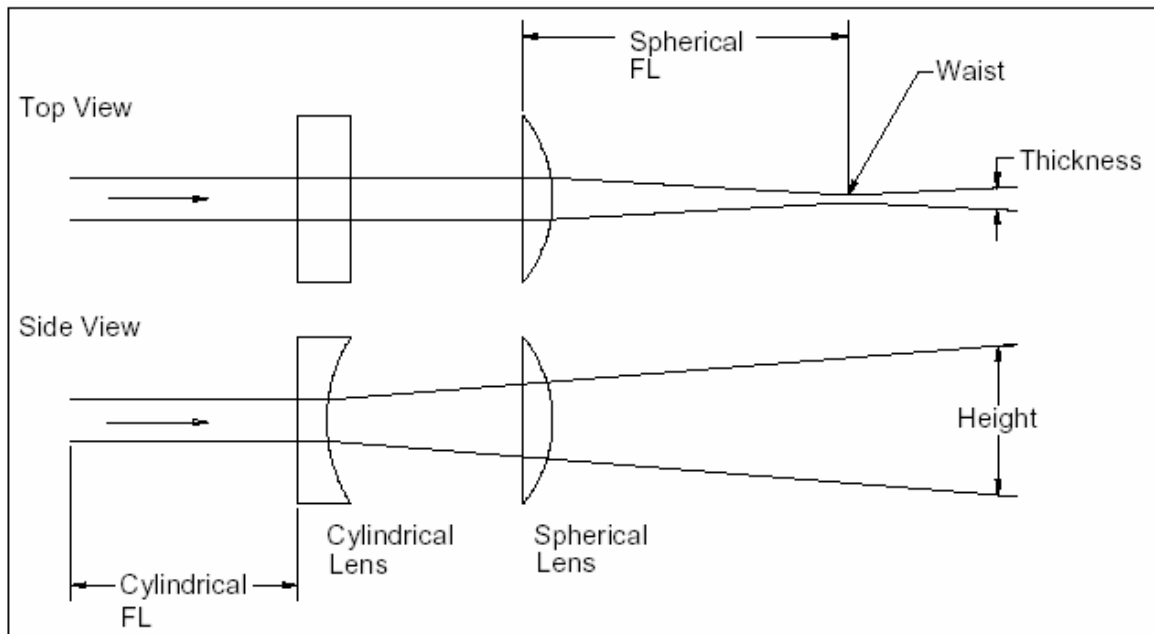


Figure 2.40. Light sheet optics

direction after passing through negative focal length cylindrical lens. The positive focal length spherical lens reduces this height divergence only a little. Typically the cylindrical lens has a much shorter focal length than the spherical lens. Typically the camera views

the light sheet near the thickness waist, where the intensity is highest, but any place along the light sheet can be used. When selecting the light sheet optics and camera viewing position the light sheet intensity should not be allowed to vary too much over the field of view.

2.3.2.3. Synchronizer system

The computer controlled Synchronizer is at the heart of all PIV systems. Synchronizer set-up is shown in the following Figure 2.41.

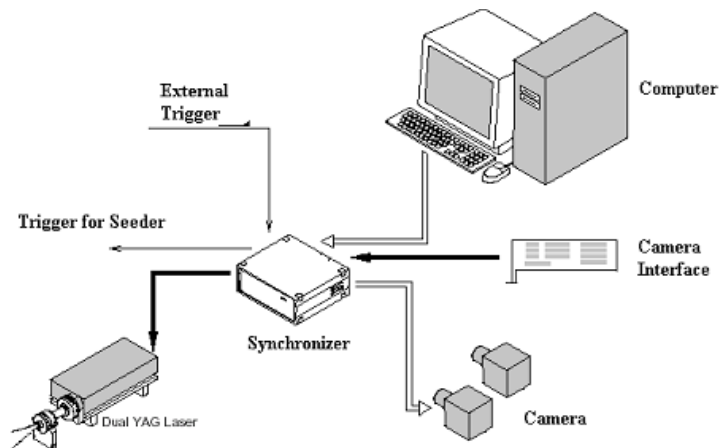


Figure 2.41. Synchronizer set-up

The primary function of a synchronizer system is that of a precise timer and a master system controller. It synchronizes the timing of image capture with the pulsing of the laser. Acting as the master controller for system components, it automates control of the timing between laser pulses, camera, camera interfaces and any external device during system set-up and image acquisition. The Synchronizer enables the system to be completely computer controlled via a serial interface. Special cross correlation cameras are employed in PIV which enable pairs of images be taken with short time between pulses. Control of such cameras is built into the synchronizer. Signals for the laser flash lamps and Q-switches, the camera and time grabber are generated and automatically synchronized for effortless image acquisition. For PIV applications, pulse delay time and

the time between pulses necessary to collect frame-straddling images are controlled by the software. The synchronizer has an auxiliary output for controlling various devices in an experimental rig. For periodic flows, where phase locked velocity measurements are desirable, the Laser pulse synchronizer can be externally triggered using a TTL signal from the experimental apparatus. That is, images can be captured at a certain angular position or at certain events in order to be ensemble averaged. The synchronizer system provides all the needed control signals and does not need further adjustments for the cameras, lasers and other devices. The few techniques in synchronization are shown in the Figure 2.42.

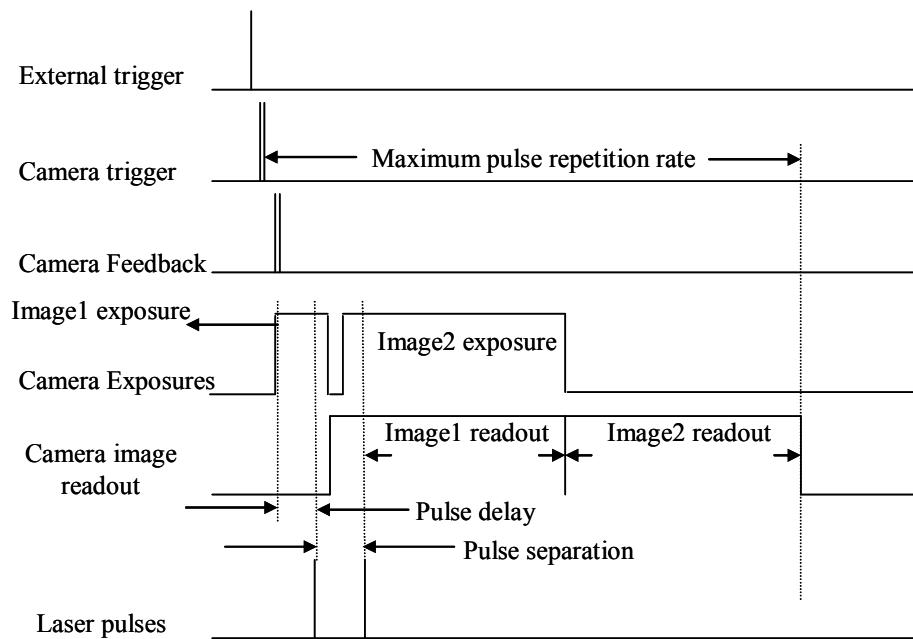


Figure 2.42. Frame straddle timing diagram for PIV

Frame straddling technique allows very short time between laser pulses and thus provides the capability to measure higher and higher speed flows. Frame straddling requires a close synchronization between the camera exposure and the pulsing of the laser. Key camera specification is the time from the end of one exposure to the start of the next exposure, the minimum frame straddling time. When trying to make the highest flow velocity measurement, the first pulse is delayed until the last moment of exposure 1,

and the second pulse happens at the first moment of exposure 2. Actual frame straddling time requires that Image1 be removed from the pixels before the second exposure starts. The time to move the image from the pixels depends on the image brightness. Actual frame straddle times can vary with experimental set-up. Figure 2.43 shows the pulse separation and repetition rate.

The few terms which need to be understood in synchronization are as follows:

Camera trigger: The synchronizer triggers the camera to start a double exposure sequence. The frame grabber is also triggered at this time to capture the next two images.

An external trigger can initiate the camera trigger.

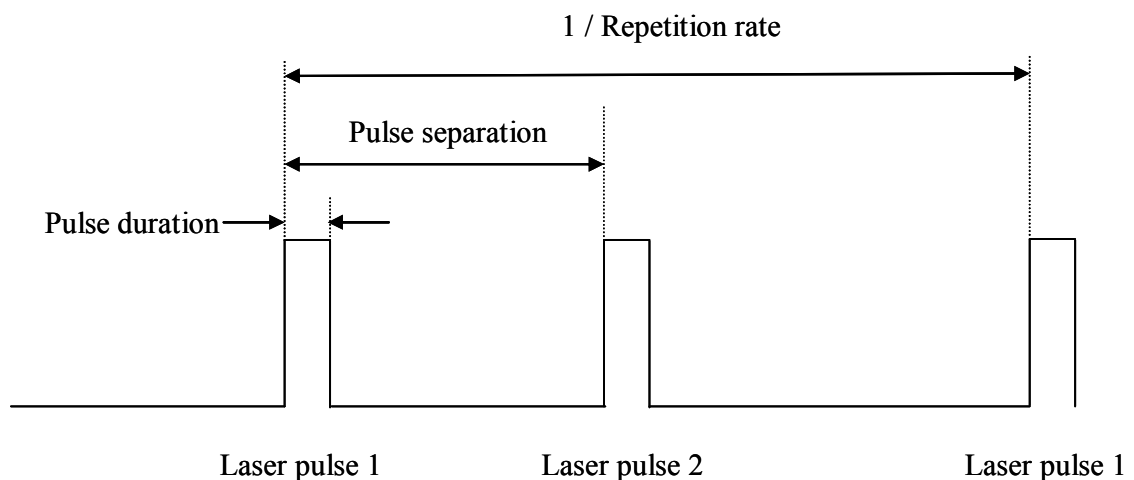


Figure 2.43. Pulse separation and repetition rate

Camera shutter feedback: After a short time the shutter feedback signals the start of the first frame exposure.

Camera exposure: The two frame exposure includes a short frame 1 exposure and a longer frame 2 exposure. The first exposure is just long enough to Q-switch a Nd:YAG laser, During the second exposure, image in frame 1 is readout.

Camera digital video image output: The first image (frame 1) moves quickly from the light sensitive pixels to the readout registers. It then takes one frame time to transfer the image out of the camera and to the frame grabber. The second image cannot end until all of the first image has been read out of the camera.

Laser pulses: The first laser pulse must end before the end of exposure 1. The second pulse must start after the beginning of exposure 2.

2.3.2.4. CCD sensor details

There are three basic CCD designs, full frame transfer, frame transfer and interline transfer. In all CCD architectures, the image is read out serially from the horizontal shift registers determines the maximum camera frame rate. The difference between the various CCD architectures is the process to move image from the light sensitive pixels to the horizontal shift register. In full frame transfer and frame transfer CCDs the pixels also act as vertical shift registers, while the interline transfer CCD has separate pixels and vertical shift registers. Interline transfer CCD camera typically has a high frame rate and allows very small time between frames. With 2048 x 2048 pixel cameras, high spatial resolution can be achieved to resolve finer scales or larger fields of view can be captured with adequate resolution. As given earlier, frame-straddling allows cross correlation of separate PIV images which enhances the dynamic range with no directional ambiguity. Frame straddling cameras with cross correlation analysis can be used from a few mm/s till supersonic flows. Herein, the cameras can still be used for multiple exposure image capture with auto correlation analysis for extremely high speed flows. Without frame straddling, frames can be captured at the camera frame rate. But this value of the time between pulses is applicable for only low velocity flows. The camera shutter defines the start and stop of each pulse instead of the laser pulsing. To measure extremely low velocity flows, the time between images can be increased by not grabbing every frame from the camera. In large area measurements the field of view can

be greater than 500 mm. To do this the tracer particle size need to be larger, so that image covers enough pixels.

2.3.2.5. Image capture

System set-up, laser pulse sequencing, image capture, data analysis and display are accomplished using a comprehensive software package. This software provides a comprehensive approach to experiment set-up, synchronization, image capture, analysis, storage and display. The analysis/display algorithm analyzes the image information and displays the vector field. Double exposed particle image fields are analyzed using cross correlation algorithms.

2.3.2.6. Stereoscopic technique

The image displacements for the images captured by the two cameras are obtained using the cross-correlation approach used for 2D PIV measurements. The correlation approach is desirable because the three-dimensional velocity vectors can be obtained on uniform grids, and the problem of matching individual particle image pairs is solved automatically. To assure good measurements of the out-of-plane component of velocity, the viewing angles between the stereo lenses must be substantial, of the order of thirty degrees, and the time between exposures of the images must be small enough that the particles remain within the thickness of the light sheet. The relationship (mapping function) between the fixed points in the flow field and their corresponding image (pixel) locations in the two cameras is established through the calibration process. A calibration grid with markers at known locations defines the positions in the flow field. Placing this within the light sheet and imaging the markers with the two cameras provides the data to create the mapping function. Using this, the reverse process of going from image

displacements obtained at the different grid locations in the camera to corresponding particle displacements (and hence the velocity) in the flow field is easily accomplished.

The most common approach to three-component velocity measurements using PIV is to get the three-dimensional velocity vector field using a laser light sheet illumination. This is a natural extension to the two-dimensional planar PIV and provides the third component of velocity normal to the light sheet plane. In this way, the number of vectors is the same as in two-dimensional planar PIV, but the determination of the third velocity component contributes significantly to the experimenter's capability to visualize and understand the flow dynamics. The measuring volume (as in two-dimensional PIV) is decided by the area imaged by the camera and the thickness of the light sheet.

Other approaches to three-dimensional flow measurements include volume illumination and Holographic recording of image displacements. Holographic systems require a unique set of techniques and apparatus, and they place demands on the optical access required to view the flow field. The velocity vector in the light sheet (AB) shown in the Fig 2.44 is viewed as a two-dimensional projection (ΔX , ΔY) on the image plane (detector plane) on the left side.

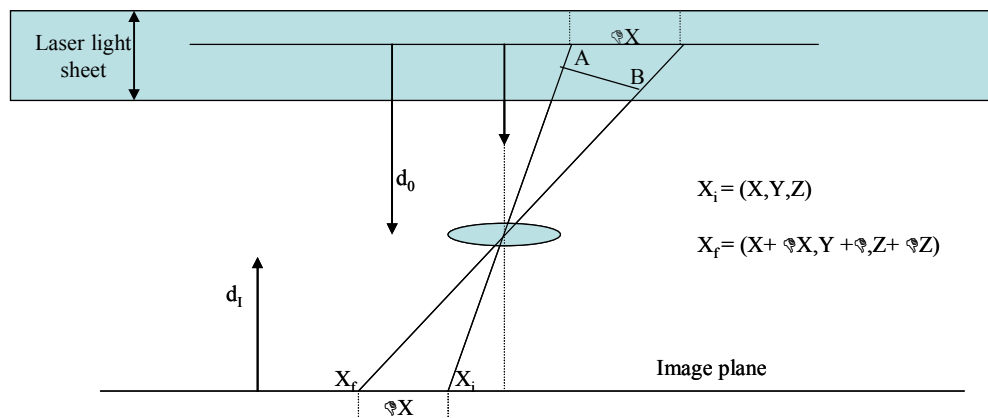


Figure 2.44. Velocity vector in the light sheet

Similarly the projection of the vector is also viewed by the image plane on the right side (using the second camera). Combining the two projected vectors on the two image planes, the three orthogonal velocity components are obtained.

2.3.2.7. Scheimpflug stereoscopic arrangement

The Scheimpflug stereoscopic camera configuration (shown in the Figure 2.45) can be achieved by mounting the camera lens with an angular offset, as in the angular offset stereoscopic camera configuration and then tilting the camera body (with respect to the lens).

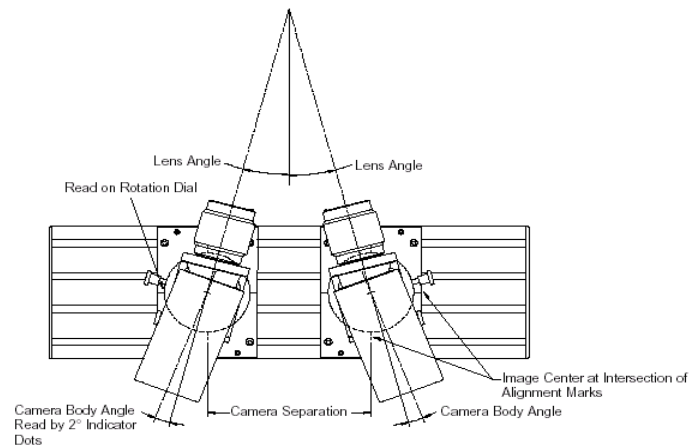


Figure 2.45. Stereoscopic Camera Arrangement

The correct focus and tilt angles are achieved when all of the particles within the camera field of view are in good focus. The on-line update of images captured by the camera makes this setup process straight forward. The Scheimpflug arrangement allows one to keep the plane of best focus in the plane of light sheet for both air and water flows while having the camera view the light sheet from an off-axis angle. This allows the lens aperture settings to be the same as that for two-dimensional PIV.

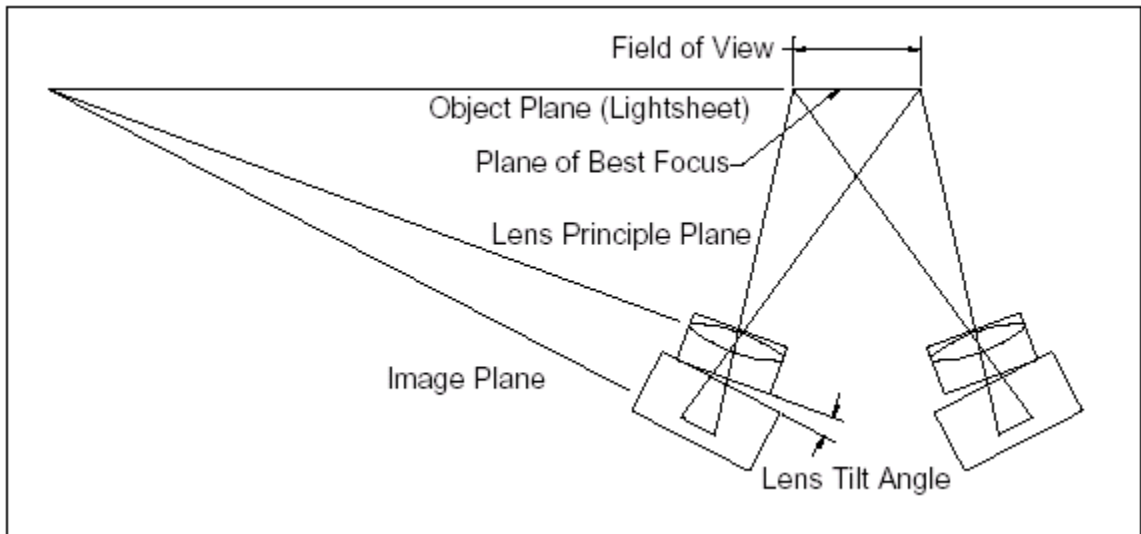


Figure 2.46. Scheimpflug Stereoscopic Arrangement

It also has the image sensor near the lens optical axis so that the image intensity is similar to the angular offset camera system. The arrangement shown in Figure 2.46 clearly shows the plane of best focus. The Scheimpflug camera arrangement introduces perspective distortion to the images causing a rectangle in the light sheet plane to be imaged as a trapezoid on the image sensor. The perspective effect due to camera tilt is shown in Figure 2.47.

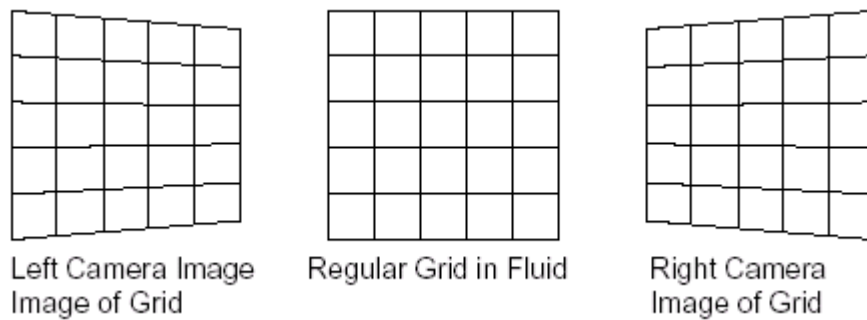


Figure 2.47. Perspective Effect due to Camera Tilt

In order to use the images recorded with the cameras in the Scheimpflug condition the velocity vectors must be transformed to convert them from this image space to the fluid space.

When an aberrating medium is placed between the object plane and the cameras, a calibration procedure to correct for the aberrations is necessary. Depending upon the configurations of the two cameras, variable magnifications may be introduced which will cause systematic bias errors into the measurement of fluid velocity and the location of velocity vector. These influences can be corrected by an appropriate technique. The approach is to perform a calibration to generate a mapping function for the correction of distortion, aberration and misalignment of the cameras. This approach eliminates the need to mechanically register the pixel arrays of two cameras, replacing the process by a simple mathematical registration. In addition, the mapping function approach provides a natural framework to combine the images of two or more cameras to obtain the three dimensional velocity fields.

2.3.3. Data Processing of PIV

2.3.3.1. Image evaluation methods for PIV

In principle, a high data density is required on the PIV vector maps, especially for the comparison of experimental data with results of numerical calculations. This demand requires a medium concentration of the images of tracer particles in the PIV recording (Adrian and Yao, 1985). Medium image concentration is characterized by the fact that matching pairs of particle images, due to subsequent illuminations cannot be detected by visual inspection of the PIV recording. Hence statistical approaches are used wherein, after statistical evaluation, tracking algorithms can be additionally applied in order to achieve sub window spatial resolution of the measurement. However, since the extraction of the displacement information from individual particle images requires spatially well resolved recordings of the particle images, those techniques are more

appropriate to increase the spatial resolution of photographic PIV recordings than that of digital recordings.

2.3.3.2. Image shifting

The autocorrelation function produces two displacement peaks for each particle image pair. These are of equal strength and 180° apart. The forward peak is the distance from the first image to the second and the reverse peak is the distance from the second image to the first. When there are no flow reversals, the correct peak is found by selecting the peak search half-plane: left, right, up, down. However, when there are no flow reversals, no single search half plane is correct for the entire flow. Directional ambiguity is thus a problem with autocorrelation processing.

Mirror image shifting uses a rotating mirror that is placed between the light sheet and the camera. The mirror rotates in the time between the laser pulses and adds the image shift velocity to the flow velocity. The short duration of the laser flash effectively freezes the mirror at two angular positions. The first pulse is taken with the mirror at one position and the second pulse after the mirror has rotated. An object in the flow with no velocity is recorded in two locations. The distance between the two images of a stationary object is the image shift distance. This displacement is added to the displacement due to the particle images movement. When the image shift displacement is larger than the largest flow reversal displacement, all correct displacements may be found in a single search half-plane. The peak is at distance equal to the velocity displacement plus the image shift displacement. By subtracting the image shift displacement from the measured peak location, displacement due to the flow can be found. While selecting the image shift direction, the image shift is usually provided in

one direction only. When the autocorrelation function is searched for displacement peaks only one half is searched.

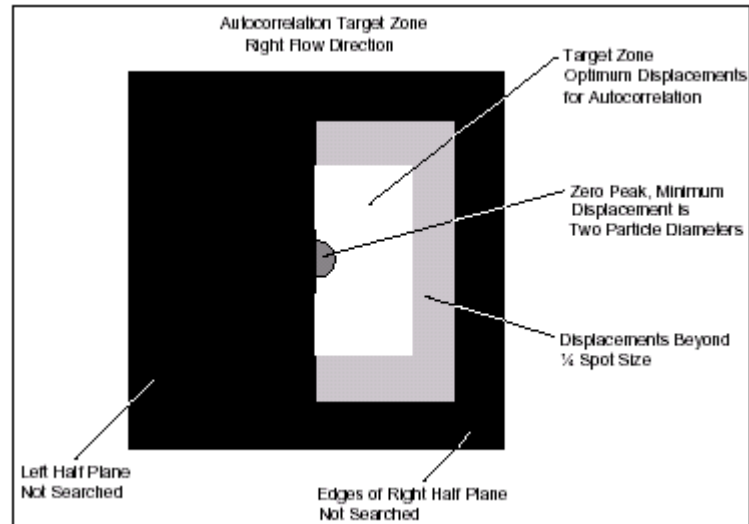


Figure 2.48. Autocorrelation target zone

This is since the autocorrelation function is symmetrical and searching the other half plane gives a peak with negative displacement, directional ambiguity. Also, the edges of the autocorrelation are not searched since the peaks too close to the edge are likely to go off the edge and aliasing might occur. Using the autocorrelation target zone as shown in the Figure 2.48 is helpful in deciding the direction and magnitude of the image shift. For the best measurements, all particle image displacement should be inside autocorrelation zone. The image shift displacement is a translation of the particle displacement across the autocorrelation. To make successful measurements without directional ambiguity all of the particle image displacements must fall within the peak search area.

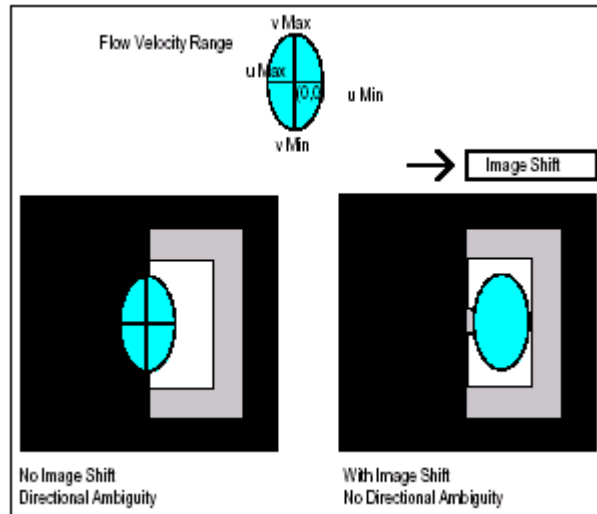


Figure 2.49. Displacement range

When there are flow reversals, some of the forward displacement peaks may be in the right half plane and some in the left. By using image shifting and selecting the correct interrogation spot size and dT , the range of particle image displacements can be made to fit into the peak search area. The Figure 2.49 shows that after the image shifting, the displacement peaks are inside the selected search half plane.

2.3.3.3. Processing of PIV vector field

The post-processing of PIV data is characterized by the following steps:

Validation of raw data: After automatic evaluation of the PIV recordings, a certain number of obviously incorrectly determined velocity vectors (so-called outliers) can usually be found by visual inspection of the raw data. In order to detect these incorrect data the raw flow field data have to be validated. For this purpose, special algorithms have to be developed, which must work automatically.

Replacement of incorrect data: For most post-processing algorithms (e.g., calculation of vector operators) it is required to have complete data fields as is quite naturally the case for numerically obtained data. Such algorithms will not work if gaps (data drop-outs) are

present in the experimental data. Thus, means to fill the gaps in the experimental data must be developed.

Data reduction: It is quite difficult to inspect several hundred velocity vector maps and to describe their fluid mechanical features. Usually techniques like averaging (in order to extract the information about the mean flow and its fluctuations), conditional sampling (in order to distinguish between periodic and non-periodic parts of the flow), and vector field operators (e.g. vorticity, divergence in order to detect structures in the flow) are applied.

Analysis of the information: At present this is the most challenging task for the user of the PIV technique. PIV being the first technique to offer information about complete instantaneous velocity vector fields allows new insights in old and new problems of fluid mechanics. New tools for analysis such as proper orthogonal decomposition (POD) (Wiegel and Fischer, 1995) or neural networks (Carosone et al, 1995).

A vector field is generated from the input images. The grid engine breaks the input images up into smaller spots for processing and initializes the vector field. For each grid point, the process manager copies the pixels from the input images into the spots and passes the spots to the spot mask engine. The spot mask engine conditions the spots for processing and passes the spots to the correlation engine. The correlation engine computes the correlation function and returns it as a correlation map. The peak engine finds the peak location in the correlation map. The process manager then stores the velocity, and export plugin data into the vector. This loop continues until all of the grid points have been processed. If a multi-pass grid engine is being used and there are more processing passes to go, the vector field is validated using the pass validate macro. The pass validate macro is set to filter out bad vectors and fill in holes with interpolated vectors. This preliminary vector field is then fed into the Grid engine and used to optimize the next processing pass spots based on the displacements measured in the previous pass. The new optimized list of grid points is then processed. If the processing

was the final pass, the vector field is validated using final validate macro. The macro validate is used to remove bad vectors, interpolate vector holes, and smooth the vector field before saving to a vector file. The final validate macro is typically less aggressive than the pass validation in interpolating and filling holes. The vector field is then saved to disk and a message sent to Tecplot for advanced flow field analysis and display.

Hart correlation processing: In Hart correlation processing, the compression ratio is used to set the number of pixels used in computing the correlation. With a compression value of 0.9, the 90 % of pixels with the least significance are excluded and the 10 % of the spot pixels that are most significant are used in computing the correlation. A high compression ratio will include more pixels in the correlation and may or may not increase the correlation map signal-to-noise ratio. The effect of the compression ratio may be seen in the Process Monitor in the Masked Spots images. In the masked spots the pixels that were removed by compression are set to 0. If particle images are missing from the masked spots, the compression ratio is set too high.

Spot reduction: This is a plugin parameter and is the amount the spot size is reduced between processing passes. A spot reduction of 2.0 indicates that the spot size is $\frac{1}{2}$ the width and $\frac{1}{2}$ the height of the previous processing pass increasing the number of vectors 4 times. If the spot reduction were increased to 4, the spot width and height would be $\frac{1}{4}$ the previous spot size and the number of vectors will increase by 16 times. If the final spot sizes are smaller than the starting spot sizes, the spot size will be reduced by a factor of 2 and the number of vector rows and columns increased by a factor of 2, giving 4 times the number of vectors with each pass. When the central difference offset is set to off, spot A is centered on the vector (x,y) location, spot B is offset by the particle image displacement distance. By offsetting the spots by the particle image displacement distance, lost pairs due to in-plane motion are eliminated increasing the correlation

signal-to-noise ratio. Offsetting the spots by the particle image displacement distance also allows for smaller spots since the $\frac{1}{4}$ displacement rule no longer applies. Using recursive grid algorithms allow for more accurate and higher density flow measurements. The double correlation validation is a unique validation scheme essential for validation of smaller spot sizes and increases peak selection accuracy. Herein, the spot offset algorithm moves both spot A and B by one-half the particle image displacement measured in the previous processing pass, relative to the vector (x,y) location. This allows the determination of the dominant peak, which increases the cross correlation peak selection accuracy.

2.3.3.4. Stereo PIV: mapping function generation

Since the cameras in the Scheimpflug configuration are generally not normal to the light sheet, angular viewing must be accounted for. A rectangular grid structure imaged in such an arrangement appears as a trapezoid, a situation easily compensated for using a comprehensive mapping function. The influences of refraction through walls and similar optical influences are also overcome. The mapping function that establishes the unique relationship between the object plane, or the measurement plane in the flow, and the image planes in the cameras is generated using a target. A dual plane dual side target that has multiple planes of markers on both sides allows the mapping function generation without traversing the target. This allows the two cameras in a stereoscopic system to be setup in any desired fashion. They can be placed on either side of the light sheet or both on the same side to suit the experimental facility geometry. The target has a built-in mirror to position it in the light sheet plane. A unique advantage of this on-line calibration approach is that camera angles and other parameters need not be measured, even for an asymmetrical camera arrangement.

The calibration grid target is first aligned with the center of the light sheet and centered on the camera system optical axis. Images of the target from the two cameras are captured and saved. The calibration grid images are analyzed and the centroid of each calibration marker stored in a target file. The locations of the marker points in the fluid are also stored in the target files. The set of calibration point locations in the fluid and the set of measured marker centroids are used to generate the calibration polynomial equations for each camera. Using high order polynomials allows other image distortions such as those caused by lens aberrations and distortions of access windows to be corrected by the calibration process. A set of mapping functions are generated from the calibration polynomial equations. The mapping functions are used during stereo PIV processing to generate three component velocity vectors. To improve signal to noise ratio, the gray scale for each image can be modified by changing the offset, gain and threshold.

2.3.3.4. Guidelines

In order to get best results from a PIV experiment, the following control parameters need to be optimized: Laser energy, Δt , image shift, interrogation spot size (area), camera magnification, light sheet dimensions, seed particles and their concentration. Interrogation area must be small enough such that one vector describes the flow at that spot. This puts a limit on the velocity gradient in an interrogation region. If the gradient is too large, then the displacement peak will become broader with a lower peak height. When this happens, measuring on noise is more likely. There should be three or more particle pairs per interrogation spot. Improvement in accuracy is small for cases for more than 5 pairs of images. Maximum in-plane displacement should be $\frac{1}{2}$ of interrogation spot size, while the minimum in-plane displacement could be zero. The maximum out of plane displacement should be less than $\frac{1}{4}$ of light sheet thickness. The

procedure should be to visually verify the flow field first, i.e., varies the control parameters to obtain a believable flow field vectors. The next step should be to verify that the conditions describes above are met.

Velocities can be measured using one of the three correlation processes: Autocorrelation, 1-Frame Cross-Correlation and 2-Frame Cross-Correlation. The differences in these correlation techniques is the image window areas for the first and second particle images. In autocorrelation, the same image window is used for both the first and second image window. In 1-frame cross-correlation, the second image window is offset from the first image window on the same frame. In 2-frame cross, the first image window is on frame 1 and the second image window is on frame 2. Each of these processing techniques has advantages for some applications. Autocorrelation is for multiple exposure images where the particle motion and image shift together give less than $\frac{1}{4}$ of the interrogation spot image displacement. This is the classical PIV processing technique. 1-frame cross-correlation is also a multiple exposure technique. It is used when the image shift displacement is large relative to the particle motion displacement. By offsetting the second image window from the first by the mean particle image displacement, distance high resolution measurements can be made. Else, it would prohibitively require large interrogation spot sizes for autocorrelation processing. By offsetting the second image window by the mean particle image displacement, the interrogation spot size can be reduced and fewer lost pairs relative to autocorrelation will result. 2-frame cross-correlation measures the distance which particles have moved between exposures on two image frames. Each of these frames has only one pulse of light. By knowing the sequence of the first pulse images and the second pulse images, the processing signal-to-noise ratio relative to the single frame techniques is improved. 2-frame cross-correlation can measure zero displacements and reversing flows without

image shifting. It can also be used with image capture systems with an effective frame rate high enough so that the particle images on two successive frames give particle image displacements in the measurable range.

2.3.3.5. Rules of thumb for autocorrelation PIV analysis:

Rule 1: Interrogation spot size should be small enough so that one vector describes the flow within that spot.

Rule 2: There should be more than ten particle image pairs per interrogation spot.

Rule 3. Maximum in plane displacements should be less than $\frac{1}{4}$ of the interrogation spot size.

Rule 4.: Maximum out of plane displacement should be less than $\frac{1}{4}$ of the light sheet thickness.

Rule 5: Minimum in-plane displacement should be two-particle diameters.

Rule 6: Exposure must be large enough to clearly show the particles.

2.3.3.6. PIV image processing to estimate bubble size

Bubbles reflect very high intensity laser light, which is very bright compared to seeding particles because of their larger size. To circumvent this problem, fluorescent seeding particles are used, and camera is fitted with red filter. Thus, reflected green laser light from original light sheet is not captured by the camera and PIV records the liquid velocity. However, bubbles do reflect this fluorescent light also, which can be detected by proper image processing. In this, the particle image is brightened by histogram correction, and then filtered to remove seeding particle image. This is accomplished by spatial low-pass filter (similar to blurring the image) based on morphological image

reconstruction. This step basically separates the PIV image processing algorithm from high speed camera image processing for bubble sizing. After filtering, the image is thresholded, holes are filled and objects in the image are detected to measure their properties like pixel area, maximum and minimum dimension, and centroid.

The image processing sequence is illustrated in Figure 2.50.

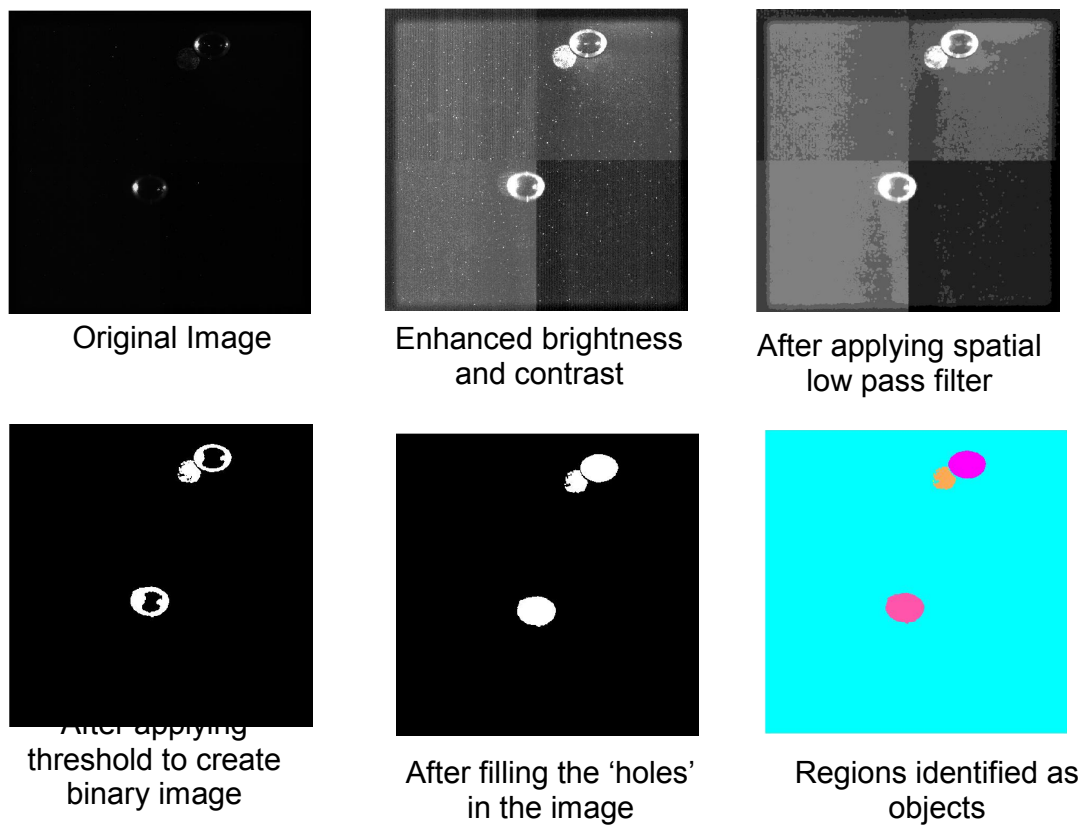


Figure 2.50 PIV Image processing to identify bubbles

2.4. Shadow Imaging

2.4.1. Previous Work

A common method in dispersed two-phase flows is shadowgraphy. A shadow image of the gas bubbles is recorded on the CCD camera and the velocity distribution of the gas bubbles is evaluated with a particle tracking velocimetry (PTV) algorithm. The velocity of the liquid cannot be determined with the shadowgraphy technique. Therefore this technique is often combined with a PIV measurement. Tokuhiko et al. (1998) used two cameras facing each other for combined PIV and shadowgraphy measurements on a single bubble. They did not use the information of the position of the bubble for their PIV evaluation, but they deleted all PIV velocity information at the area of the gas bubble in a post processing procedure.

Lindken and Merzkirch (1999) used two cameras under a 30° angle, one for PIV measurements and the other for shadowgraphy measurements, to measure the velocity with 2D PIV and the bubble velocity with 3D PTV. The 3D bubble velocity was measured very inaccurately because of the weak signal from the gas bubble in the PIV measurement. With this set-up they were able to determine the position of the bubbles relative to the 2D-PIV measurement plane.

In another work, Bröder and Sommerfeld (2003) report PIV measurement based on shadow imaging in a rectangular airlift reactor. Double pulsing LED backlight was used to generate the particle and bubble shadow images. The discrimination between particles and bubbles was achieved by the size difference between seeding particles and bubbles (150 µm vs. few mm). Diaz and Riethmuller (1998) carried out PIV and shadowgraphy measurements for Taylor bubbles.

2.4.2. Equipment

For shadow image recording, any camera can be used with backlight. In the current work, a high speed camera (Photron Fastcam super 10kc) and a frame straddled PIV camera have been used. Images were recorded at low frame rate of 30 fps or lower with high shutter speed of 1/1000 s. The low frame rate was principally selected to avoid repetition of the same bubbles.

The schematic of the setup used for image recording is shown in fig 2.51. A high intensity white backlight was used to generate silhouettes of bubbles. A diffuser plate was used in between the light and the column to even out the intensity gradients in the background, again to aid image processing. At a time, 700 images were recorded for subsequent analysis to find bubble size distribution. Before recording, a marker plate was inserted in the column in the area of measurement, for calibration in the image processing program. An area of 50x50 mm was selected for bubble size measurement, just below the hole made in the column for mounting pressure sensor.

Bubble image generation

The silhouette images of bubbles are generated by using the principle of total internal reflection, as illustrated in figure 3.2. When light travels from denser to rarer medium or vice versa, it bends the path of motion and the ratio of the sines of the angle is given by refractive index (Snell's law).

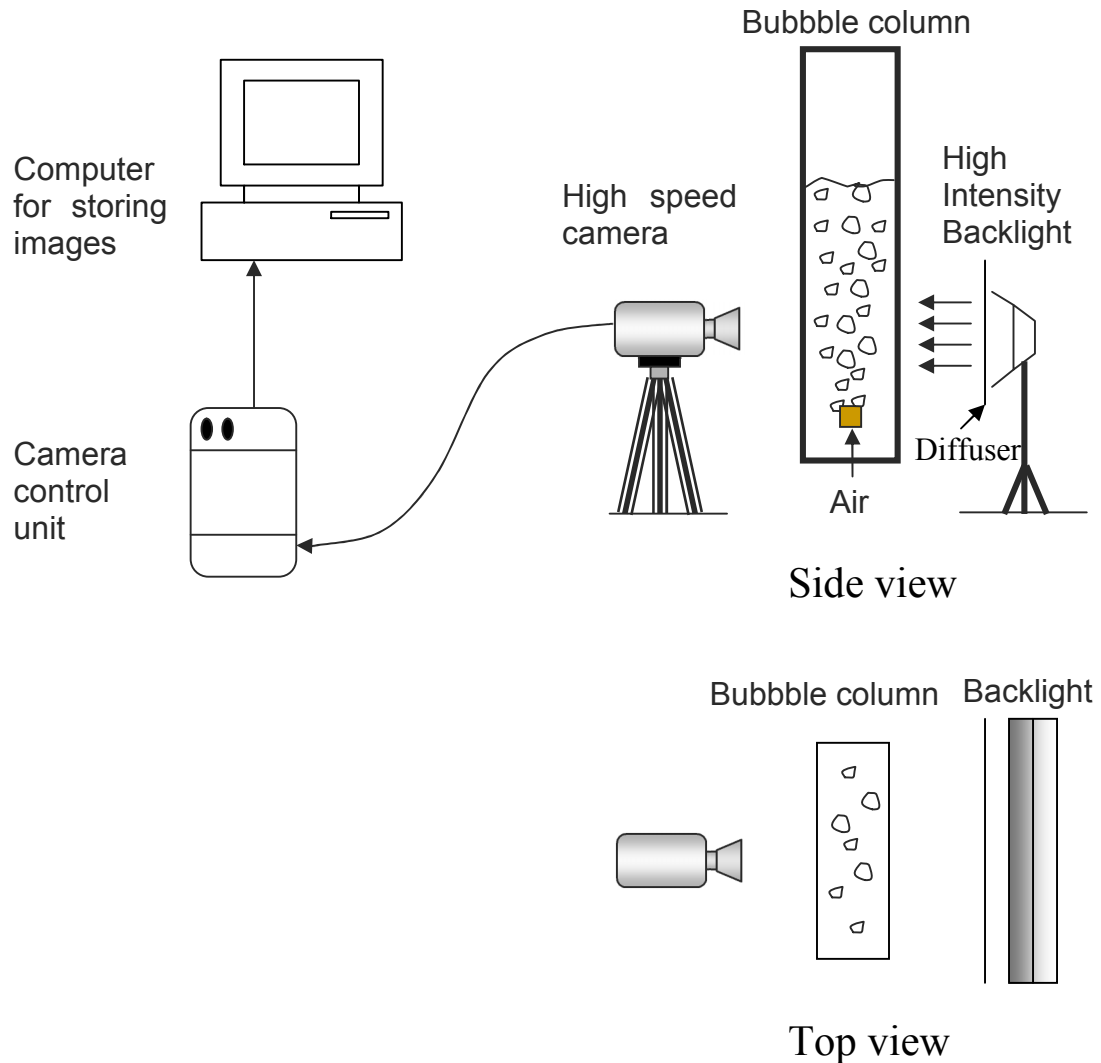


Figure 2.51: Experimental setup for high speed photography in bubble column

However, when light travels from denser to rarer medium (say from water to air) the light ray bends in direction outward from the surface normal. If the incident angle w.r.t. surface normal is higher than a critical angle, the angle of light ray leaving from the surface w.r.t. surface normal is higher than 90° and the ray reflects back in the medium instead of refracting. This is called total internal reflection. As illustrated in figure 2.52, curvature of bubble surface causes the parallel input rays from backlight to subtend different angles with local surface normal on bubble surface. When this subtended angle becomes higher than a critical angle, the rays reflect back towards water, and image generated on camera is dark in these regions which is called a 'Silhouette' image. However, instead of being completely dark, there is a bright spot in

the central region of a bubble, and it appears as if there is a hole in the bubble in the image, as an artifact. This needs to be corrected in the subsequent image processing steps, by identifying and ‘filling’ the ‘holes’ generated due to this phenomena.

Shutter speed required to obtain blur-free images

The shutter speed decides the time for which image is focused on the CCD chip of camera. If the object of interest is moving, then its image also moves on the ccd, and the same image gets recorded on multiple pixels. This causes the image to be blurred and poses difficulty in deciding dimensions of the object. Thus, the fastest of shutter speed must be chosen to virtually ‘freeze’ the motion of bubbles. However, very high shutter speed means very low exposure time, causing a very low intensity image. Thus, an optimum shutter speed has to be calculated, which just suffices to minimize the blur and still maintains the brightness of the recorded image.

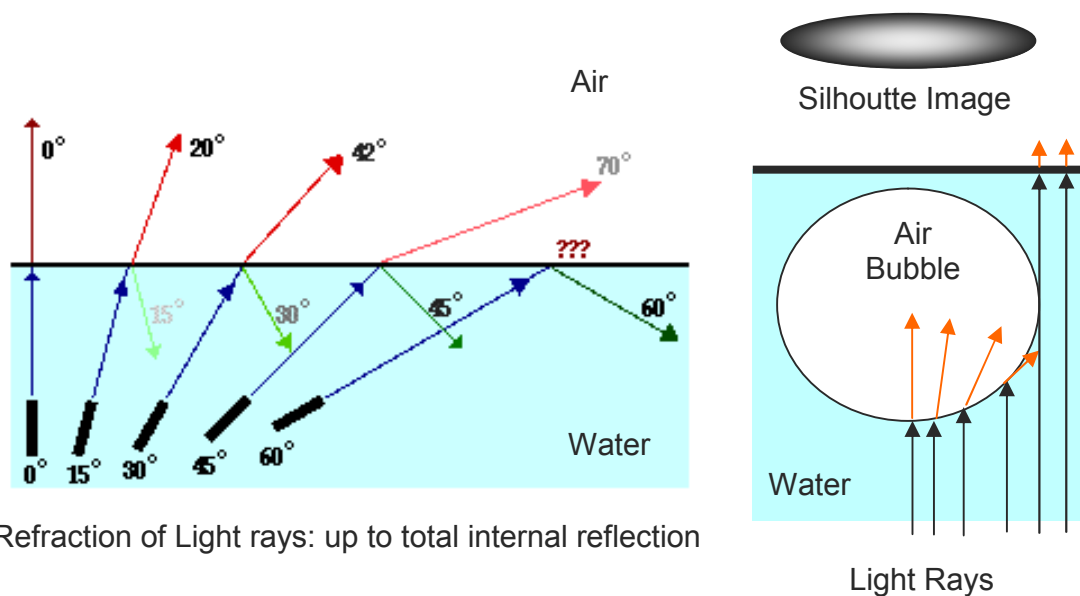


Figure 2.52: Illustrating total internal reflection

A simple criterion for estimating the blur is the fraction of the dimension of bubble traveled by bubble in the shutter opening time. Smaller bubbles cause greater of this blur because of their less diameter. Calculating the time required by 3 mm bubble to travel a distance equal to its diameter, by using its terminal rise velocity gives:

$$t_{blur} = 0.05 \times \frac{d_b}{v_b} = 0.05 \times \frac{0.003}{0.2} = 0.00075s$$

And for 20 mm bubbles the same calculation shows:

$$t_{blur} = 0.05 \times \frac{d_b}{v_b} = 0.05 \times \frac{0.02}{0.33} = 0.00303s$$

Thus, the shutter opening time required is less than 1 ms for blur free images while allowing the bubbles to travel less than 5% of their diameter. In this work, the shutter speed chosen is 1/2000 in order to strike a balance between the image brightness and the blur.

2.4.3. Data Processing of Shadow Images

2.4.3.1. High speed photography

The images recorded with high speed camera were processed to identify different bubbles and to obtain the corresponding bubble size distribution. The background illumination with high intensity, flicker free light along with diffuser plate makes a uniformly bright white background. The bubbles appear dark against this, because of the total internal reflection phenomena. This makes it easy to separate bubbles from background. The camera being a color camera, records images with 3 components (Red, green and blue) with 8 bit precision, i.e. their intensity values vary from 0 to 255. These images are first converted to grayscale images for further data processing. The images were processed by programs written in MATLAB. The sequence of processing is illustrated in figure 2.53.

2.4.3.2. Image processing for estimation of bubble size distribution

The bubble image was inverted (i.e. subtracted from maximum intensity, 255) so as to make the bubbles appear brighter in contrast to dull background. This is a favorable composition for image processing. The background image was separately recorded by focusing on the measurement area without aeration, thus capturing the non-uniformity in the illumination and the noise caused by scratches etc. on the column wall. This background image was subtracted from the bubble image to make the background image uniformly illuminated and easily separable from the bubble image. After subtracting the background, the image becomes fairly dull, because of non-uniform intensity reduction due to background subtraction. This is corrected to some extent by technique of histogram correction. In this, the intensity values in grayscale image matrix are mapped to new values such that 1% of data is saturated at low and high intensities of original image. This increases the contrast of the output image, thus further easing the separation and improving the robustness of the program.

This background subtracted and corrected image is then subjected to thresholding, which is the real separation step for isolating bubbles from background. In this, pixels having value larger than a threshold are assigned value of 1, while others are assigned zero. This makes a black and white image out of the supplied grayscale image. There are 'Holes' in the bubbles thus isolated, because some light rays manage to pass through the region near the center of the bubble. These holes are filled by morphological reconstruction, which detects the local minima, and flood fills them, to remove the holes in the image. This prepared image is then subjected to object decomposition, which is based on a different morphological operation, and this also labels the local maxima. The bubbles in images are now appearing bright, and each bubble comprises of the local maxima. This detected region is labeled in sequence, and analyzed for its various

properties like pixel area, centroid, maximum and minimum dimension, dimension of the ellipse fitting the region etc. In figure 2.53, each of these identified regions is labeled with a different color, and their centroid is marked by a '+' symbol at the centroid location in image.

The diameter of a bubble is reported as the diameter of a circle having area equal to the represented by a particular bubble in the image. These values are appended to a data file containing the data of the bubbles identified in the subsequent images in the given image set at the same gas flow rate. At least 200 images were processed to obtain the bubble size distribution.

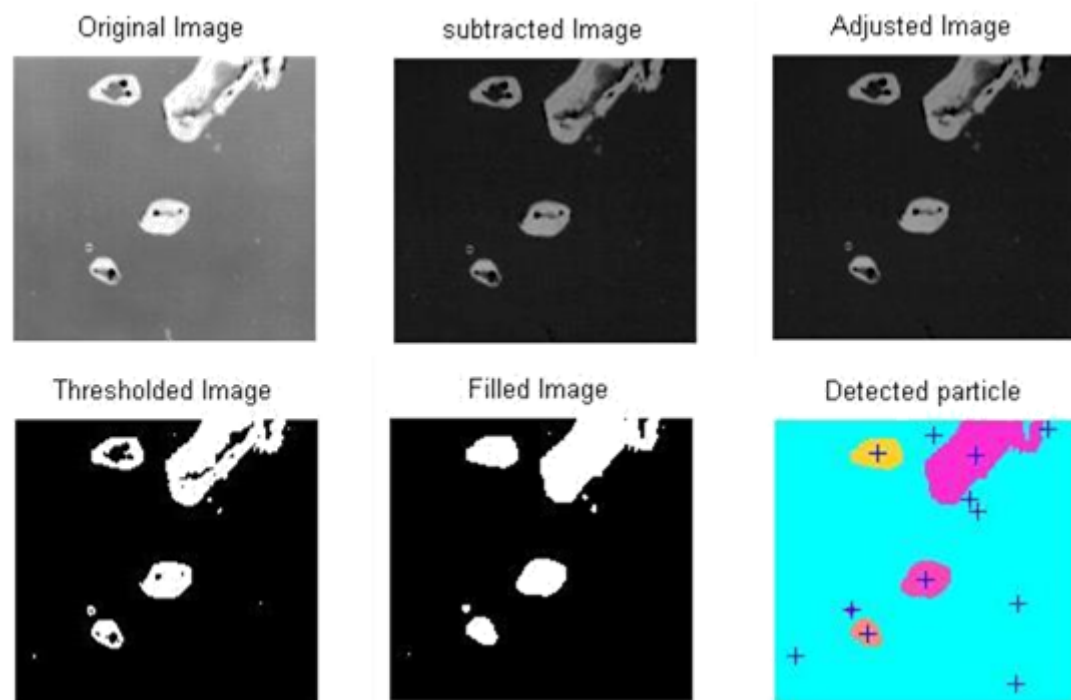


Figure 2.53: Image processing of high speed camera images

2.5. Planar Laser Induced Fluorescence (PLIF)

Planar laser induced fluorescence (PLIF) technique is principally based on the temperature dependence of fluorescence, induced by laser radiation of organic dye. It is a non intrusive optical method and has the similar basic components as that of PIV. A typical application of PLIF is temperature measurement in the domain either, gaseous media (Gross et al., 1987) or in liquid media for the study of heat transfer. In many cases, this technique has been used together with velocity measurements, with either PIV (Nakajima et al., 1990; Sakakibara et al., 1993) or LDA (Lemoine et al., 1999). The PLIF technique used in the present work is simultaneously with PIV. The image capturing, synchronization for PLIF is same as in PIV described in previous section.

2.5.1. Literature Review

Planar laser-induced fluorescence (PLIF) is an excellent technique for measurement of the two-dimensional local concentration and for mixing studies in flowing systems. Several researchers (e.g. Houcine et al. 1996; Karasso and Mungul 1997; Muhlfriedel and Baumann 2000) have reported quantitative measurement in liquid flows. Most of these researchers used a single dye as a fluorescent tracer. Coppeta and Rogers (1996) have presented an overview of dye characteristics and possible sources of error for PLIF. Sakakibara and Adrian, (1999) introduced the two dyes approach for the PLIF measurement accounting for intensity variation of laser sheet. Dahikar et al. (2010) describe the use of two color PLIF combined with PIV for simultaneous velocity and temperature measurement. Sathe et al. (2010) describe the use of combined PIV/PLIF in refractive index matched liquid-liquid dispersion for drop size and liquid hold up, along with the continuous phase velocity measurement.

2.5.2. *Equipment*

2.5.2.1. *Principle of PLIF*

The working of PLIF is based on the concentration and temperature dependence of fluorescence of organic dyes dissolved in a liquid medium. This dependence on the temperature of fluorescence is referred to the literature by many authors (Andre and Molinari, 1976; Walker, 1987) and it is strongly influenced by the fluorescent molecule itself. The fluorescence dependence on the temperature of fluorescein sodium is 0.3 % per K and is about 5% per K for rhodamine B (C₂₈H₃₁ClN₂O₃). (Guibault, 1973). Hence rhodamine B seems to be an adequate tracer for temperature.

When a laser beam passes through a liquid medium seeded with an organic fluorescent dye, the fluorescence intensity is affected by the absorption of incident laser beam and by re-absorption of fluorescence itself, across the absorbing medium. According to Beer's law, the fluorescence intensity can be written as follows (Lemoine et al 1999):

$$I = k_{opt} \varepsilon_1 \eta C e^{-C(\varepsilon_1 b + \varepsilon_2 e)} \quad (2.36)$$

where, ε_1 and ε_2 are constants depends on the type of tracer and laser.

For very low concentrations, the above equation indicates that the intensity is proportional to dye concentration. Thus

$$I = k_{opt} \varepsilon_1 \eta C \quad (2.37)$$

The temperature dependence of the fluorescent emission appears on the one hand in the absorption coefficient ε_1 and on the other hand in the fluorescence quantum yield, where quenching phenomena are involved. The absorption coefficient ε_1 is proportional to the

Boltzmann fractional population of the molecules in the absorbing state (Hiller and Hanson 1990). However, in condensed media, where large band-width energy levels are involved, at low temperatures (0-100⁰C), the fractional Boltzmann population is quite insensitive to temperature. The major part of the temperature dependence can be found in the fluorescence quantum yield. The fluorescence quantum yield corresponds to the ratio between the number of quanta emitted by fluorescence and the number of absorbed quanta. The quenching of the excited state is involved in the fluorescence quantum yield. Quenching phenomena, which compete with the fluorescence emission, are all the more important when temperature is high. These phenomena correspond to non-radiative transitions, which tend to reduce fluorescence intensity. The total number of possible transitions (radiative or not) per unit of time is $A_{21} + Q$, where A_{21} is the spontaneous emission Einstein coefficient and Q the quenching rate. Considering the fluorescence natural quantum efficiency η_0 , only $\eta_0 A_{21}$ transitions per unit of time are radiative. The natural fluorescence quantum yield is the quantum yield in quenching absence, and typical values of η_0 range from 0.9 to 0.95 (Glowacki 1964). The other transition processes are unknown.

Both the spontaneous emission Einstein coefficient A_{21} and the natural fluorescence efficiency depend only on the fluorescent molecule. The fluorescence quantum yield is defined by (Andre and Molinari, 1976):

$$\eta = \frac{\eta_0 A_{21}}{A_{21} + Q} \quad (2.38)$$

Q , the quenching rate is proportional to the concentration in quenchers $[M]$:

$$Q = k_q [M] \quad (2.39)$$

k_q is the quenching constant, which depends strongly on temperature. For very low tracer concentrations, the quenchers are only the water molecules, whose concentration is assumed to be constant. According to Glowacki (1964), the quenching constant k_q can be modeled as follows:

$$k_q = k_{q_0} e^{-Ea/RT} \quad (2.40)$$

Ea is the activation energy involved in collisions between a fluorescent molecule and a molecule of the solvent and k_{q_0} is a constant. Both depend only on the properties of the fluorescent tracer and of the solvent. It can be also noted that the quenching phenomena have a much larger importance than the radiative one. This assumption is verified in gases, at pressure higher than a few 10^3 Pa (Lemoine and Leporcq, 1995) and in condensed media:

$$Q \gg A_{21} \quad (2.41)$$

According to the previous assumptions, fluorescence intensity can be expressed as a function of temperature as

$$I = k_{opt} \frac{\eta_0 A_{21}}{k_{q_0} [M]} C e^{-Ea/kT} \quad (2.42)$$

Two constants, K_{spec} and β , depending only on the physical and spectroscopic properties of the fluorescent molecule, can be defined:

$$k_{spec} = \frac{\eta_0 A_{21}}{k_{q_0} [M]} \quad (2.43)$$

and

$$\beta = \frac{Ea}{k} \quad (2.44)$$

The expression of the fluorescence signal as a function of temperature can be derived from Eq. (2.25):

$$I_f = k_{opt} k_{spec} C e^{-\beta/T} \quad (2.45)$$

2.5.2.2. Experimental set-up

The schematic of experimental set up is shown in Figure 2.54. In these measurements, the laser source (L) was a pulsed Nd:YAG (make: New Wave Research Inc.) having pulse duration of 6 ns and was synchronized with the camera using a synchronizer (S). The optics included a combination of cylindrical and spherical lenses, attached in view of creating a thin laser sheet (thickness \sim 1mm). The images were captured using two high resolution 4M CCD cameras (of 15 Hz frequency), one (C1) was placed perpendicular to the laser sheet, and the other (C2) in front of a dichroic mirror (M, placed at 45° between the Camera (C1) and the laser sheet). Three kinds of optical filters (a dichroic mirror, a narrow band pass optical filter and long wave pass filter) were used to separate the laser induced fluorescence (LIF) lights from scattered laser lights, and then recorded them separately to obtain PLIF and PIV images simultaneously. A dichroic mirror separates the LIF light ($\lambda \sim$ 670 nm) for PLIF and scattered light ($\lambda =$ 532 nm) for PIV images. LIF light directly passes to the Camera (C1) through high wave pass filter, while scattered light is reflected to camera (C2) through a low band pass filter.

2.5.2.3. PLIF calibration

In order to quantify the intensities, calibration images at known uniform concentration or temperature conditions with laser and camera operating with same settings as in experiment are required. Particularly, for temperature determination two calibration images are required, while for concentration determination one image is sufficient using origin as the location of the second point as shown in Figure 2.55.

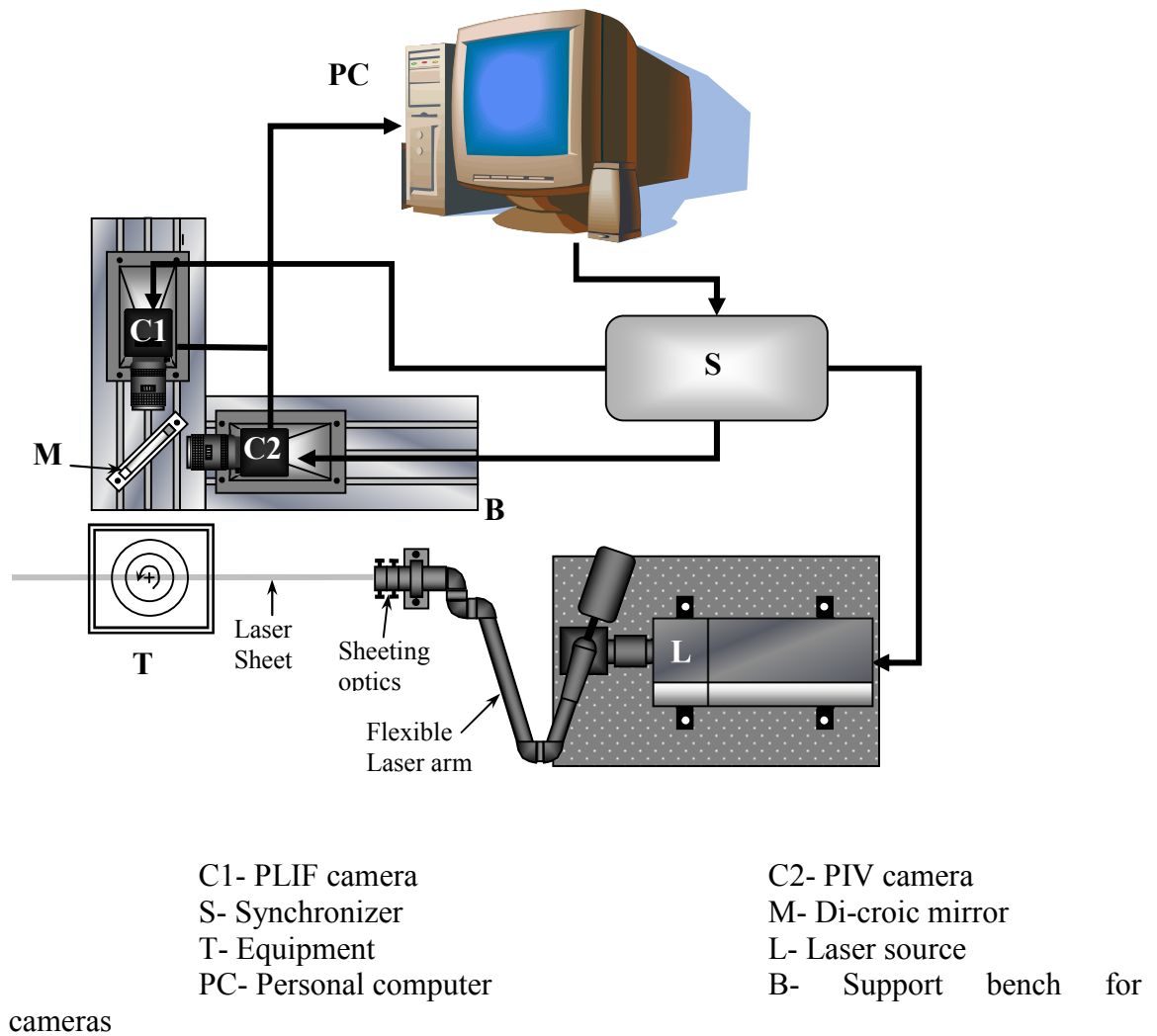


Figure 2.54. Schematic of experimental set up of PIV and PLIF

2.5.3. Processing of PLIF Images

The processing of PLIF images in stage-wise manner. Initially the pixel by pixel calibration is performed followed by the conversion of image intensity to scalar quantities. The various difficulties in calibration are (i) special variation in laser sheet intensity (ii) camera noise (iii) unwanted background signals. These problems can be corrected by subtracting background images from PLIF images. To convert the image intensity to scalar quantities the following PLIF processing methods can be used:

Ratiometric method

For each pixel in PLIF images, the two closest calibration points in terms of pixel intensity are used to compute the scalar quantity at that pixel using a two-point linear equation.

Linear Fit Method

For each pixel in PLIF images, all the calibration points are used to obtain a linear equation between intensity and scalar quantity, which is then used to compute the scalar quantity at that pixel.

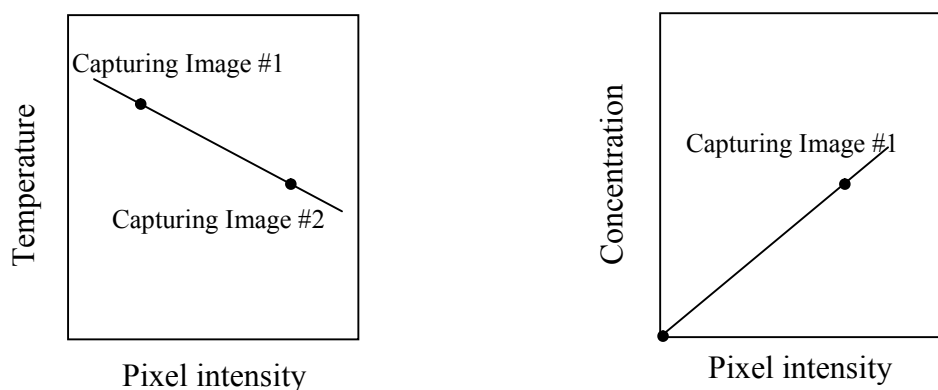


Figure 2.55 PLIF calibration

2.6. Miniature Pressure Sensor Arrays

2.6.1. Previous Work

For bubble columns, pressure based techniques have been extensively used in past for identification of flow regimes (Letzel et al., 1997; Lin et al., 2001), identification of oscillation frequency of central plume in a two dimensional column (Buwa and Rannade, 2002) and estimation of average bubble size in slurry bubble column (Chilekar et al., 2005). In context to the attempt towards the identification of the flow structures using pressure signals is concerned, liquid circulation velocity has been estimated so far based on the cross-correlation between two pressure sensors located at some distance (Drahos et al., 1991; Vial et al., 2000; Kulkarni and Joshi, 2006). Gandhi et al. (2007) have described the use of wall pressure fluctuations for estimation of mass transfer coefficient in surface aereator.

Application of stochastic estimation using wall pressure fluctuations for the extraction of the coherent motion in turbulent flows was first proposed by Adrian (1975). Down the time, the technique has been successfully applied to quantify large scale structures in turbulent flows like, identification of the conditional eddies of isotropic turbulence (Adrian and Moin, 1988), extraction of the spatio-temporal flow field characteristics of turbulent boundary layer structures (Guezennec, 1989), jet mixing layer (Cole et al., 1992), separated flows (Stokes and Glauser, 1999). However, Naguib et al., (2001) was the first to investigate the flow structures associated with surface pressure events in a turbulent boundary layer using stochastic estimation, followed by Ukeiley and Murray, (2005) for open cavity system and Hudy et al., (2007) for separated flow, both using PIV for flow field identification.

2.6.2. Equipment

Pressure fluctuation measurements involve pressure sensors having sufficiently high dynamic accuracy; a transmitter to amplify the signal from sensors; a junction box (channel box) for connecting multiple sensors at one point; and the A/D converter, which converts the analog signal to equivalent digital magnitude. The accuracy of the measurement and the bandwidth is collectively the result of all three components.

2.6.2.1. Pressure measurement

Pressure sensors used for dynamic measurement are based on the principle of capacitance measurement, strain gauge, piezoresistive and piezoelectric. A transmitter supplies the excitation voltage for sensor, and also amplifies the signal from sensor. The analog signal from the signal conditioner is then subjected to digitization. The data was acquired by using an external USB data acquisition card NI DAQPAD 6020E and Lab View software was used to interface the card with a Pentium-4 personal computer.

Further details pertaining to hardware part and instrumental tests pertaining to pressure fluctuation measurement are discussed in detail in following sub-section.

Aspects	Specifications
Principle	Miniature IS silicon diaphragm
Make	Kulite Inc., USA (Model 19C003GK1)
Working principle	Piezoresistive
Pressure range	5 psig
Bandwidth	150 kHz (Resonant frequency)
Size	19 mm
Type	Threaded mount (XTL 190) Cylindrical tube (XCQ 093)
Location on bubble column	L1
Signal conditioner (make)	Dewetron, USA

2.6.2.2. Rectangular bubble column

Pressure fluctuation signals were measured in rectangular bubble column principally for the calibration of bubble size measurement technique. Pressure time series was recorded simultaneously at two locations in the column: one near to sparger and one at the location of the measurement. The acquired signal is then processed for the bubble size measurement. The rectangular column used is having cross section 15x200 mm. Two different spargers viz. single nozzle and multi nozzle (with 5 nozzles) with same free area (0.165 %) were used to observe the sparger effect on the bubble sizes obtained. The single nozzle was of 2. mm Id while in multi nozzle sparger, 5 needles with ID of 1.15 mm were used. The liquid height in column was 550 mm with single nozzle and 450 mm with multi nozzle sparger case. The superficial velocity was varied from 0.000787-0.016 m/s for single nozzle sparger and from 0.00196-0.04 m/s for multi nozzle sparger. The sensor locations are schematically shown in Figure 3.3.

2.6.2.3. Cylindrical bubble column

The method of bubble size measurement from pressure fluctuations was employed for measurement in the cylindrical bubble column with 385 mm diameter. Three axial locations were selected at the heights corresponding to H/D ratio of 1, 2 and 3. The radial locations selected were r/R of 0, 0.5 and 1.

The Sensor near sparger was mounted at 70 mm height from the sparger. The measurements were carried out for superficial gas velocities ranging from 0.02- 0.1 m/s. The pressure time series were acquired at two data rates: 100 Hz and 10000 Hz to subject them to different signal analysis. The Dual sensor probe

for velocity measurement was inserted through a special fitting into the column. The same opening made in the column for the single pressure sensors for bubble sizing was utilized for this purpose.

The schematic of the entire experimental setup is shown in Figure 2.56.

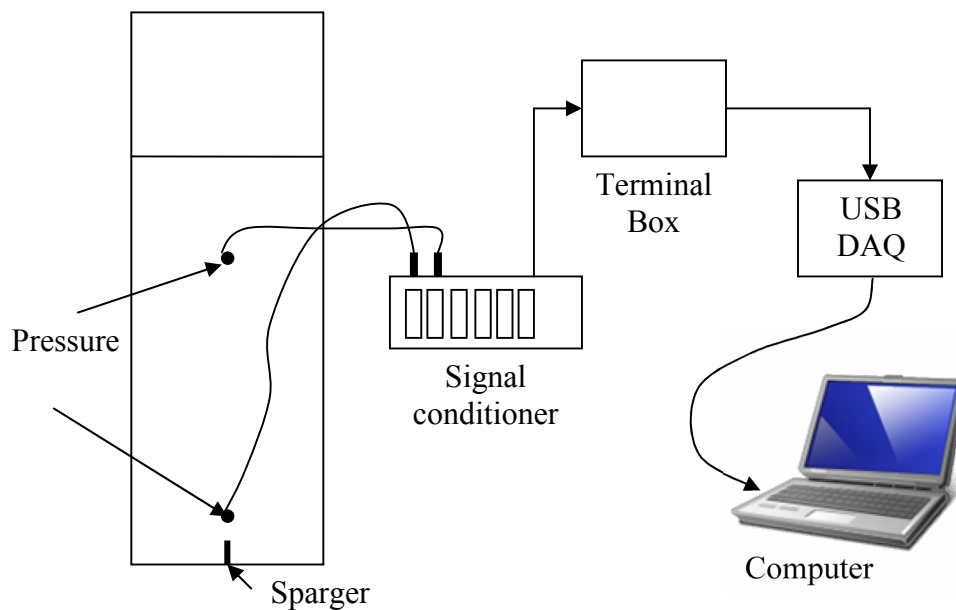


Figure 2.56 : Experimental setup for acquiring PFS in bubble column

2.6.2.4. Pressure sensors

Pressure sensors used for dynamic measurement are based on the principle of capacitance measurement, strain gauge, piezoresistive and piezoelectric. In first three categories of pressure sensor, there exists a diaphragm element, made up of metal or metal-coated quartz element, which is exposed to process fluid. Pressure is applied by process fluid on diaphragm element, which induces strain in the element. This flex in the diaphragm changes the capacitance, in case of capacitance sensors; resistance of the thin wire etched on the backside of the diaphragm, in case of strain gauge based sensor; and the resistance of the silicon element in case of piezoresistive sensors. In case of

piezoelectric sensors, a crystal, which produces measurable charge when compressed, twisted or distorted (piezoelectric effect) is used to measure pressure.

The silicon-based piezoresistor is known to provide electrical output much large, as high as 100 times, that usual strain gage wires. The dynamic range of piezoresistive sensor is comparatively high.

Piezoresistive Sensor:

Principle and operation: Piezoresistivity is a material property, particularly with semiconductors, where the bulk resistivity is influenced by the mechanical stresses applied to the material. Change in resistance of semiconductor element is proportional to the change in the strain of diaphragm element, induced by process pressure. The piezoresistors are implanted into a single homogeneous thin silicon diaphragm, which is integrated with force sensing element. These piezoresistors constitutes a part of a wheatstone bridge, to which a constant DC voltage is applied. The resistance R4 is the resistance offered by piezoresistive element, hence by pressure, while rest all three resistances; R1, R2 and R3 are constant value resistance. The output voltage V_o across the junction BD can be formulated, as by knowing the constant input voltage, called as excitation voltage.

$$V_o = V_{AB} - V_{AD} = \frac{V_{in}}{R_1 + R_2} R_1 - \frac{V_{in}}{R_4 + R_3} R_4 \quad (2.46)$$

Simplifying equation (2.46), we get

$$V_o = V_{AB} - V_{AD} = \frac{R_1 R_3 - R_2 R_4}{(R_1 + R_2)(R_4 + R_3)} V_{in} \quad (2.47)$$

2.6.2.5. Signal conditioner

Two-wire transmitter provides a constant DC voltage of 12 V to the sensor's bridge and also amplifies the output of sensor in a series of amplifiers, and provides output of 0-5 V. The gain of the amplifiers in the signal conditioner is variable, and can be adjusted by switches provided on the front panel. The conditioner also features adjustable low pass filter with cutoff frequency adjustment. However, no hardware filtering was used, and the raw signal was recorded for subsequent signal processing. The transmitter couples the excitation voltage and the output of the pressure sensors, which offers less noise at the output. The single ended output voltage obtained from sensor is subjected to digitization through a common junction box in between signal conditioner and A/D converter.

2.6.2.6. Analog to digital conversion:

The analog signal obtained from the transmitter, is subjected to digitization using analog to digital converter (ADC). An ADC transforms the information into the equivalent digital form of input analog signal, hence performs digital reading of input analog signal. Different principles for electronic reading, i.e. digitization, are a) Wilkinson's ADC, b) Successive approximation, ADC and c) Flash ADC. In case of Wilkinson's ADC, a capacitor is charged by, the incoming analog signal and then discharged at constant rate by a controlled timer. Time required for discharging till the base value of capacitor is then measured, which is proportional to the amplitude of the analog signal. In successive approximation, the controlled timer serially activates each bit of the reference input voltage range. A comparator compares the analog voltage with each bit. The bit contribution which does not exceed the analog voltage is the digitized value of the input analog signal. In case of flash ADCs, there exist a set of comparators,

hence its resolution and bandwidth is usually highest. Normally Storage Oscilloscopes have flash ADCs. In the present investigation, National Instruments DAQPAD 6020 E, multi functional DAQ is used. The ADC has resolution of 12-bit and maximum sampling rate of 100kS/s. For data acquisition, National instruments Lab View software was used. After initiation of program it asks for the file name. On declaring the file name program will continuously acquire the data, unless and until it is stopped from the respective key on the front panel.

2.6.3. Data Processing

2.6.3.1. Accuracy and resolution of pressure measurement

Accuracy in amplitude domain, i.e. voltage, hence pressure, is mainly governed by the accuracy and resolution digitizer. For example, a signal conditioner generates a voltage level of say 10V at full scale pressure. The full scale pressure of sensors is say, 3 psig $\equiv 20.684E+03$ Pa. The resolution of digitizer is say 8-bit. The overall resolution then comes out to be 80.797 Pa, and accuracy at full scale becomes ± 40.398 Pa. The specified accuracy of sensor is to be ± 0.1 % at full scale then it works out to be ± 20.68427 Pa at full scale, which is an order of magnitude higher as compared to that from the digitizer, also the sensitivity of the sensor is known to be much higher as compared to above value. Hence the range of the pressure sensor and resolution of digitizer need to carefully select to cover the whole range of measurement. In the present investigation, pressure resolution of 0.5 Pa was obtained.

Regarding the resolution in time domain, sensor and signal conditioner plays a major role, rather than digitizer. However examining the frequency range of interest for bubble column experiments, designed for investigating the macroscopic structures,

frequency response of even 100 Hz gives satisfactory results. This frequency range is less by several orders of magnitude as compared with the response time. As per manufacturer's specification of both the sensors, it is 150 kHz (natural resonant frequency) for Kulite XCQ-64.

2.6.3.2. Noise analysis and data acquisition

One of the main problems in non-linear time series sequence analysis has to do with the fact that time signals from natural phenomena, especially physical systems, are corrupted by noise. The unwanted electronic fluctuation in analog signal, which are not associated with the pressure changes from the system, is another factor, which decides the overall resolution and the quality of the time series. This unwanted part of the signal is called as noise. Although one can do one's best to limit the amount of noise in the time signal as much as possible by carrying out a very-well controlled measurement, a complete separation between the deterministic component in the signal, if present, and the noise is impossible. The signal will always contain some noise due to inaccuracies that can never be ruled out completely. These inaccuracies may be caused by e.g. (i) the measuring device (relative and absolute accuracies), (ii) the analogue-to-digital conversion (discretization errors) or (iii) minor fluctuations in settings of important system parameters (e.g. flow, pressure or temperature in physical experiments).

The explicit noise sources are pick-up signals from various external sources, and vibrations. There is no standard methodology for determination of this kind of noise in terms of magnitude and frequency. Hence need to be accounted *at actual*. However following are few known sources of pick-up.

- 1) Power supply pick-up, the frequency of this noise is essentially the same as that of power supply mains (50Hz in India) or its harmonics, as 100Hz, 150Hz, 200Hz, etc.
- 2) Improper earthing creates ground loops and induces an *emf* in the circuit.
- 3) The high-tension cables.
- 4) All the possible sources of EMI radiation, as compute monitors, mobiles, power supply cables, tube-lights, electrostatic field around the DAQ units, magnetic sources, etc.
- 5) Improper grounding and pick-up noise at a point induces the cross talks between the channels and induces a biased in estimates.
- 6) Any material in the neighborhood of measurement station, which is capable to absorb moisture, including the equipments itself.
- 7) Heavy-duty equipments in the neighborhood of sensors, which induces vibrations to the sensors.

The pick-up noise induced in cables, cabinets, and connectors by the above sources is induced in the measurement signal. Following are precaution taken to reduce this type of noise, which, to a large extent, reduces the noise.

- 1) Earthing should be proper
- 2) Multiple earthing should always be avoided
- 3) Use of spike suppressors (particularly the inductors) at the mains.
- 4) Use shielded and preferably twisted pair cables.
- 5) Avoiding the carriage of voltage signal over a long distance, specifically from sensor to signal conditioner.
- 6) The cables, sensors, should be away from any electric, magnetic, and electromagnetic fields.

7) The instruments need to be protected from dirt and moisture and the causes.

To deal with the problem of noise, one could propose three basic approaches (Cor *et al.*, 1993).

Method 1 (Before Measurement) – Try to calculate or measure the time series as accurately as possible. This means in the case of measured time series: (i) use an accurate measuring device (e.g. inaccuracy less than 1.0% or even 0.1% of the full scale); (ii) use the full scale as close as possible to the maximum difference between measured data points that can be expected; (iii) do the analogue-to-digital conversion with at least 12 bit precision (1:4096), though in many cases even 16 bit (1:65536) precision may be required.

Method 2 (During measurement) – Remove high frequency components in the signal using a low-pass filter. While doing so, one should be sure that still relevant and characteristic time scales in the signal are not removed. In general it may be possible to recognize these in the (unfiltered) power spectrum. A useful first estimate would be that one should not apply a low pass filter frequency smaller than about 10 times the dominant frequency in the time signal.

Method 3 (After measurement) – Try to clean the data set by a noise reduction algorithm or apply singular value decomposition and then pass the cleaned time signal through a dimension and entropy estimation routine. However, a disadvantage of these methods may be that they alter the original time series in a way that is not known a priori. Therefore it might be better to just use the unmodified time signal without any prior noise reduction.

In a bubble column, small gas bubbles are introduced at the sparger. These small bubbles coalesce and grow in size as they rise in the column. Liquid is dragged along

with the bubbles, which results in a global liquid circulation throughout the column. Liquid circulations influence the path of the rising bubbles and also the breakup of bubbles. Bubbles eventually escape from the liquid at the surface.

2.6.3.3. Bubble size estimation

The entire phenomena generate pressure fluctuations either locally or globally in the column. The local pressure fluctuations are caused by pressure sources such as liquid velocity fluctuations and gas holdup fluctuations. The liquid velocity fluctuations are mainly generated due to rising gas bubbles, large liquid eddies, and liquid turbulence. And the gas holdup fluctuations are directly related to the passage of large gas bubbles. The global pressure fluctuations are caused by pressure sources such as bubble formation, bubble coalescence, bubble breakup, bubble eruption, oscillations of the gas–liquid suspension, and mechanical vibrations of the column. The local and global sources can be differentiated based on the propagation velocity of the related pressure sources. The pressure fluctuations from local sources travel with the speed of the source and are measured only in the direct vicinity of the source. These pressure fluctuations have a low propagation velocity (2 m/s). Global sources generate pressure waves that travel with the velocity of sound in the gas–liquid suspension, which is given as:

$$c^2 = \frac{P}{\rho_s \epsilon_G (1 - \epsilon_G)} \quad (2.48)$$

where c the velocity of the sound in the gas–liquid suspension, P is the atmospheric pressure, ρ_s is the density of the slurry, and ϵ_G is the gas holdup. Equation 4.1 gives minima for velocity of sound at $\epsilon_G = 0.5$, which is 20 m/s. The global sources thus have a high propagation velocity (>20 m/s), and are measured almost instantaneously throughout the column.

The gas bubbles in a BC are classified into two distinct classes: small bubbles (2–8 mm dia) and large bubbles (>8 mm dia). The volume-averaged bubble diameter estimated from the local pressure fluctuations is related to the small and the large bubble classes. The contribution of the small bubbles, however, is negligible compared to that of the large bubbles. These gas bubbles show a distinct axial distribution in size in the column. Small bubbles are present near the sparger up to the equilibrium height above which the large bubbles are dominant. Above this equilibrium height, turbulent flow is completely developed and the bubbles do not grow further in size by coalescence. In the developed turbulent flow, the large bubbles are uniformly distributed along the radius of the column. At any location above the equilibrium height, the average bubble size is constant. Thus the average bubble diameter measured above the equilibrium height can be considered as the representative diameter of the large bubbles present in the column.

The pressure time series measured above this height will capture the pressure fluctuations resulting from all the large bubbles passing the vicinity of the sensor and thus will be representative for all the large bubbles rising in the column. Theoretically, rising bubbles generate most of the local pressure fluctuations, so these local pressure fluctuations can be used to estimate the average bubble diameter of rising bubbles. The liquid circulations in the BC also generate local pressure fluctuations as a result of changes in the liquid velocity field influenced by its interaction with the rising bubbles.

Rising bubbles also generate pressure fluctuations at the measurement position because of changes in the static liquid head above the measurement position. These pressure fluctuations are termed as holdup pressure fluctuations. This holdup pressure fluctuation is seen to be proportional to the volume of the gas bubbles and in turn proportional to the square of the bubble diameter in a 2-D column and to the cube of the bubble diameter in a 3-D column:

$$2\text{-D bubble: } P_h(t) \propto d_b^2 \quad (2.49)$$

$$3\text{-D bubble: } P_h(t) \propto d_b^3 \quad (2.50)$$

In summary, the amplitude of the local pressure fluctuation in a BC is proportional to a certain power of the large bubble diameter. This power is expected to be between 1.5 and 2 for the 2-D large bubbles and between 2 and 3 for the 3-D large bubbles.

2.6.3.4. Spectral analysis of pressure time series

Different time series analysis can be employed to characterize the dynamic behavior of multiphase systems. Van der Schaaf et al. (2002) developed a technique to extract information related to the average large bubble diameter from the Fourier transform of pressure time series measured simultaneously in a gas–solid fluidized bed at different column positions. On similar grounds, Chilekar et al. (2005) applied Fourier analysis to the pressure time series measured at the wall in SBCs. The pressure time series measured at the axial measuring position x , consists of the sum of pressure fluctuations by local and global sources as:

$$P_x(t) = P^{Glob}(t) + P_x^{Loc}(t) \quad (2.51)$$

Another pressure time series measured simultaneously at axial position y in the column is given as

$$P_y(t) = a_y P^{Glob}(t + \Delta t) + P_y^{Loc}(t) \quad (2.52)$$

where a_y is the attenuation of the global fluctuations at position y as compared to position x and Δt is the time lag. The attenuation is the measure of the dampening of the amplitude of the global fluctuations measured at two different locations, and the time lag

gives the time shift of a global pressure fluctuation between the two measurement points.

In this section, the separation of the local and the global pressure fluctuations in the measured pressure time series using Fourier analysis is mathematically explained.

Fourier transform

The Fourier transform converts the pressure time series from the time domain to the frequency domain as:

$$F_x(f) = \frac{1}{T} \int_0^T P_x(t) e^{-2\pi i f t} dt \quad (2.53)$$

A recorded pressure time series is discrete in time, with a constant sampling frequency.

A discrete Fourier transform (Fast Fourier Transform) algorithm is used to convert this measured pressure time series into the frequency domain. The Fourier transforms of the pressure time series are:

$$F_x(f) = F_x^{loc}(f) + F_x^{glob}(f) \quad (2.54)$$

$$F_y(f) = F_y^{loc}(f) + a_y F_y^{glob}(f) \quad (2.55)$$

The above equations show that the Fourier transform of a pressure time series is the sum of the separate Fourier transforms of the local pressure fluctuations and the global pressure fluctuations.

2.6.3.5. Power spectral density

The power spectral density (PSD) of a pressure time series at a measuring position x ,

Φ_{xx} , is defined as:

$$\phi_{xx}(f) = \frac{1}{T} E[F_x(f).F_x^*(f)] \quad (2.56)$$

where E is the expectation of F_x , F_x^* is the complex conjugate of the Fourier transform. By applying Eq. 2.56 to Eq. 2.54, the PSD of the pressure time series at position x is calculated as

$$\phi_{xx} = E\{[F_x^{loc}(f) + F^{glob}(f)].[F_x^{loc}(f) + F^{glob}(f)]^*\} \quad (2.57)$$

$$\phi_{xx}(f) = |F_x^{loc}(f)|^2 + |F^{glob}(f)|^2 + 2E[F_x^{loc}(f).F^{glob}(f)]^* \quad (2.58)$$

The local and global fluctuations are created by different pressure sources as mentioned in the previous section. These pressure fluctuations cannot be cross-correlated with each other in a pressure time series and thus can be assumed independent of each other. Consequently, the product of their Fourier transforms becomes equal to zero. Thus, in Eq. 2.58, the last term is equated to zero, which gives

$$\phi_{xx}(f) = |F_x^{loc}(f)|^2 + |F^{glob}(f)|^2 \quad (2.59)$$

Similarly, the PSD at position y is given by

$$\phi_{yy}(f) = |F_y^{loc}(f)|^2 + a_y^2 |F^{glob}(f)|^2 \quad (2.60)$$

The cross-power spectral density (CSD) between two time series is given as

$$\phi_{xy}(f) = \frac{1}{T} E[F_x(f).F_y^*(f)] \quad (2.61)$$

Substituting the Fourier transform of the pressure time series in the above equation gives

$$\begin{aligned} \phi_{xy}(f) = & E[F_x^{loc}(f).F_y^{loc*}(f)] + E[F_x^{loc}(f).a_y F^{glob*}(f)] \\ & + E[F^{glob}(f).F_y^{loc*}(f)] + a_y |F^{glob}(f)|^2 \end{aligned} \quad (2.62)$$

In Eq. 4.15, the first three terms are equal to zero because, by definition, the local pressure sources at different measurement positions are not correlated with each other. At the same time, the local and global pressure sources are also independent of each other as mentioned earlier. Consequently,

$$\phi_{xy}(f) = a_y |F^{glob}(f)|^2 \quad (2.63)$$

Eq. 4.16 shows that the CSD corresponds to the cross correlation of the two time series. It is a measure of the global pressure fluctuations recorded in the two time series and gives its power over the complete frequency spectrum. The global pressure fluctuations cannot be simply subtracted between the two pressure time series to obtain the local pressure fluctuations, because of the attenuation of the signal a_y and the time shift Δt , of the same sources in the two signals. The so-called coherence is therefore used to separate the local fluctuations from the global fluctuations.

2.6.3.6. Coherence

The pressure fluctuations caused by global pressure sources have a high propagation velocity and thus they generate a constant time shift when measured at two different heights in the column. Because of this, they are coherent over the height of the column. Local pressure sources, such as large gas bubbles, undergo a change in shape and velocity as they rise in the column. The time shift from these sources is therefore not constant. Local pressure sources are thus globally incoherent. In gas–solid fluidized beds, this characteristic difference between local and global pressure sources has been used to successfully separate them using the so-called coherence. The Coherence is defined as the CSD of the two time series normalized by the PSDs of the individual time series

$$\gamma_{xy}^2(f) = \frac{|\phi_{xy}(f)|^2}{\phi_{xx}(f)\phi_{yy}(f)} \quad (2.64)$$

A constant phase lag created by a pressure source gives a coherence of unity at its characteristic frequency. If the phase lag is not constant then the coherence is less than unity and its value varies between zero and one. For completely uncorrelated signals the coherence is zero. From equations 2.59, 2.60, 2.63, and 2.64 the coherence between the two time series x and y is obtained as

$$\gamma_{xy}^2(f) = \frac{a_y^2 |F^{glob}(f)|^4}{[|F_x^{loc}(f)|^2 + |F^{glob}(f)|^2][|F_y^{loc}(f)|^2 + a_y^2 |F^{glob}(f)|^2]} \quad (2.65)$$

The product of the coherence (between the measurement position and the sparger position) and the PSD (at the measurement position) gives the so-called coherent output power (COP) that is present in the signal at the measurement position. The COP at position y is calculated as:

$$COP_y(f) = \gamma_{xy}^2(f)\phi_{yy}(f) \quad (2.66)$$

From Eqs. 4.13 and 4.18, the above equation is further simplified as

$$COP_y(f) = \frac{a_y^2 |F^{glob}(f)|^4}{|F_x^{loc}(f)|^2 + |F^{glob}(f)|^2} \quad (2.67)$$

Equation 2.67 clearly demonstrates that the local pressure fluctuations at measurement position x influence the COP calculated at the measurement position y . Thus, the measurement position x needs to be chosen such that the local pressure fluctuations at this position are minimum or are almost absent. This is possible when this pressure measurement is done in the plenum or just above the gas distributor, where large gas

bubbles have not yet been formed, while as yet there are also no large liquid velocity fluctuations. With a measurement position x close to the gas distributor, it can be assumed that

$$|F_x^{loc}| \approx 0$$

and the COP in Eq. 2.67 is simplified to,

$$COP_y(f) = a_y^2 |F^{glob}(f)|^2 \quad (2.68)$$

Equation 2.68 shows that the COP gives the power in the PSD related to the global pressure fluctuations along with its attenuation at that particular measurement position y . The residual power in the PSD is the so-called incoherent output power (IOP). This IOP at the measuring position y is given as

$$IOP_y(f) = [1 - \gamma_{xy}^2(f)] \phi_{yy}(f) \quad (2.69)$$

Simplifying Eq. 2.69, using Eqs. 2.63 and 2.65 gives

$$IOP_y(f) = |F_y^{loc}(f)|^2 + a_y^2 \frac{|F_x^{loc}(f)|^2 |F^{glob}(f)|^2}{|F_x^{loc}(f)|^2 + |F^{glob}(f)|^2} \quad (2.70)$$

Simplifying Eq. 2.70 gives

$$IOP_y(f) = |F_y^{loc}(f)|^2$$

$$\text{If } |F_x^{loc}(f)| \rightarrow 0 \text{ or } |F^{glob}(f)| \rightarrow 0 \quad (2.71)$$

Equation 2.71 shows that the IOP at measurement position y contains only the local pressure fluctuations present in the pressure time series measured at the position y ,

provided the measurement position x is such that either F_x^{loc} or F^{glob} is close to zero, that is, in the plenum or just above the gas distributor. The above analysis shows that the coherence effectively separates the local pressure fluctuations (IOP) from the global pressure fluctuations (COP) in a measured pressure time series. Parseval's theorem states that the area under the curve of the incoherent output power as a function of frequency is equal to the variance of the incoherent part of the signal, σ_i^2 in the pressure time series.

$$\sigma_i^2 = \sum_f IOP_y(f) \quad (2.72)$$

This variance is therefore a measure of the power of the pressure fluctuations produced by the rising large bubbles and, as mentioned earlier, is considered to be a function of the average large bubble diameter in the SBC.

$$\sigma_p^2 = \sigma_i^2 + \sigma_c^2 \quad (2.73)$$

σ_i^2 is separated from σ_p^2 using the spectral analysis method as explained in the previous section. σ_i^2 can then be related to the average large bubble diameter as follows,

$$\sigma_i^2 = \frac{1}{N} \sum_{n=1}^N f_{s,n} \sigma_{s,n}^2 = \frac{1}{T} \sum_T |P_b(t)|^2 = \rho_s^2 g^2 f(d_{b,avg}) \quad (2.74)$$

where s refers to a source of local pressure fluctuation (such as the rising bubble pressure fluctuation, the gas holdup fluctuation, or the liquid velocity fluctuation) and n refers to the different classes of bubble size present. In Eq. 2.74 each class of bubbles contributes to the incoherent standard deviation σ_i , depending on its own standard deviation and frequency of occurrence of that class of bubbles. In other words, the incoherent standard deviation is the standard deviation of the local pressure fluctuations and is a function of the average large bubble diameter as in Eq. 2.74. For example, from Eqs. 2.49 and 2.50,

we can expect in a 3-D SBC that the incoherent standard deviation is proportional to the average large bubble diameter to the power of 2 to 3. This is the basis used for the pressure fluctuations technique explained in this report, that is, $\sigma_i \sim d_b^m$ with $m = 2$ to 3. It is important to mention here that liquid velocity fluctuations are inherently a part of the incoherent pressure fluctuations caused by the rising large gas bubbles. Therefore, Eq. 2.74 also contains the power in the pressure fluctuations resulting from liquid velocity fluctuations along with the rising bubble fluctuations. It is important to mention here that liquid velocity fluctuations are inherently a part of the incoherent pressure fluctuations caused by the rising large gas bubbles.

2.6.3.7. Liquid velocity estimation

As mentioned in the introduction of analysis of PFS for bubble size, the local pressure fluctuations are caused by the passage of bubble as well as dynamic pressure changes caused by large eddies. Cross correlation can be used to detect the similarity between two pressure time series recorded simultaneously at two locations at D_x distance apart. The cross correlation function is given as:

$$R_{xy}(\tau) = \frac{1}{T} \int_0^T x(t)y(t-\tau)dt \quad (2.78)$$

This function generates distinct peak at zero time lag and one secondary peak. The separation between sensors and the time lag corresponding to this secondary peak is used to calculate the circulation velocity.

Notations

a, b, c	Coefficients from calibration, (-)
A_{21}	Einstein spontaneous emission coefficient
A_{film}	projected film surface area, m ²
A_W	Heat transfer area of film, m ²
a_y	Attenuation coefficient, -
C	molecular concentration, kmol/m ³
c	velocity of light, m/s
d_0	size of beam waist, m
d_b	Diameter of bubble, m
dx	height of measuring volume, m
dy	width of measuring volume, m
dz	length of measuring volume, m
$-E_a$	activation energy, J
E_i	Eddy energy, J
e_i	unit vector in the direction of incoming light, m/s
e_s	unit vector in the direction of scattering light, m/s
F	Fourier transform coefficients, Pa
f_0	Frequency corresponding to zero velocity, Hz
f_D	Doppler frequency, Hz
f_i	frequency of incoming light, Hz
f_p	frequency of incoming light with respect to seeding particle, Hz
f_s	frequency of light scattered towards receiver, Hz

DEVELOPMENT OF EXPERIMENTAL TECHNIQUES AND CFD SIMULATIONS OF MULTIPHASE DISPERSIONS

F_C	center frequency
F^{glob}	Power spectral density of global pressure fluctuations, Pa ²
F^{loc}	Power spectral density of local pressure fluctuations, Pa ²
h	heat transfer coefficient of the film, Wm ⁻² K ⁻¹
I	input current, A
I	fluorescence intensity, %
I	Number of counts in presence of flow medium, -
I_f	fluorescence intensity as a function of temperature, %
k_1, k_2	yaw coefficients, (-)
k_i	eddy energy, J
k_{opt}	optical constant
k_q	quenching constant
k_{spec}	constant dependent on fluorescent molecule
l_e	Eddy length scale, m
m	Interpolation factor, -
$[M]$	quenchers concentration, kmol/m ³
n	number of elements in time series
N_f	number of fringes
P	atmospheric pressure, Pa
p^{Glob}	Global pressure fluctuation, (Pa)
P_h	Pressure fluctuation, (Pa)
p^{Loc}	Local pressure fluctuation, (Pa)
P_x, P_y	Pressure time series acquires simultaneously, (Pa)
Q	quenching rate,

DEVELOPMENT OF EXPERIMENTAL TECHNIQUES AND CFD SIMULATIONS OF MULTIPHASE DISPERSIONS

r	Radius, m
R	Radius of the column, (m)
$R(z)$	wave front radius, m
R_1, R_2, R_3, R_4	Bridge resistances, Ω
R_{film}	resistance of the film, W
T	temperature, K
t_{blur}	time required to blur the bubble image completely, s
T_f	temperature of the fluid, K
T_{film}	temperatures of the film, K
T_{Ref}	reference temperature, K
T_W	temperatures of the film, K
t_{int}	time interval for interpolation, s
t_R	residence time of particle within measuring volume, s
Δt_i	eddy lifetime
u_1, u_2, u_3	velocity in x_1, x_2, x_3 directions respectively, $m\ s^{-1}$
u_i	average velocity if i^{th} segment, m/s
u_x	x-component of velocity, m/s
U	velocity vector, $m\ s^{-1}$
U	particle velocity vector, m/s
U_1, U_2	velocity component after decomposition, $m\ s^{-1}$
v_b	Rise velocity of bubble, m/s

v_f	flow velocity, m s ⁻¹
V	Y component of velocity vector, m s ⁻¹
V_{AB}, V_{AD}	Junction voltage, V
V_{in}	Input voltage, V
V_L	Averaged liquid velocity, m/s
V_o	Output voltage, V
V_S	Slip velocity, m/s
x_1, x_2, x_3	co-ordinate system
$x_j(i)$	scale wise wavelet transformed reconstruction, m/s
\hat{x}_j	Energy of scale wise wavelet transformed reconstruction, m ² /s ²
z	distance from beam waist, m

Greek Letters

α	beam divergence
β	Cosntant in equation for temperature dependence of fluorescence intensity, -
Δf	Doppler shift
Δt	time gap between velocity crossing, s
δf	distance between fringes, m
ε_1	absorption coefficient for the laser beam
ε_2	absorption coefficient for the fluorescence emission

DEVELOPMENT OF EXPERIMENTAL TECHNIQUES AND CFD SIMULATIONS OF MULTIPHASE DISPERSIONS

ϕ	angle between velocity vector and direction of measurement, $^{\circ}$
η	fluorescence quantum yield, %
η_0	fluorescence natural quantum yield, %
λ	wavelength, m
θ	angle between incoming laser beams, $^{\circ}$
θ_B	tilt angle of Brag cell, $^{\circ}$
ϵ	Fractional gas hold-up, -
ρ_s	density of the suspension, kg/m^3
Φ_{xx}	Series X power spectral density, Pa^2
Φ_{xy}	Cross spectral power spectral density, Pa^2
Φ_{yy}	Series Y power spectral density, Pa^2
γ_{xy}^2	Coherence, -
σ_c^2	Variance of coherent output power
σ_i^2	Variance of incoherent output power
σ_p^2	Total energy of pressure fluctuations

Subscript

g	gas phase
I	incident light

Abbreviations

A/D	Analog to digital
CCA	constant-current anemometer
COP	coherent output power
CTA	constant-temperature anemometer
DAQ	data acquisition card
HFA	hot film anemometry
IOP	incoherent output power
LDV	laser doppler anemometry
LIF	laser induced fluorescence
LIM	local intermittency measure
PIV	particle image velocimetry
PLIF	planar laser induced fluorescence
POD	proper orthogonal decomposition
SNR	Signal to noise ratio

References: -

- Adrian, R. J. 1975. On the role of conditional averages in turbulence theory. Proceedings of the Fourth Biennial Symposium on Turbulence in Liquids, Princeton, NJ, 323-340.
- Adrian, R. J., Moin, P. 1988. Stochastic estimation of organized turbulent structure: Homogenous shear flow. *Journal of Fluid Mechanics* 190, 531-541.
- Adrian, R.J., 1983. Laser velocimetry in fluid mechanics measurements. In R.J. Goldstein (Ed.) Washington, D.C.: Hemisphere, 155-240.
- Andre, J.C., Molinari, J., 1976. Mise au point sur les differents facteurs physicochimiques influant sur la mesure de concentration de traceurs fluorescents et leurs consequences pratiques en hydrologie, (in french). *J. Hydrol.* 30, 257-285.
- Bröder, D. and Sommerfeld, M., 2002. An advanced LIF-PLV system for analyzing the hydrodynamics in a laboratory bubble column at higher void fractions. *Experiments in Fluids*, 33, 826–837.

- Bröder, D. and Sommerfeld, M., 2003. Combined PIV/PTV-measurements for the analysis of bubble interactions and coalescence in a turbulent flow. *Canadian Journal of Chemical Engineering*, 81, 756.
- Bruun, H. H. 1995 *Hot Wire Anemometry: Principles and Signal Analysis*. Oxford University Press.
- Buwa, V.V., Rannade, V.V. 2002. Dynamics of gas-liquid flow in a rectangular bubble column: experiments and single/multiple-group CFD simulations. *Chemical Engineering Science* 57 (22-23), 4715-4736.
- Carosone, F., Cenedese, A., Querzoli, G., 1995. Recognition of partially overlapped particle images using the Kohonen neural network. *Experiments in Fluids* 19, 225-232.
- Chen, R.C. and Fan, L.S., 1992. Particle image velocimetry for characterizing the flow structure in three-dimensional gas-liquid-solid fluidized beds. *Chemical Engineering Science*, 47 (13/14), 3615-3622.
- Chilekar, V. P., Warnier, M. J. F., van der Schaaf, J., Kuster, B. F. M., Schouten, J. C., van Ommen, J. R., 2005. Bubble size estimation in slurry bubble columns from pressure fluctuations. *A.I.Ch.E. Journal* 51(7), 1924-1937.
- Cole, D., Glauser, M., Guezennec, Y. 1992. An application of stochastic estimation to the jet mixing layer. *Physics of Fluids A* 4(1):192-194.
- Coppeta, J. and Rogers, C., 1998. Dual emission laser induced fluorescence for direct planar scalar behavior measurements. *Exp Fluids*, 25, 1-15.
- Dahikar, S. K., Sathe, M. J. and Joshi, J. B., 2010. Investigation of flow and temperature patterns in direct contact condensation using PIV, PLIF and CFD. *Chemical Engineering Science*, 65 (16), 4606-4620.
- Deen, N.G., Delnoij, E., Westerweel, J., Kuipers, J.A.M. and Van Swaaij, W.P.M., 1999. Ensemble correlation PIV applied to bubble plumes rising in a bubble column. *Chemical Engineering Science*, 54, 5159-5171.
- Delnoij E, Westerweel J, Deen NG, Kuipers JAM, Swaaij WPM van (1999) Ensemble correlation PIV applied to bubble plumes rising in a bubble column. *Chem Eng Sci* 54:5159-5171.
- Deshmukh, S.S.; Joshi, J.B. and Koganti, S.B., 2008. Flow Visualization and 3D CFD simulations of Annular Region of Annular Centrifugal Extractor. *Industrial & Engineering Chemistry Research*, 47, 3677-3686.
- Diaz, I. and Riethmuller, M. L., 1998. PIV in two-phase flows: simultaneous bubble sizing and liquid velocity measurements. *Proceedings of 9th International Symposium on Applications of Laser Techniques to Fluid Mechanics*, Lisbon, Portugal.
- Drahos, J., Zahradnik, J., Puncochar, M., Fialova, M., Bradka, F. 1991. Effect of operating conditions on the characteristics of pressure fluctuations in a bubble column. *Chemical Engineering Process* 29(2), 107-115.
- Durst F., Stevenson W.H., 1976. Visual modeling of laser Doppler anemometer signals by moiré fringes. *Applied Optics* 15, 137-144.
- Durst, F., Melling, A., Whitelaw, J.H., 1981. *Principles and Practice of Laser-Doppler Anemometry* (second ed.), Academic Press, London.

DEVELOPMENT OF EXPERIMENTAL TECHNIQUES AND CFD SIMULATIONS OF MULTIPHASE DISPERSIONS

- Gandhi, A. B., Joshi, J. B., Jayaraman, V. K. and Kulkarni, B.D., 2007. Data-Driven Dynamic Modeling and Control of a Surface Aeration System. *Ind. Eng. Chem. Res.*, 46, 8607–8613.
- Glowacki, J., 1964. Further investigations into fluorescence quenching of dyes by neutral salts. *Acta Physica Polonica* 15, 767-780.
- Gross, K.P., McKenzie, R.L., Logan, P., 1987. Measurements of temperature, density, pressure, and their fluctuations in supersonic turbulence using laser-induced fluorescence. *Experiments in Fluids* 5, 372-380.
- Guezennec, Y. G. 1989. Stochastic estimation of coherent structures in turbulent boundary layers. *Physics of Fluids A* (1), 1054-1060.
- Guibault, G., 1973. *Practical fluorescence: theory, methods and techniques*. Marcel Dekker, New York.
- Haut, B., Ben, A. H., Coulon, L., Jacquet, A., Halloin, V., 2003. Hydrodynamics and mass transfer in a Couette-Taylor bioreactor for the culture of animal cells. *Chemical Engineering Science* 58, 774.
- Hiller, B., Hanson, R.K., 1990. Properties of the iodine molecule relevant to laser-induced fluorescence experiments in gas flows. *Experiments in Fluids* 10, 1-11.
- Houcine., I., Vivier, H., Plasari, E., David, R. and Villiermaux, J., 1996. Planar laser induced fluorescence technique for measurements of concentration fields in continuous stirred tank reactors. *Exp Fluids*, 22, 95–102.
- Hudy, L. M., Naguib, A., Humphreys, W.M. 2007. Stochastic estimation of a separated-flow field using wall-pressure-array measurements. *Physics of Fluids* 19, 1-18.
- Ibrahim K.M., Werthimer, G.D., Bachalo, W.D. 1990. Signal processing considerations for laser Doppler and phase Doppler applications. *Proceedings of the 5th International Symposium on Applications of Laser Techniques to Fluid Mechanics*, Lisbon, Portugal.
- Karasso, P.S., Mungal, M.G., 1997. PLIF measurements in aqueous flows using the Nd:Yag laser. *Exp Fluids*, 23, 382–387
- Karlsson, R., Johansson, T., 1998. LDV measurement of higher order moments of velocity fluctuations in a turbulent boundary layer. In *Laser Anemometry in Fluid Mechanics-III*, pp. 273–289. Lisbon: LADOAN.
- Kulkarni, A. V., Joshi, J.B. 2006. Estimation of hydrodynamic and heat transfer characteristic of bubble column by analysis of wall pressure measurement and CFD simulations. *Chemical Engineering Research and Design* 84(A7), 601-609.
- Kulkarni, A. A., Joshi, J. B., Ravi Kumar, V. and Kulkarni, B. D., 2001. Application of multiresolution analysis for simultaneous measurement of gas and liquid velocities and fractional gas hold-up in bubble column using LDA. *Chemical Engineering Science*, 56,5037–5048
- Lance, M. & Bataille, J. 1991 Turbulence in the liquid phase of a uniform bubbly air–water flow. *J. Fluid Mech.* 222, 95–118.
- Lemoine, F., Antoine, Y., Wolff, M., Lebouche, M., 1999. Simultaneous temperature and 2D velocity measurements in a turbulent heated jet using combined laser-induced fluorescence and LDA. *Experiments in Fluids* 26, 315-323.

- Lemoine, F., Leporcq, B., 1995. An efficient optical pressure measurement in compressible flows: laser-induced fluorescence. *Experiments in Fluids* 19, 150-158.
- Letzel, H. M., Schouten, J. C., Krishna, R., Van den Bleek, C. M. 1997. Characterization of regimes and regime transitions in bubble columns by chaos analysis of pressure signals. *Chemical Engineering Science* 52 (24), 4447-4459.
- Lin, T.J., Juang, R.C., Chen, Y.C., Chen, C.C. 2001. Predictions of flow transitions in a bubble column by chaotic time series analysis of pressure fluctuation signals. *Chemical Engineering Science* 56, 1057-1065.
- Lindken R, Merzkirch W (1999) Phase-separated PIV and shadow image measurements in bubbly two-phase flows. In: *Proceedings of the 8th International Conference on Laser Anemometry Advances and Applications*, 6–8 September 1999, Rome, Italy, pp 165–171
- Lindken, R., Gui, L., Merzkirch, W., 1999. Velocity measurements in multiphase flow by means of particle image velocimetry. *Chemical Engineering and Technology*, 22, 202–206.
- Lui, S., Meneveau, C., Katz, J., 1994. On the properties of similarity subgrid-scale models as deduced from measurements in a turbulent jet. *Journal of Fluid Mechanics* 275, 83-119.
- Luk, S., Lee, Y.H., 1986. Mass Transfer in Eddies Close to Air-Water Interface. *A.I.Ch.E. Journal* 32, 1546-1554.
- Luther, S., Rensen, J., van der Berg, T. H. & Lohse, D. 2005 Data analysis for hot-film anemometry in turbulent bubbly flow. *Expl. Therm. Fluid Sci.* 7, 821–826.
- Martinez-Mercado, J., Gomez, D.C., Gils, D.V., Sun, C. And Lohse, D., 2010. On bubble clustering and energy spectra in pseudo-turbulence. *Journal of Fluid Mechanics*, 650, 287–306.
- Mayo, W.T., 1978. Spectrum measurements with laser velocimeters. *Proceedings of Dynamic Flow Conference on Dynamic Measurements in Unsteady Flows*, DISA Electroic NS. Denmark, 851-868.
- Mudde, R. F., Groen, J. S. & van den Akker, H. E. A. 1997 Liquid velocity field in a bubble column: LDA experiments. *Chemical Engineering Science* , 52, 4217–4224.
- Muhlfriedel, K., Baumann, K. H., 2000. Concentration measurements during mass transfer across liquid-phase boundaries using planar laser induced fluorescence (PLIF). *Exp Fluids*, 28, 279–281.
- Naguib, A. M., Wark, C. E., Juckenhofel, O. 2001. Stochastic estimation and flow sources associated with surface pressure events in a turbulent boundary layer. *Physics of Fluids A* 13 (9), 2611-2626.
- Nakajima, T., Utsunomiya, M., Ikeda, Y., Matsumoto, R., 1990. Simultaneous measurement of velocity and temperature of water using LDV and fluorescence technique. *5th Int Symp on Application of Laser Technique to Fluid Mechanics*, Lisbon, 2.6.1-2.6.6 .
- Nishimura, T., Inaba, S., Hishida, K., Maeda, M., 2000. Measurements of flow around inclined jets by stereoscopic PIV. In: *Lisboa: 10th International Symposium on Applications of Laser Techniques to Fluid Mechanics*.

- Ohba, A. K., Kishimoto, I., & Ogasawara, M., 1977. Simultaneous measurement of local liquid velocity and void fraction in bubbly flows using a gas laser. Tech. Rep. of the Osaka University, vol. 27, no. 1358.
- Rensen, J., Luther, S. and Lohse, A. 2005 The effect of bubbles on developed turbulence. *Journal of Fluid Mechanics*, 538, 153–187.
- Riboux, G., Risso, F. and Legendre, D., 2009. Experimental characterization of the agitation generated by bubbles rising at high Reynolds number. *Journal of Fluid Mechanics*, 643, 509-539.
- Roy, M., RaviKumar, V., Kulkarni, B.D., Sanderson, J., Rhodes, M., Van der Stappen, M., 1999. Simple denoising algorithm using wavelet transform. *A.I.Ch.E. Journal*, 45, 2461.
- Sakakibara, J., Adrian, R. J., 1999. Whole field measurement of temperature in water using two-color laser induced fluorescence. *Exp. Fluids* 26, 7-15.
- Sakakibara, J., Hishida, K., Maeda, M., 1993. Measurements of thermally stratified pipe flow using image-processing techniques. *Experiments in Fluids* 16, 82-96.
- Sathe, M. J., Deshmukh, S. S., Joshi, J. B. and Koganti, S. B., 2010. Computational fluid dynamics simulation and experimental investigation: Study of two-phase liquid-liquid flow in a vertical Taylor-couette contactor. *Industrial and Engineering Chemistry Research*, 49, 14-28.
- Theofanous, T. G. & Sullivan, J. P., 1982. Turbulence in two-phase dispersed flows. *Journal of Fluid Mechanics* 116, 343-362.
- Tokuhiro, A., Maekawa, M., Iizuka, K., Hishida, K. and Maeda, M., 1998. Turbulent flow past a bubble and an ellipsoid using shadow-image and PIV techniques. *International Journal of Multiphase Flow*, 24, 1383–1406.
- van der Schaaf, J., Schouten, J. C., Johnsson, F., van den Bleek, C. M., 2002. Non-intrusive determination of bubble and slug length scales in fluidized beds by decomposition of the power spectral density of pressure time series. *International Journal of Multiphase Flow* 28, 865-880.
- Vial, C., Camarasa, E., Poncin, S., Wild, G., Midoux, G., Bouillard, J. 2000. Study of hydrodynamic behaviour in bubble columns and external loop lift reactors through analysis of pressure fluctuations. *Chemical Engineering Science* 55(15), 2957-2973.
- Walker, D.A., 1987. A fluorescence technique for measurements of concentration in mixing liquids. *Journal of Physics E: Scientific Instruments* 20, 217-224.
- Webster, D. R., Longmire, E. K., 1997. Vortex dynamics in jets from inclined nozzles. *Physics of Fluids* 9, 655-666.
- Webster, D. R., Roberts, P. J. W., Raad, L., 2001. Simultaneous DPIV/PLIF measurements of a turbulent jet. *Experiments in Fluids*, 65, 65-72.
- Wiegel, M., Fischer, M. 1995. Proper orthogonal decomposition applied to PIV data for the oblique transition in a Blasius boundary layer. *Proceedings of S.P.I.E.* 2546, 87-97.

Chapter 3

ESTIMATION OF DESIGN PARAMETERS

3.1. Residence Time distribution in Annular Centrifugal Extractors

3.1.1. Introduction

Annular centrifugal extractor (ACE) is used for liquid-liquid extraction, in chemical, nuclear, and biotechnology industries. It has a unique feature of acting as a mixer and settler in a single device. In ACE, mixing takes place in the annular space, stratification occurs inside the inner cylinder, and separation takes place in the weir system (Bernstein et al., 1973). Two-fluid Taylor-vortex based ACE offers several advantages in liquid-liquid extraction processes such as centrifugally accelerated settling, short residence times, low hold-up volumes, flexible phase ratios, and high throughput. These are desirable in applications where throughput (petroleum industry), safety (nuclear fuel processing), or facilitated settling (biological separations) are required. Further, Taylor vortex equipment are also used as bioreactors (Tsao et al., 1994), emulsion polymerization (Imamura et al., 1993), synthesis of silica particles (Ogihara et al., 1995), heterogeneous catalytic reactions (Sczechowcki et al., 1995), enzymatic and cell reactions (Gandhi et al, 2000; Joshi et al., 1996). Due to the advantages offered by ACE as well as the commercial success of the equipment, these type of equipment have been investigated over the past 3 decades (Bernstein et al., 1973; Leonard et al., 1981; Leonard, 1988; Vedantam and Joshi, 2006). The complexity of the hydrodynamics prevailing in ACE has resulted into empiricism in design, scale-up, and optimization procedures.

3.1.2. Previous Work

The flow patterns in ACE are in close resemblance to turbulent Taylor vortex flow. Substantial work has been done in the past few decades for understanding Taylor-Couette flows. These include analytical studies (Taylor, 1923; Chandrasekhar, 1962) as

DEVELOPMENT OF EXPERIMENTAL TECHNIQUES AND CFD SIMULATIONS OF MULTIPHASE DISPERSIONS

well as experimental findings (Taylor, 1923; Coles, 1965; Andreck et al., 1986; Lueptow et al., 1992). The various transitions with rotational speeds in the absence of axial flow have been reported by Coles (1965) and Andreck et al. (1986), while Lueptow et al (1992) reported such transitions in the presence of axial flow. Many researchers have investigated the axial dispersion in Taylor–Couette flow. The dispersion studies in Taylor-Couette contactors for different flow regimes have been summarized by Vedantam and Joshi (2006). In the case of laminar flows, investigations include the RTD experiments and the description of axial dispersion either by one parameter model (Kataoka et al., 1975; Pudijiono et al., 1992; Legrand and Coeuret, 1986) (dispersed plug flow model or tanks in series model) or two parameter model (Desmet et al., 1996a). The laminar Taylor vortex regime, is characterized by well defined vortices. The work of Kataoka et al. (1975) provided a basis for the assumption of treating each vortex as a well mixed reactor. They performed two-point RTD measurements, and concluded that there is no vortex-intermixing. Thus, with very high aspect ratio (ratio of height of annulus to annular gap), the global flow was expected to reach plug flow. The mixing for laminar flow was later investigated by Desmet et al. (1996a). The authors found that, under laminar flow conditions, intravortex transport is slow compared to the intervortex transport; thus, a single vortex can not be treated as a well mixed reactor. They studied both the inter- and intravortex transport and indicated the need for at least a two parameter model. However, when the Taylor vortex flow is turbulent, intravortex transport is faster than the intervortex flow (Desmet et al., 1996b). Vedantam et al (2006a) used CFD for estimating the mixing time and RTD in a Taylor-Couette flow. They obtained very good agreement between the CFD predictions and the experimental findings reported in the literature. However, such an analysis was performed in the low

range of Taylor number (Ta) for Taylor-Couette flow and needs to be extended for the case of ACE and over a wide range of Ta.

The flow patterns in ACE have been investigated using CFD are reported in chapter 3.4 and 3.5, and the predictions were found to be in good agreement with the experimental measurements. The simulations were performed for the laminar as well as turbulent condition. The transition from the laminar to turbulent conditions was also simulated. For instance, for the case of ($\eta=0.75$, $\Gamma=11$) the transition occurs when the Taylor number (Ta) exceeds 2.1×10^6 . The rotational velocity of the fluid was found to be about 0.5 times the surface velocity of the inner cylinder. Further, the rotational velocity of fluid was at least 5-10 times higher than axial and radial velocities. Most importantly, it was found that the flow pattern in ACE is markedly different from that in a Taylor-Couette flow because of the low aspect ratio and the presence of bottom plate and vanes thereon. For such geometry, it was thought desirable to investigate systematically, the characteristics of axial mixing. An attempt has been made to reduce the axial mixing by introducing internals. Such an investigation consists of two steps (i) the effect of geometrical parameters on the flow pattern and (ii) the relationship between flow pattern and axial mixing. These work elements form the subject of the present chapter.

3.1.3. Experimental

The experimental work was aimed at measuring the RTD in a continuous annular centrifugal extractor (ACE) using pulse response technique. The Important characteristic of ACE is small residence time. To measure the RTD for such small time intervals, a conductivity probe with interface circuitry has been developed. The details of the

measurement technique and geometry of contactor are described in the following subsections.

3.1.3.1. Geometrical details and operating conditions

The experimental geometry has been schematically shown in Figure 3.1 and the geometrical details of the ACE have been summarized in Table 3.1. The rotor (A) i.d., stator (B) i.d., and bottom clearance were 39, 52, and 8 mm, respectively. Six vanes (D) were provided on the bottom plate. Each vane had a height of 5 mm each, thickness of 3 mm and length of 20 mm. The gap between the inside diameter of the outer cylinder and the outer edge of a vane was 1.5 mm. This means that, at the center, a circular portion of 9 mm diameter was vane free and the clearance in this region (between the bottom plate of stator and the bottom face of the rotor) was 8 mm. The clearance between the top edge of the vane and the bottom face of the rotor was 3 mm. The stator (B) was provided with two inlets (E and F) which were diametrically opposite to each other, and the outlet was at the centre of the bottom plate. The two inlets and the outlet (G) had 5 mm diameter. The rotor and outer vessel has been made of transparent acrylic. The measurements were performed for single phase flow in the annulus. The gravity flow has been used for the inflows using constant head tank. To avoid the entrapment of air in the annulus the stationary outer cylinder was kept in a square tank (H) filled with the working liquid (Figure 3.1) and the level in the square tank was kept above the height of outer cylinder (I) and a top wall (J) was provided with a small clearance around rotor. The level was maintained by adjusting the drain valve. The solution of NaCl (1.367 mol/lit) was used as a tracer and 0.25 ml of it was injected at location 1 through a needle in less than 0.5 s, which could be considered as pulse input, while the conductivity of the liquid was measured at the outlet, where electrodes were placed (location 2).

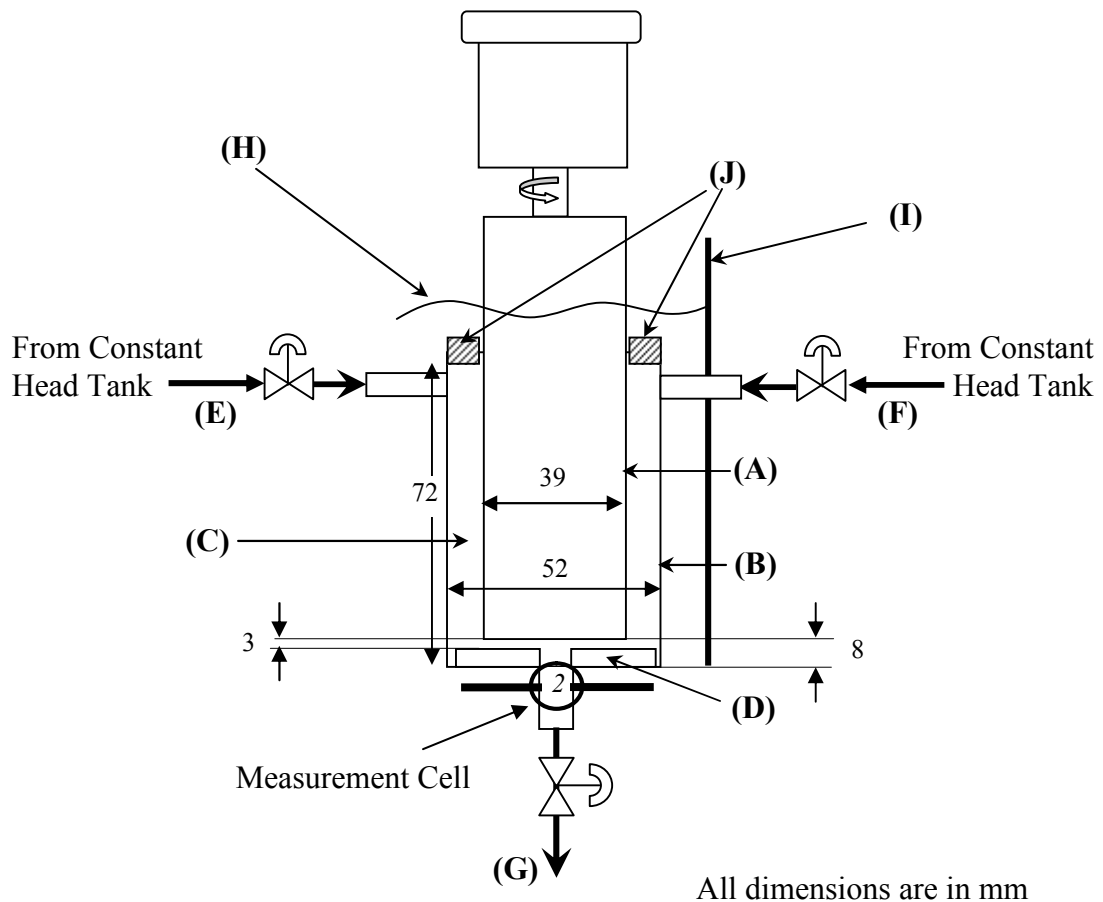


Figure 3.1. Experimental geometry (A) rotor (B) stator (C) annular Space (D) vanes (E) inlet 1 (F) inlet 2 (G) outlet (H) liquid level (I) square tank (J) top wall

Table 3.1. Details of Geometry for RTD experiments

Rotor Diameter	39 mm
ID of Stationary Cylinder	52 mm
Height of vanes on the bottom plate	5 mm
Distance between the Rotor bottom to the top edge of the vanes	3 mm
Total liquid height in flow domain	72 mm
Diameter of outlet	5 mm
Diameter of inlets	5 mm
Volume of flow domain	74.9 ml

DEVELOPMENT OF EXPERIMENTAL TECHNIQUES AND CFD SIMULATIONS OF MULTIPHASE DISPERSIONS

Water ($\rho=998 \text{ kg/m}^3$; $\mu=0.9\text{cP}$) has been used as a working fluid. The rotor speed was varied from 10 to 30 r/s. Total throughput was varied from 2 mL/s to 6.94 mL/s. The inlet flow ratio (ratio of flow rate at inlet 1 with respect to inlet 2) was varied from 0.73 to 2.4. For this range of flow rates, the mean residence time varies from 11 to 38 s.

3.1.3.2. Measurement principle

A conductivity probe was employed in the present work to measure the concentration of tracer at the exit of the contactor. Sodium chloride solution was used as a tracer. The probe actually measures the electrical conductivity of solution passing through the measurement cell located at the outlet shown in Figure 3.1. The conductivity cell and interface circuit are schematically shown in Figure 3.2.

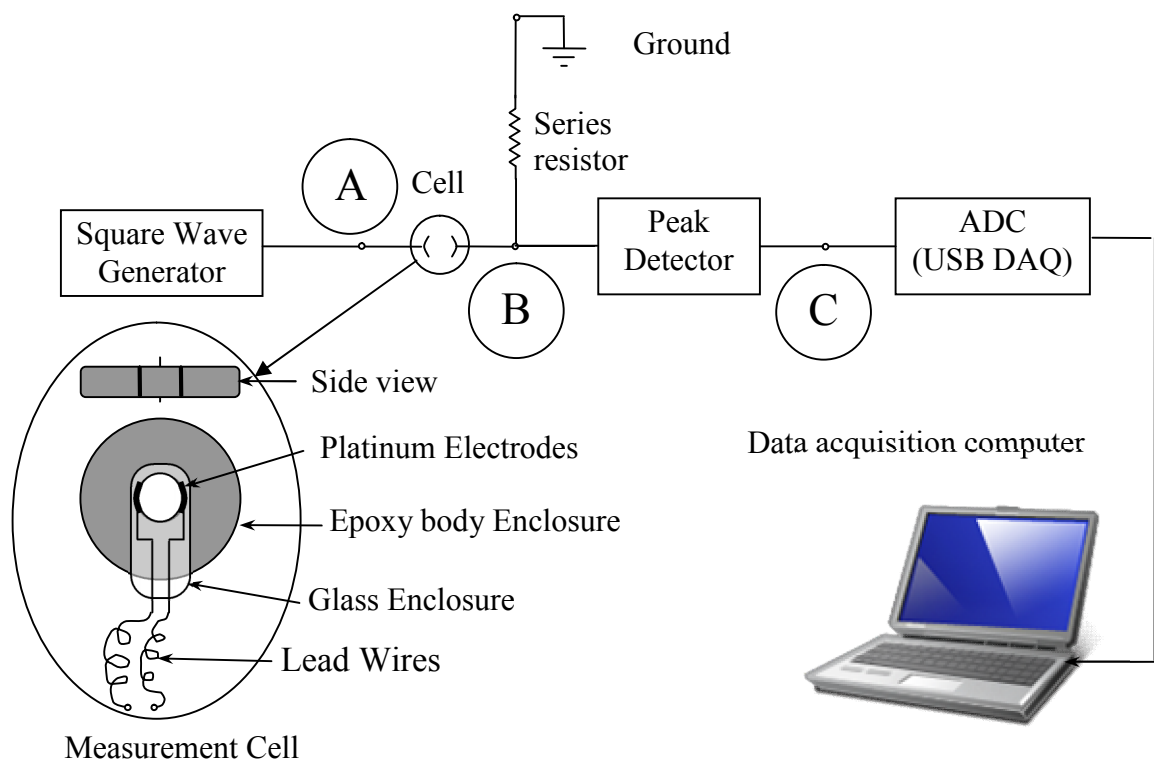


Figure 3.2. Details of conductivity cell and interface circuit

The probe comprises of two parallel, thin platinum plates of $5\text{mm} \times 5\text{mm}$ size, separated by 5 mm distance between them. The plates were fixed to the wall by means of epoxy adhesive and were excited by an AC square wave, with the frequency of 33 kHz.

DEVELOPMENT OF EXPERIMENTAL TECHNIQUES AND CFD SIMULATIONS OF MULTIPHASE DISPERSIONS

The amplitude of the excitation wave was 15 V, in order to have high strength signal which facilitates an easy denoising at a later stage. The current passing through the electrodes comprises mainly of faradaic, coulombic and ohmic currents. These currents result respectively from the capacitance of the solution, oxidation and reduction of the electrolyte ions at the electrodes, and ionic conductance. The alternating voltage causes successive oxidation and reduction of the electrodes, thus canceling the effect of coulombic current. Similarly, positively and negatively changing voltage causes the capacitance to charge and discharge sequentially, thus canceling the effect of coulombic current. The schematic of AC waveforms generated at locations A, B, and C, in the circuit (see Figure 3.2) are shown in Figure 3.3.

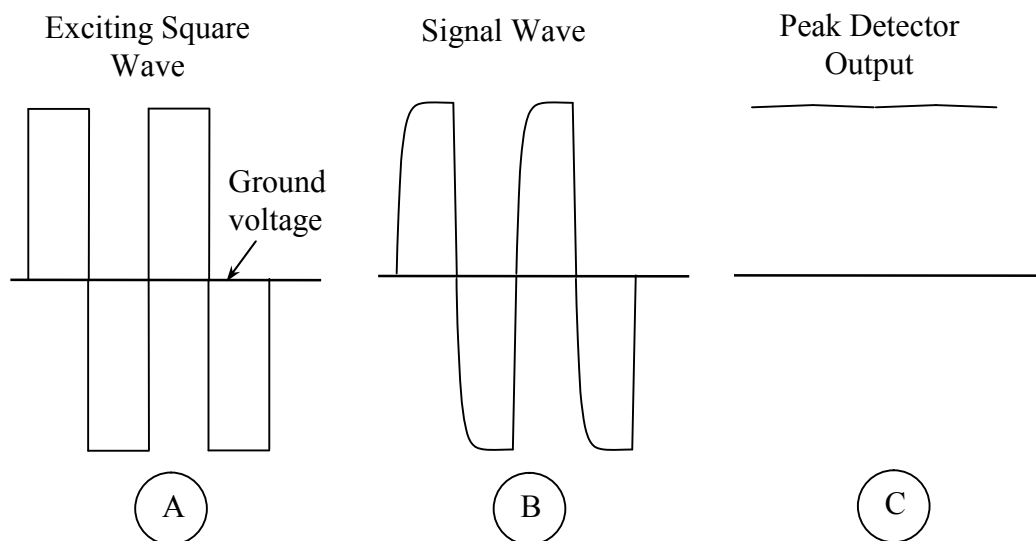


Figure 3.3 Schematic of AC waveforms at locations A, B, and C

A peak detector circuit was used to store the peak value as the output voltage having a refresh time of 0.01 s. Thus, the sampling frequency required to register a peak value was reduced from 15000 Hz to 100 Hz, which reduced the amount of data to be stored and processed. The response of the probe was represented by first order dynamics. The step response curve was obtained by dipping the probe in the solution of known electrical conductivity. The time required to reach 63.5 % of the ultimate steady state

voltage gives the value of time constant which was estimated to be 0.16 s. The typical rise time values range between 1.5-2 s, which is much higher than the estimated probe response time.

The interface circuit comprising of square wave generator and peak detector was built in-house. A square wave generator has been made by using function generator IC 8038 and a comparator (LM 339). The peak detector circuit requires use of high slew rate and input resistance Op-amp (CP3140). The output of peak detector was a stable voltage, which was read by a NI USB 6210 data acquisition card having 16 channels with 16 bit data acquisition capability and was connected to a 2.13 GHz Core 2 Duo PC by means of USB connectivity.

3.1.3.3. Probe calibration and data acquisition

The probe was calibrated using a solution of reagent grade sodium chloride with known concentrations. The solution was kept in a beaker with mild agitation using magnetic stirrer. The probe was dipped into this solution and the steady voltage reading was recorded with the help of a digital multimeter. The calibration curve is depicted in Figure 3.4. The calibration curve was obtained by plotting the concentration against the output voltage of the signal conditioning circuit. Two sets of calibration readings were taken in order to check the repeatability of the probe. The solid line indicates the polynomial fit with the polynomial of degree 6 (R^2 value of 0.9999), and is given by the following equation:

$$C = 0.0042V^6 - 0.068V^5 + 0.36V^4 - 0.3V^3 - 3.37V^2 + 11.75V - 11.69 \quad (3.1)$$

The tap water also contains some dissolved salts which cause the variation in the conductivity of the water, which is used as a working fluid. To compensate for these

extra salts, the initial concentration obtained from the corresponding voltage recorded before injecting the tracer pulse was subtracted from C curve. Data were acquired for 200 s at a sampling frequency of 100 Hz.

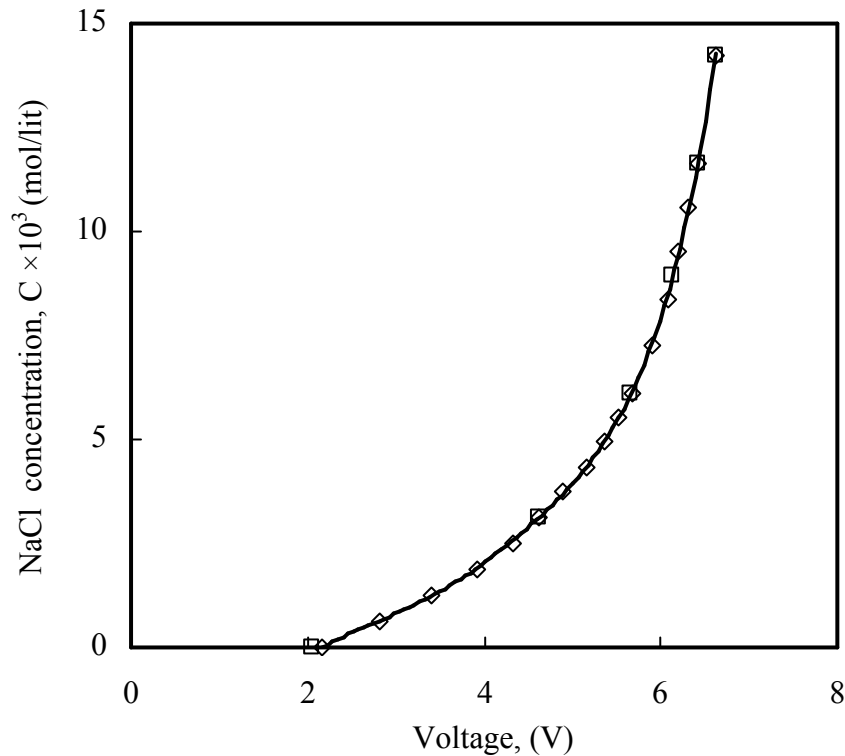


Figure 3.4. Calibration curve for the RTD measurements
◇ Run1 □ Run2 — Calibration Curve

3.1.4. Mathematical Modeling

The details of model equations for CFD are given in chapter 3.5. For turbulence modeling, Reynolds Stress Model (RSM) has been used.

3.1.4.1. Model formulation for species transport

After a fully developed flow field is obtained, the mixing of a passive tracer is simulated. The following assumptions have been made: (i) the diffusion process is isothermal, (ii) the tracer does not undergo any chemical reaction, and (iii) the amount of tracer in the system is sufficiently small as well as all the physical properties of the tracer

DEVELOPMENT OF EXPERIMENTAL TECHNIQUES AND CFD SIMULATIONS OF MULTIPHASE DISPERSIONS

are practically the same as that of the working liquid so that the flow will not get disturbed after the introduction of the tracer.

Zero tracer concentration was specified for the entire solution domain except for the predetermined computational cells wherein, the tracer concentration was defined as unity. The transient mass balance expresses the dispersion of the tracer as follows:

$$\frac{\partial c}{\partial t} + \nabla \cdot (\langle u_i \rangle c) = -\nabla \cdot (D_{eff} \nabla c) \quad (3.2)$$

c is the local concentration of the tracer and D_{eff} is the effective diffusion coefficient, given by:

$$D_{eff} = D_m + D_t \quad (3.3)$$

where, D_m is the molecular diffusion coefficient and D_t is the eddy diffusion coefficient.

In the present case, the value of turbulent Schmidt number (Sc_t) has been assumed to be

1. Thus, the value of the eddy diffusivity is given by following equation:

$$D_t = C_\mu \frac{k^2}{\varepsilon} \quad (3.4)$$

3.1.4.2. Data analysis

RTD curves were obtained for a wide range of rotor speeds and inlet flow ratios. The nature of curve indicates back-mixed flow. These curves have been used for the estimation of number of tanks in “tanks in series” model. The experimentally obtained curves were compared with the RTD prediction of CFD with water as a working fluid. The validated CFD model was then applied for studying the effect of geometric variations such as annular gap and provision of radial baffles in the annulus. The measurements have been also carried out in geometry with radial baffles. The prediction

**DEVELOPMENT OF EXPERIMENTAL TECHNIQUES AND CFD
SIMULATIONS OF MULTIPHASE DISPERSIONS**

of RTD by CFD for this case was also in good agreement. The following step wise procedure was employed:

The average tracer concentration at the outlet is given by:

$$\bar{C}(t) = \frac{\int_0^{2\pi} \int_0^{r_{out}} curdrd\theta}{\int_0^{2\pi} \int_0^{r_{out}} urdrd\theta} \quad (3.5)$$

The E curve can be obtained from the recorded tracer concentration-time data and is given by:

$$E = \frac{\bar{C}(t)}{\sum \bar{C}(t)\Delta t} \quad (3.6)$$

The model equation for E curve using tanks in series model is (Levenspiel, 1999),

$$\tau E = \left(\frac{t}{\tau}\right)^{N-1} \frac{N^N}{(N-1)!} e^{-tN/\tau} \quad (3.7)$$

Where, $\tau = N\tau_i$ and $\sigma^2 = \frac{\tau^2}{N}$. The value of N was estimated by using a least-square fit

of Eq. (3.7) to the experimentally obtained E curve.

3.1.4.3. Numerical simulation

With the finite volume formulation, all the simulations were carried out using 3D grids. The commercial software FLUENT (version 6.2.16) has been used in all the studies, using around 600,000 non-uniform hex grids. A segregated implicit solver method was used for the momentum equations. The momentum equations have been discretized with the QUICK upwind scheme, and for the pressure velocity coupling, PISO scheme has been used which is recommended for transient simulations (FLUENT, 2004). For the Pressure equation, PRESTO scheme was used. In all the cases, for the axial flow, the simulations were initially performed for the specified axial flow without the rotation of inner cylinder. After the steady state was attained the rotational speed of

the rotating cylinder was specified and the transient simulations were performed. Data has been collected at specified points to track the development of the flow and confirm that the asymptotic solution was reached.

Once the steady state was attained, the tracer concentration was defined as unity in predetermined computational cells and the model has been solved for the species transport equation mentioned above. The concentration of the tracer at the outlet surface was monitored, and the RTD curve was obtained from the monitored data.

3.1.5. Results and Discussion

3.1.5.1. RTD experiments

The RTD has been measured for four different rotational speeds viz. 10, 12, 20 and 30 r/s. Equal flow rates from each inlet (2.08 mL/s) were supplied during the measurements so that the total throughput was 4.16 mL/s. Figure 3.5 shows the E curves for different rotational speeds. As expected, as the rotational speed increases, the extent of back-mixing increases. When the tanks in series model was applied for the RTD curves, it resulted in a single back-mixed tank for all the rotational speeds. In view of this result, one is tempted to visualize the existence of a single circulation in the flow domain. This is in contradiction with the studies in chapter 3.4 and 3.5. The explanation was obtained using CFD simulation and has been provided in the later section.

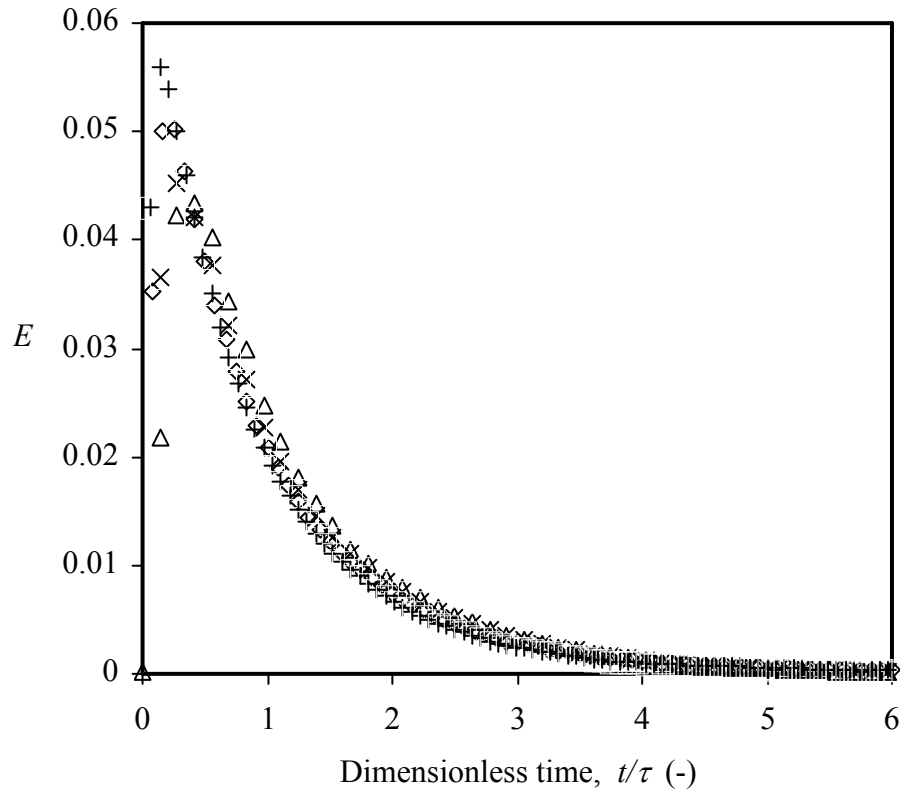


Figure 3.5. Experimentally measured RTD curves at various rotational speeds

Δ 9 r/s ($Ta=1.46 \times 10^7$) \times 13 r/s ($Ta=3.06 \times 10^7$)
 \diamond 20 r/s ($Ta=7.24 \times 10^7$) $+$ 30 r/s ($Ta=16.3 \times 10^7$)

Since, in an ACE, two liquids enter from the diametrically opposite ends, it was thought that the inlet flow ratios are likely to affect the RTD in ACE. Hence, three inlet flow ratios (flow rate at inlet 1/flow rate at inlet 2) viz. 0.73, 1 and 2.4 were employed for investigation. It should be noted that the tracer has been injected at inlet 1 in all the cases. The total flow rate through the ACE is then 3.60, 4.16 and 6.94 mL/s for the respective flow ratios and the rotational speed was kept constant (20 r/s) for all the flow ratios. The average residence time for three the flow conditions are as follows: 20.8, 18, 10.8 s, respectively. The E curves for different flow ratios are shown in Figure 3.6. Again, all these cases were found to be equivalent to one well-mixed stage.

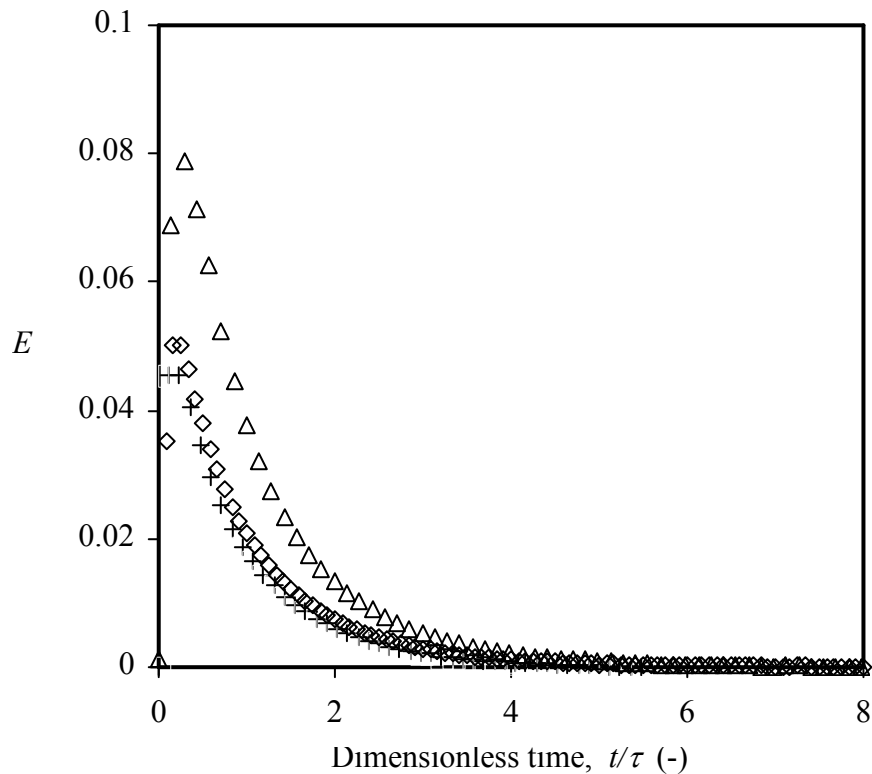


Figure 3.6. Experimentally measured RTD curves at various inlet flow ratios

+ 0.73 ◇ 1 Δ 2.4

3.1.5.2. CFD predictions of RTD

If a single vortex can be considered as a well-mixed tank, it is expected that the number of tanks represented by the tanks in series model should be equal to the number of counter-rotating vortices. However, the experimental RTD studies have revealed only one well mixed tank. For understanding such a behavior, it was thought desirable to undertake CFD simulation of flow pattern and distribution of tracer. It was also thought desirable to compare the predicted and the experimental RTD curves.

The CFD predictions and the experimental measurements were in good agreement with each other. For the case of rotational speed equal to 30 r/s, the total flow rate of 4.16 mL/s with inlet flow ratio equal to 1, the comparison of the E curves

obtained by CFD with those observed by experimental measurements is shown in Figure 3.7.

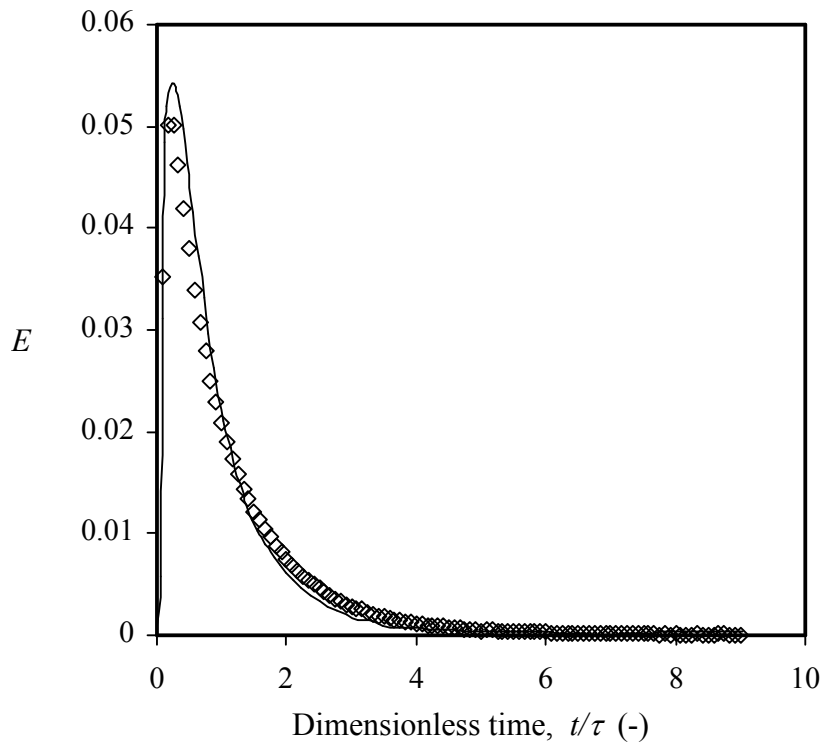


Figure 3.7. Comparison between the experimental and CFD studies for RTD at 30 r/s.

_____ CFD \diamond Experimental

Although, the results are comparable to each other, very little under prediction can be seen in the case of CFD. However, in terms of tanks in series model, the CFD simulation also gives one back-mixed stage. Figure 3.8 shows the contours of molar tracer concentration in a vertical plane passing through the rotational axis and bisecting the inlets for the above operating conditions. It shows the tracer distribution in the flow domain. The injected tracer first starts spreading in the vortex rotating closer to inlet (referred as local dispersion or intravortex transport). Further, before attaining the local homogeneity of tracer in first vortex, some tracer gets entrained in the outer layer of neighboring vortex below it, which then spreads in that vortex. This entire process of

DEVELOPMENT OF EXPERIMENTAL TECHNIQUES AND CFD SIMULATIONS OF MULTIPHASE DISPERSIONS

spreading of tracer from one vortex to the next and finally to the outlet of the domain has been referred to as global dispersion or global axial mixing. In the case of local dispersion within the first vortex near the inlet, tracer gets quickly distributed in radial and axial direction (~ 0.3 s) compared to that of dispersion in tangential direction (~ 1.1 s). On the other hand it should be noted that the time required for global dispersion is about $1/6^{\text{th}}$ times the average residence time. It takes about 3 s to obtain near-uniform concentration of tracer in the entire annular region of ACE. This uniformity indicates the absence of the dead zones inside the annulus. The mixing time, in general, depends on the transport of tracer by convection, molecular diffusion, and turbulent dispersion. For turbulent flows, the transport by molecular diffusion is negligible. The relative contribution of convection and turbulent dispersion can be compared using the time scales for convective transport and the turbulent dispersion. Further, there are two levels of mixing viz. mixing in a single vortex (local mixing) and mixing in the entire annular region (global mixing), to be considered. The calculation procedure is given below.

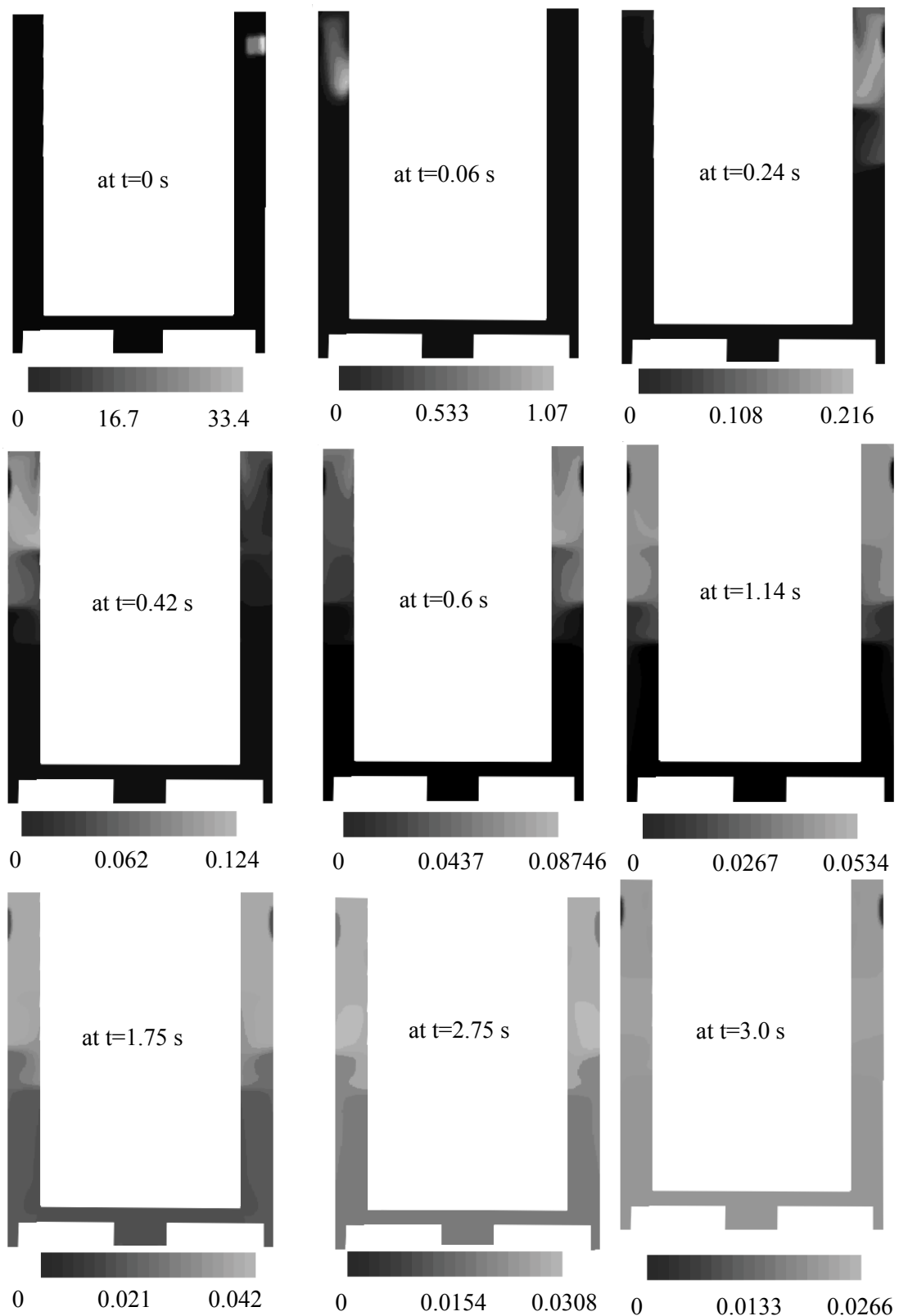


Figure 3.8 Contours of molar tracer concentration (kmol/m³) in a vertical plane passing through the rotational axis and bisecting the inlets at different flow times

3.1.5.2.1. Convective Transport

Mixing in a single vortex:

For a single vortex, (Figure 3.9) the circulation time can be calculated by:

$$t_{c,rz} = \frac{2(l_r + l_z)}{u_{rz}} \quad (3.8)$$

Where l_r and l_z are the radial and axial sizes of a single vortex and u_{rz} is the average circulation velocity within the vortex.

For the tangential direction, the circulation time can be calculated by:

$$t_{c,\theta} = \frac{l_\theta}{u_\theta} \quad (3.9)$$

Where, l_θ and u_θ are the tangential mixing length and the tangential velocity, respectively.

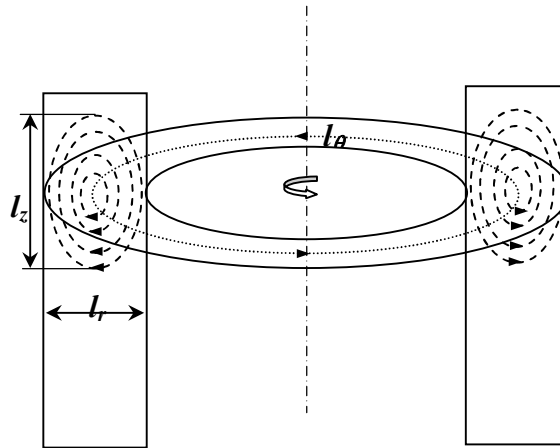


Figure 3.9 Schematic of single vortex and corresponding length scale

Mixing in entire annulus:

The circulation time can be calculated (for a 2D case) by:

$$t_{c,G} = \frac{2(d+H)}{u_c} \quad (3.10)$$

DEVELOPMENT OF EXPERIMENTAL TECHNIQUES AND CFD SIMULATIONS OF MULTIPHASE DISPERSIONS

Where d and H are the annular gap and the height of the annulus, respectively and u_c is the average circulation velocity. It was calculated using the CFD results. The mixing time was then assumed to be 5 times the respective circulation time (Van de Vusse, 1962).

3.1.5.2.2. Turbulent transport

The mixing time due to turbulent transport is given by:

$$\theta_{m,t} = 0.5 \times l^2 / D_t \quad (3.11)$$

Where l is the length scale in respective direction and D_t is eddy mass diffusivity, which plays an important role in turbulent mixing. The DNS results of Bilson and Bremhorst (2007) show that, in case of turbulent Taylor-Couette flow, the maximum turbulence intensities do not occur in the vortex centers and these occur between the vortices. In the light of these observations, it was thought desirable to present this work for the case of $d_o=52$ mm, $d_i=39$ mm, $d=6.5$ mm, $F=11$, and $\omega=30$ r/s. Figure 3.10 shows: (A) the vortex flow and the contour plot for turbulent intensities (u'/u_{avg}), and axial profiles for (B) radial velocity (u_r), (C) turbulent kinetic energy (k), (D) eddy diffusivity (ν_t) and, (E) energy dissipation rate (ε). The maxima (at $z = 0.032$ m and $z = 0.052$ m) and minima (at $z = 0.041$ m) in radial velocity profile indicate vortex boundaries. The maxima in (u'/u_{avg}), k , and the ε profiles are seen between the vortices. These results are in agreement with the literature (Bilson and Bremhorst, 2007). Thus ν_t is directly proportional to the square of turbulent kinetic energy and inversely proportional to the dissipation rate. The profiles of ε show that the values of ε are also maximum near the vortex boundary. However, the decrease in ε at vortex core is much steeper than the decrease in turbulent kinetic energy, giving higher values for eddy diffusivity near the vortex core and lower values in between the vortices (at $z = 0.032$;

m).

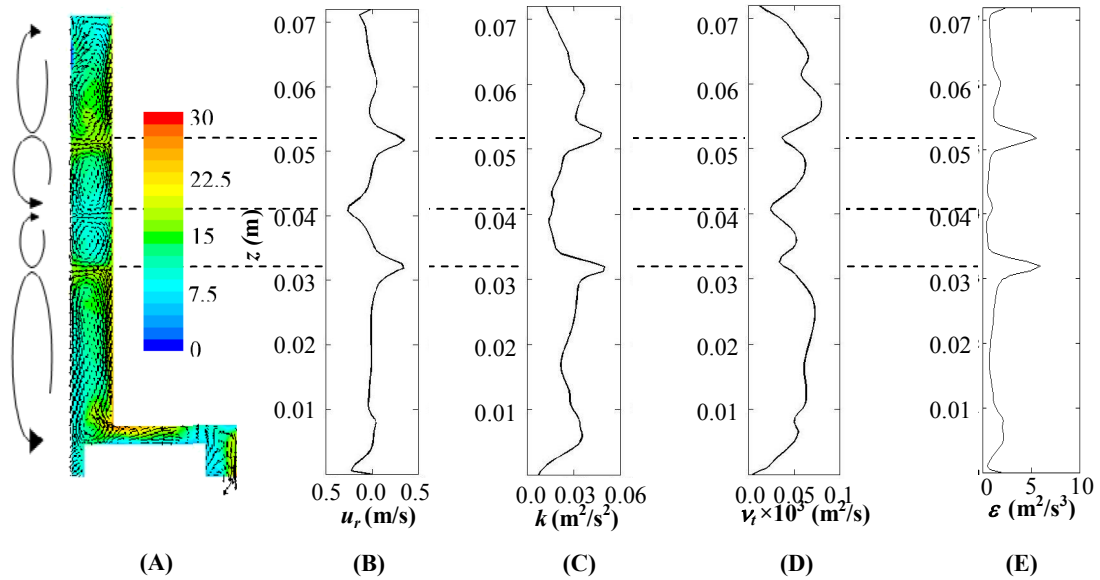


Figure 3.10. The flow patterns and turbulent properties at 30 r/s and total flow rate 4.16 mL/s at the centre of annulus [A] Contours of turbulent intensities (%) [B] Radial velocity profile [C] Turbulent kinetic energy profile [D] Turbulent viscosity profile [E] Turbulent energy dissipation profile

For a typical case of 30 r/s, with aspect ratio (Γ) equal to 11 and $d = 6.5$ mm, the values of $t_{c,rz}$, $\theta_{m,rz}$, $t_{c,\theta}$, $\theta_{m,\theta}$, $t_{c,G}$, $\theta_{m,G}$, $\theta_{mt,r}$, $\theta_{mt,z}$, $\theta_{mt,\theta}$, $\theta_{mt,G}$, were estimated using above equations, (3.8 to 3.11) and these are given below:

Convective Transport

$$l_r=6.5 \text{ mm}, l_z=18 \text{ mm}, u_{rz}= 0.2 \text{ m/s}, t_{c,rz}= 0.245 \text{ s}, \theta_{m,rz}= 0.98 \text{ s (Eq 3.8)}$$

$$l_\theta=143 \text{ mm}, u_{\theta}= 1.35 \text{ m/s}, t_{c,\theta}= 0.106\text{s}, \theta_{m\theta}= 0.53\text{s (Eq 3.9)}$$

$$d=6.5 \text{ mm}, H=72 \text{ mm}, u_c= 0.145 \text{ m/s}, t_{c,G}= 0.5 \text{ s}, \theta_{m,G}= 2.5 \text{ s (Eq 3.10)}$$

Turbulent Transport (Eq 3.11)

DEVELOPMENT OF EXPERIMENTAL TECHNIQUES AND CFD SIMULATIONS OF MULTIPHASE DISPERSIONS

Radial: $l=6.5$ mm, $D_t=3.6 \times 10^{-5}$ m²/s, $\theta_{m,r}= 0.58$ s

Axial : $l=18$ mm, $D_t=3.6 \times 10^{-5}$ m²/s, $\theta_{m,z}= 4.45$ s

Tangential: $l=143$ mm, $D_t= 3.6 \times 10^{-5}$ m²/s, $\theta_{m,\theta}= 280$ s

Global: $l=H=72$ mm, $D_t= 3.6 \times 10^{-5}$ m²/s, $\theta_{m,G}= 71.2$ s.

It can be seen that the mixing time by convective mechanism is an order of magnitude lower than the mixing time by turbulent transport. Further, the values of global mixing time observed experimentally are closer to those estimated by the convective mechanism.

The residence time for a single vortex estimated from the tanks in series model considering each vortex as a well mixed tank comes out to be 4.5 s. It can be observed that the mixing time required by convective transport is 0.58 s, while that required by turbulent dispersion is 4.45 s in axial and 280 s in tangential direction. The actual mixing time is 13 % of the mean residence time in the vortex, confirming the well mixed behavior of individual vortex. The mixing time required by turbulent dispersion is much higher than that required by convection and even the mean residence time, indicating negligible contribution of turbulent transport. Similar observations have been made for all other cases considered in the present work. Table 3.2 summarizes the mixing due to these two mechanisms for the other cases.

3.1.5.2.3. Relation between the number of vortices and number of tanks in series

The liquid phase mixing can also be modeled on the basis an alternative approach given by Joshi (1980). The relation between the Peclet number (Pe) and the number of vortices (n) is given by the following equation (Mecklenburgh, 1974):

$$Pe = \frac{n}{\frac{1}{2} + f} \quad (3.12)$$

DEVELOPMENT OF EXPERIMENTAL TECHNIQUES AND CFD SIMULATIONS OF MULTIPHASE DISPERSIONS

Where, f is recirculation ratio defined as the ratio of inter-vortex circulation velocity to the superficial velocity. The values of f were estimated from CFD. The effective number of tanks (N) is then equal to $Pe/2$ (this relation of $Pe/2$ is to be used when Pe is typically greater than 4). When Pe is less than 1, then the system can be considered completely back-mixed. The value of f can be estimated using CFD. For a typical case of (30 r/s, $\Gamma = 11$ and $d = 6.5$ mm), the inter vortex circulation velocity was 0.0243 m/s while the superficial velocity was 0.00447 m/s and the value of f is 5.44. The number of vortices was 4. Thus from eq 3.12 the Pe works out be equal to 0.67, which represents strong back-mixed flow or $N=1$. The estimations for the other cases are summarized in Table 3.2.

It can be seen that the predictions of number of tanks in series are in good agreement with that of RTD study carried out using experiments as well as CFD. It may be pointed out that the strong intervortex circulation is responsible for the axial mixing behavior of the ACE.

3.1.5.3. Effect of aspect ratio

The flow pattern in the annulus strongly depends upon the aspect ratio, Γ . In the case of very high aspect ratio (Taylor-Couette flow), the size of vortex typically equals to the annular gap between the cylinders. When the aspect ratio becomes small (either increasing the annular gap or reducing height of annulus), the end effects alter the sizes of vortices and reduces the total number of vortices in the flow domain. The aspect ratio variation is thus expected to affect the RTD for ACE. The CFD simulations have been used to understand this effect. For this purpose, four aspect ratios (Γ) have been considered viz. 45 ($d=1.5$ mm), 24 ($d=3$ mm), 16, ($d=4.5$ mm) and 11 ($d=6.5$ mm).

Table 3.2. Mixing in a ACE

Q (mL/s)	ω (r/s)	τ (s)	Ta	Re	Γ	n	f	d (mm)	Pe	mixing time due to convective transport (s)		mixing time due to turbulent transport (s)					
										local		global		local		global	
										$r-z$	θ	$r-z$	θ	r	z	θ	z
2.5	10	30	1.81×10^7	7964	11	7	8.83	6.5	0.75	2.24	2.04	9.74	1.14	2.85	549	139	
4.16	20	12.5	2.52×10^7	11027	16	9	3.13	4.5	2.48	1.25	0.57	8.86	0.41	1.30	379	105	
4.16	20	8.7	7.72×10^6	7351	24	11	2.14	3	4.18	0.76	0.66	6.45	0.42	1.99	820	245	
4.16	20	5.5	1.00×10^6	3676	48	18	1.55	1.5	7.80	0.55	0.71	8.316	0.18	1.31	1326	425	
4.16	20	18	7.25×10^7	15928	11	4	4.92	6.5	0.74	1.4	0.95	7.21	0.68	5.23	329	84	
10	10	7.5	1.81×10^7	7964	11	5	2.05	6.5	1.96	1.4	1.52	8.98	0.69	3.39	334	85	
4.16	30	18	1.63×10^8	23892	11	4	5.44	6.5	0.68	0.61	0.53	3.98	0.58	4.45	280	71	
4.16	10	18	1.81×10^7	7964	11	7	5.09	6.5	1.26	3.36	1.43	10.16	1.14	2.85	549	139	
4.16	40	18	2.90×10^8	31856	11	4	9.28	6.5	0.40	1.31	0.48	3.75	0.26	1.98	125	32	

The other geometrical parameters such as height of vanes on the bottom plate, gap between the top of vanes and the bottom of rotor have been kept same in all the four annular gaps. The total throughput was 4.16 mL/s. The values of average residence times were 5.5, 8.7, 12.5 and 18 s for the respective aspect ratios. Figure 3.11 shows the RTD curves for the different annular gaps considered. The number of vortices was higher in larger aspect ratio than the smaller one ($\Gamma = 45, 25, 16$ and 11 correspond to 18, 12, 6, and 4 number of vortices, respectively). From the figure it can be seen that the RTD curve shifts away from back-mixed behavior (for 6.5 mm gap) to 2, 3 and 4 tanks for cases of 4.5, 3 and 1.5 mm gaps, respectively.

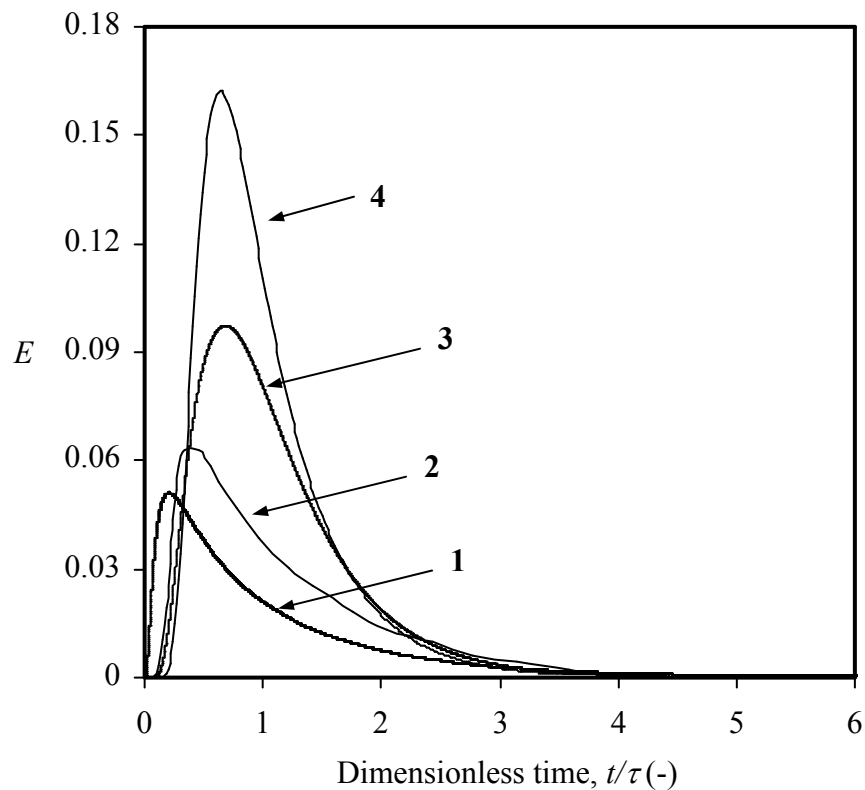


Figure 3.11. Comparison between RTD studies using CFD at 20 r/s for different annular gaps with the total throughput 4.16 mL/s.

[1] 6.5 mm ($Ta=7.24 \times 10^7$)

[2] 4.5 mm ($Ta=2.49 \times 10^7$)

[3] 3 mm ($Ta=7.74 \times 10^6$)

[4] 1.5 mm ($Ta=1.02 \times 10^6$)

3.1.5.4. Reduction in back-mixing by providing internals

Increase in rotational speed leads to increased back-mixing in the ACE. For the reduction of back-mixing, one of the suggestions was the use of radial baffles and divide the annulus in compartments (chapter 3.4.5). Thus the entire annulus was divided into four compartments providing three equally spaced radial baffles. The width of baffles was selected equal to half of the annular gap. Simulations were performed for the rotational speed of 20 r/s, and total throughput equal to 4.16 mL/s. All the other geometrical parameters were kept the same. The flow pattern in Figure 3.12A shows that each compartment consists of two counter rotating vortices. In the presence of net axial flow and radial baffles, the difference can be seen in the vortex pattern compared to that in absence of net axial flow. In the absence of net flow, the existence of counter-rotating vortices has been observed in each compartment, on contrary when there is a net flow, the compartment at the inlet shows single circulation vortex. Further, the vortex was found to rotate with the same direction as that of adjacent vortex in the next compartment (refer enlarged part of Figure 3.12A).

Figure 3.13 shows the RTD curve for the modified geometry of ACE as compared with the geometry in absence of annular baffles at the same rotational speed (20 r/s). The average residence time in this case was found to be 25 s. The baffles can be seen to reduce the extent of back-mixing. When the tanks in series model is applied to the RTD curve, the flow was represented by three tanks in series.

An attempt has been made to reduce the back-mixing further by increasing the width of radial baffles. The length of vanes below the rotor has been selected such that vanes would not protrude beyond the rotor circumference. The width of baffles was kept 2.5 mm so that the clearance between the rotating cylinder and the radial

***DEVELOPMENT OF EXPERIMENTAL TECHNIQUES AND CFD
SIMULATIONS OF MULTIPHASE DISPERSIONS***

baffle was 1 mm. Thus the annulus was divided into 12 compartments each of height equal to 5 mm. The experiments as well as CFD simulations have been performed, and the results are shown in Figure 3.13 in the form of E curves. For the rotational speed equal to 20 r/s, the flow was represented by 5 tanks in series. When the rotational speed was increased to 30 r/s, the number of tanks reduced to 4. It should be noted from Figure 3.12 B that, each compartment in this case has a single vortex as against a pair of counter rotating vortices as shown in Figure 3.12 A.

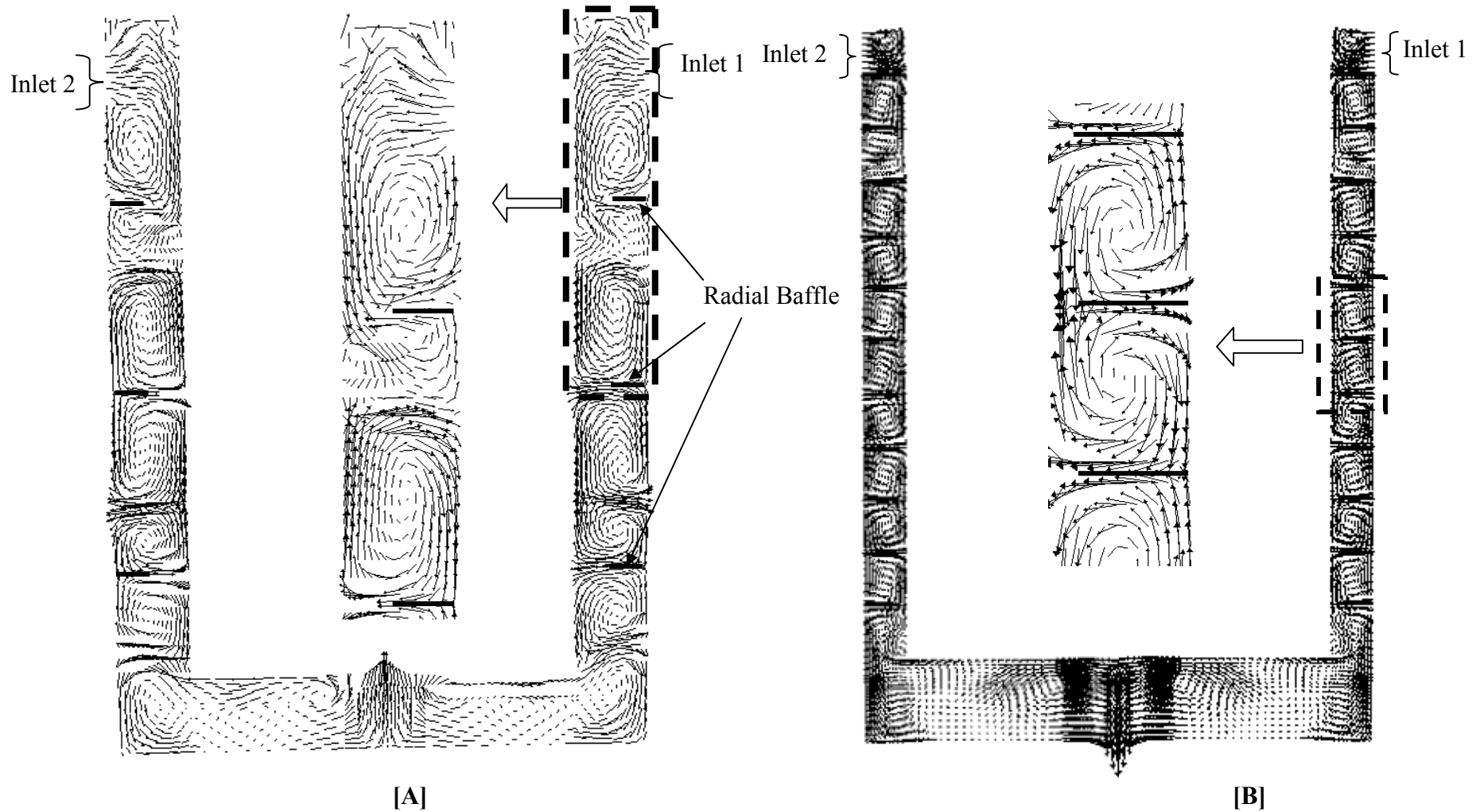


Figure 3.12. Vector plot representing the flow patterns at 20 r/s and total flow rate 4.16 mL/s in presence of radial baffles in annulus
 [A] $d = 6.5$ mm, Baffle width= $d/2$, No. of baffles = 3 [B] $d = 3.5$ mm, Baffle width= 2.5 mm, No. of baffles = 11

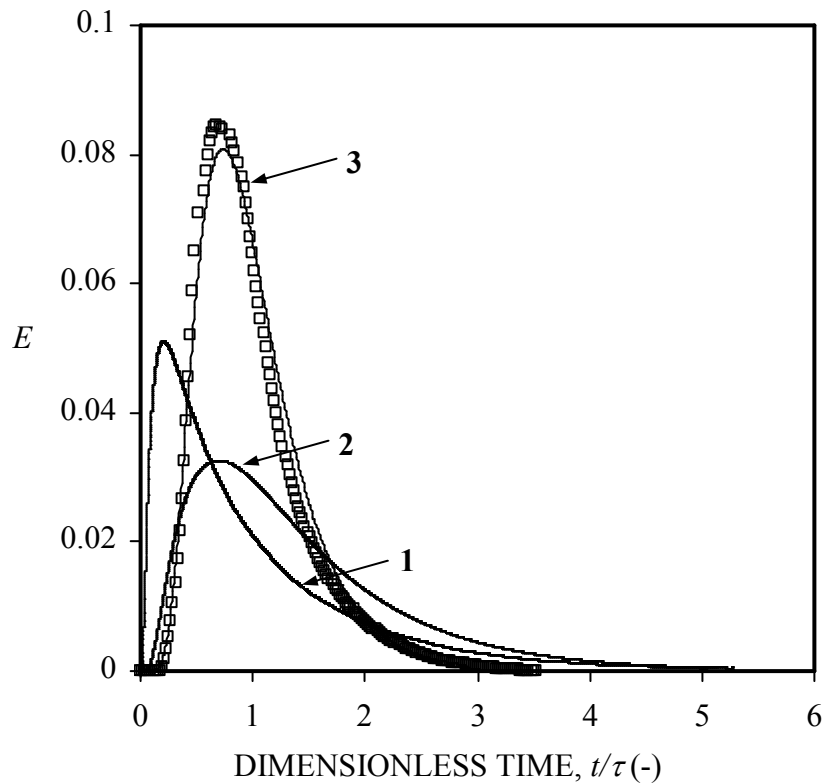


Figure 3.13. Comparison between RTD studies using CFD at 20 r/s in presence and absence of radial baffles in the annulus and total flow rate 4.16 mL/s

[1] Absence of radial baffles in annulus ($\tau=18\text{s}$) [2] Presence of radial baffles in annulus ($d=6.5\text{ mm}$, Baffle width= $d/2$, No. of baffles = 3, $\tau=18\text{s}$) [3] Presence of radial baffles in annulus ($d=3.5\text{ mm}$, Baffle width= 2.5 mm, No. of baffles = 11, $\tau=11\text{s}$) \square Experimental presence of radial baffles in annulus ($d=3.5\text{ mm}$, Baffle width= 2.5 mm, No. of baffles = 11, $\tau=11\text{s}$)

3.1.6. Conclusions

(1) An experimental technique has been developed which is capable of picking the quick response in the apparatus like Annular Centrifugal Extractors (ACEs). RTD for the annular region of ACEs has been studied experimentally as well as computationally.

- (2) An explanation has been provided for the mechanism of mixing. The convective motion has been shown to control the rate of mixing, and the role of turbulent diffusion has been found to be negligibly small.
- (3) The results obtained experimentally as well as computationally are in agreement with each other.
- (4) The RTD studies indicated the existence of a single back-mixed stage, in spite of the presence of multiple vortices in the annulus.
- (5) The number of tanks in series depends on the aspect ratio.
- (6) An attempt has been made to reduce the axial mixing by providing radial baffles, which has been shown to give practically plug flow behavior.

3.2. Estimation of Turbulent Energy Dissipation Rate in Jet loop Reactor

3.2.1 Introduction

Jet loop reactors (JLR) are frequently employed in the process industry as an alternative to impeller mixers due to the existence of relatively high convection currents leading to enhanced rate of macro-mixing at the same power consumption. In a JLR, part of the content of the vessel is recirculated by drawing it through a pump and returning it at high speed through a nozzle. The resulting high speed jet entrains some of the surrounding liquid and creates a circulation pattern within the vessel. Figure 3.14 shows the schematic of JLR and the inside flow pattern. These equipment are easy to install, operate and maintain with no requirement of any structural reinforcement of the tank and are normally cheaper in cost as compared to the conventional stirred tank reactors. Further, JLR also give improved heat and mass transfer rates (Dihn et al., 1999). Because of these advantages, JLRs are widely used in environmental and biological applications (Oldshue, 1983; Simon and Fonade, 1993) and in nuclear reactors (Dihn et al., 1999). In addition, these are used for fast, competitive-

consecutive reactions having a mixing sensitive product distribution (Baldyga et al., 1994; Forney and Nafia, 2000).

In view of these important considerations, a large number of theoretical and experimental investigations have been undertaken during the past five decades. The published work is concerned with the experimental measurements and the mathematical modeling (including CFD simulations) of (1) flow pattern and (2) mixing time. The present paper is concerned with the first objective and a brief review of the published information is given in the following sub-section.

3.2.2 Previous Work

The literature on the experimental studies of liquid jets discusses various flow aspects such as jet length, jet spread, flow regimes, liquid entrainment, recirculation rate, identification of dead zones, and turbulence aspects like energy spectrum and turbulent structures, etc. The design criteria are mainly dependent on these flow fields as well as the turbulence parameters and hence are important for the effective optimization. Various experimental tools have been used in the literature such as photography with colored dye, hot film anemometry (HFA)/ hot wire anemometry (HWA), laser Doppler velocimetry (LDV), high speed photography with seeding particles, laser based photography, optical tomography, and particle image velocimetry (PIV).

Donald and Singer (1959) proposed the jet angle for the condition of no recirculation (i.e., free jet) and estimated its relation to kinematic viscosity of fluid. Rossler and Bankoff (1963) sought for a relationship of mean dimensionless velocity as well as integral length scale with dimensionless axial distance and was found to be linear. Sadakata and Kunii (1972) compared the turbulence intensity as well as isotropy in free and recirculatory jets.

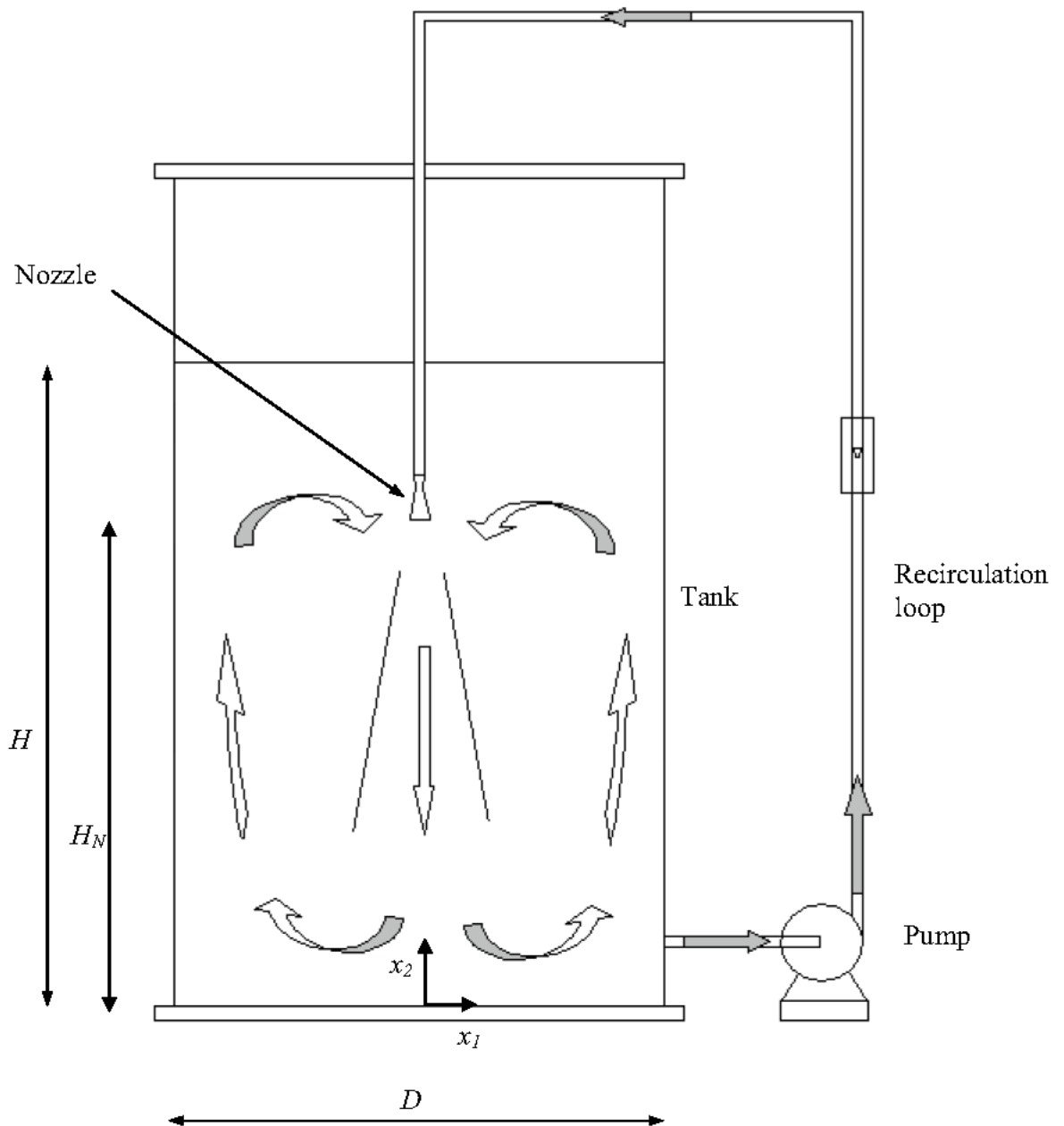


Figure 3.14: Schematic Diagram of JLR.

Usui and Sano (1980) evaluated the average velocities and length scale using high speed photographic technique and confirmed the results with LDV measurements. Lane and Rice (1982) studied the variation of cone angle with increasing Re over the range of laminar as well as turbulent regime and further found the relationship between centerline velocity as well as recirculation velocity; both as a function of the jet velocity. Boyle and Golay (1983)

DEVELOPMENT OF EXPERIMENTAL TECHNIQUES AND CFD SIMULATIONS OF MULTIPHASE DISPERSIONS

studied the flow patterns in 2D cell for transient flow using LDV and evaluated transient variation of flow and turbulent properties. Yianneskis (1991) studied the variation of type of the vortex formation with respect to jet angle, Re as well as aspect ratio. Mewes and Renz (1991) identified the location of dead zones with respect to Re , nozzle position as well as aspect ratio. Lui et al. (1994) evaluated the value of ε from 2D energy spectrum and proposed a priori analysis by evaluating the energy flux and Leonardo stress (L_{ij}) from PIV data. Webster and Longmire (1997) studied the effect of variation of nozzle face inclination as well as forcing frequency on the variation of vortex pairing and vortex spacing in the jet region. Nishimura et al. (2000) evaluated vorticity structures and the variation of its size and periodicity with respect to distance from jet. Webster et al. (2001) studied the planar variation of velocity and concentration simultaneously and proposed the self similarity in mean as well as turbulent characteristics. To summarize, the previous work regarding flow patterns in JLR reports the experiments carried out on the JLR using HFA, LDV, photography, laser sheet based photography and PIV. LDV was mainly used to compare the mean flow profiles with the CFD predictions as well as with the other measurement techniques. This is mainly because of the high accuracy with which the mean velocities can be measured using LDV. On the other hand, turbulence characteristics have been evaluated mainly using HFA. In the recent past, PIV has been used to study the local flow structures and their dynamics. The forgoing section briefly summarizes the previous work. On the basis of the analysis of the previous work, it was thought desirable to undertake a systematic experimental investigation of JLR. In particular: (1) scanty information is available in the published literature regarding the distribution of turbulent energy dissipation rate in JLR. In fact, the estimation of ε has been an outstanding problem needing closer attention. In the design of chemical process equipment, the dissipation of energy inside the most effective way ensures the energy efficient operation. e.g., when the jet is used for solid suspension, most of the energy should

DEVELOPMENT OF EXPERIMENTAL TECHNIQUES AND CFD SIMULATIONS OF MULTIPHASE DISPERSIONS

be dissipated near the bottom, where solids are settled otherwise. Similarly, in the case of jet employed for mixing (blending) of input stream to the bulk of liquid, most of the energy dissipation should be around the jet. Thus, the spatial distribution of ε inside the contactor is of prime importance while designing the contactor based on the understanding of flow patterns. Therefore, in this work, an attempt has been made to estimate using the measurements made by LDV, HFA and PIV. For this purpose, the method of eddy isolation model (Ranade et al., 1992; Sahu et al., 1995), energy spectrum (inertial range) and the method of structure function relation (Lindborg, 1999; Pope, 2000; Kang et al., 2003) have been employed for the three measurement techniques, respectively. Such estimations have been made throughout the tank and the relative comparison of all these methods has been presented. Further, if the ε distribution is known throughout the tank, its volume integral gives the total energy dissipation rate (E_D) in the tank. This value has been compared with the energy introduction rate through the nozzle ($E_I = Q_J \langle u_{2,J} \rangle^2 \rho / 2$). (2) a close observation of the energy spectrum showed the existence of flow instabilities and flow structures in the jet as well as in the bulk region. For understanding these flow phenomena it was thought desirable to undertake detailed PIV measurements and LES simulations. (3) the present work also includes comprehensive experimental measurements using HFA, LDV and PIV. HFA and LDV are the instruments for point wise measurement with high data acquisition rate. This information was used for analyzing flow characteristics in wavenumber domain. In particular, the data rate of HFA is very high (20 kHz) and hence was used for generating energy spectrum up to wave number covering good part of the dissipation scales. Note that the ability of HFA to have highest sampling frequencies up to those corresponding to dissipation regime has been utilized. However, we might still not be able to achieve sampling frequencies corresponding to Kolmogorov scale. Further, PIV was used for high spatial resolution thereby enabling the use of structure function analysis. An effort has been made to

DEVELOPMENT OF EXPERIMENTAL TECHNIQUES AND CFD SIMULATIONS OF MULTIPHASE DISPERSIONS

use the LDV, HFA and the PIV measurements in a complimentary way. The strength and the limitations of these measurement techniques will be described in the experimental section.

3.2.3 Experimental

The measurements were performed in a cylindrical plexiglass tank of 0.3 m internal diameter and 0.4 m height. This tank was enclosed in another tank of square cross-section and space between the two was filled with water to minimize refraction effects. The liquid was circulated using an external 0.5 HP centrifugal pump. The nozzle position was fixed at $H_N/D = 1$ with downward orientation (Figure 3.14). The experiments were conducted for the nozzle diameter of 20 mm. Also three flow rates (0.287, 0.416, 0.542 kg/s) were selected to investigate the effect of the nozzle velocity on the flow pattern. For measurement, PIV, LDV and HFA were employed.

3.2.3.1 Particle Image Velocimetry

The PIV apparatus consisted of a pulsed dual head Nd:YAG laser from New Wave having pulse duration of 6 ns and was synchronized with the camera using synchronizer. Optics included a combination of cylindrical and spherical lenses, attached in view of creating a thin laser sheet of 0.5 mm thickness. A high resolution 4M CCD camera (Powerview 4MP, TSI) of 15 Hz frequency was placed at right angle to the laser sheet. A zoom lens (AF micro Nikkor, 60 mm) from Nikon was used for capturing the window size of 45 mm \times 45 mm. The images were recorded with resolution of 2048 \times 2048 pixels. The flow was seeded with hollow glass-silver particles of 20 μ m diameter and 1050 kg/m³ making sure that the Stokes number for the measurement be small enough for particles to follow the path of the fluid. The recorded images were divided into interrogation area of 64 \times 64 pixels with a 50 % overlap, resulting in approximately 4000 vectors for the image. Thus, a vector spacing of 0.750 mm was obtained. Note that, the spatial resolution of PIV is decided mainly by the size of measurement window (the size of the area captured by camera used for PIV),

DEVELOPMENT OF EXPERIMENTAL TECHNIQUES AND CFD SIMULATIONS OF MULTIPHASE DISPERSIONS

the resolution of camera, the seeding size and seeding concentration in the recorded image. The smallest interrogation window size is mainly determined by the requirement of having a minimum 5-15 seeding particles in each interrogation window. The factors like out of plane motions of particles require the use of larger interrogation window. The techniques like multi-pass processing and deformation window processing allow usage of smaller window sizes like 16×16 pixels compared to a typical of 64×64 pixels used in conventional Nyquist grid processing. However, they provide no solution for particles moving out of plane. Even after using the smallest interrogation window sizes, the vector spacing may correspond to several Kolmogorov scales. However, it still might be sufficient to describe the time averaged velocity profile nicely. In the present study, use of advanced multi-pass algorithms like deformation grids has improved the physical resolution. However, relatively coarse grid guarantees enough number of particles inside each window and hence less number of invalid vectors; ultimately increasing the accuracy of estimation of higher order statistics like the third order structure functions. The time difference between the two laser pulses was optimized based on Nyquist criterion. Thus, a time delay of $400 \mu s$ was used. This ensures that velocities of up to 1 m/s are captured accurately without significant number of particles moving out of the interrogation window. A nonlinear calibration analysis was carried out in order to obtain accurate values of the velocities. The personal computer functioned as a central data acquisition and also processing unit. The possibility of error occurs in various stages of measurements viz. calibration, image capture and image analysis (Aldrian, 1996, 2005; Kompenhans and Tropea, 1997). During calibration, grid plate alignment is required to be in the plane of the laser. A change in angle of 3° results in significant error in the projected vector. This error is minimized by carefully aligning the grid in plane based on the mirror fixed on it. The overlapping of input and reflected image ensures the accurate alignment. Other important consideration is the focusing of camera in the plane of laser and

the depth of focus. While capturing the images, factors that require attention are intensity and uniformity of two consecutive laser pulses, size concentration and distribution of seeding particles, pulse delay, etc. These parameters can be adjusted based on trial error method to obtain a good visibility and even distribution of seeding in the captured image. The pulse delay is set depending upon the flow velocity to be captured and window size covered such that particle pairs are visible. In view of obtaining good cross-correlation, 10-12 particle pairs per interrogation spot are desired to give very high reliable data for image processing. In order to cover the entire plane below the jet, 4 windows in radial direction and 7 windows in the axial direction have been recorded during PIV measurements. Enough number of images were captured for each small window such that third order statistics was also independent of more number of images.

3.2.3.2 Laser Doppler Velocimetry (LDV)

Three beam LDV was used to make simultaneous measurement of two velocity components. The LDV set-up comprised of Dantec 55 X modular series optics along with electronic instrumentation and a personal computer. A 5 W, Spectra Physics Argon-ion laser was used as a source. Laser and the other optics were mounted on a bench. To identify the flow reversals correctly, a frequency shift was given to one of the beams by means of Bragg cell with electronic downmixing. Data validation and signal processing were carried out with the help of a Dantec 57N21 Burst spectrum analyzer. The personal computer functioned as a central data acquisition as well as a processing unit. Forward scatter optical arrangement was employed in all the measurements. Further, details may be obtained from Ranade and Joshi (1990) and Ranade et al. (1992). The velocity information was collected with an average validated data rate of about 200 Hz in low velocity region and with 800 Hz in high velocity regions. The measurements have been carried out for axial and radial components of liquid

DEVELOPMENT OF EXPERIMENTAL TECHNIQUES AND CFD SIMULATIONS OF MULTIPHASE DISPERSIONS

velocity at 20 radial locations (from $x_1 = 0.0$ m to $x_1 = 0.14$ m), 3 axial locations (viz. $x_2 = 0.1$ m, 0.2 m and 0.28 m) and at the flow rates of 0.287, 0.416 and 0.542 kg/s.

3.2.3.3 Hot Film Anemometer (HFA)

The HFA (Dantec make) was used for the simultaneous measurement of two velocity components by employing X-Film type dual probe (quartz fiber probe 55R63, covered by Ni thin film of thickness $0.1 \mu\text{m}$, sensor diameter $70 \mu\text{m}$, overall fiber length 3 mm, sensor length 1.25 mm). A Constant Temperature module (CTA) was used in the system, which gives velocity versus voltage data profile for every fiber film. Built-in signal conditioners were provided for high pass and low pass filtering and for amplification of the CTA signal. The acquired signal then moves through computer via A/D board, which controls various operating parameters such as number of channels, resolution, sampling rate and external triggering. Further, personal computer functioned as the central data acquisition and a controller to all the modules such as CTA, signal conditioners, A/D board and traverse unit. The calibration of the probe was performed on the same setup at 50 mm below the nozzle at centerline axis. Local velocities were obtained by LDV and corresponding voltages for both the films acquired using HFA at various flow rates (0 to 3.5 m/s) and temperatures (24°C to 40°C). The calibration curves for velocity and temperature have been incorporated into an in-house code which processes the voltage-time data into velocity-time data. In case of HFA measurements, evaluation of probe response at high frequency is essential. It was executed and optimized using the square wave test i.e. by applying a square wave signal to the bridge top. Optimization involves selection of the filter for the pre-amplified bridge unbalance signal (to avoid high frequency noise and folding of spectra), selection of gain of the servo loop amplifier (amplification of the output from probe to utilize the A/D converter best possible) and tuning the cable inductance. In this case the value of frequency response was optimized with 13 % under shoot (Bruun, 1996; Dantec Dynamics, 2000), where the

DEVELOPMENT OF EXPERIMENTAL TECHNIQUES AND CFD SIMULATIONS OF MULTIPHASE DISPERSIONS

response frequency was 65 kHz. Hence the measurements were carried out at 20 kHz in order to avoid noise at high frequency. In the present case, effect of temperature change was nominal, hence the temperature response frequency was less important. The HFA measurements were carried out at Heights of 0.28 m, 0.25 m, 0.2 m, 0.15 m, 0.1 m and 0.05 m, at a radial spacing of 10 mm for further analysis.

3.2.3.4 Need for Multiple Measurement Technique

The relative merits of the three measuring techniques are summarized in Table 3.3 wherein advantages and limitations of HFA, LDV and PIV have been highlighted. HFA gives equispaced velocity dataset at high data rate (20 kHz) which enables spectral analysis, but its accuracy is highly dependent upon successful calibration of voltage measurement to velocity data. While, LDV is factory calibrated, it obtains the velocity dataset with a poisson distribution, and suffers from velocity bias and particle rate filter. Both of these techniques lack spatial resolution. On the other hand, PIV gives planar measurements and good spatial resolution, and enables two and three component measurements possible. Note that, the term 'limited spatial resolution' (Table 3.3) is highly relative. The spatial resolution should be considered with reference to the length scales of interest for the typical experiment under consideration. For instance, Kolmogorov length scale for typical turbulent air flow is around few millimeters (Lindborg, 1999); while in water it corresponds to few micrometers for similar Reynolds number [Table 3.4]. The relative performance of these measuring techniques in obtaining the mean and turbulent quantities, and in computing energy spectrum is outlined in Table 3.3. For mean flows, only LDV and PIV need to be used.

DEVELOPMENT OF EXPERIMENTAL TECHNIQUES AND CFD SIMULATIONS OF MULTIPHASE DISPERSIONS

Table 3.3: Multiple Measurement Techniques

Table 3.3 A : Relative merits of different measurement techniques			
No	Technique	Advantages	Limitations
1.	Hot Film Anemometry	<ol style="list-style-type: none"> 1. Very high data rate (20 kHz) 2. Equispaced data 3. Evaluation of entire energy spectrum possible 	<ol style="list-style-type: none"> 1. Intrusive technique 2. Voltage velocity calibration is critical 3. Limited response at high frequencies 4. Voltage stability crucial 5. Variation in temperature is crucial 6. Negative velocity cannot be measured and therefore the results of mean velocity cannot be reported
2.	Laser Doppler Velocimetry	<ol style="list-style-type: none"> 1. Non-intrusive technique 2. Factory calibrated 3. Micron size seedings are traceable 	<ol style="list-style-type: none"> 1. Non-equispaced data 2. Interpolation is needed 3. High frequency values of energy are anomalous (particle rate filter) 4. Velocity bias
3.	Particle Image Velocimetry	<ol style="list-style-type: none"> 1. Planar measurements 2. Two and Three component measurements possible 3. Evaluation of spatial derivatives is possible 4. Velocity measurement over wide range possible 	<ol style="list-style-type: none"> 1. Low data rate 2. Window size limits the spatial resolution 3. Strong velocity gradients

Table 3.3 B : Performance of different measurement techniques				
No	Performance Parameter	HFA	LDV	PIV
1	Mean	Cannot be estimated	Accurately measured	Accurately measured
2	Turbulence kinetic energy	Gives good estimate	Gives good estimate	Gives good estimate
3	Energy dissipation rate	Obtained using energy spectrum	EIM method + dimensional analysis	Structure function
4	Energy spectrum	3D energy spectrum gives correct values	Equispacing required	Structure function method

DEVELOPMENT OF EXPERIMENTAL TECHNIQUES AND CFD SIMULATIONS OF MULTIPHASE DISPERSIONS

Table 3.4. Flow Parameters Obtained using PIV/HFA (Case of 0.542 kg/s)

Axial Location	x_2 (m)	0.28			0.2			0.1		
Radial Location	x_1 (m)	0	0.01	0.05	0	0.01	0.05	0	0.01	0.05
Mean	$\langle u_2 \rangle$ (m/s)	-2.07	-0.686	0.02	-1.18	-0.96	-0.085	-0.75	-0.82	-0.21
RMS Velocity	u_{1RMS} (m/s)	0.4	0.32	0.051	0.3	0.31	0.155	0.19	0.185	0.108
	u_{2RMS} (m/s)	0.5	0.42	0.047	0.38	0.382	0.146	0.25	0.274	0.11
Isotropy ratio	I (-)	1.2	1.31	0.922	1.27	1.232	0.942	1.31	1.481	1.02
Turbulent Kinetic Energy dissipation rate	ε (m ² /s ³)	16.2	32.1	0.005	8.7	14.57	0.008	4.57	2.24	0.028
Taylor Microscale	λ (m)	2.0×10^{-4}	2.8×10^{-4}	2.9×10^{-3}	4.1×10^{-4}	4.72×10^{-4}	2.1×10^{-3}	8.9×10^{-4}	8.6×10^{-4}	1.9×10^{-3}
Kolmogorov Length scale	η (m/s)	1.2×10^{-5}	1.3×10^{-5}	1.2×10^{-4}	1.7×10^{-5}	1.8×10^{-5}	9.6×10^{-5}	3.1×10^{-5}	2.0×10^{-5}	8.0×10^{-5}

DEVELOPMENT OF EXPERIMENTAL TECHNIQUES AND CFD SIMULATIONS OF MULTIPHASE DISPERSIONS

HFA cannot be employed to estimate the mean flows owing to its inability in predicting the flow direction, and the negative velocities associated with flow reversals. HFA is based on the temperature change arising out of the convective motion of flow, which is a scalar. Hence, it gives only the absolute magnitude of the velocity. On the other hand, LDV measurements are based on the Doppler shift principle and hence velocity is a linear function of frequency shift. The velocity direction is determined on the basis of the detected value of scattered beam frequency with respect to value of frequency of shifted beam (40 MHz). Thus, LDV is capable of measuring the direction of velocity and hence gives the mean values correctly. Similarly, PIV measurements are based on the cross-correlation technique; thus it also measures the direction of the flow and hence PIV also measures the mean values accurately. For the measurement of turbulent kinetic energy (k), all the three techniques can be employed equally accurately. However, similar statement can not be made for the estimation of ε . It is known that, ε can be accurately evaluated from HFA data by constructing 3D energy spectrum. Alternate methodology based on structure functions can be used for HFA data provided the minimum possible distance between the two probes would be sufficiently short to lie in the inertial range. This methodology is not suitable for LDV mainly because the LDV based energy spectrum is relatively less reliable than that based on HFA data. However, for both the cases of HFA and LDV, the simultaneous measurement at two neighboring locations is rarely practiced. Additionally, the LDV data is inherently non-equispaced and hence, first step before calculation of spectra is equispacing. Further, the Fourier transform is evaluated for estimate the energy as a function of frequency. The correction is obtained for change of axis from frequency to wavenumber as $\kappa = 2\pi f / \langle u \rangle$. Because of inaccuracies related to the equispacing, the anomalous behavior is

DEVELOPMENT OF EXPERIMENTAL TECHNIQUES AND CFD SIMULATIONS OF MULTIPHASE DISPERSIONS

seen for higher frequencies in the energy spectra. There have been alternative methods developed based on the slotting technique from the randomly placed data using autocorrelation (Maanen et al., 1998, 1999) but they are compute intensive and hence less popular. In the framework of these limitations of HFA and LDV, the PIV is a useful technique because it gives simultaneous measurements at several locations. In PIV case, ε is evaluated on a plane using the structure function based method by maintaining the spatial resolution to lie within inertial range. From the foregoing discussion it can be seen that, each measurement technique has its own strength and limitations. The advantageous aspects of one measuring technique help in verifying measurements obtained using other measurement techniques.

1. HFA needs calibration. This can be best achieved by measurement using HFA and LDV over a wide range of flow behavior particularly the regions of sharp velocity gradients. Further, it would be fortunate coincidence if such measurements are made in an equipment for which extensive HFA data are to be collected.

2. HFA is more useful for getting turbulence information. It can not be used for getting accurate mean flow pattern for which LDV is known to be suitable equipment.

3. If LDV is to be used as a major tool, it has a limitation of constructing energy spectrum. First of all, LDV gives velocity information which is unequispaced in time. All the methods of equispacing have limitations. It is desirable to verify the LDV based spectrum with HFA. Further, LDV has a limitation of wavenumber up to which energy spectra can be constructed.

4. estimation from PIV may require some support of HFA data (this subject will be discussed in the section of results and discussions).

5. Spatial derivatives cannot be evaluated from HFA/LDV data. Only PIV can be used for this purpose. Further, PIV gives a lot more space information on flow instabilities and about non-coherent and coherent turbulent structures.

3.2.3.5 Processing Method

3.2.3.5.1 PIV data processing

PIV data were further processed in order to eliminate the spurious vectors. The data were first subjected to the high and low pass filters to eliminate out-of-range vectors. Further, the data was double-correlated to find the relative direction of neighboring vectors and thus deciding the flow governing vectors and removing the noise (Adrain, 1996, 2005). The processed data was tested and was used further for the calculation of mean and turbulence information.

3.2.3.5.2 LDV/HFA data processing

The velocity data were first of all subjected to the elimination of noise and then processed to find mean and turbulence information. The methodology for the estimation of energy dissipation rate (ε) using energy spectrum has been discussed in detail in results and discussions.

3.2.4 CFD Simulations

3.2.4.1 Model formulation and boundary conditions

The equation of continuity and motion for a three dimensional system can be represented in the following form ,

$$\frac{\partial u_i}{\partial t} + \frac{\partial u_i}{\partial x_i} = 0 \tag{3.13}$$

$$\frac{\partial u_i}{\partial t} + \frac{\partial u_i u_j}{\partial x_j} = -\frac{1}{\rho} \frac{\partial P_i}{\partial x_i} + \frac{\partial}{\partial x_j} \left(\nu \frac{\partial u_i}{\partial x_j} \right) \quad (3.14)$$

In the present case, in order to set the exact inlet boundary condition, the nozzle was separately simulated with known inlet flow conditions. The outlet profiles of the nozzle were stored in order to use them as a boundary condition at the inlet of the reactor. The diameter of outlet of reactor was set to be 0.0254 m, and was located at the peripheral radial location at $x_2=0.05$ m. The velocity at the outlet was determined such that global mass balance is obtained and the outlet pressure was set at atmospheric condition. The tank walls and the base of the tank are specified as impermeable boundaries. Thus velocity component normal to the surface is set to zero. Standard wall functions were used to specify the gradients of velocities at the wall. The top liquid surface was simulated as a flat interface. The normal flux and the gradients of the other quantities were specified to be zero. The prediction of the fluctuations of the top liquid surface is assumed to be flat.

3.2.4.2 Turbulent models and method of solutions

3.2.4.2.1 LES Model

The LES model equations have been derived and obtained as follows:

$$\frac{\partial}{\partial t} (\overline{u_i}) + \frac{\partial}{\partial x_j} (\overline{u_i u_j}) = \frac{\partial}{\partial x_j} \left(\nu \frac{\partial \overline{u_i}}{\partial x_j} \right) - \frac{1}{\rho} \frac{\partial \overline{P}}{\partial x_i} - \frac{\partial \overline{\tau_{ij}}}{\partial x_j} \quad (3.15)$$

$$\overline{\tau_{ij}} = \overline{u_i u_j} - \overline{u_i} \overline{u_j} \quad (3.16)$$

$$\overline{\tau_{ij}} - \frac{1}{3} \overline{\tau_{kk}} \delta_{ij} = -2\nu_{SGS} \overline{S_{ij}} \quad (3.17)$$

$$\overline{S_{ij}} = \frac{1}{2} \left(\frac{\partial \overline{u_i}}{\partial x_j} + \frac{\partial \overline{u_j}}{\partial x_i} \right) \quad (3.18)$$

DEVELOPMENT OF EXPERIMENTAL TECHNIQUES AND CFD SIMULATIONS OF MULTIPHASE DISPERSIONS

In case of LES modeling, one equation sub-grid scale (SGS) model has been used for closure in Fluent 6.2. In this model, model coefficient has been calculated based on Leonard stresses. The hexahedral grid was taken and about 0.66 million node points were employed. The inlet boundary condition has been given from a separate simulation of nozzle same as that of in the earlier model cases. The fluctuations have been artificially given to the inlet profile by random number generation program. The details of model equations can be obtained in (Pope, 2000; Mathpati and Joshi, 2007). The simulations have been performed with a staggered grid arrangement and with bounded central difference discretization scheme for momentum. For pressure-velocity coupling, PISO description scheme was employed. The second order implicit time discretization has been adapted with time increment of 0.0005 sec. The time required to converge the steady state RANS model was of the order of 4-5 hours. On the contrary, LES required higher mesh size as well as parallel computational resources. The transient simulation for 30 seconds on two processors of AMD 3.0 GHz machine required approximately 25 days. Thus, when the aim is to study the steady state properties, RANS models would suffice provided their parameters have been finely tuned for corresponding experimental results. In order to optimize the systems for transient effects in critical conditions, LES would be essential tool, however, in order to resolve the wavenumbers in the inertial range higher grid numbers and computational time is essential.

3.2.5 Results and Discussion

3.2.5.1 Flow Characteristics: Comparison of PIV results with LDV Measurement

Figure 3.15A shows a comparison of mean axial velocity at a flow rate of 0.542 kg/s and at $x_2 = 0.1$ m. It can be seen that both the techniques give practically the same results, the maximum difference being at the center which is about 3 percent. The comparison of RMS

DEVELOPMENT OF EXPERIMENTAL TECHNIQUES AND CFD SIMULATIONS OF MULTIPHASE DISPERSIONS

velocities using LDV and PIV has been shown in Figure 3.15B. A reasonably good agreement is seen among the two data sets.

The hydrodynamic parameters have been obtained from the experimental data set, (with LDV and PIV and at various locations). These include isotropy ratio $I = u_{2RMS}/u_{1RMS}$, turbulence intensity $u_{2RMS}/\langle u_2 \rangle$, turbulent energy dissipation rate ε (procedure described in the next section), the Taylor micro-scale $\lambda = (15u_{2RMS}^2\nu/\varepsilon)$ and the Kolmogorov length scale $\eta = (\nu^3/\varepsilon)^{1/4}$. The results have been summarized in Table 3.3 at three axial locations and only at three radial locations (the values across all the radial locations have not been reported for keeping brevity of the manuscript). The three radial locations bring out the characteristic features of the central jet region, shear region as well as the bulk pool. It can be clearly observed from Table 3.4 that, in the central jet region as well as in the shear region, anisotropy exists, with shear region showing relatively high anisotropy.

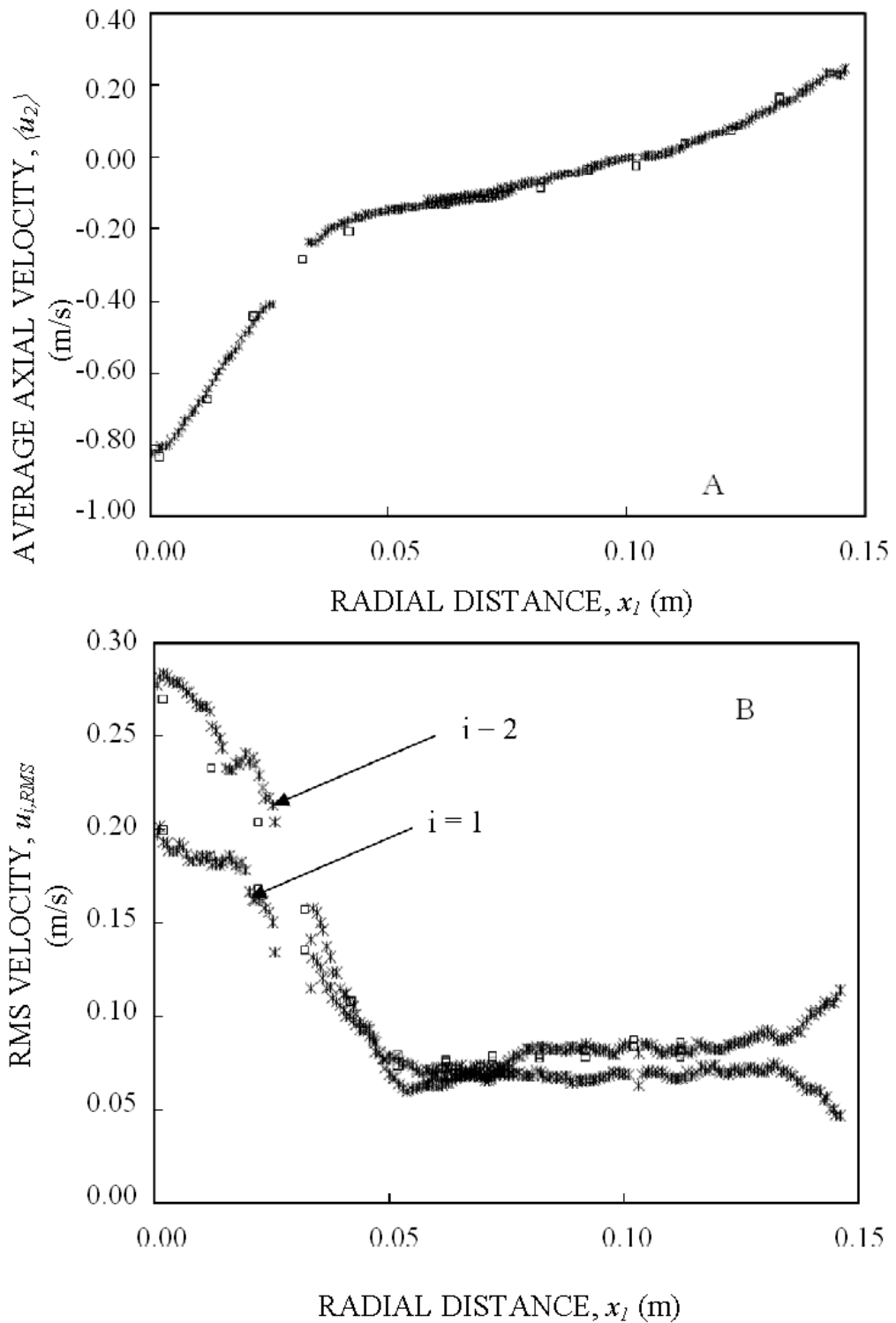


Figure 3.15: Radial profiles of mean and RMS velocity measured by PIV and LDV at $x_2 = 0.1$ m. (A) Mean Axial Velocity, u_2 (m/s); (B) RMS Velocity (m/s), $u_{i,RMS}$ where $i=1$ Radial; $i=2$ Axial : * PIV Results; \square LDV Results.

On the other hand, in the bulk region ($0.04 \text{ m} < x_1 < 0.09 \text{ m}$) nearly isotropic conditions can be seen to prevail.

3.2.5.2 Estimation of Turbulent Energy Dissipation Rate per unit Mass (ε)

The literature describes various methodologies wherein energy spectra have been used to estimate the value of ε . Few of these methods were devised for the data obtained from single point HFA probe (Obukhov, 1962; Sffiman, 1970; Frisch, 1994; Sreenivasan, 1999; Pearson et al., 2002; Tsuji, 2004). The methods are mainly based on the Taylor series approximations and have been studied mainly for the cases of homogeneous and isotropic turbulence. These methods have linked the energy spectra and the structure functions exponents by an algebraic relationship. In an another approach, the methodology of structure function using multiple HFA probes has essentially been illustrated in the literature by Lindborg (1999), Pope (2000) and Kang et al. (2003) to calculate ε for the conditions where the spatial distance between the two points is maintained such that they lie in the inertial range. In this approach, using the array of probes, the methodology become more robust, and the correlations among the neighboring successive probe velocity give the information about the parameters in the form of structure functions. These in turn give values of the turbulence parameters such as ε . Thus, the relationship between the structure function and the energy spectrum has been made generalized by simultaneously solving the set of nonlinear equations. In the present study, an attempt has been made to apply the later methodology for PIV data which otherwise are difficult to estimate accurately using conventional methods.

DEVELOPMENT OF EXPERIMENTAL TECHNIQUES AND CFD SIMULATIONS OF MULTIPHASE DISPERSIONS

3.2.5.2.1 Method of Third Order Structure Function using PIV Data

Since the measurement vector spacing (0.750 mm) has been found to be about 20 times more than the Kolmogorov length scale η , the dissipation scale is not sufficiently resolved in the present experiments. Therefore, turbulent energy dissipation rate (ε) cannot be obtained accurately from the derivative variance and Lindborg (1999), Pope (2000) and Kang et al. (2003) have suggested a procedure on the basis of structure functions for multiple probe HFA. The procedure has been extended for PIV as described below. Second and third order structure functions (Frisch, 1994; Sreenivasan, 1999) can be obtained as:

$$D_{uu} = \langle [(u_2(x_1 + r_D, x_2) - u_2(x_1, x_2))]^2 \rangle \quad (3.19)$$

$$D_{uuu} = \langle [(u_2(x_1 + r_D, x_2) - u_2(x_1, x_2))]^3 \rangle \quad (3.20)$$

In the present study, the r_D has been evaluated based on the radial direction being the maximum gradient direction. Further, the relationship between D_{uuu} and ε can be obtained as:

$$D_{uuu} = -\frac{4}{5} \varepsilon r_D + 6\nu \frac{\partial D_{uu}}{\partial r_D} - \frac{3}{r_D^4} \int_0^{r_D} r_D' r_D'^4 \frac{\partial D_{uu}}{\partial t} dr_D' \quad (3.21)$$

The second term on the right hand side of eq (3.21) shows the effect of diffusivity, while the last term represents the decay in the mean flow direction. To calculate $\frac{\partial D_{uu}}{\partial t}$ in eq (3.21), Kolmogorov's second similarity hypothesis ($D_{uu} = C\varepsilon^{2/3}r_D^{2/3}$) and the $k-\varepsilon$ model for the decay of the dissipation ($\frac{\partial \varepsilon}{\partial t} = -C_{\varepsilon 2} \frac{\varepsilon^2}{k}$) were used. The values of C and $C_{\varepsilon 2}$ have been varied in the range 1.6 - 2.3 and 1.6 - 2.1 respectively. Thus eq (3.21) becomes:

$$\frac{D_{uuu}}{\varepsilon r_D} = -\frac{4}{5} + C \left[4 \left(\frac{r_D}{\eta} \right)^{-4/3} + \frac{2\sqrt{2}C_{\varepsilon 2}}{\sqrt{5}} \frac{\nu}{k\lambda} \left(\frac{r_D}{\eta} \right)^{2/3} \right] \quad (3.22)$$

ε in eq (3.22) has been determined by iterative process. [Discussed in subsection 5.2.3].

3.2.5.2.2 Energy Spectrum using LDV/HFA Data

The energy spectrum can be obtained from LDV/HFA data by using the functional form given by Pope (2000) and Kang et al. (2003) :

$$E(\kappa) = C_{\kappa} \varepsilon^{2/3} \kappa^{-5/3} \left[\frac{\kappa l}{[(\kappa l)^{\alpha_2} + \alpha_1]^{1/\alpha_2}} \right]^{5/3 + \alpha_3} e^{-\alpha_4 \kappa \eta} \times \left[1 + \alpha_5 \left(\frac{1}{\pi} \tan^{-1} \{ \alpha_6 \log_{10}(\kappa \eta) + \alpha_7 \} + \frac{1}{2} \right) \right] \quad (3.23)$$

where, C_{κ} , α_1 , α_2 , α_3 , α_4 , α_5 , α_6 and α_7 are the parameters in eq (3.23). In this

equation, $\kappa^{-5/3}$ represents the main scaling in the inertial range, $\left[\frac{\kappa l}{[(\kappa l)^{\alpha_2} + \alpha_1]^{1/\alpha_2}} \right]$

reproduces the energy spectrum at low wavenumber $\kappa < l^{-1}$ where $l = 0.1$ m. Factor $e^{-\alpha_4 \kappa \eta}$ represents the high wavenumber decay in the dissipation region. Further, arctangent factor varies from 1 at low wavenumber to $1 + \alpha_5$ at high wavenumber which considers the change in slope from the inertial range to the dissipation range. Further, one-dimensional energy spectrum is related to the 3D energy spectrum as given by the following equations:

$$E_{11}(\kappa_2) = \frac{1}{2} \int_1^{\infty} \frac{x^2 - 1}{x^3} E(\kappa_2 x) dx \quad (3.24)$$

$$E_{22}(\kappa_2) = \frac{1}{2} \int_1^{\infty} \frac{x^2 + 1}{x^3} E(\kappa_2 x) dx \quad (3.25)$$

DEVELOPMENT OF EXPERIMENTAL TECHNIQUES AND CFD SIMULATIONS OF MULTIPHASE DISPERSIONS

To find α_i ($i=1,7$), one-dimensional energy spectra were estimated using eq (3.24) and (3.25) with $E(\kappa)$ written as in eq (3.23) with some assumed set of parameter values. Results are compared to the measured longitudinal spectra and the procedure was repeated until a good agreement between the fitted and original one-dimensional spectra was achieved. In the case of JLR, it is necessary to determine 3D energy spectrum mainly because evaluation of $E(\kappa)$ from eq (3.23) requires the calculation of derivatives which are difficult to estimate accurately at this resolution. Secondly, the flow is not at very high Reynolds number across the entire tank and universality of constants may not be valid; thus it is necessary to fine tune the parameters. Additionally, the flow is anisotropic and hence equations proposed for isotropic conditions cannot be used directly. Hence an iterative process is required in order to evaluate the value of $E(\kappa)$ based on eq (3.23).

3.2.5.2.3 Optimization algorithm

The methodologies mentioned in the earlier sub-section consist of set of parameters which in turn decide the value of ε . Hence, the sensitivity of each of the methods has to be evaluated. Further, a common methodology is essential in order to find the correct parameters in the system. For this purpose, both PIV and HFA/LDV data have been used complementary to each other to find optimized parameters and thereby accurate prediction of ε is obtained. The following stepwise procedure has been employed in the present work (the procedure is also summarized in the form of flow chart in Figure 3.16):

1. The value of energy dissipation rate (ε) is estimated by analyzing the PIV data over the entire plane using method discussed in the previous sub-section. The measurement window contains 64×64 vectors ($45 \text{ mm} \times 45 \text{ mm}$) and solution was evaluated based on 1024 vector sets for the solution of variables in eqs (3.20)-(3.23).

DEVELOPMENT OF EXPERIMENTAL TECHNIQUES AND CFD SIMULATIONS OF MULTIPHASE DISPERSIONS

2. 3D Energy spectra are obtained using eq (3.23) with assumed values of parameters α_i ($i = 1, 7$) and the value of ε from step 1.
3. 1D energy spectrum is calculated from eqs (3.24) and (3.25).

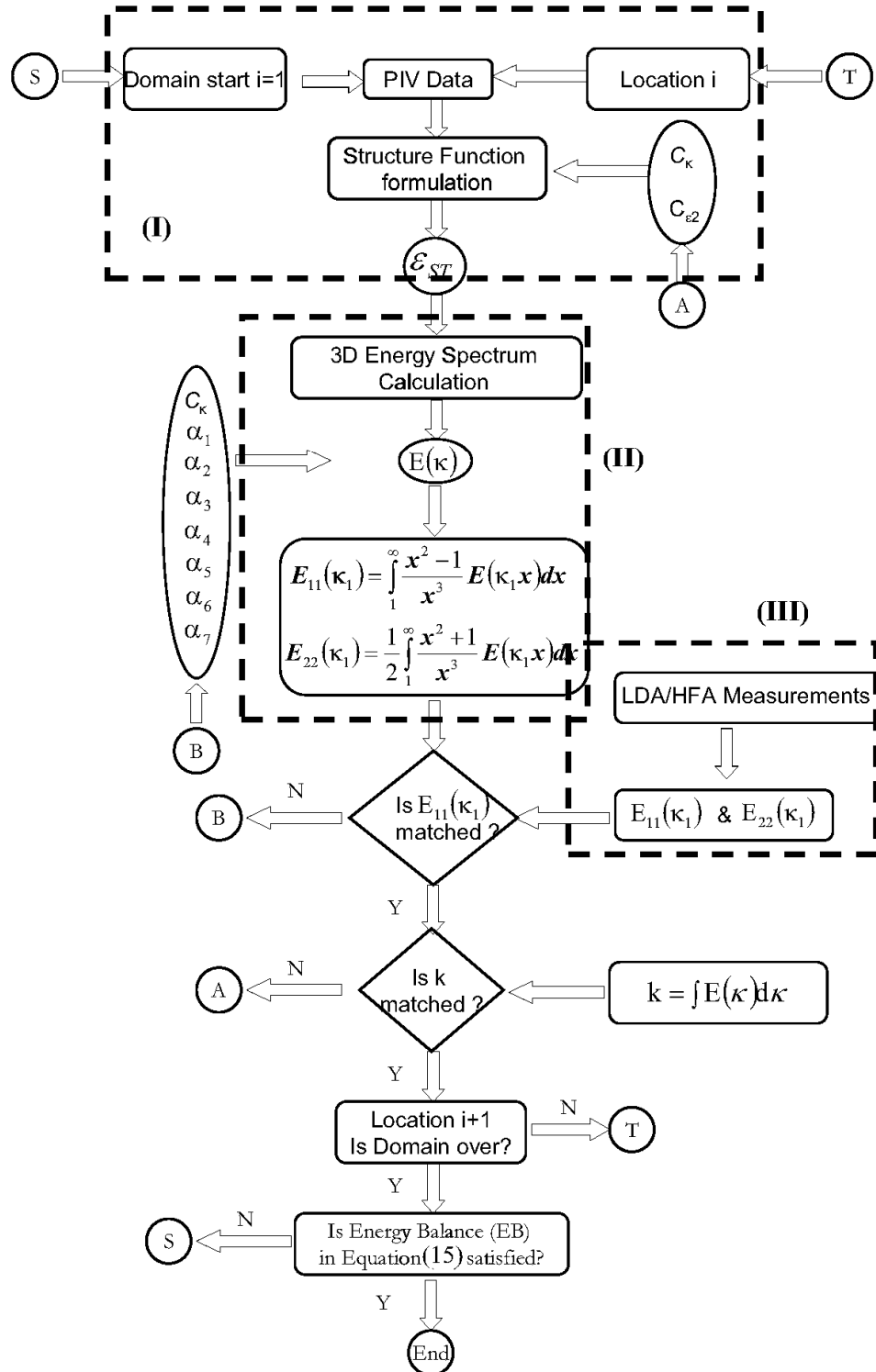


Figure 3.16: Flow chart for estimation of ϵ by iterative procedure from PIV and HFA data.

DEVELOPMENT OF EXPERIMENTAL TECHNIQUES AND CFD SIMULATIONS OF MULTIPHASE DISPERSIONS

4. 1D energy spectrum is plotted using LDV/HFA data.
5. The energy spectra from steps 3 and 4 are quantitatively compared.
6. Steps 2-3 are repeated till step 5 is satisfied by variation of parameters α_i ($i = 1, 7$) in eq (3.24).
7. The turbulent kinetic energy of the 3D energy spectrum is obtained as:

$$k = \int E(\kappa) d\kappa \quad (3.26)$$

This value is matched with that obtained from fluctuating components u_i' . All the three components of velocity have been obtained by independent measurements of axial-radial and axial-tangential simultaneous measurements.

The flowchart has three main parts (I) PIV data and structure function method (II) theoretical 3D and 1D energy spectra evaluation, and (III) 1D energy spectra evaluation based on HFA data. The parameters have been estimated based on iterative procedure and various checks have been placed such as k balance at each location and global energy balance.

8. Steps 1-7 are repeated till step 7 is satisfied with variation of parameters C and $C_{\varepsilon 2}$ in eq (3.22) and C_κ in eq (3.23). The error minimization between theoretical and experimental k values has been the criteria at each location within 1 %. This satisfies the local criterion for the evaluation of at a point.

9. Steps 1-8 are repeated at all the locations where PIV and LDV/HFA data co-exist.
10. PIV data are used for all the locations with final set of parameters as per step 1.
11. As a final step, the estimated values of ε have been integrated over the volume to check the energy balance as

$$\frac{P_{in}}{\rho \int_V dV} = \frac{\int_V \varepsilon dV}{\int_V dV} \quad (3.27)$$

where

$$P_{in} = \frac{1}{2} Q_J \left(\frac{\sum_{r=0}^{d/2} \langle u_2(r) \rangle (2\pi r^2)}{\sum_{r=0}^{d/2} (2\pi r^2)} \right)^2 \quad (3.28)$$

12. Error in eq (3.27) has been reduced based on setting the value of ε as a new guess for steps 1-11 with special emphasis on step 10 where the variation in the local values of parameters have been evaluated based on the criteria of local isotropy ratio by varying the cutoff value. The criterion for convergence is set to be less than 10 % error in the energy balance.

3.2.5.2.4 Results of ε

Third order structure functions were evaluated using PIV data for the substitution in eq (3.21). Further, function $\frac{D_{uuu}}{\varepsilon r_D}$ was evaluated with respect to r_D . For isotropic and homogeneous flow at high Re , according to Kolmogorov's similarity hypothesis, this value comes out to be 4/5. However, for anisotropic and/or intermittent flow behavior, the deviation from this value is observed. As shown in the Figure 3.18A the value of $\frac{D_{uuu}}{\varepsilon r_D}$ was found to be below 0.8 which is in line with the literature obtained for air jet (Lindborg, 1999) (Figure 3.17). Thus, necessity of eq (3.23) as well as anisotropic nature of the flow has been verified.

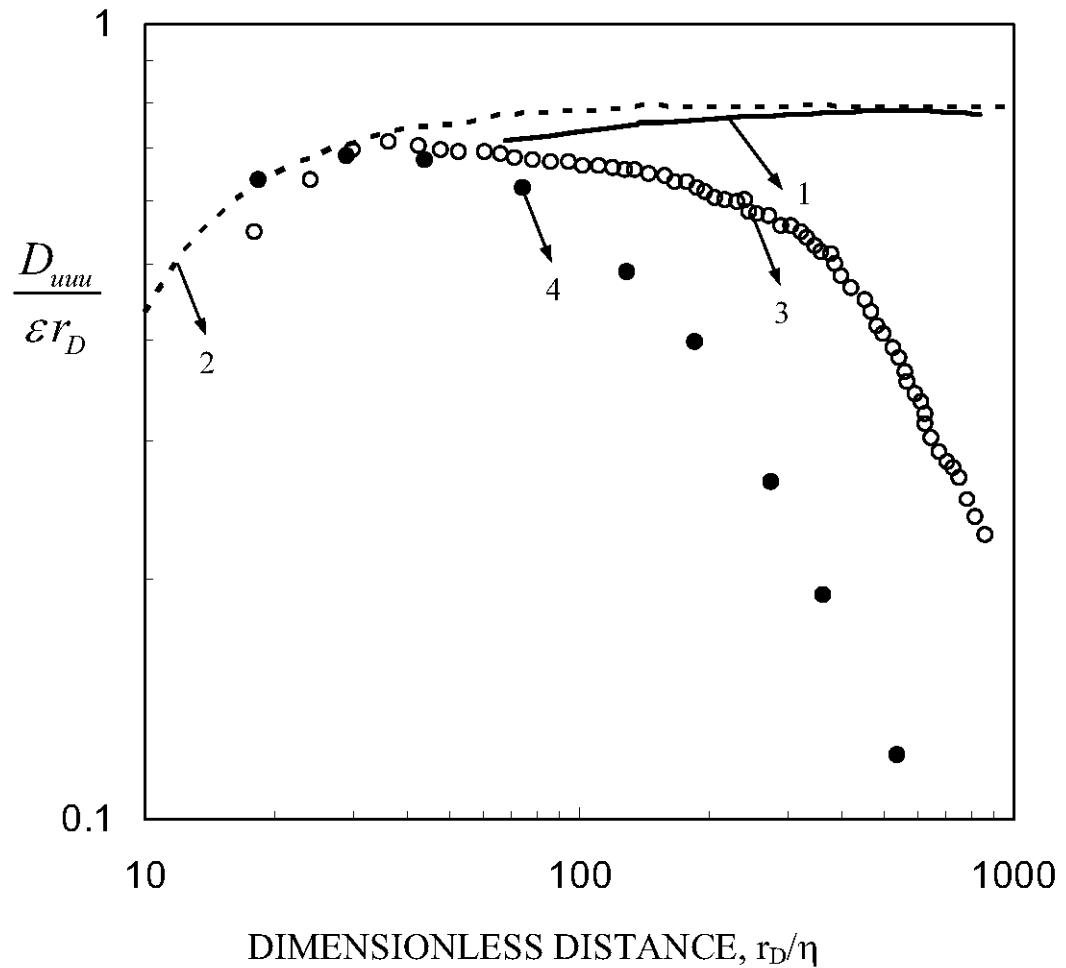


Figure 3.17: $\frac{D_{uuu}}{\epsilon r_D}$ vs $\frac{r_D}{\eta}$ profile 1. Present case flow rate = 0.542 kg/s. (2-4)

Literature data for jet experiments [10] : 2 From stationary data; 3 Grid turbulence $Re_\lambda = 449$; 4 Grid turbulence $Re_\lambda = 99$.

Similarly, energy spectrum was obtained from HFA data. Figure 3.18A shows one dimensional longitudinal energy spectra of axial velocity component $E_{22}(\kappa_2)$ and longitudinal energy spectra of radial velocity component $E_{11}(\kappa_2)$, where, κ_2 is the longitudinal wavenumber. Statistically well converged spectra were calculated by partitioning the data set into O(1000) segments (with 50 % overlapping) of 2^{15} points each.

DEVELOPMENT OF EXPERIMENTAL TECHNIQUES AND CFD SIMULATIONS OF MULTIPHASE DISPERSIONS

Comparison from Figure 3.18B shows the overlapped spectrum of $E_{11}(\kappa_2)$ and $E_{22}(\kappa_2)$ which clearly shows the deviation in the low wavenumber region. This observation indicates the existence of an anisotropic behavior due to the presence of large scale motion having size comparable to the nozzle diameter. In the inertial range, both the spectra get overlapped and the turbulence was found to be isotropic in the inertial and dissipation region. As seen from Figure 3.18A, HFA measurements cover the wavenumber range up to 10^4 , while LDV measures up to 10^3 . Further, the LDV measurements show the deviation in the energy spectra due to anomalous behavior at high frequencies. This has been highlighted in detail in Section 3.4. Further, Figure 3.18B shows one dimensional energy spectrum at two axial locations. As observed in Figure 3.18B at $x_2 = 0.28$ m, the inertial range is delayed because of the convective flow generated from the nozzle and the start of an inertial range is seen at a wavenumber of around 200, i.e., half/one-fourth of the diameter of the nozzle. However, at farther location, i.e., at $x_2 = 0.1$ m, a change of slope occurred at around wavenumber of 50. This observation is also reflected in the form of variations in integral length scale as well as the Taylor microscale at respective locations. The integral length scale represents the start of the inertial range while the Taylor microscale is seen to lie approximately at the transition between inertial range and dissipation range (Table 3.3 and Figure 3.18A). Also, the plots show an increased slope of -5 in the dissipation range.

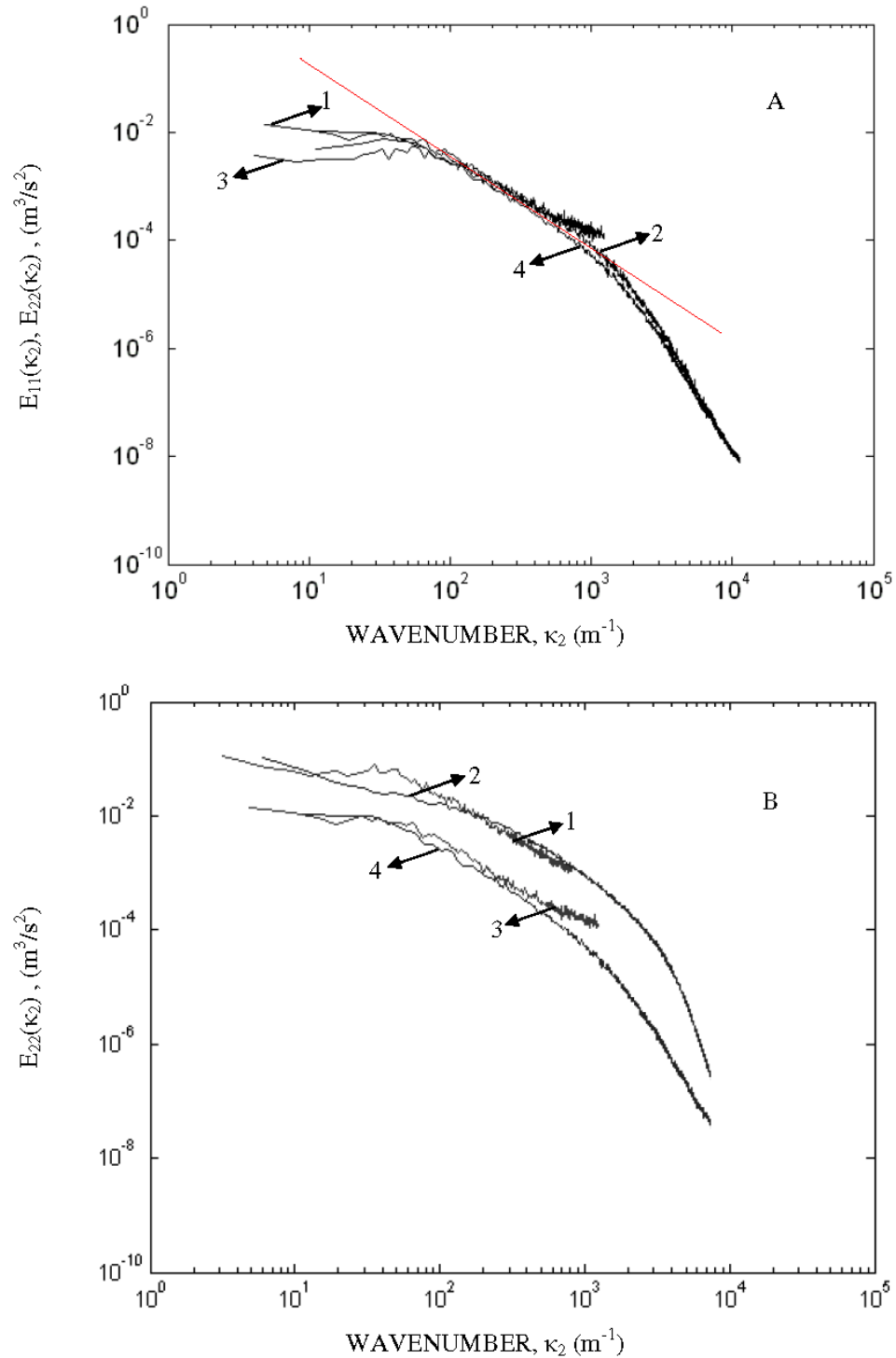


Figure 3.18: One dimensional energy spectrum for HFA and LDV (A) $x_1 = 0$ m : 1 $E_{22}(\kappa_2)$ of LDV at $x_2 = 0.1$ m; 2 $E_{22}(\kappa_2)$ of HFA at $x_2 = 0.1$ m; 3 $E_{11}(\kappa_2)$ of LDV at $x_2 = 0.1$ m; 4 $E_{11}(\kappa_2)$ of HFA at $x_2 = 0.1$ m; (B) $E_{22}(\kappa_2)$ vs κ_2 $x_1 = 0$ m: 1 LDV at $x_2 = 0.28$ m; 2 HFA at $x_2 = 0.28$ m; 3 LDV at $x_2 = 0.1$ m; 4 HFA at $x_2 = 0.1$ m.

To look further insight in to the variation in the energy spectra, the compensated energy spectra have been plotted (Figure 3.19) over the normalized scale for u_2 . The spectra show the variation of start of the inertial range at $x_2=0.28$ and 0.1 m. The two zones are observed on either side of the maxima location in the inertial range, namely α and β with positive and negative slopes, respectively, as described by Tsuji (2004). At $x_2=0.28$ m, the inertial range was observed to start at larger wavenumbers, which is also discussed earlier in the section. Further, this region was found to be spread over the one order of wavenumber with maxima approximately at $\kappa_p=600 \text{ m}^{-1}$. The α and β slope regions are narrow and have covered almost equal range of wavenumber. This intermittent behavior is found to be prominent in the near nozzle zone because of higher entrainment from the surrounding and sharp shear driven vortex effects due to nozzle proximity. On the other hand, the inertial range was observed to be spread over the wider range, i.e., two orders of κ_2 . The α as well as β slopes are found to be smaller at $x_2=0.1$ m as compared to that at $x_2=0.28$ m. The slope was also found to change sharply after the β region both the cases. The coefficient C_κ are observed in the similar range for both the cases at approximately 0.6. The value is observed to be decreased away from the nozzle towards 0.45 (Figure not shown). This would reflect on the overall trend of the parameters in the theoretical spectrum. As seen from the Figure 6, the local energy and κ_p show large variation across the tank and hence the conventional methodologies are insufficient to predict the value of ε accurately and therefore, a coupled technique using HFA and PIV has been used to estimate the parameters more closely to the reality.

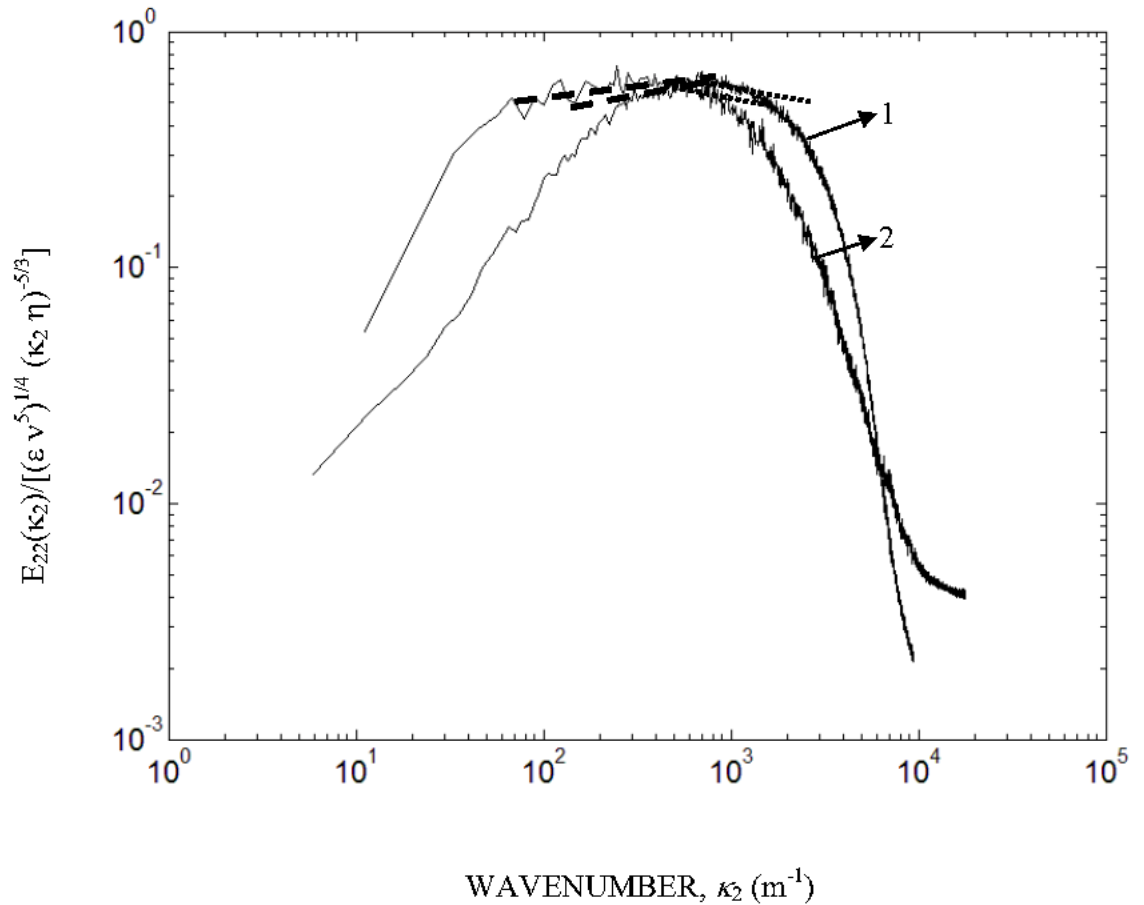


Figure 3.19: One dimensional compensated energy spectrum for HFA; Plot of $E_{22}(\kappa_2)/[(\epsilon v^5)^{1/4} (\kappa_2 \eta)^{-5/3}]$ vs κ_2 ; at locations 1. $x_1 = 0$ m and $x_2 = 0.28$ m; 2 $x_1 = 0$ m and $x_2 = 0.1$ m. The plot shows α slope () and β slope (···) regions.

The three dimensional energy spectra were plotted using methodology described in the previous sub-section. The range of parameters selected are $C_\kappa = 1.6-2.3$, $\alpha_1 = 0.2-0.39$, $\alpha_2 = 0.4-1.2$, $\alpha_3 = 4.0$, $\alpha_4 = 2.0-12$, $\alpha_5 = 0.522$, $\alpha_6 = 10.0$ and $\alpha_7 = 12.58$. These values produce good agreement with the measured longitudinal spectra across the radial locations, in the inertial range as well as dissipation range. As mentioned above, major variation was obtained in the values of C_κ , α_1 , α_2 , α_3 , α_4 across the radial distance. Figure 3.20 shows a

DEVELOPMENT OF EXPERIMENTAL TECHNIQUES AND CFD SIMULATIONS OF MULTIPHASE DISPERSIONS

comparison of 1D energy spectrum evaluated from HFA data and that based on the eq (8) while, Figure 7B shows the plot of 3D energy spectrum obtained from eq (6). The results show good agreement between the experimental and correlation based energy spectrum and it predicts the anisotropic region as well as dissipation range very well.

Thus, based on the optimization strategy discussed earlier, the final set of parameters is listed in Table 3.5.

Table 3.5: Optimized Parameters Obtained from the Algorithm

Parameters	$\langle u_2 \rangle > 0.1 \langle u_{2,\phi} \rangle$, $I > 1.05$	$\langle u_2 \rangle < 0.1 \langle u_{2,\phi} \rangle$, $I < 1.05$
C	1.9	1.8
$C_{\varepsilon 2}$	1.8	1.92
C_{κ}	1.7	1.6
α_1	0.2	0.4
α_2	0.5	1.2
α_3	4	4
α_4	8	12
α_5	0.522	0.522
α_6	10	10
α_7	12.58	12.58

The values of parameters have been set differently based on a criterion of mean velocity and the isotropy ratio at a specific location. It can be observed from Table 3.5 that, the deviation is mainly seen in parameters α_1 , α_2 , α_3 corresponding to low wavenumber range which signifies the effect of turbulence production in the shear region. It can further be seen from Table 3.5 that, since α_4 signifies the beginning of dissipation zone, it becomes sensitive in the high wavenumber region. Figure 3.21 shows the ε profile with respect to

DEVELOPMENT OF EXPERIMENTAL TECHNIQUES AND CFD SIMULATIONS OF MULTIPHASE DISPERSIONS

radial locations at $x_2 = 0.1$ m and flow rate of 0.542 kg/s. Further, the value of ε is integrated over the volume and average value is compared with that of energy input as given in eq (3.26). The comparison is presented in Table 3.6, which shows a good agreement between the two. It may be pointed out that the energy balance has been obtained within 10 %.

Table 3.6: Total Energy Balance Obtained from PIV Measurements

Mass Flow Rate	Power Supplied	ε	ε	ε
(kg/s)	per unit mass	m^2/s^3	m^2/s^3	m^2/s^3
	W/kg or m^2/s^3	Expt. (PIV)	CFD ($k-\varepsilon$)	CFD (LES)
0.542	0.092	0.0853	0.0827	0.0846
0.287	0.0127	0.0108	0.0098	0.0102

The constants derived from this work can be used to estimate the ε in jets and free shear flows, provided spectral data at few locations viz. in shear layer and far from shear layer to put a check on the obtained energy dissipation distribution. The processing flow chart using the constants reported here is depicted in Figure 3.22. number of PIV frames captured should be sufficient in order to give reasonably accurate values of higher order statistics (second and third order structure functions). The uncertainty in the data is significantly reduced by increasing the number of frames from 256 to 1024 (Figure 3.21).

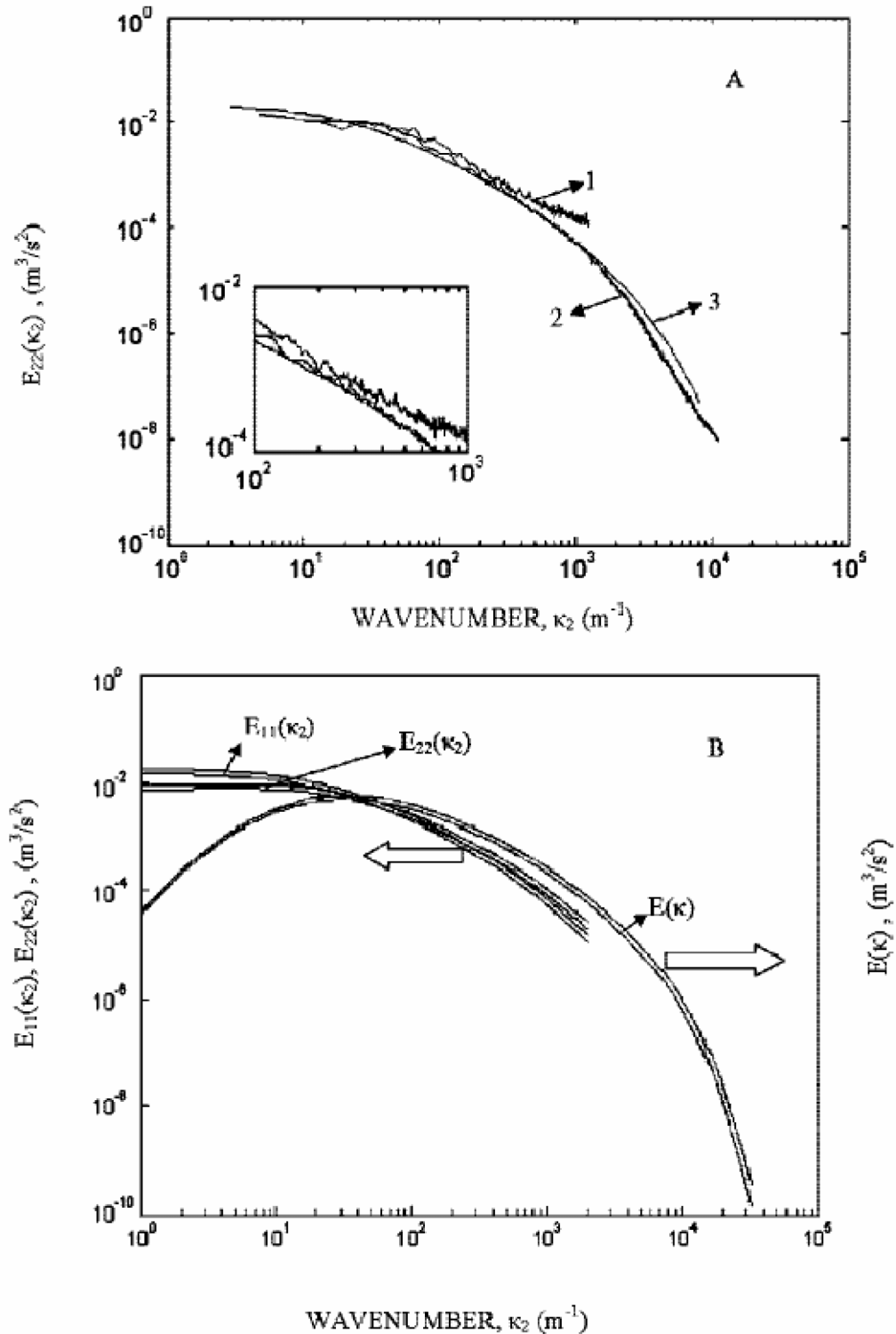


Figure 3.20: Evaluation of 3D energy spectrum (A) $E_{22}(\kappa_2)$ vs κ_2 at $x_1 = 0 \text{ m} : 1$ LDV; 2 HFA; 3 $E_{22}(\kappa_2)$ evaluated based on correlation; (B) $E(\kappa)$ vs κ , $E_{11}(\kappa_2)$ vs κ_2 and $E_{22}(\kappa_2)$ vs κ_2 from correlation.

DEVELOPMENT OF EXPERIMENTAL TECHNIQUES AND CFD SIMULATIONS OF MULTIPHASE DISPERSIONS

These ε profiles throughout the equipment necessarily give the deeper insight into the nature of flow inside it, and provide the guideline for intensification of the operation. These profiles have been used as a bench mark to study CFD predictions in the next subsection.

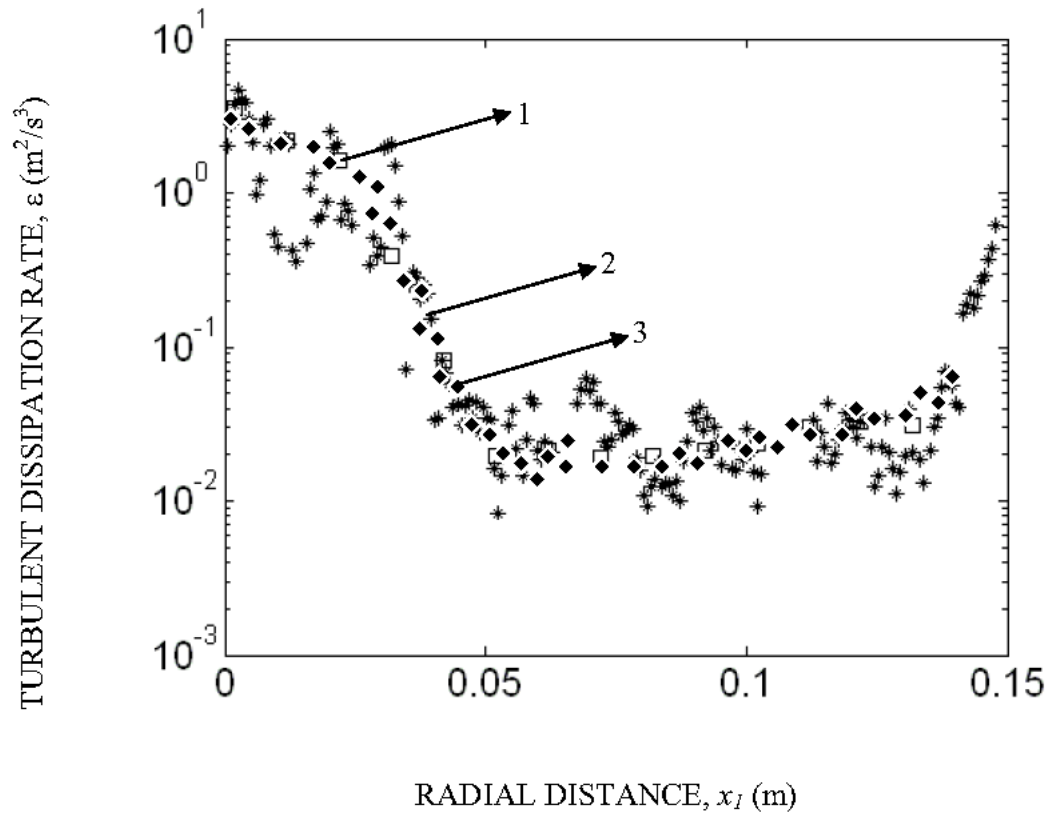


Figure 3.21: ε profile at $x_2 = 0.1$ m 1(□): HFA; 2(*): PIV data with 256 frames; 3 (◆): PIV data with 1024 frames.

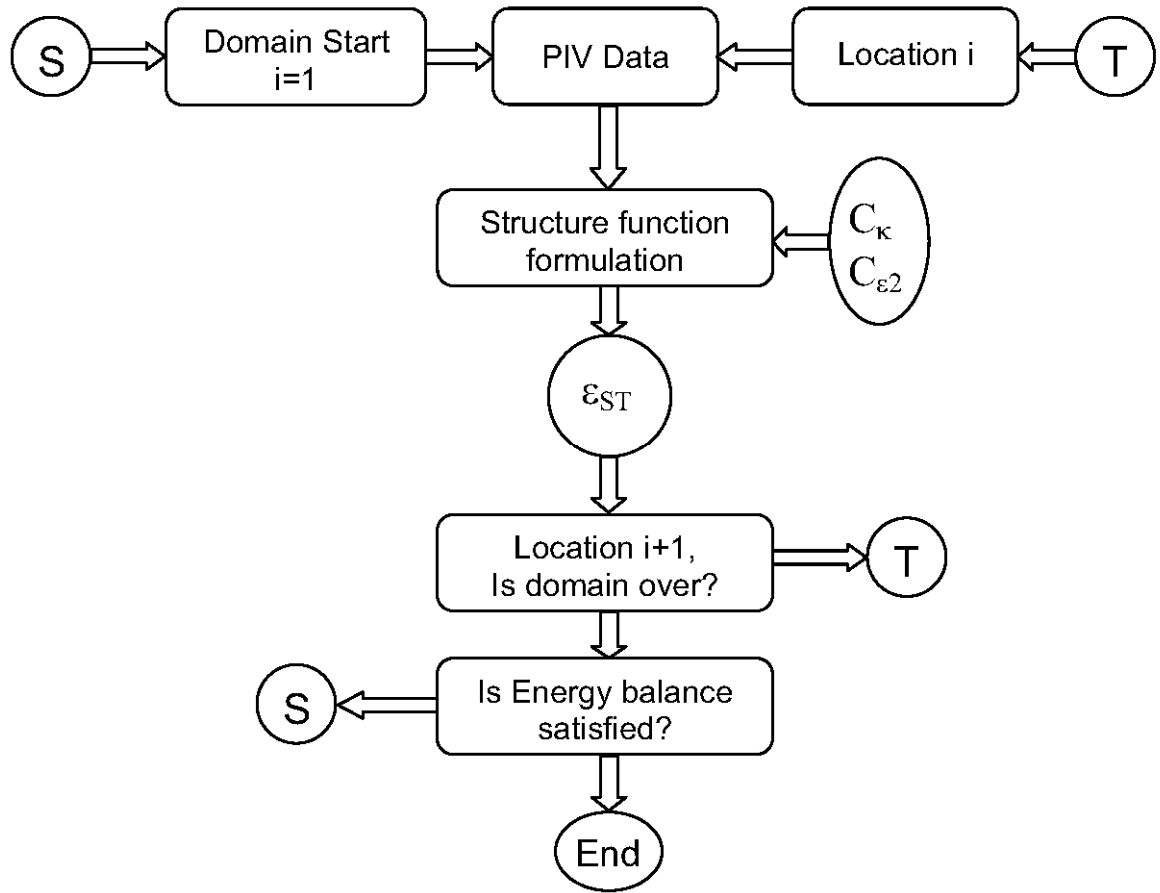


Figure 3.22: Flow chart for estimation of ε from PIV data.

3.2.5.3 CFD Simulations

The values of mean velocity and ε have been further utilized to compare the predicted values obtained from LES model. The CFD predictions have been compared in order to show an application of the methodology in brief and thereby gaining lot of scope for the future work in terms of designing and controlling the turbulence within the reactor.

3.2.5.3.1 Mean Velocity Profiles

Figure 3.23 shows the comparison for radial profile of axial velocity. The axial flow is distinctly downward in the central region with very high velocities, while an upward counter flow is observed in the near wall region. The point of flow reversal is clearly seen at a radial location of around 0.1 m (Figure 3.23B, 3.23C), while it is shifted closer to central plane near the nozzle. At $x_2 = 0.28$ m, crossover is observed around 0.04 m (Figure 3.23A). It can be observed that the LES model perform excellent for $x_2 = 0.28$ m except in the shear region. At $x_2 = 0.1$ m and 0.2 m, also LES predictions show excellent agreement with the experiments. Overall comparison shows that the standard $k-\varepsilon$ model (Pope, 2000) (with model parameters C_μ , $C_{\varepsilon 1}$ and $C_{\varepsilon 2}$ equal to 0.09, 1.44 and 1.92, respectively) deviates from the experimental values away from the nozzle.

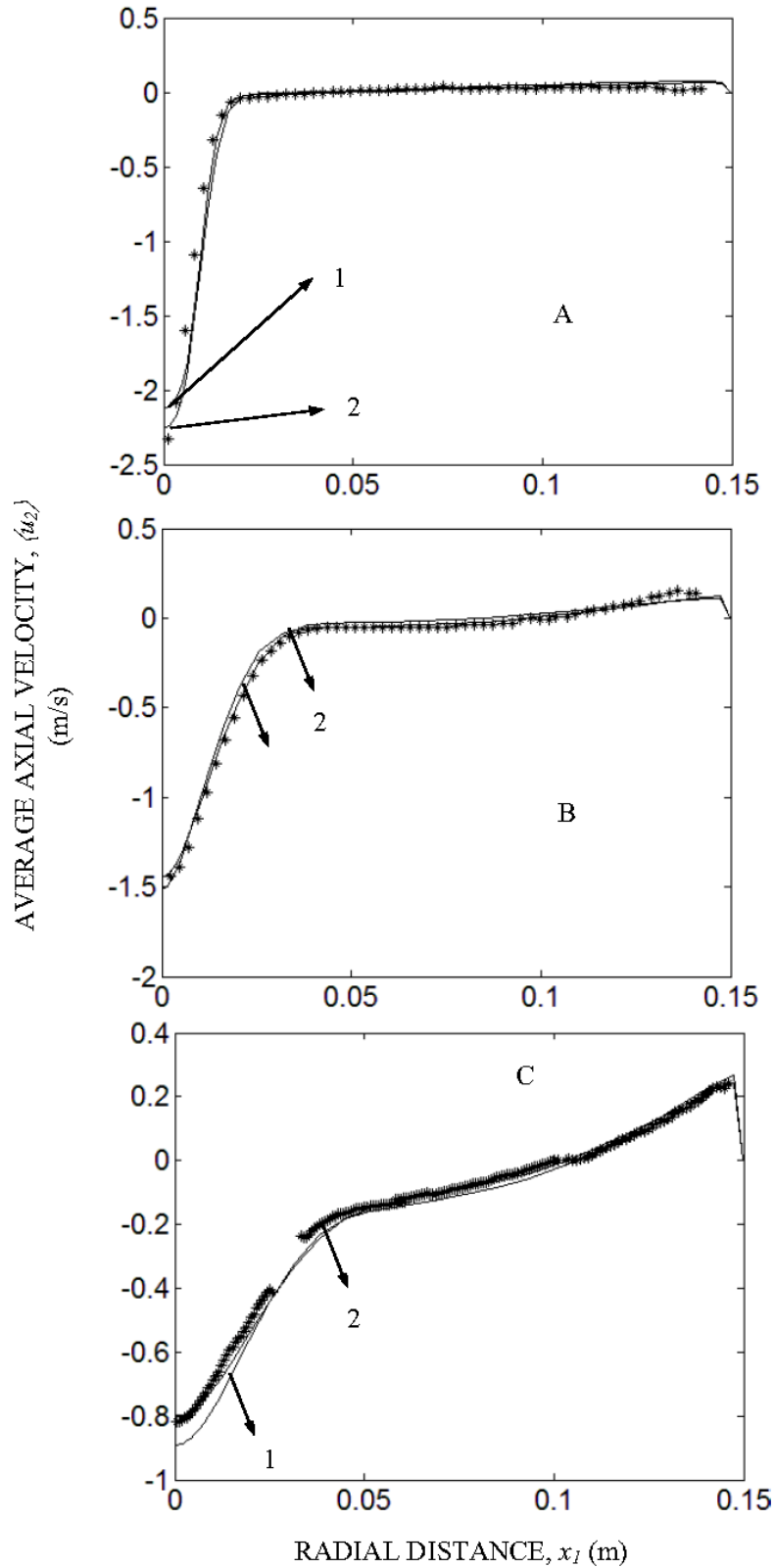


Figure 3.23: Comparison of mean velocity profiles from LES with experimental data in JLR. 1 $k-\varepsilon$ model; 2 LES model; * PIV Results.

3.2.5.3.2 ε Profiles

The comparison of turbulent dissipation rate has been shown in Figure 3.24 for the flow rate of 0.542 kg/s. Maximum dissipation rate is near $x_1 = 0$ m. The $k - \varepsilon$ profiles show qualitative as well as quantitative trend which are the same as those of experimental results. In this model, ε formulation is assumed to be isotropic in nature. This is again in line with the experimental observation in the earlier section, where the inertial as well as dissipation range is found to be isotropic. The dissipation rate at $x_2 = 0.28$ m (Figure 3.24A) and $x_2 = 0.2$ m (Figure 3.24B) shows underprediction as compared to the experimentally evaluated values with maximum deviation at the center. It indicates the need for the study of variation of model constants in the vessel. Major deviation is observed at $x_2 = 0.1$ m (Figure 3.24C). For LES model, ε is estimated based on the SGS viscosity obtained as

$$\varepsilon_{SGS} = \overline{\tau_{ij} S_{ij}} = -2\nu_{SGS} \overline{S_{ij} S_{ij}} = -(C_s \Delta)^2 |\overline{S_{ij}}|^3 \quad (3.29)$$

Figure 3.24 shows the comparison of ε predicted from the LES simulations, which is in line with the experimental results. Table 3.6 shows the comparison of energy balance over the entire volume for computational methods as well. The analysis showed that the LES could also capture the average energy balance for the system. The values of $k - \varepsilon$ model have also shown in the plot which deviate more from the experimental values.

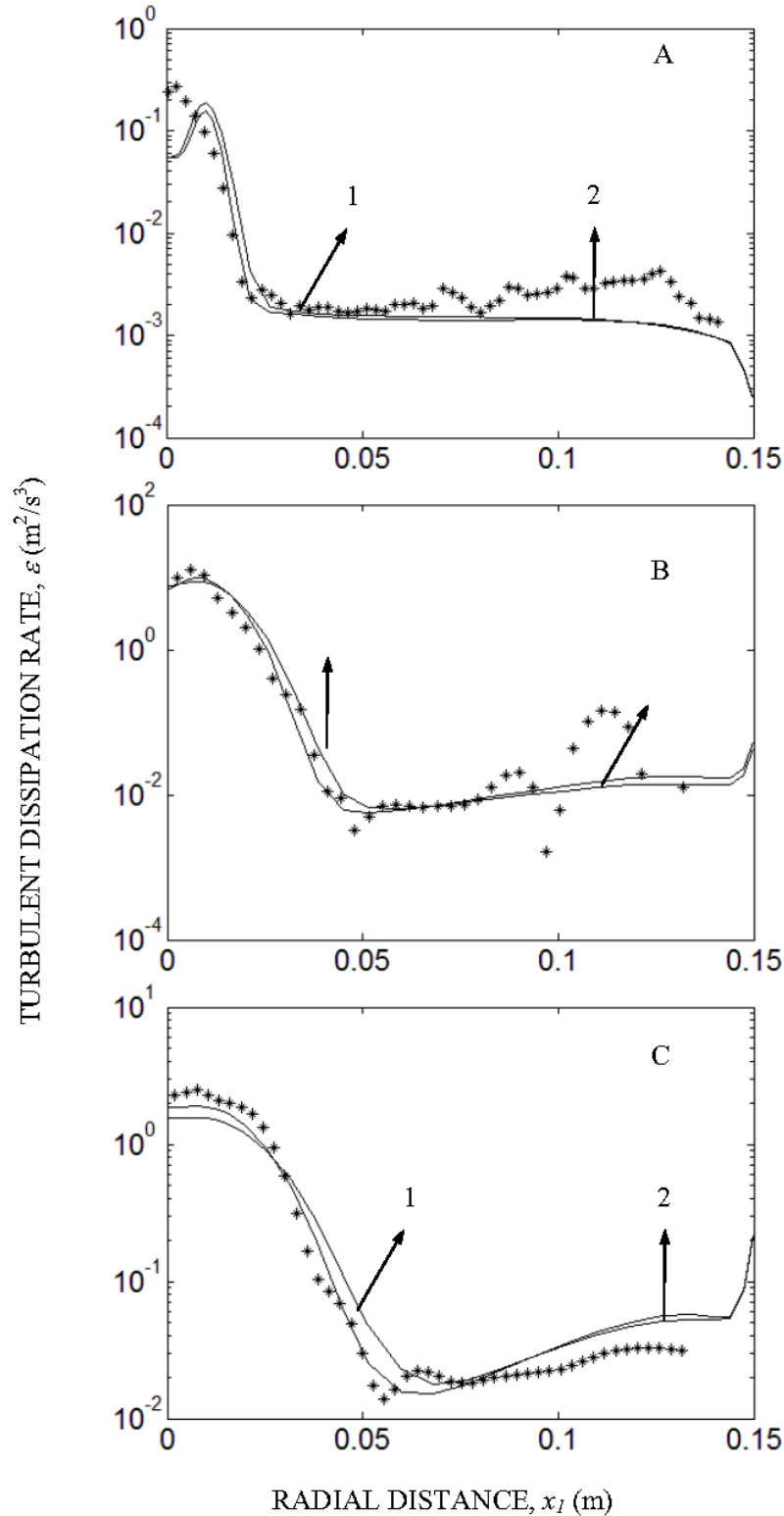


Figure 3.24: Comparison of energy dissipation rate profiles from LES with experimental data in JLR. 1 $k-\epsilon$ model; 2 LES model; * PIV Results.

3.2.5.4. Application of the Methodology for Design of Reactor

As shown in the earlier section, the energy balance has been obtained within 10 % . Further, good agreement has been shown in the measured and predicted ε profiles as well as mean velocity. Such a knowledge of both mean and turbulence is useful for the design of reactors. For instance the blending (or homogenization or macromixing), the solid suspension and the heat transfer, are mainly controlled by the by the mean flow. Our study (unpublished work) has shown that, for a given tank dimension and power consumption per unit mass, the mean liquid circulation velocity increases with an increase in the nozzle diameter. For instance, for the ratio of nozzle diameter (d) to tank diameter (D) of 0.066, 0.166 and 0.33 (and $D = H = 0.3$), the values of liquid circulation velocity were found to be 6.7, 8.3 and 9.3 L/S, respectively. Further, it has also been found that the d/D ratio of 0.066 gives 10 % high mixing time as compared with that given by a hydrofoil impeller (very efficient impeller among all the impeller designs). On contrast, the d/D ration of 0.33 gives 40 % less mixing time. Thus the CFD simulation is expected to give optimum selection of d, D, liquid height and the nozzle location.

As an other extreme of micromixing controlled operation, particularly instantaneous reactions or reactive precipitation, the feed point of reactants need to be at the location where ε profiles and hence suggests the optimum location of feed point. Thus, the desired design objective can be achieved by the procedure proposed in the present work.

3.2.6 Conclusions

In the present work, measurements have been made in JLR using PIV, LDV and HFA. We conclude the following:

DEVELOPMENT OF EXPERIMENTAL TECHNIQUES AND CFD SIMULATIONS OF MULTIPHASE DISPERSIONS

1. LDV, HFA as well as PIV have merits and limitations. Importance of each of the techniques has been pointed out for measurement of mean and turbulence quantities. Thus, mean flow pattern has been evaluated by LDV, turbulence parameters by HFA and turbulence structures by PIV.

2. A strategy has been proposed for the evaluation of ε from PIV and HFA measurements. It involves the formulation and estimation of structure function relationships. A stepwise iterative procedure has been suggested for the evaluation of parameters in the structure function relationship and hence the 3D energy spectrum. Overall energy balance has been satisfied implicitly to make the algorithm more robust.

3. Using the constants obtained by the optimization in current work, the ε variation can be obtained from PIV data. The ε profiles throughout the equipment necessarily give the deeper insight into the nature of flow inside it, and provide the guideline for intensification of the operation.

4. The experimental data has been further utilized for the validation of the large eddy simulation prediction. The analysis shows that the mean as well as energy rate of dissipation have been found within 10 % as against the experimental values at various locations in the JLR.

5. The comparison of CFD predictions show an application for the present methodology for design of turbulence by utilizing the local values of ε for optimization. More work in this direction would be carried out.

DEVELOPMENT OF EXPERIMENTAL TECHNIQUES AND CFD SIMULATIONS OF MULTIPHASE DISPERSIONS

Notations

c	local tracer concentration, g/lit
C	tracer concentration, g/lit
\bar{C}	average tracer concentration, g/lit
C_μ	turbulent parameter (=0.09)
$C_{\varepsilon 2}$	model parameter in ε equation, -
C_κ	Kolmogorov constant
d	gap width, m
D	tank diameter, m
D_t	eddy diffusion coefficient, m^2/s
D_{eff}	effective diffusion coefficient, m^2/s
D_m	molecular diffusion coefficient, m^2/s
D_{uu}	second order velocity structure function, m^2/s^2
D_{uuu}	third order velocity structure function, m^3/s^3
E	Dimensionless concentration,-
$E(\kappa)$	energy spectrum in wavenumber domain, m^3/s^2
$E_{11}(\kappa_2)$	1D energy spectrum in longitudinal wavenumber domain for axial direction, m^3/s^2
$E_{22}(\kappa_2)$	1D energy spectrum in longitudinal wavenumber domain for radial direction, m^3/s^2

DEVELOPMENT OF EXPERIMENTAL TECHNIQUES AND CFD SIMULATIONS OF MULTIPHASE DISPERSIONS

E_D	total energy dissipation rate, W
E_I	energy induction rate, W
f	ratio of inter cell circulation velocity to the superficial velocity
H	annulus height, m
H_N	nozzle clearance from front surface (i.e. for upward nozzle distance from top surface while, for downward nozzle distance from bottom surface), m
I	isotropy Ratio = $\frac{u_{2RMS}}{u_{1RMS}}$, -
k	turbulent kinetic energy, m^2/s^2
l	length scale magnitude = κ^{-1} , m
l_i	integral length scale in i direction, m
L_{ij}	Leonardo stress for LES model = $\overline{u_i u_j} - \overline{u_i} \overline{u_j}$, m^2/s^2
n	number of vortices in annular centrifugal extractor
N	number of tanks
P_{in}	total power input, W
Pe	Peclet number, -
Q	volumetric flow rate, m^3/s
r_D	difference in the two locations for calculation of structure function, m
r	radial direction, m
t	time, s

DEVELOPMENT OF EXPERIMENTAL TECHNIQUES AND CFD SIMULATIONS OF MULTIPHASE DISPERSIONS

t_c	circulation time due to convective transport, s
Ta	Taylor number, $\frac{2\eta^2}{(1-\eta^2)} d^4 \left(\frac{\Omega}{\nu} \right)^2$, -
$\langle u_{2,j} \rangle$	nozzle velocity, m/s
u	velocity component, m/s
u_c	average circulation velocity, m/s
u_i	instantaneous velocity of component i , where $i = 1,2,3$ corresponds to radial,axial and tangential component of velocity, m/s
u_{iRMS}	RMS velocity of component i (m/s) = $\sum_{i=1}^N u_i / N$ where N=number of points in time series, m/s
$\langle u_i \rangle$	time average of velocity, m/s
\bar{u}_i	filtered velocity of component i for LES model
u_i'	fluctuating part of velocity of component i , m/s
u_{rz}	average circulation velocity within the vortex, m/s
$\langle u \rangle$	time average velocity, m/s
V	voltage, V
x	directional coordinate
z	axial direction, m
x_i	co-ordinate distances in i direction where $i = 1,2,3$, m

DEVELOPMENT OF EXPERIMENTAL TECHNIQUES AND CFD SIMULATIONS OF MULTIPHASE DISPERSIONS

$$x \quad \frac{\kappa}{\kappa_2} \text{ [in eq 3.24 and 3.25]}$$

Greek letters

α_i	parameter constants in eq 6 ($i = 1-7$)
δ_{ij}	Kronekar delta, $\delta_{ij} = 1$ if $i = j$; $\delta_{ij} = 0$ if $i \neq j$
ε	energy dissipation rate, m^2/s^3
κ	resultant wavenumber, m^{-1}
κ_2	wavenumber in longitudinal direction, m^{-1}
λ	Taylor microscale, m
ν	kinematic viscosity, m^2/s
ρ	density of liquid, kg/m^3
η	ratio of radii of inner to outer cylinder, -
Γ	aspect ratio, H/d , -
μ	molecular viscosity, Pa.s
σ^2	variance, s^2
τ	mean residence time, s
τ_i	mean residence time of i^{th} reactor in series, s
θ	azimuthal direction
θ_m	mixing time due to convective transport, s
$\theta_{m,t}$	mixing time due to turbulent transport, s

DEVELOPMENT OF EXPERIMENTAL TECHNIQUES AND CFD SIMULATIONS OF MULTIPHASE DISPERSIONS

ω revolution per seconds, r/s

Ω angular velocity, rad/s

Subscripts

G Global

rz axial-radial direction

i, j, k co-ordinates in generalized form with value 1, 2 and 3 corresponds to radial, axial and tangential direction

J variable value at nozzle exit

$'$ fluctuating component

$-$ LES filtered component

References

- Adrian, R.J., 1996. Bibliography of particle velocimetry using imaging methods. 1917-1995. TSI inc., St. Paul, Minnesota.
- Adrian, R.J., 2005. Twenty years of particle image velocimetry. *Experiments in Fluids* 39, 159-169.
- Andereck, C.D., Liu, S. S., Swinney, H. L., 1986. Flow regimes in a circular Couette system with independently rotating cylinders. *Journal of Fluid Mechanics* 164, 155.
- Baldyga, J., Bourne, J.R., Zimmermann, B., 1994. Investigation of mixing in jet reactors using fast competitive-consecutive reactions. *Chemical Engineering Science* 49, 1937-1946.
- Bernstein, G. J., Grodsvenor, D. E., Lenc, J. F., Levitz, N. M., 1973. Development and performance of a high-speed annular centrifugal contactor. Argonne National Laboratory Report, ANL- 7968.
- Bilson, M., Bremhorst, K., 2007. Direct numerical simulation of turbulent Taylor-Couette flow. *Journal of Fluid Mechanics* 579, 227.

DEVELOPMENT OF EXPERIMENTAL TECHNIQUES AND CFD SIMULATIONS OF MULTIPHASE DISPERSIONS

- Boyle, D.R., Golay, M.W., 1983. Measurement of a recirculating, two-dimensional, turbulent flow and comparison to turbulence model predictions II: transient case. *Journal of Fluid Engineering* 105, 447-454.
- Bruun, H.H., 1996. *Hot wire anemometry: principles and signal analysis*. Oxford University Press.
- Chandrasekhar, S., 1962. The stability of spiral flow between rotating cylinders. *Proceedings of Royal Society London A*. 265, 188.
- Coles, D., 1965. Transition in circular Couette Flow. *Journal of Fluid Mechanics* 21, 385.
- Desmet, G, Verelst, H., Baron, G.V., 1996a. Local and global dispersion effects in Couette-Taylor flow-I. Description and modeling of the dispersion effects. *Chemical Engineering Science* 51, 1287.
- Desmet, G, Verelst, H., Baron, G.V., 1996b. Local and global dispersion effects in Couette-Taylor flow-II. Quantitative measurements and discussion of the reactor performance. *Chemical Engineering Science* 51, 1299.
- Dihn, T.N., Bui, V.A., Nourgaliev, R.R., Green, J.A., Sehgal, B.R, 1999. Experimental and analytical studies of melt jet-coolant interactions: a synthesis. *Nuclear Engineering and Design* 189, 299-327.
- Donald, M.B., Singer, H., 1959. Entrainment in turbulent fluid jets. *Transactions of Institute of Chemical Engineers* 37, 255-267.
- Forney, L.J., Nafia, N., 2000. Eddy contact model: CFD simulations of liquid reactions in nearly homogeneous turbulence. *Chemical Engineering Science* 55, 6049-6058.
- Frisch, U. *Turbulence: the Legacy of A.N. Kolmogorov*. University Press, Cambridge, 1994.
- Gandhi, N.N., Patil, N.S., Sawant, S.B., Joshi, J.B, Wangikar, P.P., Mukesh, D. 2000. Lipase catalyzed esterification. *Catalytic Reviews –Science and Engineering* 42, 439-480.
- Imamura, T., Saito, K., Ishikura, S., 1993. A new approach to continuous emulsion polymerization. *Polymer International* 30, 203.
- Joshi, J.B., 1980. Axial mixing in multiphase contactors-a unified correlation. *Transactions of I.Ch.E.* 58, 155.
- Joshi, J.B., Elias, C.B., Patole, M.S. 1996. Role of hydrodynamic shear in cultivation of animal, plant and microbial cells. *Chemical Engineering Journal* 62, 121-141.
- Kang, H.S., Chester, S., Meneveau, C., 2003. Decaying turbulence in an active grid generated flow and comparisons with large eddy simulations. *Journal of Fluid Mechanics* 480, 129-160.
- Kataoka, K., Doi, H., Hongo, T., Fugatawa, M., 1975. Ideal plug-flow properties of Taylor-vortex flow. *Journal of Chemical Engineering Japan* 8, 472.
- Kompenhans, J., Tropea, C., 1997. Special issue: Particle image velocimetry. *Measurement science and technology* 8,1379-1583.

DEVELOPMENT OF EXPERIMENTAL TECHNIQUES AND CFD SIMULATIONS OF MULTIPHASE DISPERSIONS

- Lane, A.G.C., Rice, P., 1982. The flow characteristics of a submerged bounded jet in a closed system, short communication. *Trans ICHME Symposium Series 64*, 245-248.
- Leonard, R. A., 1988. Recent advances in centrifugal contactor design. *Separation Science Technology 23*, 1473.
- Leonard, R. A., Bernstein, G. J., Pelto, R. H., 1981. Liquid-liquid dispersion in turbulent Couette flow. *A.I.Ch.E. Journal 27*, 495.
- Levenspiel, O., 1999 *Chemical Reaction Engineering*, 3rd ed., John Wiley and Sons, Inc., Singapore.
- Lindborg, E., 1999. Correction to the four-fifth law due to variations of the dissipation. *Physics of Fluids 11*, 510-512.
- Lueptow, R. M., Docter, A., Min, K., 1992. Stability of axial flow in an annulus with a rotating inner cylinder. *Physics of Fluids A 4*, 2446.
- Lui, S., Meneveau, C., Katz, J., 1994. On the properties of similarity subgrid-scale models as deduced from measurements in a turbulent jet. *Journal of Fluid Mechanics 275*, 83-119.
- Mathpati, C.S., Joshi, J.B., 2007. Insight into theories of heat and mass transfer at the solid-fluid interface using direct numerical simulation and large eddy simulation. *Industrial and Engineering Chemistry Research 46*, 8525-8557.
- Mecklenburgh, J.C., 1974. Backmixing and design: a review. *Transactions of I.Ch.E. 52*, 180.
- Mewes, D., Renz, R., 1991. Jet mixing of liquids in storage tanks. 7th European Congress on Mixing, Brugge, Belgium.
- Nishimura, T., Inaba, S., Hishida, K., Maeda, M., 2000. Measurements of flow around inclined jets by stereoscopic PIV. 10th International Symposium on Applications of Laser Techniques to Fluid Mechanics, Lisboa.
- Obukhov, A.M., 1962. Some specific features of atmospheric turbulence. *Journal of Fluid Mechanics 13*, 77-81.
- Ogihara, T., Matsuda, G., Yanagawa, T., Ogata, N., Fujita, Nomura, M. 1995. Continuous synthesis of monodispersed silica particles using Couette-Taylor vortex flow. *Journal of Ceramic Society Japan International 103*, 151.
- Oldshue, J.Y., 1983. *Fluid Mixing Technology*. Mcgraw Hill Pub. Co., New York.
- Pearson, B.R., Krogstad, P.A., Van de Water, W., 2002. Measurements of the turbulent energy dissipation rate. *Physics of Fluids 14*, 1288-1290.
- Pope, S.B., 2000. *Turbulent flows*. Cambridge University Press.
- Pudijiono, P.I., Tavaré, N.S., Garside, J., Nigam, K.D.P., 1992. Residence time distribution from a continuous Couette flow device. *Chemical Engineering Journal 48*, 101.

DEVELOPMENT OF EXPERIMENTAL TECHNIQUES AND CFD SIMULATIONS OF MULTIPHASE DISPERSIONS

- Ranade, V.V., Joshi, J.B., 1990. Flow generated by a disc turbine: part I Experimental. *Trans IChemE* 68A, 19-33.
- Ranade, V.V., Mishra, V.P., Saraph, V.S., Deshpande, G.B., Joshi, J.B., 1992. Comparison of axial flow impellers using LDA. *Industrial and Engineering Chemistry Research* 31, 2370-2379.
- Rosler, R.S., Bankoff, S.G., 1963. Large-scale turbulence characteristics of a submerged water jet. *AIChE Journal* 9, 672-676.
- Sadakata, M., Kunii, D., 1972. Recirculation and turbulence by jet flow confined in vessel. *Journal of Chemical Engineering Japan* 5, 355-360.
- Saffman, P.G., 1970. Dependence on Reynolds number of high order moments of velocity derivatives in isotropic turbulence. *Physics of Fluids* 13, 2193-2194.
- Sahu, A.K., Joshi, J.B., 1995. Simulation of flow in stirred vessels with axial flow impellers: effects of various numerical schemes and turbulence model parameters. *Industrial Engineering Chemistry and Research* 34, 626-639.
- Sahu, A.K., Kumar, P., Patwardhan, A.W., Joshi, J.B., 1999. CFD modeling and mixing in stirred tanks. *Chemical Engineering Science* 54, 2285-2293.
- Simon, M., Fonade, C., 1993. Experimental study of mixing performances using steady and unsteady jets. *Canadian Journal of Chemical Engineering* 71, 507-513.
- Sreenivasan, K. R., 1998. An update on the energy dissipation rate in isotropic turbulence. *Physics of Fluids* 10, 528.
- Sreenivasan, K.R., 1999. Fluid turbulence. *Reviews of Modern Physics* 71, 383-395.
- StreamLine/ StreamWare: Installation and user's manual. Dantec Dynamics A/S, Denmark, 2000.
- Taylor, G. I., 1923. Stability of a viscous liquid contained between two rotating cylinders. *Philosophical Transactions of Royal Society London A*. 223, 289.
- Tsao, Y. M. D., Boyd, E., Spaulding, G., 1994. Fluid dynamics within a rotating bioreactor in space and earth environments. *Journal of Space and Rockets* 31, 937.
- Tsuji, V., 2004. Intermittency effect on energy spectrum in high-Reynolds number turbulence. *Physics of Fluids* 16, L43-L46.
- Usui, H., Sano, Y., 1980. Turbulent structure of submerged jets of dilute polymer solutions. *Journal of Chemical Engineering Japan* 13, 401-404.
- Van De Vusse, J.G., 1962. A new model for the stirred tank reactor. *Chemical Engineering Science* 17, 507.
- Van Maanen, H.R.E., Nobach, H., Benedict, L.H., 1999. Improved estimator for the slotted autocorrelation function of randomly sampled LDA data. *Measurement Science and Technology* 10, L4-L7.

DEVELOPMENT OF EXPERIMENTAL TECHNIQUES AND CFD SIMULATIONS OF MULTIPHASE DISPERSIONS

- Van Maanen, H.R.E., Oldenziel, A., 1998. Estimation of turbulence power spectra from randomly sampled data by curve-fit to the autocorrelation function applied to laser-Doppler anemometry. *Measurement Science and Technology* 9, 458-467.
- Vedantam, S. Joshi, J.B., Koganti, S.B., 2006a. Three dimensional CFD simulation of stratified two-fluid Taylor-Couette flow. *Canadian Journal of Chemical Engineering* 84, 279-288.
- Vedantam, S., Joshi, J.B., 2006. Annular centrifugal Contactors: A review. *Chemical Engineering Research and Design* 84, 522-542.
- Webster, D.R., Longmire, E.K., 1997. Vortex dynamics in jets from inclined nozzles. *Physics of Fluids* 9, 655-666.
- Webster, D.R., Roberts, P.J.W., Raad, L., 2001. Simultaneous DPIV/PLIF measurements of a turbulent jet. *Experiments in Fluids* 65, 65-72.
- Yianneskis, M., 1991. The effect of flow rate and tracer insertion time on mixing times in jet-agitated vessels. *Proc. of 7th European Conference on mixing*, 121-128, Brugge, Belgium.

Chapter 4

EFFECT OF TURBULENCE ON BUBBLE RISE CHARACTERISTICS

4.1. Introduction

Gas-liquid contacting is involved in many important processes like fermentation, polymerization, hydrogenation, Fisher-Tropsch synthesis etc. It is also important for separation processes like distillation. The fluid mechanical aspects of gas-liquid two phase flows have not been clearly understood, introducing empiricism and uncertainty in the design of such equipment. Recent advances in Experimental Fluid Dynamics (EFD) and Computational Fluid Dynamics (CFD) are promising in terms of gaining deeper insight into the flow patterns in multiphase dispersions. CFD involves numerical solution of the governing equations of fluid flow: the equations of continuity and momentum. These equations include equations for continuity and momentum transfer in all three directions. In case of multiphase flows, separate set of equations needs to be solved for each phase, and the coupling between these equations is represented by momentum exchange terms. Different models are used to approximate the two phase flow viz. Mixture model, Euler-Euler model, Euler-Lagrange model, Volume of Fluid (VOF) model, Lattice-Boltzmann method and the direct numerical simulation (DNS). The mixture model solves a single set of momentum equations and approximates the mixture properties from the individual fluid properties and their respective void fractions. The mixture model approximates the interaction between phases by defining a specific slip velocity. In Euler-Euler model, the two phases are modeled as interpenetrating continua; and one set of momentum equations is solved for each of the phase. In this framework, the interaction between phases is modeled using different formulations for the interfacial forces like drag, lift and virtual mass. With DNS, a finite number of particles are incorporated in the control volume and trajectories are determined via the equation of motion. The instantaneous forces acting on a particle are obtained from local flow statistics. The VOF model, the Lattice Boltzmann and DNS methods are computationally much more expensive and hence find niche applications

like study of the flow patterns around individual bubbles to much greater detail. As far as modeling of industrial scale contactors is concerned, Euler-Euler approach presents a balance between approximations introduced while modeling and the computational requirements and hence is most popular. The major approximation in Euler-Euler framework lies in representation of dispersed phase as a continuum and hence requirement of fictitious terms like interfacial area concentration which is the amount of interfacial area present per unit volume of the element under consideration. This brings in the requirement of carefully selecting the dispersed phase diameter and the grid size for solution of the flow equations. Another feature of this model which introduces empirical correlations in the solution procedure is the interaction between phases which is represented by momentum exchange terms in momentum equation. These terms are ensemble-averaged momentum exchange between the phases, due to interface forces like drag, lift, virtual mass and turbulent dispersion. The drag force is dominant in terms of its magnitude out of all these interaction forces. Thus, it has attracted the focus of the efforts from numerous researchers since last 4 decades. The drag force is significantly different for bubbles, drops and particles of same size. This is primarily caused by the different slip conditions occurring at fluid boundary, viz. full slip to no slip. A number of different empirical correlations have been devised to include the effect of several parameters like particle diameter, shape, and particle Reynolds number etc. These correlations perform satisfactorily for individual particles moving in quiescent fluids. However, it still remains a major challenge to devise a generalized correlation which also includes the effect of free stream turbulence on the drag force besides all these parameters. In number of scenarios, surfactant molecules are present in the liquid. They get adsorbed onto the gas-liquid interface forming partial slip boundary conditions. The process is known to be dynamic in nature i.e. bubble rise velocity in surfactant solution is

time dependent. Thus, it was thought desirable to study the effect of surfactant concentration as well as free stream turbulence on the rise velocity of individual bubbles as well as bubbles rising in chains.

4.2. Literature Review

Panidis and Papailiou (2002) studied the influence of a swarm of bubbles on the structure of a nearly isotropic turbulent flow field behind a grid. A vertical channel was used with the volumetric upflow of the liquid maintained constant, Reynolds number of the liquid flow based on 30mm mesh spacing was 8000. Using photographic techniques, it was ascertained that mean bubble diameter and slip velocity were respectively 3mm and 250mm/s, respectively. The regions of peak voidage depended on the air flux into the system, being central for low air intake and at roughly the midpoint between the centre and the wall at higher air flow rates. The void distribution had a close link with the local velocities, it was inferred that this arose due to enhanced liquid velocity by the buoyancy of bubbles and interfacial drag between the phases carrying liquid upwards.

Panidis and Papailiou (2002) also looked at turbulence intensity measurements with a view to ascertaining whether the turbulence isotropy remains in the system. It was found that the longitudinal turbulence intensity component generally increased more markedly than the transverse components for similar reasons as outlined above. Therefore the presence of bubbles destroys the isotropy of turbulence for this system.

Poorte and Biesheuvel (2002) performed experiments on the motion of gas bubbles behind grid turbulence in order to validate the theoretical modeling analysis of previous work by Spelt and Biesheuvel (1997). For weak turbulence of ‘intermediate’ length scales, they presented the following semi-analytical solution to the equation of bubble motion.

$$\frac{U_s}{U_T} = 1 - 0.75\pi \frac{\bar{u}^2 \tau_b}{U_T \ell} \quad (4.1)$$

The authors suggest that bubbles are slowed by the turbulence because lift forces redirect them laterally to regions of relative downflow, viscous forces then make the bubbles adapt their speed to the fluid velocity fluctuations.

Experiments were conducted in a vertical water tunnel of 0.45m square edge. Isotropic turbulence was generated by means of an active grid; interlaced shafts with flaps at regular intervals would make up the grid, these shafts rotated by motors with both random speed and duration. This latter specification was designed to eliminate periodicities in the flow. In addition the flaps (or wings) were mounted in a staggered orientation along each shaft, thus helping to promote isotropy of the generated turbulence (Poorte and Biesheuvel, 2002).

The bubble size was not directly measured; rather the authors were confident that their technique of bubble generation could produce bubbles of constant diameter. A certain number of bubbles (~20) were collected and allowed to coalesce to form a plug inside a known diameter tube to determine bubble size. The non intrusive real-time measurement of bubble velocity was carried out using a position-sensitive detector (PSD).

Experimental results from Poorte and Biesheuvel (2002) show that turbulence can result into decrease in the rise velocity up to 35% for a number of scenarios. The results were within 9% of the SB theoretical predictions (Spelt and Biesheuvel, 1997). Two of the data points demonstrate an increase in slip velocity associated with turbulence, which is observed in the literature generally for solid particles. The authors

did not present any explanation for this result, which went against their theoretical predictions.

In view of the flexible and partial slip behavior, it was thought desirable to present some of the reported work on drag modification of droplets. Friedman and Katz (2002) investigated the rise rates of droplets of diesel fuel in water (density ratio of 0.85) at isotropic turbulent conditions. In quiescent water, it was found that droplets of size 0.5 – 3mm remain spherical within a few percent and possess almost the same drag coefficient as solid spheres (slightly lower). The authors performed a force balance on the system and found that the velocity profiles were dependant on four dimensionless variables. The Stokes number is used to characterize the turbulence in the flow. It is dependent on the local Reynolds number, the ratio of drop diameter to turbulence length scale and the ratio of RMS fluctuating velocity to the terminal drop velocity.

The experimental setup consisted of two rectangular tanks with four rotating grids on each corner with different sizes and thus allowed for varying levels of turbulence. PIV was used for flow characterization, while shadowgraphy was applied to track the droplet motion. Their results indicate that at high turbulence levels with RMS velocity beyond 4 times the settling velocity and at the low turbulence level with the RMS velocity comparable to settling velocity, the settling velocity is independent of Stokes number. However, at intermediate turbulence levels St does strongly affect settling velocity. The authors suggest that the small droplet motion is enhanced by means of the trajectory biasing effect whilst motion of large droplets is suppressed due to non-linear drag.

Aliseda et al. (2002) studied motion of heavy particles in homogeneous isotropic turbulence. The flow system comprised of spraying the water droplets in a wind tunnel

containing honeycomb grids. The settling velocity of droplets was observed to depend on the Stokes number and the ratio of particle terminal velocity to characteristic turbulence velocity. These parameters were defined as functions of the Kolmogorov scale. Initially, clean air was passed through the system in order to study the single phase turbulence characteristics using hot-wire anemometry. Measurements of the dispersed phase were done using Phase Doppler Particle Analysis (PDPA), with two-phase flow visualization also performed via a high resolution digital camera setup.

By using hot wire anemometry and PDPA, large datasets of droplet velocity were available for analyzing droplet behaviour in the system. The data was classified into bins according to the droplet diameter. The instantaneous vertical velocity of drops in each size class was averaged to compute the mean settling velocity for that size. When the velocity data was plotted against their Stokes number (St), all of the data exhibited an increase in settling velocity associated with turbulence, the maximum such increase corresponding roughly with $St_k = 1$. The authors also examined the influence of particle loading and found that settling velocity was further enhanced as the volume fraction was raised. The authors claim that their range of volume fractions adopted ($\epsilon \leq 8 \times 10^{-5}$) is such that turbulence is not significantly affected by the particles. In general, these experimental results support the notion that turbulence promotes clustering of heavy particles which is one of the mechanisms responsible for faster settling.

Kubie (1999) modeled the settling velocity of droplets in turbulent pipe flow using the equation of motion. It was mentioned that when the linear drag law applies to the particle, settling velocity in isotropic turbulence would be the same as for stagnant fluid (the system examined may not have exhibited the trajectory biasing effect). A retardation coefficient was introduced, being smaller than one, and representing the slowing of settling velocity due to turbulence. Values obtained were between 0.8 – 1.

The work was designed to prove the decrease in settling velocity due to turbulence (although limited to effects of drag).

Maxey et al. (1996) also present an equation of particle motion for low Reynolds numbers (on the basis of slip velocity and also fluid velocity gradients), applicable for particles smaller than the Kolmogorov scale. Treating the particles as ‘points’ allows for the fluid acceleration in the virtual mass term to be determined relative to the particle centre rather than global estimate using the substantial time derivative. Low Reynolds number brings significant simplification for drag and lift because the particles are in Stokes flow. Lift forces are thus absent and Stokes drag is linear in Re .

Concerning the motion of particles in turbulence, it is mentioned that settling (possibly also rising) of particles is what triggers the crossing trajectories effect (otherwise known as trajectory biasing or preferential accumulation). This effect limits dispersion of particles relative to fluid elements and thus has been known to enhance settling. Dispersion is governed by large eddies but Maxey et al. (1996) point out that the rate of settling is more strongly influenced by small-scale turbulence. The smaller Kolmogorov eddies contribute most to the vorticity and rate of strain distributions, when the particle response time greatly exceeds the Kolmogorov time then they are controlled by the larger scale eddies. The authors state that no confirmation of trajectory biasing has been produced for such large scale interactions thus far. Also non-linear drag is expected to oppose the settling (rise) enhancement if $Re_{(slip)} > 1$, but accumulation should still occur under the appropriate conditions.

With regards to bubbles, the analysis shows that bubbles strongly accumulate in regions of high vorticity or low strain rate. Bubble rise velocities are thus reduced in extent compared to stagnant conditions. This vortex trapping effect is incidentally

expected to be stronger than the corresponding crossing trajectories effect of denser particles.

Bunner and Tryggvason (2002) performed numerical simulations on systems of buoyant bubbles in turbulent systems. The focus was on uncovering details of the ensuing turbulence when a cluster of bubbles rise. It was mentioned that in numerical simulations of particulate flows the Kolmogorov length scale was assumed to be larger than particle size in order to uphold the point force approximation. Physically this does not concur with bubbly flows and so work dealing with bubbles must account for all scales of turbulence (Bunner and Tryggvason, 2002).

Mazzitelli et al. (2003) performed numerical simulation on tiny bubbles with diameter up to 0.1 mm in turbulent liquid. They found that microbubbles in turbulence accumulate preferentially on the downflow vortices thus slowing their rate of ascent. The means by which this was thought to be achieved was the lift force. It was also found that the abovementioned effect was most pronounced when the bubble relaxation time coincided with τ_k ($St = 1$). It was suggested that bubbles act to reduce the dissipation rate (ϵ) of the established turbulence supposedly because as they accumulate in downflow regions, rising bubbles transfer momentum upwards thus reducing the intensity of vertical velocity fluctuations.

Liao et al. (2004) describe the study of rise velocity characteristics for a small bubble with size 0.69 mm rising through quiescent solution of 2.3×10^{-7} molar Triton X-100 (nonionic surfactant). They found the bubble shape remained essentially spherical since its injection, and the bubble rise velocity initial increased to a value above the terminal rise velocity and then decreased slowly to its terminal rise velocity. The significance of this study is to establish time dependent nature of surfactant adsorption.

They modeled the adsorption and transport of the surfactant on the bubble interface and tried to explain this behavior with their numerical simulations. The simulations were able to capture this increase of rise velocity above its terminal velocity; however the quantitative agreement was poor. This was attributed to initial contamination of bubbles at the time of their formation, because they are held stationary for ~ 0.8 s before getting detached.

Sharifullin and Luebbert (2001) studied the variation of rise velocity of bubbles in dilute solutions of Proxanol P-268 (nonionic surfactant) and Sodium oleate (anionic surfactant) up to concentrations of 2 g/l. The experiments were carried out in a glass column 30 mm in diameter which was filled with the solution under study. The time it took for a bubble to travel through the surfactant-containing water layer was measured with a stopwatch. The bubble diameter was varied from 3-6.6 mm. They also found the general effect of decrease in rise velocity with increase in surfactant concentration. The decrease in rise velocity with increase in bubble diameter at lower surfactant concentrations was attributed to the change in the shape of bubbles. At higher concentration of surfactants, however, the bubble velocity increased steadily with bubble diameter indicating rigid interface. As a part of their study, they also varied clear liquid height (and hence residence time of bubble in surfactant) and observed the effect on rise velocity. For weak surfactant (Proxanol) the effect was negligible; while for strong surfactant (Sodium oleate) the rise velocity was found to oscillate with the residence time of the bubble. This indicated the dependence of bubble motion on balance between adsorption and desorption of surfactant at gas-liquid interface.

Recently, Saito et al. (2008) studied the effect of surfactant on the liquid-phase motion around a single zigzagging-ascent bubble using a more advanced measurement technique, viz. PIV and shadowgraphy. They discussed the effects of surfactant concentration on the surrounding liquid motion (i.e. intensity of the vorticity, size of the vortices and the structure of a hairpin-like vortex) as well as those on centre-of-gravity

and surface motion of the bubble. They used a very small amount of 1-pentanol solutions with concentration up to 500 ppm. Although the bulk surface tension was almost the same as that of purified water, the bubble motion and the surrounding liquid motion in the solutions (i.e. contaminated system) were very different from those in purified water. They found out a critical concentration of a surfactant at which, the intensity and size of the vorticity becomes the largest. They observed the coupling between the asymmetric surface motion of the bubble and the surrounding liquid motion, concluding the Marangoni stress owing to a concentration gradient of the adsorbed surfactant on the bubble surface plays a great role.

It is apparent from the literature review that besides a large number of works undertaken, the state of the art is far from providing a clear, quantitative description of the drag force in presence of turbulence and surfactant in the liquid surrounding the bubbles. The principle reason for this was the lacunae of the measurement techniques available to researchers till date. With the limited information available from manual measurement of the rise time of bubbles in usually narrow columns, with practically no means to simultaneously measure the bubble rise characteristics and the surrounding liquid flow field. The use of computational models like level sets, lattice-Boltzmann simulations or front tracking to calculate the flow field surrounding bubbles is certainly more powerful to discern to flow pattern surrounding the interface at a high spatial and temporal resolution and can generate deeper insight into the effect of turbulence, the presence of surfactant and interface mobility. However, these methods are computationally intensive. Thus, it was thought desirable to conduct a systematic experimental study of the effect of free stream turbulence and surfactant concentration on single bubbles and bubbles rising in a chain. In the current work, we have employed an advanced measurement technique using simultaneous stereo PIV and shadowgraphy

along with detailed image processing to get further insight into bubble motion under turbulent conditions. The details of the measurement techniques, experimental setup and different experiment conditions are described in the following subsections.

4.3. Experimental methods

The experimental setup consisted of 3 main parts: (1) Turbulence generator (2) Bubble generator and (3) The PIV/Shadowgraphy system with related electronics. Details of each individual subassembly are described in the following subsections.

4.3.1. Turbulence Generator

In the present study, an oscillating turbulence generator described by Doorodchi et al. (2008) was employed to produce stationary near isotropic turbulent flow fields. In such devices, the oscillating grids generate a system of wakes and jets that merge with each other to produce a sustained turbulence with zero mean flow (De Silva and Fernando, 1994). The turbulent intensity can be varied simply by changing the vibration frequency, the size of the strokes and/or the separation distance between the grids. A relationship between these operational parameters and the characteristics of the resultant turbulent field has been already established (Shy et. al. 1997).

A schematic representation of the turbulence generator is shown in Figure 4.1A. The device consisted of a rectangular Perspex tank with a width of 300mm containing a pair of vertically oriented grids of size 150mm×150 mm. The grids were made of 6mm thick aluminum sheets with 30 mm distance between centers of two successive openings, having an overall opening of 64% (Figure 4.1B). Perfect horizontal and vertical alignments of the square-openings were achieved using a high precision laser cutting technique. These design specifications were set according to the literature to prevent formation of unstable flow structures (Yang and Shy, 2003). Connecting rods supported by linear bearings were then used to connect the grids to stepper motors through

eccentric cams. To minimize the possibility of transmitting vibration from motors to the flow field, the tank was installed on a separate supporting bench.

The system was designed to operate at different frequencies and strokes of up to 10 Hz and 50 mm, respectively. In the present work, the stroke was fixed at 20mm while the mean separation distance between the grids was set at 110 mm. The motors were setup so that the grids moved in-and-out together, rather than side-to-side. The flow characteristics of turbulence under these conditions for particular frequencies have been reported by Yang and Shy (2003) using a Laser Doppler Velocimetry (LDV) system while the length scale of the turbulence was estimated to be about 3mm for frequencies varying from 3 to 8 Hz. A summary of the flow characteristics is presented in Table 4.1.

Table 4.1. Turbulent flow characteristics [Yang and Shy, 2003]

Grid frequency (Hz)	r.m.s. turbulent velocity (mm/s)	Integral lengthscale (mm)
3	7.2	3
4	9.6	3
5	12.0	3
6	14.4	3
7	16.8	3
8	19.2	3

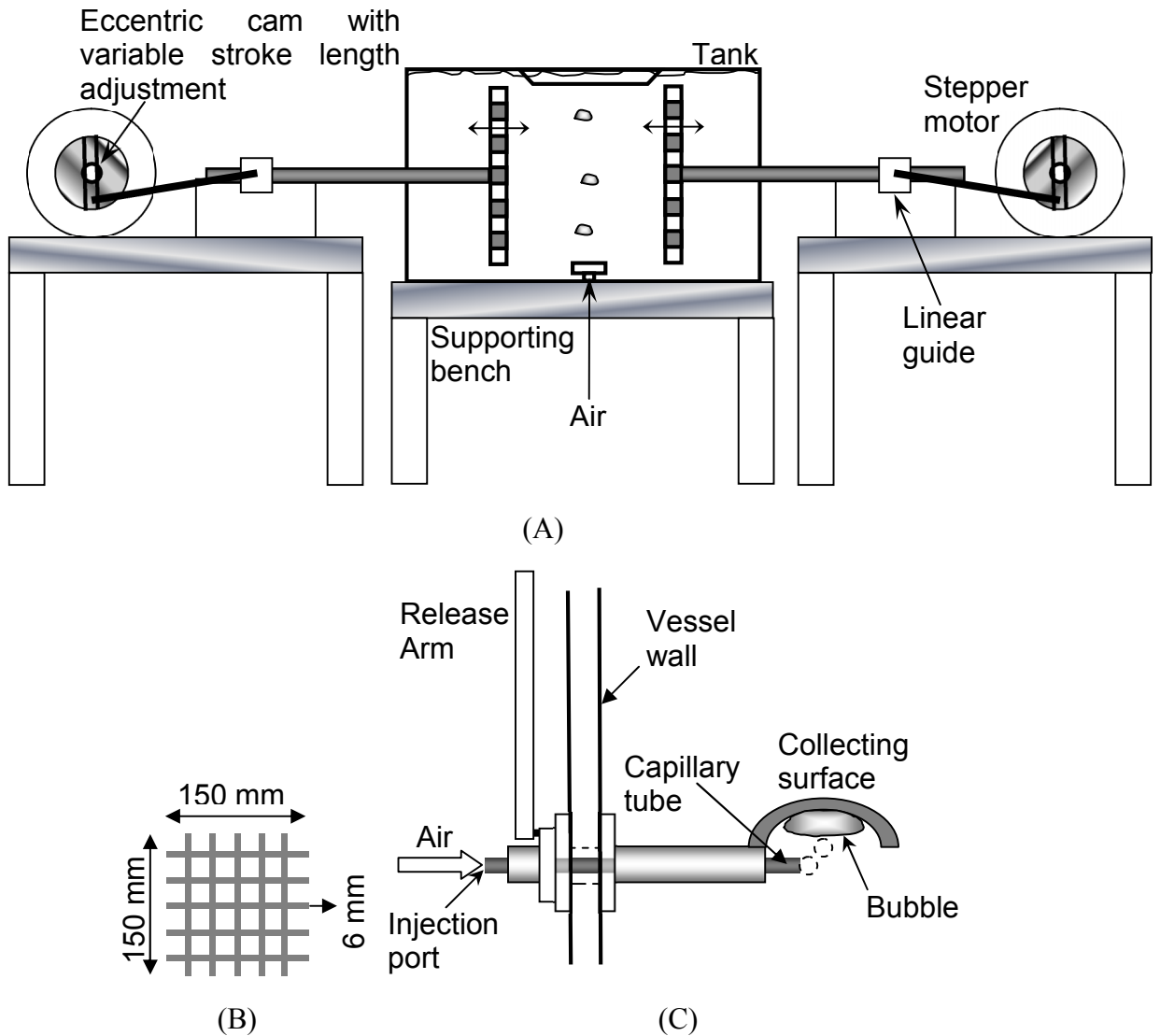


Figure 4.1 (A) A schematic representation of the turbulent generator, (B) the grid geometry (C) Bubble generator

4.3.2. Bubble Generator

Two types of bubble generators were employed. An orifice with 2 mm hole diameter was used to generate the chain of bubbles having similar diameters. The gas was sparged with a miniature compressor and the gas flow rate was measured using pre-calibrated precision rotameter with capacity of 0-100 cc/minute of air. To generate single bubbles of different diameters, a special bubble generator described by Lane et al. (2007) was used to generate single bubbles of different sizes. The schematic of this generator is shown in Figure 4.1C. A known amount of gas is injected using a precision gas-tight syringe. This gets collected below the concave collector plate. This is flipped to release

the gas all at once, generating bubbles with diameter dependent on the volume of gas injected before release. This allowed generation of bubbles having different sizes ranging from 3 mm-15 mm with good reproducibility.

4.3.3 Measurement Principle

Figure 4.2A shows the schematic of the experimental setup for combined PIV/LIF with fluorescent tracer particles and shadow imaging of the gas bubbles. Like conventional PIV, a dual head Nd:YAG laser illuminates a 2D light sheet in the multiphase flow at 532 nm wavelength. A frame straddled camera is used to capture the two images at the desired time interval. The major difference between the conventional PIV and the current methodology lies in the ability to separate bubble images from the raw particle images. The refractive index of gas is orders of magnitude lower than the liquids. Hence, the laser light is bent to very large extent by the bubbles. This results in speckles and very high intensity flaring at the bubble interface. The reflected laser intensity is high enough to damage the CCD/CMOS sensor of the camera, besides resulting in extremely poor contrast of the particle image. Since the size of bubbles used in current work is 3 order of magnitude larger than the PIV seeding particles (4 mm vs 12 microns), the scattered laser light intensity is also orders of magnitude higher than seeding particles. Thus, the very intense reflection from bubble surface must be blocked from reaching the camera CCD. This is achieved by using florescent tracer particles. Fluorescent tracer particles in the flow reflect part of the light and they emit light at a wavelength of 555–585 nm with an emission peak at 566 nm. Thus, the reflected light from seeding particles is a mixture of 532 nm laser light and the longer wavelength fluorescent light.

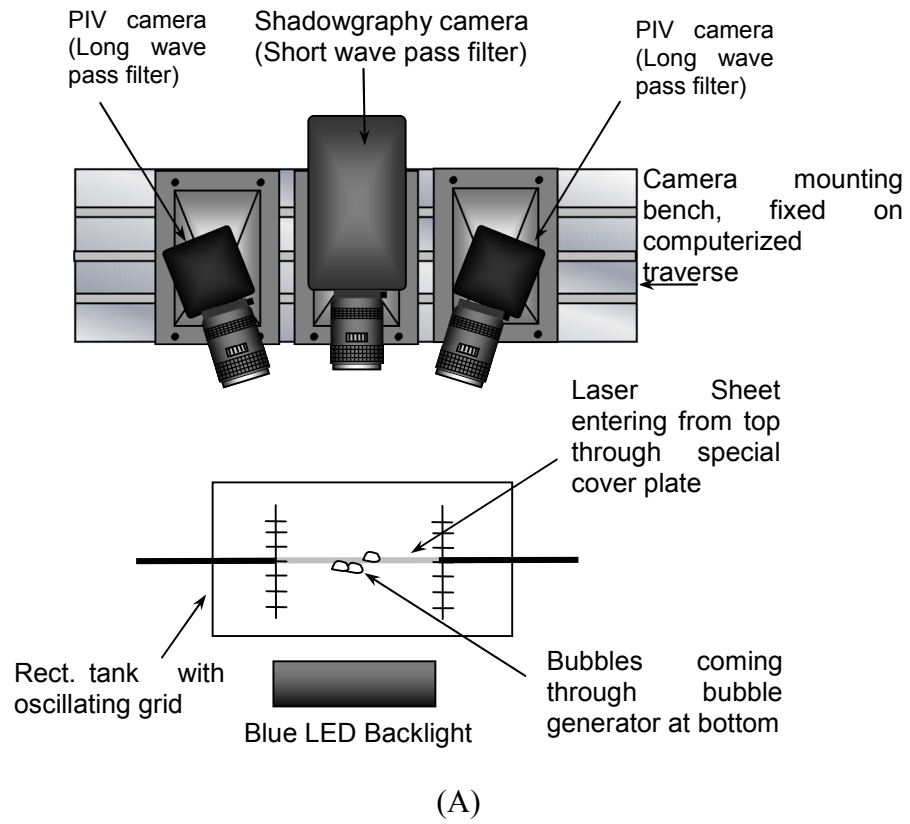


Figure 4.2 (A) Schematic of combined stereo PIV and shadowgraphy setup (B) Photograph of the setup

An optical long wave pass filter with a steep transmission edge at $570 \text{ nm} \pm 5 \text{ nm}$ is fitted on camera to block the green laser light to a great extent. While allowing most of the fluorescent light to be recorded by the CCD. The laser intensity needs to be adjusted to minimize the intensity of leakage light from the filter. Bubbles are still detected by CCD chip in the long wave pass filtered image. However, part of the image containing reflections is completely blocked when mask generated from the shadow image is applied.

Both sets of information from the tracers and from the bubbles are recorded by different cameras. A double-pulsed high-power light emitting diode (LED) array backlight and a high speed camera is used for shadowgraphy. The backlight has emission wavelength of 470 nm corresponding to blue color. A short wave pass filter allowing transmission of wavelengths less than 475 nm is used in front of the shadowgraphy camera. The blue light passes the optical low pass filter and the shadow image is recorded on the detector of the camera. The green/red light used with PIV recordings is almost completely blocked. This particular combination of the blue, green and red light allows better isolation of each individual wavelength by respective filters, allowing use of high intensity backlighting. Even after choosing such a wide difference in the wavelengths of backlight and fluorescence from seeding, the backlight intensity has to be carefully adjusted in order to get least interference in the images used for PIV processing. Using this method, we are able to achieve a good contrast in shadow images at very fast shutter speeds.

4.3.4 The Measurement System

Experiments were performed with a modified commercial PIV system, consisting of a Quantel BrilliantB dual head Nd:YAG laser with up to 400 mJ per pulse and two Dantec Hisense cameras with 1200×1024 pixels and 12-bit resolution. A Dantec system

hub was used to control the PIV system. Additionally, the pulsed LED array is integrated in the PIV measurement set-up as shown in Figure 4.2. The pulsed LED array consists of 144 high-power diodes with a small emission angle. A diffuser plate is used in front of the LED array. The LEDs are operated in pulsed mode (19 Volts for less than 1 ms). This increases the light emission and the moving bubbles do not cause blurring of the image.

An in-house developed timing card fires the LED array in synchronization with laser pulses. The timing sequence for Shadowgraphy+PIV measurements used in the current work is similar to that used by Lindken and Merzkirch (2002). Further details of timing are described in Sathe et al. 2008. This combination is used to record the bubble trajectories with liquid velocity field. PIV exposure is 800 μ s. Within 1 μ s, the data is removed from the light sensitive part of the pixels. After a time interval $dt=1000 \mu$ s, the laser and the LED array are triggered again, and the information is recorded in the second frame of the PIV recording.

LED illumination circuit was designed following the recommendations of Lindken and Merzkirch (2002). The resultant short pulse duration allows the use of LED for illumination of fast moving objects (up to few m/s) without blur. Slight discrepancy in the background intensity between the two frames is taken care of by the dynamic histogram based threshold in the image processing algorithm. For recording with high speed camera, the LEDs were kept on for 20 ms, during which the high speed camera recorded 5 images at 500 Hz. This frame rate is sufficient to capture the relatively smooth trajectory of bubble needed to deduce the bubble velocity and acceleration.

4.3.5 Outline of the Experiments

The experimental studies were carried out for bubbles rising in chain for different turbulence intensities and surfactant concentrations. The typical bubble diameter was

about 4 mm for most of the experiments. The terminal velocity in a quiescent liquid was also obtained experimentally for clean water as well as water containing surfactant.

A systematic approach was adopted in the experimental work. First, the tank was rinsed thoroughly with Reverse osmosis treated water. The Reverse osmosis treated water was used for clean water experiments. The surfactant solutions were prepared by dissolving the appropriate volume of surfactant (MIBK/IPA) into Reverse osmosis water. Since the surfactants employed in current work are volatile, the tank was allowed to dry thoroughly before filling it with clean water or water with surfactant solution. Then, the operational parameters including the grid oscillation frequency, the size of the stroke and the distance between the grids were set. A turbulent flow field was then established by out of phase oscillation of the grids. The gas flow rate through the sparger was then adjusted to give the desired bubble frequency. The bubble motion was captured using a simultaneous stereo PIV and high speed video camera. The measurement window was in the near isotropic turbulent region, which has a width of approximately 40mm and height of about 100mm located in the centre between the grids. The rise characteristics for each bubble were determined from the image processing program written in MATLAB. Each run was repeated a number of times with the velocity being reported as the average value. For single bubbles, the bubble slip velocity is equal to its rise velocity since the liquid mean velocity relative to the wall is zero in the current study. The rise velocity of bubbles rising in chain is higher compared to single bubbles. This increase in rise velocity can be attributed to modified bubble drag coefficient and the upward liquid motion setup by the rising bubbles. The mean velocity of liquid in the vicinity of bubbles was quantified using PIV. To calculate the slip velocity of bubbles, this local liquid velocity was subtracted from the bubble rise velocity obtained using shadow image sequence processing. To verify that the bubble is intersecting the plane of measurement

of PIV, the bubble silhouettes isolated from PIV images were used as projections of the bubble shape additional to shadow image. These two projections were used to fit a 3D ellipsoid, to deduce bubble orientation and its position with respect to light sheet. Figure 4.3 shows one such snapshot of a bubble behind the measurement plane. Only those bubbles which were intersecting the measurement plane were used for the estimation of slip velocity using PIV and shadowgraphy.

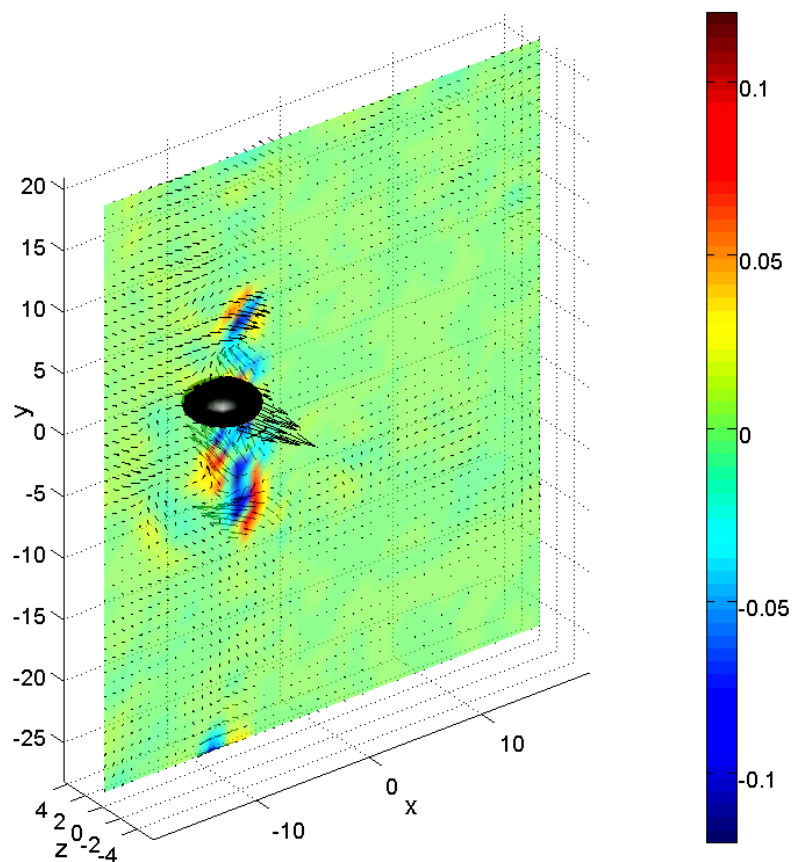


Figure 4.3 Ellipsoid approximating the bubble shape superimposed over stereo PIV vectors and vorticity contour for air flow rate $500 \text{ mm}^3/\text{s}$ and grid oscillation frequency of 2.5 Hz

4.4. Data Processing

4.4.1 Image Processing

The shadow images were processed by the image processing routines programmed in MATLAB R2007a. The grayscale images from the high speed camera are read, and corrected with first order perspective correction to obtain complete overlap between PIV and High speed camera image. This is verified by comparing the images captured by a calibration target in the focal plane of the square tank used for the experiments. After this, the images are binarized to black and white using an optimum threshold value. This threshold is calculated on the basis of intensity histogram of the grayscale image, and has to be optimized in the case of non-uniform background illumination. However, artifacts such as a dark border on either side of the image remain, and they are removed before image registration to detect bubbles. After binarization, the ‘holes’ in the bubble image, primarily caused by the curvature of the bubble, are removed by morphological image processing, which involves subsequent dilation and erosion of image. After ‘filling’ the holes, the image registration detects bubbles as isolated regions of the image with the type of pixel connectivity specified. Every region is labeled for different properties like equivalent area in pixel squared units, and location of the centroid. The detected bubble image is used as a digital mask to blank the PIV images in these regions, because even after using a high pass filter in front of the PIV camera, leakage through the filter allows the bubble silhouette to be recorded as a blurred boundary, which must be blanked to avoid spurious vectors caused by weak cross correlation between these hallows.

Finally, the centroid locations exported from the image processing routine are processed to track the particles by an open source code available from Daniel Blair and Eric Dufresne. The routine searches for particles with similar location from the location

array provided. This was tested on dummy images before being applied to ‘Rough’ images caused by bubbles. The routine works satisfactorily even with more than 100 bubbles present in the image. However, care must be taken while capturing the images, by adjusting the Δt such that the bubbles do not move farther than half the diameter of individual bubbles. Additional check of both the identified bubbles having same area was implemented in the particle tracking code. The tracking code returns the trajectory as array of centroid locations. Then, a 4th degree polynomial is fitted to this trajectory. This polynomial is used to evaluate the first and second derivative of the bubble trajectory, which yield the bubble velocity and acceleration, respectively.

The bubble projections isolated using morphological image processing are processed to get equivalent ellipse (ellipse having same second moment of area as that of the bubble silhouette) and the solidity. Solidity is the parameter describing wobbling nature of the interface quantitatively. This is illustrated in Figure 4.4. A Convex hull is generated using peripheral pixels of the binarized silhouette image, and the ratio of the original area of the silhouette to the area covered by the convex hull is reported as solidity. More the concave dents on the interface, the lesser is the solidity value. Similarly, a higher solidity value describes a smoother interface with least dents/waves ensuring more streamlined shape of the body.

4.4.2 PIV Processing

The digital PIV recordings were evaluated using the Dantec FlowManager software. Since the two phases, bubbles and water, move with different velocities it is necessary to separate the signals from the two phases in the PIV recordings. The bubble image derived from the shadowgraph using the methodology described in section 4.3.1 was used as the digital mask.

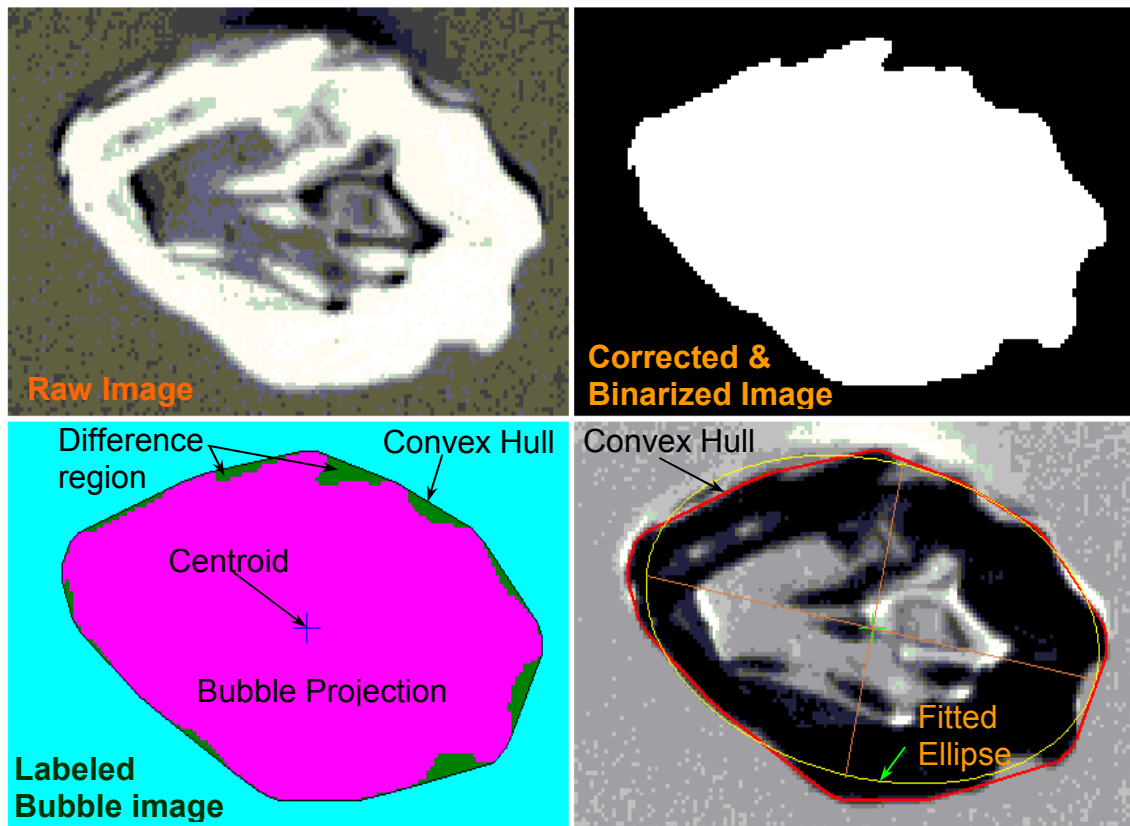


Figure 4.4. sample images illustrating solidity and fitted ellipse characteristics to a sample bubble image

The flow velocity of water was obtained from the masked tracer particle image, while that of the bubbles was obtained from particle tracking applied to the bubble image pairs obtain from shadow images. The Fluorescent tracer particle image also contained faint images of bubbles resulting from leakage through the filter. These portions were effectively masked by the binary mask generated from the shadow images of bubbles. A composite image generated from 5 shadowgraphs recorded along with the stereo PIV images. The trajectory of the bubble was used to calculate the rise velocity and acceleration corresponding to the flow field reported in Figure 4.3.

The recursive PIV processing was employed to evaluate the velocity vectors. It requires significantly more computational time than Nyquist grid. However, it is more effective in resolving the small scale velocity fluctuations and velocity gradients caused by passage of the bubbles, and allows for very small interrogation spot size of 16x16

pixels, giving output of 128x128 vectors corresponding to the spatial resolution of 0.52 mm over a field of view of 66x66 mm.

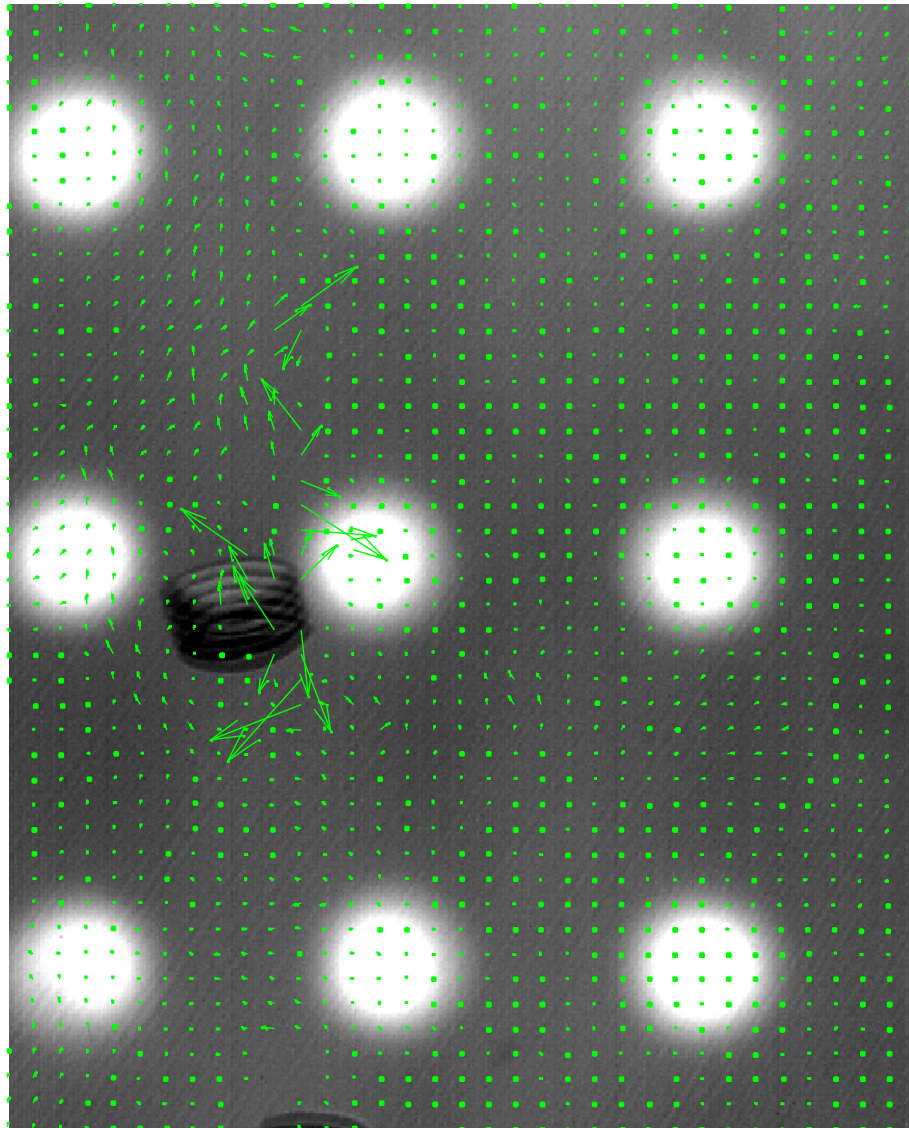


Figure 4.5. Velocity vectors obtained from PIV superimposed over the composite bubble trajectory image generated using the image sequence captured with high speed camera at 500 Hz

4.4.3 Particle Response Time and Stokes Number

The Stokes number (St) is a measure of the time taken for a particle to respond to an interacting turbulent eddy. It is defined as:

$$St = \frac{\tau_p}{T_L}, \quad (4.2)$$

where τ_p is the particle relaxation time and T_L is the turbulent integral time scale. In an isotropic turbulence, in which the flow characteristics are statistically independent of direction, the integral time scale can be defined as: $T_L = L/u_0$ where L is the integral length scale and u_0 is the r.m.s. velocity of turbulence.

The relaxation time of a particle can be calculated according to Bel F'dhila and Simonin (1992):

$$\tau_p = \frac{\rho_p + C_A}{\rho} \frac{1}{\left(\frac{3}{4}\right)\left(\frac{C_D}{d}\right)U_T} \quad (4.3)$$

where C_D is the drag coefficient in stagnant liquid, ρ_p is the particle density, ρ is the fluid density, d is the particle size and $C_A = 0.5$ is the added mass coefficient (Spelt and Biesheuvel, 1997). The relaxation time for bubbles, the integral time scale and the corresponding stokes numbers for different grid oscillation frequencies reported in current work have been reported in Table 4.2.

Table 4.2. Time scales and Stokes number for experimental conditions

Grid frequency (Hz)	Bubble response time (dB= 3.9 mm) (s)	Integral time scale (s)	Stokes Number (-)
2.5	0.0359	0.5	0.0719
4.5	0.0359	0.278	0.1294
6.5	0.0359	0.192	0.1869
8	0.0359	0.156	0.2299
10	0.0359	0.125	0.2875

4.5. Results and Discussion

The bubble frequency in the chain was varied by controlling the flow rate of air through the orifice. The experiments have been carried out for 2 air flow rates of 500 mm³/s and 833 mm³/s, corresponding to bubble frequencies of 14 and 24 bubbles/s, respectively. Clean water and 0.1 % v/v isopropyl alcohol was used to study the effect of the presence of surfactant. The grid oscillation frequency was varied from 0 to 8 Hz. Figure 4.6 describes the effect of turbulence on the rise velocity of bubbles rising in a chain. Figure shows the general trend of a consistent decrease in rise velocity of bubbles for all four cases under consideration.

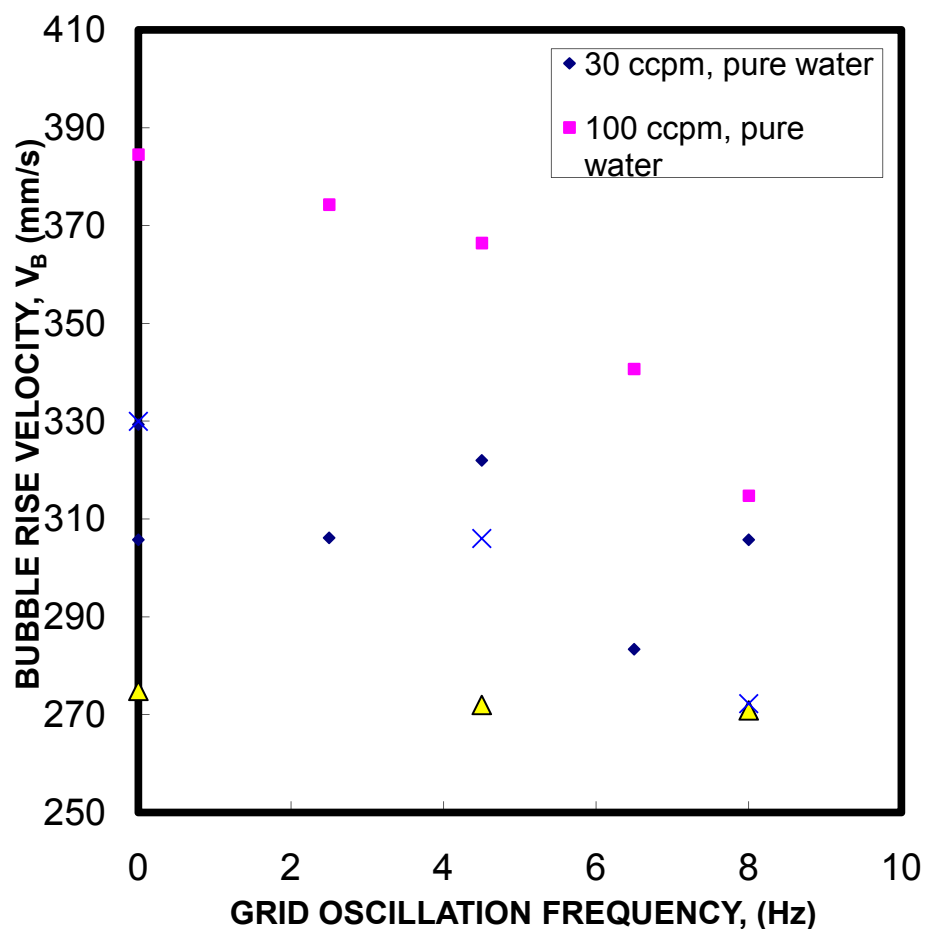


Figure 4.6 Effect of grid generated turbulence on bubble rise velocity for: ◆ Pure water, air flow rate 500 mm³/s; ■ Pure water, 1667 mm³/s; 785 ppm IPA, ▲ air flow rate 500 mm³/s; × 785 ppm IPA, air flow rate 833 mm³/s

The decrease in rise velocity is more prominent for the higher bubble frequency. This can be attributed to the increase in the spread of the bubble plume at higher degree of turbulence, which can be observed from the overlapped trajectories of several bubbles displayed in Figure 4.5. The spreading of the plume reduces the peak hold-up in the narrow region of the plume, reducing the driving force to induce the liquid circulation along the chain of rising bubbles. The addition of isopropyl alcohol has reduced the rise velocity of the bubbles. This effect is attributed mainly to the decreased mobility of the interface caused by the accumulation of surfactant at gas-liquid interface. This reduces the mobility of the interface, increasing the shear stress and corresponding increase in the overall drag force on the bubble.

To further study the effect of surfactant addition on the rise velocity of the bubbles, a systematic increase in surfactant concentration was employed instead of a strong step change (0 to 750 ppm IPA). In this case, a commonly used frother (Methyl Iso Butyl Ketone, MIBK) was used. Three grid oscillation frequencies of 0, 4.5 and 8 Hz were studied for each concentration of surfactant. The MIBK concentration was varied from 0 to 100 ppm.

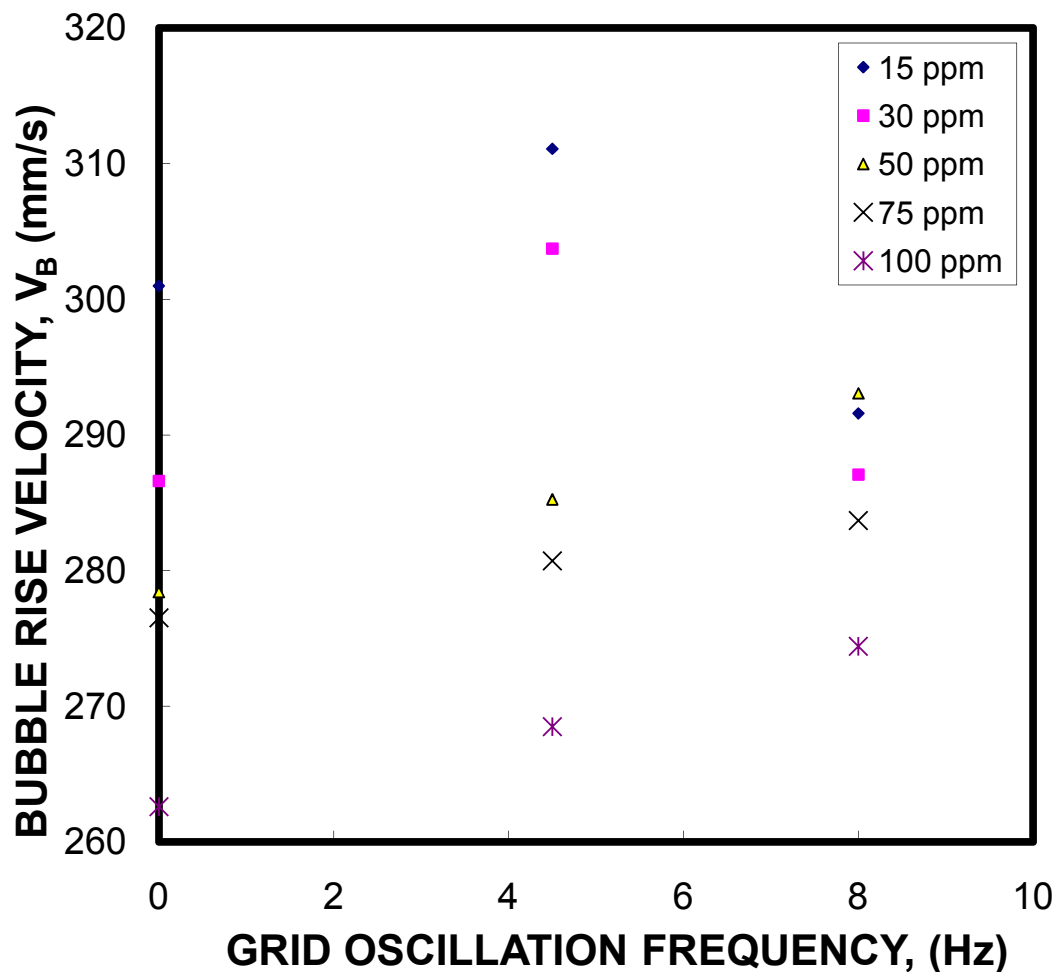


Figure 4.7 Effect of grid generated turbulence on bubble rise velocity: air flow rate of 167 mm³/s, ◆ 15 ppm MIBC; ■ 30 ppm MIBC; ▲ 50 ppm MIBC; × 75 ppm MIBC; ✖ 100 ppm MIBC

The results are summarized in Figure 4.7. The rise velocity of the bubbles decreases with an increase in the MIBC concentration. The rise velocity shows a maximum with respect to grid frequency at lower MIBC concentrations while it shows a sustained increase with respect to grid frequency in case of higher MIBC concentration. However, the positive effect of grid frequency on rise velocity is smaller compared to the

negative effect of the increased surfactant concentration, and in general the rise velocity at all turbulence intensities is lower for higher MIBC concentration.

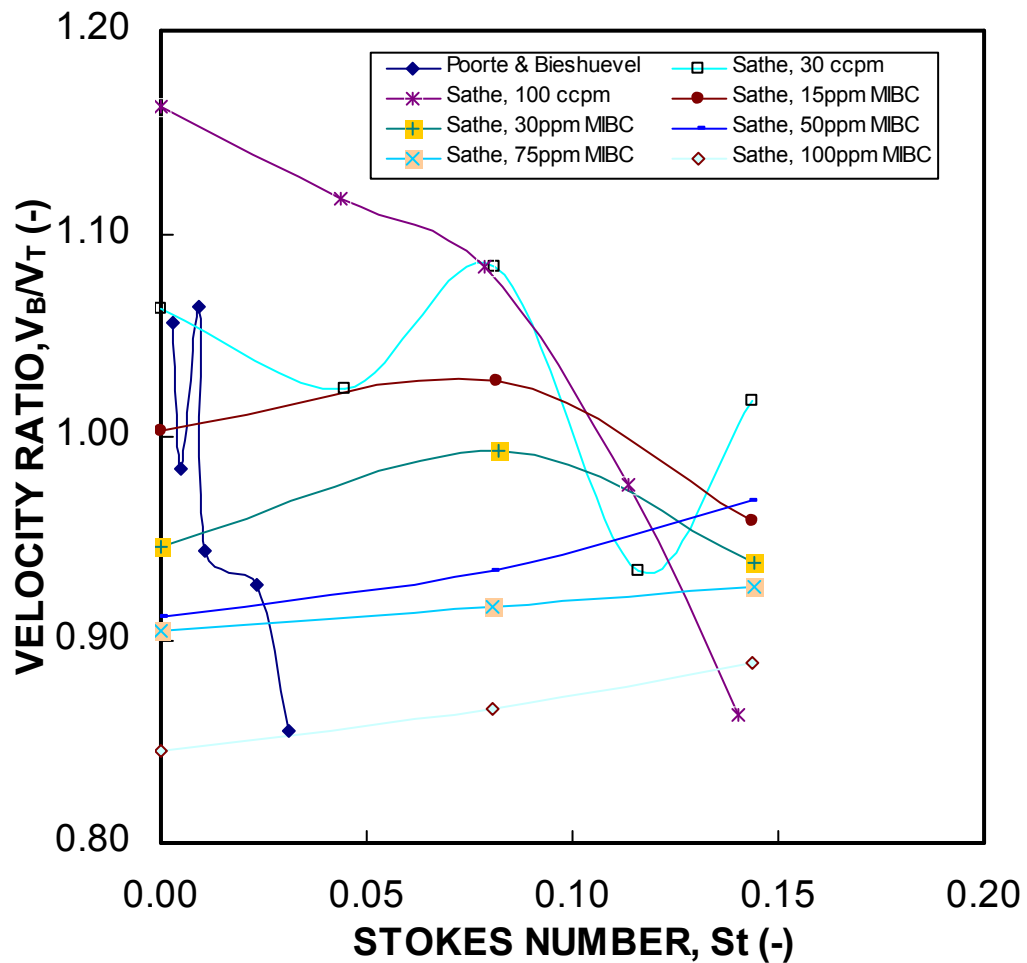


Figure 4.8 Comparison of the data obtained in current work with that obtained by Poorte and Biesheuvel (2002)

The drag reduction at higher turbulence can be attributed to the dynamics of the surfactant adsorption at the interface as well as the shape change of the bubble. Enhanced turbulence can significantly enhance the rates of surfactant adsorption and desorption. Also, the turbulent structures encountered by bubbles at higher free stream turbulence tend to hit and deform the bubble interface locally, making it wavy. This can significantly alter the wake separation angle, and the magnitude of surface vorticity generation. For example, the dimples on the surface of the golf ball delay the wake

separation and hence reduce the drag force. However, in order to quantify the effect of free stream turbulence clearly on adsorption/desorption of surfactant, the bubble wake characteristics and the vorticity generation at interface must be studied in much greater detail, which is beyond the scope of the current work. Figure 4.8 shows the comparison of the results obtained in current work with those of Poorte and Biesheuvel (2002).

The variation in bubble shape and size with surfactant concentration was analyzed using high speed camera images to get further insight into bubble behavior at different surfactant concentrations. The individual bubbles were allowed to rise in the dilute MIBC solution with desired concentration. The MIBC concentration was varied from 0-800 ppm. At least 100 bubbles were used to get the statistics of bubble shapes presented in subsequent Figures. Figure 4.9 shows the variation of the projected bubble diameter with MIBC concentration. The projected bubble size varies by a greater extent at lower MIBC concentrations. The spread is primarily caused by higher flexibility of the interface at lower surfactant concentration, causing the oblate ellipsoid shape of bubble. These flatter bubbles move with greater wobbling motion than the near-spherical bubbles at higher surfactant concentration, causing higher projected area fluctuations. The mean bubble size is nearly the same for all surfactant concentration. The mean bubble diameter is also governed by the bubble diameter at the orifice which is affected by the surface tension change due to the addition of MIBC.

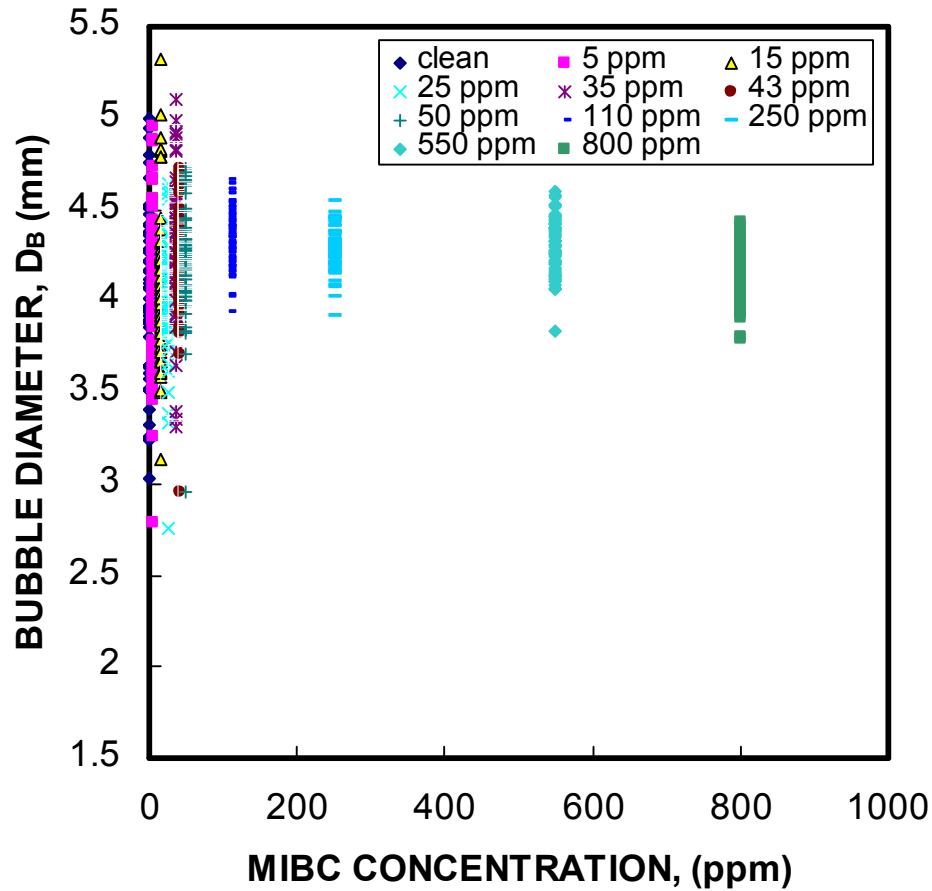


Figure 4.9 Effect of MIBC concentration on bubble diameter: ◆ Clean; ■ 5 ppm; ▲ 15 ppm; × 25 ppm; * 35 ppm; ● 43 ppm; + 50 ppm; - 110 ppm; - 250 ppm; ◆ 550 ppm; ■ 800 ppm

Figure 4.10 shows the variation of the shape attributes of the bubbles viz. the solidity and the eccentricity. The solidity of the bubbles characterizes the waviness of the interface. The solidity is observed to increase and the plateau with MIBC concentration of about 200 ppm indicating bubble interface becoming more rigid and smoother. Similarly, the eccentricity of the bubble reduces with MIBC concentration and reaching a plateau around similar MIBC concentration of 200 ppm. This behavior shows that the interfacial transport of surfactant reaches to an equilibrium around this concentration.

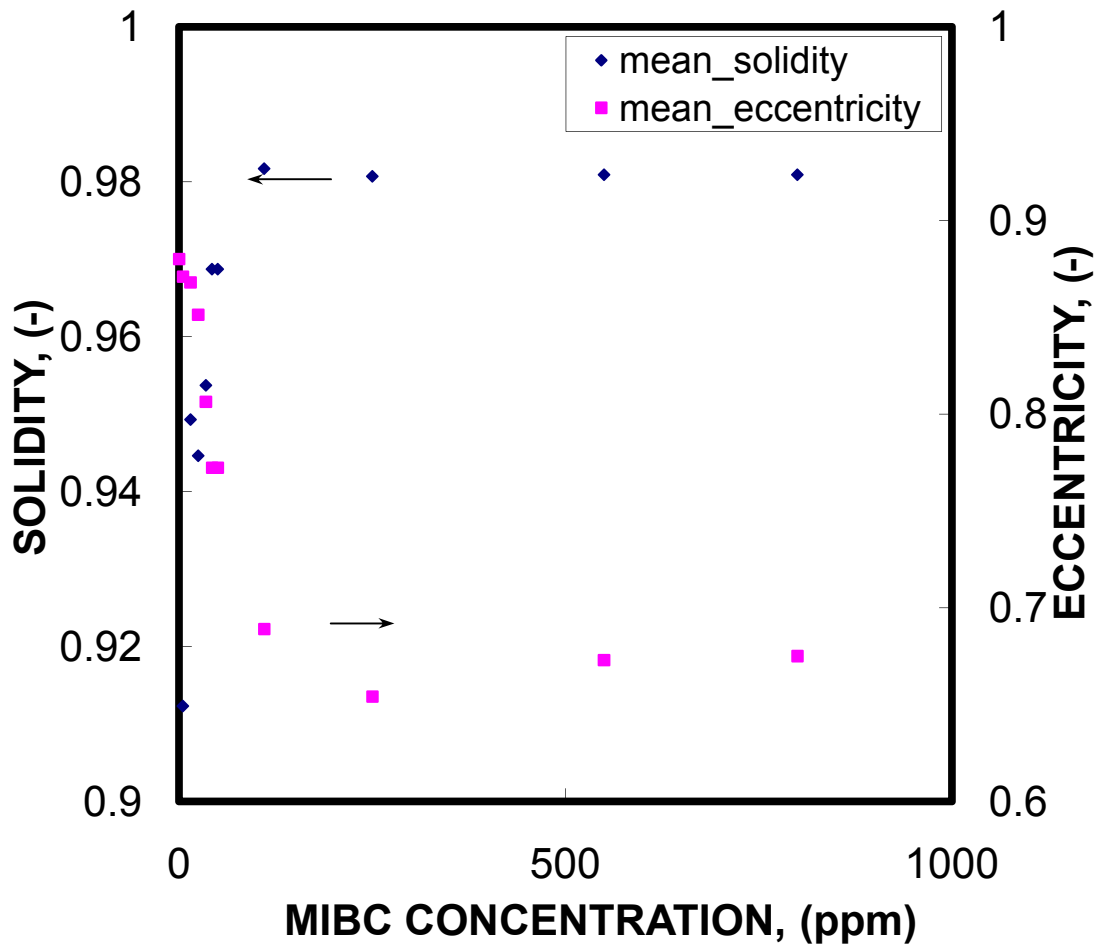


Figure 4.10 Effect of MIBC concentration on bubble characteristics: ◆ Solidity; ■ Eccentricity

The detailed image processing methodology was applied to the bubble image sequences obtained using the high speed camera. Figure 4.11 shows the results for a single bubble rising in quiescent water. Using the averaged rise velocity and projected bubbles diameter, the bubble Reynolds number turns out to be 1170. The bubble trajectory is shown in Figure 4.11A. It clearly shows the oscillatory motion which is primarily caused by wake detachment. The bubble also undergoes significant shape oscillations during this wobbling motion. Figure 4.11B shows the variation in major and minor axis of the projected bubble image. There is significant increase in the major axis while the bubble changes its orientation (represented by a turn in the trajectory, Figure 4.11B).

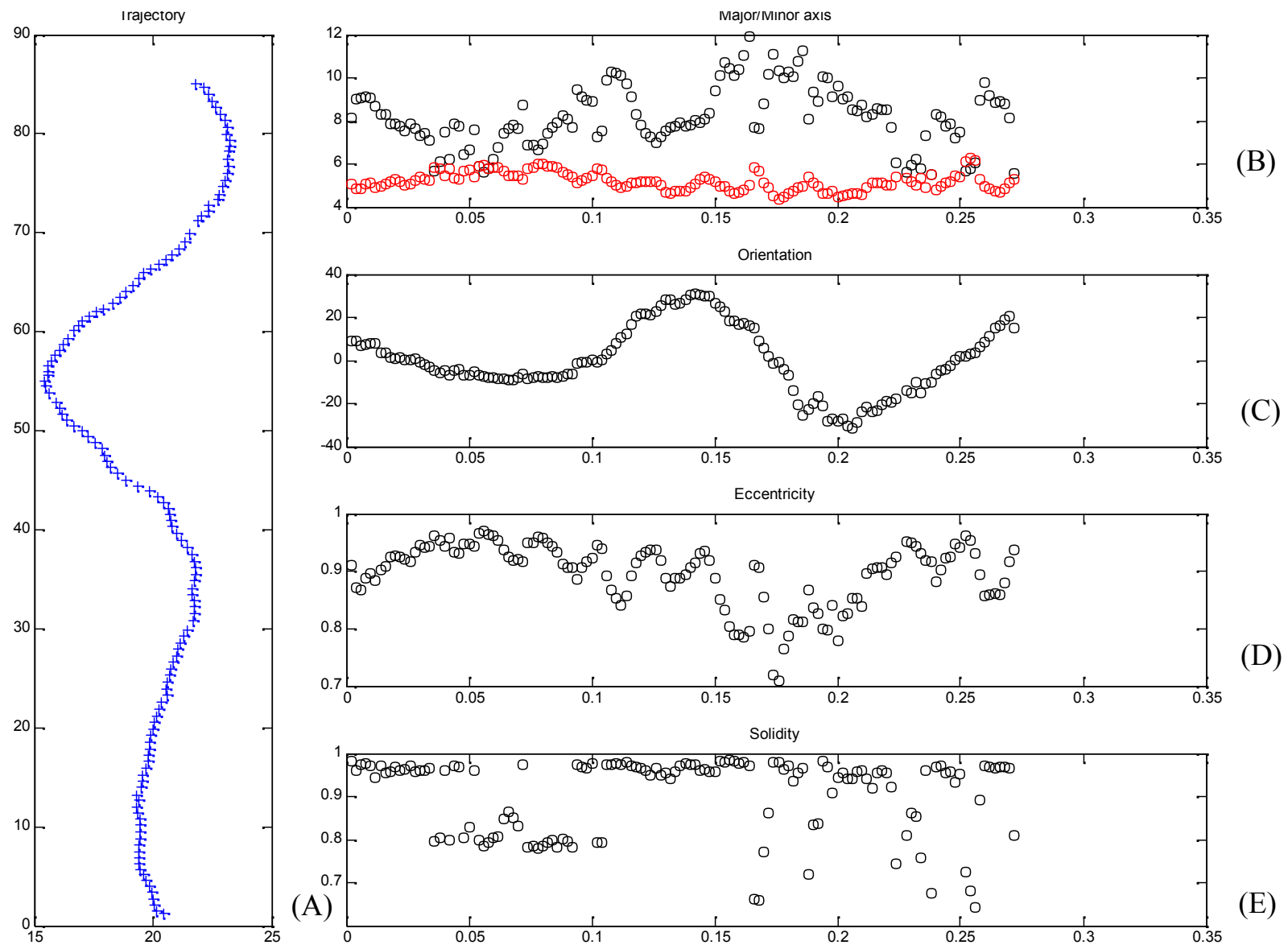


Figure 4.11 (A) Bubble trajectory, (B) variation of bubble major/minor axis (C) variation of orientation (D) variation of eccentricity (E) variation of and solidity with time, for a single bubble of 3.9 mm diameter rising through quiescent water

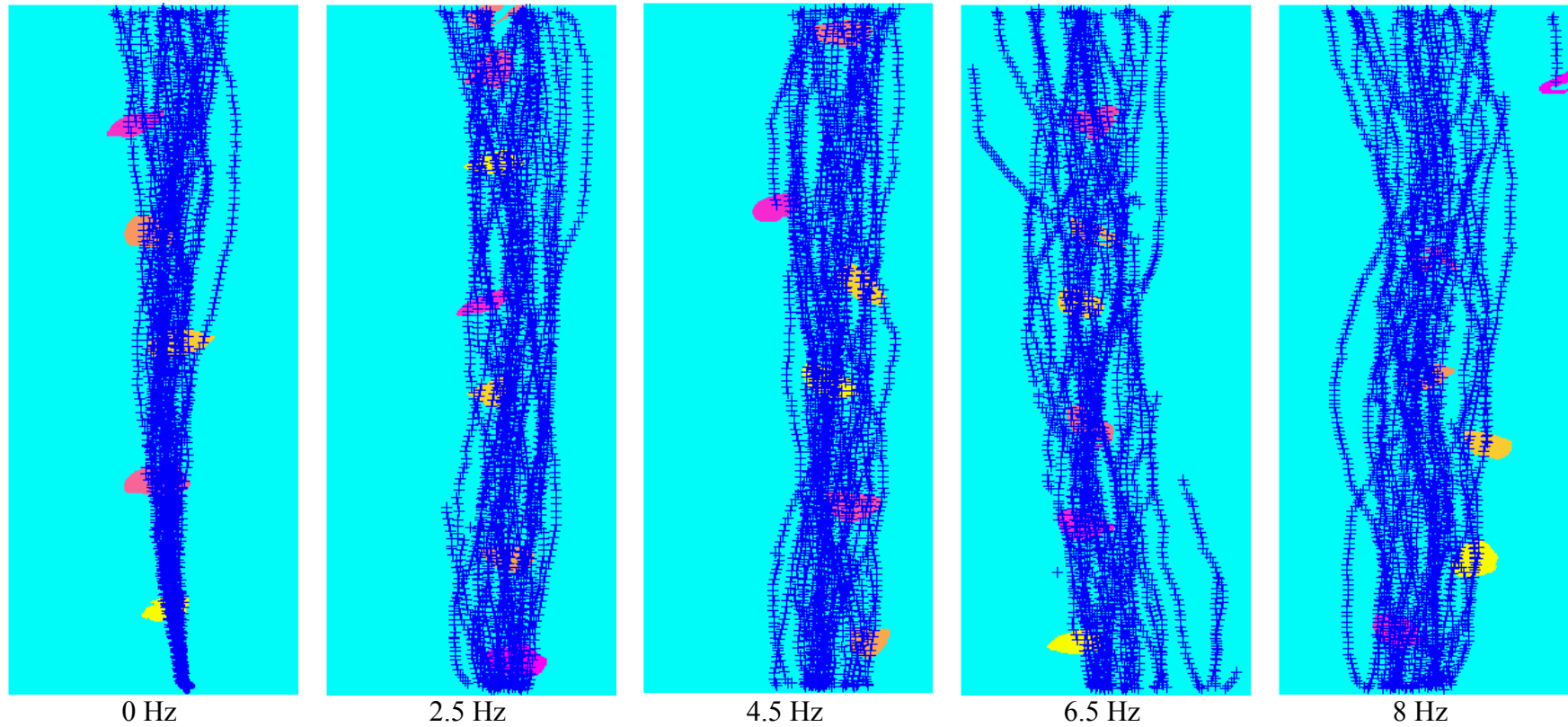


Figure 4.12 Variation of bubble trajectories in clean water with different grid oscillation frequencies for air flow rate of $1667 \text{ mm}^3/\text{s}$

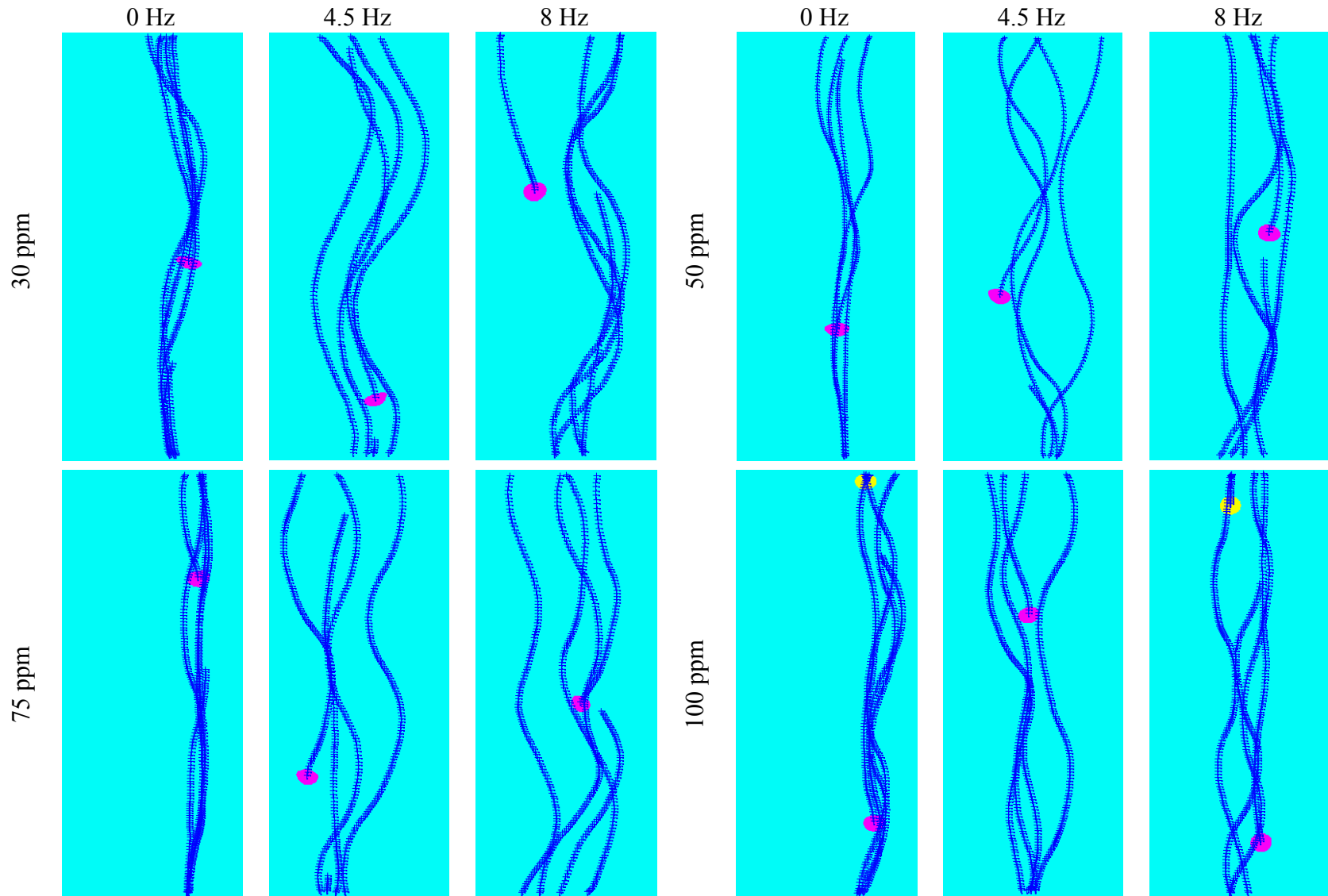


Figure 4.13 Bubble trajectories for different MIBC concentrations and grid oscillation frequencies

DEVELOPMENT OF EXPERIMENTAL TECHNIQUES AND CFD SIMULATIONS OF MULTIPHASE DISPERSIONS

The orientation of the bubble changes from 30 to -30 degrees with respect to horizontal axis during the course of the rise. It is interesting to observe the fluctuations in the eccentricity of the bubble and the solidity. These clearly bring out the small scale oscillation and wobbling of the bubble along with the four major turns visible from bubble trajectory during the course of the bubble rise. The major oscillation of bubble has similar period as that in quiescent water. However, the fluctuations in horizontal as well as vertical velocity increase, and bubble motion in transverse direction is altered significantly as becomes apparent from Figure 4.12. It also shows the variation in bubble trajectories as a function of the grid oscillation frequency for the case of bubbles rising in chain. The spread of the trajectories was found to increase with an increase in the grid oscillation frequency. The bubble plume has a structure similar to that of a buoyant jet, with lower spread near bottom and higher near top. This spread alters the gas hold-up profiles, affecting the liquid circulating velocity and hence the rise velocity of bubbles in swarms.

Figure 4.13 shows the variation of bubble trajectories with MIBC concentration and grid oscillation frequency. The general trend of increased spread with increased grid oscillation frequency is maintained at all MIBC concentrations. The overall trajectories are quite similar for all 4 cases considered. At no grid generated turbulence, the trajectory has 3 major oscillations along with small scale fluctuations. However, the rise velocity of bubbles averaged over entire length of tank reduces consistently with increase in surfactant concentration, as shown in Figure 4.4.

Figures 4.14 and 4.15 show the velocity profiles of water at different heights along with the bubble chain obtained using PIV for air flow rate of 500 and 1667 mm³/s, respectively.

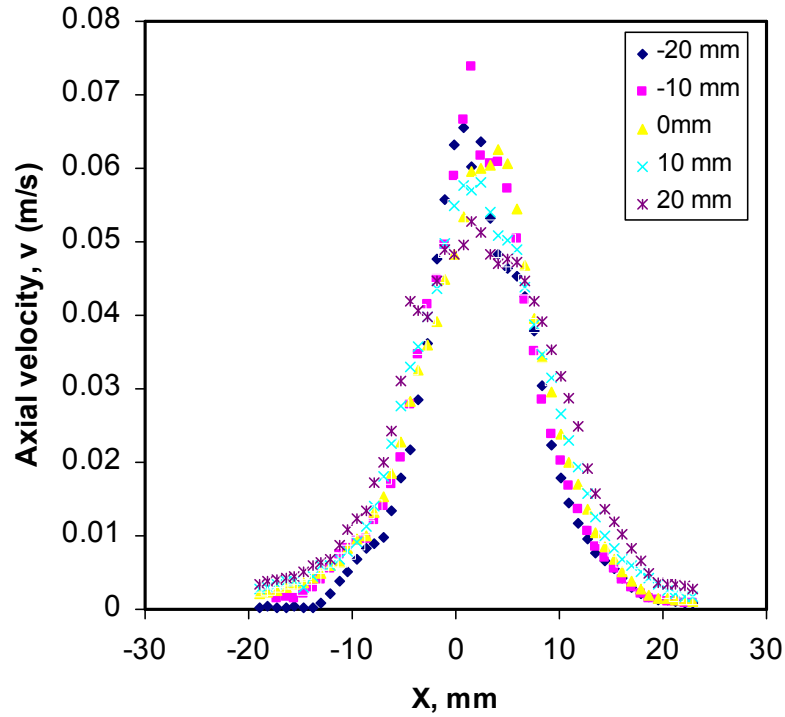


Figure 4.14 Velocity profiles obtained from PIV for bubbles rising in chain for air flow rate of $500 \text{ mm}^3/\text{s}$ for different axial locations

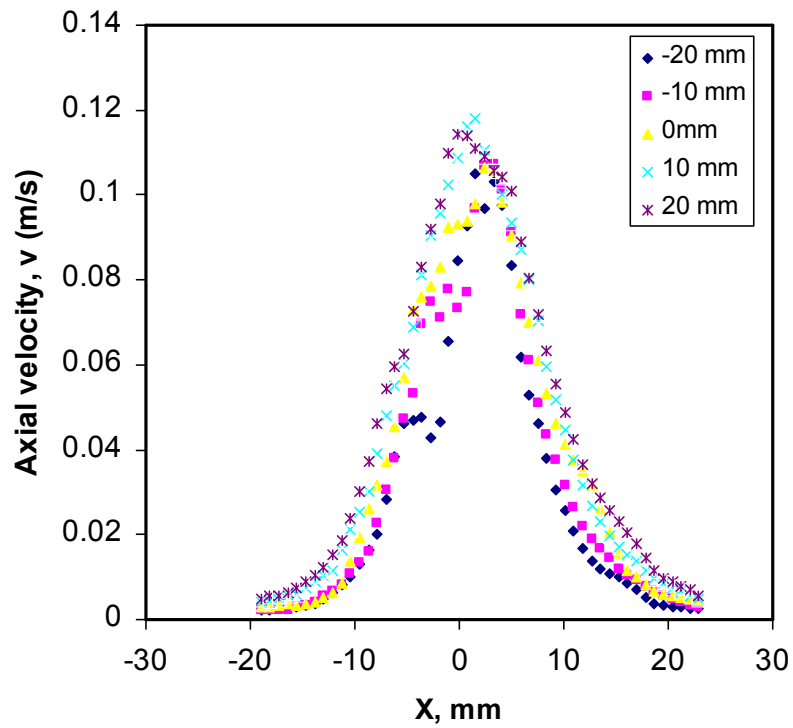


Figure 4.15 Velocity profiles obtained from PIV for bubbles rising in chain for air flow rate of $1667 \text{ mm}^3/\text{s}$ for different axial locations

DEVELOPMENT OF EXPERIMENTAL TECHNIQUES AND CFD SIMULATIONS OF MULTIPHASE DISPERSIONS

The centerline velocity was found to be 0.055 m/s for 500 mm³/s and 0.11 m/s for 1667 mm³/s air flow. These values of the liquid rise velocity should be subtracted from the bubble rise velocity in chains in order to get an approximation of individual bubble rise velocity. For these two cases, it works out to be 259 mm/s and 276 mm/s respectively. Both of these values are higher than the velocity corresponding to clean bubble correlation of Clift et al. (1978) which corresponds to 240 mm/s. Thus, it can be observed that the bubbles rising in chains experience effectively lower drag force than single bubbles, even after compensating for the liquid rise velocity. To clearly understand the phenomena, PIV data at finer resolution and more rigorous data analysis needs to be employed to clearly describe flow field surrounding individual bubbles in swarms.

4.6. Conclusions

The study of the bubble rise velocity modification by the free stream turbulence and surfactant concentration has been carried out using an advanced PIV/Shadowgraphy system. The experiments have been carried out for the case of single bubbles as well as bubbles rising in chains in grid generated turbulence. The data on rise characteristics of the bubbles along with liquid flow pattern have been reported for the first time for the bubbles rising in surfactant solution in presence of controlled turbulence.

The results indicated that the settling velocity generally reduces with increase in surfactant concentration and the turbulence intensity. The rise velocity shows a maximum with respect to turbulence intensity at lower MIBC concentrations while it shows a sustained increase with respect to turbulence intensity in case of higher MIBC concentration. However, the positive effect of grid frequency on rise velocity is smaller compared to the negative effect of the increased surfactant concentration, and in general the rise velocity at

DEVELOPMENT OF EXPERIMENTAL TECHNIQUES AND CFD SIMULATIONS OF MULTIPHASE DISPERSIONS

all turbulence intensities is lower for higher MIBC concentration. The rise velocity increased with bubble frequency. The effect of rise velocity reduction by increase in turbulent intensity and the surfactant concentration were more pronounced at higher bubble frequencies.

The details of bubble shape oscillations obtained from image processing reveal that the increased surfactant concentration increases the rigidity of the interface, hence causing the reduction in eccentricity of the ellipsoid as well as the reduction in the wobbling of the interface. The complex behavior of reduction and enhancement of the bubble rise velocity with respect to surfactant concentration, turbulence intensity and the bubble frequency require further study with finer spatial and temporal resolution of flow field around the bubble along with advanced image processing to characterize the interface characteristics of the bubble.

Notations

d	Bubble diameter, (m)
u_0	RMS velocity, ($\text{m}\cdot\text{s}^{-1}$)
C_A	Virtual mass coefficient, (-)
C_D	Drag coefficient, (-)
L	Integral length scale of turbulence, (m)
St	Stokes number, (-)
T_L	Integral time scale of turbulence, (s)
U_T	Terminal settling velocity of particle, ($\text{m}\cdot\text{s}^{-1}$)

DEVELOPMENT OF EXPERIMENTAL TECHNIQUES AND CFD SIMULATIONS OF MULTIPHASE DISPERSIONS

Greek symbols

ρ_p Density of particle, (kg.m⁻³)

ρ Density of Liquid, (kg.m⁻³)

τ_p Particle relaxation time, (s)

References

- Aliseda, A., Cartellier, A., Hainaux, F. and Lasheras, J. C., 2002. Effect of preferential concentration on the settling velocity of heavy particles in homogeneous isotropic turbulence, *J. Fluid Mech.*, 468, 77-105.
- Bel F'dhila, R. and Simonin, O., 1992. Eulerian prediction of turbulent bubbly flow downstream of a sudden pipe expansion, in: *Proceedings of Sixth Workshops on Two-Phase Flow Prediction*, Erlangen, Germany, 264–273.
- Bunner, B. and Tryggvason, G., 2002. Dynamics of homogeneous bubbly flows - Part 2. Velocity fluctuations. *J. Fluid Mech.*, 466, 53-84.
- Clift, R., Grace, J.R. and Weber, M. E., 1978. *Bubbles, drops and particles* New York: Academic Press.
- De Silva, I.P.D. and Fernando, H.J.S., 1994. Oscillating grids as a source of nearly isotropic turbulence. *Phys. Fluids*, 6 (7), 2455–2464.
- Doroodchi, E., Evans, G.M., Schwarz, M.P., Lane, G.L., Shah, N. and Nguyen, A., 2008. Influence of turbulence intensity on particle drag coefficients. *Chem. Eng. J.*, 135, 129–134.
- Friedman, P. D. and Katz, J., 2002. Mean rise rate of droplets in isotropic turbulence. *Phys. Fluids*, 14 (9), 3059-3073.
- Fung, J. C. H., 1998. Effect of nonlinear drag on the settling velocity of particles in homogeneous isotropic turbulence, *J. Geo. Res.*, 103 (C12), 27905-27917.
- Kubie, J., 1980. Settling Velocity of Droplets in Turbulent Flows. *Chem. Eng. Sci.*, 35, 1787-1793.
- Lane, G., 2005. *Computational Modelling of Gas-Liquid Flow in Stirred Tanks*. PhD Thesis, University of Newcastle, Australia.
- Liao, Y., Wang, J., Nunge, R.J. and McLaughlin, J.B., 2004. Comments on “Bubble motion in aqueous surfactant solutions”, *J. Coll. and Int. Sci.*, 272, 498–501.
- Maxey, M. R., Chang, E. J. and Wang, L. P., 1996. Interactions of Particles and Microbubbles with Turbulence. *Exp. Therm. Fluid Sci.*, 12, pp. 417-425.
- Mazzitelli, I. M., Lohse, D. and Toschi, F., 2003. The effect of microbubbles on developed turbulence. *Phys. Fluids*, 15 (1), pp. L5-L8.

DEVELOPMENT OF EXPERIMENTAL TECHNIQUES AND CFD SIMULATIONS OF MULTIPHASE DISPERSIONS

- Panidis, T. and Papailiou, D. D., 2002. Water air bubble grid turbulence. *Chem. Eng. and Tech.*, 25(4), 455-458.
- Poorte, R. E. G. and Biesheuvel, A., 2002. Experiments on the motion of gas bubbles in turbulence generated by an active grid. *J. Fluid Mech.*, Vol 461, 127-154.
- Risso, F., 1999. Experimental investigation of the motion of a bubble in a gradient of turbulence. *Phys. Fluids*, 11(11), 3567-3569.
- Saito, T., Sakakibara, K., Miyamoto, Y. and Yamada, M., 2008. A study of surfactant effects on the liquid-phase motion around a zigzagging-ascent bubble using a recursive cross-correlation PIV. Article In Press, *Chem. Eng. J.*, doi:10.1016/j.cej.2008.07.021
- Sathe, M. J.; Thaker, I. H.; Strand, T. E.; Joshi, J. B., 2008. An advanced PIV/LIF and shadowgraphy system to visualize flow structure in two-phase bubbly flows. 4th Int. Symp. on Appl. Laser Techniques to Fluid Mechanics, July 07 – 10, Lisbon, Portugal.
- Sharifullin, V. N. and Luebbert, A., 2001. Adsorption Processes and the Velocity of a Bubble Rising in the Presence of Surfactants. *Theoretical Foundations of Chemical Engineering*, 35 (4), 357–360.
- Shy, S.S., Tang, C.Y. and Fann, S.Y., 1997. A nearly isotropic turbulence generated by a pair of vibrating grids. *Exp. Therm. Fluid Sci.*, 14, 251–262.
- Spelt, P. D. M. and Biesheuvel, A., 1997. On the motion of gas bubbles in homogeneous isotropic turbulence. *J. Fluid Mech.*, 336, pp. 221-244.
- Yang, T.S., and Shy, S.S., 2003. The settling velocity of heavy particles in an aqueous near-isotropic turbulence. *Phys. Fluids*, 15 (4), 868–880.
- Zellouf, Y., Dupont, P., Peerhossaini, H., 2005. Heat and mass fluxes across density interfaces in a grid-generated turbulence. *Int. J. Heat Mass Transfer*, 48, 3722–3735.

Chapter 5

CHARACTERIZATION OF TURBULENCE IN HOMOGENEOUS AND HETEROGENEOUS DISPERSED FLOWS

5.1. Introduction

The characterization of turbulence in dispersed flows is of utmost practical and theoretical interest. It bears its characteristic similarities and differences from the grid generated turbulence, which has been the most explored type of the turbulent flows. The decaying turbulence behind the grid is fairly isotropic, stationary and is nearly homogeneous upto a certain distance in the flow direction. The particle generated turbulence and grid generated turbulence bear the similarity of the nature of turbulence generation- both are generated by the array of turbulence generating elements. The interaction between vortices develops the so called 'true turbulent' flow. The turbulence generated by the swarm of bubbles is called as 'pseudo turbulence' on the contrary. Primary reason for this treatment is the nature of generation of the turbulent kinetic energy by the sinuous movements of the bubbles. However, the description of turbulence based on sinuous motion is not general for all bubbly dispersions. In addition, no such description is used for the turbulence in the swarm of solid particles, or fluidized bed (as it is generally referred). One can expect the physical similarity in the flow field in the close vicinity of the grid of bars and grid of particles. It is interesting to note that active grids, in which the regular elements of the grid have random motion have afforded to generate better quality of isotropy than passive grids; and hence this further strengthens the ground for considering the turbulence generated by the active grid and the array of randomly moving solid particles (or spherical bubbles) on the same platform of regular turbulence generators. There is, however a complete different treatment given to each of these cases in the literature. In the current work, we try to investigate the turbulence generated by the bubbles and particles, both inside the dispersion as well as in the region where the liquid exits the bed. In addition, we examine the characteristics of the turbulence in both the types of dispersed flows: homogeneous and heterogeneous. For

this purpose, we have used experimental techniques like PIV, shadowgraphy and refractive index matching.

5.1.1. Characterization of Turbulence of Interest to Present Work

The term ‘turbulence’ has been used to describe the pseudorandom, highly energetic state of flow. So far the turbulence generated through different sources has been named with the source, like the grid turbulence, wake turbulence, etc. One important subset of this wide variety is the particle or bubble generated turbulence. The bubbles/particles moving with a relative velocity in the fluids may cause high local velocity gradients, which then combine in case of multiple particles and result into an overall turbulent motion. This flow resembles in many respect to fully developed turbulence like grid generated turbulence. The local, instantaneous velocity and scalar values are difficult to predict. However, their statistics are well conserved. In order to characterize the turbulence, it is important to have clear description of the parameters that cause the generation of turbulent kinetic energy. The bubbles and particles are nearly similar except the bubble interface is deformable, and the full slip boundary condition exists at the clean gas-liquid interface while there is no slip condition at the solid-liquid interface. However, the general descriptors for both the particles and bubbles is expected to be the same. The major descriptors are the bubble/particle size, the Reynolds number based on slip, the Weber number and Eotvos number. This description is sufficient to describe the motion of single particle/bubble in quiescent liquid. In the case where large number of particles are present, the information of local void fraction and the void fraction variation throughout the cross section of vessel is important. When the void fraction is constant across the entire vessel, the flow is homogeneous while the nonuniform void fraction marks the heterogeneity of the flow. During both the flow regimes of the dispersed

flows, the net velocity of the continuous phase (termed ‘superficial velocity’) as well as the local, instantaneous velocity are of interest.

The major descriptors of turbulence which are of interest to current work are described below.

5.1.2. Profiles of Dispersed Phase Hold-up, Continuous Phase Velocity and Turbulent Kinetic Energy

As mentioned earlier, the structure of two phase flow is largely governed by the distribution of the dispersed phase hold-up along the cross section of the vessel. The available literature on turbulence in bubbly flows is mostly concentrated with the homogeneous regime where dispersed phase hold-up is uniform over the cross section. However, in the homogeneous regime of operation also the bubbles are observed to form horizontal and/or vertical clusters. Several experimental and numerical studies are available on this subject (Zenit et al., 2001; Cartellier and Reviere, 2001; Risso and Ellingson, 2002; Esmaeeli and Tryggvasan, 2005; Martenez-Mercado et al., 2010).

Hydrodynamic interaction between the two phases and the particle inertia, under certain conditions, are observed to generate inhomogeneous distribution of both particles and bubbles. Assuming potential flow, rising bubbles form horizontally aligned rafts. The deformability effect also plays a crucial role in determining the orientation of the clustering. Esmaeeli and Tryggvasan (2005) carried out DNS simulations for both the spherical non-deformable bubbles ($N=216$, $Re=12-30$, $\epsilon_G = 0.24$ and $We=1$) and deformable bubbles ($N=27$, $Re=26$, $\epsilon_G = 0.06$ and $We=3.7$). Spherical pairs of bubbles probably aligned horizontally, whereas, the non-spherical bubbles align in the vertical orientation. For deformable bubbles, weak vertical clustering was observed. The reason for this phenomenon was mentioned to be that the larger Re (100) enhances the wobbling motion of bubbles, producing perturbations which do not allow bubbles to align

vertically and promotes breakup of any probable clusters. Zenit et al (2001) observed mild horizontal clustering for bubbles with $Re > 100$. Cartellier and Reviere (2001) observed moderate horizontal accumulation for bubbles with Re of $O(10)$. Higher probability of the pair density in horizontal plane, and reduced bubble density behind the wake of a test bubble was observed. Risso and Ellingson (2002) experimented with bubble Re $O(800)$. They did not find clustering. For hold-up less than 0.0105, they found weak influence of hydrodynamic interaction between bubbles.

5.1.3. Particle/Bubble Slip Velocity as a Function of Void Fraction

The description of high-Reynolds-number bubbly flow involves the dynamics of both the bubbles and the liquid. The mean bubble rise velocity is an important indication of the influence of turbulence on bubble rise characteristics. The mean bubble rise velocity in homogeneous regime is generally found to decrease with an increase in the bubble concentration (ϵ_G) whereas the normalized vertical fluctuation $V_{z,rms}/V_z$ increases (Davidson and Harrison 1966; Lance and Bataille 1991; Zenit et al. 2001; Panidis and Papailiou 2002; Poorte and Biesheuvel 2002; Risso and Ellingsen 2002; Bunner and Tryggvason 2003; Martinez-Mercado, Palacios-Morales and Zenit 2007). . The hindrance mechanism require a very small volume fraction (<0.1 %) to develop. Roig and Larue de Torunemine (2007) showed that potential flow theory is sufficient to predict bubble rise velocity for $\epsilon < 0.02$. The liquid flux entrained in the wake becomes predominant for larger ϵ ($\epsilon > 0.1$). Garnier et al. (2002) observed that $\langle V \rangle$ scaled as $\epsilon^{1/3}$. Risso and ellingson (2002) found that the bubble agitation was similar to that of a single rising bubble for $0.005 < \epsilon < 0.01$. It was thus driven by vortex shedding that occurred in the wake.

However the mean bubble rise velocity has been reported to increase for large bubbles in case of heterogeneous flow regimes (Griffith and Walis 1961; Davidson and

Harrison 1966; Zahradnik et al 1997; Thakre and Joshi, 1999) The general interpretation for decrease in the rise velocity in homogeneous regime is the enhanced rate of momentum transfer with an increase in the intensity of the liquid turbulence. In heterogeneous regime, the bulk liquid motion modifies the bubble rise velocity with respect to the external observer. Since the bubble concentration is higher in the central core region where the bulk motion is upwards, the net effect of bubble and liquid motion results into an increase in the bubble rise velocity with respect to external observer.

The quality of turbulence in the homogeneous bubble column has been experimentally investigated by Zenit, Koch and Sangani (2001), Risso and Ellingsen (2002) and Martinez-Mercado, Palacios-Morales and Zenit (2007) and using DNS simulations by Bunner and Tryggvason (2002,2003) and Esmaeeli and Tryggvason (2005). There is no general model for decrease in mean rise velocity of bubbles with increase in gas void fraction. Martinez-Mercado et al. (2007) suggest that it is likely to depend on both the Re (Flow regime) and We (Bubble shape).

It has been observed that a very small increase of volume fraction than zero results in noticeable decrease in mean bubble rise velocity.

5.1.4. Statistics of Dispersed Phase Slip Velocity and Continuous Phase Velocity: Bubble Rise Velocity Fluctuations

PDF of bubble velocities in pseudo turbulence were also measured by Zenit et al (2001) and Martinez-Mercado (2007). The later authors, showed that the variance of the bubble velocity remained almost constant for bubble volume fractions of at least 0.1. Thus, the bubble agitation depends neither on the bubble rise velocity nor on the liquid dynamics, which both depend on ϵ . Risso and Ellingson (2002) showed that the liquid velocity functions normalized by $V_0 \epsilon^{0.4}$ are similar.

Panidis and Papailiou (2002) also looked at turbulence intensity measurements with a view to ascertaining whether the turbulence isotropy remains in the system. It was found that the longitudinal turbulence intensity component generally increased more markedly than the transverse components for similar reasons as outlined above. Therefore the presence of bubbles destroys the isotropy of turbulence for this system.

For non-deformable bubbles (Bunner and Tryggvason 2002b), the PDFs of velocity fluctuations have a Gaussian distribution. If deformability is considered (Bunner and Tryggvason 2003), the PDF of only one horizontal component of the velocity keeps a Gaussian shape while the non-Gaussianity in the PDFs was stronger at the lowest concentration $\alpha = 2\%$, recovering a Gaussian distribution for $\alpha = 6\%$. However in that numerical work only a limited number of bubbles ($N_b = 27$) could be considered and the different behavior in the two different horizontal directions reflects the lack of statistical convergence. Experimental PDFs of bubble velocities in pseudo-turbulence have been obtained by Zenit et al. (2001) and by Martinez-Mercado et al. (2007).

5.1.5. Wake Attenuation and Wake Interactions

At vanishing Re , the Stokes solution shows that the velocity disturbance decays as r^{-1} where r is the distance from the bubble. Calfish and Luke (1985) concluded that the summation of the flow disturbances generated by homogeneously distributed swarm of bubbles leads to divergence of variance of the fluctuations with the size of container. Parthasarathy and Faeth (1990) concluded that the linear summation of all individual bubble contributions also leads to the divergence of variance.

Koch (1993) proposed a screening mechanism for $1 < Re < 100$ due to deficit of particles in the wake of a test particle. It causes the disappearance of the wake disturbance at a distance that depends on the ϵ and scales as $d\epsilon^{-1}$.

Cartellier and Riviere (2001) experimentally observed wake attenuation for the deficit of particles in the wake of a test particle for $Re \sim O(10)$. Hunt and Eames (2002) showed that sequence of positive and negative strains cause diffusion and cancellation of vorticity leading to wake attenuation. Thus, at large Re , a non-uniform distribution of bubbles is not required to observe wake attenuation.

Exponential wake attenuation with a length scale proportional to $dC_D^{-1}\epsilon^{-1}$ was observed. It shows that mixing of vorticity components of opposite signs belonging to neighbor wakes can make themselves disappear rapidly. Risso et al. (2008) experimentally observed an exponential attenuation in bubbly flows for Re of several hundreds. Exponential wake attenuation with a length scale independent on ϵ_G was observed for $0.01 \leq \epsilon \leq 0.14$.

Variation of the longitudinal turbulent intensity as a function of void fraction shows the existence of the two turbulent flow regimes. The regime transition depends on the hydrodynamics interaction between the bubbles. At low void fractions, the turbulent kinetic energy is approx. sum of the turbulent kinetic energy in absence of bubbles and the pseudo turbulent contribution.

5.1.6. Spectral Slope for Continuous Phase Energy Spectrum in Inertial and Near Dissipation Subrange

In bubbly flows, one must distinguish between the energy input due to the bubbles and the energy input due to some external mechanism: both of them can be important, however, likely to provide different mechanism for turbulence generation. The characteristic features of the turbulence generated by different mechanisms may be different. For instance, one important feature of the liquid agitation is the spectral distribution of the turbulent energy with the wavenumber k . Lance and Bataille (1991) suggested the ratio of the bubble-induced kinetic energy and the kinetic energy of the

flow without bubbles as an appropriate dimensionless number to characterize the type of the bubbly flow. Rensen, Luther and Lohse (2005) called this ratio the bubble parameter b , defined as

$$b = \frac{1}{2} \frac{\alpha U_r^2}{u_0'^2}, \quad (5.1)$$

where ϵ_G is already defined, U_r is the bubble rise velocity in still water and u_0' is the typical turbulent vertical fluctuation in the absence of bubbles. Lance and Bataille (1991) measured the liquid phase power spectrum in bubbly turbulence and observed a gradual change of the slope with increasing void fraction. At low concentrations the slope of the spectrum was close to the Kolmogorov value of $-5/3$. By increasing ϵ_G , the principal driving mechanism changed – the turbulence generation from bubbles now becomes dominant compared to the bulk turbulence originally present in the flow. Under these conditions, the slope was close to $-8/3$. Having in mind eq. 5.1 one may expect different scaling behaviour, depending on the nature of the energy input that is dominant, namely $b < 1$ for dominant turbulent fluctuations or $b > 1$ for dominant bubble-induced fluctuations.

Indeed from Table 1 of Rensen et al. (2005) one may draw the conclusion that the slope is around $-5/3$ for $b < 1$ and around $-8/3$ for $b > 1$. Also Riboux et al. (2010) obtained a spectral slope of about -3 in the wake of a swarm of rising bubbles in still water ($b = \infty$). Moreover, in numerical simulations Sugiyama et al. (2001) obtained spectral slope of -3 for the velocity fluctuations caused by up to 800 rising light particles, i.e. $b = \infty$, with finite diameter ($Re \approx 30$). However, there are also counter-examples, e.g. Mudde et al., (1997) and Cui and Fan (2004) obtained a slope of around $-5/3$, though $b = \infty$. Therefore, in this paper we want to re-examine the issue of the spectral slope in pseudo-turbulence ($b = \infty$).

The comparison between the different works is not straight forward for two reasons. The first reason is that the spectra are generally computed from signals which are interpolated during the intervals when bubbles are present at the measuring point; the exponent of the spectra may therefore depend on the interpolation method that is used. The second reason arises from the fact that the shear-induced turbulence is in most cases also present; it can be generated at the wall, such as in pipe flows, or due to large mean velocity gradients when the gas distribution is inhomogeneous, such as in unstable bubble columns. Larue de Tournemine (2001) also obtained a spectrum evolving as k^{-3} . It seems therefore likely that bubble-induced turbulence generates a spectral range in k^{-n} , with an exponent n close to 3. However, the wavelength at which this range starts and stops is still not clear. Generally speaking, we can say that a satisfactory description of the bubble-induced turbulence requires the knowledge of the characteristic scales of the various spectrum ranges.

Currently there is no universal agreement in the literature on the slope of the energy spectrum for bubbly two-phase flows. A detailed review on the topic is presented in Bolotnov et al. (2008). Quite a few experiments and DNSs report a slope of $-5/3$, or one “slightly less steep than $-5/3$ ” (Rensen et al., 2005), while others have found different slopes. To properly analyze the slopes of the energy spectrum one must be careful to look at the same range and the same system of coordinates when comparing these slopes. Generally, we may have two separate slopes in the energy spectrum; one slope in the inertial subrange and a steeper slope before the dissipation range. For example, Lance and Bataille (1991) report a $-5/3$ slope for the inertial subrange of turbulent single-phase flow and $-8/3$ for their corresponding bubbly two-phase flow experiments.

However, a careful analysis of their two-phase spectrum that Lance and Bataille (1991) actually had a slope between $-8/3$ and $-11/3$ in the high wave number dissipation range and a $-7/6$ slope in the inertial subrange of the corresponding single phase flow. Since $-7/6$ is slightly less steep than $-5/3$, their results are in substantial agreement with the data of Rensen et al. (2005). Bunner and Tryggvason (2003) performed a 3-D DNS of 27 deformable bubbles rising in a periodic domain. They analyzed the induced turbulent kinetic energy spectrum in the liquid phase and found a -3.6 slope in the dissipation region. This slope is very close to a $-11/3$ slope (i.e., -3.67) which, as noted above, can also be seen in the data of Lance and Bataille (1991).

Besides, while comparing the different spectra on single platform we should keep in mind that the flow patterns are completely different for these cases. Lance and Bataille (1991) use a co-current flow of bubbles and liquid. Rensen et al. (2005) used a counter-current flow of liquid to the upward rising bubbles. Riboux et al. (2009) performed experiments in the bubble column where the liquid was in batch mode. Martinez-Mercado et al. (2010) injected bubbles inside a water tunnel, with no liquid flow (effectively proving to be a bubble column). It should be noted that all these flows correspond to the homogeneous regime of operation. The works of Mudde et al. (1997) and Cui and Fan (2004) used the bubble column with liquid in batch mode and in heterogeneous flow regime.

The above discussion applies to the slope of the spectrum in inertial and dissipation subrange. Typically, it has been observed in the current work that the integral turbulent kinetic energy in these subranges is 20 % of the total turbulent kinetic energy of the liquid. While, 80 % of the energy is contained in scales larger than the bubble size. None of the published work looks at the details of large scale structures, their

characteristics and the role of the low frequency, high energy structures while characterizing the turbulence in dispersed flows.

5.2. Experiments and Methods

5.2.1. Fluidized Bed and Bubble Column

A laboratory scale fluidized bed has been used to obtain the homogeneous dispersed flow. The schematic setup is presented in Figure 5.1A. The fluidized bed is the square channel with cross section of $30 \times 30 \text{ mm}^2$, having length of 300 mm. The fluidized bed is made of float glass plates having thickness 5 mm to ensure maximum transparency and stability to high intensity of laser. A distributor plate with holes of 2 mm diameter at the square pitch of 5 mm was used at the bottom of fluidized bed as liquid inlet. A diffuser bed of 6 mm diameter soda-lime glass spheres was used as the calming section prior to the distributor in order to ensure uniform liquid dispersion throughout the cross section. Borosilicate spheres with mean diameter of $3 \pm 0.03 \text{ mm}$ have been used as fluidized particles. Sodium Iodide solution with refractive index=1.465 was used as the fluidization liquid, which matches the refractive index of the borosilicate glass hence the liquid-solid dispersion becomes optically homogeneous. Thus, the PIV measurements were possible inside the fluidized bed. The particle Reynolds number, Re_p is 320.

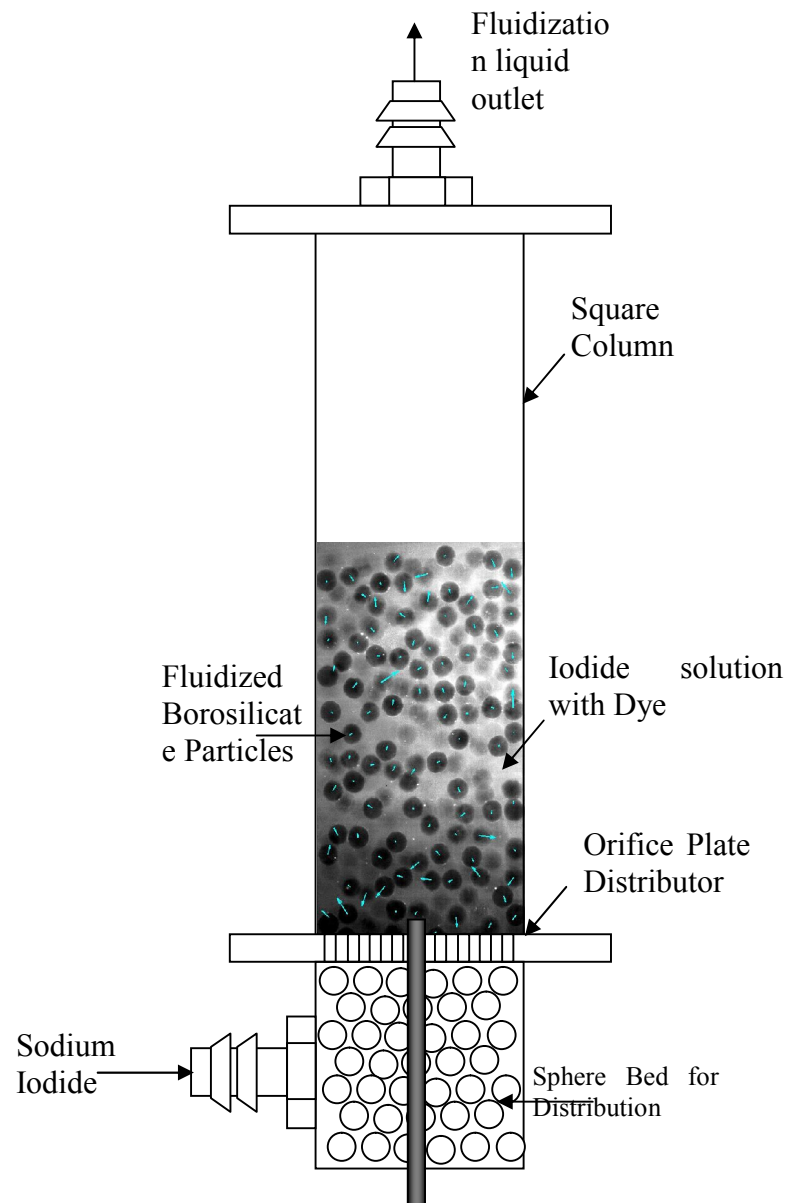


Figure 5.1A Schematic of Experimental set-up for Refractive index matched PIV/LIF measurement in square fluidized bed

The refractive index match of the liquid with borosilicate particles was optimized by watching the spread of the laser beam passing through the particle bed through which the solution was flowing. The spread of the laser beam was minimized to ensure the best possible refractive index match. Due care was taken by filtering and degassing the sodium iodide solution to ensure the clarity of the solution. The sodium iodide solution is highly hygroscopic. Hence, due care was taken during the experiment to ensure the RI match by checking the dispersion of the laser beam through the bed.

A fluorescent dye, Rhodamine B was added to the sodium iodide solution for the visualization of the glass particles. Under planer illumination of Nd:Yag laser, the dye emits fluorescent light in the range of 570 nm, while the particle cross sections appear as dark circles. Fluorescent tracer particles of Styrene-DVB of 8 μm mean diameter, containing same dye (Rhodamine B) were used for particle image velocimetry. The concentration of the dye in liquid was kept to an optimum value between the lowest concentration required for good detection of the spherical glass particles and the highest concentration which will mask the fluorescent tracer particles. Hence, single PIV camera was able to capture the motion of fluidized particles and the tracer particles. An image processing routine was applied to isolate the regions of the fluidized particles from the PIV image by using the intensity criteria, while standard PIV routine was applied on the remainder of the image pair to get the liquid velocity field in the interstices between the particles.

The superficial liquid velocity–voidage relationship of this bed in the operating regime was confirmed to follow the behavior predicted by Richardson-Zaki correlation, hence the homogeneous operation of fluidized bed was ensured. The superficial liquid velocity was varied form 6.1 mm/s to 51.7 mm/s, where fractional liquid hold-up varied from 0.42 to 0.76.

The bubble column set-up is depicted in Figure 5.1B. The test section is a plexiglass rectangular bubble column of 1000mm height with a cross-section of 200 mm width and 15 mm depth. Since it is very difficult to get optical access to the measurement plane to acquiring the bubble images at higher void fractions, a narrow depth of column was used to facilitate imaging at relatively high void fractions compared to the earlier works. It should be noted that, the column depth is thrice the mean bubble diameter observed in cylindrical column for the desired superficial gas velocity, hence the flow in the column is essentially different from the 2D flow like hele shaw cell. Owing to very less depth of the column the flow pattern is expected to be different than cylindrical column; however the characteristics of heterogeneous bubbly flow like the formation of plume and plume oscillations are retained.

The column operated with liquid in batch mode, with tap water being the continuous phase. Filtered air was injected form bottom with an oil free diaphragm compressor. At lowest gas flow rates, the bubbles rise in trains. Upon increasing the flow, the trains become unstable. With a further increase in the gas flow rate the large-scale liquid circulation starts owing to the instability of flow. This heterogeneous regime of operation is of principle interest to this work.

In order to examine the effect of sparger during the heterogeneous operation, different spargers were employed. Three spargers were used, with single capillary, three capillary and five capillaries each. SS capillaries having ID of 0.8 mm were employed to inject the gas. The capillaries were positioned equidistant in all the three cases. The distance between needles was 50 mm for the 3 capillary sparger while it was 33 mm for 5 capillary sparger. The single capillary was placed at the center of the column. The gas flow rate was varied from 0-60 ml/s corresponding to the maximum superficial gas velocity of 20 mm/s. The overall gas volume fraction($\bar{\alpha}$) corresponding to the superficial

gas velocity of 20 mm/s was found to be 0.0475, while the local gas volume fraction $\bar{\alpha}$ varied up to 0.1.

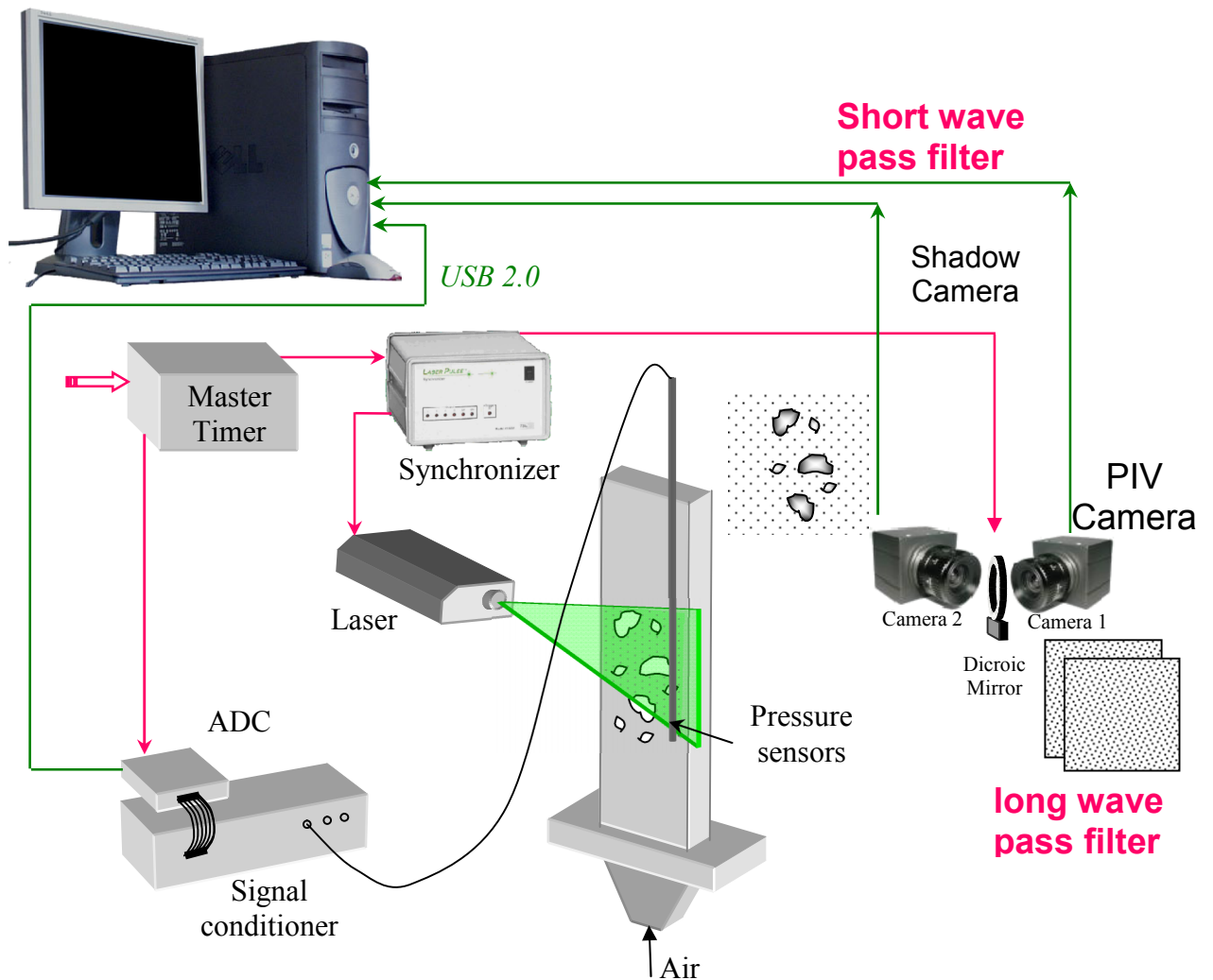


Figure 5.1B. Schematic of Experimental set-up for pressure sensor, PIV/LIF and shadowgraphy measurement in rectangular bubble column

A soap film meter was used to measure the gas flow rate. Since the void fraction varies from centerline of the column to wall, a modified Pitot tube probe was used to measure local void fraction. The local void fraction was calculated in similar way to the manometric technique reported in earlier work (Rensen et al. 2005). However, instead of manometer a miniature absolute pressure sensor has been used. The manometric technique gives the cross sectional averaged hold-up. Using the two point static pressure

probe, local static pressure at two different heights at the required lateral location was measured. The local gas hold-up was calculated using this static pressure difference.

Since the column is operating in the heterogeneous regime, a wide bubble size distribution is observed. The bubble size immediately after release from sparger was found to have a monomodal distribution with mean bubble size of 5 ± 1 mm. The observed polydispersity of bubbles at sparger is contributed by the fact that the developed circulation in the column affects the bubble generation by altering the flow of liquid down to vicinity of the sparger. A wider bubble size distribution was observed in the column because of the coalescence and breakup of bubbles. The typical bubble sizes observed were between 0.9-22 mm. Because of the heterogeneity of the flow bubbles encounter different fluid velocities. The Reynolds number Re corresponding to the measured bubble rise velocity was 5-8240, the corresponding Weber number We was 0.000154-47.9 and the Eötvös number was 0.11-52.82. Thus, study of bubble column in heterogeneous mode has allowed us to explore a much wider range of Re , We and Eo compared to the studies of homogeneous bubbly flows. In Martínez Mercado et al. (2010), Re was of the order 100, the We was in the range 2–3 and the Eo was around 3–4, while in Riboux et al. (2009) the Re range was 540-760 and We range was 2.6-3.4.

5.2.2. Particle Image Velocimetry and Shadowgraphy

The experiments were performed with a modified commercial PIV system. A New wave dual head Nd:YAG laser with up to 120 mJ per pulse was used as the laser source to create the light sheet. A TSI Powerview 4MP camera with 2048×2048 pixels and 12-bit resolution were used for PIV to carry out liquid velocity measurements. A TSI synchronizer was used to control the overall timing of PIV system. Considering the low velocity of bubbles, the time difference between the capture of PIV image pair Δt was adjusted between 500-1000 μs . This range of Δt also ensured higher exposure time for

frame A of PIV image pair, yielding brighter particle image pair with lesser background noise of CCD.

For shadowgraphy measurements, a Photron Fastcam 10KC high speed camera was used along with a pulsed LED array as the backlight. The pulsed LED array consisted of 144 high-power diodes emitting blue light of wavelength 470 nm with a small viewing angle. A diffuser plate was used in front of the LED array. The LEDs were excited by pulses of 19 Volts of duration of $\sim 80 \mu\text{s}$. This increased the light emission from LEDs as well as ensured safety against burnout. The small flashing time of LEDs ensured that the moving bubbles are not blurred in the shadow image. The high speed camera recorded 2 images synchronized with PIV camera. The trigger pulse for LED array was supplied by PIV synchronizer, ensuring simultaneous measurement of PIV and shadow image pairs. The trigger pulse was used to fire the LED array in above mentioned voltage sequence using an in-house developed timing card. The high speed camera had a shutter speed of $1/1000 \text{ s}$. These camera and LED time settings enabled capturing the images with significant sharpness, which aided the image processing program to deduce the bubble velocity and shape more accurately.

The large number of LEDs used to form the backlight causes slight nonuniformity in the background intensity. Besides, the temperature of individual LED varies between the two frames because of heating effect of the exciting current. However, by carefully adjusting the exciting voltage it has been ensured that this intensity variation is taken care of by the dynamic histogram based threshold in the image processing algorithm. The shadow image sequence of the bubbles is subjected to image processing to get the bubble diameter, bubble centroid location and bubble shape.

5.2.3. Miniature Pressure Sensors

Kulite XTL-100 sensors were used to acquire pressure fluctuation signals (PFS). These are absolute pressure, piezoresistive pressure sensors with very small outline (cylindrical, with 2mm OD and 8mm length) with frequency response up to 150 kHz. The pressure sensors were mounted into a Pitot tube configuration. Three sensors were mounted to register the impact pressure and static pressure at the measurement location along with the static pressure at a known height difference from the measurement point. The details of probe construction are shown in Figure 5.2. The sensors were mounted in a copper tube with ID of 4 mm. The tube had been cut along the axis to form 4 slots of 0.5 mm width. These sensors were fixed to the inner wall of the tube with a silicon rubber sleeve. Another silicon rubber sleeve on the outside of the tubes covered most of the tube length to leave the small portion in front of the static pressure sensor open, forming static pressure tap. The gas hold-up was measured from the mixture density available from static pressure difference recorded by two static pressure taps. The mixture density was calculated from static pressure difference. The upward mixture velocity was estimated using the impact pressure, the static pressure and mixture density. The probe was traversed inside the column to obtain the liquid velocity and hold-up distribution. The radial pressure profiles were measured at 6 x/L values of 0, 0.1, 0.2, 0.4, 0.6, 0.8 and 0.95 in order to cover half the width of the column at given cross section. The measurements were carried out at the height of 50mm (H/D=0.25), 200mm (H/D=1), 400mm (H/D=2) from sparger, totaling 18 locations.

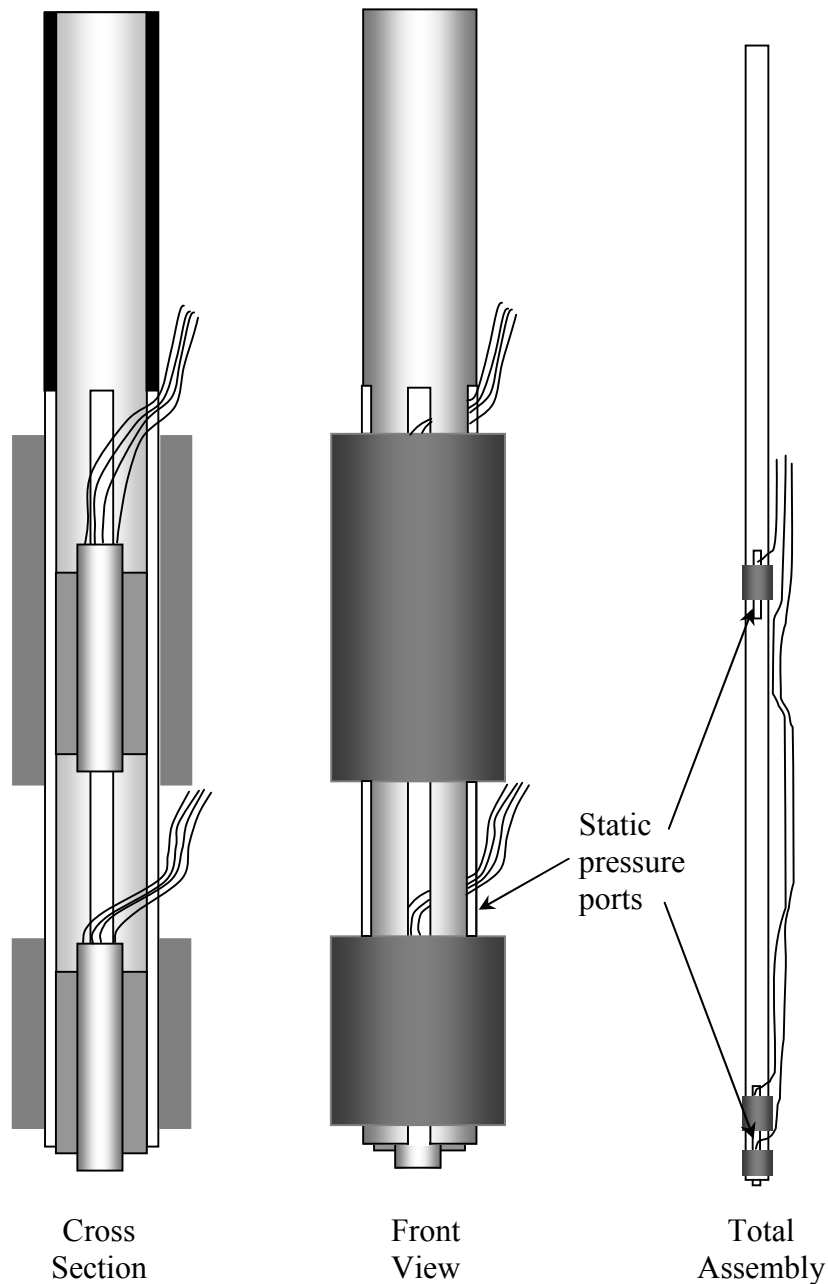


Figure 5.2. Details of 3 sensor pressure probe used for instantaneous velocity measurements in bubbly flows

The sensors were calibrated for absolute pressure in the column itself. The water level was incremented from 5mm to 500mm above the sensor level, with the increment of 20 mm in the column. This corresponds to the pressure increase of 4890 Pa. The voltage time series was recorded for the level range in order to have sufficient calibration

points in the available height of the column. Each individual sensor had its own gain and offset adjustment in a separate channel of signal conditioner. The gain and offset of each sensor was adjusted to give voltage swing of 4-7 voltage from minimum (5mm) to maximum (650 mm) head expected above the sensor. As can be anticipated, the instantaneous absolute pressure can go outside the calibration range (especially when negative pressures are encountered). However, this was taken care by the allowance provided on the lower and upper limits of the calibration voltage and the linear calibration curves obtained for all sensors.

5.3. Data Processing

5.3.1. Image Processing to Generate Bubble/Particle mask

The raw PIV images were processed using the image processing routines programmed in MATLAB R2009a. The calibration constants are obtained from the images of a calibration target placed in the focal plane of the square tank used for the experiments. The perspective corrected images are binarized to black and white using a threshold value. The threshold is calculated on the basis of intensity histogram of the grayscale image. This process takes care of the non-uniform background illumination. The bubbles appear in PIV images because of the leakage of very high intensity laser light from the long pass filter along with the reflected fluorescence light. The raw PIV image is applied with median filter to remove seeding particles and blurred using Gaussian filter of 5x5 pixel size. This filtered image is applied with a threshold to create a binary raw image.

The bubbles contain 'holes' in the binary image. These artifacts are primarily caused by the curvature of the bubble. These are removed using morphological image processing, which involves dilation operation on the image followed by erosion

operation. The negative of the ‘filled’ bubble image is used as a digital mask to blank the PIV images in these regions. The residual light passing through the filter assembly allows the bubble silhouette to be recorded as a blurred boundary in the seeding particle image. The regions corresponding to the bubbles are set to value ‘0’ to avoid spurious vectors caused by cross correlation between the reflections from bubble surface. Even after applying median filters and taking due care in applying the threshold values based on the image intensity histogram, certain artifacts from seeding particles and speckles remain in the form of small dots in images. These are removed by eroding and dilating the binary image 3-5 times depending on the requirements of the image.

The image processing to isolate particles from PLIF images is similar; except the step of taking negative of the raw PLIF image. In these images, the particles appear as dark patches on bright background. This is caused by the absence of the fluorescent dye inside the fluidized particles.

The ‘filled’ binary bubble/particle images are used as the mask image to generate the phase discrimination marker matrix, described in next subsection. The value of marker function within the detected particle/bubble is set to zero; while that outside the bubbles/particles (liquid region) is set to 1.

5.3.2. PDF of Liquid Velocity and Structure Functions

A phase discrimination marker matrix is obtained using image processing of PIV images. The marker function definition is similar to that used by Rensen et al. (2005), which is defined by:

$$\xi = \{\xi_{i,j}\}_{i=1,j=1}^{i=M,j=N} \quad (5.2)$$

Where $\xi_{i,j} = 1$ for fluid while $\xi_{i,j} = 0$ for bubble or particle; M and denote the number of rows and column in the 2D vector field.

For the calculation of PDFs, the elements with marker function values of zero were omitted from the number of points in particular velocity bin. The mean velocity can be calculated by:

$$\langle V \rangle = \frac{\sum_{i=1}^M \sum_{j=1}^N \xi_{i,j} v_{i,j}}{\sum_{i=1}^M \sum_{j=1}^N \xi_{i,j}} \quad (5.3)$$

Similarly, the RMS velocity is calculated by:

$$V^2 = \frac{\sum_{i=1}^M \sum_{j=1}^N \xi_{i,j} (v_{i,j} - \langle V \rangle)^2}{(\sum_{i=1}^M \sum_{j=1}^N \xi_{i,j})^2} \quad (5.4)$$

The pth-order longitudinal structure function of the velocity is

$$D_p(r_x) = \langle |v(x + r_x, t) - v(x, t)|^p \rangle \quad (5.5)$$

Where $v(x, t)$ is the local vertical water velocity at a point in space x at time t . Since PIV data is used, no use of Taylor's hypothesis is involved as in reported literature (Lance and Bataille, 1991; Rensen et al., 2005; Martinez Mercado et al., 2010). However, since this is no longer a point velocity time series, the structure functions were evaluated over a small region in space which was locally homogeneous (negligible variation of time averaged velocity over the spatial domain where structure functions are evaluated) and then averaged over time. The regions selected for fluidized bed and decaying fluidized bed were horizontal bands with small height width ratio, while the regions selected for bubble column were vertical bands with high height to width ratio. Such a selection was made by observing the time averaged velocity and turbulent stress profiles along height and width in respective geometries.

Using the notation of eq. 5.3 the structure function of a dispersed flow signal can be obtained by using the following equation:

$$D_P(r_x) = \frac{\sum_{x=0}^{x=L-r_x} \sum_{y=y_{min}}^{y=y_{min}} \xi_{x,y} \xi_{x+r_x,y} |v(x+r_x,t) - v(x,t)|^p}{\sum_{x=0}^{x=L-r_x} \sum_{y=y_{min}}^{y=y_{min}} \xi_{x,y} \xi_{x+r_x,y}} \quad (5.6)$$

The structure functions of second, third and fourth order are evaluated for fluidized bed, decay region above fluidized bed and bubble column with single and five point sparger. The extended Self similarity is the plot of fourth order structure function versus the compensated third order structure function. It has also been calculated for all the above geometries. The results are presented in section 5.4.

5.3.3. Evaluation of Energy Spectrum

Evaluation of turbulence energy spectrum in dispersed flows poses two main difficulties: The turbulence is heterogeneous and the presence of dispersed particles in the flow domain makes the space (or time) series of fluid velocity discontinuous. Many approaches to evaluate energy spectra in such circumstances have been described in recent literature. Riboux et al. (2009) constructed the spatial spectrum of the vertical velocity S_{zz} by means of a fast Fourier transform (FFT) for each vertical column of the two-dimensional PIV velocity field and then averaging over all the columns. Although this represents some form of spatial averaging and we lose the information regarding the heterogeneity of the turbulence; it has to be resorted to in order to evaluate the contribution of the large scale eddies. The largest eddy that can be evaluated using this technique is half the height of the measurement window, which corresponds to 25 mm in their case. However, Riboux et al. (2009) carried out PIV measurements only in the region behind the bubble swarm, and hence no bubbles appeared in PIV measurement window. Martínez Mercado et al. (2010) carried out PTV and hot wire anemometry in the presence of bubbles at low void fractions ($0.002 < \alpha < 0.022$). PTV measurements

were carried out to measure bubble velocities, while phase sensitive hot wire anemometry was used for liquid velocity measurement. They used an indicator function to mark the presence of bubbles. The energy spectrum was calculated using FFT of the liquid velocity series between two bubbles only. The spectra evaluated with many fragments were then averaged to get the energy spectrum for entire velocity time series. This approach limits the smallest frequency (largest length scale) to the inverse of half the time between two consecutive bubble passages. This may not create any problem for very small void fractions since the separation between the bubbles is large. However, at larger void fraction and in presence of small bubbles the number density of bubbles is very high and the corresponding separation between bubbles is small. Hence, very small fragments of time series are available making it biased towards high frequencies.

To overcome these difficulties, we have adopted a modified approach to evaluate the energy spectrum in presence of bubbles. The liquid velocity along the vertical lines of flow field from PIV is used to calculate the vertical component of energy spectrum. The raw PIV images are multiplied with a mask image which has value of zero in the regions of bubbles while 1 in presence of liquid. The mask image is evaluated from the shadow images captured simultaneously with PIV. The PIV and shadow images are captured at the same location and same time by ensuring synchronization between cameras and focusing them on the same planer calibration target. Using the masked raw images for PIV processing, the velocity in the regions corresponding to the dispersed phase is set to zero. The velocity vectors appearing in the boundary of bubbles are set to zero again by applying the mask to PIV vector field. Effectively, the liquid velocity is set to zero inside the bubbles. This is coherent with the physics in the way that the liquid is absent inside bubbles hence the magnitude of its velocity must be considered zero. Having isolated the liquid velocity vectors using this technique, the 2D array of liquid

velocity vectors is subjected to the FFT in the same way as Riboux et al. (2009) in order to calculate the energy spectrum. This is advantageous in the sense that the maximum eddy size evaluated still corresponds to half the measurement window height irrespective of the spacing between bubbles.

5.4. Results and Discussion

5.4.1. Turbulence Inside Fluidized Bed and In the Decay Region Downstream of Fluidized Bed

Figure 5.3 shows a PIV snapshot of liquid velocity field near the top section of the fluidized bed. The fluidized particles in the cross section of the measurement window are seen as the black circles. The array of jets and wakes is visible near the interface of the fluidized bed. It also shows three marked regions inside the fluidized bed, just above the interface of fluidized bed and 40 mm away from fluidized bed interface. The regions have size of 10 mm × 30 mm. The turbulence parameters are spatially averaged within this rectangular region to obtain profile of lateral variation of each turbulence parameter. The axial variation of each variable was found to be much less within each region.

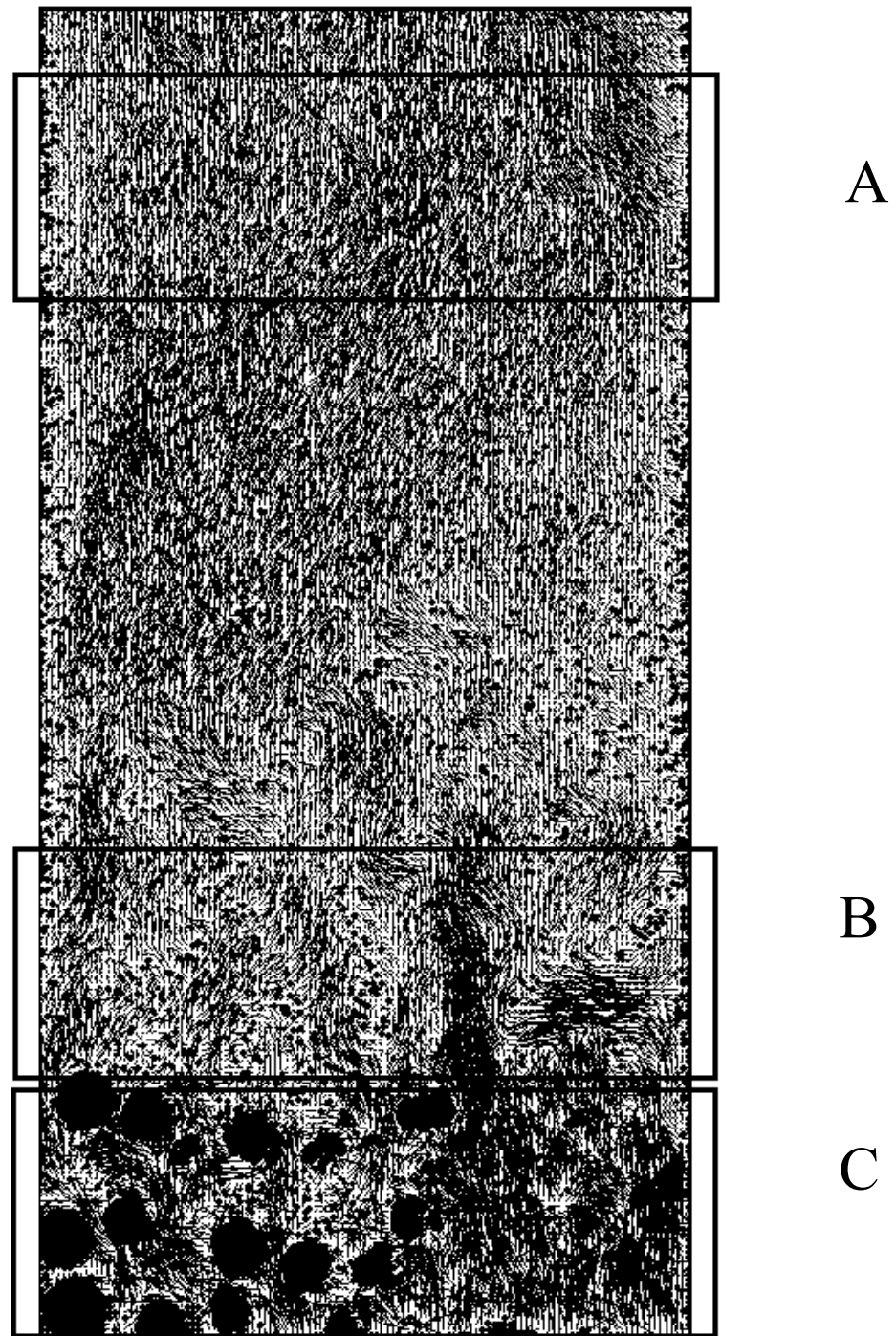


Figure 5.3. Instantaneous PIV snapshot of liquid velocity in fluidized bed, showing the regions of interest to evaluate the structure functions and ESS: (A) Far from the interface of the bed (B) Just above the interface of the bed (C) Inside the fluid bed

In order to establish the homogeneity of turbulence inside fluidized bed, the power spectrum of liquid velocity fluctuations has been calculated over 6 lateral bands having thickness of 5 mm each. Figure 5.4, 5.5 and 5.6 show these spectra for bed voidages of 0.42, 0.6 and 0.65 respectively. It can be observed that the variation of spectra with respect to the radial location is very less. The turbulent kinetic energy is successively higher for higher bed voidage, however the nature of the spectrum in terms of characteristic slope is the same for all three cases. A region having slope $-5/3$ is followed by a region of slope less steeper than $-5/3$, before the dissipation regime.

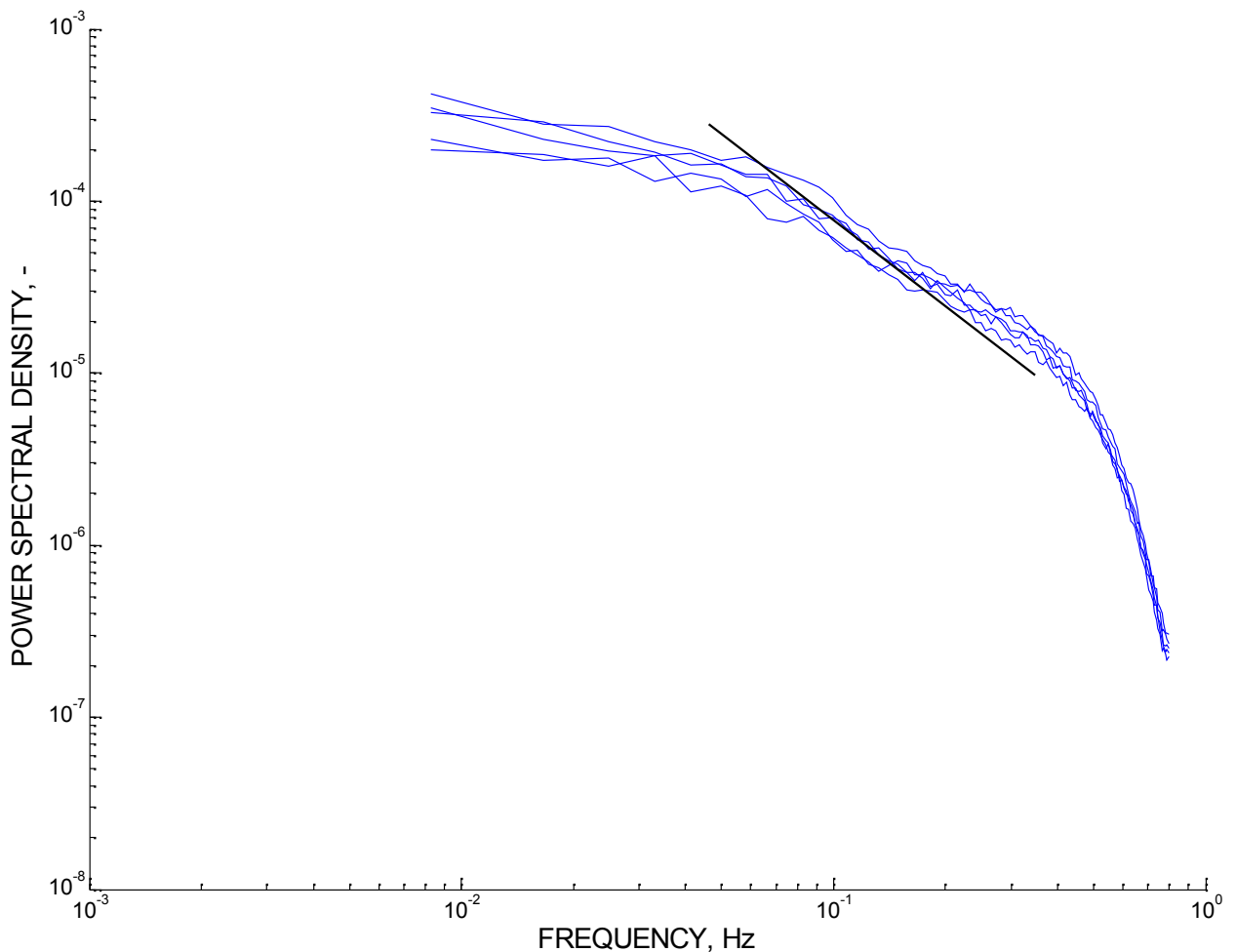


Figure 5.4. Radial variation of spectra in fluid bed for bed voidage of 0.42

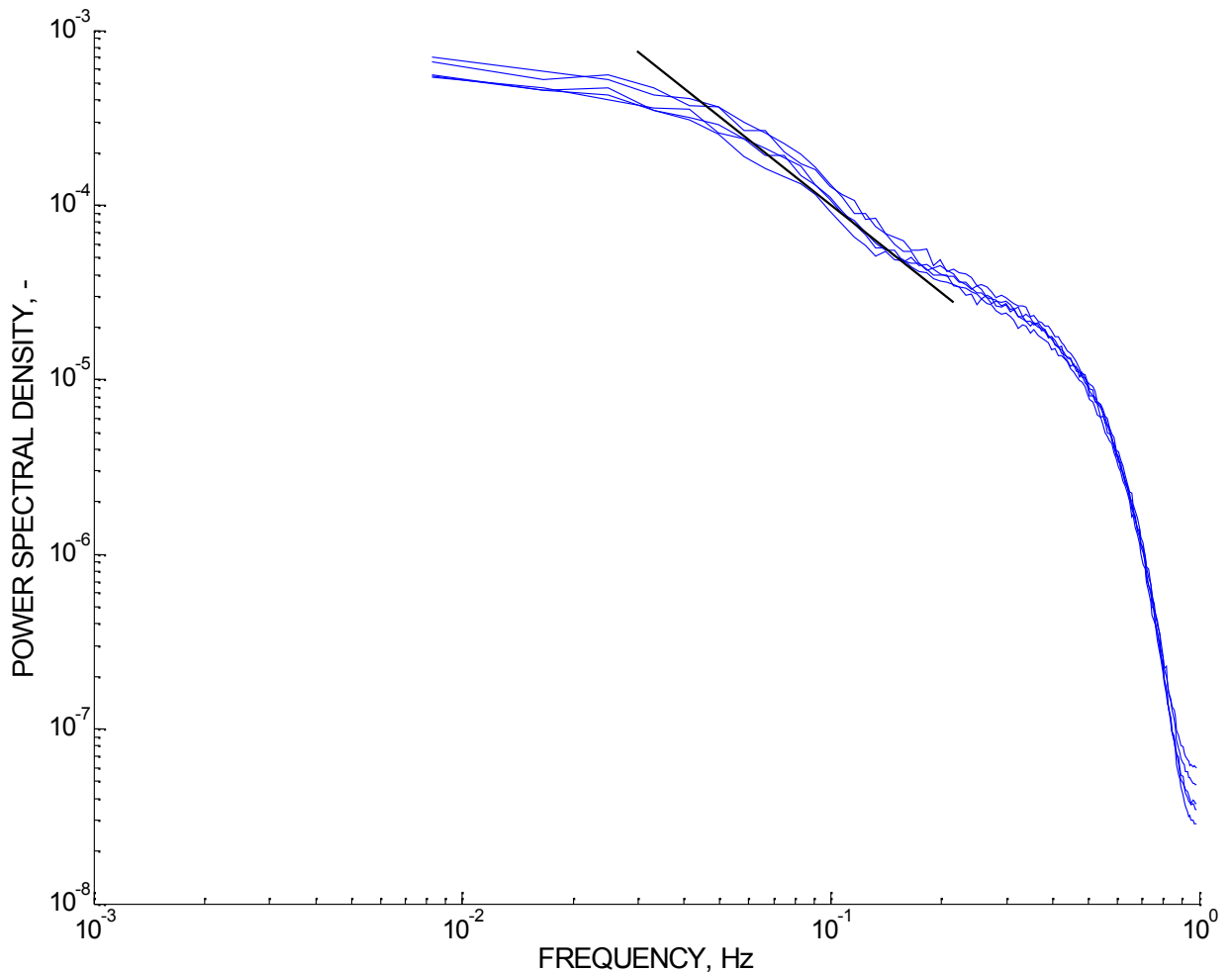


Figure 5.5. Radial variation of spectra in fluid bed for bed voidage of 0.6

The flow pattern in the decay region downstream of the fluidized bed is interesting because it compares more with the grid generated turbulence which has been widely characterized in the literature. In the current work we compare the turbulence characteristics of this region with the decaying grid turbulence in order to establish that the fluidized bed is a source of homogeneous turbulence, like the bar of grids. Thus, the fluidized bed can be used as the turbulence source to study the effect of free stream turbulence on the motion of bubbles, drops and particles. Fluidized bed also has the advantage of higher turbulence intensity compared to decaying grid or oscillating grid turbulence.

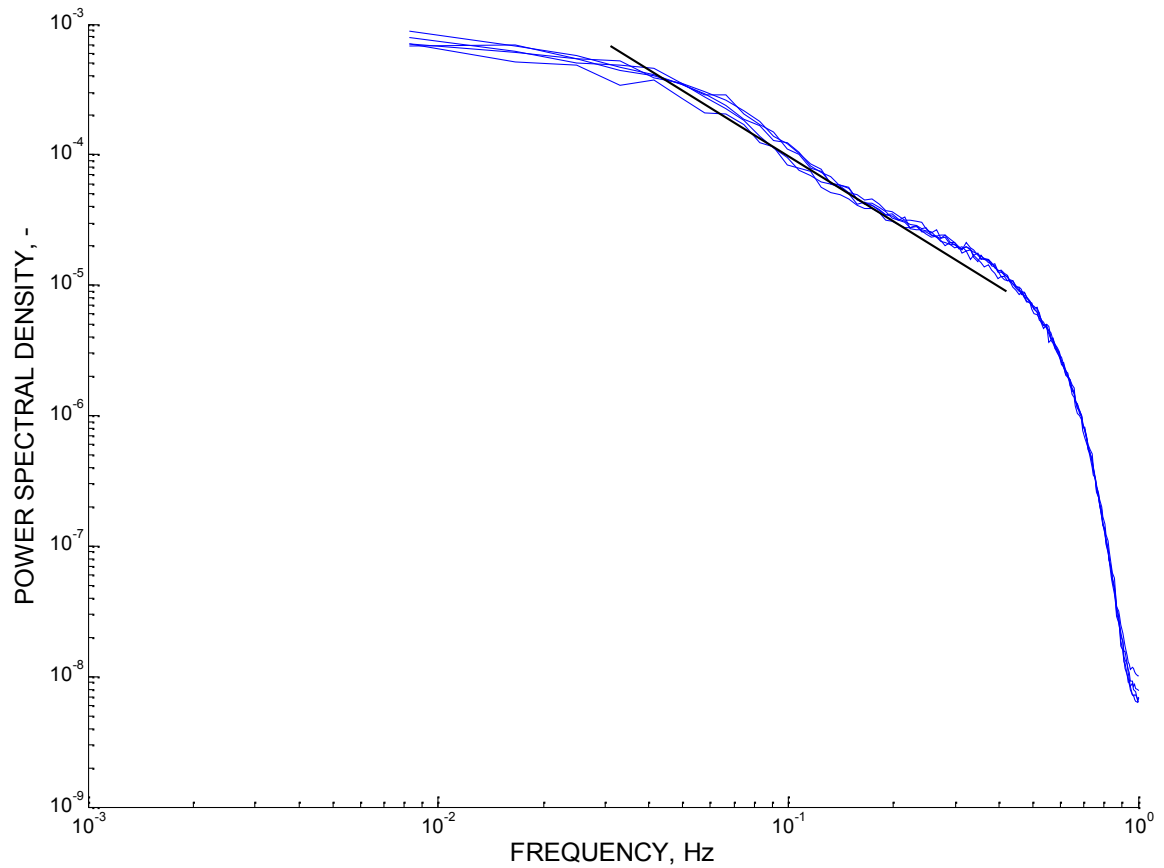


Figure 5.6. Radial variation of spectra in fluid bed for bed voidage of 0.65

5.4.2 PDF of Liquid Velocity in Fluidized Bed

PDF of local velocity fluctuations provide the simplest measure for intermittency. The deviation from gaussian PDF indicate the presence of intermittency in the velocity field. Figure 5.7, 5.8 and 5.9 show the PDF for lateral and axial velocity for bed voidage of 0.42, 0.6 and 0.65 respectively. It can be observed that the PDF attains Gaussian behavior far from the fluidized bed. Inside the fluidized bed and near the interface of the fluidized bed the PDFs are non Gaussian, with more deviation inside the fluidized bed for all three bed voidages. The Effect is more pronounced for axial velocity than lateral velocity.

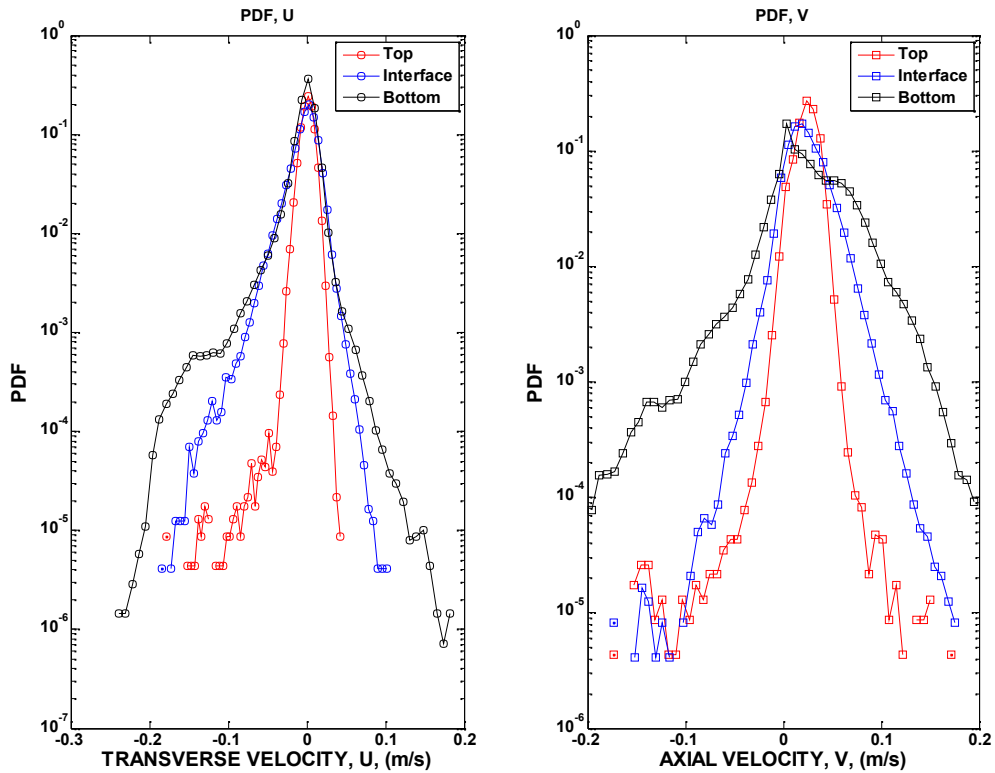


Figure 5.7. PDF of liquid velocity for bed voidage of 0.42

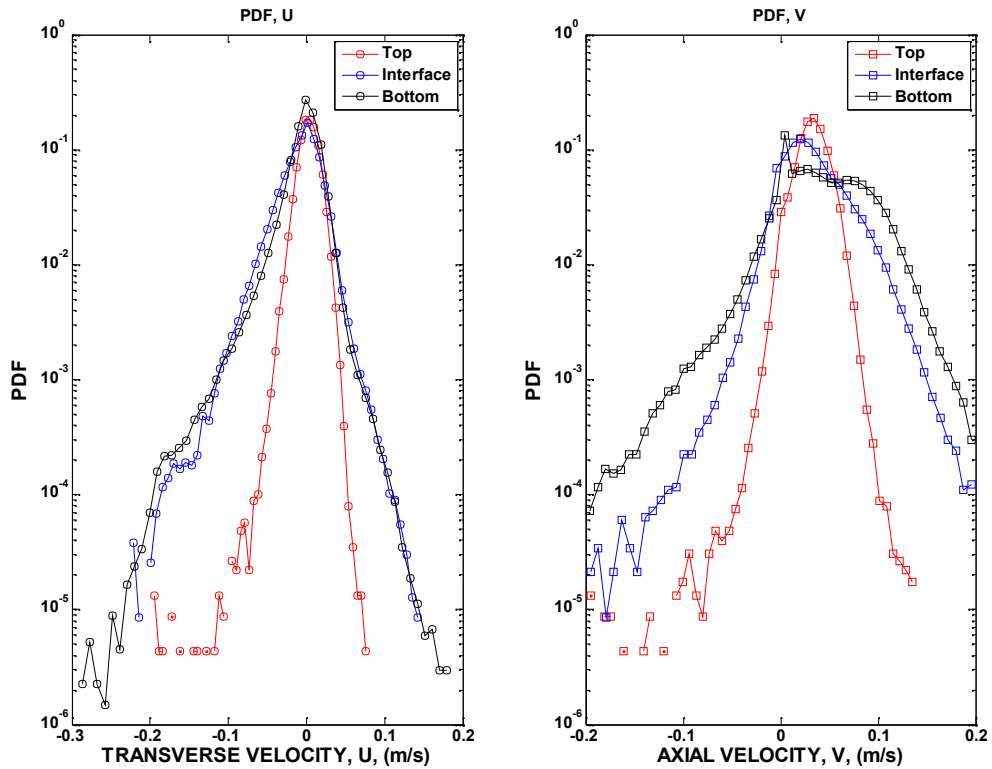


Figure 5.8. PDF of liquid velocity for bed voidage of 0.6

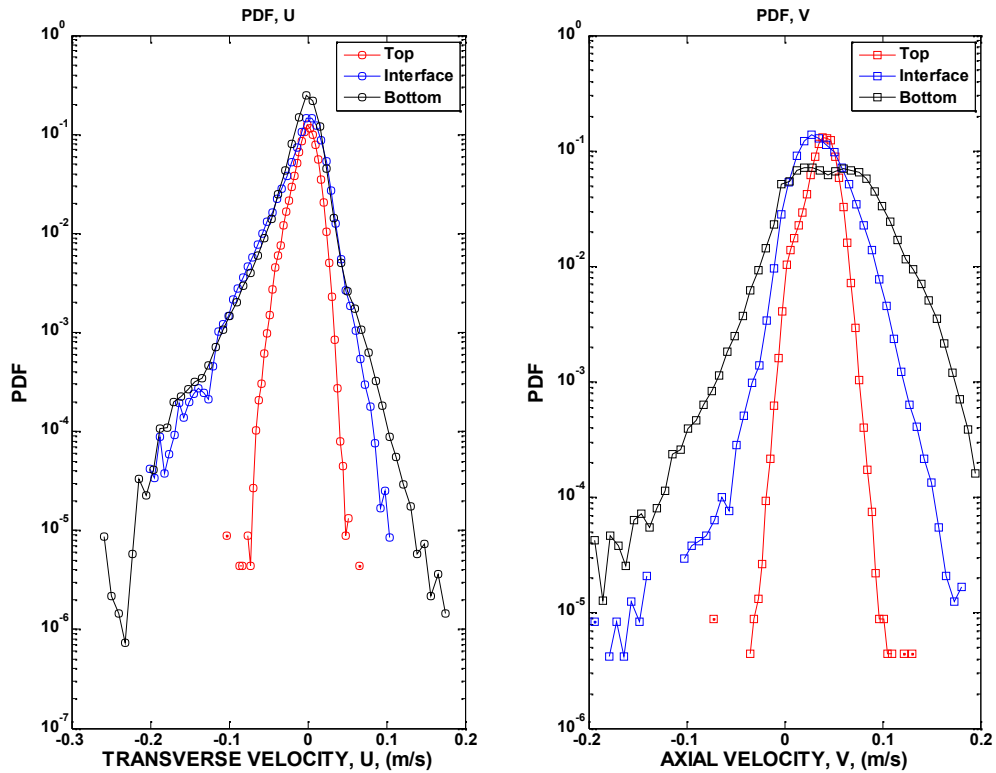


Figure 5.9. PDF of liquid velocity for bed voidage of 0.65

5.4.3. Structure Functions of Liquid Velocity in Fluidized Bed

The structure functions of second, third and fourth order have been calculated for same three regions marked in Figure 5.3 for three bed voidages of 0.42, 0.6 and 0.65. The results are plotted in Figure 5.10-5.12. It can be observed that all three structure functions show highest energy in the bottom region, which comprises of fluidized bed, followed by the region near interface and the region far from fluidized bed. This shows uniform decay of turbulence. In the next section we describe the decay law that is similar to grid generated turbulence. The Nature of the structure function variation with spatial separation r is similar for all the cases. The nature of the structure function curves is similar to those obtained for gas liquid dispersions by Rensen et al. (2005).

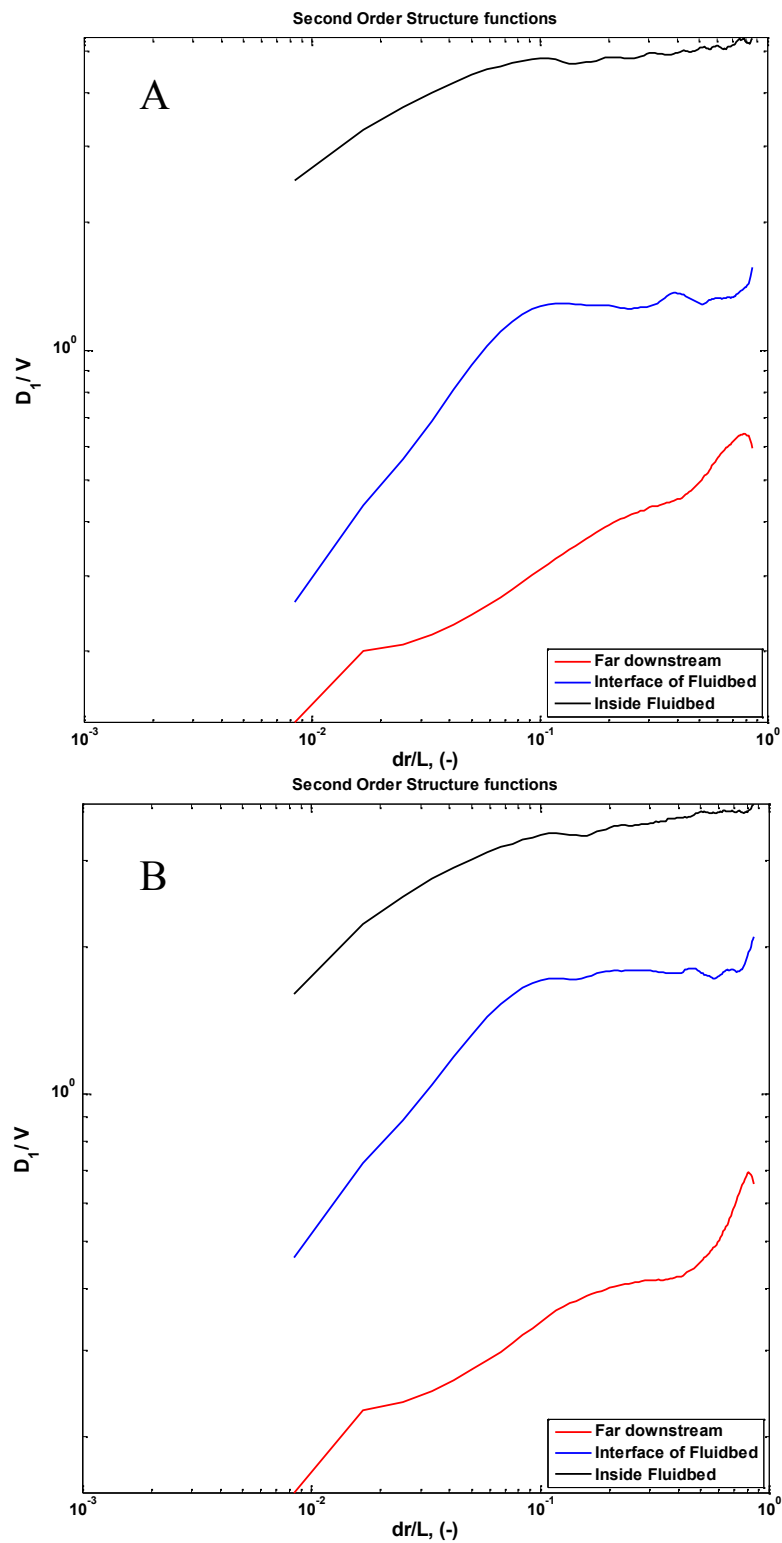


Figure 5.10. Second order structure functions for (A) Fluid bed at voidage of 0.42 and (B) Fluid bed at voidage of 0.6

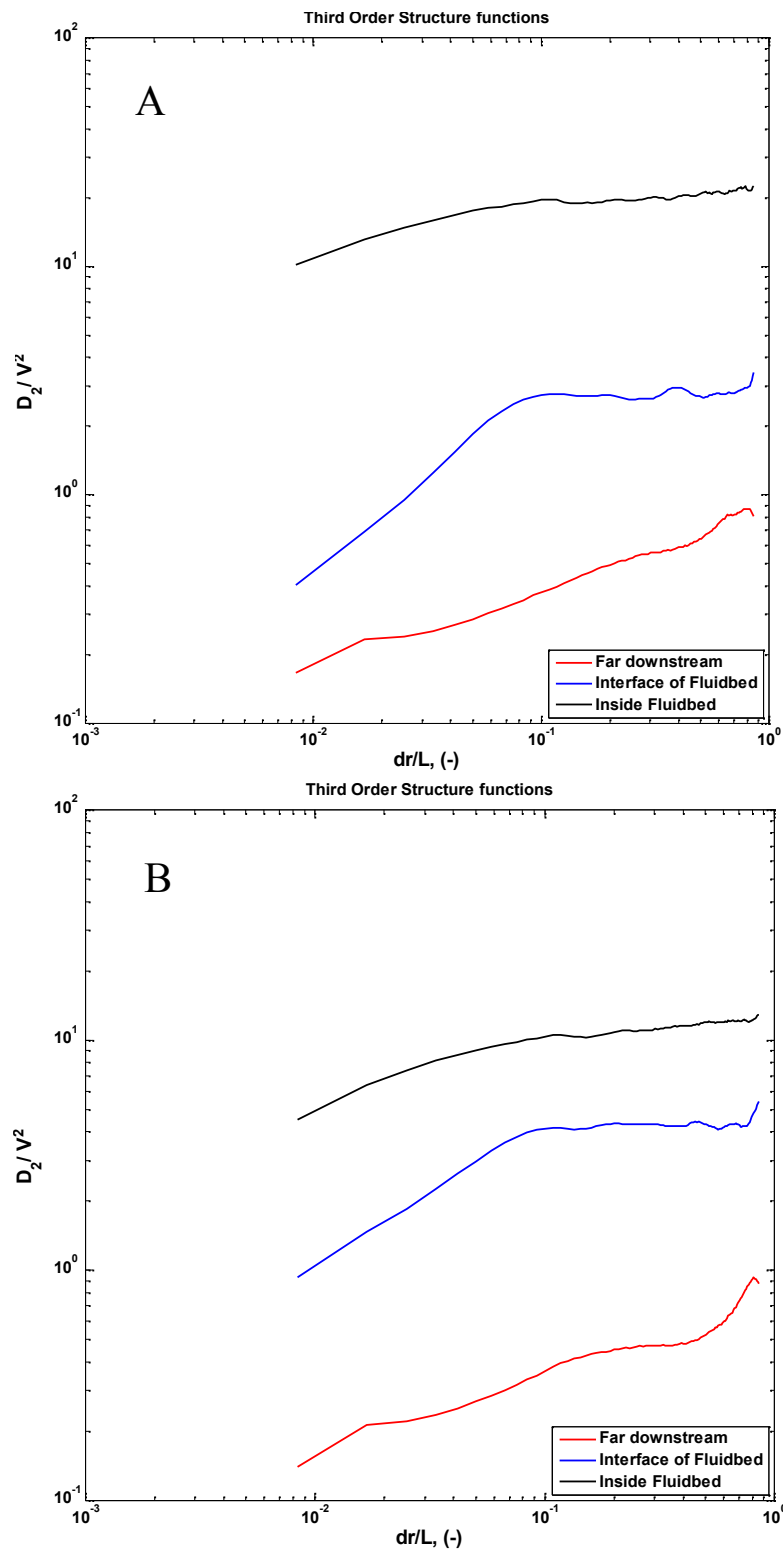


Figure 5.11. Third order structure functions for (A) Fluid bed at voidage of 0.42 and (B) Fluid bed at voidage of 0.6

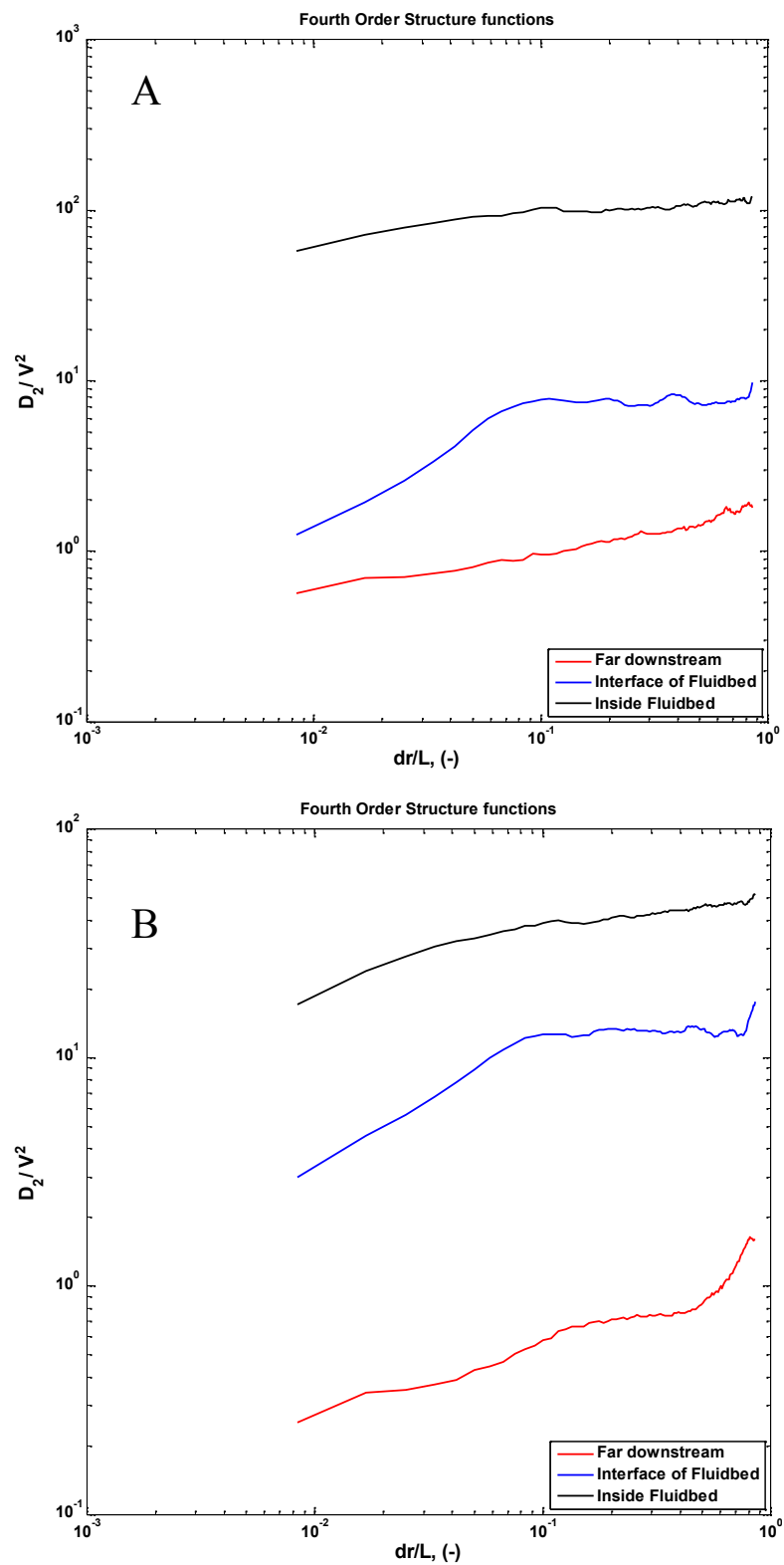


Figure 5.12. Fourth order structure functions for (A) Fluid bed at voidage of 0.42 and (B) Fluid bed at voidage of 0.6

However, with the current resolution of PIV we are able to resolve up to r/L value of ~ 0.01 ; hence the structure function values for smaller r could not be evaluated. However, the resolution is small enough to bring out the characteristics of energy decay of turbulence.

5.4.4. Integral Length Scale, RMS Velocity and the Decay Law for Flow Downstream the Fluidized Bed

As mentioned in earlier sections, in order to compare the decay of turbulence above fluidized bed with that of the turbulence behind the grid, we compared the decay of integral length and velocity scales. There are two characteristic models proposed for such decay: Batchelor turbulence and Saffman turbulence. For Batchelor turbulence, the quantity $u^2 l^5$ is constant, where u is the RMS velocity and l is the integral length scale. For Saffman turbulence, $u^2 l^3$ is constant.

The integral length scale is calculated using the autocorrelation function of axial velocity in radial direction. The autocorrelation function is averaged over certain height for 100 PIV snapshots. To note the effect of this vertical averaging on the trend of increase in integral length scale with height, two band thickness of 10 and 5 mm were analyzed. The results are shown in Figure 5.13-5.16. Table 1 summarizes the results for all the cases of different bed voidages and band height. Figure 5.13 shows the autocorrelation function with 5 bands for bed voidage of 0.42, and Figure 5.16 shows the autocorrelation with 10 bands for same bed voidage. It can be observed that the integral length scale smoothly increases downstream of the fluidized bed. As can be observed from Table 1, the variation is $u^2 l^3$ is much less than $u^2 l^5$ which shows a trend of uniform increase with height. Hence, the decay of turbulence in fluidized bed resembles to Saffman turbulence.

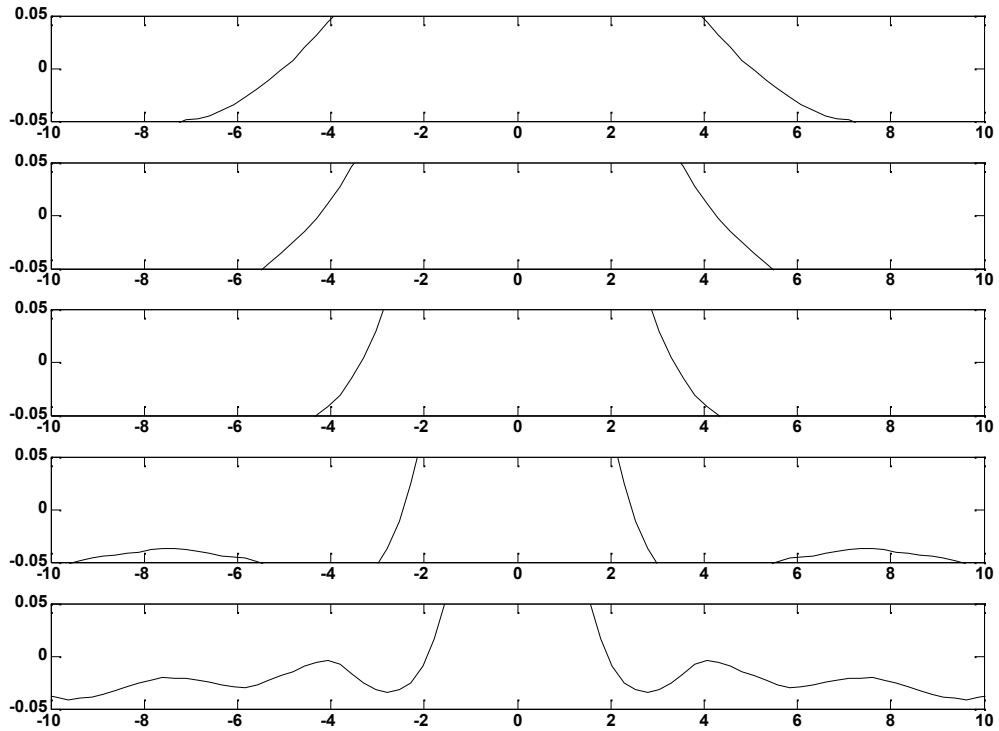


Figure 5.13. Variation of autocorrelation function with height for fluid bed at voidage of 0.42

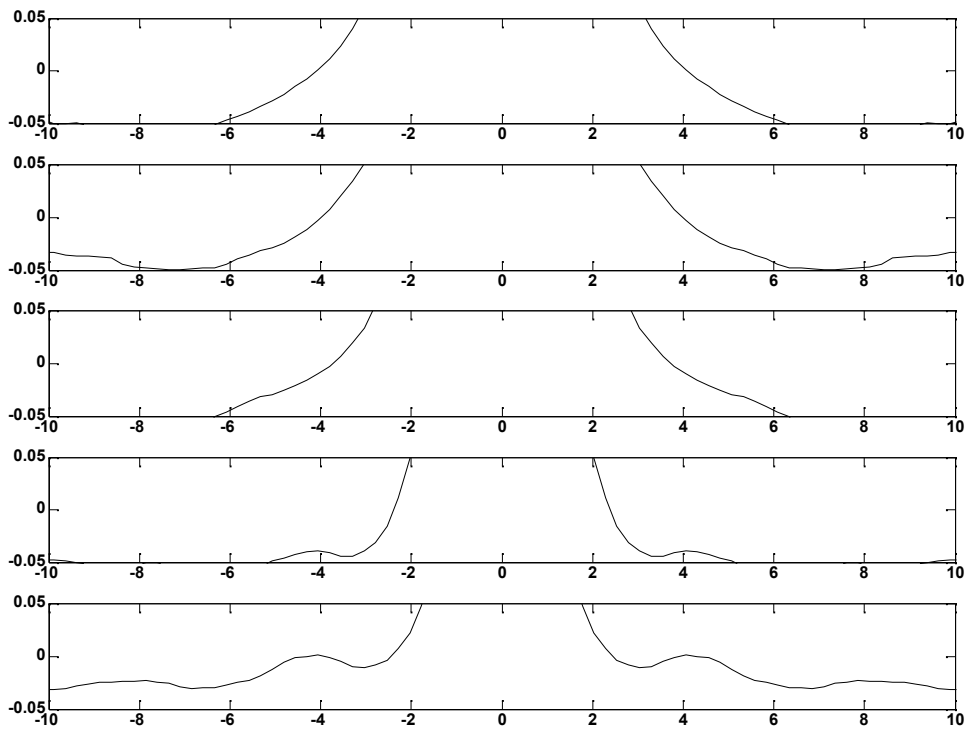


Figure 5.14. Variation of autocorrelation function with height for Fluid bed at voidage of 0.6

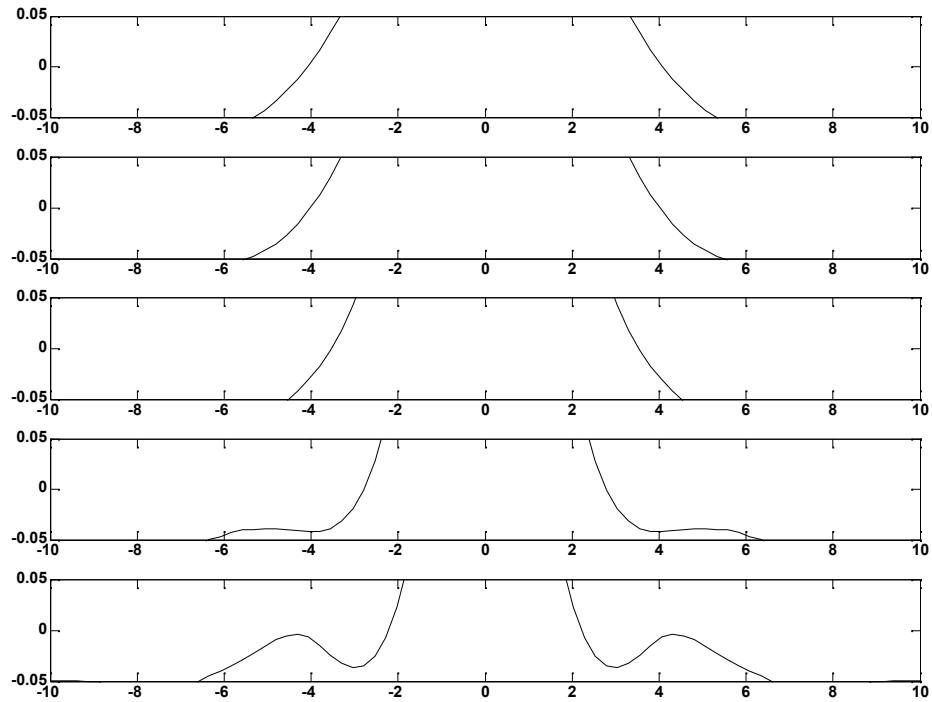


Figure 5.15. Variation of autocorrelation function with height for Fluid bed voidage of 0.65

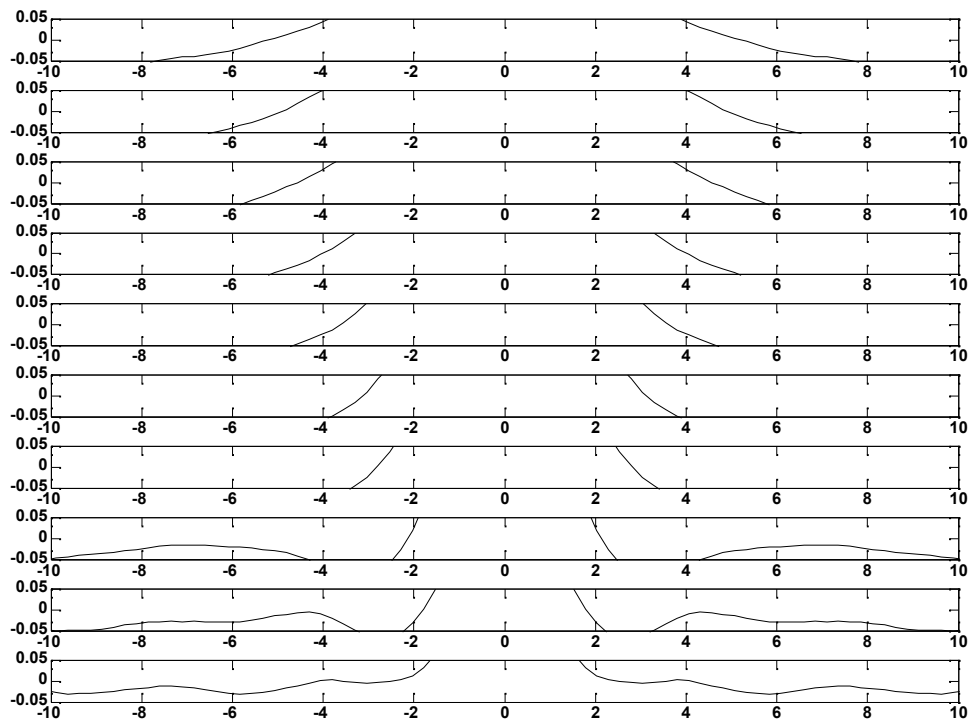


Figure 5.16. Variation of autocorrelation function with height for Fluid bed at voidage of 0.42: 10 vertical bands

Table 1: Integral length scale, RMS velocity and decay law for flow downstream of the fluidized bed

75 mm, 5 bands					110 mm, 5 bands					130 mm, 5 bands				
h (mm)	u	L	u^2L^3	u^2L^5	h (mm)	u	L	u^2L^3	u^2L^5	h (mm)	u	L	u^2L^3	u^2L^5
54	0.0112	4.6112	0.0122	0.26	54	0.0157	4.0368	0.0162	0.2644	54	0.0138	4.0372	0.0125	0.203
42	0.0114	3.844	0.0074	0.1087	42	0.0176	3.6234	0.0147	0.1933	42	0.0147	3.5864	0.0099	0.1276
30	0.0135	3.2401	0.0062	0.0655	30	0.0201	3.3724	0.0155	0.1758	30	0.0175	3.0712	0.0088	0.0834
18	0.0201	2.1065	0.0038	0.0168	18	0.0334	2.1775	0.0115	0.0547	18	0.0246	2.2889	0.0072	0.0379
6	0.0382	1.6123	0.0061	0.0159	6	0.0452	2.1187	0.0194	0.0871	6	0.041	1.835	0.0104	0.0349

75 mm, 10 bands					110 mm, 10 bands					130 mm, 10 bands				
h (mm)	u	L	u^2L^3	u^2L^5	h (mm)	u	L	u^2L^3	u^2L^5	h (mm)	u	L	u^2L^3	u^2L^5
57	0.0112	4.9386	0.0152	0.3703	57	0.0153	4.0398	0.0154	0.2521	57	0.0136	4.0459	0.0123	0.2017
51	0.0111	4.7487	0.0132	0.2976	51	0.0161	4.0329	0.017	0.2762	51	0.0139	4.0269	0.0126	0.2036
45	0.011	4.0751	0.0082	0.1364	45	0.0167	3.563	0.0126	0.1602	45	0.0143	4.036	0.0134	0.2183
39	0.0117	3.6045	0.0064	0.0837	39	0.0184	3.6935	0.0171	0.2335	39	0.015	3.6416	0.0109	0.1448
33	0.0126	3.4974	0.0068	0.0828	33	0.0191	3.9905	0.0233	0.3709	33	0.0163	3.4159	0.0106	0.1242
27	0.0144	2.9574	0.0054	0.0472	27	0.021	3.1878	0.0142	0.1446	27	0.0185	3.2195	0.0115	0.1187
21	0.0166	2.765	0.0059	0.0448	21	0.0266	2.3962	0.0097	0.0558	21	0.021	2.8402	0.0101	0.0813
15	0.0231	1.925	0.0038	0.0141	15	0.0393	1.9537	0.0115	0.044	15	0.0277	2.1585	0.0077	0.0359
9	0.0359	1.7656	0.0071	0.0221	9	0.0455	2.0861	0.0188	0.0816	9	0.041	1.9141	0.0118	0.0431
3	0.0404	2.0896	0.0149	0.0649	3	0.0448	2.1626	0.0203	0.0951	3	0.0401	2.1659	0.0163	0.0767

5.4.5. Flow Pattern in Bubble Column

The bubble column is taken as the case of dispersion of deformable particles with complete slip (bubbles) to demonstrate the similarity in the structure of turbulence with the dispersion of rigid spherical particles with no slip boundary condition in fluidized bed. The flow pattern in the rectangular bubble column considered in the current study is heterogeneous. However, when we look at the structure functions and energy spectrum for bubble column bring out similarity in the nature of the spectrum with ‘True turbulent’ spectrum in the qualitative sense that it shows continuous decrease in the energy with increase in the wavenumber. However, the slopes of them differ in certain subranges; owing to the difference in the turbulence generation and attenuation by the particles and bubbles.

Figure 5.17 shows the quiver plot of time averaged liquid velocity and the contours of radial and axial RMS liquid velocity for two superficial gas velocities, $V_G=10$ mm/s and 20 mm/s for five point sparger at $H/L= 2$. The RMS velocities are higher for higher superficial gas velocity. The quiver plot shows downflow near the wall and upflow near column center. This circulation marks the presence of heterogeneity. Figure 5.18 shows mean and RMS velocities for bubble column with five point sparger at $V_G=10$ mm/s. It can be observed that the RMS vertical velocity has a maxima near the wall while the RMS lateral velocity has the maxima near the column center. Figure 5.19 shows similar graphs for $V_G=20$ mm/s. Similar trend is observed, except for higher mean and RMS velocities.

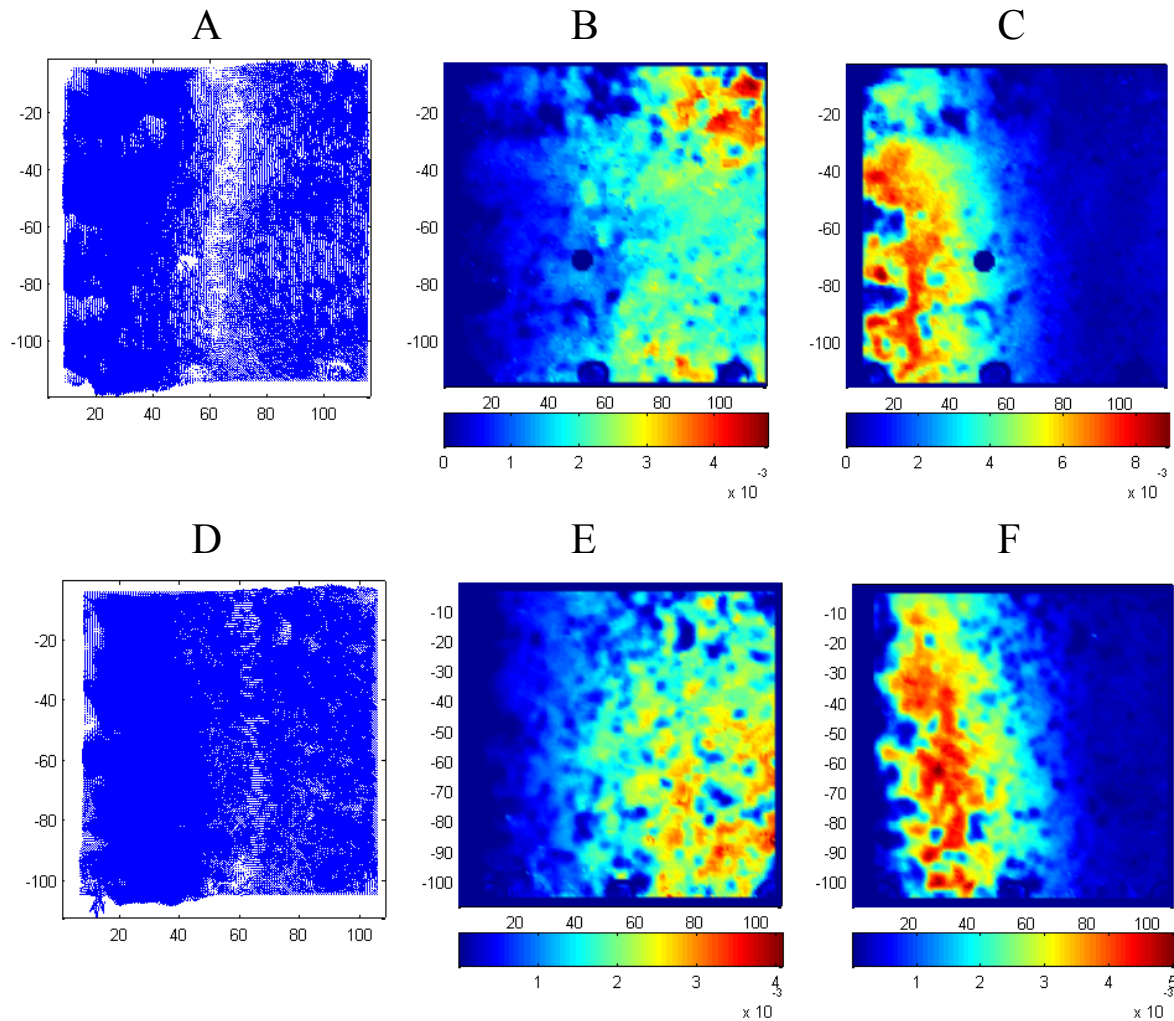


Figure 5.17. Statistics of velocity for bubble column with five point sparger at $H/L=2$: (A) Quiver plot of time averaged velocity field, $V_G=10$ mm/s (B) U_{RMS} , $V_G=10$ mm/s (C) V_{RMS} , $V_G=10$ mm/s (D) Quiver plot of time averaged velocity field, $V_G=20$ mm/s (E) U_{RMS} , $V_G=20$ mm/s (F) V_{RMS} , $V_G=20$ mm/s

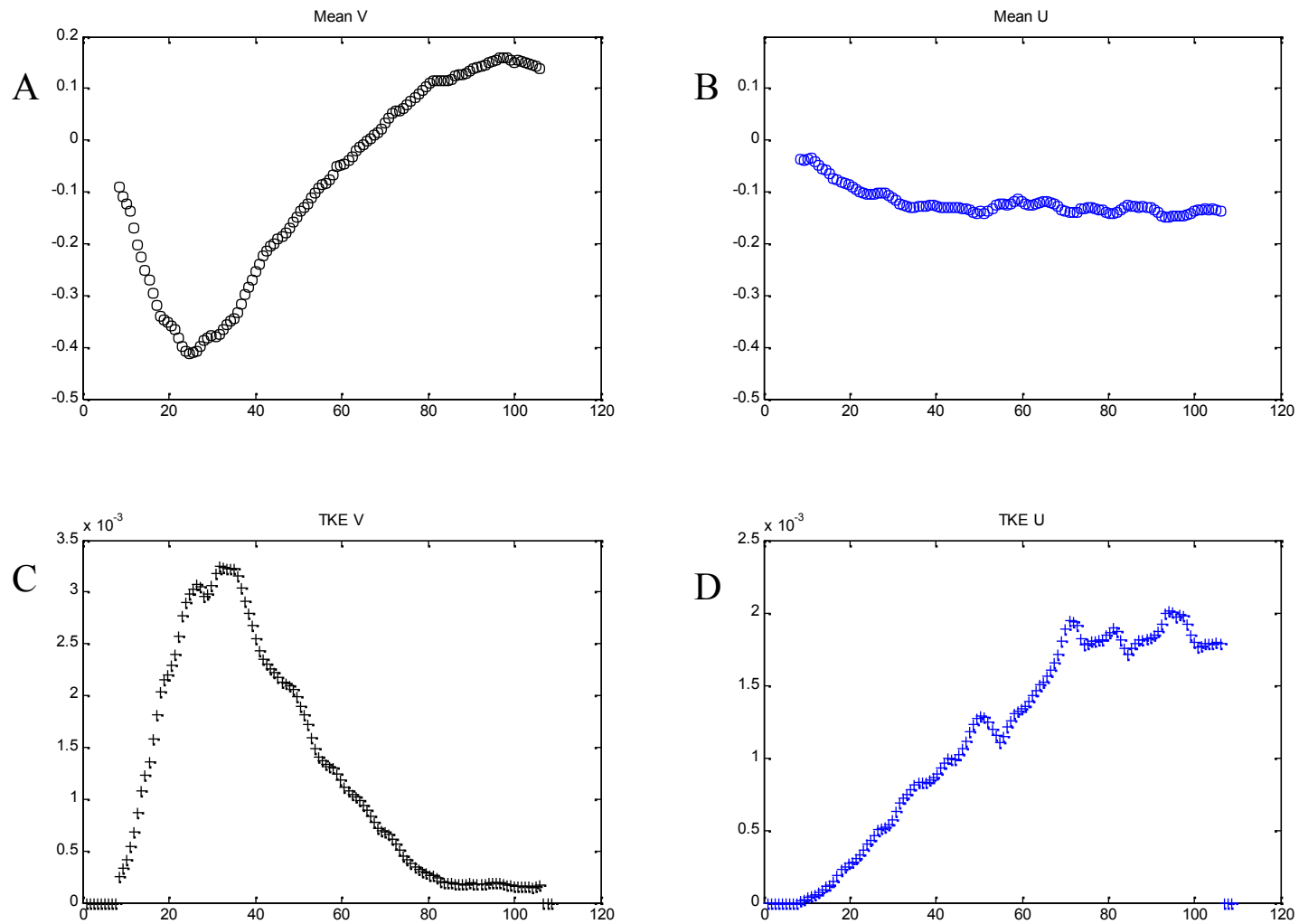


Figure 5.18. Mean and RMS velocity profiles for bubble column with five point sparger at $H/L=2$ for $V_G=10\text{mm/s}$ (A) \bar{V} (B) \bar{U} (C) V_{RMS} (D) U_{RMS}

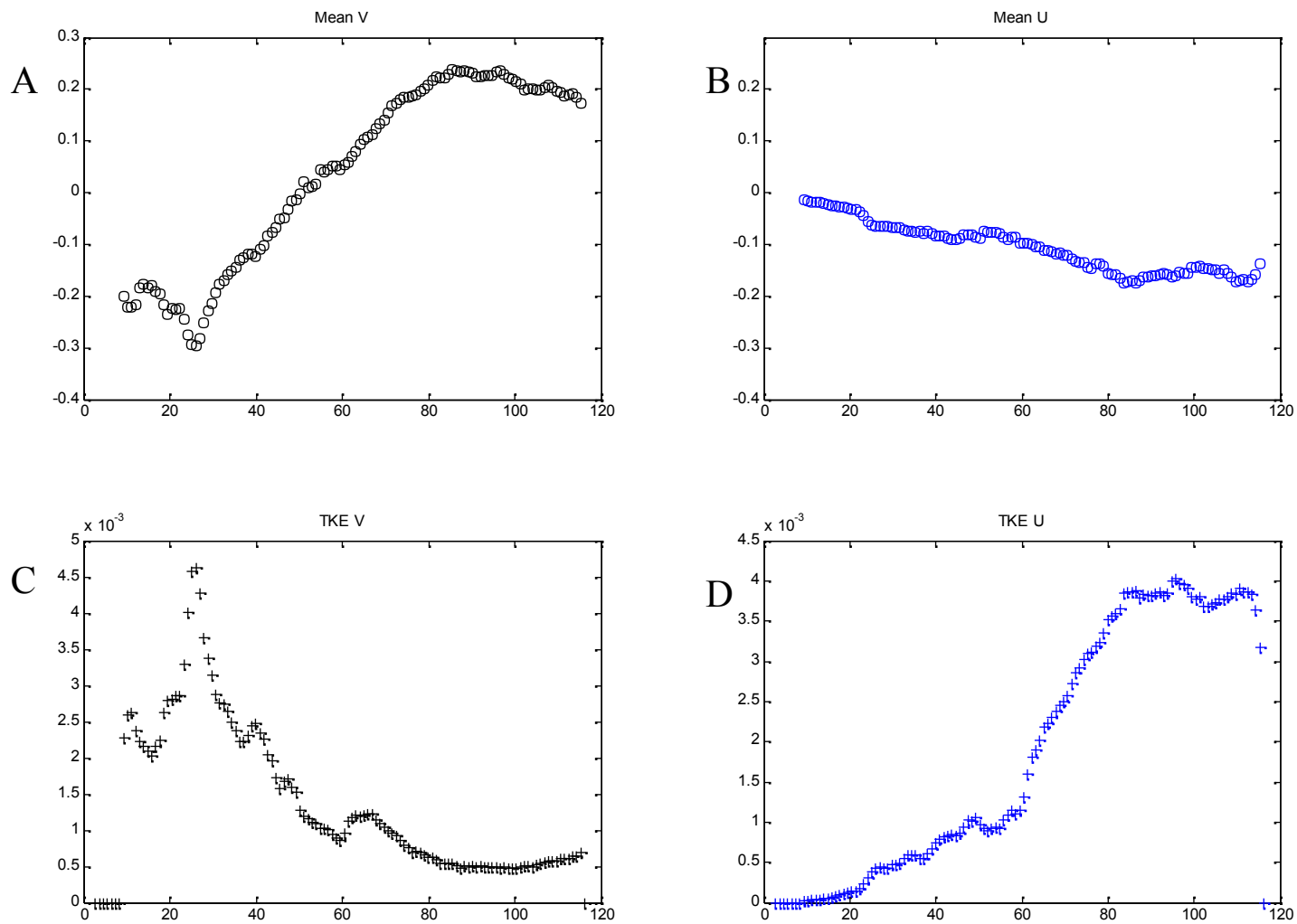


Figure 5.19. Mean and RMS velocity profiles for bubble column with five point sparger at $H/L=2$ for $V_G=20\text{mm/s}$ (A) \bar{V} (B) \bar{U} (C) V_{RMS} (D) U_{RMS}

5.4.6. Structure Functions and Energy Spectra in Bubble Column

Figure 5.20 is the plot of second, third and fourth order structure functions for bubble column with single point sparger, for $V_G=10$ and 20 mm/s. As can be observed, all three structure functions maintain similar trend; however their energies differ. It can also be observed that the general trend of all the structure function plots resembles the structure function plots of grid turbulence with continuous increase in the energy with r , with slope decreasing as r increases. Hence, the turbulence in bubble column bears similarity with ‘true turbulence’ and it is not completely the ‘pseudo turbulence’ which is formed by interaction between the sinuous trajectories of bubbles. Figure 5.21 shows similar plots for five point sparger with $V_G=10$ and 20 mm/s. The difference in the curves is more prominent at higher values of r . However, the trend of higher energy for higher superficial gas velocity is maintained.

The structure functions plotted in Figure 5.20 and 5.21 are averaged over time and vertical bands with width of $L/8$ (4 vertical bands). Structure functions for each band are marked with lines of different color. In all the 12 plots, the energy of structure functions is higher at intermediate bands (between centerline of column and column wall). The energies are less for column center as well as column wall, marking stronger correlation of velocity at these locations.

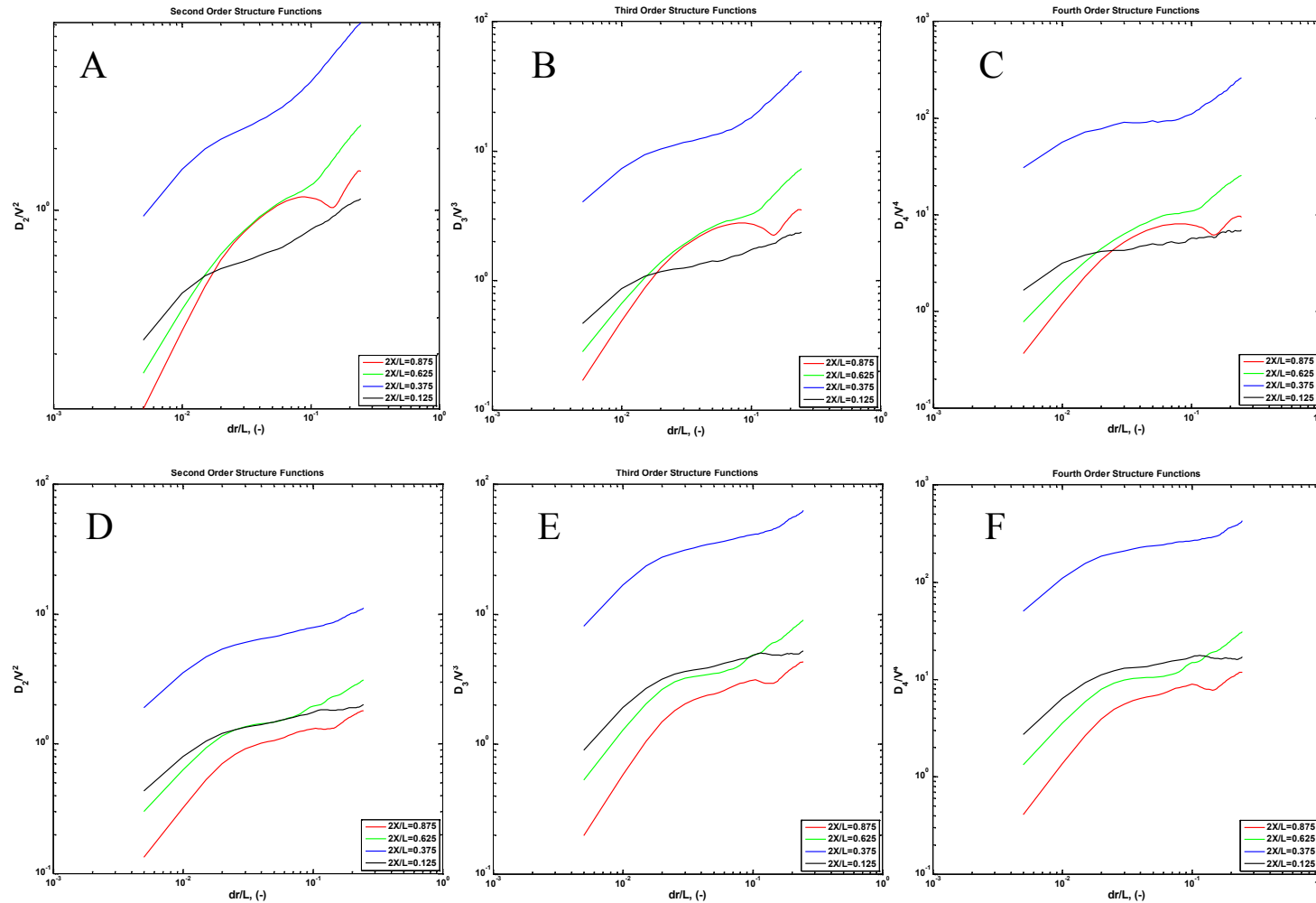


Figure 5.20. Structure functions of vertical velocity for bubble column with single point sparger at $H/L=2$: (A) D_2 , $V_G=10\text{mm/s}$ (B) D_3 , $V_G=10\text{mm/s}$ (C) D_4 , $V_G=10\text{mm/s}$ (D) D_2 , $V_G=20\text{mm/s}$ (E) D_3 , $V_G=20\text{mm/s}$ (F) D_4 , $V_G=20\text{mm/s}$

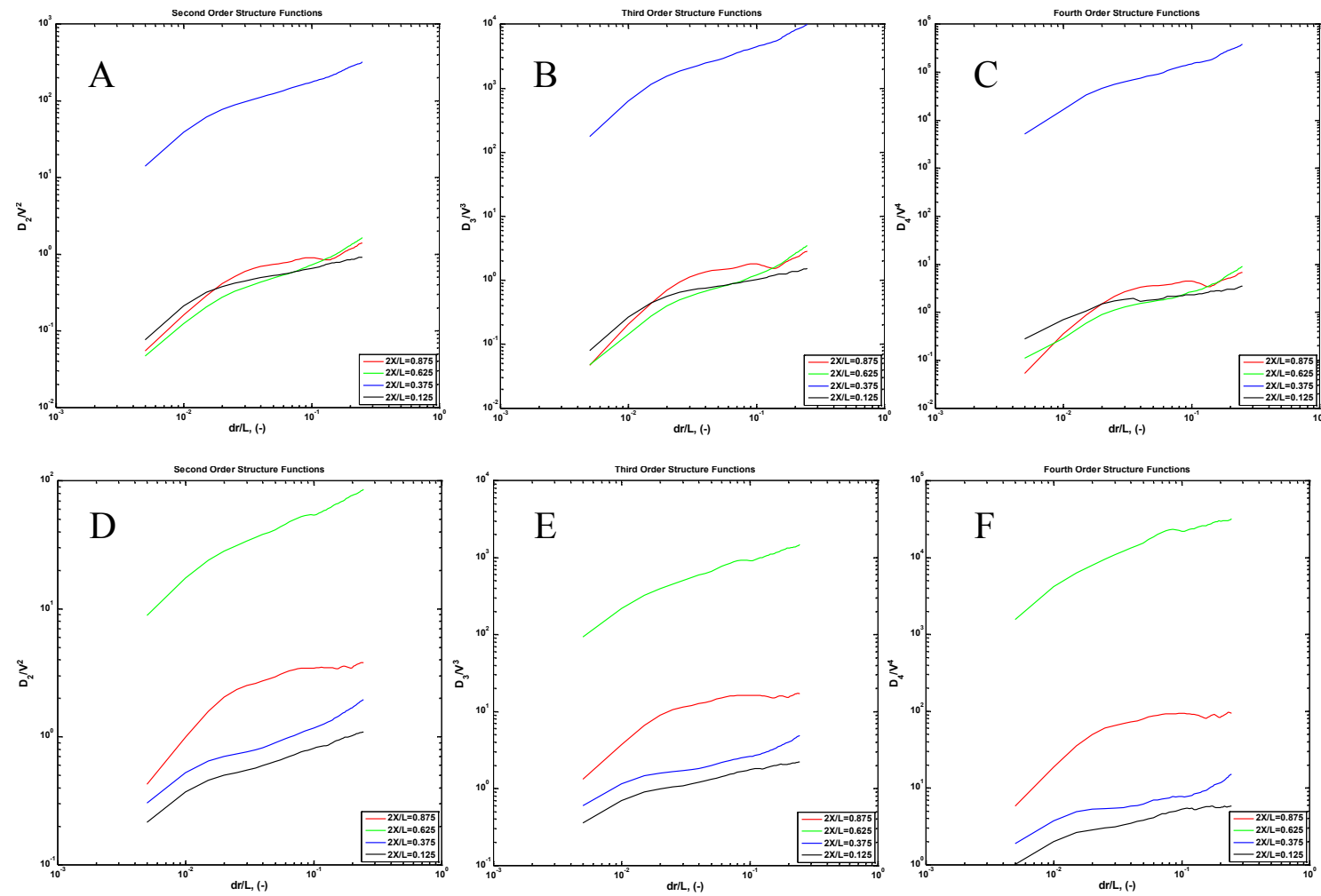


Figure 5.21. Structure functions of vertical velocity for bubble column with five point sparger at $H/L=2$: (A) D_2 , $V_G=10\text{mm/s}$ (B) D_3 , $V_G=10\text{mm/s}$ (C) D_4 , $V_G=10\text{mm/s}$ (D) D_2 , $V_G=20\text{mm/s}$ (E) D_3 , $V_G=20\text{mm/s}$ (F) D_4 , $V_G=20\text{mm/s}$

Finally, to complete the description of turbulence in heterogeneous bubbly flow, the energy spectrum averaged over time and same vertical bands is presented. Figure 5.22 shows the energy spectrum for single point sparger for $V_G=10$ and 20 mm/s. The spectrum with highest energy is corresponding to the band near wall, while the spectrum corresponding to each consecutive band from wall to centerline has successively lesser energy. This is in accordance with the observed RMS velocity profile of axial velocity. This also proves that the procedure of using zero liquid velocity in the regions pertaining to bubbles does not introduce huge artifacts in the spectrum. The characteristic slope of $-5/3$ is visible in the initial part of the spectrum, followed by a steeper slope till the dissipation regime starts. This can be signature of bubble induced turbulence in accordance with the published literature. Figure 5.23 shows the energy spectrum for bubble column with five point sparger for $V_G=10$ and 20 mm/s. It shows trend similar to Figure 5.22.

Comparing the spectra for heterogeneous flow in Figure 5.22-5.23 with the spectra in homogeneous flow in [Figure 4-6](#), we can clearly observe the effect of heterogeneity in the form of variation in the integral of the spectrum. However, the trend of two slopes and the magnitude of the slope of the spectrum is maintained while the integral energy of the spectrum varies. This shows that there exists a similarity in the structure of turbulence along the cross section of bubble column, even if the turbulent kinetic energy varies from center to wall. In the next sections, the flow parameters resulting into heterogeneity are described.

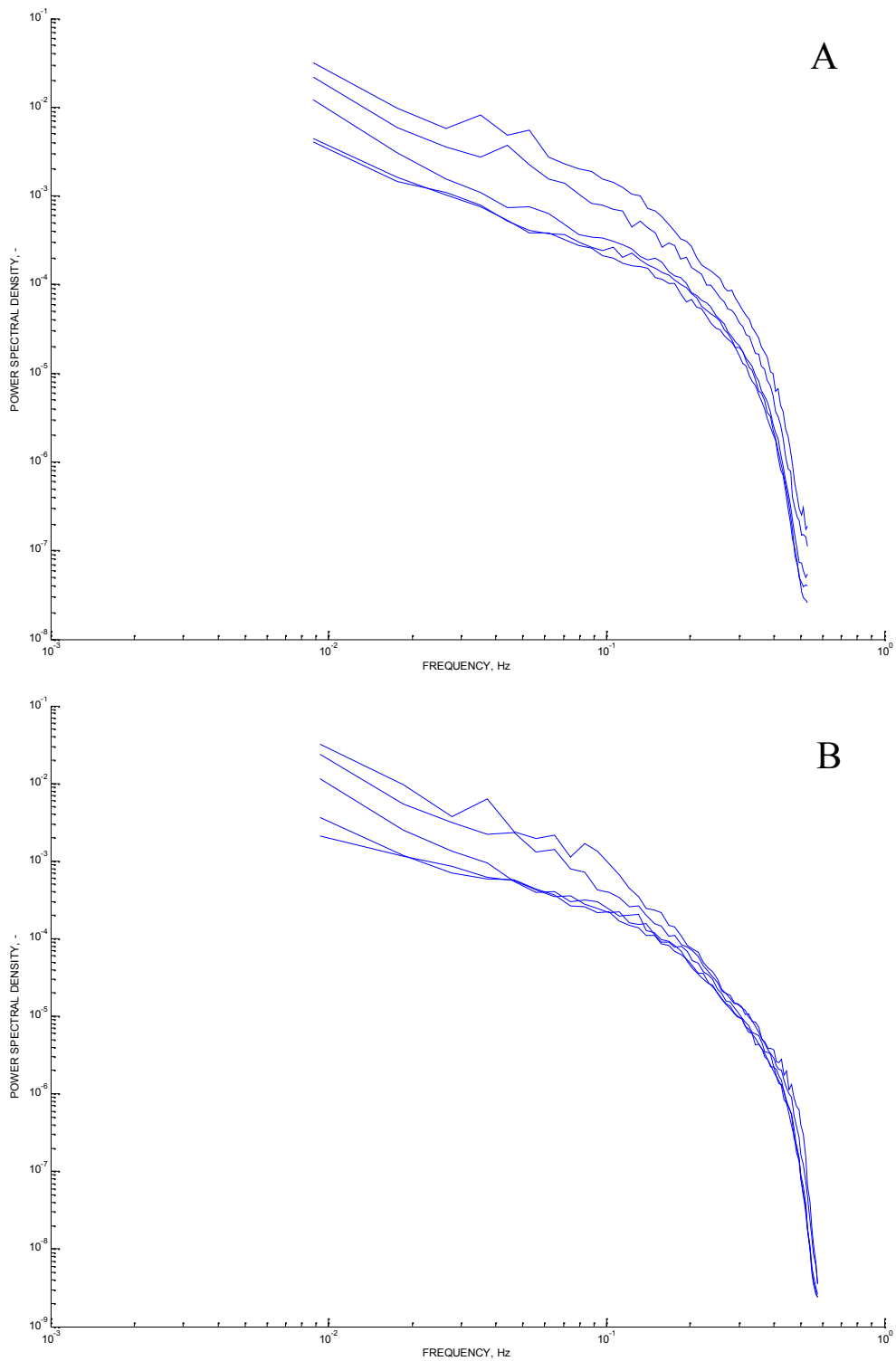


Figure 5.22. Radial variation of energy spectrum for bubble column with single point sparger (A) $V_G = 10$ mm/s (B) $V_G = 20$ mm/s

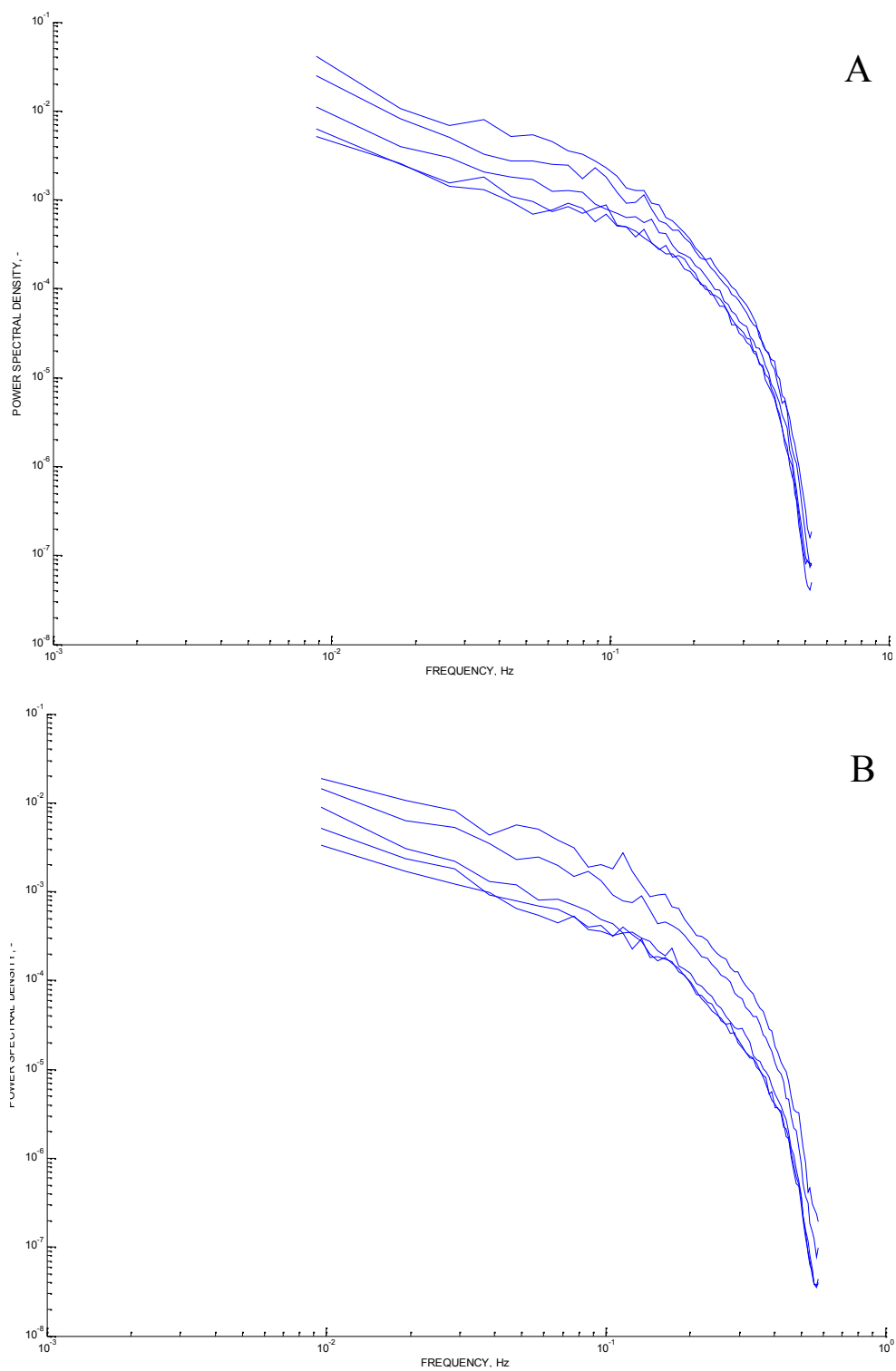


Figure 5.23. Radial variation of energy spectrum for bubble column with five point sparger (A) $V_G = 10$ mm/s (B) $V_G = 20$ mm/s

5.4.7. Bubble Size Distribution

Figure 5.24 shows the bubble size distribution at $H/D=2$ for 5 point sparger for different gas flow rates. Two types of distributions are shown: number density distribution and the volume weighted distribution. The smaller gas flow rates correspond to nearly homogeneous regime while the higher flow rates correspond to the heterogeneous flow regime. It can be observed that at the smallest gas flow rates, the bubble size distribution has a distinct peak around the bubble size at sparger. This implies least coalescence and breakup of bubbles. As the gas flow rate is increased, the number of bubbles is approximated by the inverse of bubble diameter. Also, much larger bubbles start appearing. This implies that the bubble breakup and coalescence are set up inside the column in heterogeneous regime. Although the number of small bubbles is large, it must be noted that a single bubble of 6 mm diameter has a volume 216 times larger than that of a 1 mm diameter bubble. This implies that the higher number density of small bubbles does not represent the true mean diameter of the gas phase. A more rational representation is the volume weighted distribution. It signifies the volume fraction of bubbles having a typical diameter. Figure 5.24B clearly shows the trend of increase in volume fraction of gas in large bubbles. The large and small bubbles are not equally distributed along the column cross section. This fact will be elaborated later in this section.

Figure 5.25A shows the lateral gas hold-up distribution obtained with 3 point pressure probe, while Figure 5.25B shows the axial liquid velocity distribution along the lateral direction in the bubble column with 5 point sparger for the superficial gas velocity (V_G) of 20 mm/s.

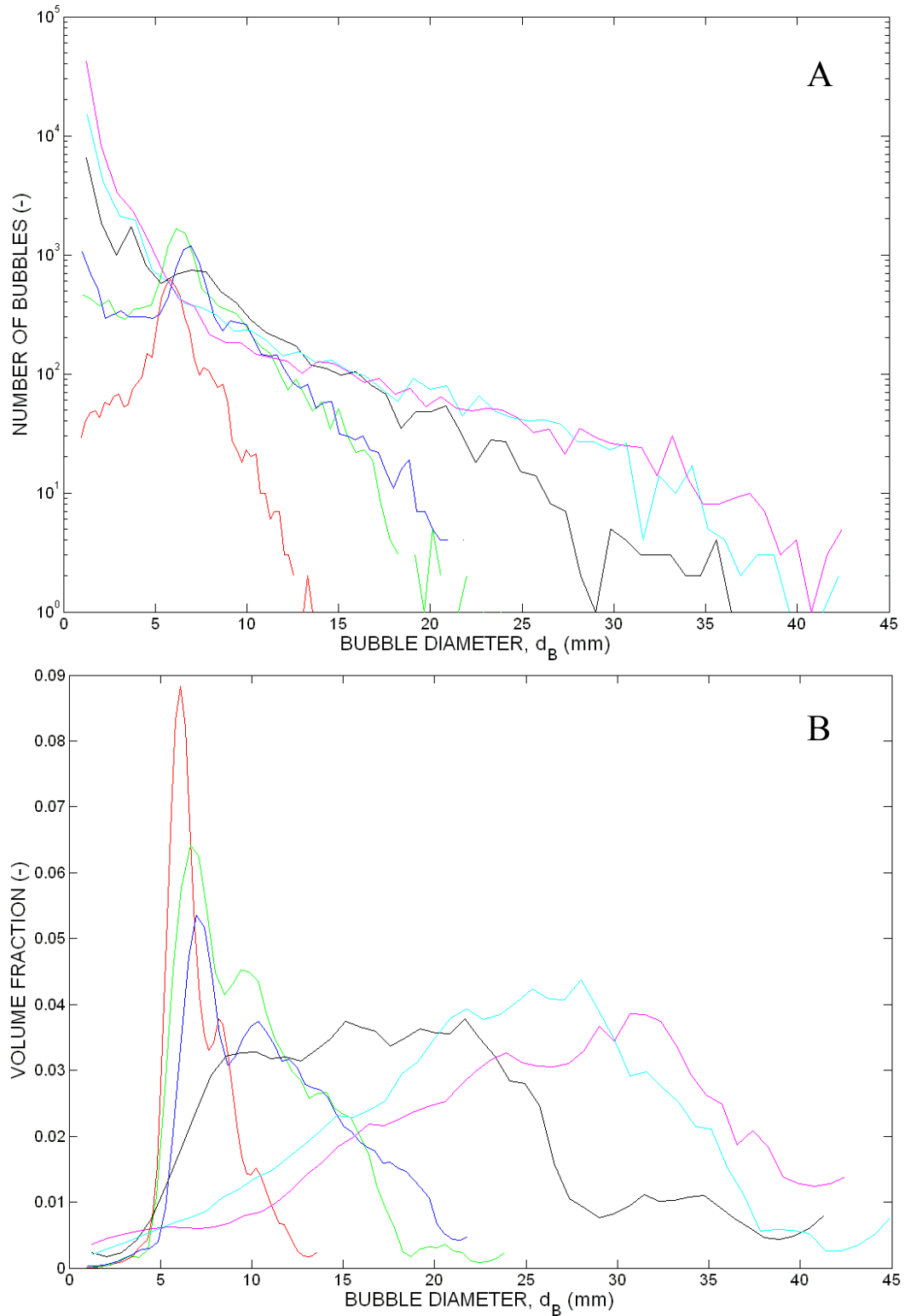


Figure 5.24 (A) Number distribution and (B) volume weighted distribution for 5 point sparger and different gas flow rates: — $10 \times 10^3 \text{ mm}^3/\text{s}$, — $30 \times 10^3 \text{ mm}^3/\text{s}$, — $40 \times 10^3 \text{ mm}^3/\text{s}$, — $60 \times 10^3 \text{ mm}^3/\text{s}$, — $88 \times 10^3 \text{ mm}^3/\text{s}$, — $128 \times 10^3 \text{ mm}^3/\text{s}$

It can be observed that the liquid velocity as well as the gas hold-up are maximum near the column center. The liquid velocity is negative near the wall implying liquid recirculation which is characteristic of the heterogeneous flow regime. Figure 5.26A and 5.26B show the lateral variation of bubble size obtained using shadowgraphy measurement at superficial gas velocity of 10mm/s and 20 mm/s, respectively. The flow at $V_G=10$ mm/s is weakly heterogeneous than the flow at $V_G=20$ mm/s. However, in both the cases it can be observed that the bubbles having diameters significantly different than the bubble size at sparger are present. This non uniform bubble size along with the non uniform gas hold-up distribution helps sustaining the liquid circulation maintaining heterogeneity.

For $V_G=10$ mm/s, a large number of bubbles have similar size to the bubble size at sparger. This is indicated by the region between two dotted lines marking bubble size between 5 and 7 mm. For $V_G=20$ mm/s, the largest number of bubble have the size smaller than the bubble size at sparger. Also, the number of bubbles having diameter greater than 10 mm are more in case of $V_G=20$ mm/s. This implies that increased energy input rate because of the increase in gas sparging rate enhances the bubble coalescence and breakup. The overall result is the reduction in bubble size with an increase in the gas velocity. Another important fact that can be observed from Figure 5.26 is that the more number of large bubbles are present near the column center than near the wall. Also, the small bubbles are present throughout the column cross section, it should be noted that the smaller bubbles account for less volume fraction of the gas (as it has been clarified in Figure 5.24). Hence, the volume weighted bubble diameter is more near the column center while it is less near the column wall.

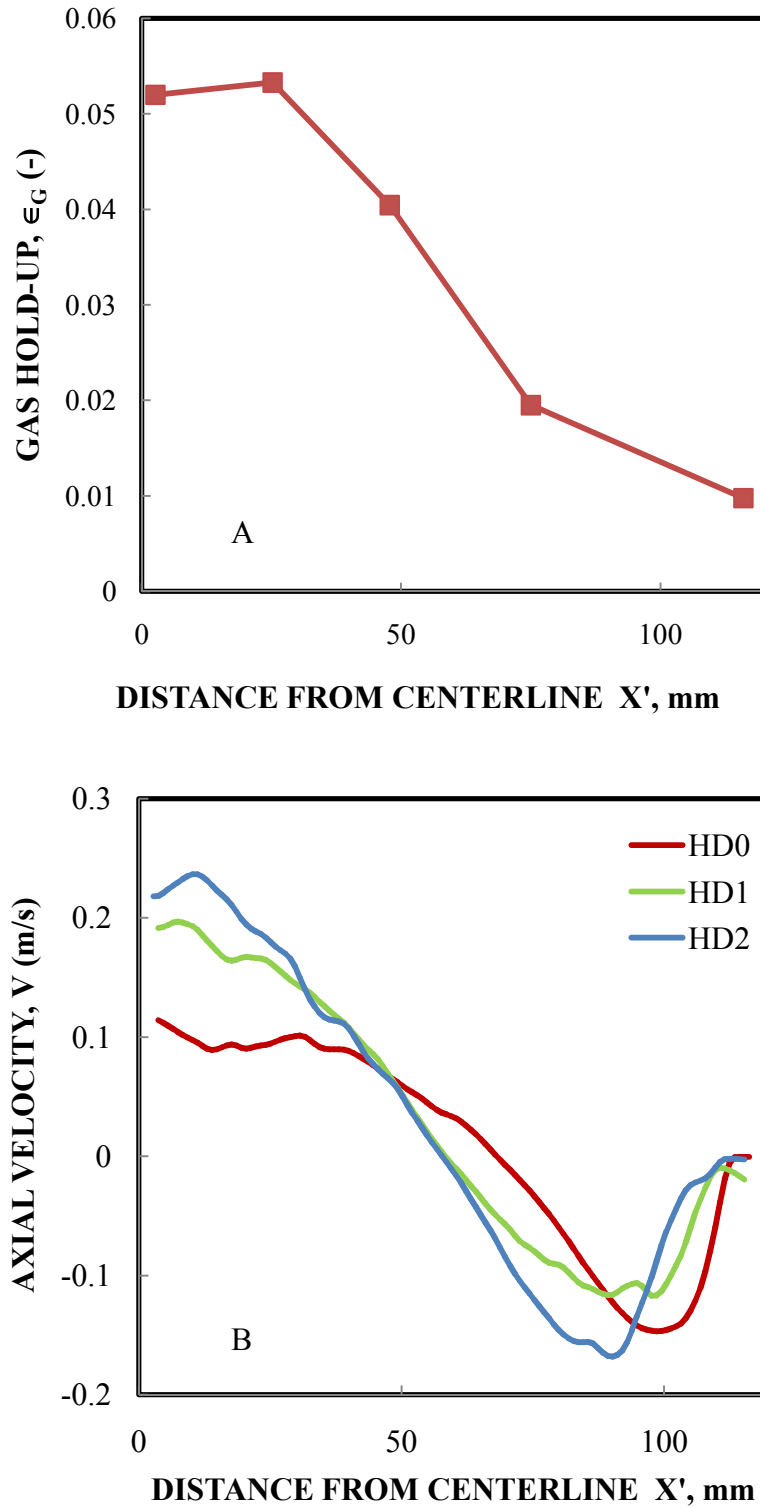


Figure 5. 25. Lateral variation of (A) volumetric gas hold-up (B) liquid velocity as a function of lateral distance form centerline of column for 5 point sparger for

$$V_G=20 \text{ mm/s}$$

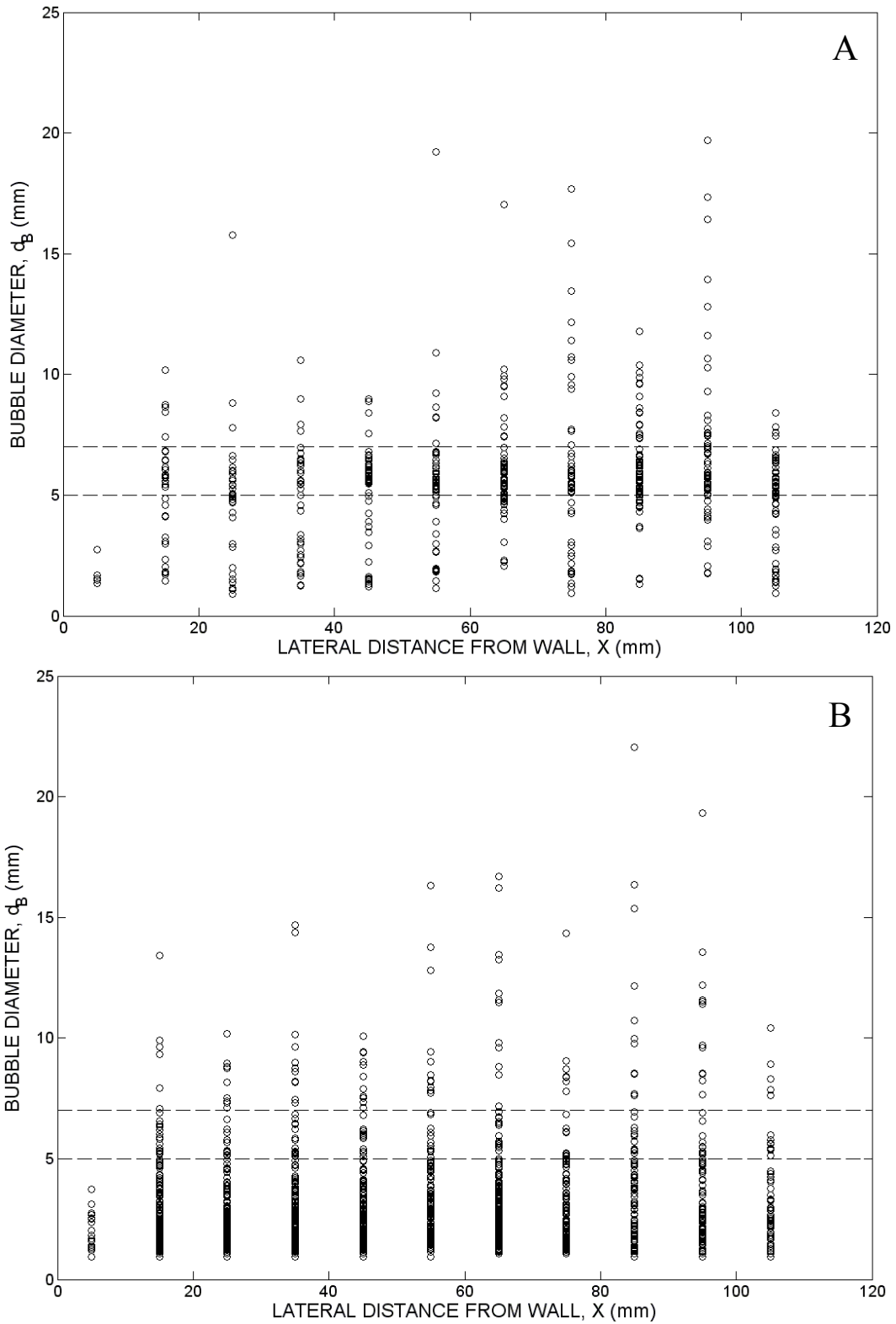


Figure 5.26. Bubble size as a function of lateral distance from wall for 5 point sparger for (A) $V_G=10$ mm/s (B) $V_G=20$ mm/s

This should be viewed in the light of the action of the lift force. For the larger bubbles the lift force is negative (in the direction of higher liquid velocity) while the lift force on small bubbles is negative (in the direction of the smaller liquid velocity). This finding has been confirmed for small Morton numbers (high viscosity liquids). The sustained presence of larger bubbles in the region of higher liquid velocity confirms the presence of negative lift coefficient for larger bubbles in heterogeneous regime. From Figure 5.26 it also becomes clear that the large bubbles mainly experience the positive liquid velocity- both in time averaged as well as instantaneous sense. Hence the velocity of the bubble with respect to stationary observer increases and hence it explains the anomalous increase in the rise velocity of the large bubbles with increasing gas hold-up, while the bubble rise velocity is generally found to decrease with an increase in the gas hold-up.

5.4.8. Bubble Rise Velocity

Figure 5.27A and 5.27B show the instantaneous rise velocity of bubbles as a function of the bubble diameter for $V_G=10$ mm/s and $V_G=20$ mm/s, respectively. The velocities are measured using simultaneous PIV and shadowgraphy. The bubble rise velocity was measured by particle tracking from a pair of shadow images of bubbles acquired at a known time interval. Hence, the bubble rise velocities in Figure 6 are instantaneous and should be differentiated from the usual notion of time averaged bubble rise velocities. Figure 5.27 also shows the rise velocity of single bubble in quiescent liquid using empirical correlations by Nguyen et al (for tap water) and Clift et al (for contaminated water).

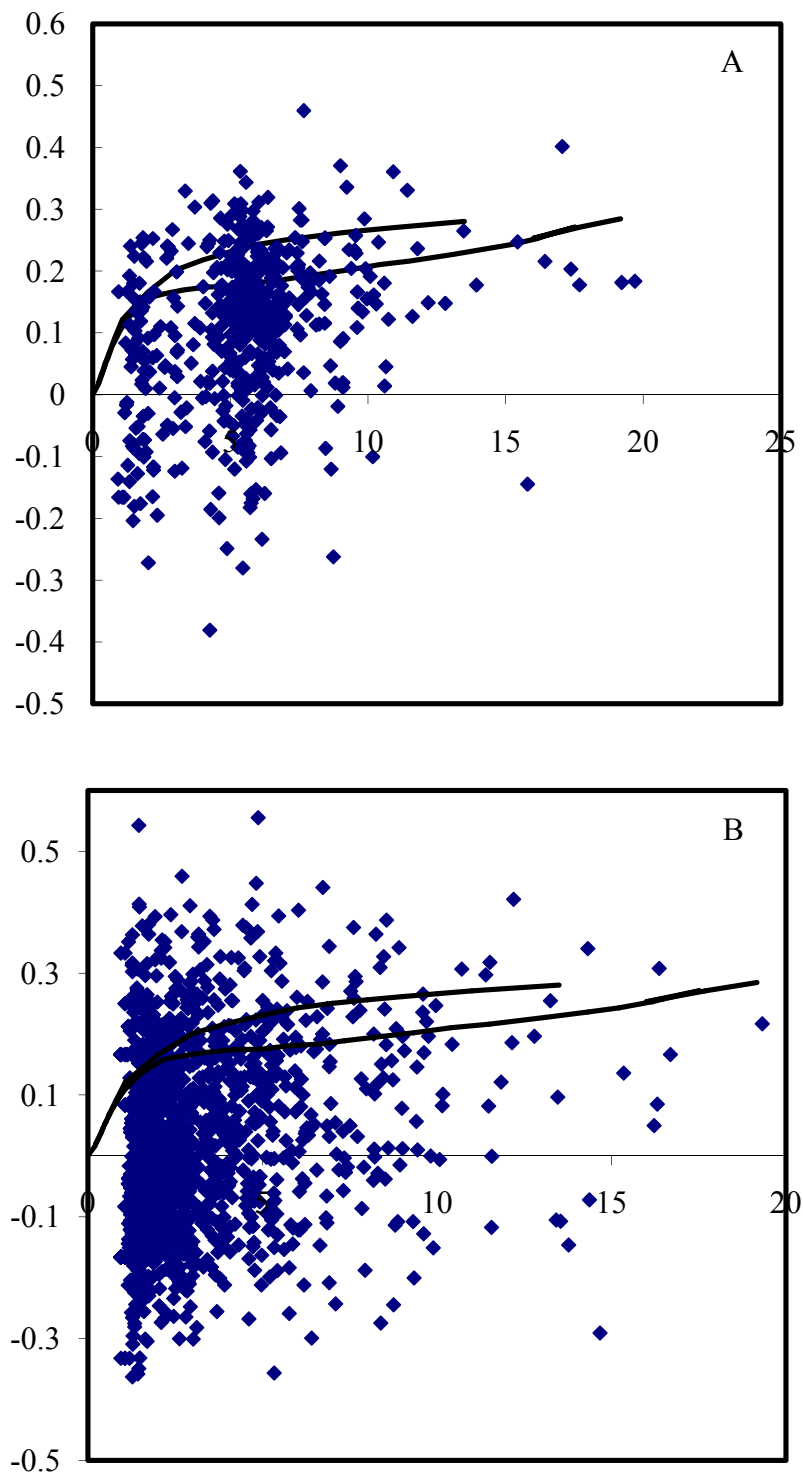


Figure 5.27. Rise velocity of bubbles as a function of bubble diameter for 5 point sparger for (A) $V_G = 10$ mm/s (B) $V_G = 20$ mm/s

It can be observed that the bubble rise velocity shows both the positive and negative deviations from the rise velocity of individual bubbles. The principle reason for this deviation is that the bubbles now rise in a heterogeneous turbulent flow field. It can also be noted that, on an average the bubble rise velocities are lower for higher gas superficial velocity. Hence, hinderence in bubble rise velocity due to turbulence is confirmed.

Figure 5.28A and 5.28B show the plot of axial liquid velocity and instantaneous bubble velocity for $V_G=10$ mm/s and 20 mm/s respectively. To calculate liquid velocity in the vicinity of the bubble, the liquid velocity field obtained using PIV was applied with a low pass filter with size corresponding to twice the mean bubble diameter in the plane. The smoothed velocity field was then interpolated at the bubble centroid in order to obtain the ‘Pseudo far field’ velocity of the liquid around the bubble. The points below diagonal in Figure 5.28 indicate the bubble velocity higher than the surrounding liquid velocity (and hence positive slip velocity). However, the points above the diagonal indicate the bubble velocity lower than the surrounding liquid and hence negative slip velocity. It should be noted that the velocities plotted in Figure 5.28 are instantaneous, and to have instantaneous negative slip velocity is not physically impossible considering the dynamic nature of flow field along with flow reversals. The radial motion of the bubbles under the influence of lift force also exposes them to different vertical velocity and hence the bubble experiences constant change in accelerations. Under these circumstances, the bubble might rise slower than liquid for the time period equivalent to the relaxation time of the bubble.

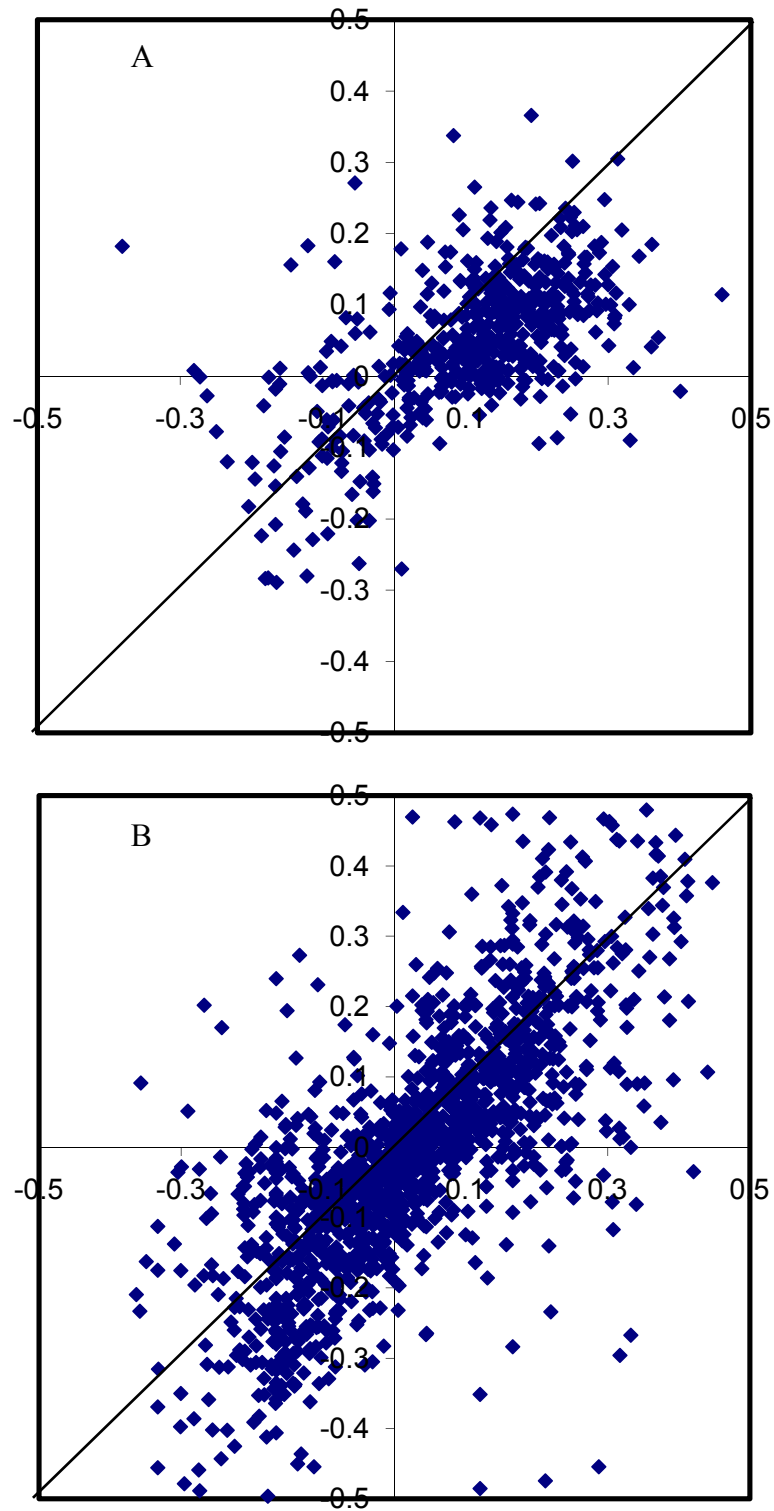


Figure 5.28. Local liquid velocity vs. bubble velocity for 5 point sparger for
(A) $V_G = 10$ mm/s (B) $V_G = 20$ mm/s

5.4.9. Energy Spectrum of Turbulence in Dispersed Flows

The turbulence inside the particulate dispersions (bubbles or particles) has long been referred to as ‘pseudo turbulence’ and considered to be different than ‘true turbulence’. The pseudo turbulence is caused mostly by the random motion of the bubbles as they rise through the liquid. It should be noted that, the turbulence is also caused by vortex shedding from the bubbles. It is also caused by the downflowing fluid elements from the top interface where the wakes are released. The latter contribute more to the ‘true turbulence’ rather than the pseudo turbulence. In the case of heterogeneous regime of operation, vorticity is also imparted to liquid in terms of steady circulation patterns. These large scale circulations form the third source to liquid turbulence by cascading in a way similar to the other turbulent flows where largest of the scale extract the kinetic energy and it is finally dissipated at the smallest scales. In the current paper, we show the features of the turbulence in gas-liquid as well as the solid liquid dispersions, inside the dispersion and describe its features in different regimes of spectrum.

Figure 5.29 shows the bubble trajectories for $V_G = 3.33$ mm/s, $V_G = 10$ mm/s and $V_G = 30$ mm/s. It can be observed from Figure 5.29A that the bubbles rise in nearly sinuous paths at small gas hold-up. However, it can be observed that their sinuous trajectories are disturbed by large scale circulation at $V_G = 10$ mm/s. This indicates the setting up of heterogeneity in the flow. On further increase in V_G , the flow is turbulent, with bubble trajectories losing their correlation rapidly. It can be observed in Figure 5.29C that the trajectories near centerline are relatively smooth, because they have been marked by large bubbles with larger relaxation time and hence less responsive to the fluctuating

liquid velocity. From the characteristics of the bubble traces in Figure 5.29C, it can be observed that they do not represent any sort of periodic motion and hence the flow is truly turbulent.

The reported work on turbulent spectra in bubbly flows has been plagued by the unavailability of a non-intrusive, spatially resolved measurement technique. Development of Particle image velocimetry in recent years has allowed us to explore the flow field inside the bubble swarm and solid-liquid fluidized bed. Present work is first attempt to evaluate turbulent spectrum inside the dispersion of particles and bubbles using PIV. The following subsection provides the discussion of the turbulence spectrum obtained using this method.

The simultaneous recording of PIV and shadow images allowed us to mark the regions where the bubbles are present and hence liquid and gas velocity can be obtained from high accuracy. Especially, the liquid in the vicinity of the bubbles can also be evaluated with enhanced precision since the reflections from the bubble interface are blocked by use of the fluorescent tracer particles. The use of camera with high resolution (2048x2048 pixels) allowed us to use the larger field of view than previous literature (10000 mm² compared to 2500 mm²). Using the interrogation area of 16x16 pixels, the accuracy of PIV evaluation was enhanced, while 128x128 vectors were obtained in the measurement window. The spatial series of the liquid velocity was used to evaluate the energy spectrum inside the heterogeneous bubble swarm using the methodology described in section 5.2.4.

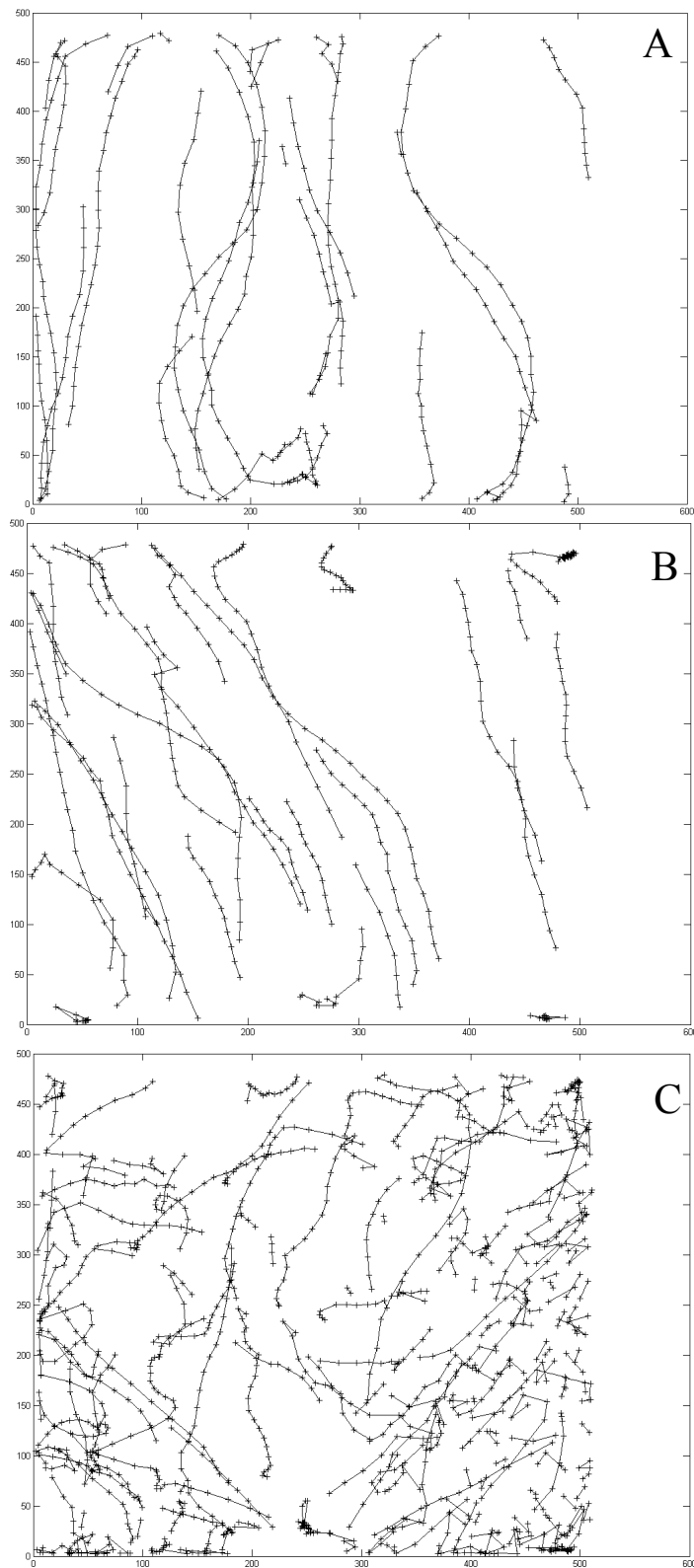


Figure 5.29. Bubble trajectories for different gas flow rates for 5 point sparger
(A) $10 \times 10^3 \text{ mm}^3/\text{s}$ (B) $30 \times 10^3 \text{ mm}^3/\text{s}$ and (C) $88 \times 10^3 \text{ mm}^3/\text{s}$

Figure 5.30 shows the energy spectrum of vertical component of liquid velocity for five point sparger, at $H/D=2$ for $V_G=10\text{mm/s}$ and 20 mm/s respectively. It can be observed that the spectrum has a well marked inertial subrange followed by a steeper slope of -3 (which has been described as the signature of the bubble induced turbulence). The regime of -3 slope is followed by the dissipation subrange with further steep slope till the spatial resolution has reached its limit and the spectrum shows aliasing at the highest resolved wavenumbers.

Figure 5.31 shows the energy spectrum of the vertical component of liquid velocity for three point sparger at $H/D=2$, for $V_G=10\text{mm/s}$ and 20 mm/s respectively. It can be observed that both the spectra have quite similar trend with the five point sparger. This implies that despite of difference in sparging locations, the heterogeneity attains its own self similar state. It can also be observed that transition in the slope from $-5/3$ to -3 is smooth in case of $V_G=20\text{ mm/s}$ while it shows an inflection in case of $V_G=10\text{ mm/s}$. It should be noted from the spatial bubble size distributions in [Figure 5](#) that the heterogeneity is less developed at $V_G=10\text{ mm/s}$. Hence, the turbulence intensity itself is less implying lesser developed cascade. Also, the bubble sizes, and hence the length scales of liquid circulations induced by the bubbles have wider distribution at higher superficial gas velocity which leads to a well developed spectrum.

The flow inside the heterogeneous bubble column is unsteady, and Figure 5.32 shows the time variation of the spectrum for 3 point sparger case. It can be observed that the integral turbulent kinetic energy fluctuates with respect to time. However, the trend of the spectrum is similar during all the time variations, for both the superficial gas velocities.

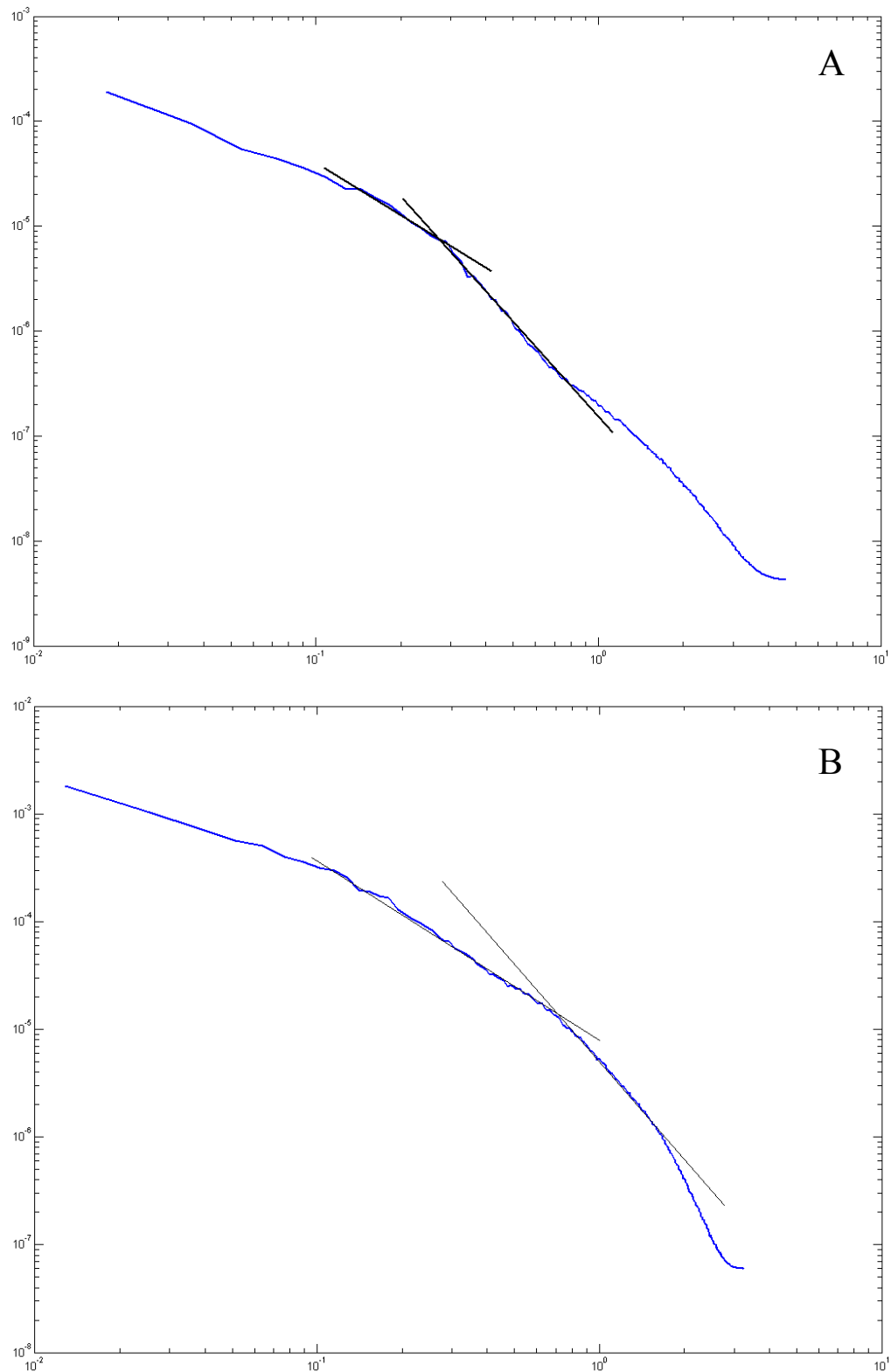


Figure 5.30. Power spectrum of vertical liquid velocity fluctuations for 5 point sparger
(A) $V_G = 10$ mm/s (B) $V_G = 20$ mm/s

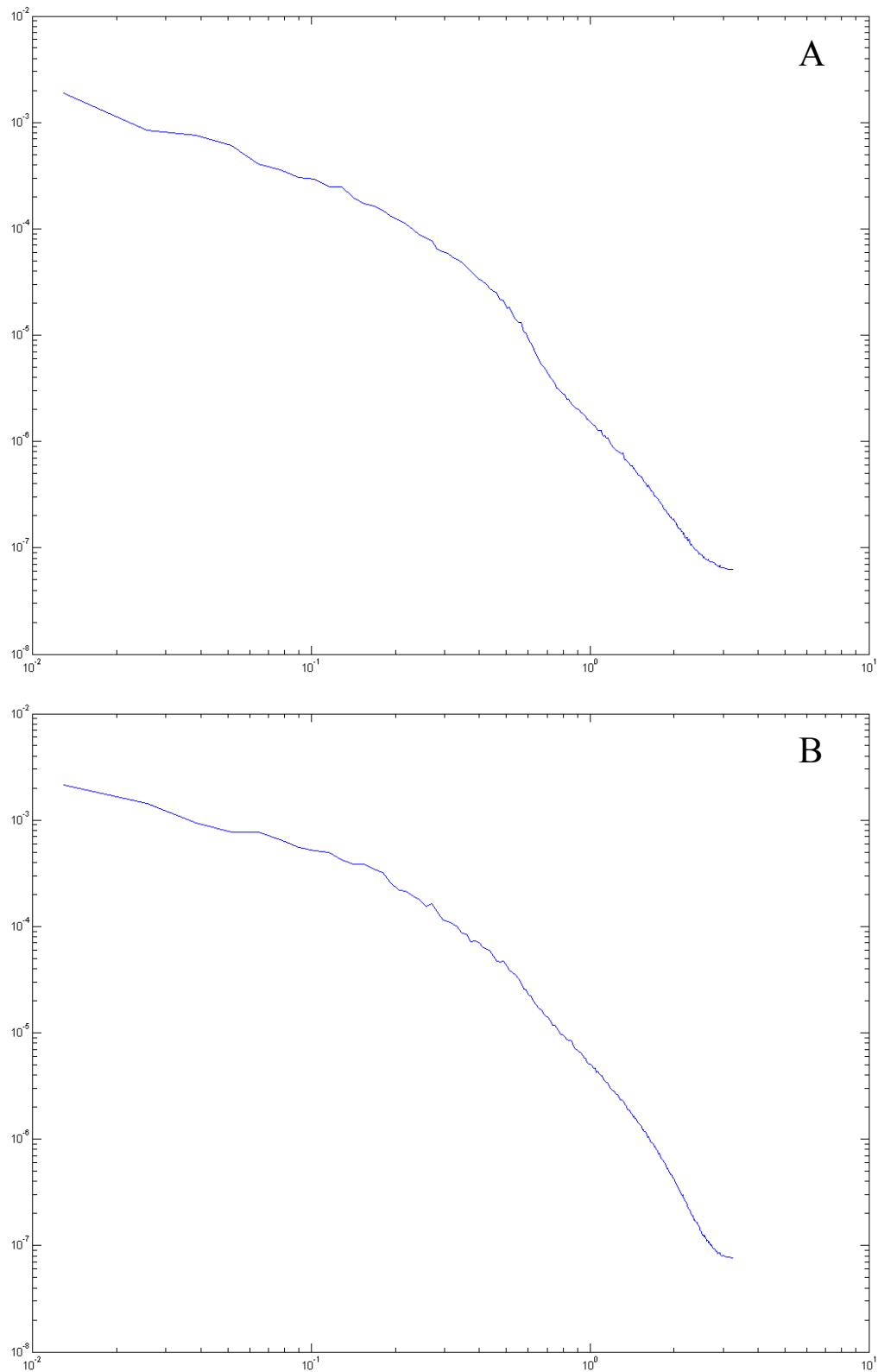


Figure 5.31. Power spectrum of vertical liquid velocity fluctuations for 3 point sparger
(A) $V_G = 10$ mm/s (B) $V_G = 20$ mm/s

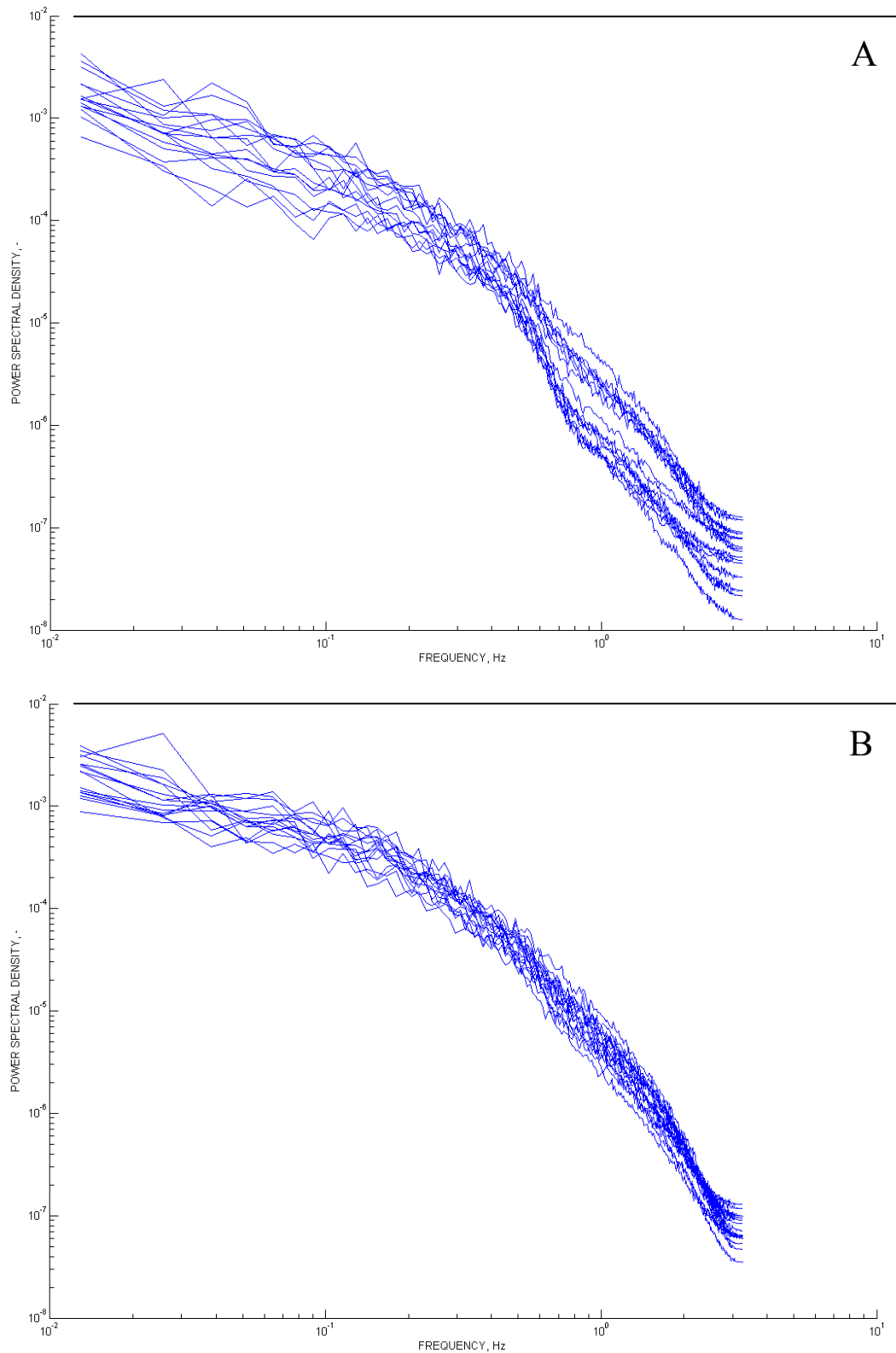


Figure 5.32. Time evolution of Power spectrum for 3 point sparger

(A) $V_G = 10$ mm/s (B) $V_G = 20$ mm/s

The spectrum with slope of $-5/3$ before the slope of -3 is different from the findings of Riboux et al. (2009) and Martinez Mercado et al. (2010). To understand the difference between the energy spectrum behind the swarm of bubbles and inside the swarm of bubbles, it was thought desirable to study a similar system of the flow over the fluidized bed of the spherical solid particles. The flow around the particles and the bubbles is different from the point of view of deformability of the bubbles and the difference in the slip boundary condition at the bubble interface. However, the flow in swarm of bubbles and particles is similar from point of view of the turbulence generated by interaction of vortices generated by the random motion and reversing flow around individual particles. Riboux et al. (2009) assumed that the turbulence behind the rising bubble swarm has similar characteristics to that inside the swarms. Figure 5.33 shows the turbulent kinetic energy of the liquid above the interface of the solid-liquid fluidized bed. This is just the reverse for the rising swarm through the liquid. It can be observed that the turbulent kinetic energy decreases with increase in the height- hence the turbulence is inhomogeneous. Although the decay occurs very fast immediately above the boundary of the fluid bed, the turbulent kinetic energy is very high inside the fluidized bed which cannot be neglected.

Figure 5.34A, 5.34B and Figure 5.35A show the turbulent energy spectrum of the liquid above the fluidized bed. The spectra have been calculated in similar fashion with Riboux et al. (2009) for three different bed voidages (and hence solid hold-up). These three spectra have similar trend of having slope -3 which is followed by slope of $-5/3$. Figure 5.35 B shows time variation of the spectrum. It can be observed that although the integral turbulent kinetic energy is fluctuating, the spectra are maintaining their shape.

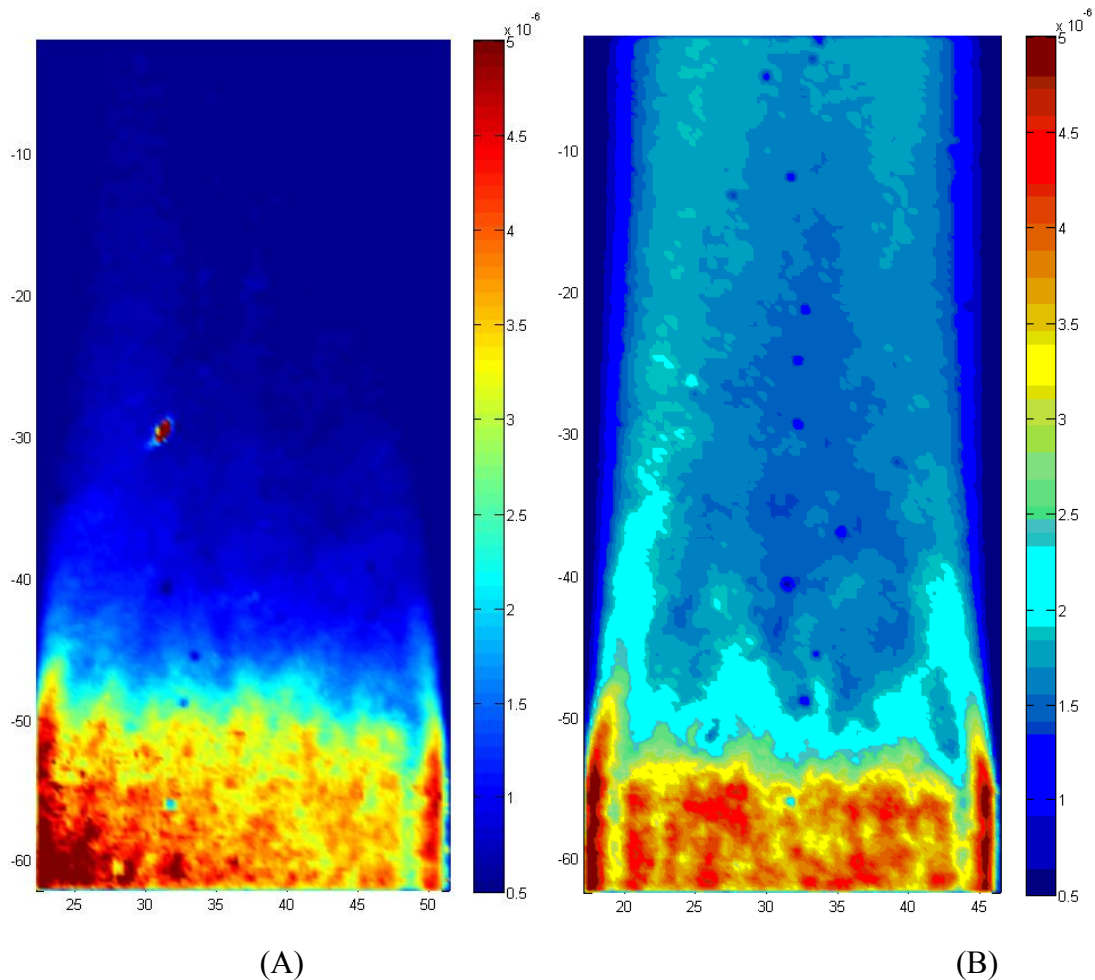


Figure 5.33. Turbulent kinetic energy contours above the homogeneous fluidized bed
(A) bed voidage of 0.6 (B) bed voidage of 0.65

While drawing any conclusion, it must be noted that the spectra have been obtained for the spatial series in which the turbulent kinetic energy is variable- and hence it is bound to have artifacts of this neglected kinetic energy variation ('the trend' in the terminology of signal processing) within the spatial series of velocity.

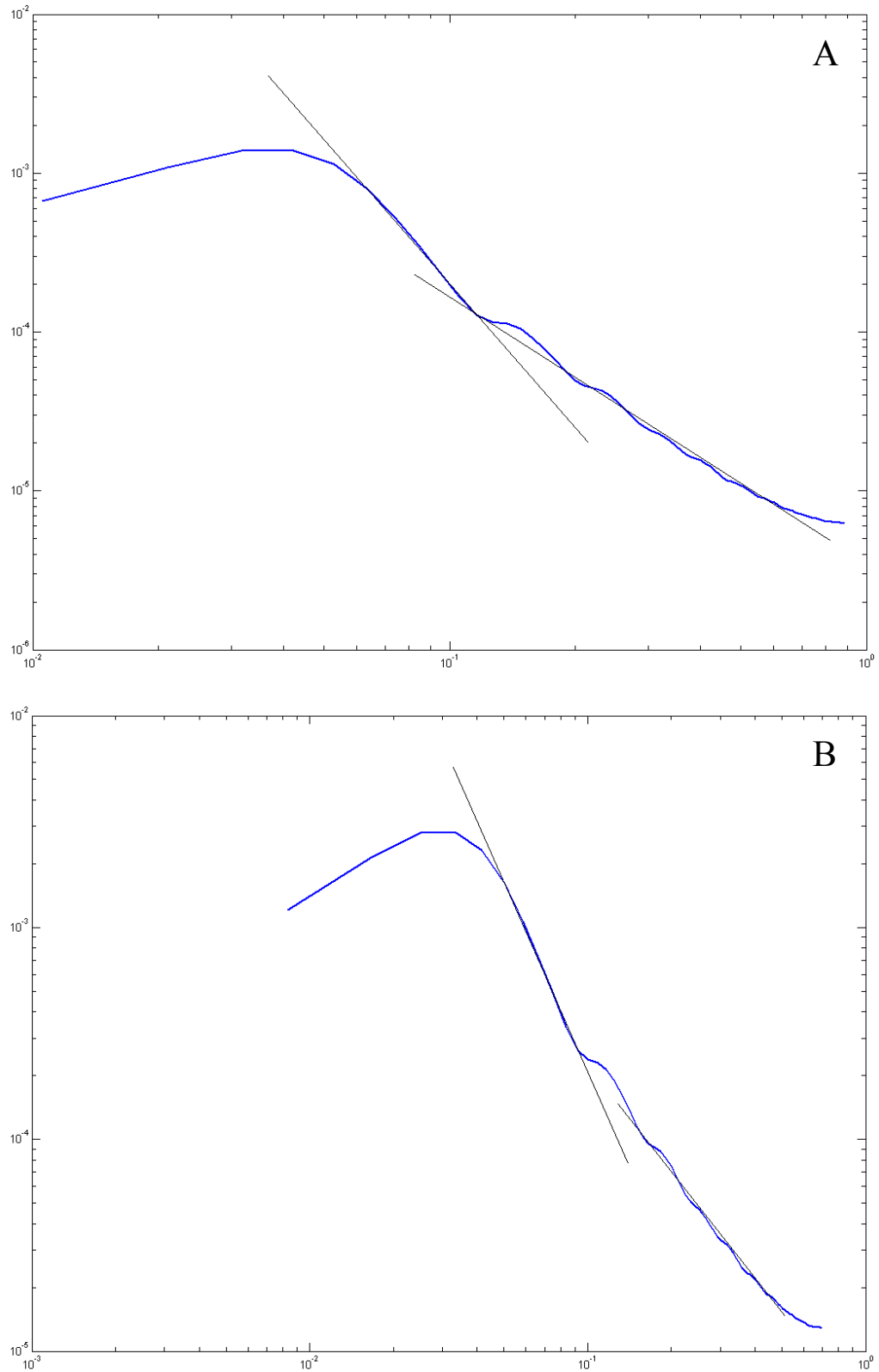


Figure 5.34. Power spectrum in decaying turbulence over fluidized bed

(A) bed voidage of 0.6 (B) bed voidage of 0.65

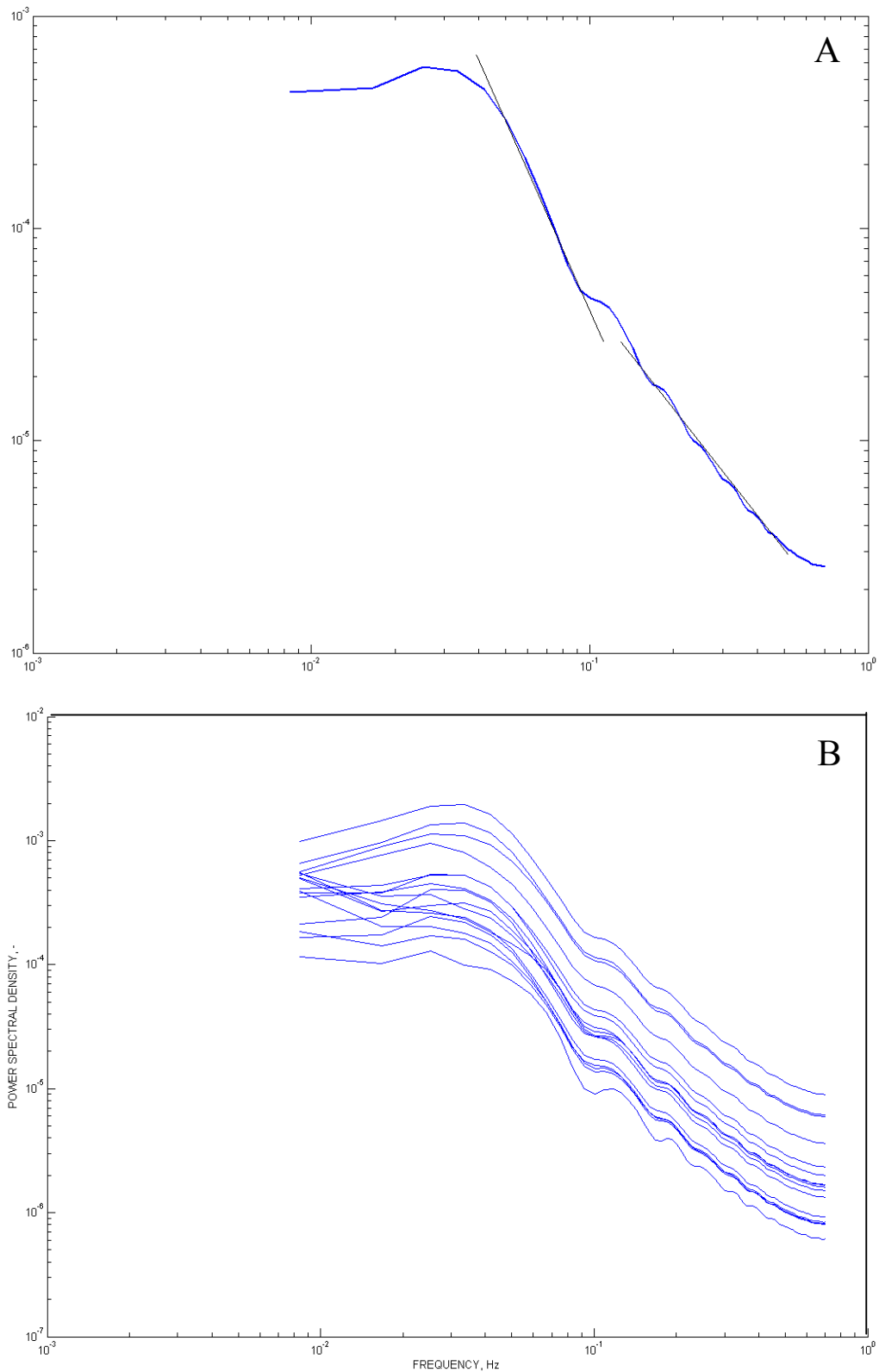


Figure 5.35. Power spectrum for decaying turbulence from fluidized bed (A) bed voidage of 0.7 (B) time variation of spectrum for bed voidage of 0.7

5.5. Conclusions

Measurement of turbulence in solid-liquid fluidized bed and rectangular bubble column is described. The experimental data is analyzed for various quantifiers like PDF of velocity, structure functions and energy spectrum. The turbulence in fluidized bed was observed to be homogeneous. The decay of turbulence downstream the fluidized bed was found to have similar behavior as that of the decay of grid generated turbulence, i.e. Saffman turbulence. This implies that the fluidized bed generates turbulence similar to a grid of bars. The liquid velocity within fluidized bed was measured with refractive index matched particle image velocimetry. Using this flow field, the parameters like turbulent kinetic energy and energy spectra were calculated. The results clearly indicate that the turbulence is homogeneous. Hence, the fluidized bed can be used as the turbulence generator for the study of drag coefficients of bubbles and particles in turbulent flows. It will prove to be better than decaying grid turbulence or the turbulence created by oscillating grids in the light of its homogeneity and a wide variation of turbulent kinetic energy possible by selecting appropriate fluidization particles.

The heterogeneous flow inside bubble column was characterized using PIV/PLIF technique. The results indicate that even in heterogeneity of the turbulence, the structure of turbulence is preserved in the form of the behavior of energy spectra. The energy spectrum in bubble column calculated using current methodology was found to agree qualitatively with the available literature, with certain difference. Both the slope of -3 and -5/3 are present in the energy spectrum of bubble column. Hence, the contribution from both- the bubble induced turbulence (Pseudo turbulence) and true turbulence both are present simultaneously in the flow field.

Nomenclature

N_b	number of bubbles, -
Re	Reynolds number, -
We	Weber number, -
ϵ_G	fractional gas hold-up, -
ϵ	liquid hold-up, -
V	Axial liquid velocity, m/s
V_{RMS}	RMS axial liquid velocity, m/s
$\langle V \rangle$	Time averaged liquid axial velocity, m/s
V_G	Superficial gas velocity, m/s
d	diameter of bubble/particle, m
C_D	drag coefficient, -
r	distance from the bubble, m
k	wavenumber
b	bubble parameter, -
U_r	bubble rise velocity, -
u_0'	turbulent vertical fluctuation, m/s
Re_p	particle Reynolds number, -
$\langle \alpha \rangle$	overall gas volume fraction
α	local gas volume fraction
t	time, s
H	height, m
ξ	Phase discrimination marker function, -
ν	Kinematic viscosity, m^2/s
r_x	Separation between two points, m
D_p	Particle diameter, m

References

- Bolotnov, I. A., Lahey, R. A. Jr., Drew, D. A. and Jansen, K. E., 2008. Turbulent cascade modeling of single and bubbly two-phase turbulent flows. *International Journal of Multiphase Flow*, 34, 1142–1151.
- Bunner, B. and Tryggvason, G. 2002a Dynamics of homogeneous bubbly flows. Part 1. Rise velocity and microstructure of the bubbles. *Journal of Fluid Mechanics*, 466, 17–52.
- Bunner, B. and Tryggvason, G. 2002b Dynamics of homogeneous bubbly flows. Part 2. Velocity fluctuations. *Journal of Fluid Mechanics*, 466, 53–84.
- Bunner, B. and Tryggvason, G. 2003 Effect of bubble deformation on the properties of bubbly flows. *Journal of Fluid Mechanics*, 495, 77–118.
- Calfish, R. E. and Luke, H. C. 1985 Variance in the sedimentation speed of a suspension. *Physics of Fluids*, 28, 759–760.
- Cartellier, A. and Riviere, N. 2001 Bubble-induced agitation and microstructure in uniform bubbly flows at small to moderate particle Reynolds number. *Physics of Fluids*, 13, 8.
- Clift, R., Grace, J.R. and Weber, M. E., 1978. *Bubbles, drops and particles* New York: Academic Press.
- Cui, Z. and Fan, L. S. 2004 Turbulence energy distributions in bubbling gas–liquid and gas–liquid–solid flow systems. *Chemical Engineering Science*, 59, 1755–1766.
- Davidson, J. F. and Harrison, D., 1966. The behavior of a continuously bubbling fluidized bed. *Chemical Engineering Science*, 21, 731–738.
- Esmaeeli, A. and Tryggvason, G. 2005 A direct numerical simulation study of the buoyant rise of bubbles at $O(100)$ Reynolds number. *Physics of Fluids*, 17, 093303.
- Garnier, C., Lance, M. and Marié, J. L. 2002 Measurement of local flow characteristics in buoyancy driven bubbly flow at high void fraction. *Experimental Thermal and Fluid Science*, 26, 811–815.
- Griffith, P. and Wallis, G. B., 1961. Two-phase slug flow. *Journal of Heat Transfer*, 83, 307–320.
- Hunt, J. C. R. and Eames, I. 2002 The disappearance of laminar and turbulent wakes in complex flows. *Journal of Fluid Mechanics*, 457, 111–132.
- Koch, D. L. 1993 Hydrodynamic diffusion in dilute sedimenting suspensions at moderate Reynolds numbers. *Physics of Fluids A*, 5, 1141–1155.
- Lance, M. and Bataille, J. 1991 Turbulence in the liquid phase of a uniform bubbly air–water flow. *Journal of Fluid Mechanics*, 222, 95–118.
- Lance, M. and Bataille, J. 1991 Turbulence in the liquid phase of a uniform bubbly air–water flow. *Journal of Fluid Mechanics*, 222, 95–118.
- Larue de Tournemine, A 2001 Etude expérimentale de l’effet du taux de vide en écoulements diphasiques à bulles. PhD thesis, University of Toulouse.

DEVELOPMENT OF EXPERIMENTAL TECHNIQUES AND CFD SIMULATIONS OF MULTIPHASE DISPERSIONS

- Martínez-Mercado, J., Palacios-Morales, C. and Zenit, R. 2007 Measurements of pseudoturbulence intensity in monodispersed bubbly liquids for $10 < \text{Re} < 500$. *Physics of Fluids*, 19, 103302.
- Martinez-Mercado, J., Gomez, D.C., Gils, D.V., Sun, C. And Lohse, D., 2010. On bubble clustering and energy spectra in pseudo-turbulence. *Journal of Fluid Mechanics*, 650, 287–306.
- Mudde, R. F., Groen, J. S. and van der Akker, H. E. A. 1997 Liquid velocity field in a bubble column: LDA experiments. *Chemical Engineering Science*, **52**, 4217–4224.
- Nguyen, A.V., 1998. Prediction of bubble terminal velocities in contaminated water. *AIChE Journal*, 44, 226-230.
- Panidis, T. and Papailiou, D. D. 2002. Water air bubble grid turbulence. *Chemical Engineering and Technology*, 25, 455-458.
- Parthasarathy, R. N. and Faeth, G. M. 1990 Turbulence modulation in homogeneous dilute particle-laden flows. *Journal of Fluid Mechanics*, **220**, 485–514.
- Poorte, R. E. G. and Biesheuvel, A. 2002 Experiments on the motion of gas bubbles in turbulence generated by an active grid. *Journal of Fluid Mechanics*, 461, 127–154.
- Rensen, J., Luther, S. and Lohse, A. 2005 The effect of bubbles on developed turbulence. *Journal of Fluid Mechanics*, **538**, 153–187.
- Riboux, G., Risso, F. and Legendre, D., 2009. Experimental characterization of the agitation generated by bubbles rising at high Reynolds number. *Journal of Fluid Mechanics*, 643, 509-539.
- Risso, F. and Ellingsen, K. 2002 Velocity fluctuations in a homogeneous dilute dispersion of high-Reynolds-number rising bubbles. *Journal of Fluid Mechanics*, 453, 395–410.
- Risso, F., Roig, V., Amoura, Z., Riboux, G. and Billet, A.-M. 2008 Wake attenuation in large Reynolds number dispersed two-phase flows. *Philosophical Transactions of Royal Society A*, **366**, 2177–2190.
- Roig, V. and de Tournemine, L. 2007 Measurement of interstitial velocity of homogeneous bubbly flows at low to moderate void fraction. *Journal of Fluid Mechanics*, 572, 87–110.
- Sugiyama, K., Takagi, S. and Matsumoto, Y. 2001 Multi-scale analysis of bubbly flows. *Computational Methods for Applied Mechanical Engineering*, **191**, 689 –704.
- Thakre, S. S. and Joshi, J.B., 1999. CFD Simulation of Flow in Bubble Column Reactors: Importance of Drag Force Formulation. *Chemical Engineering Science*, **54**, 5055-5060.
- Zahradnik, J., Fialova, M., Ruzicka, M., Drahos, J., Kastanek, F. and Thomas, N.H., 1997. Duality of the gas–liquid flow regimes in bubble column reactors. *Chemical Engineering Science*, 52, 3811–3826.
- Zenit, R., Koch, D. L. and Sangani, A. S. 2001 Measurements of the average properties of a suspension of bubbles rising in a vertical channel. *Journal of Fluid Mechanics*, 429, 307–342.

Chapter 6

LARGE EDDY SIMULATION OF BUBBLE COLUMN REACTORS

6.1. Introduction

In this type of reactor, local flow, turbulence and gas hold-up distribution are interrelated in a complex way with the operating and design variables; hence the extensive knowledge of prevailing hydrodynamics is crucial. Development of detailed fluid dynamic model is therefore essential to understand these complex interactions, which is beneficial for the reliable and efficient design of these reactors. The complex hydrodynamics of bubble columns has inhibited the development of design procedures from first principle. Hence, during the past 45 years, vigorous attempts have been made to understand the flow pattern using various techniques of flow visualization and mathematical modeling in bubble columns. Joshi (2001) and Sokolichin et al. (2004) have critically analyzed the investigations and have made a coherent presentation of the current status. Joshi (2001) has classified the entire modeling effort into three phases. Phase I and II models were made simple by making many assumptions which ultimately incorporate fair degree of empiricism. In the Phase III models, the foremost emphasis has been given on the reduction of empiricism by ensuring completeness of the formulation of continuity and momentum equations. Moreover, the comprehensive developments in the Computational Fluid Dynamics (CFD) in the past few decades have strengthened the Phase III models, which has generated hope of complete understanding of fluid mechanics with a caution of the arduous task ahead thus giving a better knowledge of existing hydrodynamics.

It is well known that a major problem in realizing a CFD code is to capture the physics behind the phenomena occurring in bubble columns. The interaction between the dispersed gas phase and the continuous liquid phase affects the interphase forces (e.g. drag force, lift force and added mass force) and turbulence in the column. Therefore, the correct modeling of interphase forces and turbulence is of prime importance for

capturing the physics correctly. Several models for interphase forces have been reported in the literature, a detailed account of which is provided by Joshi (2001) and recently by Rafique et al.(2004). Another critical issue in the CFD modeling of bubble column is the proper description of turbulence in the continuous phase. Researchers have tested different closures [standard $k-\varepsilon$ model, Reynolds Stress Model (RSM), Large Eddy Simulation (LES)] for turbulence, and amongst these, the standard $k-\varepsilon$ model is the most adopted one owing to its simplicity and lesser computational requirement.

LES equations of turbulent flows are formally derived by applying a filtering operation to the Navier-Stokes equation and assuming that filtering and differentiation operators' commute (Leonard, 1974). The filtering process effectively filters out the eddies whose scales are smaller than the filter width or grid spacing used in the meshing. The resulting equations have the structure as the original equation plus additional terms, called subgrid scale stresses (SGS). The filtered equations are used to compute the dynamics of the large-scale structures, while the effect of the small scale turbulence is modeled using a SGS model. The motivation behind LES is the recognition that the large scales of the turbulence often dominate mixing, heat transfer, and other quantities of engineering interest, while the small scales are only of interest because of how they affect the large ones. Furthermore, large scales are not universal and vary according to the geometry and flows under consideration, while small scales exhibit a more or less universal behavior, which considerably simplifies the task of modeling the SGS stresses.

6.2. Literature review

Lakehal et al. (2002) were the first ones to employ LES model for a bubbly flow. Their system involved a vertical bubbly shear flow at a very low void fraction (1.9 %). From their study, they suggested that for obtaining better results the optimum cut off filter should be 1.5 times the bubble diameter. They observed that the dynamic approach

of Germano does not perform better than Smagorinsky model, which they felt could be due to the inadequate dimensions of their computational domain. This study suggested that the LES approach can be promising for predicting the phase velocities and the void fraction, and it emphasized on the need to carry out more LES simulations on complex systems such as buoyancy driven flow operating at higher void fractions. In this context, Deen et al. (2001) were the first one to apply the LES model to simulate a bubble column, and they reported observing a better resolved flow using LES than $k-\varepsilon$ model, as discussed previously.

Bove et al. (2004) used the same geometry as Deen et al. (2001) to study the influence of different numerical schemes, of different drag models and of initial flow conditions on LES performance. They observed that the use of a second order FCT scheme for LES simulation enhanced its performance. But they suggested the need to carry out more tests on LES with higher order schemes and finer grid resolutions, before identifying the best numerical scheme for LES simulations. It was seen that the LES results were very sensitive to initial boundary conditions. In this work it seems that the sparger (individual holes in it) was not modeled due to difficulties in adapting the mesh grid to the geometry. The modeling of holes as source points could have made this work more interesting. This work also suggested that there is a need to pay attention towards near wall region as the sub-grid scale models do not account for near wall region processes which can lead to erroneous prediction of frictional stresses at the wall.

Bombardelli et al. (2006) used a finite element based LES code for simulating and analyzing the phenomena of wandering bubble plumes as in experiments conducted by Becker et al. (1994). They observed that LES was been able to capture the instability associated with wandering more vividly as compared to $k-\varepsilon$ simulation. They analyzed the plume for coherent structures arising out of interplay of eddies and bubbles by

studying the vorticity contours. Their work showed the evolution of number of eddies and their interrelation with the bubble plume. In this work, the velocity conditions at the wall were set so as to enforce the law of the wall using the LES-Near Wall Modeling (NWM) approach, but the effect this approach has on the simulation results, as compared to the conventional LES-Near Wall Resolution (NWR) approach is not yet known.

Zhang et al. (2006) took forward the work of Deen et al. (2001) by investigating the effect of smagorinsky constant and the interfacial closures for drag, lift and virtual mass force in two columns having different aspect ratio ($H/D=3,6$). They have considered two set of interfacial closures; (1) as proposed by Tomiyama (2004), and (2) The Ishii-Zuber (1979) drag model, along with lift and added mass forces having a constant coefficient value of 0.5. They observed that, by increasing the value of smagorinsky constant, the bubble plume dynamics dampens, and consequently a steep mean velocity profile is seen. They obtained good agreement with experimental results when the value of smagorinsky constant was used in the range of 0.08-0.10. They also suggested that, for taller columns ($H/D = 6$), interfacial force closures proposed by Tomiyama (2004) gave better agreements with experiments.

6.3. Equipment

The Two columns are considered for simulation: a narrow rectangular column and a cylindrical bubble column. The rectangular column had width of 200 mm, depth of 15 mm and height of 800 mm. Two spargers were used: Single point and 5 point. The superficial gas velocity was 20 mm/s. The cylindrical column had diameter of 150 mm and height of 800 mm. The simulations were carried out for same superficial velocity of 20 mm/s.

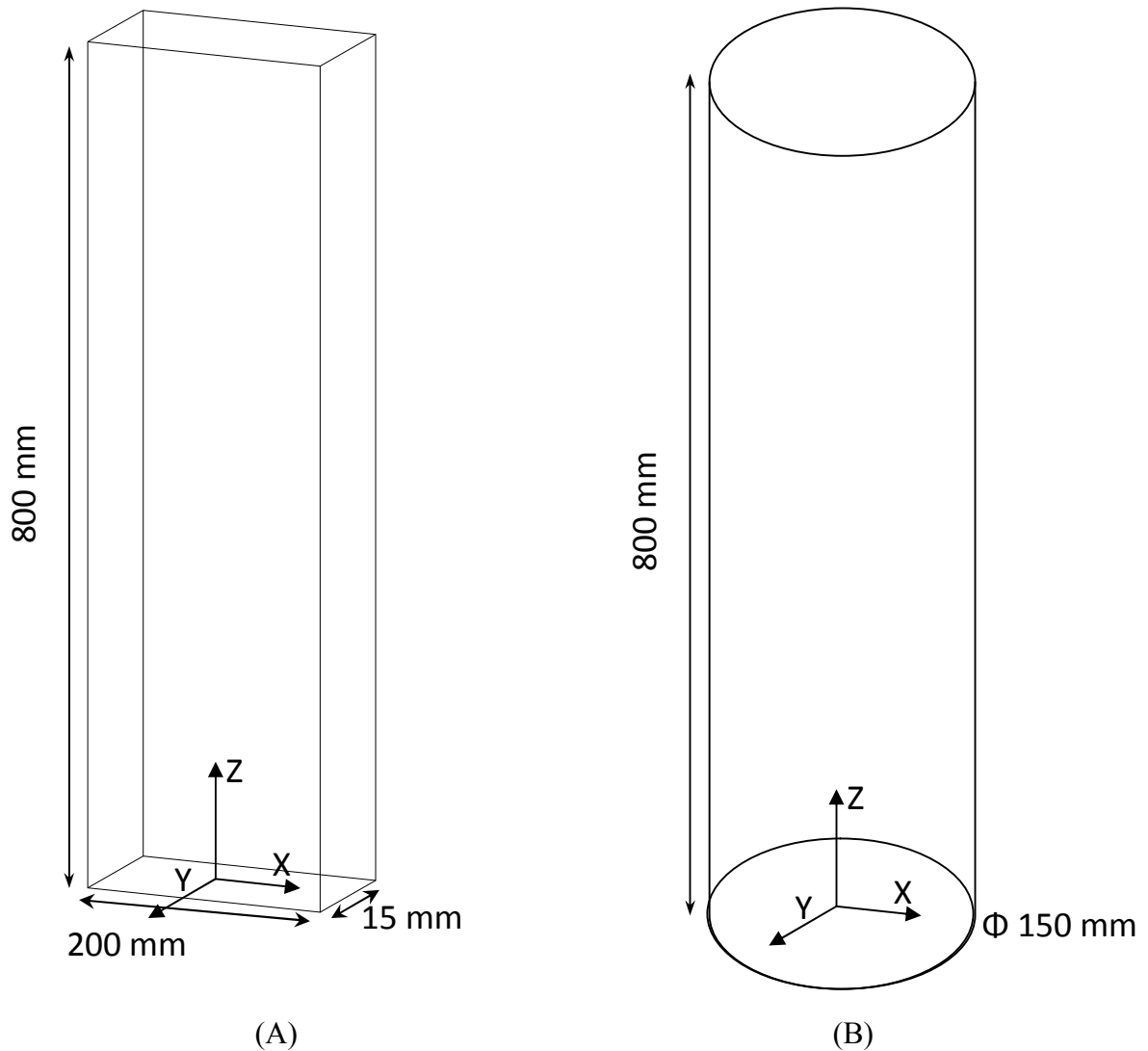


Fig. 6.1: Geometry of rectangular column (A) Rectangular column (B) Cylindrical column

6.4 Details of Simulation

A typical grid layout for two different geometries is shown in Fig. 6.1. Maximum mesh size of around 100 times the kolmogorov length scale was used, which worked out to be about 3 mm at the centre. The hexahedral grid with 200000 nodes was used for rectangular column, while hexahedral grid with 1600000 nodes was used for cylindrical bubble column. The kolmogorov length scale was calculated using integral energy dissipation results of the k- ϵ model. While near the wall, the mesh size is around 0.1 mm.

The gas inlet through the spargers was incorporated by creating mass source points at the specified position to mimic the exact sparger. Based on the superficial gas velocity (0.02 m/sec), the mass flow rate was specified for each source point. Along the walls, no-slip boundary conditions were adopted. A degassing outlet (which allows only gas phase to pass through) at the outlet of the column was used, with the atmospheric pressure as boundary condition.

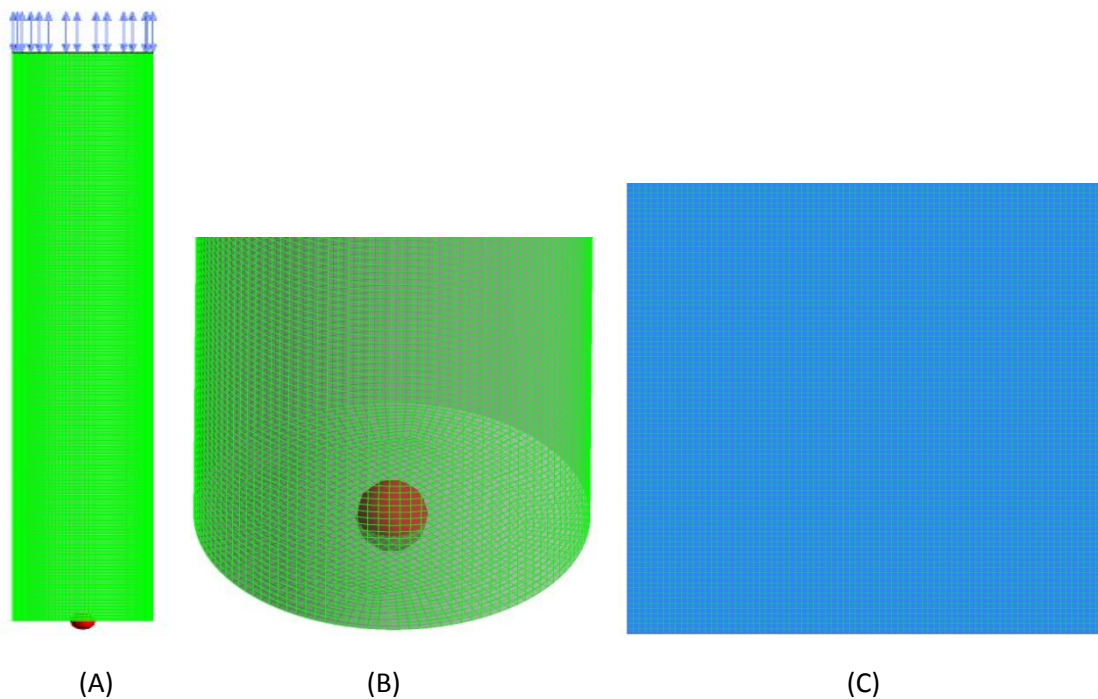


Fig. 6.2. Grid used for LES simulation of (A,B) Cylindrical column (C) Rectangular column

The conservation equations were discretized using the control volume technique. The velocity-pressure linkage was handled through the SIMPLE procedure. The hybrid-upwind discretization scheme was used for the convective terms. A time step of 0.001 sec was used for LES simulations.

6.5. Equations for Large eddy simulation

Following are the flow governing equations for LES.

$$\frac{\partial \rho}{\partial t} + \frac{\partial \rho}{\partial x_i} = 0 \quad (6.1)$$

$$\frac{\partial \rho}{\partial t} (\overline{u_i}) + \frac{\partial \rho}{\partial x_j} (\overline{u_i u_j}) = \frac{\partial}{\partial x_j} \left(\nu \frac{\partial \overline{u_i}}{\partial x_j} \right) - \frac{1}{\rho} \frac{\partial P}{\partial x_i} - \frac{\partial \tau_{ij}}{\partial x_j} \quad (6.2)$$

Where τ_{ij} in Eq 6.2 is the subgrid scale (eddies smaller than grid spacing) stress is defined by

$$\tau_{ij} = \overline{u_i u_j} - \overline{u_i} \overline{u_j} \quad (6.3)$$

The major difference between the Reynolds averaged Navier Stokes equations and the above equation is that the dependent variables are filtered quantities rather than the mean quantities. The subgrid scale stresses resulting from the filtering operation are unknown and require modeling. Most of the past work on LES of stirred vessels employed algebraic models in which subgrid-scale stresses are parameterized using the resolved velocity scales. The underlying assumption is the local equilibrium between the transferred energy through the grid-filter scale and the dissipation of kinetic energy at small sub-grid scales. The subgrid-scale turbulence can be better modeled by accounting for the transport of the subgrid-scale turbulence kinetic energy. The dynamic kinetic energy SGS model in FLUENT replicates the model proposed by Kim and Menon (1997), which has been used in the present work. The subgrid-scale kinetic energy is defined as (Kim and Menon , 1997):

$$k_{sgs} = \frac{1}{2} \left(u_k^2 - (\overline{u_k})^2 \right) \quad (6.4)$$

This is obtained by contracting the subgrid-scale stress in Eq. 6.2. The subgrid-scale eddy viscosity, ν_t , is computed using k_{sgs} as (Kim and Menon, 1997):

$$v_t = C_k k_{sgs}^{1/2} \Delta \quad (6.5)$$

The subgrid-scale stress can then be written as

$$\tau_{ij} = \frac{2}{3} k_{sgs} \delta_{ij} = -2C_k k_{sgs}^{1/2} \Delta \bar{S}_{ij} \quad (6.6)$$

k_{sgs} is obtained by solving its transport equation given by:

$$\frac{\partial \bar{k}_{sgs}}{\partial t} + \frac{\partial \bar{u}_j \bar{k}_{sgs}}{\partial x_j} = -\tau_{ij} \frac{\partial \bar{u}_j}{\partial x_j} - C_\varepsilon \frac{k_{sgs}^{3/2}}{\Delta} + \left(\frac{\partial}{\partial x_j} \frac{v_t}{\sigma_k} \frac{\partial \bar{k}_{sgs}}{\partial x_j} \right) \quad (6.7)$$

In the above equations, the model constants, C_k and C_ε , are determined dynamically.

6.5.1. Euler--Euler description of the flow field

In the two-fluid model description of a bubbly flow, we have one set of governing equations per phase, plus the expressions for the interface exchange terms. To keep the number of unknowns equal to the number of equations, we assume the pressure to be the same for both phases. The governing equations for the conservation of mass, with no mass exchange between the phases, takes the form

$$\frac{\partial}{\partial t} (\gamma \rho)_\alpha + \nabla (\gamma \rho \bar{\mathbf{u}})_\alpha = 0 \quad (6.8)$$

in which t is time, α is the phase indicator, γ , ρ , and $\bar{\mathbf{u}}$ are the volume fraction, density, and resolved (filtered) velocity of phase α . Momentum conservation is expressed by the following equation:

$$\frac{D(\gamma \rho \bar{\mathbf{u}})_\alpha}{Dt} = -\nabla (\gamma \mu \bar{S}_{ij})_\alpha - \gamma_\alpha \nabla p + (\gamma \rho)_\alpha \mathbf{g} + \mathbf{M}_\alpha - \nabla (\gamma \tau_{ij})_\alpha \quad (6.9)$$

Where $\bar{S}_{ij} = \nabla \bar{\mathbf{u}} + (\nabla \bar{\mathbf{u}})^T$ is the strain rate of the resolved velocity field, p is the pressure, is the SGS stress tensor, \mathbf{g} is the gravity vector, and M_α is the momentum exchange between the phases due to interface forces. The D/Dt operators denote the substantial derivatives. The SGS stress tensor and momentum exchange terms from Eq. (6.9) require modelling, and will be discussed below. Eqs. (6.8) and (6.9) are usually derived by ensemble averaging. However, the same form of equations are obtained if one performs filtering (volume averaging) of the governing equations (Drew and Passman, 1999). This is of practical importance for LES, because it means that the same numerical tools developed for ensemble averaged Euler--Euler equations, can be used for LES.

The Boussinesq hypothesis is used in all turbulence models used in this work, so Eq. (6.9) can conveniently be written as

$$\frac{D(\gamma \rho \bar{\mathbf{u}})_\alpha}{Dt} = -\nabla \left(\gamma \mu_{eff} \bar{S}_{ij} \right)_\alpha - \gamma_\alpha \nabla p + (\gamma \rho)_\alpha \mathbf{g} + \mathbf{M}_\alpha - \nabla \left(\gamma \tau_{ij} \right)_\alpha \quad (6.10)$$

where μ_{eff} is effective viscosity, defined as

$$\mu_{eff} = \mu + \mu_T + \mu_{BIT} \quad (6.11)$$

Here μ_T is turbulent (eddy) viscosity, obtained from a turbulence model, and μ_{BIT} is viscosity due to BIT.

6.5.2. LES of turbulence

Turbulence is modelled for the continuous (liquid) phase. The dispersed gas phase is modelled as laminar. For the sake of brevity, the index of the liquid phase is dropped from the equations describing turbulence models.

Velocities in Eqs. (6.8) and (6.9) represent the part of the velocity field resolved by the numerical method and are defined as follows:

$$\bar{\mathbf{u}} = \mathbf{u} - \mathbf{u}' \quad (6.12)$$

where \mathbf{u} is the true velocity and \mathbf{u}' is the SGS part, not resolved by the numerical simulation. These SGS parts of velocity components, gives rise to additional stress terms and interface forces. The SGS stress terms of phase are related to the resolved scale

strain tensor $\left(S_{ij} \right)$ described as

$$\tau_{ij} - \frac{1}{3} \tau_{kk} \delta_{ij} = 2\mu_T S_{ij} \quad (6.13)$$

Eq. (6.13) shows that we are modelling only the deviatoric part of the SGS, while its

trace $\left(\tau_{kk} \right)$ is implicitly added to the pressure. This means that the information on the

amount of SGS kinetic energy $\left(k_{sgs} \right)$ is lost in algebraic models, unless one introduces a model equation to account for it.

Two different SGS models are used to compute μ_T . One is the dynamic procedure proposed by Germano, and the other is a one-equation transport equation for SGS kinetic energy.

6.5.3. Dynamic procedure

The dynamic procedure used in this work is based on the Smagorinsky model.

The turbulent viscosity is calculated from the Smagorinsky model as follows:

$$\mu_{T,L} = \rho_L \left(C_S \Delta \right)^2 \left| \bar{S}_{ij} \right| \quad (6.14)$$

where C_S is a model constant and $|\overline{S}_{ij}|$ is the magnitude of the strain rate tensor, and Δ is filter width, in this work taken as the grid spacing, which is equal in all coordinate directions. A dynamic procedure is used to calculate model constant C_S from the expression:

$$\left(C_S \Delta\right)^2 = \frac{1}{2} \frac{L_{ij} M_{ij}}{M_{ij} M_{ij}} \quad (6.15)$$

where

$$L_{ij} = \widehat{\widehat{u_i u_j}} - \widehat{u_i} \widehat{u_j} \quad (6.16)$$

and

$$M_{ij} = \frac{\widehat{\Delta}}{\Delta} \left| \widehat{\widehat{S}_{ij}} \right| \widehat{S}_{ij} - \left| \overline{S}_{ij} \right| \overline{S}_{ij} \quad (6.17)$$

and the wide hat indicates a second filter, usually called the test filter, which is twice the mesh size in the present study. This is a standard procedure, and details can be found elsewhere (Germano et al., 1991; Germano, 1992; Lilly, 1992).

An advantage of the dynamic procedure is that it calculates the model constant, in our case the Smagorinsky constant C_S . It should, theoretically model the backscatter as well (energy transfer from small to large scales), but in practical simulations this means that expression $(C_S \Delta)^2$ from Eq. (6.15) becomes negative, leading to negative eddy viscosity, making the solution procedure unstable. To avoid this problem, we trim the negative values of eddy viscosity.

6.5.4. *One-equation model*

Although the dynamic procedure calculates C_s , making the SGS modelling free of specifying constants, it does not provide information on the SGS kinetic energy (k_{sgs}). In this work, a transport equation for (k_{sgs}) is introduced. The trace of τ_{ij} defines the SGS kinetic energy:

$$k_{sgs} = \frac{1}{2} \tau_{kk} \quad (6.18)$$

The transport equation for k_{sgs} reads (Davidson, 1997)

$$\frac{Dk_{sgs}}{Dt} = \nabla \left[(\mu + \mu_T) \nabla k_{sgs} \right] + P_{k_{sgs}} - C_\varepsilon \frac{k_{sgs}^{3/2}}{\Delta} \quad (6.19)$$

where $P_{k_{sgs}}$ is the production term, defined as

$$P_{k_{sgs}} = \mu_T \overline{S_{ij}^2} \quad (6.20)$$

Eddy viscosity is calculated from

$$\mu_T = C_k \Delta k_{sgs}^{1/2} \quad (6.21)$$

Model constants are $C_\varepsilon = 1.05$ and $C_k = 0.07$, as suggested by Davidson (1997).

6.5.5. *Interface force modelling*

The term M_l in Eq. (6.9) represents the interface forces, and is given as

$$M_l = M_g = M_{D,l} + M_{L,l} + M_{VM,l} + M_{TD,l} \quad (6.22)$$

where subscripts l indicates the liquid phase and g the gas phase. The terms on the right-hand side of Eq. (6.22) are respectively: drag, lift, virtual mass, and turbulent dispersion

force. All these forces have grid scale and SGS component. In previous works on EELES (Smith and Milelli, 1998; Deen et al., 2001; Zhang et al., 2006), the SGS components of these forces were neglected, but in this work we make an attempt to envisage a way model the SGS turbulent dispersion force. Note that the grid scale turbulent dispersion is resolved as the fluctuating component of the drag force.

6.5.5.1. Drag force

A drag force occurs due to the resistance experienced by a body moving in the liquid. Viscous stress creates skin drag, whereas the pressure distribution around the moving body creates form drag. The drag force per unit volume is written in the following form (Clift et al., 1978):

$$\mathbf{M}_{D,l} = \frac{3}{4} \gamma \rho l \frac{C_D}{d_B} \left| \mathbf{u}_g - \mathbf{u}_l \right| \left(\mathbf{u}_g - \mathbf{u}_l \right) \quad (6.23)$$

The drag coefficient C_D depends on the flow regime and the liquid properties. The Reynolds number covered in the present work falls under the inertial range and as known from experimental visual observations bubbles become distorted in this regime. We calculate C_D for distorted bubbles following (Ishii and Zuber, 1979):

$$C_D = \frac{2}{3} Eo^{1/2} \quad (6.24)$$

where Eo is the dimensionless Eötvös number $\left(Eo = \frac{g \Delta d_B^2}{\sigma} \right)$.

6.5.5.2. Lift force

A bubble traveling through a fluid in shearing motion will experience a lift force transverse to the direction of motion. The effect of shearing motion in the liquid phase on the movement of the gas phase is modelled through the lift force as (Drew and Lahey, 1987; Zun, 1990):

$$\mathbf{M}_{L,l} = \frac{3}{4} \gamma_g \rho_l C_L (\mathbf{u}_g - \mathbf{u}_l) \times \nabla \times \mathbf{u}_l \quad (6.25)$$

where C_L is a model coefficient, set to a constant value of 0.5 for all simulations reported in this work.

6.5.5.3. Virtual mass force

The virtual mass force accounts for the additional work performed by the bubbles in accelerating the surrounding liquid (Jakobsen et al., 1997), and is given by

$$\mathbf{M}_{VM,l} = \gamma_g \rho_l C_{VM} \left(\frac{D\mathbf{u}_g}{Dt} - \frac{D\mathbf{u}_l}{Dt} \right) \quad (6.26)$$

where the virtual mass coefficient C_{VM} is generally shape dependent and is taken to be 0.5 for individual spherical bubbles. At the start of each run, initially the virtual mass force was deselected and this effect was taken into account by simply using an enhanced gas density (Smith and Milelli, 1998):

$$\rho_g' = \rho_g + C_{VM} \rho_l \quad (6.27)$$

in the acceleration term of the gas momentum conservation equation.

6.5.5.4. Turbulent dispersion force

It should be noted that the drag and lift forces depend on the actual relative velocity between the phases, but the ensemble equations of motion for the liquid only provide information regarding the mean flow field. To account for the random influence of the turbulent eddies, the concept of a turbulent dispersion force has been advanced. By analogy with molecular movement, the force is set proportional to the local bubble concentration gradient (or void fraction), with a diffusion coefficient derived from the turbulent kinetic energy.

In LES velocities are decomposed into a resolved and an SGS part, by filtering. We explicitly compute the resolved part of the turbulent dispersion. However, some transport is present at SGS level as well. The concept derived by Lopez de Bertodano et al. (1994) is used to approximate the turbulent diffusion of the bubbles by the liquid eddies. It is formulated as

$$\mathbf{M}_{TD,l} = C_{TD} \rho_l k_{sgs} \nabla \gamma_g \quad (6.28)$$

where C_{TD} is the turbulent dispersion coefficient. In the above equation we replace the total kinetic energy by the SGS contribution, which is based on the assumption that only SGS motions contribute to SGS transport of bubbles. The exact shape of these motions is unknown, but their intensity is represented in k_{sgs}

6.5.5.5. Bubble induced turbulence

Although the turbulence is modeled in the liquid phase only, the dispersed gas bubbles traveling through the liquid induce turbulence. The influence of BIT can be accounted for by increasing the eddy viscosity, using the model of Sato and Sekoguchi (1975):

$$\mathbf{M}_{D,l} = C_{BI} \rho_l \gamma_g d_B \left| \mathbf{u}_g - \mathbf{u}_l \right| \quad (6.29)$$

This approach is suitable for algebraic SGS models and it was explored by Deen et al. (2001). In this work, in addition to the Sato model, we explore the influence of BIT by adding the extra production terms into equation, following the procedure described by Pflieger and Becker (2001).

$$P_{BIT} = C_k \left| \mathbf{M}_{D,l} \right| \left| \mathbf{u}_g - \mathbf{u}_l \right| \quad (6.30)$$

where P_{BIT} is the extra production term in Eq. (6.19) and $\mathbf{M}_{D,l}$ is defined by Eq. (6.23).

C_k is defined following the rationale from (Pflieger and Becker, 2001), i.e. it corresponds to C_k in Eq. (6.19).

6.6. 3D Gaussian Filtering

Three dimensional Gaussian filter has been used in current work owing to its simplicity, symmetry and smoothness in spatial and frequency domain. The Gaussian weighting function in three dimensions is given by:

$$f = \frac{1}{\sqrt{2\pi(r_x + r_y + r_z)}} e^{-\frac{(x^2 + y^2 + z^2)}{2(r_x + r_y + r_z)}}$$

Where r_x , r_y and r_z are the filter width in x y and z direction, respectively. The filtering operation is performed by making a discrete Gaussian matrix and taking scalar product of this filter matrix with the volume data. However, this becomes computationally too demanding for large volumetric data sets. A more computationally efficient approach is to apply 1D Gaussian filter in each direction consecutively in all three directions over entire volume dataset. The filter coefficients are chosen so that filter width is different in three directions, to match the aspect ratio of the column. The slice plot of the chosen Gaussian filter is shown in Fig. 6.3.

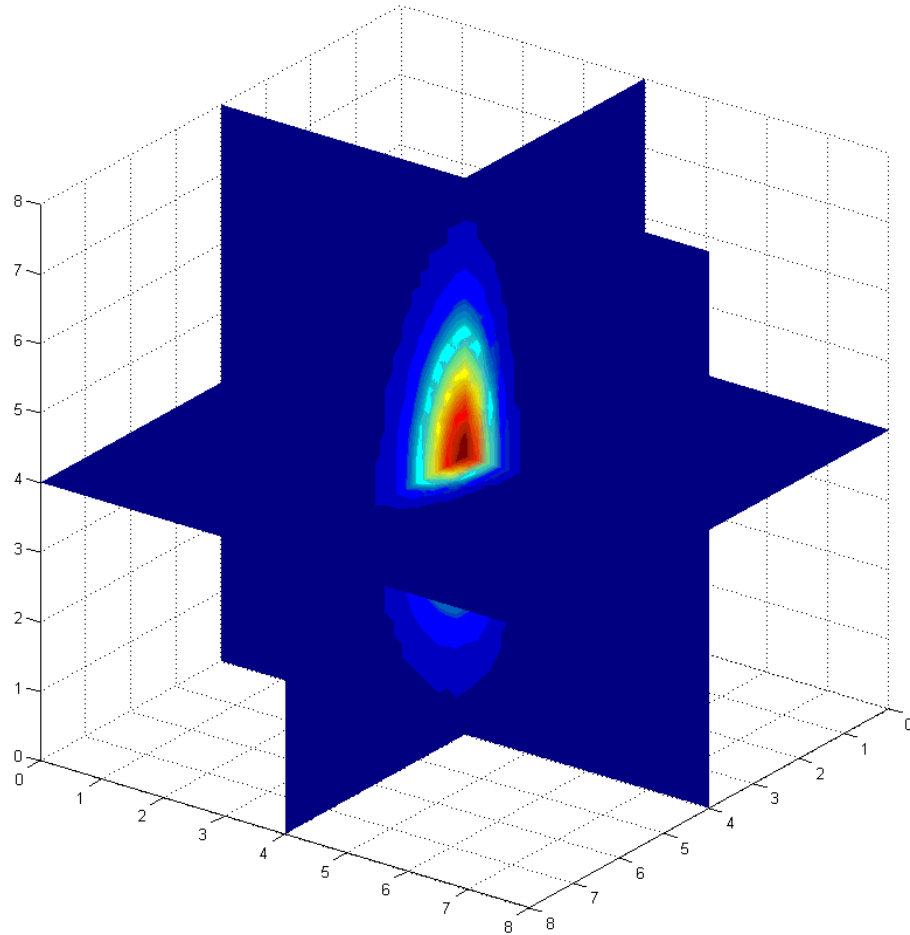


Fig. 6.3: Slice plot of the 3D Gaussian filter used for the analysis

For the purpose of demonstration, three stage filtering is performed over the volume data. The volume velocity data is first filtered with smallest filter size. This filters out the small wavenumber fluctuations. The smoothed data is subjected to higher size filter, resulting into further separation. A Threshold is applied to the three filtered sets to generate the boundaries of flow structures.

6.7. Results and discussion:

6.7.1. Cylindrical bubble column

Figure 6.4A shows the contour plots of instantaneous air volume fraction while Fig 6.4B shows the contours of instantaneous liquid velocity magnitude for cylindrical column with single point sparger. A plume region in center of the column with high gas hold-up and the liquid velocity magnitude is clearly visible. The flow structures with different size and shapes are also clearly visible. In order to check the validity of the simulations, the results were compared with LDA data of Kulkarni et al. (2007).

Fig. 6.5 shows the comparison of time averaged liquid velocity and volumetric gas hold up profiles at $H/D=4$. It can be observed that, the results are in good agreement with the experimental data. Hence, the results from LES can be used for further analysis of volumetric data.

6.7.2. Rectangular bubble column

Fig. 6.6 shows the flow patterns for rectangular bubble column. Fig. 6.6A shows the streamlines for bubble column with single point sparger. Traveling cells with the size approximately equal to column width can be clearly observed, along with small scale velocity fluctuations and central bubble plume with high upward velocity.

Fig. 6.6B shows streamlines for five point sparger. The flow structure similar to single point sparger at higher height can be observed. However, circulation cells are not as well marked as single point sparger due to more uniformity of sparging. Fig. 6.6C shows the velocity magnitude for the same case as Fig. 6.6B.

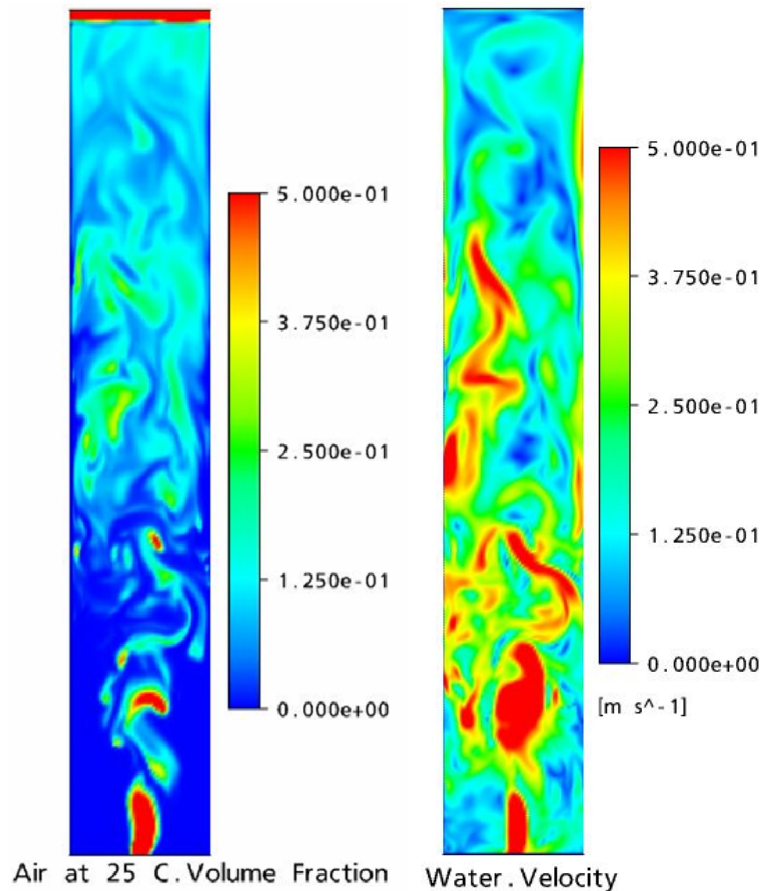


Fig. 6.4. Flow pattern in cylindrical column with single point sparger at superficial gas velocity of 20 mm/s (A) gas hold-up (B) Liquid velocity magnitude

Fig. 6.7 shows the pressure contours for five point sparger. It can be observed that the dynamic pressure has strong radial variation, while the absolute pressure is constant along the width. This signifies strong circulatory flow with zero lateral mass flux. It can also be observed that the static pressure sensors at wall would be less sensitive to the flow fluctuations since they are measuring only static pressure. To get more sensitivity of pressure fluctuations with respect to local axial velocity, the sensors should be put inside the column in pitot tube configuration to register impact (total) pressure.

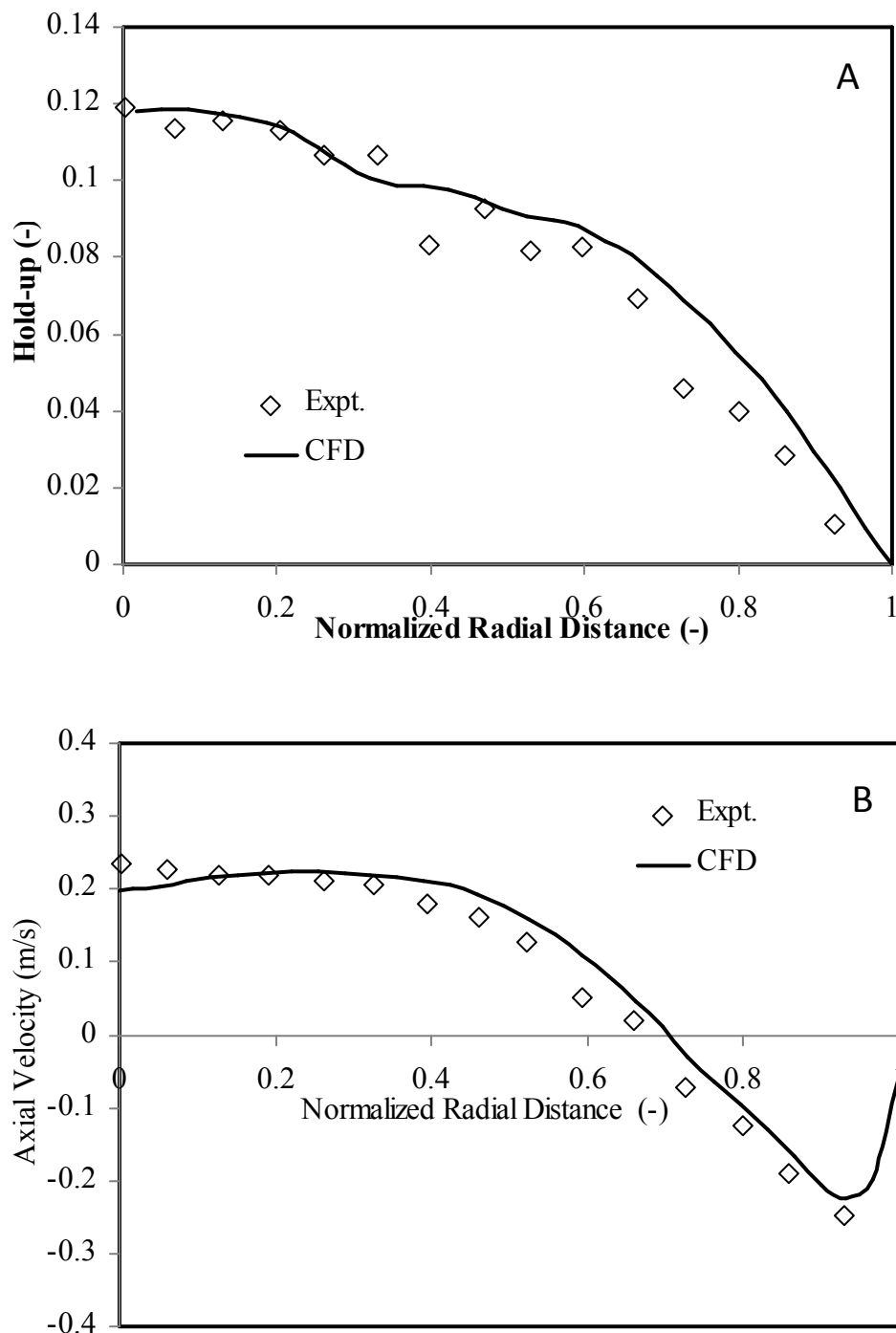


Fig. 6.5: Comparison of LES results with experimental data: (A) gas hold-up (B)

Axial Liquid velocity

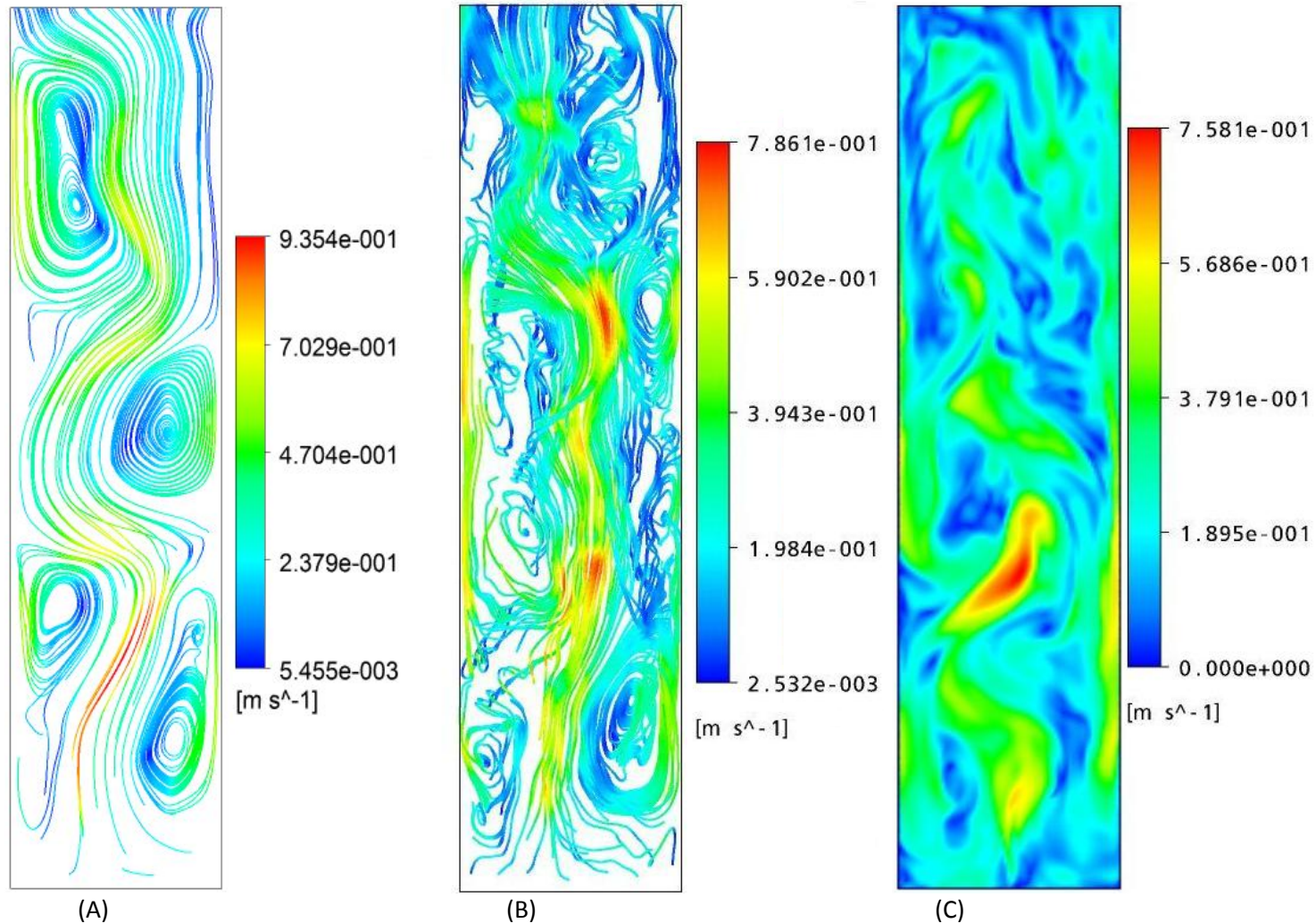


Fig. 6.6: Flow patterns for rectangular bubble column: (A) Streamlines for single point sparger (B) streamlines for five point sparger (C) Contour of velocity magnitude for five point sparger

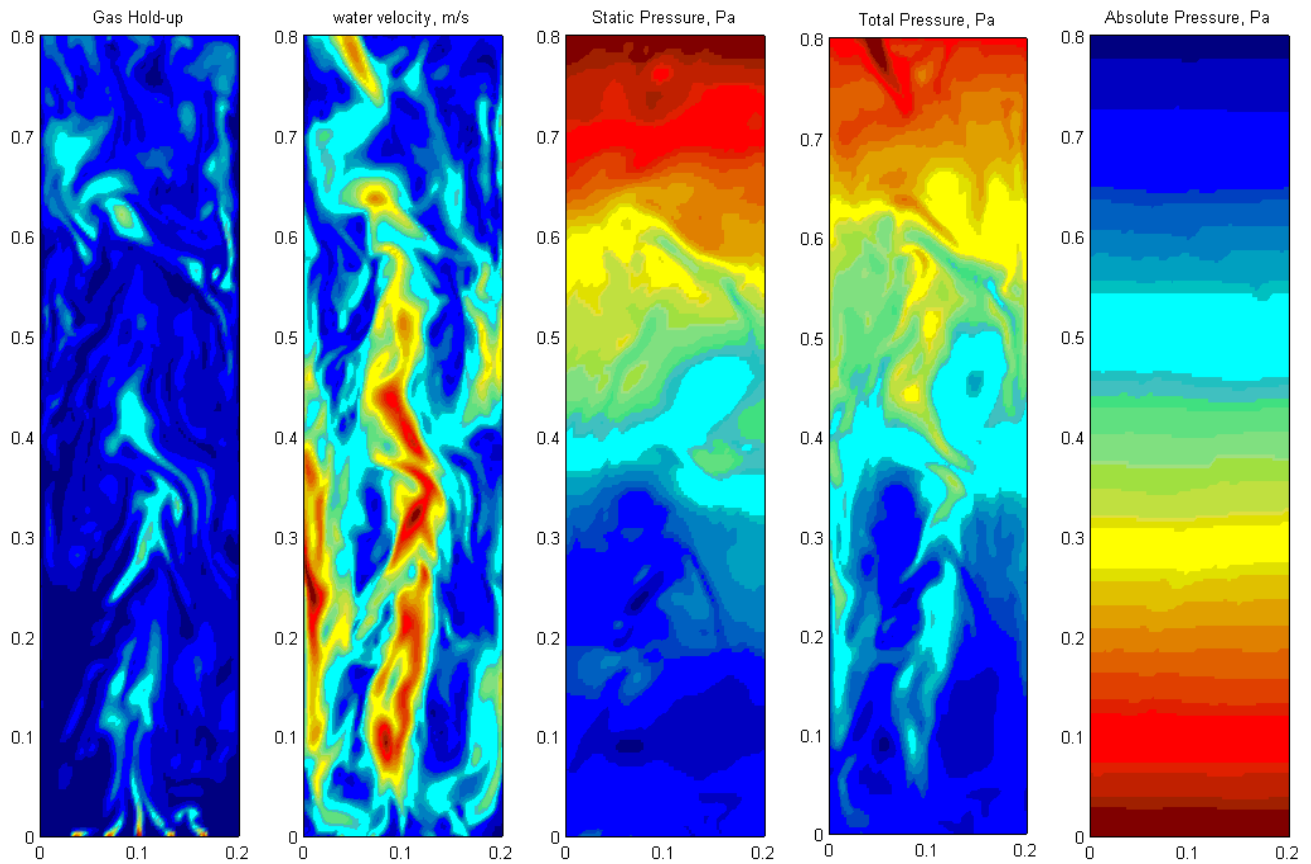


Fig. 6.7: Contours of gas hold-up, velocity magnitude, static pressure, total pressure and absolute pressure for five point bubble column for $V_G=20$ mm/s

6.7.3. Volume visualization with 3D filtering

Due to computational limitations, only rectangular column data have been processed with three dimensional filtering. Fig. 6.8 shows the filtered velocity field for single point sparger. Each closed envelopes of isosurface marks the boundary of one flow structure. It can be observed that, multiple structures are overlapping. Maximum small wavelength structures are concentrated around the plume. Large scale structures are uniformly spread over column cross section. The energy of each individual structure can be calculated by evaluating volume integral of the filtered velocity field over the envelope marking the boundary of the structure.

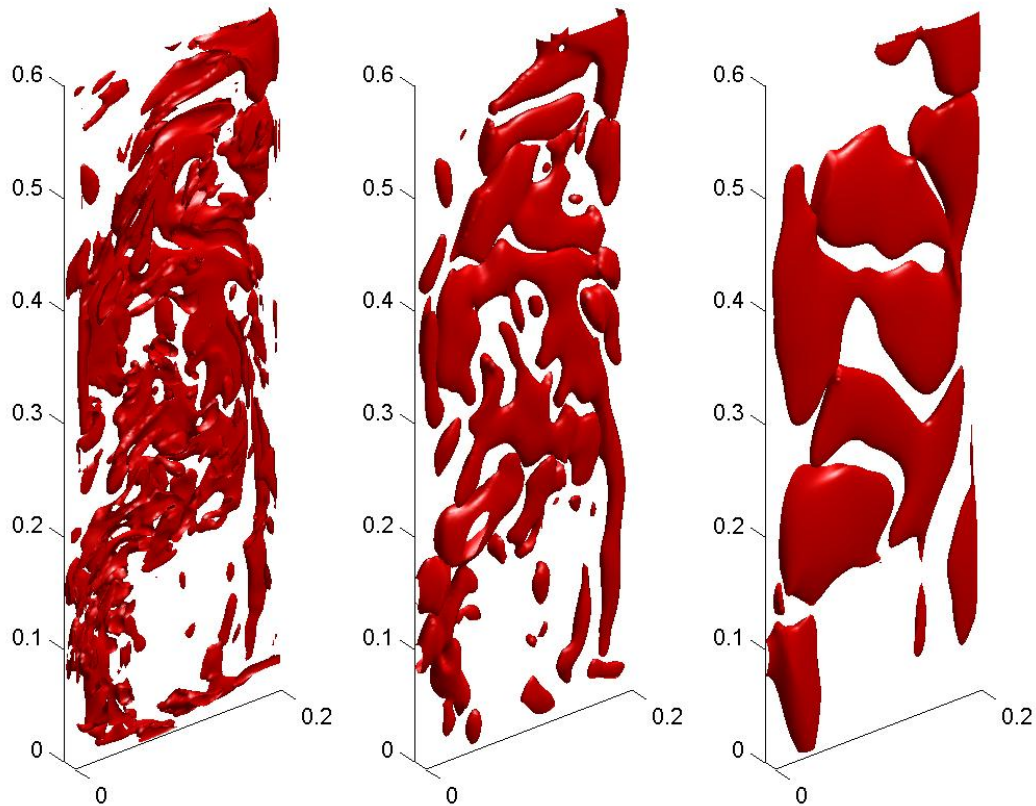


Fig. 6.8. isosurfaces of filtered velocity for rectangular column with single point sparger

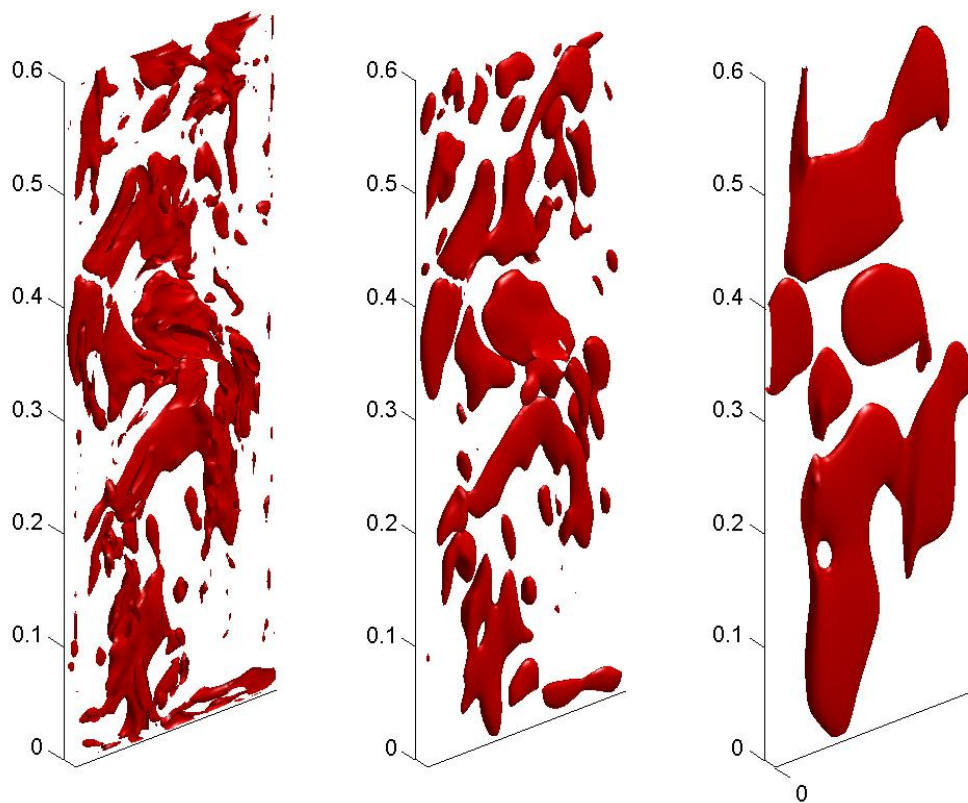


Fig. 6.9. isosurfaces of filtered velocity for rectangular column with five point sparger

Fig. 6.9 shows similar isosurface for five point sparger. It can be observed that the smaller wavelength structures are scattered more in the column than single point sparger, indicating improved homogeneity. Deeper insight into flow field can be achieved once the properties of each individual structure are registered to give distributions of structure size, shape and energy distribution.

6.8. Conclusions

Large eddy simulation of rectangular and cylindrical bubble column has been carried out. The results of time averaged liquid velocity are in agreement with experimental data. The three dimensional Gaussian filter is applied to the volume data generated by LES. Several flow features can be distinctly visualized using filtered velocity field, including advection, stretching and breakup of flow structures. This technique has the potential to detect three dimensional shapes of flow structures from volume data of LES, to relate the flow structure properties with transport phenomena.

Nomenclature

C_k, C_ε	SGS model, (-)
C_L	coefficient of lift force, (-)
C_S	model constant in Eq. 6.14, (-)
C_{TD}	turbulent dispersion coefficient, (-)
C_{VM}	virtual mass coefficient, (-)
D_ε	turbulent diffusion of dissipation, ($m^2 s^{-4}$)
f	gaussian weighing function, (s^{-1})
g	acceleration due to gravity, ($m^2 s^{-1}$)

k	turbulent kinetic energy, ($\text{m}^2 \text{s}^{-2}$)
M_α	momentum exchange between the phases due to interface forces
p	pressure, (N m^{-2})
R_{ij}	Reynolds stress tensor, (N m^{-2})
r_x	filter width in x direction
r_y	filter width in y direction
r_z	filter width in z direction
$\overline{S_{ij}}$	strain rate of the resolved scales, (s^{-1})
t	time, (s)
u	true velocity, (m s^{-1})
$\langle u_i \rangle$	time average of velocity, (m s^{-1})
$\langle u_1 \rangle$	time averaged radial velocity, (m s^{-1})
$\langle u_2 \rangle$	time averaged axial velocity, (m s^{-1})
$\langle u_3 \rangle$	time averaged tangential velocity, (m s^{-1})
$\overline{u_i}$	filtered velocity, (m s^{-1})
z	axial coordinate, (m)

Greek Letter

l_o	characteristic length scale, (m)
ε	turbulent energy dissipation rate, ($\text{m}^2 \text{s}^{-3}$)
μ	viscosity, ($\text{kg m}^{-1} \text{s}$)
μ_{BIT}	viscosity due to BIT

μ_T	turbulence viscosity, (kg m ⁻¹ s)
μ_{eff}	effective viscosity, (kg m ⁻¹ s)
ν	kinematics viscosity, (m ² s ⁻¹)
ν_{sgs}	sub-grid scale eddy viscosity, (m ² s ⁻¹)
ν_t	eddy viscosity, (m ² s ⁻¹)
σ_k	turbulent prandtl number for the turbulent kinetic energy
σ_ε	turbulent prandtl number for the dissipation rate
τ_{ij}	shear stress in <i>i</i> -direction, (N m ⁻²)
τ_{sgs}	subgrid-scale stress, (N m ⁻²)
ρ	density of the fluid, (kg m ⁻³)
ρ_g	density of the gas, (kg m ⁻³)
ρ_l	density of the liquid, (kg m ⁻³)
τ_o	characteristic time scale, (s)
δ	kornecker delta
Δ	filter width, (m)
$\hat{\Delta}$	test filter in Eq. 6.16, (-)
ϕ_ε	turbulent destruction of dissipation, (m ² s ⁻⁴)
θ	tantential coordinate, (rad)
γ	volume fraction
α	individual phase

Subscripts and Superscripts

i, j, k	axis indexes of space coordinates
g	gas phase
l	liquid phase
sgs	subgrid scale
t	turbulence
$'$	fluctuating quantity

References

- Becker, S., Sokolichin, A., Eigenberger, G., 1994. Gas-liquid flow in bubble columns and loop reactors: Part II. Comparison of detailed experiments and flow simulations. *Chemical Engineering Science* 49, 5747-5762.
- Bombardelli, F. A., Buscaglia, G. C., García, M. H., Dari, E. A., 2006. Simulation of bubble-plume wandering phenomena in a bubble plume using a k- ϵ model and a large-eddy-simulation (LES) approach. *Mecanica Computacional XXIII*, 1969-1994.
- Bove, S., Solberg, T., Hjertager, B. H., 2004. Numerical aspects of bubble column simulations. *International Journal of Chemical Reactor Engineering* 2A1, 1-22.
- Clift, R., Grace, J.R., Weber, M.E., 1978. *Bubbles, Drops and Particles*. Academic Press, New York, USA.
- Davidson, L., 1997. Large eddy simulations: a note on derivation of the equations for the subgrid turbulent kinetic energies. Technical Report No. 97/12, 980904, Chalmers University of Technology, Gothenburg, Sweden.
- Deen, N. G., Solberg T., Hjertager, B. H., 2001. Large eddy simulation of gas-liquid flow in a square cross-sectioned bubble column. *Chemical Engineering Science* 56, 6341-6349.
- Drew, D.A., Lahey, R.T., 1987. The virtual mass and lift force on a sphere in a rotating and straining flow. *International Journal of Multiphase Flow* 13, 113-121.
- Drew, D.A., Passman, S.L., 1999. *Theory of Multicomponent Fluids*. Springer, New York, USA.
- Germano, M., 1992. Turbulence: the filtering approach. *Journal of Fluid Mechanics* 238, 325-336.
- Germano, M., Piomelli, U., Moin, P., Cabot, W.H., 1991. A dynamic subgrid-scale eddy viscosity model. *Physics of Fluids A* 3, 1760-1765.
- Ishii, M., Zuber, N., 1979. Drag coefficient and relative velocity in bubbly, droplet or particulate flows. *A.I.Ch.E. Journal* 25, 843-855.
- Jakobsen, H.A., Sannæs, B.H., Grevskott, S., Svendsen, H.F., 1997. Modeling of vertical bubble-driven flows. *Industrial & Engineering Chemistry Research* 36, 4052-4074.

- Joshi, J. B., 2001. Computational flow modeling and design of bubble column reactors. *Chemical Engineering Science* 56, 5893-5933.
- Kim, W. W., Menon, S., 1997. Application of the Localized Dynamic Subgrid-Scale Model to Turbulent Wall-Bounded Flows. Technical Report AIAA-97-0210, American Institute of Aeronautics and Astronautics, 35th Aerospace Sciences Meeting, Reno.
- Kulkarni, A.A., Ekambara, K., Joshi, J.B., 2007. On the development of flow pattern in a bubble column reactor: Experiments and CFD. *Chemical Engineering Science* 62, 1049-1061.
- Lakehal, D., Smith, L. B., Milelli, M., 2002. Large-eddy simulation of bubbly turbulent shear flows. *Journal of Turbulence* 3, 1-21.
- Leonard, A., 1974. Energy cascade in large-eddy simulations of turbulent fluid flow. *Advances in Geophysics* 18A, 237-248.
- Lilly, D.K., 1992. A proposed modification of the Germano subgrid-scale closure method. *Physics of Fluids A* 4, 633-635.
- Lopez de Bertodano, M.A., Lahey, R.T., Jones, O.C., 1994. Development of a $k - \epsilon$ model for bubbly two-phase flow. *Journal of Fluids Engineering---Transactions of the ASME* 116, 128-134.
- Pfleger, D., Becker, S., 2001. Modeling and simulation of the dynamic flow behaviour in a bubble column. *Chemical Engineering Science* 56, 1737-1747.
- Rafique, M., Chen, P., Duduković, M.P., 2004. Computational modeling of gas-liquid flow in bubble columns. *Reviews in Chemical Engineering* 20, 225-375.
- Sato, Y., Sekoguchi, K., 1975. Liquid velocity distribution in two-phase bubble flow. *International Journal of Multiphase Flow* 2, 79-95.
- Smith, B.L., Milelli, M., 1998. An investigation of confined bubble plume. In: *Proceedings of the 3rd International Conference on Multiphase Flow, ICMF '98, 8-12 June 1998, Lyon, France.*
- Sokolichin, A., Eigenberger, G., 2004. Simulation of buoyancy driven bubbly flow: Established simplifications and open questions. *A.I.Ch.E. Journal* 50, 24-45.
- Tomiyama, A., 2004. Drag, Lift and Virtual mass forces acting on a single bubble. *Third International Symposium on Two phase flow modelling and experimentation, Pisa, Italy, 22-24 September.*
- Zhang, D., Deen, N. G., Kuipers, J.A.M., 2006. Numerical Simulation of dynamic flow behavior in a bubble column: A study of closures for turbulence and interface forces. *Chemical Engineering Science* 61, 7593-7608.
- Zun, I., 1990. Mechanism of bubble non-homogeneous distribution in two-phase shear flow. *Nuclear Engineering and Design* 118, 155-162.

Chapter 7

INVESTIGATION OF FLOW STRUCTURES AND TRANSPORT PHENOMENA IN BUBBLE COLUMNS USING PARTICLE IMAGE VELOCIMETRY AND MINIATURE PRESSURE SENSORS

7.1. Introduction

Bubbles are dispersed in a continuous liquid phase in many important equipment like bubble column reactor to carry out important reactions like oxidation, hydrogenation, Fischer–Tropsch, fermentation, boilers and nuclear reactors. Because of the buoyant force, the bubbles move at the different velocity than the surrounding liquid. While moving in swarms, the collective motion of bubbles induces circulation cells with length scales comparable to the size of vessel besides the small scale velocity disturbances having length scale of the order of the bubble size. This bubble-induced motion, often called pseudo-turbulence in bubbly dispersion generates the turbulent stresses in near wall region as well as the bulk of the dispersion. The enhancement of turbulent stresses is affected by the classic shear induced turbulence from the large and intermediate scales as well as the bubble generated turbulence. The quantification of the coupling between these two mechanisms forms the foundation of transport phenomena in multiphase dispersions.

7.1.1. Bubble Column as a Building Block of Understanding of Transport Phenomena in Multiphase Contactors

The types of particles encountered in two phase flow- bubbles, drops and solid particle are identical from fluid mechanics point of view in the sense that all of these represent submerged bodies in continuous fluid medium like liquid or gas. However, their surface characteristics are different like bubbles in surfactant free liquid offer free slip boundary conditions while the particles offer no-slip boundary condition at the interface. Besides the interface characteristics, solid particles offer the highest rigidity in terms of shape followed by drops and bubbles. In all these three form of particles, bubbles offer a unique advantage of offering the broadest range of interface characteristics and the rigidity in shape. The interface boundary conditions can vary from

free slip (clean interfaces) to no slip (contaminated interfaces) while the shapes range from rigid spherical (small bubbles) to completely deformable shapes (large bubbles) dependent on surrounding fluid properties. Hence, the understanding of flow pattern around single bubbles and bubble swarms offers a chance to characterize the entire fraternity of multiphase reactors in terms of two and three phase dispersions.

7.1.2. General Nature of Flow Pattern in Bubble columns

In bubble columns, the gas exists as a dispersed bubble phase in a continuous liquid phase. The gas hold-up profile within the column results in a profile of static pressure, which is lower in the central region as compared to the near-wall region. As a consequence, intense large scale liquid circulation flow pattern is developed. The time averaged liquid velocity is upward in the central region and downwards near the column wall. However, the instantaneous flow pattern consists of a spectrum of flow structures and the largest ones appear as circulation cells (Joshi, 1980; Zehner, 1982) as shown in Figure 7.1. The maximum size of this circulation cell is of the order of column diameter and can be considered as the largest eddy in the column, also known as large scale structures.

These large scale flow structures within a reactor affect the local turbulence, and play an important role in enhancing the local transport phenomena. It has become evident that these structures play a vital role in enabling the better design of the reactor by influencing mixing and heat transfer, etc within the multiphase system.

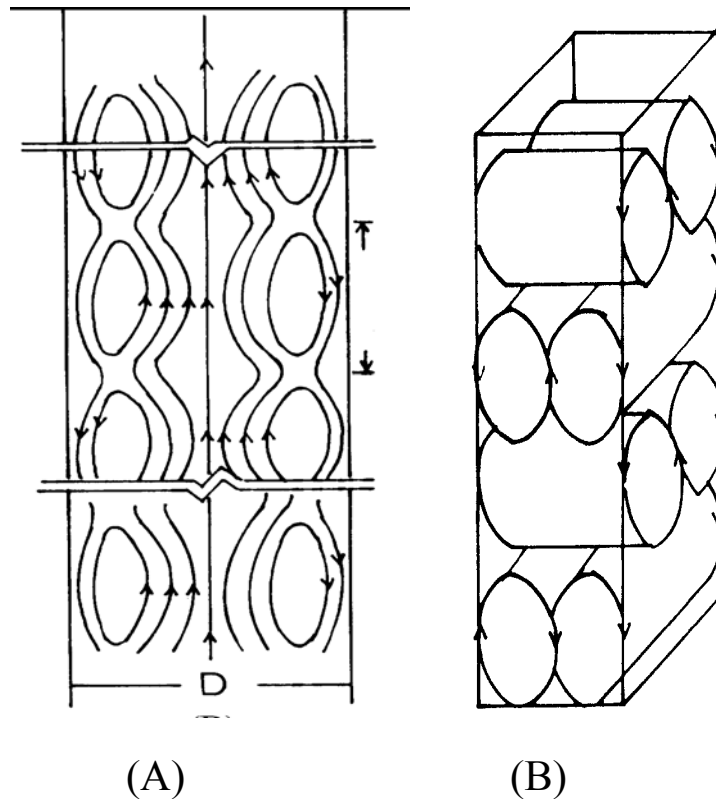


Figure 7.1 Schematic of circulation cells in bubble column (A) Joshi (1980) and (B) Zehner (1982)

7.1.3. Evaluation of Mass Transfer Coefficient using Flow Information

Calculation of mass transfer coefficient from first principles is important to have a clear understanding of the transport phenomena. This is essential to eliminate the uncertainty involved in using the empirical correlations for mass transfer, which are based on time averaged, space integral flow properties like superficial gas velocity and volumetric gas hold up. The enhancement in overall rate of transfer by turbulence is well correlated and forms the basis for theory of transport phenomena. Using the theories of transport phenomena, the mass or heat transfer from interface can be modeled in similar fashion as the momentum transfer. The rate of mass transfer is proportional to local temperature gradient, and the proportionality constant is summation of the molecular and turbulent diffusivity. The turbulent diffusivity can be calculated using the value of

turbulent momentum diffusivity (eddy viscosity) and turbulent Schmidt number. Analogous procedure is employed to evaluate turbulent thermal diffusivity using eddy viscosity and turbulent Prandtl number. Thus, in order to evaluate the heat and mass transfer characteristics in turbulent flow, the local molecular diffusivity, eddy viscosity and turbulent Prandtl/Schmidt numbers must be known for given contactor.

The current study is focused onto two principal objectives: (i) to develop a methodology to quantify the flow structures from data obtained using advanced measurement and data processing techniques (ii) to use the flow structure properties to calculate the mass transfer coefficient in bubble column reactor.

7.1.4. Approaches to use Flow Information to Derive Transport Characteristics: Heuristics and Analytical Approaches

As mentioned above, eddy viscosity and eddy diffusivity are two important parameters to quantify the transport phenomena in turbulent flows. A number of heuristic and analytical approaches have been proposed over last 125 years to calculate the turbulent Prandtl/Schmidt number. These are usually referred to as ‘Theories of heat and mass transfer’ or analogies between momentum and heat/mass transfer. These models are broadly classified into two categories: Heuristic models, which are based on the visualization of the flow behavior in the vicinity of the interface and the analytical approaches which are based on the velocity and turbulent viscosity profiles.

The simplest model is the film model of Lewis and Whitman (1924). This model postulates that resistance to the heat and mass transfer occurs across a thin layer of stagnant fluid, of thickness δ , situated at the interface, and that the bulk fluid below is well mixed. Calculation of the mass transfer coefficient, k_L , is very simple, and is given by:

$$k_L = \frac{D}{\delta} \quad (7.1)$$

where D is the diffusion coefficient. The assumption of constant δ is a great simplification. δ is a function of the local hydrodynamics.

Higbie (1935) developed a model (Penetration Model) based on a surface renewal argument. The role of turbulence was considered to bring up elements of bulk liquid to the interface, where unsteady heat and mass transfer takes place for a prescribed time T_E , after which the element returns to the bulk and is replaced by another element. In the penetration model it is assumed that the frequency of surface renewal is set by the flow. The mass transfer coefficient is calculated from,

$$k_L = \sqrt{\frac{D}{\pi T_E}} \quad (7.2)$$

where, T_E , the age of the liquid element at the interface, is supposed to be obtained from the turbulence structure. This model considers the effect of coherent structures in at least time-averaged sense.

Danckwerts (1951) modified the theory of Higbie (1935) by considering the age distribution of fluid elements at the wall. He proposed one parameter model based on the surface renewal rate, S . He stated that the replacement of fluid elements is irrespective of their age and considered a probability distribution function of the exponential form for the ages of the fluid elements. Using this concept mass transfer coefficient is given by,

$$k_L = \sqrt{DS} \quad (7.3)$$

The time distribution of surface renewing eddies was arbitrary and it could only account for the quasi-periodicity in the time, but spatial distribution (the distance up to which eddies could move up to the wall) was not considered.

The major problem of these models is the inability to explain the experimental observations regarding the dependency of mass transfer coefficient on the diffusivity values. Film theory predicted direct proportionality, whereas penetration and surface renewal theories predicted square-root dependency. The experimentally observed value ranges from 0.5 to 1. This fact led to the development of number of models for the prediction of heat and mass transfer rates in turbulent shear flows. These models, though based on the same concept (random surface renewal) differ with regard to the assumptions, near wall modeling concept and mathematical formulations. These models can be broadly classified as the film penetration models, growth breakdown models or periodic viscous sublayer models, the random surface renewal models, the surface rejuvenation models. Mathpati and Joshi (2007) give a critical assessment of the published literature about these theories.

The heuristic models make simplifying assumptions in order to keep the model mathematically tractable. These models are mathematically formulated analogous to the unsteady state conduction problems in between two surface renewals, however quantification of model parameters has been the limiting factor in terms of their applicability. Theories with extreme speculations, such as from “consideration of stagnant film of liquid in the film theory” to “the entire sublayer becoming turbulent in case of periodic growth-breakdown models”, are available in the published literature. All these theories have certainly contributed to the understanding of transport phenomena in the time period those were developed, however none of these could answer all the questions in isolation. All the theories (except film theory) consider the effect of fluid elements coming and going away from the wall to renew the interface. There are different opinions regarding the question, “how close eddies can reach the interface?”. The experimental and DNS/LES investigations have contributed significantly in

understanding the movement of surface renewing eddies, called as coherent structures. None of the heuristic models could till date take into account all the features of the coherent structures. These features of coherent structures are listed below and Table 7.1 provides information about the features which are not incorporated by heuristic models (at least in qualitative sense).

1. Viscous sublayer flow is unsteady and three-dimensional.
2. Wall normal ejections and wallward sweep of fluid elements happen at almost all the times and at all the locations near the wall.
3. Distance up to which eddies can penetrate depends upon their energy content.
4. Fluid elements while moving in streamwise direction also moved in spanwise direction.
5. Turbulent mixing of fluid elements from wall region with turbulent core occurs due to the instability in the viscosity dominated region.
6. Turbulent sweeps and ejections are quasi-periodic in space and time.
7. In single phase channel and pipe flows, streaks have spanwise extent of 10-100 and streamwise extent of 100-1000 in terms of wall units (i.e. non-dimensionlized using u_τ and ν) .
8. Mean contact time of eddies at the wall can be properly scaled with inner variables which are solely governed by Reynolds number.
9. The whole cycle of turbulent burst process repeats itself.
10. A thin layer of fluid ($y^+ < 1$) exists where velocity profile is essentially linear all the times.
11. Only in a time-averaged sense, $u^+ = y^+$ is a good approximation for viscous sublayer.

Figure 7.2 shows the heuristic pictures of different models and visualizations using DNS/LES.

DEVELOPMENT OF EXPERIMENTAL TECHNIQUES AND CFD SIMULATIONS OF MULTIPHASE DISPERSIONS

Table 7.1. Features of Bursting Process Incorporated by Heuristic Models

Model	formulation	investigator(s)	features not incorporated
Film theory	$D \frac{\partial^2 C}{\partial y^2} = 0$ $y=0 \quad C = C_i$ $y=\delta \quad C = C_b$	Lewis and Whitman (1924)	1-9, 11
Surface renewal theory	$\frac{\partial C}{\partial t} = D \frac{\partial^2 C}{\partial y^2}$ $t=0 \quad y > 0 \quad C = C_b$ $t > 0 \quad y=0 \quad C = C_i$ $t > 0 \quad y = \infty \quad C = C_b$	Higbie (1935) Danckwerts (1951)	1, 3-8, 10, 11 1,3-5,7,8,10,11
Film-penetration theory	$\frac{\partial C}{\partial t} = D \frac{\partial^2 C}{\partial y^2}$ $t=0 \quad y > 0 \quad C = C_b$ $t > 0 \quad y=0 \quad C = C_i$ $t > 0 \quad y=L \quad C = C_b$	Toor and Marchello (1958) Brusset et al (1973).	1, 3-5, 7, 8, 11 1, 3-5, 7, 8, 11
Periodic growth-breakdown theory	$\frac{\partial u}{\partial t} + u \frac{\partial u}{\partial x} + v \frac{\partial u}{\partial y} = \nu \frac{\partial^2 u}{\partial y^2}$ $\frac{\partial C}{\partial t} + u \frac{\partial C}{\partial x} + v \frac{\partial C}{\partial y} = D \frac{\partial^2 C}{\partial y^2}$ $t=0 \quad x \geq 0 \quad y \geq 0 \quad u = u_b \quad C = C_b$ $t > 0 \quad x=0 \quad y > 0 \quad u = u_b \quad C = C_b$ $t > 0 \quad x > 0 \quad y=0 \quad u=0 \quad C = C_i$ $t > 0 \quad x \rightarrow 0 \quad y \rightarrow \infty \quad u = u_b \quad C = C_b$	Einsten and Li (1956) Ruckenstein (1958) Meek and Baer (1970) Pinczewski and Sideman (1974)	2-4, 7, 10 2-4, 2-4 2-4
Random surface renewal theory	$\left(\frac{u(y,t)}{u_b} \right) \frac{\partial C}{\partial t} = D \frac{\partial^2 C}{\partial y^2}$ $t=0 \quad y > 0 \quad C = C_b$ $t > 0 \quad y=0 \quad C = C_i$ $t > 0 \quad y = \infty \quad C = C_b$	Hanratty (1956) Fortuin and Klijn (1982) Fortuin et al. (1992)	1, 3-5, 7, 8, 10 3, 4, 7 3, 4, 7
Surface rejuvenation theory	$\frac{\partial C}{\partial t} = D \frac{\partial^2 C}{\partial y^2}$ $t=0 \quad y > 0 \quad C = f(y)$ $t > 0 \quad y=0 \quad C = C_i$ $t > 0 \quad y = \infty \quad C = C_b$	Harriott (1962) Thomas et al. (1975) Thomas (1978) Thomas (1980) Loughlin et al. (1985)	1, 4, 5, 7, 8, 11 1, 4, 5, 7, 8, 11 1, 4, 5, 7, 8, 11 1, 4, 5, 7, 8, 11 1, 4, 5, 7, 8, 11

DEVELOPMENT OF EXPERIMENTAL TECHNIQUES AND CFD SIMULATIONS OF MULTIPHASE DISPERSIONS

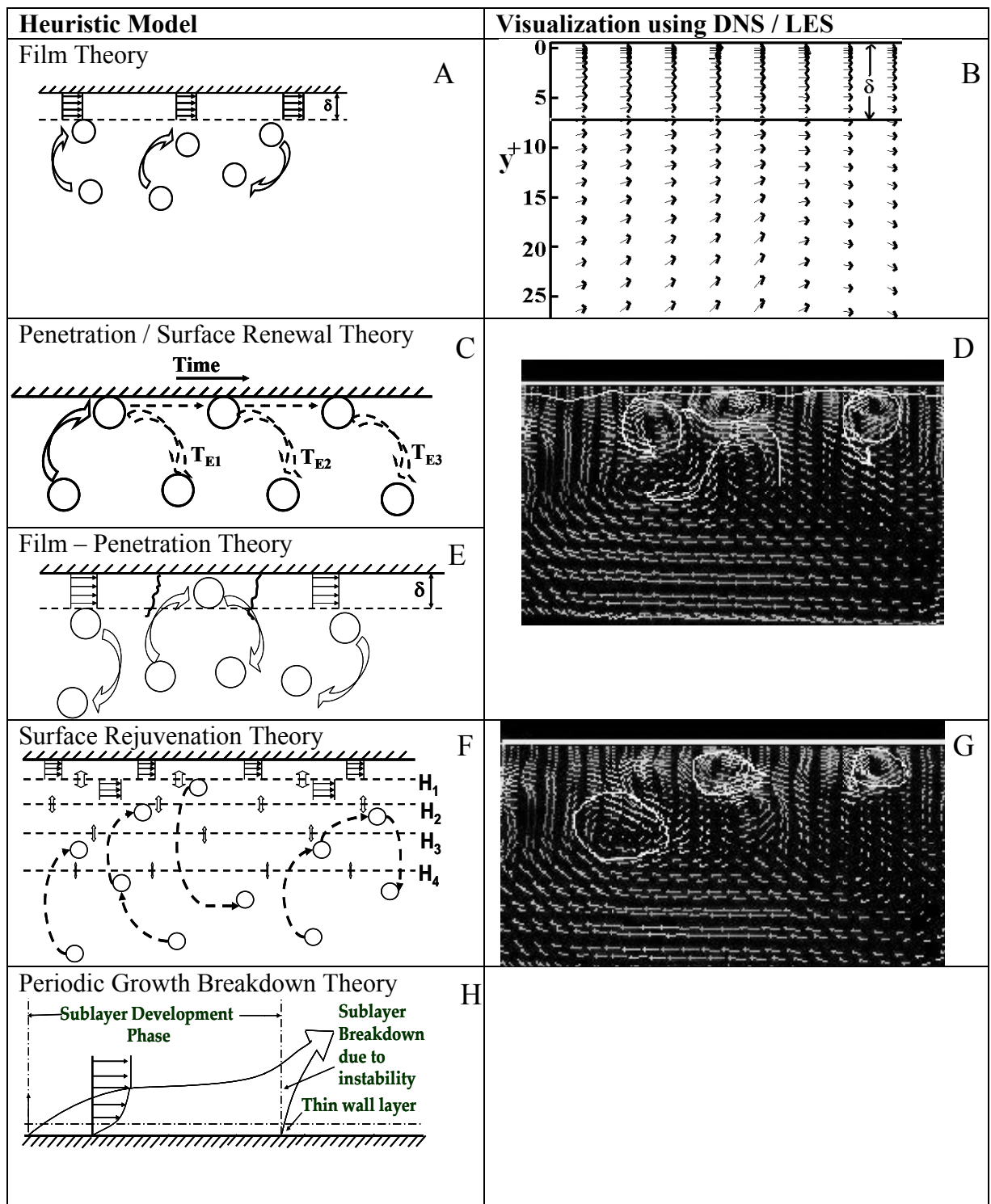


Figure 7.2. Schematic representation of different theories of mass transfer (A) Film theory (B)LES visualization of constant velocity ‘Film’ near interface (C) Penetration/surface renewal theory (D) LES visualization of eddies near interface (E) Film-penetration theory (F) Surface Rejuvenation theory (G) LES visualization for surface rejuvenation theory (H) Periodic growth/breakdown theory

As we know that the near wall turbulence is very complex and confining it into simplified pictures of heuristic models is not possible. But still deliberate attempt is made to see these simplified pictures using DNS / LES. As shown in Figure 7.2A, according to film theory, eddies cannot penetrate up to the wall, there is a thin film of thickness ' δ ', in which only molecular motions prevail. Figure 2B shows visualization using DNS at $Re = 5600$ in which one can observe a small layer near the wall where fluid elements are moving almost parallel to the wall, which one can call as "film" as in film theory. But DNS at different Re and / or Pr show different thickness of such layer, which is not at all quantified by film theory. In case of penetration / surface renewal theory (Figure 7.2C), concept of film is disregarded and eddies are assumed to reach up to wall and eddies may spend exactly same amount of time at the wall (penetration theory) or random amount of time (surface renewal theory). Figure 7.2D shows vector plots from LES indicating the movement of eddies close to and away from the wall. But no eddy has the ability to go straight up to the wall.

In literature, different kind of distribution functions are available to predict transfer coefficients from surface renewal theory. The distribution functions are discussed here, and listed in Table 7.2. The simplest age distribution function of Higbie (1935) considers constant contact time of eddies at the wall. Danckwerts (1951) discarded the concept of constant contact time and considered exponentially decaying function. But this model predicts that the most probable age of fluid elements at the wall is equal to zero. This distribution can also be identified as the RTD function of well-mixed vessel, whereas Higbie's model as plug flow system. Perlmutter (1961) suggested that the correct distribution function should lie somewhere in between these two. So he proposed a distribution function for a system of ' m ' well-mixed vessels in series. Special case of $m = 1$, reduces to Danckwerts' distribution and $m = \infty$ gives Higbie's

DEVELOPMENT OF EXPERIMENTAL TECHNIQUES AND CFD SIMULATIONS OF MULTIPHASE DISPERSIONS

distribution. Perlmutter (1961) also considered imperfect mixing of interfacial fluid using concept of dead time. He took into account the presence of stagnant, unreplaced fluid elements through delayed exponential distribution. Fortuin et al. (1992) carried out LDA measurements to predict the age distribution and they correlated age of the fluid elements with friction factor. But even if one considers any type of distribution for contact time, the variation in predicted transfer coefficients is only 13 %. It means that there must be some other reason which is not yet understood. It can be eddy size, shape, energy or the eddy approach (to wall) distribution.

Table 7.2. Age Distribution Functions Available in Literature

Investigator	Age distribution function
Higbie (1935)	$\phi(\theta) = \begin{cases} 1/\tau & 0 < \theta < \tau \\ 0 & \theta > \tau \end{cases}$ <p>θ is mean contact time</p>
Danckwerts (1951)	$\phi(\theta) = S \exp(-S\theta)$ <p>S is rate of surface renewal</p>
Perlmutter (1961)	<p>Tanks-in-series model</p> $\phi(\theta) = \frac{m^m \theta^{m-1}}{(m-1)! \tau^m} \exp\left(\frac{-m\theta}{\tau}\right)$ <p>m = no. of tanks in series</p> <p>Delayed exponential function</p> $\phi(\theta) = \begin{cases} \frac{1}{\tau + A} & 0 \leq \theta \leq A \\ \frac{1}{\tau + A} \exp\left[\frac{-(\theta - A)}{\tau}\right] & \theta \geq A \end{cases}$ <p>A is dead time</p>
Fortuin et al. (1992)	$\phi(\theta) d\theta = e^{-\theta/\tau} d(\theta/\tau)$ <p>θ is mean contact time</p>

The models after Danckwerts (1951) attempted to include some of the above mentioned points, such as film-penetration model considered variable film thickness and penetration theory was superimposed over that (Figure 7.2E). Figure 7.2D shows the vector plot using LES which partially support film-penetration model. Surface rejuvenation theory takes into account the distribution of heights (H_1, H_2, H_3, \dots) up to

which eddies can penetrate as well as distribution of contact time (Figure 7.2F). Figure 7.2G shows the vector plot using LES, from which one can see that not all eddies penetrate up to same depth. But all these attempts in heuristic models can be considered as forceful, as the major objective was to explain $k_L \propto D^{0.5-1}$, without much physical basis. Periodic growth-breakdown theory (Figure 7.2H) is somewhat closer to the bursting phenomena observed experimentally by Kline et al. (1967). This theory is an explanation of sublayer events over a time period of single burst. It is almost impossible to show this theory in a single visualization, but this theory can be very well explained by the animations using DNS/LES data.

This discussion clearly points out that the heuristic models are too much simplified as a one-dimensional problem (only periodic growth-breakdown model is two-dimensional), whereas sublayer flow is essentially three-dimensional. Vector plots of velocity and temperature provide a direct tool to analyze the heuristic arguments in these models.

7.1.5. 'Wish List' for Desired Flow Parameters in Order to Clearly Understand Transport Phenomena

Based on the discussion in section 7.1.4, DNS of the flow field around the solid-fluid or fluid-fluid interface is essential in order to completely resolve the anomalies in the transport coefficients predicted by different models. The following parameters should be obtained with maximum precision over the widest possible range of fluid and interface properties:

1. Eddy size distribution
2. Eddy age distribution
3. Eddy penetration depth distribution

4. Eddy energy distribution
5. Eddy shape distribution
6. Turbulent viscosity profile near interface
7. Turbulent Prandtl number
8. Turbulent Schmidt number

Once these parameters are quantified, clear account of effect of flow pattern on enhancement of transport processes by turbulence can be pointed out. This extracted information will be greatly useful in pointing out the lacunae in the existing modeling approach and implementing the corrections in the current practices to improve the reliability of model predictions in transport phenomena.

7.2. State of the Art on Estimation of Mass Transfer Coefficient in Bubble Column

There exists a large volume of literature reporting the experimentally measured mass transfer coefficient in bubble column for a wide variation of geometry and flow conditions. Principle approach to express the data is in the form of correlations emerging from dimensional analysis and methods based on artificial intelligence to fit the large pool of data. A comprehensive review of these methods can be found in Gandhi et al. (2009). The estimation of mass transfer coefficient from experimental or computational fluid dynamics data has also been carried out. A good literature review on this subject can be found in Joshi et al. (2002), Kulkarni and Joshi (2006), Kulkarni (2007) and Wang and Wang (2007). The estimation based on theories of transport phenomena is however difficult, owing to the fact that the turbulence is not homogenous inside the reactor. Besides the turbulence, the bubble size is variable throughout the reactor. The theories have succeeded to certain extent owing to the stationary statistics of these variables. Hence, using the overall eddy age/length scale and single, volumetric averaged bubble diameter is correlated with volumetric mass transfer coefficient for fully

developed flow in bubble columns. However, such an estimate is not free from use of empirical, adjustable constants in order to compensate for the use of the time and space averaged eddy age/length distributions, along with the distribution of bubble sizes and hold-up.

The estimation of turbulence characteristics like eddy age and length scale also faces experimental and mathematical difficulties. The use of LDA to get these parameters is described in detail by Kulkarni et al. (2001, 2004). The use of HFA has been made extensively to study the turbulence in wind tunnels, channel pipe flows and water tunnels with small volume fraction of bubbles. However, the HFA has not been employed to study the eddy ages in bubbly flows primarily because of the difficulty associated with small mean velocity in bubble column with less superficial liquid velocity.

Particle image velocimetry (PIV) in bubbly flows has advanced significantly during the last decade. Now it is possible to measure the planer velocity field with considerable spatial resolution to allow the estimation of length scales of eddies in bubbly flows (Saito et al. 2010, Sathe et al. 2010). The PIV resolution limits the smallest eddy size that can be resolved, which is typically 100 times the kolmogorov length scale. Besides, the presence of bubbles in measurement plane introduces the difficulty in developing the data processing technique used to isolate eddies from the discontinuous liquid velocity field.

7.3. Experimental Techniques

7.3.1. Bubble Column and Sparger Details

Experiments were carried out in two bubble columns: a narrow rectangular (2D) bubble column, primarily to facilitate the PIV measurements in Bubbly flow and a

DEVELOPMENT OF EXPERIMENTAL TECHNIQUES AND CFD SIMULATIONS OF MULTIPHASE DISPERSIONS

cylindrical bubble column. The 2D, Plexiglass bubble column having cross section $200 \times 15 \text{ mm}^2$ and the height 800 mm was used. Three spargers- a single nozzle sparger, 3 needle sparger and 5 needle sparger with the free area of 0.165 % were used. An oil free diaphragm compressor was used to force air through the sparger. A soap film flow meter was used to measure the gas flow rate. Tap water was used as system liquid, with a clear liquid height of 600 mm in the column, corresponding to H/D ratio of 3. Figure 3 shows the schematic of the experimental setup.

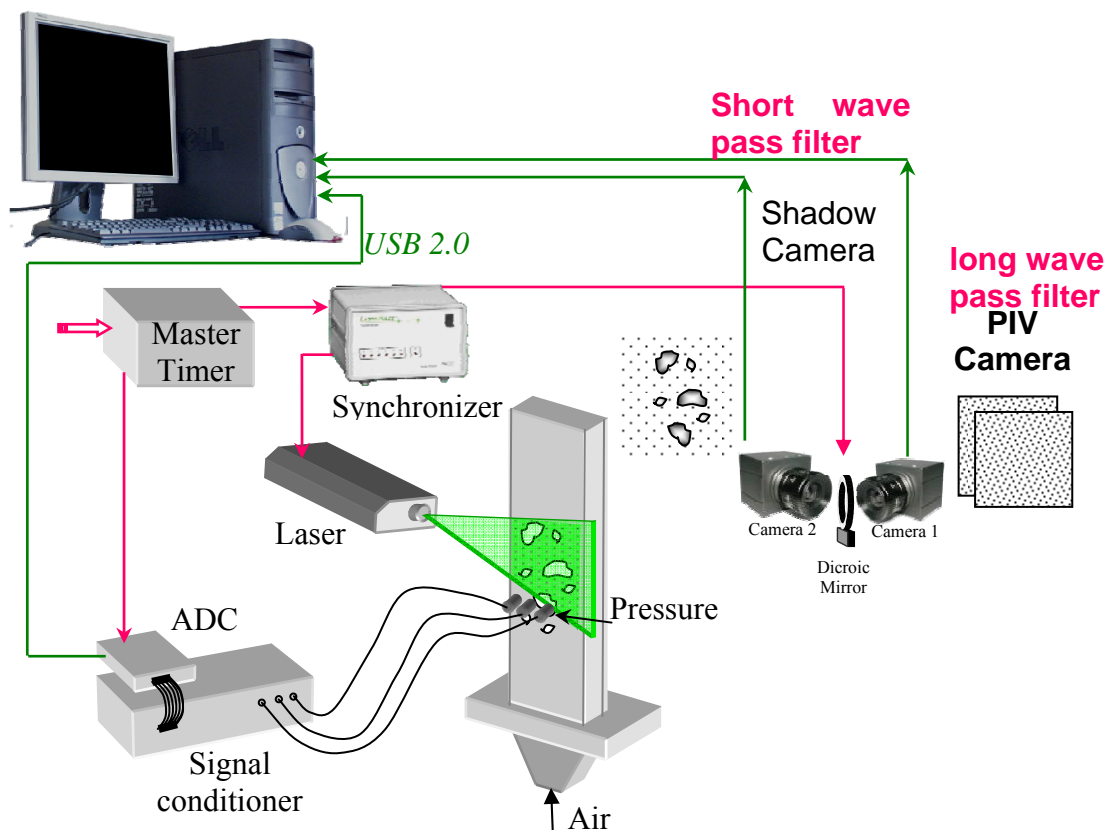


Figure 3. Experimental setup for simultaneous PFS and PIV measurement

The column was mounted on a mechanical traverse in order to have easy alignment with optics, and to facilitate proper leveling. The vertical alignment of the bubble column is a very crucial aspect for the dynamic behavior of column. It was adjusted such that the central bubble plume oscillation around the central axis of the column was symmetric and having nearly constant period of oscillation. Even the

slightest of the error in vertical alignment (up to 0.5°) can result into a biased flow of the bubble plume. The experiments were performed for a single gas flow rate of 60 cc/s, which induces strong plume oscillations with two distinct zones within the column. The central bubble plume region mainly consisted of very large bubbles rising within the liquid at very fast rate, while rest of the cross section had small bubbles with narrow size distribution.

For experiments in 3D column, a cylindrical plexiglass bubble column of 150 mm internal diameter was used. This column was enclosed in another column of square cross section and the space between the two was filled with water to minimize refraction effects. An oil free diaphragm type compressor was used to sparge air through a 20 mm sintered plate. A soap film meter was used to measure the volumetric gas flow rate. The clear liquid height of tap water in the cylindrical column was 650 mm. The experimental conditions maintained the same as the ones used by Kulkarni and Joshi (2004) so that the mass transfer coefficient measured by chemical method could be used for comparison with those calculated by the methodology of current paper.

7.3.2. LDA Measurements

Since the tap water contained sufficient dust, there was no need of any additional seeding while data acquisition with LDA. The LDA velocity measurements were carried out at an axial height of 300 mm from the sparger. At this height, measurements were made at 6 radial positions from center to wall. The average gas hold-up was also independently calculated by taking measurements of the clear liquid height and the dispersed height.

The LDA set-up comprised of a Dantec 55X modular series along with electronic instrumentation and a personal computer. A 5 W Argon-ion laser was used as a source. The laser and optics were mounted on a bench having a unidirectional traversing

mechanism. The traversing mechanism could focus the beams at 5 mm increments by displacing the front lens ($f=300$ mm) with the help of a linearly encoded stepping motor that could be operated either by computer or manually. To identify the flow reversals correctly, a frequency shift was given to one of the beams by means of a Bragg cell with electronic downmixing. Data validation and signal processing were carried out with the help of a Dantec 57N21 Burst Spectrum Analyzer (BSA). The personal computer functioned also as the central data acquisition unit. Durst et al. (1986), Groen et al. (1999), Deshpande et al. (2000), Kulkarni et al. (2001) and Mudde (2010) have discussed the LDA and its use for characterization of bubble driven fluid flow systems in detail. All the measurements were made in the forward scatter mode. It is known that the signal to noise ratio of the forward to back-scattered light is of the order of 10^2 – 10^3 . This means that, in general, forward scatter optical arrangements provide much better signal to noise ratio.

7.3.3. Pressure Sensor: Description, Mounting and Calibration

Kulite XTL-100 sensors were used to acquire pressure fluctuation signals (PFS). These are absolute pressure, piezoresistive pressure sensors with very small outline (cylindrical, with 2mm OD and 8mm length) with frequency response up to 150 kHz. The pressure sensors were mounted onto the wider side of the column wall, as shown in detail in Figure 7.3. Sensors were placed in array of 3 sensors at the height of 50mm ($H/D=0.25$), 200mm ($H/D=1$), 400mm ($H/D=2$) and 600mm ($H/D=3$) totaling 12 sensors. However, for the present study only four active sensors (P1, P2, P3 and P4) were used for analysis. The lateral distance between individual sensors was kept to 30 mm, in order to cover half the width of the column at given cross section. There has been a little concern in regards to the photosensitivity of these sensors and their accuracy for

the low pressure fluctuation range expected (~5000 Pa). However, for the current experimental configuration, the sensor performance was found satisfactory.

The sensors were calibrated for absolute pressure in the column itself. The water level was incremented from 5mm to 500mm above the sensor level, with the increment of 20 mm in the column. This corresponds to the pressure increase of 196 Pa. The voltage time series was recorded for each level in order to have sufficient calibration point in the available height of the column. Each individual sensor had its own gain and offset adjustment in a separate channel of signal conditioner. The gain and offset of each sensor was adjusted to give voltage swing of 4-7 voltage from minimum (5mm) to maximum (650 mm) head expected above the sensor. As can be anticipated, the instantaneous absolute pressure went outside the calibration range (especially slight negative pressures are encountered). However, this was taken care by the allowance provided on the lower and upper limits of the calibration voltage and fairly linear calibration curves obtained for all sensors.

7.3.4. PIV Measurements

Simultaneously with the pressure sensor-array measurements, planar PIV was used to measure two velocity-field components over a plane parallel to the x and y axes and located along the left side of the column, as shown in Figure 7.3 by box number 1, 2 and 3. The PIV system used consisted of two TSI Powerview 4MP, high-resolution, frame straddled CCD cameras with resolution of 2048×2048 pixels and dual cavity Nd:YAG laser. The flow field was seeded using fluorescent seeding particles of Styrene-DVB, having density of 1050kg/m³ and mean particle diameter of 8 μm. This particle size was found to scatter enough light to be imaged by the CCD cameras and ensure that each image contained a sufficient amount of seeding to accurately cross correlate particles within the interrogation region. A Long wave pass filter placed in front of the

DEVELOPMENT OF EXPERIMENTAL TECHNIQUES AND CFD SIMULATIONS OF MULTIPHASE DISPERSIONS

PIV camera ensured that the camera records only the red light scattered by fluorescent particles, and the green laser light scattered from bubbles is blocked. A LED array backlight with 144 High intensity Blue LEDs which are switched on in synchronization with laser, in order to have simultaneous measurement of bubble trajectory with liquid velocity. The details of measurement technique are described elsewhere (Sathe et al., 2010). A dichroic mirror reflects this low wavelength (<532 nm) light towards the shadow camera, which has additional short wave pass filter in order to allow only the blue light from LED array, almost completely blocking the green laser light reflected from bubbles. The PIV processing is done by TSI INSIGHT 3G image acquisition software platform. Deformation grid processing is used with final interrogation area of 20×20 pixels, giving a spatial resolution of 0.6 mm over a measurement window of 100×100 mm.

To synchronize the Pressure sensor and PIV acquisition, a master timer generating a single 5-V TTL pulse with duration of 1 ms was utilized. Both the Pressure sensor Data acquisition system (In-house developed signal conditioner and National Instruments USB Daq 6210) and the PIV acquisition systems were armed to start acquiring once they receive an external trigger signal. Then, the PIV synchronizer (TSI Laser Pulse 610035) sends the trigger signals for Laser pulsing, LED Flash and camera shutter operations. The timing of PIV synchronizer was controlled by INSIGHT 3G software on Mater PC. A Dell Precision 670 workstation with two 3.0 GHz, Xeon processors and 3GB of memory was used as a master PC. The data acquisition was controlled by National Instruments LABVIEW software. The final data processing of PFS, LDA data and PIV velocity field was performed using MATLAB.

7.4. Data Processing

7.4.1. Stochastic Estimation

Stochastic estimation uses the conditional information specified about the flow at one or more locations in conjunction with its statistical properties (the two-point correlation tensor) to estimate the information at the remaining locations. In this particular study SE has been used to estimate the turbulent velocity field (unknown variable) $\tilde{u}_i'(r_0 + \Delta r, t + \tau)$ and $\tilde{v}_i'(r_0 + \Delta r, t + \tau)$ within the bubble column reactor, from a known wall pressure magnitude or event, $p_{wi}'(r_0, t)$; where $r_0 = (x_0, 0, z_0)$ is the location of the event, $\Delta r = (x - x_0, y, z - z_0)$ is the offset between the estimate and event locations, and τ is the corresponding time offset.

For brevity, the following analysis will only consider the x-component of the velocity, u_i' , but the resulting equations are the same for the y-component. Basically the stochastically estimated velocity field is obtained from a Taylor series expansion of the estimate in terms of the known condition (the wall pressure in the current work) and is given by,

$$\tilde{u}_i'(r_0 + \Delta r, t + \tau) = A_{ui,lin}(\Delta r, \tau) p_{wi}'(r_0, t) \quad (7.4)$$

and

$$\tilde{v}_i'(r_0 + \Delta r, t + \tau) = A_{vi,lin}(\Delta r, \tau) p_{wi}'(r_0, t) \quad (7.5)$$

where, $A_{ui,lin}(\Delta r, \tau)$ is the coefficient of the linear estimate of u_i' . This is determined such that the long-time mean squared error between the velocity and its estimate, $e(r_0 + \Delta r)$, is minimized. Explicitly, at a specific location within the flow domain the mean squared error is:

$$e(r_0 + \Delta r) = \overline{(\widetilde{u}_i'(r_0 + \Delta r, t + \tau) - u_i'(r_0 + \Delta r, t + \tau))^2} \\ = \overline{(A_{ui,lin}(\Delta r, \tau) p_{wi}'(r_0, t) - u_i'(r_0 + \Delta r, t + \tau))^2} \quad (7.6)$$

The value of $A_{ui,lin}(\Delta r, \tau)$ that minimizes the error may be found then by requiring:

$$\frac{de}{dA_{ui,lin}} = \frac{d}{dA_{ui,lin}} \left[\overline{(A_{ui,lin}(\Delta r, \tau) p_{wi}'(r_0, t) - u_i'(r_0 + \Delta r, t + \tau))^2} \right] = 0 \quad (7.7)$$

Exchanging the order of the derivative and time integration operations:

$$\frac{d}{dA_{ui,lin}} \left[\overline{(A_{ui,lin}(\Delta r, \tau) p_{wi}'(r_0, t) - u_i'(r_0 + \Delta r, t + \tau))^2} \right] \\ = 2 \left[\overline{(A_{ui,lin} p_{wi}'^2(r_0, t) - u_i'(r_0 + \Delta r, t + \tau) p_{wi}'(r_0, t))} \right] \\ = \left[\overline{(A_{ui,lin} p_{wi}'^2(r_0, t) - u_i'(r_0 + \Delta r, t + \tau) p_{wi}'(r_0, t))} \right] = 0 \quad (7.8)$$

Eq. (7.8) is satisfied if,

$$A_{ui,lin}(\Delta r, \tau) = \frac{\overline{p_{wi}'(r_0, t) u_i'(r_0 + \Delta r, t + \tau)}}{\overline{p_{wi,rms}'^2}} = \frac{R_{p'u_i}(\Delta r, \tau)}{\overline{p_{wi}'^2}} \quad (7.9)$$

Such an estimate is known as linear stochastic estimation (LSE), where, $R_{p'u_i}(\Delta r, \tau)$ is the cross correlation function between wall pressure, p_w' and the instantaneous u_i' and the over-bar denotes time averaging. $A_{i,lin}(\Delta r, \tau)$ is the linear coefficient, which is the function of the cross-correlation between the u_i' and p_w' . These two-point correlations are computed at zero time delay between the pressure signature and the flow field; and, therefore, it is necessary to acquire both the pressure and velocity data simultaneously. An important point to recognize is that with stochastic estimation if there is no correlation between the flow field and the pressure signature, the estimation has no significant physical value. The technique provides information about the flow

structures that are directly related to the pressure signature. Thus, SE gives a physical interpretation of the dominant the flow structures associated with the pressure generation on the surface. Note that the LSE is taken to be a function of the spatial and temporal separation between the event and estimate, but not the specific time or location on the wall where the event is observed.

Linearly estimated conditional average based on the single point event is said to be single point LSE or just LSE. SE technique provides a valuable tool to evaluate estimates of single and multipoint conditional averages, however, it does not answer the fundamental question of which event(s) to observe and their relevance to the overall dynamics of the flow. In general, flow structures may imprint a pressure signature on multiple pressure sensors. Thus, when estimating the flow field above the surface from the wall pressure field, the multi-point, linear, stochastic estimation uses the pressure signature from an array of two or more pressure sensors as the condition on which to estimate the flow field. The number of pressure sensors to use in the estimate depends on the correlation of the velocity with the pressure field. In some cases a flow structure may affect the pressure seen by five or six pressure sensors only; and, therefore, only those pressure sensors would be needed in the estimation. However, it is difficult to know exactly how many pressure sensors are appropriate for reconstructing the flow field based on the pressure distribution. This problem can be remedied by using a large array of pressure sensors extending beyond the spatial range of interest for the estimation. Multipoint estimate is stricter with this condition compared to a single-point, pressure condition and is less likely to deviate from the instantaneous flow field. It has been also pointed out by Guezennec et al. (1989) that multipoint conditional averages or their stochastic estimates are far more realistic than single-point conditional averages since they allow for the observation of the interaction of events at specified length scales,

rather than events viewed in isolation. Cole et al. (1992) reaffirmed the idea of using multi-point SE by investigating utilizing multiple reference velocity points in their estimation of the dominant structures in a jet mixing layer. They presented their results in terms of percentage of energy captured by the multi-point estimates. The authors found that single-point estimates did not adequately estimate the instantaneous flow field and that at least two reference points located on opposite sides of the shear layer did represent the flow field well. Thus, the multi-point estimate is generally more effective in capturing the true nature of the flow structures, and it is one of the primary focus here, given the availability of multi-point information from the pressure-array data. The results from single-point estimation were examined first in order to assess the consequences of truncating the estimation at the linear term. Once the reasonableness of the linear estimation was established, the spatiotemporal evolution of the wall-pressure-generating structures was examined through a multipoint linear stochastic estimation (MLSE) (Ukeiley and Murray, 2005). MLSE, which is an extension of the LSE (Eq.(4) and Eq.(5)), is given by,

$$\begin{aligned} \tilde{u}_i' = & A_{u1,lin}(\Delta r, \tau) p_{w1}'(r_0, t) + A_{u2,lin}(\Delta r, \tau) p_{w2}'(r_0, t) + A_{u3,lin}(\Delta r, \tau) p_{w3}'(r_0, t) + \dots \\ & + A_{un,lin}(\Delta r, \tau) p_{wn}'(r_0, t) \end{aligned} \quad (7.10)$$

$$\begin{aligned} \tilde{v}_i' = & A_{v1,lin}(\Delta r, \tau) p_{w1}'(r_0, t) + A_{v2,lin}(\Delta r, \tau) p_{w2}'(r_0, t) + A_{v3,lin}(\Delta r, \tau) p_{w3}'(r_0, t) + \dots \\ & + A_{vn,lin}(\Delta r, \tau) p_{wn}'(r_0, t) \end{aligned} \quad (7.11)$$

where, $A_{u1,lin} - A_{un,lin}$ and $A_{v1,lin} - A_{vn,lin}$ are the linear-estimation coefficients for each pressure point used in the LSE and after mathematical rearrangement are given as,

$$\begin{bmatrix} A_{u1,lin} \\ A_{u2,lin} \\ A_{u3,lin} \\ \vdots \\ A_{un,lin} \end{bmatrix} = \begin{bmatrix} \overline{P_{w1}P_{w1}} & \overline{P_{w1}P_{w2}} & \overline{P_{w1}P_{w3}} & \cdots & \overline{P_{w1}P_{wn}} \\ \overline{P_{w2}P_{w1}} & \overline{P_{w2}P_{w2}} & \overline{P_{w2}P_{w3}} & \cdots & \overline{P_{w2}P_{wn}} \\ \overline{P_{w3}P_{w1}} & \overline{P_{w3}P_{w2}} & \overline{P_{w3}P_{w3}} & \cdots & \overline{P_{w3}P_{wn}} \\ \vdots & \vdots & \vdots & \ddots & \vdots \\ \overline{P_{wn}P_{w1}} & \overline{P_{wn}P_{w2}} & \overline{P_{wn}P_{w3}} & \cdots & \overline{P_{wn}P_{wn}} \end{bmatrix}^{-1} \begin{bmatrix} R_{p_1'u_1'} \\ R_{p_2'u_2'} \\ R_{p_3'u_3'} \\ \vdots \\ R_{p_n'u_n'} \end{bmatrix} \quad (7.12)$$

The inverse matrix in Eq. (7.12) (first matrix on the right hand side) is calculated from the wall-pressure measurements alone and it contains information on the two-point correlation among the data from all sensors. The second matrix on the right hand side of the equations represents the cross-correlation between the velocity component to be estimated and the wall-pressure at all pressure sensors. Thus, in this way a set of coefficients, $A_{u1,lin} - A_{un,lin}$, is calculated for every spatial location where the time dependence of the velocity is to be estimated. Similarly the coefficients are estimated for MLSE estimation of v_i' .

On the other hand, if the second-order term in the series is included in the estimation, a quadratic stochastic estimation (QSE) is obtained. However, Tung and Adrian (1980) studied the influence of the second, third and fourth order terms on the estimate and their results indicated that the contribution from higher order terms to the overall estimate was insignificant and the same observations were even extended for our study, hence, the focus for the current study was restricted only upto the use of LSE. For more detailed derivation of LSE and QSE equations, the reader is referred to the references cited above.

7.4.2. Image Processing

The shadow images were processed using the image processing routines programmed in MATLAB R2009a. The grayscale images from the high speed camera

are read and corrected with first order perspective correction to obtain perfect overlap between PIV and High speed camera image. The calibration constants are obtained from the images of a calibration target placed in the focal plane of the square tank used for the experiments. The perspective corrected images are binarized to black and white using a threshold value. The threshold is calculated on the basis of intensity histogram of the grayscale image. This process takes care of the non-uniform background illumination. Since the bubble shadows appear as dark patches on a white background, a negative of this image is taken where the bubbles appear bright against dark background.

The bubbles contain 'holes' in the binary image. These artifacts are primarily caused by the curvature of the bubble. These are removed using morphological image processing, which involves dilation operation on the image followed by erosion operation. The negative of the 'filled' bubble image is used as a digital mask to blank the PIV images in these regions. The residual light passing through the filter assembly allows the bubble silhouette to be recorded as a blurred boundary in the seeding particle image. The regions corresponding to the bubbles are set to value '0' to avoid spurious vectors caused by cross correlation between the reflections from bubble surface.

The 'filled' bubble images are subjected to the image registration process. In image registration, the individual bright regions of the image are isolated, which are marked by the negative of the bubble shadows. The connectivity of a pixel with its neighboring pixels is used as a criterion for a pixel to be associated to a particular region. The registration program starts from the top left corner of the image and assigns a unique number to each pixel of the image. The pixels having same label number correspond to single region (bubble). The background is labeled 0. Every labeled region is analyzed for different properties like equivalent area in pixel squared units, and location of the centroid.

Finally, the centroid locations exported from the image processing routine are processed to track the particles by an open source code implementing the algorithm of Crocker and Grier (1996). The routine searches for centroids closer to the current centroid from the location array provided. The routine was tested on dummy images before being applied to ‘rough’ images caused by bubbles. It was found to work satisfactorily even with more than 100 bubbles present in the image. However, the Δt needs to be adjusted such that the bubbles do not move farther than half the diameter of individual bubbles while capturing the shadow images. Additional check of both the identified bubbles having same area was implemented in the particle tracking code. The tracking code returns the trajectory as array of centroid locations. Then, second order differencing is used to evaluate the first and second derivative of the bubble trajectory, which yields the bubble velocity and acceleration respectively.

7.4.3. Discrete Wavelet Transform

The flow field obtained by PIV contains flow structures with different length scales. The DWT is used to separate the information content in the data from a fine scale to a coarser scale. When the data comprises of variations of different ‘scales’ of variations, spectral analysis is used to extract the information about these scales. The details of DWT to isolate the structures of different scales from PIV data is described in detail by Deshapande et al. (2008) and Sathe et al. (2010). A MATLAB program has been developed that marks the boundaries of flow structures with different scales, and calculates their length scale, velocity and time scale. The energy spectrum is obtained by taking the mean over the energy associated with each selected scale as:

$$E_{ii}(\kappa) = \frac{\sum_b W_i^{a,b}(x)}{n_b}. \quad (7.13)$$

The corresponding wavenumber κ is obtained based on scaling parameter a as $\kappa^2 = \kappa_1^2 + \kappa_2^2$ and $\kappa_i = 2\pi 2^a / \Delta x_i$. The resultant wavenumber spectrum gives an idea of the nature of turbulence in flow field.

The scalewise reconstruction of velocity field is used to calculate the vorticity field corresponding to different length scales. A threshold is applied to each one of this vorticity field, to identify the flow structures of different size. The thresholding result in the binary images marking the structures as white regions. These images are then processed by the same MATLAB routine which isolates bubbles from binarized shadow images. After isolating different eddies, this image is used as a mask on the scalewise reconstruction of the axial and radial velocity field. The resultant matrix is used to get the velocity magnitudes inside each isolated 'structure', which aid the calculation of the energy of each individual structure. The labeled binary images are analysed to get the size and centroid of every individual structure. It should be noted that, each individual region essentially represents a 2D cross section of the original 3D flow structure. The individual labeled regions can also be processed to quantify their shapes.

7.4.4. Eddy Identification Methodologies (EIM)

Two algorithms for EIM, one based on zero crossings of velocity/temperature and the other based on CWT for identification and isolation of eddies have been employed in this study. The PFS (pressure fluctuation signals) and PIV data are used to complement each other for eddy isolation in 2D column, while the PFS and LDA data are used for eddy isolation in 3D column. The data are processed for superficial gas velocity of 20 mm/s. The discussion below brings out the principles of the individual methods and their relative merits.

PFS and LDA data are point data, represented as the time series. The PIV data is planer velocity data. The regions corresponding to bubbles have been marked and removed from PIV velocity field and it is subjected to 2D EIM-CWT analysis. The individual eddies are separated form time seris using zero crossings and CWT. The methods are described below:

7.4.4.1. Eddy identification method based on zero crossings (EIM-ZC)

For the identification of eddies an approach based on zero crossings in fluctuating velocity component (Sreenivasan et al., 1983; Luk and Lee, 1986; ; Sahu et al. 1999; Kulkarni and Joshi, 2004). As an eddy passes through the measurement point, the velocity fluctuates about its mean value (Figure 7.4A). Subtracting the mean value, we obtain the fluctuating component of the velocity. As seen in Figure 7.4B, which represents a small window of the data in Figure 7.4A, the fluctuating component has both positive and negative values and therefore it crosses the time axis at many locations. Within consecutive zero crossings of the fluctuating component, the fluid elements in the measurement location would therefore have similar kinetic properties and this may be considered as the criterion for eddy identification. Thus, from a plot of fluctuating velocity (u_2') versus time, as the velocity vector crosses the time axis, the life of one eddy may be considered to end while another one begins. Alternatively stated, it may be proposed that the time gap (Δt) between two successive crossings represents one eddy. Different eddies show unequal time gaps ($\Delta t_1, \Delta t_2, \dots, \Delta t_n$) as shown in Figure 7.4 (B), and these gaps are taken as the life of respective eddies.

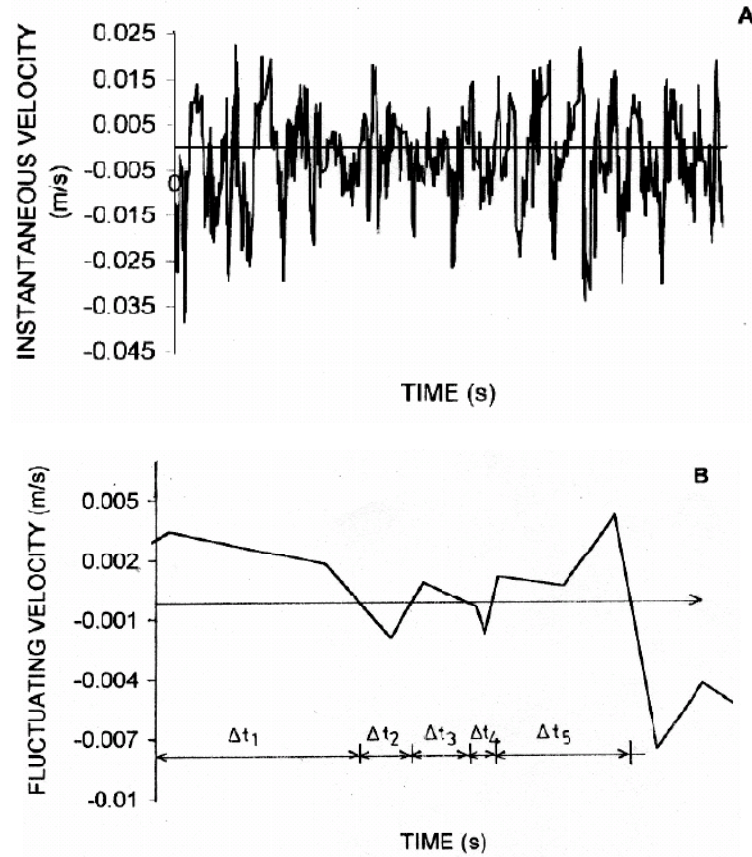


Figure 7.4 Schematic of Eddy isolation method (A) sample instantaneous velocity time series (B) zero crossings

The characteristic energy of an eddy may be obtained by squaring and summing the fluctuating components within an identified eddy as:

$$k_{E,i} = \frac{\sum_i \frac{1}{2} u_2'^2}{\sum_i} \quad (7.14)$$

The characteristic eddy velocity for i th eddy was then estimated by:

$$u_{E,i} = \sqrt{2k_{E,i}} \quad (7.15)$$

Eddy length scale (l_E) was calculated from the eddy lifetime (Δt_E) and the characteristic eddy velocity (u_E). All eddies were sorted according to their age. The age

distribution function ($\phi(t)$) was then estimated, identifying the fraction of eddies having life between t and $t + \Delta t$.

7.4.4.2. Eddy identification method based on continuous wavelet transform (EIM-CWT)

In the case of CWT, an appropriate wavelet basis function ψ is chosen to convolve the 1D data $u_2(t)$ into time-scale components by means of translations b and dilations a of ψ as given by:

$$T_i^{a,b} = \int u_2(t) \psi^{a,b}(t) dt \quad (7.16)$$

The wavelet function ψ may be selected as the n^{th} derivative of a Gaussian (DoG) function because of its advantage in computing higher order derivatives while still maintaining the compactness and scalability of the wavelet basis function, i.e.,

$$\psi^{(n)}(t) \equiv \frac{d^n}{dt^n} e^{-(1/2)t^2} \quad (7.17)$$

Using the Gaussian function, the deterministic trends up to $(n-1)^{\text{th}}$ order may be eliminated by a local polynomial fit, and then studying the residual for its multifractal properties and for extracting the masked singularities. The identified singularities relate to the presence of distinct structures in the flow (Meneveau and Sreenivasan, 1987; Muzy et al., 1991).

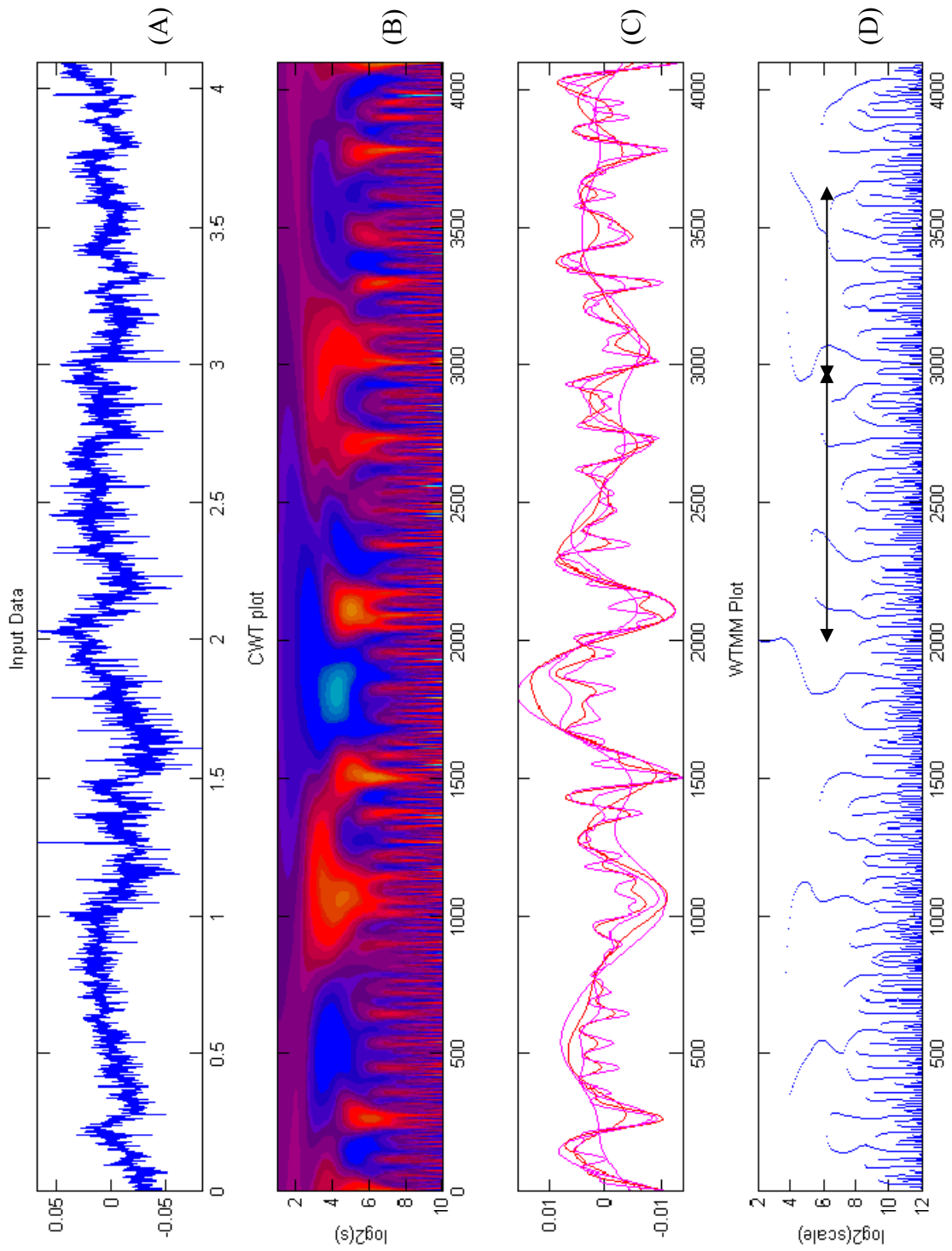


Figure 7.5 Sample CWT processing output: (A) Time series (B) CWT scalewise coefficient matrix (C) Scalewise reconstruction using CWT (D) WTTMM tracking

Further, by the methodology of wavelet transform modulus maxima (WTMM), only the local maxima of $|T_i^{(a,b)}|$ (Eq. 7.17) are chosen and grouped to obtain the loci of maxima as a function of t across the scales a . The observed maxima lines delineate structures and their passage in the multiscale WT domain. More precisely, when the WTMM is applied to the data captured near the VL and/or SL interfaces, this analyses bring out the passage of eddies in time and therefore their effects on the surface renewal phenomena may be analyzed. A proper implementation of the WTMM and scanning the modulus maxima lines systematically across wavelet scales may be used to obtain properties including the start time of eddy formation, its end time, eddy age distribution, eddy energy and their distribution, eddy break-up and energy transfer mechanism across the WT scales. Figure 7.5 shows typical results of a study by WTMM and analyzing the maxima lines for eddy identification and their properties, for pressure time series. Eddy identification was carried out by coding in MATLAB© by analyzing for array oriented data constructs on the maxima lines.

7.4.4.3. Relative merits of EIM-ZC and EIM-CWT

The main advantage of EIM-ZC is that it is possible to evaluate the eddy age distribution $\phi(t)$ in a simple way. Although, CWT requires increased computational time, it is more rigorous because eddies have been isolated on the basis of detection of singularities. The EIM-ZC shows the presence of large number of small eddies when noise is present in the data. This may lead to interpretations deviating from reality. The situation may be improved by denoising the data by suitable techniques. In the present study, we employ a procedure using discrete wavelet transform and as described in Roy et al. (1999). For EIM-CWT, because of the basis function dilated and translated over the range of scales, the frequency separation is in-situ. It identifies eddies according to frequency scales and a separation of eddies at all scales is observed. The EIM-CWT

offers the advantage of studying eddy behavior at desired scales and the effects of noise is naturally diminished.

7.4.5. Methodology for Evaluation of Flow Structures Characteristics and the Estimation of Mass Transfer Coefficient

In the current work, we propose a systematic methodology to use the pressure fluctuation signals to evaluate the characteristics of flow structures, and to use them for estimation of mass transfer coefficient. The data processing requires support of PIV and LDA data in order to provide calibration dataset for the pressure fluctuation signals to obtain liquid velocity field. This velocity time series are then employed to estimate the length scale, time scale and energy distributions of the structures which are then used to evaluate the mass transfer coefficient. The stepwise procedure is as follows:

1. Simultaneous PIV and PFS signal recording is carried out in rectangular (2D) bubble column for different spargers.
2. The planer velocity data from PIV is used as calibration set in MLSE to reconstruct the planer time averaged velocity field from pressure sensor array time series.
3. The Planer velocity field from PIV is subjected to 2D DWT analysis to obtain the energy spectrum, length and age distribution of structures.
4. The velocity time series calculated using MLSE from pressure fluctuation signals is subjected to EIM-ZC and EIM-CWT, to obtain the length and age distribution of structures. These distributions are varified against those obtained from PIV.
5. The LDA velocity profiles are used as calibration set in MLSE to obtain the velocity time series from pressure sensor signals in cylindrical (3D) bubble column.

6. The velocity time series from MLSE in 3D column is subjected to EIM-ZC and EIM-CWT, to obtain the length and age distribution of structures.
7. The age and length scale distributions in (4) and (6) are used to calculate the mass transfer coefficient in 2D and 3D bubble column.

7.5. Results and Discussion

7.5.1. MLSE of Pressure Fluctuation Signals

Figure 7.6 shows the PIV vector field and corresponding vector field calculated using MLSE of pressure fluctuation signals. The stochastic coefficients to calculate the time-dependence of the velocity fluctuations based on the time-dependence of the wall pressure fluctuations were calculated using Eq.(7.10) and Eq.(7.11). The mechanics of the estimated flow structure could be evaluated using this vector field. Multipoint linear stochastic (MLSE) estimate of the mean velocity vector field for the test data (Different from calibration data) is shown in Figure 7.6B. Comparison of Figure 7.6A with Figure 7.6B indicates the quality of each respective estimate by obtaining a realistic representation of the instantaneous character of the large-scale, organized motions in the present flow field. It is clear from Figure 7.6 that both the amplitude and phase of the velocity vector field are reasonably preserved with MLSE. The order of magnitude of the axial liquid velocity in the upward direction (central region) was found to be 0.26 m/s and the axial liquid velocity in the downward direction (near wall region) of the column was found to be 0.29 m/s.

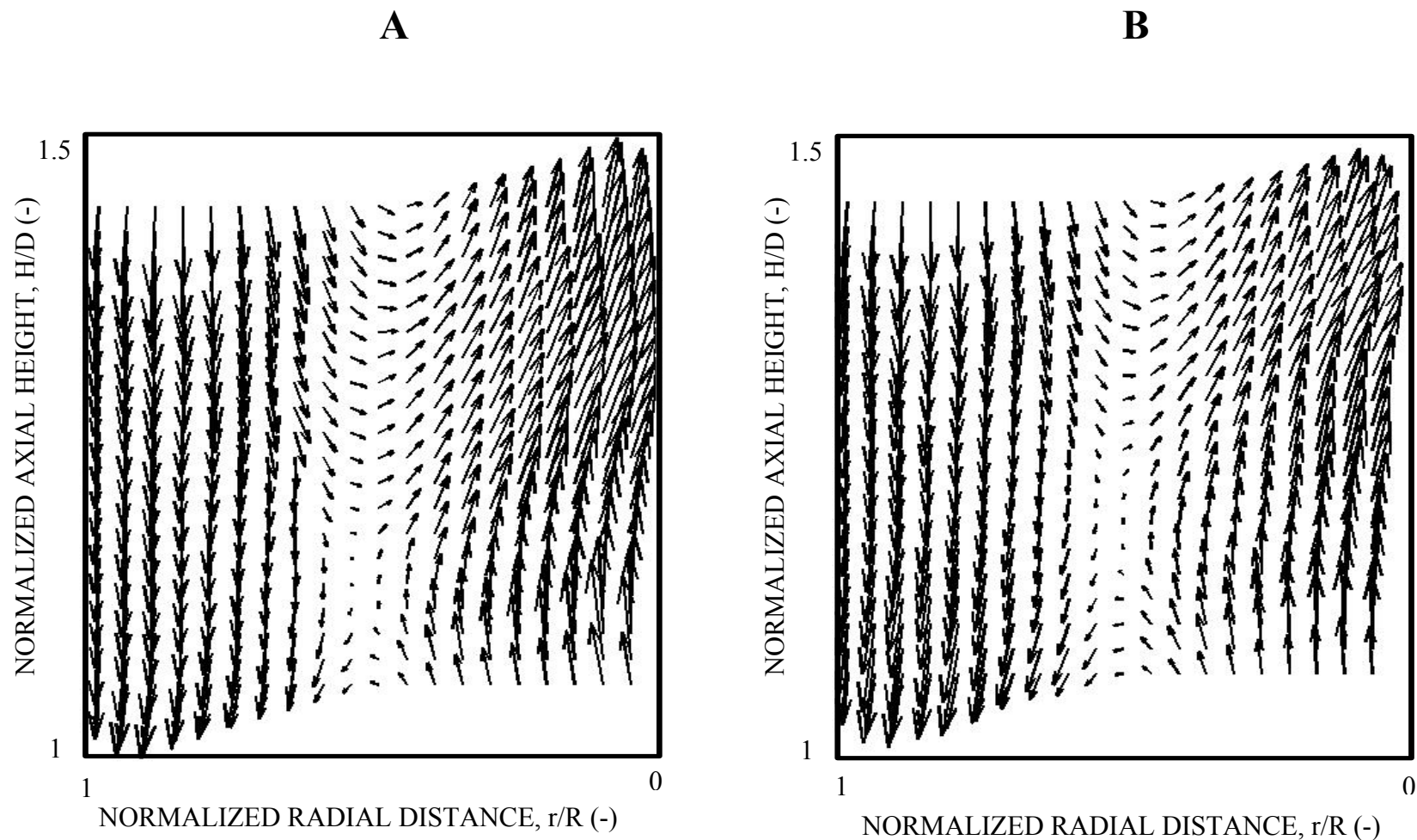


Figure 7.6 Comparison of vector field predicted by MLSE (A) PIV data (B) vector field predicted by MLSE

For clear, quantitative justification of accuracy of MLSE estimates, parity plots showing the comparison between the experimental instantaneous velocity values and those obtained using MLSE has been shown in Figure 7.7. An excellent agreement is seen between the measured and the estimated instantaneous velocity values as shown in Figure 7.7A and Figure 7.7B for u_i' and v_i' respectively.

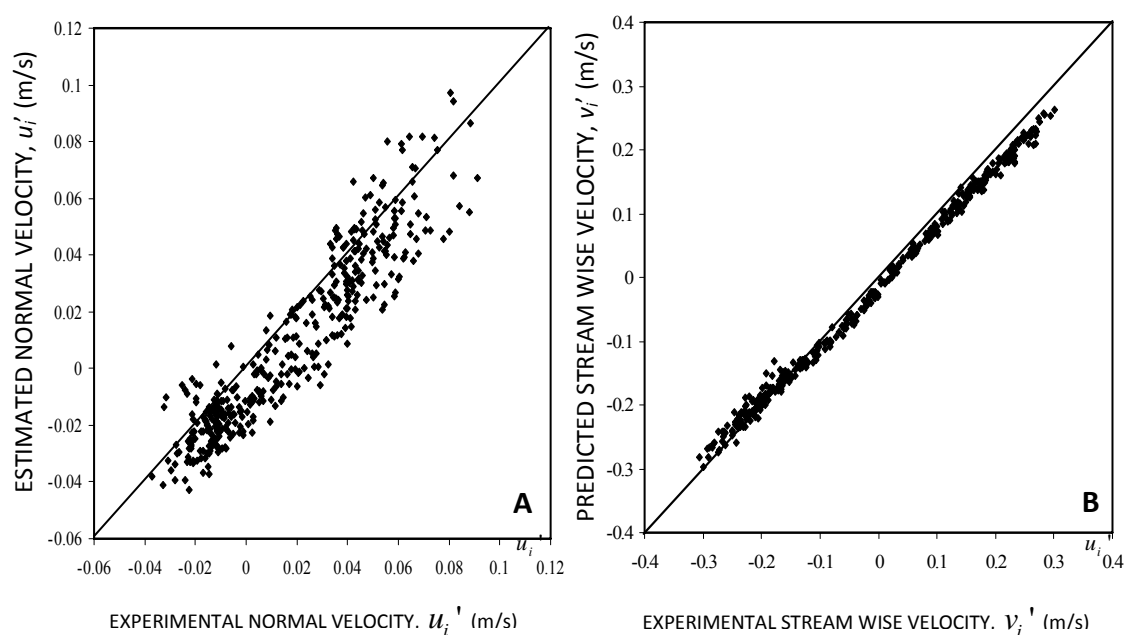


Figure 7.7 Parity plot for prediction of liquid velocity by MLSE

(A) Lateral velocity (B) Axial velocity

7.5.2. Discrete Wavelet transform

Figure 7.8 shows the velocity magnitude contour superimposed with bubble image. Figure 7.9 shows the scalewise decomposition of the vector field of the same image in Figure 7.8.

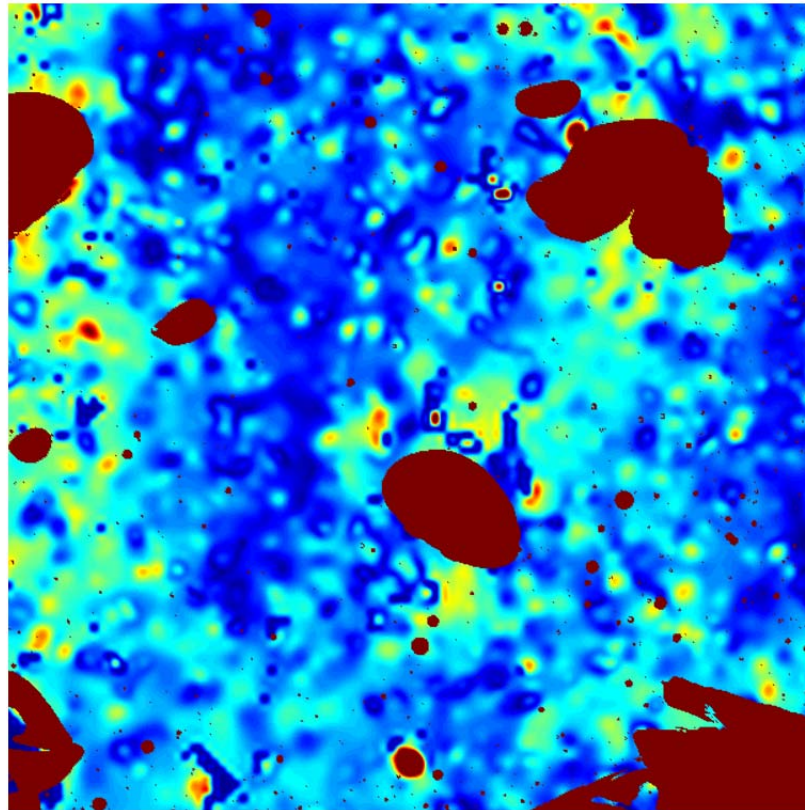


Figure 7.8 Contour of velocity magnitude superimposed with bubble image, a sample image for DWT processing

The individual structure boundaries are marked in each scale. Figure 7.9A-7.9F are consistently decreasing length scales. It can be observed that the small and large structures overlap in many regions. Thus, Figure 7.9 shows the power of DWT to isolate individual structures from PIV vector field. The velocity corresponding to the regions of bubbles has been marked as zero, hence some ‘holes’ appear in the structures of length scale larger than bubbles. A large number of such PIV images were processed to evaluate the length scale, characteristic velocity and energy of each individual structure. The data of eddy energy and length is used to plot the energy spectrum with wavenumber abscissa.

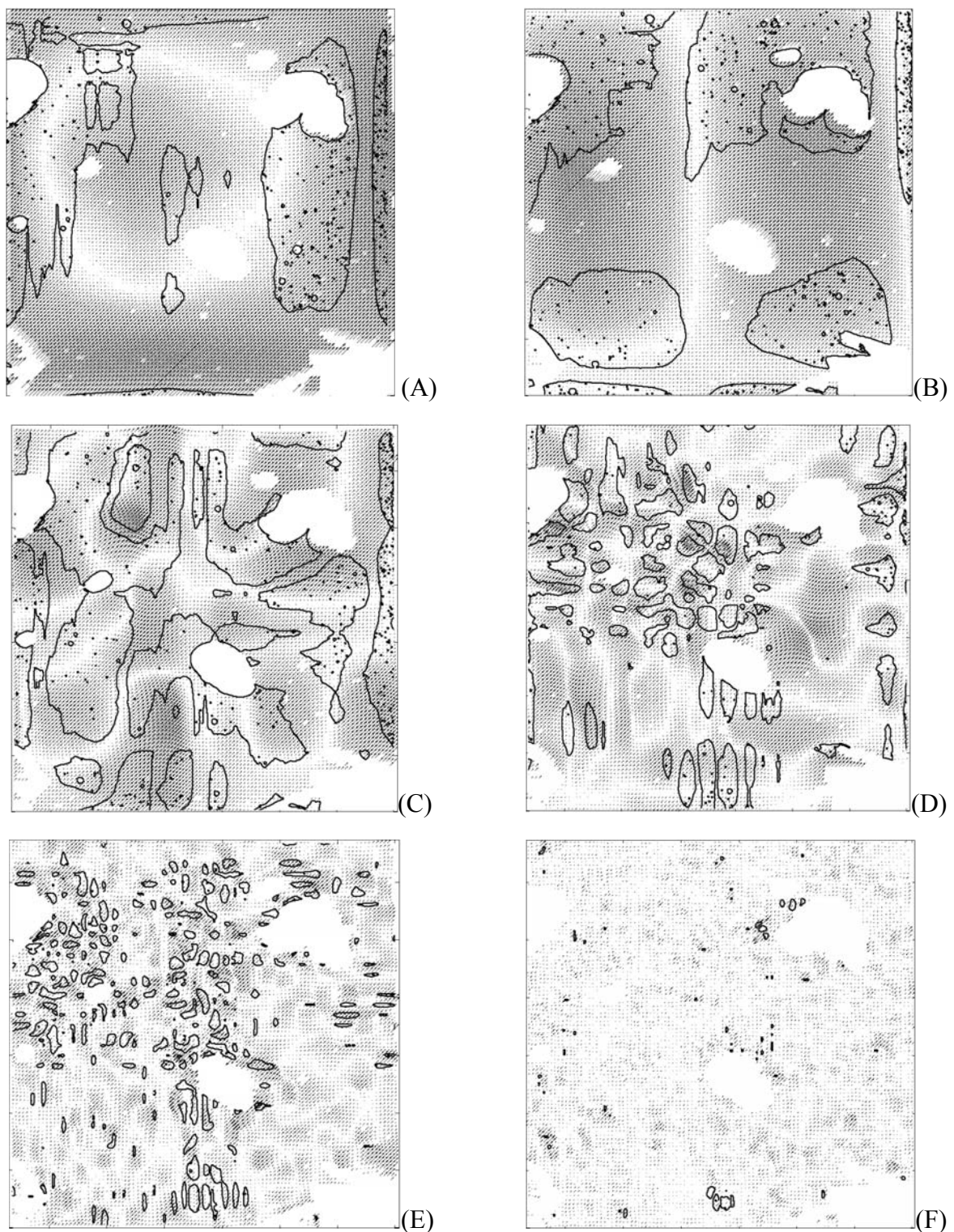


Figure 7.9 Identification of structures in scalewise reconstruction from DWT of PIV velocity field; the black lines mark the boundary of the structures

(A) Scale 2 (B) Scale 3 (C) Scale 4 (D) Scale 5 (E) Scale 6 (F)

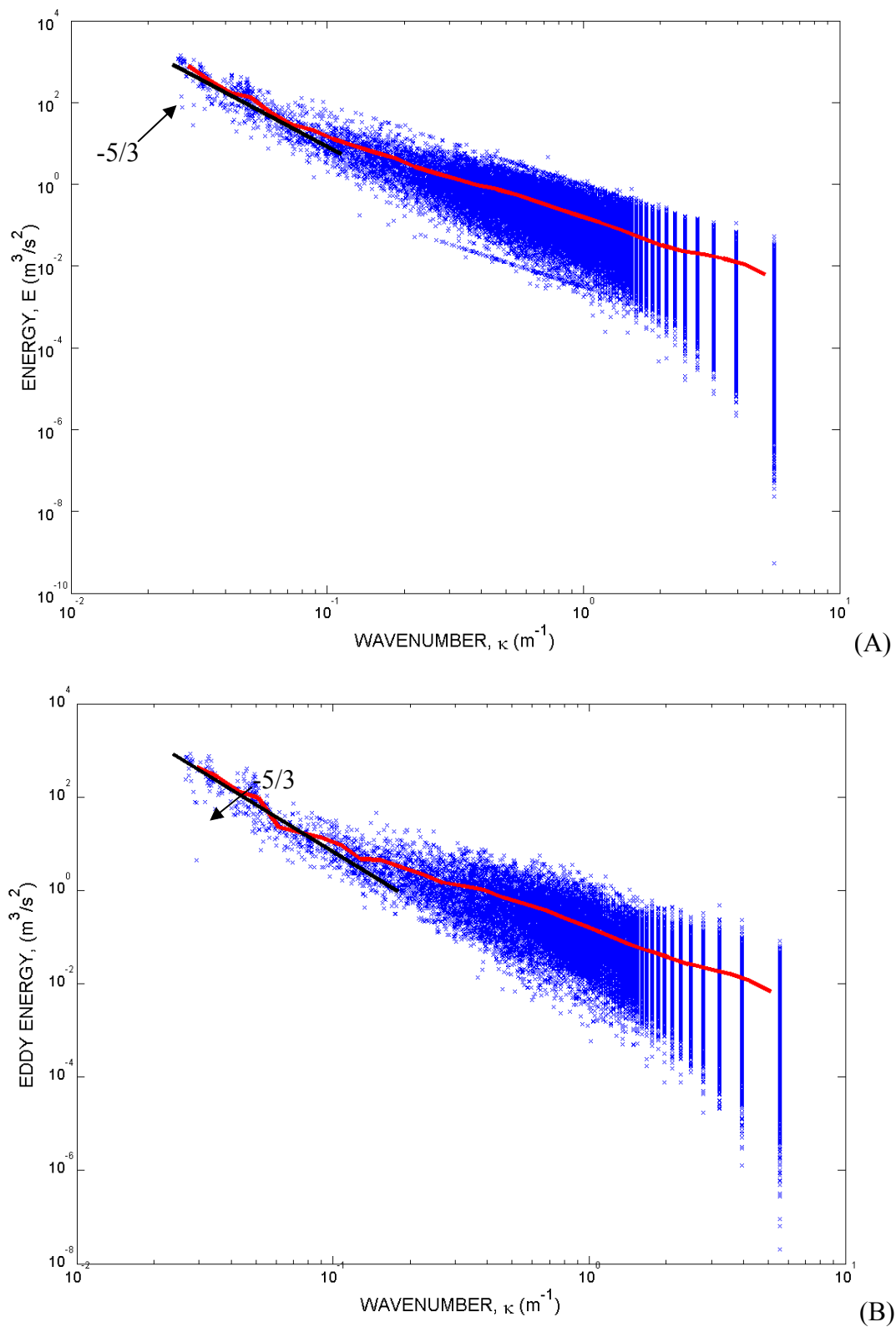


Figure 7.10 Energy spectrum calculated using DWT in 2D bubble column for

(A) Single point sparger (B) Five point sparger

Figure 7.10A shows the Energy spectrum for single point sparger and Figure 7.10B shows the energy spectrum for five point sparger in 2D bubble column. It can be observed that the spectrum has slope of $-5/3$ in lower wavenumber range, marking the inertial subrange. Thus, the resolution of the current PIV data is high enough to resolve the dissipation subrange. Hence the characteristics of flow structures extracted using the methodology in current work are suitable for prediction of mass transfer coefficient using the theories of transport phenomena.

7.5.3. Properties of Flow Structures Evaluated from Pressure Fluctuation Signals

The pressure fluctuation signals obtained in 2D and 3D column were subjected to the analysis described in section 7.4.5. The age distribution and length distributions are plotted in Figure 7.11-7.18 for 2D column and Figure 7.19-7.22 for 3D column. The collective statistics in form of mean eddy length, age and velocity are described in Tables 7.3-7.7.

Figure 7.11A, 7.11B and 7.11C show the age distributions of structures at x/W of 0, 0.5 and 0.97; and $y/H=2$ for 2D bubble column with single point sparger, calculated with EIM-CWT and EIM-ZC. Figure 7.12 A, 7.12B and 7.12C show the different model PDFs fitted to the age distribution for same location as Figure 7.11. 7 different eddy age distributions are plotted: Higbie model, Danckwerts model, Perlmutter tanks-in-series model ($m=2$), Perlmutter tanks-in-series model ($m=4$), Perlmutter tanks-in-series model ($m=6$), and Perlmutter delayed exponential model. The distributions differ mostly in higher order statistics. However, Deshpande et al. (2009) have shown that using two extreme age distribution (Constant age and exponential distribution) results in difference of 13% of predicted value in mass transfer coefficient.

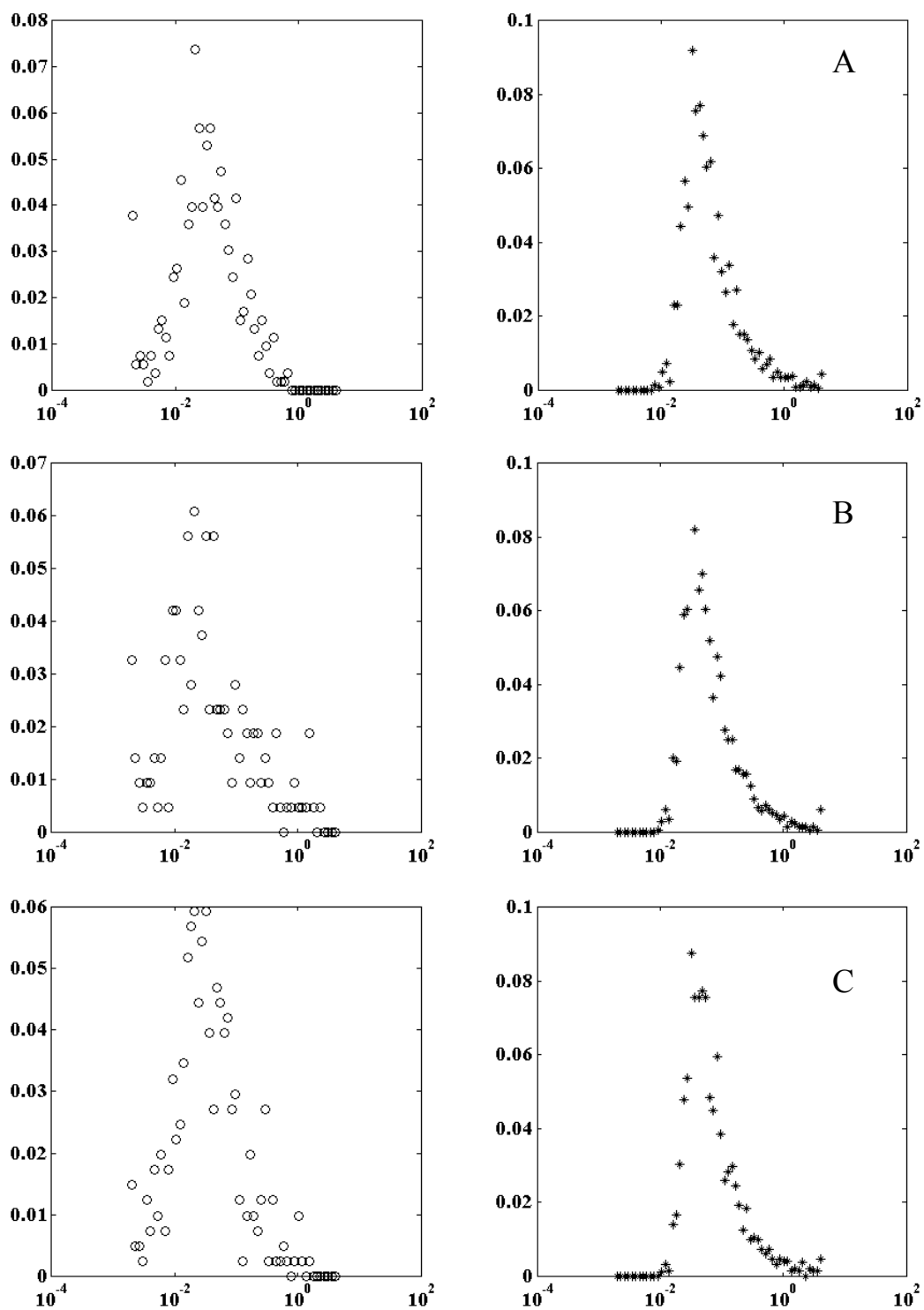


Figure 7.11 Age distribution, 2D Bubble column, Single point Sparger, (A) $x/W=0$ (B) $x/W=0.5$ (C) $x/W=0.97$ (°, EIM-ZC; *, EIM-CWT)

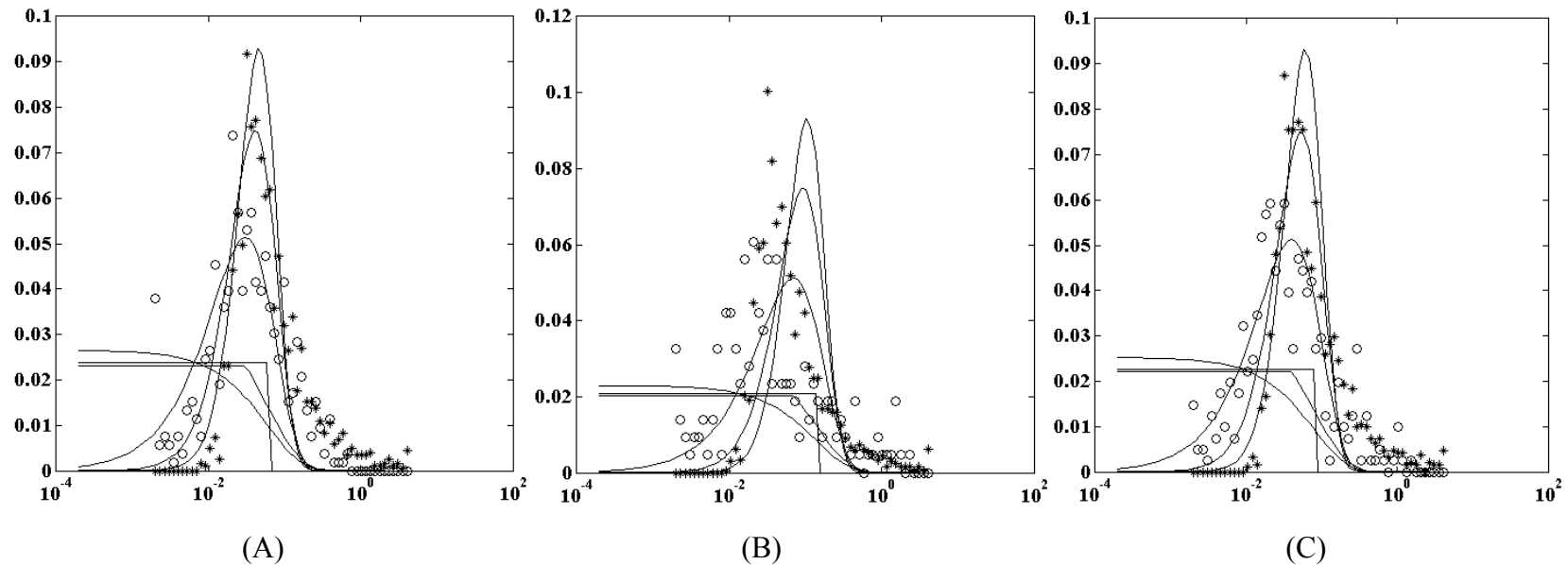


Figure 7.12: Age distribution, 2D Bubble column, Single point Sparger, (A) $x/W=0$ (B) $x/W=0.5$ (C) $x/W=0.97$; (Line 1, Higbie model; Line 2, Danckwerts model; Line 3, Perlmutter tanks-in-series model ($m=2$); Line 4, Perlmutter tanks-in-series model ($m=4$); Line 5, Perlmutter tanks-in-series model ($m=6$); Line 6, Perlmutter delayed exponential model; Line 7, Fortuin et al.; \circ , EIM-ZC; $*$, EIM-CWT)

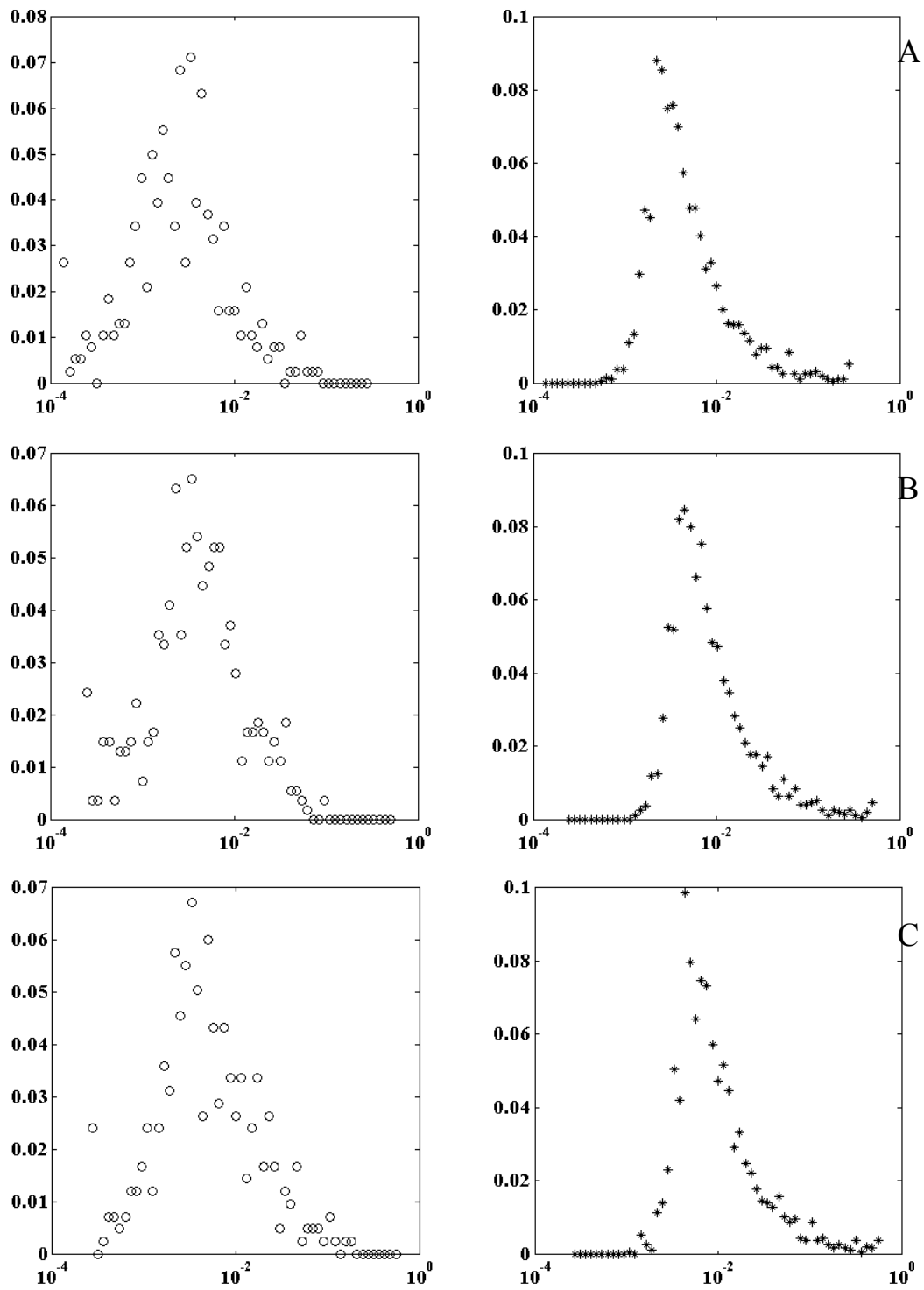


Figure 7.13 Length scale distribution, 2D Bubble column, Single point Sparger,

(A) $x/W=0$ (B) $x/W=0.5$ (C) $x/W=0.97$ (\circ , EIM-ZC; $*$, EIM-CWT)

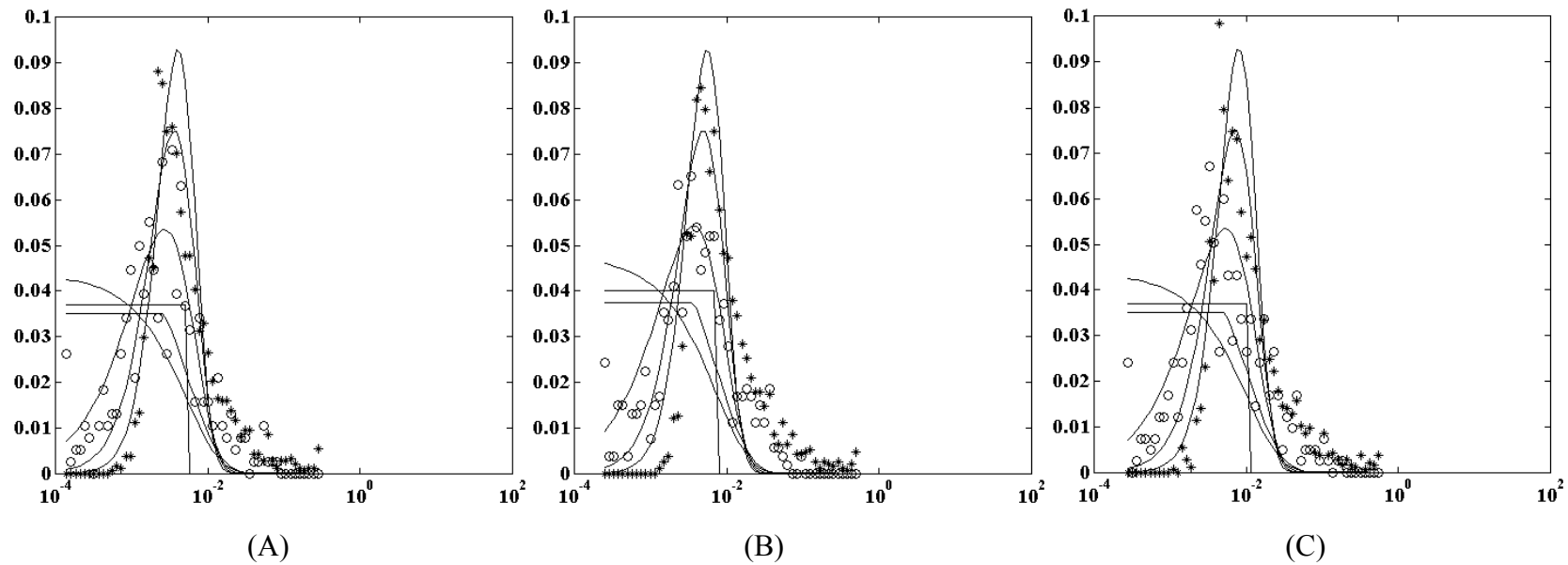


Figure 7.14 Length scale distribution, 2D Bubble column, Single point Sparger, (A) $x/W=0$ (B) $x/W=0.5$ (C) $x/W=0.97$ (\circ , EIM-ZC; $*$, EIM-CWT; lines description same as Figure 12)

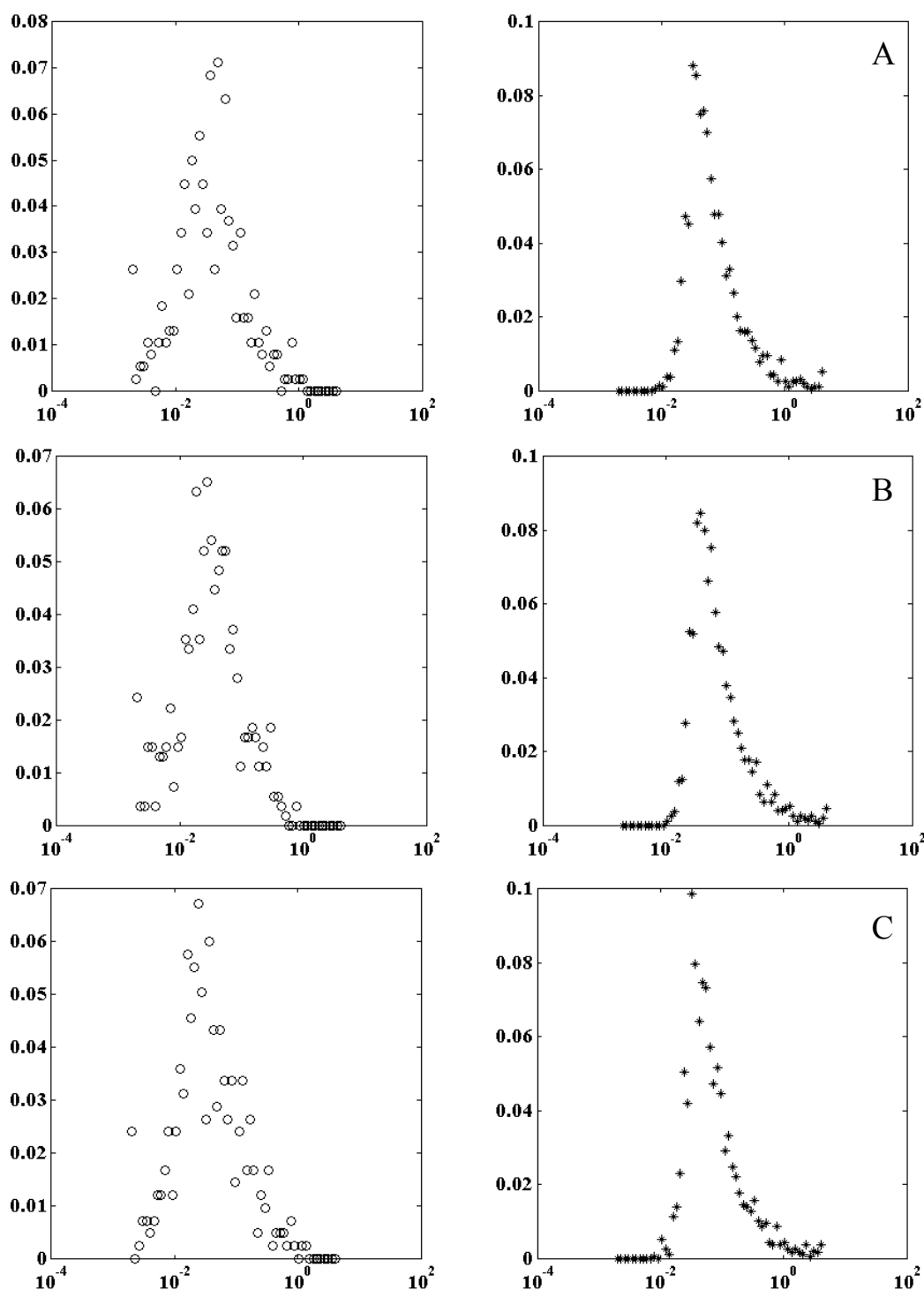


Figure 7.15 Age distribution, 2D Bubble column, Five point Sparger,
 (A) $x/W=0$ (B) $x/W=0.5$ (C) $x/W=0.97$ (\circ , EIM-ZC; $*$, EIM-CWT)

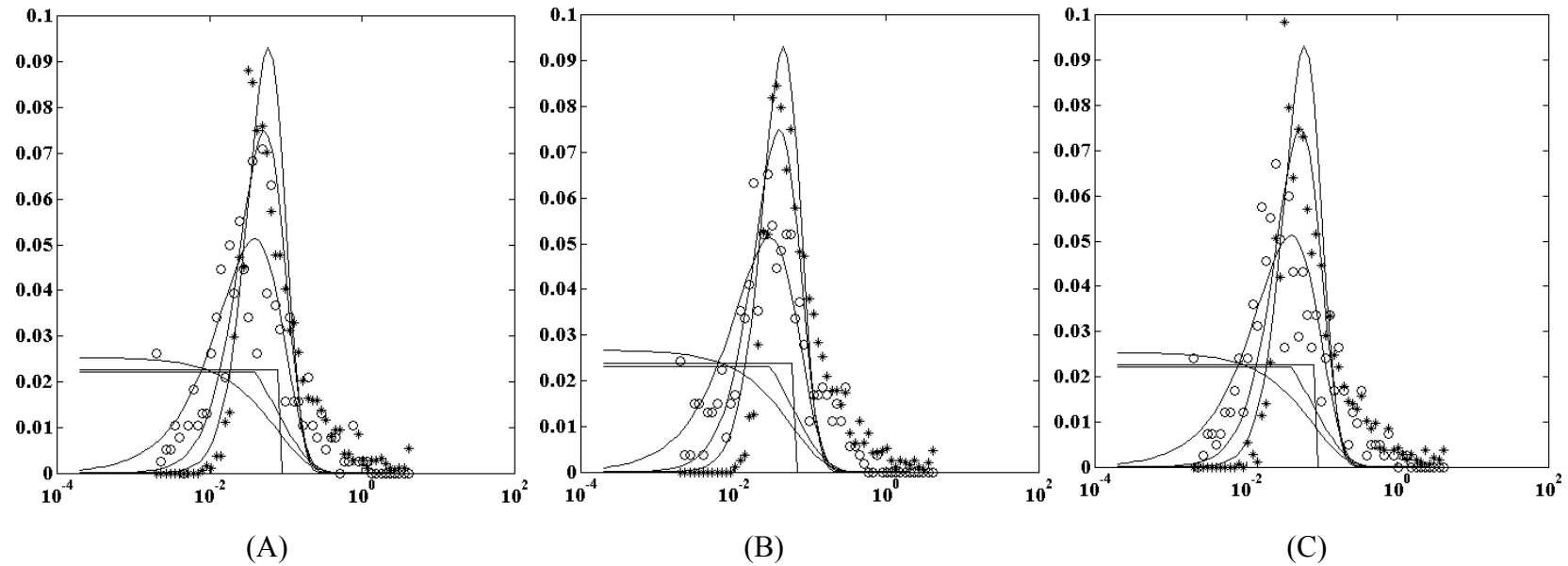


Figure 7.16 Age distribution, 2D Bubble column, Five point Sparger, (A) $x/W=0$ (B) $x/W=0.5$ (C) $x/W=0.97$ (\circ , EIM-ZC; *, EIM-CWT; lines description same as Figure 12)

The statistics of the eddy age, eddy size and velocity for single point sparger are presented in Table 7.4. Figure 7.13A, 7.13B and 7.13C show the length scale distributions of structures at x/W of 0, 0.5 and 0.97; and $y/H=2$ for 2D bubble column with single point sparger, while Figure 7.14A, 7.14B and 7.14C show the model distributions mentioned above fitted to length scale distribution.

Figure 7.15A, 7.15B and 7.15C show the age distributions of structures at x/W of 0, 0.5 and 0.97; and $y/H=2$ for 2D bubble column with five point sparger, calculated with EIM-CWT and EIM-ZC. Figure 7.16A, 7.16B and 7.16C show the different model PDFs fitted to the age distribution for same location as Figure 7.15. Figure 7.17A, 7.17B and 7.17C show the length scale distributions of structures for same sparger and location, calculated with EIM-CWT and EIM-ZC. Figure 7.18 A, 7.18B and 7.18C show the different model PDFs fitted to the age distribution for same location as Figure 7.17.

The analysis of EIM-ZC and EIM-CWT was also performed for processed pressure signals in 3D column. Figure 7.19A, 7.19B and 7.19C show the length scale distributions of structures at x/W of 0, 0.5 and 0.97; and $y/H=2$ for 3D bubble column with perforated plate sparger, calculated with EIM-CWT and EIM-ZC. Figure 7.20A, 7.20B and 7.20C show the different model PDFs fitted to the age distribution for same sparger and location as Figure 7.13. Figure 7.21A, 7.21B and 7.21C show the length scale distributions of structures at x/W of 0, 0.5 and 0.97; and $y/H=2$ for 3D bubble column with single point sparger, calculated with EIM-CWT and EIM-ZC. Figure 7.22A, 7.22B and 7.22C show the different model PDFs fitted to the length scale distribution for same location as Figure 7.21.

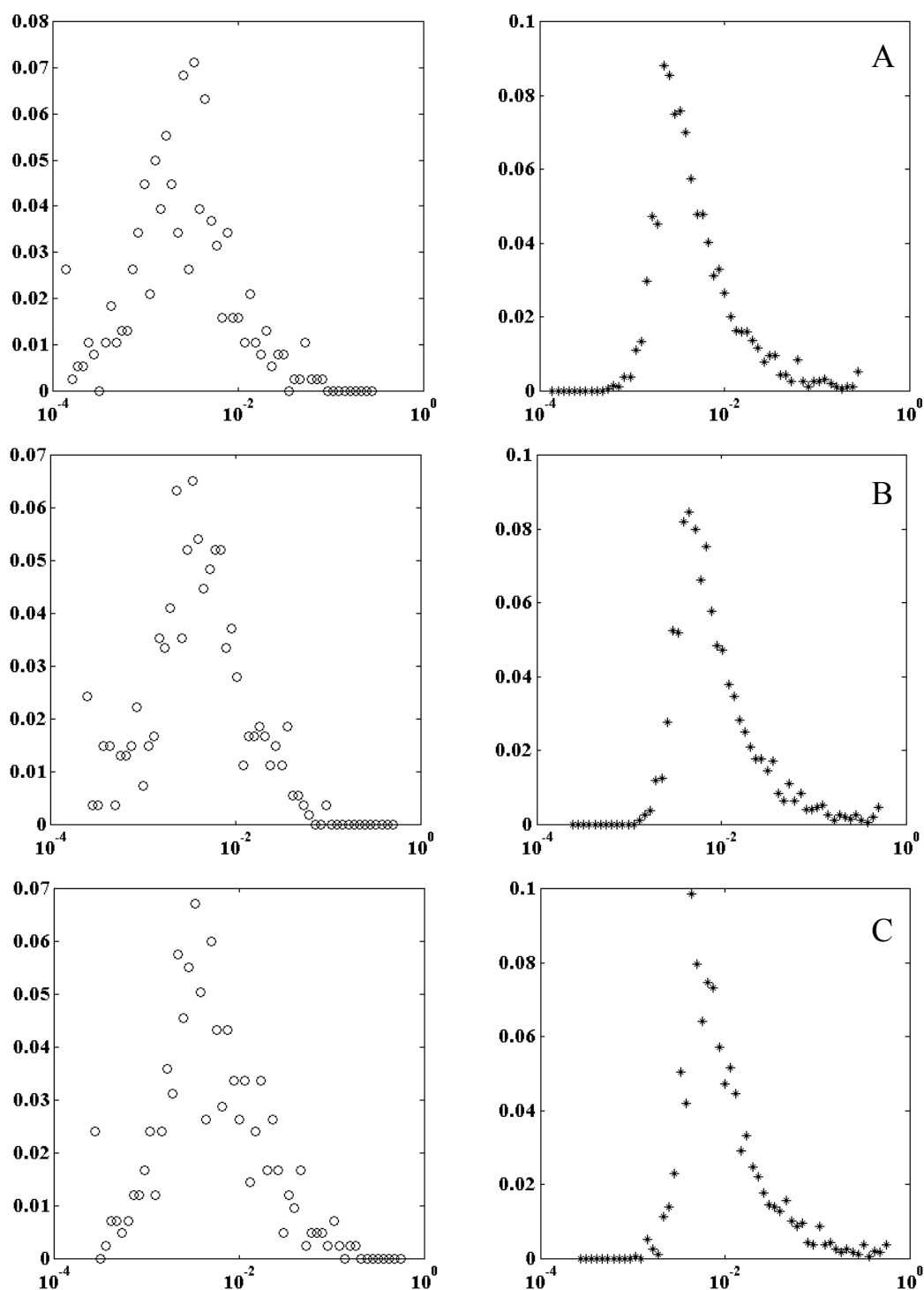


Figure 7.17 Length scale distribution, 2D Bubble column, Five point Sparger, (A) $x/W=0$
 (B) $x/W=0.5$ (C) $x/W=0.97$ ($^{\circ}$, EIM-ZC; $*$, EIM-CWT)

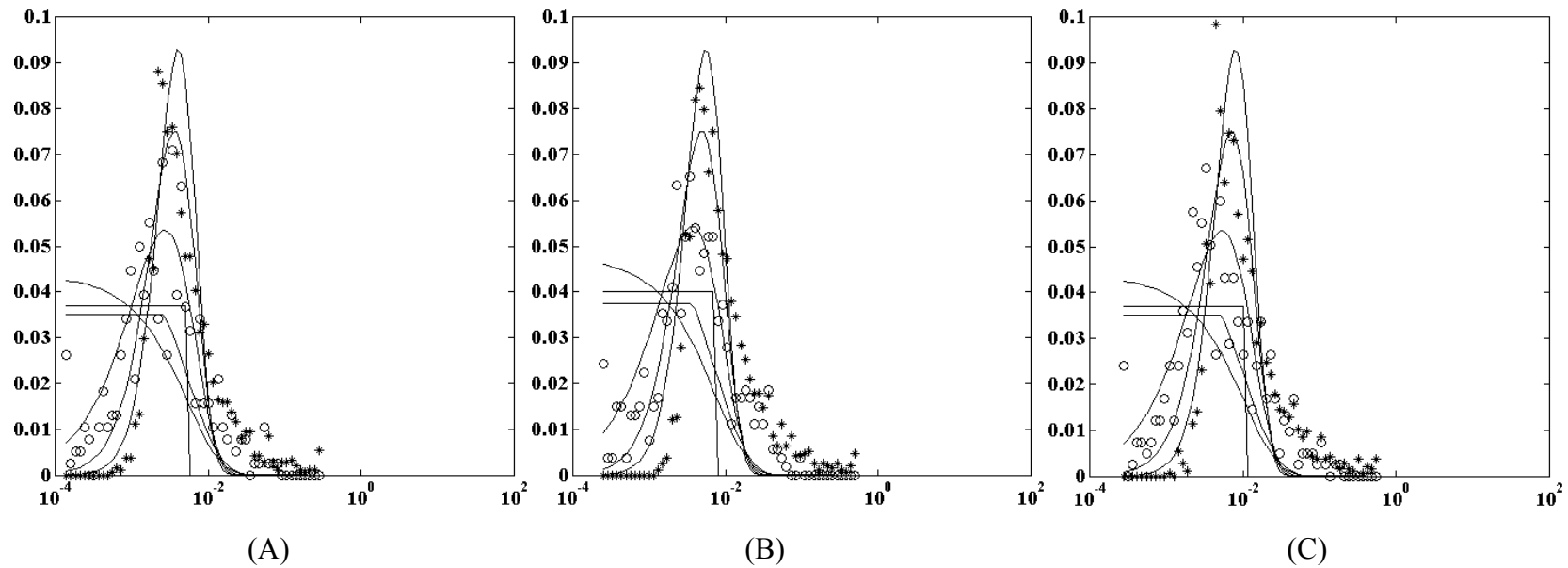


Figure 7.18 Length scale distribution, 2D Bubble column, Five point Sparger, (A) $x/W=0$ (B) $x/W=0.5$ (C) $x/W=0.97$ (\circ , EIM-ZC; $*$, EIM-CWT; lines description same as Figure 12)

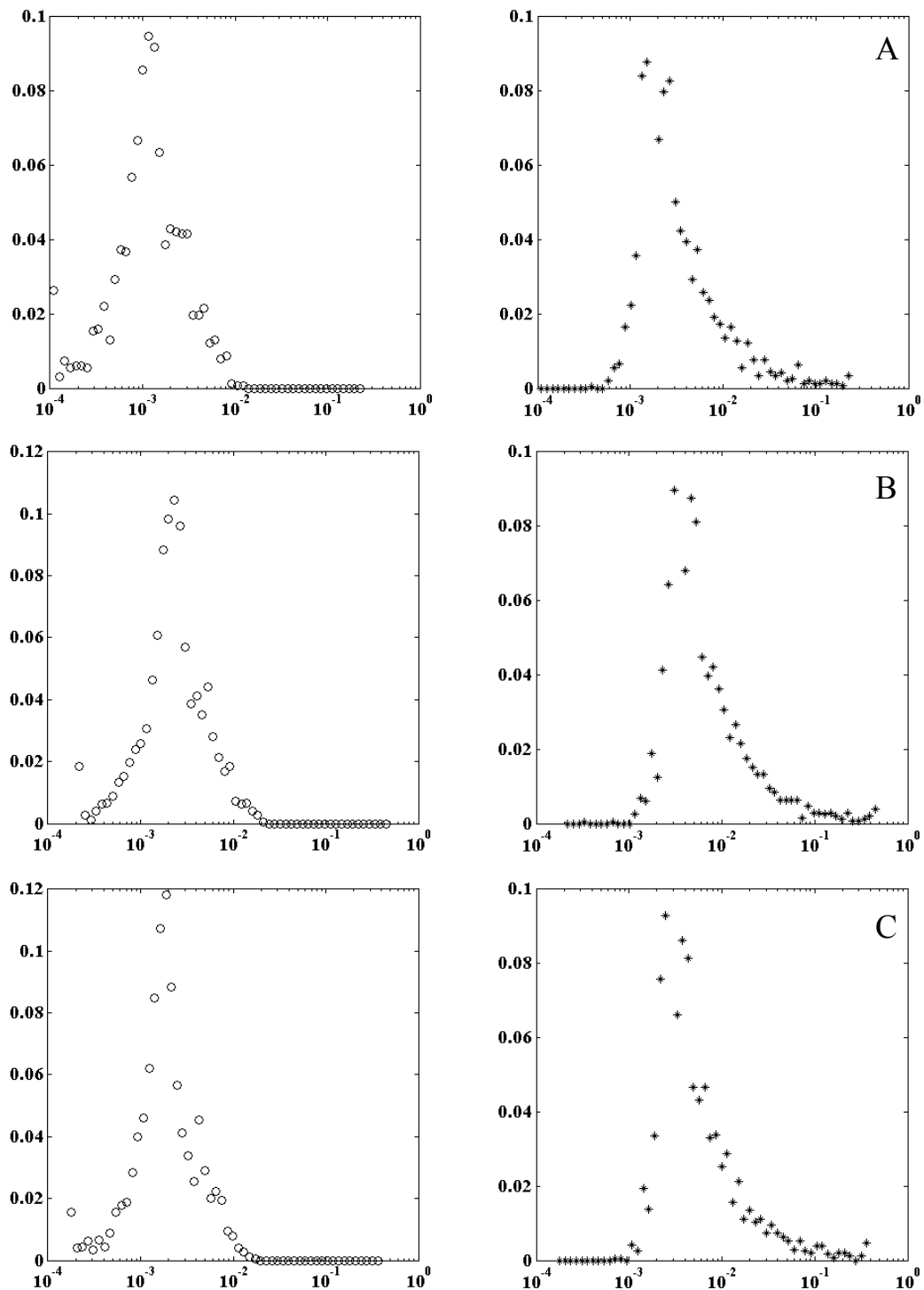


Figure 7.19 Length scale distribution, 3D Bubble column, Single point Sparger, (A) $r/R=0$
 (B) $r/R=0.5$ (C) $r/R=0.97$ (°, EIM-ZC; *, EIM-CWT)

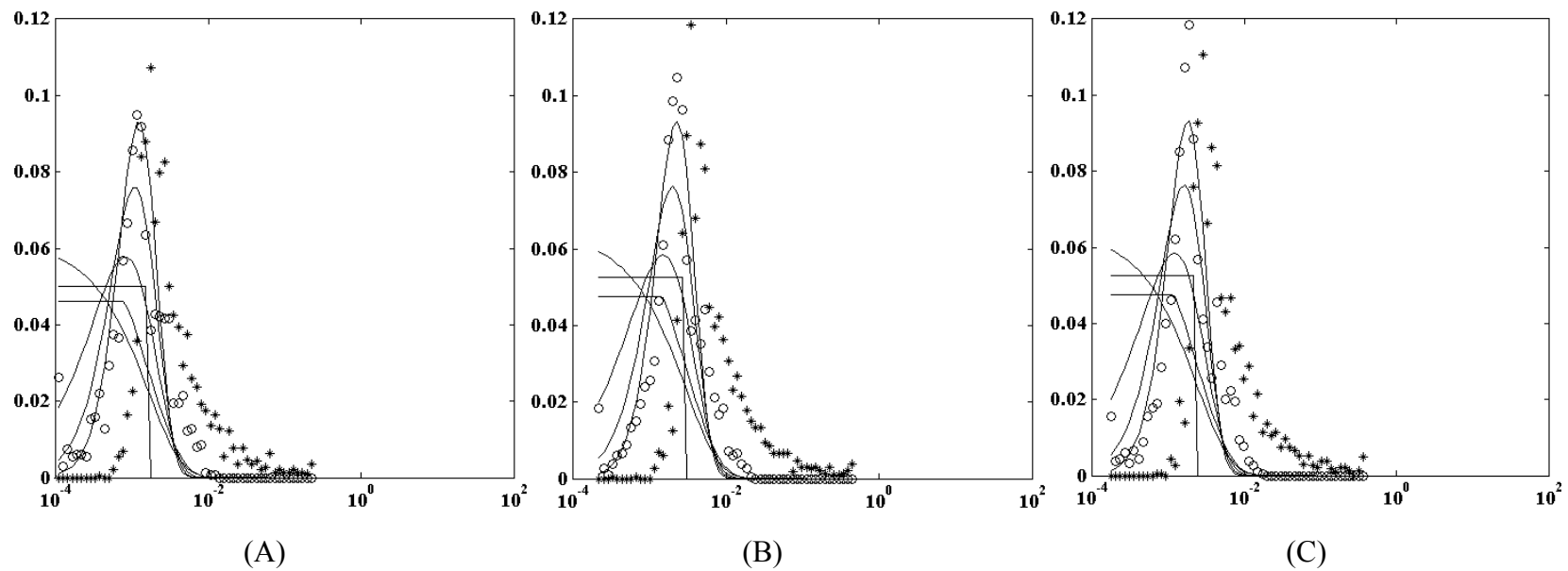


Figure 7.20 Length scale distribution, 3D Bubble column, Single point Sparger, (A) $r/R=0$ (B) $r/R=0.5$ (C) $r/R=0.97$ (\circ , EIM-ZC; $*$, EIM-CWT)

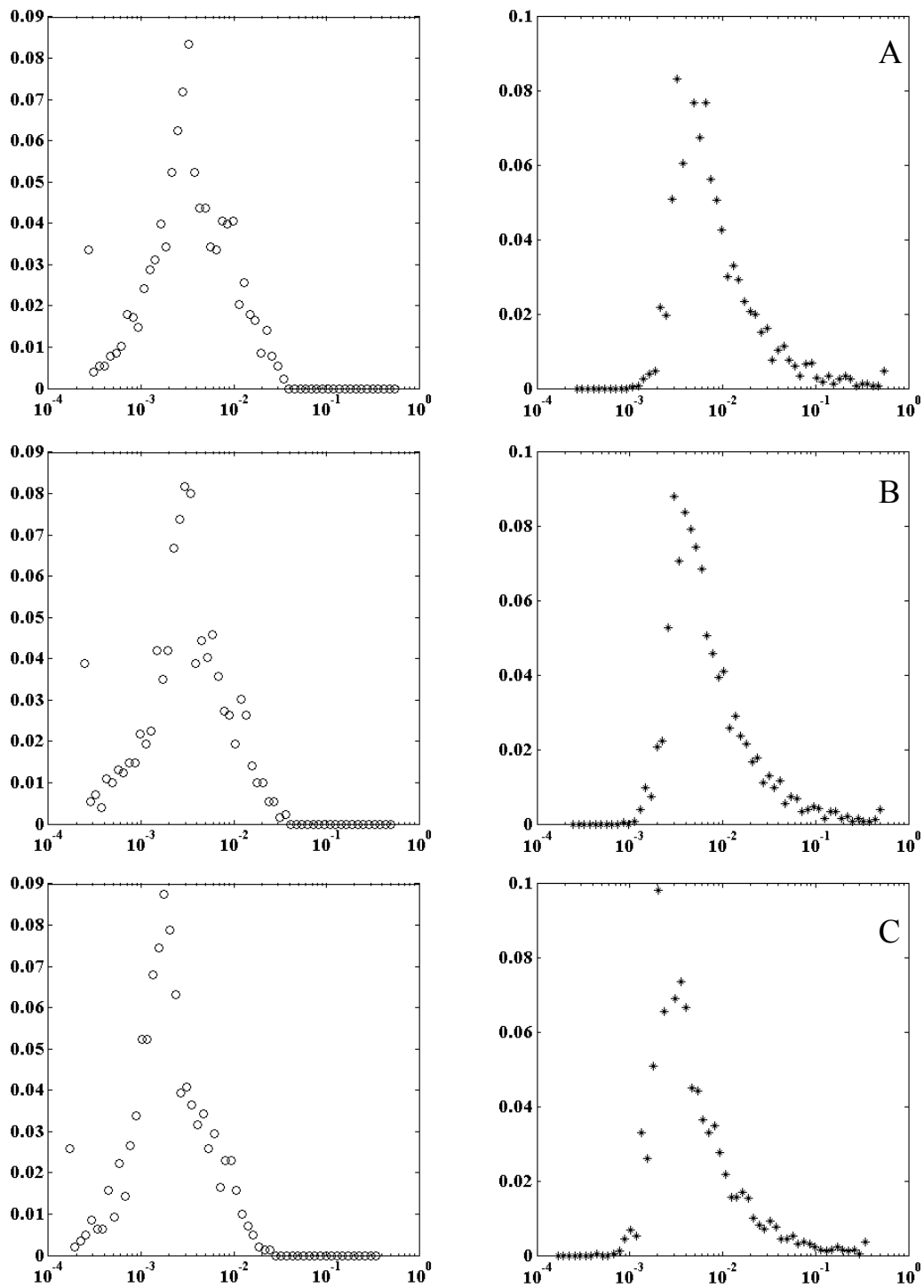


Figure 7.21 Length scale distribution, 3D Bubble column, Perforated Plate Sparger,

(A) $r/R=0$ (B) $r/R=0.5$ (C) $r/R=0.97$ (\circ , EIM-ZC; *, EIM-CWT)

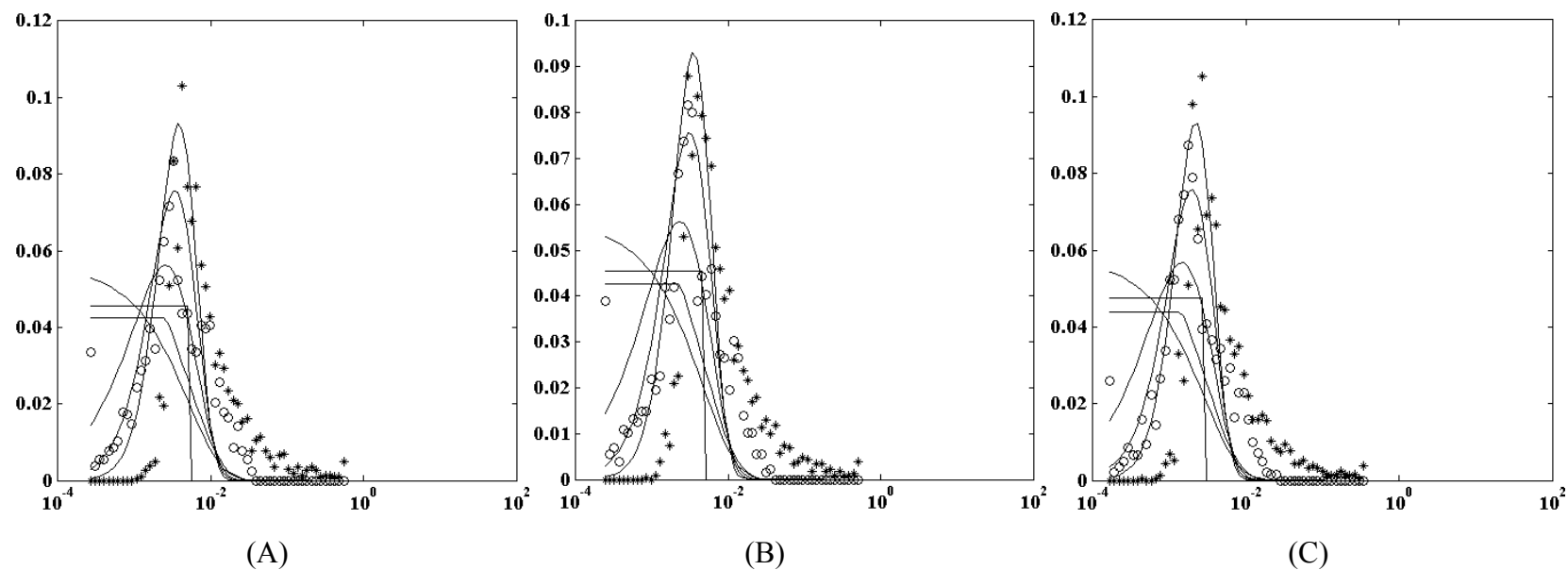


Figure 7.22 Length scale distribution, 3D Bubble column, Perforated Plate Sparger,

(A) $r/R=0$ (B) $r/R=0.5$ (C) $r/R=0.97$ (°, EIM-ZC; *, EIM-CWT)

The age and length scale distribution are a comprehensive way of presentation of results. However, the statistical properties of these distributions are easier to perceive from quantitative point of view. Table 7.3, 7.4 and 7.5 report the mean eddy age, mean eddy velocity and mean eddy length scale for single point, three point and five point sparger in 2D column respectively, for three radial locations. It can be observed that difference in the mean quantities at three location is highest for single point sparger while least for five point sparger.

Table 7.3. Mass transfer coefficient for 2D column with single point sparger

		$x/W = 0$	$x/W = 0.5$	$x/W = 0.97$
Eddy age	(s)	0.0782	0.0596	0.0783
Eddy velocity	(m/s)	0.0688	0.1228	0.1354
Eddy length	(m)	0.0054	0.0073	0.0106
Mass transfer coefficient	(m/s)	1.8×10^{-04}	2.07×10^{-04}	1.8×10^{-04}

Table 7.4. Mass transfer coefficient for 2D column with three point sparger

		$x/W = 0$	$x/W = 0.5$	$x/W = 0.97$
Eddy age	(s)	0.0738	0.0912	0.1052
Eddy velocity	(m/s)	0.0688	0.1228	0.1354
Eddy length	(m)	0.0051	0.0112	0.0142
Mass transfer coefficient	(m/s)	1.86×10^{-04}	1.67×10^{-04}	1.56×10^{-04}

Table 7.5. Mass transfer coefficient for 2D column with five point sparger

		$x/W = 0$	$x/W = 0.5$	$x/W = 0.97$
Eddy age	(s)	0.0615	0.1397	0.0804
Eddy velocity	(m/s)	0.0688	0.1228	0.1354
Eddy length	(m)	0.0042	0.0172	0.0109
Mass transfer coefficient	(m/s)	2.03×10^{-04}	1.35×10^{-04}	1.78×10^{-04}

Table 7.6 and 7.7 represent the same statistics for 3D column. The similar trend of higher heterogeneity for single point sparger is observed in 3D column as well.

DEVELOPMENT OF EXPERIMENTAL TECHNIQUES AND CFD SIMULATIONS OF MULTIPHASE DISPERSIONS

Table 7.6. Mass transfer coefficient for 3D column with perforated plate sparger

		r/R = 0	r/R = 0.5	r/R = 0.97
Eddy age	(s)	0.0384	0.0381	0.0352
Eddy velocity	(m/s)	0.1342	0.1225	0.084
Eddy length	(m)	0.0052	0.0047	0.003
Mass transfer coefficient	(m/s)	2.58×10⁻⁰⁴	2.59×10⁻⁰⁴	2.69×10⁻⁰⁴

Table 7.7. Mass transfer coefficient for 3D column with single point sparger

		r/R = 0	r/R = 0.5	r/R = 0.97
Eddy age	(s)	0.0299	0.0275	0.0272
Eddy velocity	(m/s)	0.0548	0.1095	0.089
Eddy length	(m)	0.0016	0.003	0.0024
Mass transfer coefficient	(m/s)	2.92×10⁻⁰⁴	3.04×10⁻⁰⁴	3.06×10⁻⁰⁴

7.5.4. Evaluation of mass transfer coefficient

The mass transfer coefficient is evaluated using the age distribution obtained from EIM-ZC and EIM-CWT. Unlike the penetration/ surface renewal theories, no pre determined PDF for age is assumed. Instead the mass transfer coefficient for every individual eddy is evaluated and then averaged over all the eddies. Similar method for evaluation of heat transfer coefficient is described in detail by Deshpande et al. (2009). The mass transfer coefficient is calculated using individual eddy age as:

$$k_L = \frac{2}{N} \sum_{i=1}^N \sqrt{\frac{D}{\pi t_i}} \quad (7.18)$$

Where D is the molecular diffusivity of gas in liquid, t_i is the age of individual eddy and N is the number of eddies. The mass transfer coefficient is evaluated for 2D and 3D column with different spargers. The results are summarized in Tables 7.4-7.7.

The gas-liquid mass transfer coefficient has been measured by Kulkarni et al. (2004) for bubble column with 150 mm diameter and perforated sparger for the superficial gas velocity of 22 mm/s, which is same as that used in the current work. The value of mass transfer coefficient reported by Kulkarni et al. (2004) is 2.84×10^{-4} m/s. From Table 7.6, it can

DEVELOPMENT OF EXPERIMENTAL TECHNIQUES AND CFD SIMULATIONS OF MULTIPHASE DISPERSIONS

be observed that the average mass transfer coefficient predicted using current model for 3D column with perforated plate sparger is 2.62×10^{-4} m/s, which is close to the experimental value of 2.84×10^{-4} m/s. The mass transfer coefficient for single point sparger is 3×10^{-4} m/s, which is higher than perforated plate sparger.

Similar trend of higher mass transfer coefficient for higher heterogeneity is observed in 2D bubble column, as can be observed from Table 7.4 to 7.6.

7.6. Conclusions

In the present study, the measurement of liquid velocity field in 2D and 3D bubble column has been described using three instruments, namely, pressure fluctuation signals, PIV+shadowgraphy and LDA. The main aim has been to identify and separate liquid flow structures in the complex two phase flow and to estimate mass transfer coefficient. For this purpose, the advanced data processing techniques viz. MLSE, DWT, CWT and EIM have been used. The findings of these measurements have been summarized below.

1. MLSE has been used to obtain the velocity profiles from simultaneous pressure fluctuation signals and PIV data. This method shows the effectiveness of pressure data for estimation of flow structures in the complex flow field. This method can be applied in the industrial scale reactor also.
2. Wavelet transforms (WT) have been applied to isolate individual structures from PIV data to get their shape, size and energy in 2D column. The resolution of measured data is found to be suitable for prediction of mass transfer coefficient because it captures the small eddies in the dissipative range of spectrum as well.
3. The EIM-ZC and EIM_CWT have also been used to extract the data of eddy shape size and energy. Comparison of eddy size, age and velocity scale distributions show wide variation at single point sparger while uniformity is increased for multipoint spargers.

These liquid flow structure characteristics have been subsequently used to predict the local values of mass transfer coefficient in 2D and 3D bubble column.

4. The local mass transfer coefficient for 3D column with perforated plate sparger was compared with the reported data from Kulkarni et al. (2004). The present method based on local age distribution predicts the mass transfer coefficient closer to the experimental value.
5. Considering the agreement of the estimated mass transfer coefficient with the experimental mass transfer coefficient, the methodology presented in the current work can be successfully used to predict mass transfer coefficients in bubble column. The present study shows that in single point sparger, centerline mass transfer coefficient is highest and it decreases towards the wall. Also, magnitudes of k_L in single point sparger are found to be higher than that of multi point sparger. The reason for this is clearly found in the behavior of liquid flow structures which cause interface mass transfer.

Thus, the present methodology can be extended for online estimation of mass transfer coefficient in bubble column under continuous operation at larger scale using pressure fluctuation signals.

Nomenclature

- a Scaling parameter, m
- b Translation parameter, 1/m
- D Molecular diffusivity, m²/s
- E Spectral Energy Density, m²/s

DEVELOPMENT OF EXPERIMENTAL TECHNIQUES AND CFD SIMULATIONS OF MULTIPHASE DISPERSIONS

e	Error
k	Turbulent kinetic energy, m^2/s^2
k_L	Mass transfer coefficient, m/s
$l_{E,i}$	Characteristic length scale of i^{th} eddy, m
n	Number of data points corresponding to b
p'_{wi}	Wall pressure fluctuations
r_0	Location of the event
S	Surface renewal rate, (1/s)
t	Time, s
$T_i^{a,b}$	CWT coefficient matrix
T_E	Contact time in penetration theory, s
$u_{E,i}$	Velocity of eddy for i^{th} component, m/s
u_i	Instantaneous velocity in i direction, m/s
u'_i	Fluctuating velocity in i direction, m/s
u^+	Dimensionless friction velocity
\tilde{u}'_i	Instantaneous estimated radial velocity
\tilde{v}'_i	Instantaneous estimated axial velocity
v'_i	Instantaneous PIV-based axial velocity
$W^{a,b}$	Wavelet coefficient in DWT
y^+	Dimensionless distance from wall

Greek letters

δ	Film thickness, m
----------	-------------------

DEVELOPMENT OF EXPERIMENTAL TECHNIQUES AND CFD SIMULATIONS OF MULTIPHASE DISPERSIONS

Δr Offset between the estimate and event

$\phi(t)$ Age distribution function

κ Wavenumber, 1/m

ψ Mother wavelet function

τ Time offset

References

- Banerjee, S., Rhodes, E. and Scott, D. S., 1968 Mass transfer to falling wavy liquid films in turbulent flow. *Industrial and Engineering Chemistry Fundamentals*, 7, 22-27.
- Brusset, H., Depeyre, D. and Quang T.L., 1973. An estimation of the film-penetration model parameters. *Chemical Engineering Science*, 28, 31-39.
- Cole, D., Glauser, M. and Guezennec, Y., 1992. An application of stochastic estimation to the jet mixing layer. *Physcis of Fluids A*, 4, 192–194.
- Crocker, J. C. and Grier, D. G., 1996. Methods of Digital Video Microscopy for Colloidal Studies. *Journal of Colloid and Interface Science*, 179, 298-310.
- Danckwerts, P. V., 1951. Significance of liquid film coefficient in gas. *Industrial and Engineering Chemistry*, 43, 1460-1467.
- Deshpande, N. S., Prasad, Ch. V., Kulkarni, A. A., and Joshi, J. B., 2000. Hydrodynamic characterization of dispersed two phase flows by laser Doppler velocimeter. *Transactions of Institution of Chemical Engineers*, 78 A, 903–910.
- Deshpande, S. S., Mathpati, C. S., Gulawani, S. S., Joshi, J. B. and Ravi Kumar, V., 2009. Effect of Flow Structures on Heat Transfer in Single and Multiphase Jet Reactors. *Industrial and Engineering Chemistry Research*, 48, 9428–9440.
- Deshpande, S. S., Joshi, J. B., RaviKumar, V. and Kulkarni, B.D., 2008. Identification and characterization of flow structures in chemical process equipment using multiresolution techniques. *Chemical Engineering Science*, 63, 5330-5346.
- Durst, F., Schonung, B., Selanger, K., and Winter, M., 1986. Bubble driven fluid flows. *Journal Fluid Mechanics*, 170, 53–82.
- Einstein, H.A. and Li, H., 1956. The viscous sublayer along a smooth boundary. *Transactions of American Society of Civil Engineers*, 82, 293-317.
- Fortescue, G. E. and Pearson, J. R. A., 1967. On gas absorption into a turbulent liquid. *Chemical Engineering Science*, 22, 1163-1176.
- Fortuin, J. M. H. and Klijn, P. J., 1982. Drag reduction and surface renewal in turbulent pipe flow. *Chemical Engineering Science*, 37, 611-623.
- Fortuin, J. M. H., Musschenga, E. E. and Hamersma, P. J., 1992. Transfer processes in turbulent pipe flow described by ERSR model. *AIChE Journal*, 38, 343-352.

DEVELOPMENT OF EXPERIMENTAL TECHNIQUES AND CFD SIMULATIONS OF MULTIPHASE DISPERSIONS

- Gandhi A. B., Gupta, P.P., Joshi, J. B., Jayaraman, V.K., and Kulkarni, B.D., 2009. Development of Unified Correlations for Volumetric Mass-Transfer Coefficient and Effective Interfacial Area in Bubble Column Reactors for Various Gas-Liquid Systems Using Support Vector Regression. *Industrial and Engineering Chemistry Research*, 48, 4216–4236.
- Groen, J. S., Mudde, R. F., and van den Akker, H. E. A., 1999. On the application of LDA to bubbly flow in the wobbling regime. *Experiments in Fluids*, 27, 435.
- Guezennec, Y. G., 1989. Stochastic estimation of coherent structures in turbulent boundary layers. *Physics of Fluids A*, 1, 1054-1060.
- Hanratty, T.J., 1956. Turbulent exchange of mass and momentum with a boundary. *AICHE Journal*, 2, 359-362.
- Harriott, P. A., 1962. Random eddy modification of penetration theory. *Chemical Engineering Science*, 17, 149-165.
- Higbie, R., 1935. The rate of absorption of a pure gas into a still liquid during short periods of exposure. *Transactions of AIChE*, 31, 365-385.
- Joshi, J. B. 1980. Axial mixing in multiphase Contactors—A unified correlation. *Transactions of Institution of Chemical Engineers*, 58, 155–165.
- Joshi, J. B., Vitankar, V. S., Kulkarni, A. A., Dhotre, M. T. and Ekambara, K., 2002. Coherent flow structures in bubble column reactors. *Chemical Engineering Science*, 57, 3157 – 3183.
- Kline, S. J., Reynolds, W. C., Schraub, F. A. and Runstadler, P. W., 1967. The Structure of Turbulent Boundary Layers. *Journal of Fluid Mechanics*, 30, 741-773.
- Kulkarni, A. A. and Joshi, J. B., 2004. Simultaneous Measurement of Flow Pattern and Mass Transfer Coefficient in Bubble Columns. *Chemical Engineering Science*, 59, 271.
- Kulkarni, A. A., 2007. Mass Transfer in Bubble Column Reactors: Effect of Bubble Size Distribution. *Industrial and Engineering Chemistry Research*, 46, 2205-2211.
- Kulkarni, A. A., Joshi, J. B., Ravi Kumar, V. and Kulkarni, B. D., 2001. Simultaneous Measurement of Hold-Up Profiles and Interfacial Area using LDA in Bubble Columns: Predictions by Multiresolution Analysis and Comparison with Experiments. *Chemical Engineering Science*, 56, 6437.
- Kulkarni, A. V., and Joshi, J. B., 2006. Estimation of Hydrodynamic and Heat Transfer Characteristics of Bubble column by Analysis of Wall Pressure Measurements and CFD Simulations. *Transactions of Institute of Chemical Engineers-A: Chemical Engineering Research and Design*, 84, 601-609, 2006.
- Lamont, J. C. and Scott, D. S, 1970. An eddy cell model of mass transfer into the surface of a turbulent liquid. *AICHE Journal* , 16, 512-519.
- Levich, W. G. *Physicochemical hydrodynamics*. Prentice Hall, Englewood Cliffs, NJ.
- Lewis, W. K. and Whitman, W. G., 1924. Principles of gas adsorption. *Industrial and Engineering Chemistry*, 16, 1215-1220.
- Loughlin, K.F., Abul-Hamayel, M.A. and Thomas, L.C., 1985. The surface rejuvenation theory of wall turbulence for momentum, heat and mass transfer: Application to boundary. *Chemical Engineering Science*, 7, 265-268.

DEVELOPMENT OF EXPERIMENTAL TECHNIQUES AND CFD SIMULATIONS OF MULTIPHASE DISPERSIONS

- Mathpati, C.S. and Joshi, J.B., 2007. Insight into Theories of Heat and Mass Transfer at the Solid-Fluid Interface Using Direct Numerical Simulation and Large Eddy Simulation. *Industrial and Engineering Chemistry Research*, 46, 25, 8525 – 8557.
- Meek, R.L. and Baer, A.D., 1970. The periodic viscous sublayer in turbulent flow. *AIChE Journal*, 16, 841-848.
- Meneveau, C. and Sreenivasan, K., 1987. Simple multifractal cascade model for fully developed turbulence. *Physical Review Letters*, 59, 1424–1427.
- Mudde, R. F., 2010. Advanced measurement techniques for GLS reactors. *The Canadian Journal of Chemical Engineering*, 88, 638–647.
- Muzy, J., Bacry, E. and Arneodo, A., 1991. Wavelets and multifractal formalism for singular signals: applications to turbulent data. *Physical Review Letters*, 67, 3515–3518.
- Perlmutter, D. D., 1961. Surface renewal models in mass transfer. *Chemical Engineering Science*, 16, 287-296.
- Pinczewski, W.V. and Sideman, S., 1974. A model for mass (heat) transfer in turbulent tube flow: moderate and high Schmidt (Prandtl) Numbers. *Chemical Engineering Science*, 29, 1969-1976.
- Roy, M., Ravi Kumar, V., Kulkarni, B. D., Sanderson, J., Rhodes, M., and Van der Stappen, M., 1999. Simple denoising algorithm using wavelet transform. *AIChE Journal*, 45, 2461.
- Ruckenstein, E., 1958. A note concerning turbulent exchange of heat or mass with a moderate and high Schmidt (Prandtl) numbers. *AIChE Journal*, 31, 1614-1620.
- Sahu, A.K., Kumar, P., Patwardhan, A. W., Joshi, J.B., 1999. CFD modelling and mixing in stirred tanks. *Chemical Engineering Science*, 54, 2285-2293.
- Saito T., K. Sakakibara, Y. Miyamoto, M. Yamada, 2010. A study of surfactant effects on the liquid-phase motion around a zigzagging-ascent bubble using a recursive cross-correlation PIV. *Chemical Engineering Journal*, 158, 39–50.
- Sathe, M. J., Thaker, I. H., Strand, T. E. and Joshi, J. B., 2010. Advanced PIV/LIF and Shadowgraphy System to Visualize Flow Structure in Two-Phase Bubbly Flows. *Chemical Engineering Science*, 65, 2431-2442.
- Sreenivasan, K., Prabhu, A., Narsimha, R., 1983. Zero-crossings in turbulent signals. *Journal of Fluid Mechanics*, 137, 251-272.
- Thomas, L.C., 1978. A Formulation for ϵ_M and ϵ_H based on the surface renewal principle. *AIChE Journal*, 24, 101-106.
- Thomas, L.C., 1980. A surface rejuvenation model of wall turbulence: inner laws for u^+ and T^+ . *International Journal of Heat Mass Transfer*, 23, 1099-1104.
- Thomas, L.C., Gingo, P.J. and Chung, B.T.F., 1975. The surface rejuvenation model for turbulent convective transport- An exact solution. *Chemical engineering science*, 30, 1239-1242.
- Toor, H. L. and Marchello, J. M., 1958. Film penetration model for mass and heat transfer. *AIChE Journal*, 4, 97-99.
- Tung, T.C. and Adrian, R.J., 1980. Higher-order estimates of conditional eddies in isotropic turbulence. *Physics of Fluids*, 23, 1469.
- Ukeiley, L. and Murray, N., 2005. Velocity and surface pressure measurements in an open cavity. *Experiments in Fluids*, 38, 656–671.

DEVELOPMENT OF EXPERIMENTAL TECHNIQUES AND CFD SIMULATIONS OF MULTIPHASE DISPERSIONS

- Wang, T. and Wang, J., 2007. Numerical simulations of gas–liquid mass transfer in bubble columns with a CFD–PBM coupled model. *Chemical Engineering Science*, 62, 7107–7118.
- Zehner, P., 1982. Momentum, mass and heat transfer in bubble columns. *International Chemical Engineers*, 26, 22–35.

SCOPE FOR FUTURE WORK

SCOPE FOR FUTURE WORK

1. Complete characterization of turbulence in solid-liquid and gas-liquid dispersions over a wide range of voidage, particle/bubble size and column diameters should be carried out.
2. A method should be developed to correlate the statistics of flow structures obtained from the available 1D, 2D and 3D datasets. This will enable the estimation of flow structure properties using experimental techniques which generate 1D and 2D data. A methodology should be developed to relate the flow structures obtained with such methodology with transport phenomena.
3. Efficient strategies should be developed to standardize the method of storage, retrieval and process the experimental and CFD data. Since the quest for understanding the transport phenomena based on flow structure means examining every small details of the flow field in greatest detail possible, it requires lot of resources including data exchange between interdisciplinary teams. Standard procedure for storage of all the available data that can be easily retrieved by future users is required to prevent repeated efforts due to data loss or data in improper/unfamiliar format.
4. DNS has evolved as a promising tool over last three decades. Its reach has significantly improved with the advent of computational power. Its capability needs further enhancement to cover much higher Reynolds number, bigger and complex equipment geometries and more number of dispersed phase particles (i.e. bubble/drops/ particles). This will help in understanding the forces acting on these particles as well as accurate prediction of mass and heat transfer at the interface.
5. Large eddy simulation (LES) has been standardized for single phase flows. However, it has to be exploited to study near wall structure in laboratory and industrial scale

multiphase reactors, with and without chemical reaction. The required closure models should be standardized to ensure the quality of the simulations and novel data processing techniques should be developed to isolate flow structures from the volumetric data of LES.

6. The miniature pressure sensors can provide useful information about the flow patterns in industrial scale reactors. Based on the experience gained so far with data acquisition and processing of pressure fluctuations, ruggedized probes, data acquisition electronics and software should be produced which can be used by industry as a solution for real time monitoring and control of multiphase contactors.
7. Fluid mechanics community should intensely focus on understanding the mechanism of energy transfer from dispersed phase to continuous phase or vice-versa in heterogeneous regime or in presence of accelerating particles. This can reveal many mysteries of liquid phase turbulence and its effect on overall transport phenomena in multiphase contactors.
8. Although size and shapes of structures can be obtained with the current methodology based on wavelet transforms and image processing for 2D data, it has got its limitation on the accuracy. In depth study of wavelet transforms and similar techniques should be carried out to find means to improve this accuracy. In next step, such algorithms should be extended to the 3D data processing.
9. The interaction of turbulent flow structures amongst themselves and their subsequent breakage, coalescence and energy spectra need a close attention. For this reason, LES with fine grid resolution and high speed PIV should be employed.

SYNOPSIS

INSTITUTE OF CHEMICAL TECHNOLOGY

SYNOPSIS

**OF THE THESIS TO BE SUBMITTED TO THE
INSTITUTE OF CHEMICAL TECHNOLOGY
IN PARTIAL FULFILLMENT OF THE REQUIREMENTS
FOR THE DEGREE OF
DOCTOR OF PHILOSOPHY (TECHNOLOGY)
IN THE FACULTY OF CHEMICAL ENGINEERING**

RESEARCH SCHOLAR : SATHE MAYUR JAYANTKUMAR

RESEARCH SUPERVISOR : PROFESSOR J. B. JOSHI

**TITLE OF THE THESIS : DEVELOPMENT OF EXPERIMENTAL
TECHNIQUES AND CFD SIMULATIONS
OF MULTIPHASE DISPERSIONS**

DEGREE : Doctor of Philosophy (Technology)

**INSTITUTE : Institute of Chemical Technology
Matunga, Mumbai - 400 019.**

REGISTRATION NUMBER : ICT/ 945 (19/4/08)

AND DATE

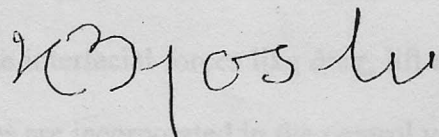
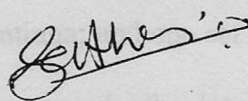
DATE OF SUBMISSION : May 26, 2010

SIGNATURE OF THE

CANDIDATE

SIGNATURE OF THE

RESEARCH GUIDE



1. Introduction

Gas-liquid contacting is involved in many important processes like fermentation, polymerization, hydrogenation, Fisher-Tropsch synthesis, etc. It is also important for separation processes like distillation. The fluid mechanical aspects of gas-liquid two phase flows have not been clearly understood, introducing empiricism and uncertainty in the design of such equipment. Recent advances in Experimental Fluid Dynamics (EFD) and Computational Fluid Dynamics (CFD) are promising in terms of gaining deeper insight into the flow patterns in multiphase dispersions.

CFD involves numerical solution of the governing equations of fluid flow: the equations of continuity and motion. In case of multiphase flows, separate set of equations needs to be solved for each phase, and the coupling between these equations is represented by momentum exchange terms. Different models are used to approximate the two phase flow viz. mixture model, Euler-Euler model, Euler-Lagrange model, volume of fluid (VOF) model, Lattice-Boltzmann method and the direct numerical simulation (DNS). The mixture model solves a single set of momentum equations and approximates the mixture properties from the individual fluid properties and their respective void fractions. The mixture model approximates the interaction between phases by defining a specific slip velocity. In Euler-Euler model, the two phases are modeled as interpenetrating continua; and one set of momentum equations is solved for each of the phase. In this framework, the interaction between phases is modeled using different formulations for the interfacial forces like drag, lift and virtual mass. With DNS, a finite number of particles are incorporated in the control volume and trajectories are determined via the equation of motion. The instantaneous forces acting on a particle are obtained from local flow statistics. The VOF model, the Lattice Boltzmann and DNS methods are computationally much more expensive and hence find niche applications

like study of the flow patterns around individual bubbles to much greater detail. As far as modeling of industrial scale contactors is concerned, Euler-Euler approach presents a balance between approximations introduced while modeling and the computational requirements and hence is most popular. The major approximation in Euler-Euler framework lies in representation of dispersed phase as a continuum and hence requirement of fictitious terms like interfacial area concentration which is the amount of interfacial area present per unit volume of the element under consideration.

Multiphase flow is characterized by enhanced turbulence in the continuous phase in presence of large number of dispersed phase particles. This turbulence is broadly classified as particle generated turbulence and shear generated turbulence. The particle generated turbulence commonly refers to the turbulence generated by linear and nonlinear interactions between wakes, while the shear induced turbulence is commonly referred to the turbulence generated by the instabilities and consequent cascading at the locations of high shear near the wall as well as in the bulk caused by the large scale circulations. The characterization of these two types of turbulence, besides the overall structure of turbulence is the key to generate more generalized models for transport coefficients in multiphase dispersions. The current work is mainly focused on development of experimental and data processing techniques to fulfill this aim.

2. Development of Experimental Techniques

The advanced techniques of experimental fluid dynamics were extended for their application to multiphase flows. Particle Image Velocimetry has been used along with Laser induced fluorescence and shadow imaging to extend its applicability to bubbly flows (Sathe et. al. 2010). Fluorescent seeding particles have been used to avoid the laser reflections from bubble interface. The PIV camera was fitted with a long wave pass filter so as to record the liquid velocity field. Simultaneous shadow imaging has been

DEVELOPMENT OF EXPERIMENTAL TECHNIQUES AND CFD SIMULATIONS OF MULTIPHASE DISPERSIONS

performed using another PIV camera along with a dichroic mirror and a blue LED backlight. The dichroic mirror reflected the light shorter than 535 nm while allowing the light with longer wavelength to pass through it. The shadow camera was fitted with a blue filter which allowed the passage of light with wavelength shorter than 470 nm. The shadow images of bubbles were processed by image processing to get bubble shape and size. The bubble centroids in two consecutive shadow PIV images were subjected to particle tracking to get bubble velocity.

Laser Induced Fluorescence has been applied to study liquid-liquid dispersion in annular centrifugal extractor (Sathe et. al. 2010). Kerosene and Sodium iodide solutions were used as the liquids. The refractive index of sodium iodide solution had been matched with that of the kerosene, hence the droplets of kerosene or sodium iodide solution presented the least optical distortion and acted as a single optical phase. A fluorescent dye, Rhodamine B was added to Sodium iodide solution. Two cameras were used: one was used to record the fluorescent light emitted by the dye while the other was used to record the green laser light reflected by the PIV seeding particles. The images of the particles and drops were then processed to get drop size, shape and dispersed phase hold-up along with the velocity field.

Although PIV is useful to generate a wealth of information regarding the planer liquid velocity field and the bubble size and velocity information, its applicability is highly hampered by the fact that it cannot handle larger column diameter or dispersed phase hold-up. Hence, it was thought desirable to develop intrusive techniques which can handle larger column diameters and higher superficial gas velocities. In house electronics has been developed for conductivity probes and pressure sensor arrays. Data from pressure sensor arrays has been subjected to cross correlation analysis to give the mean liquid circulation velocity. The multi-point pressure data was subjected to Linear

Stochastic Estimation to get the planer mean velocity field, using PIV data for calibration. Besides the wall pressure sensor arrays, a special probe with three pressure sensors in pitot tube configuration was developed in house. The impact and static sensors at the probe tip were used to calculate the local mixture velocity, while the two static sensors were used to get the mixture density and hence the dispersed phase hold-up. This probe has been used in 150 mm dia. bubble column to discern the profiles of mean velocity and gas hold up along with the energy spectrum and bubble size.

In order to generate calibration data of bubble size for three point pressure probe, endoscope along with high speed camera has been employed. The column has been illuminated near the wall using a high intensity CFL backlight. The resultant shadow image sequence was used for bubble size and velocity measurement inside cylindrical column without the restriction of column diameter or transparent wall.

A variety of equipments were studied using the above mentioned techniques like annular centrifugal extractor, jet loop reactor, direct contact steam condensation, pool boiling of water, and solid liquid fluidized beds.

3. Effect of Turbulence on Rise Characteristics of the Bubbles

In Euler-Euler model for CFD simulation for multiphase flows, the interaction between phases is represented by momentum exchange terms in momentum equation. These terms are ensemble-averaged momentum exchange between the phases, due to interface forces like drag, lift, virtual mass and turbulent dispersion. The drag force is dominant in terms of its magnitude out of all these interaction forces. Thus, it has attracted the focus of the efforts from numerous researchers since last four decades. The drag force is significantly different for bubbles, drops and particles of same size. This is primarily caused by the different slip conditions occurring at fluid boundary, viz. full slip to no slip. A number of different empirical correlations have been devised to include the

effect of several parameters like particle diameter, shape, and particle Reynolds number, etc. These correlations perform satisfactorily for individual particles moving in quiescent fluids. However, it still remains a major challenge to devise a generalized correlation which also includes the effect of free stream turbulence on the drag force besides all these parameters. In number of scenarios, surfactant molecules are present in the liquid. They get adsorbed onto the gas-liquid interface forming partial slip boundary conditions. The process is known to be dynamic in nature i.e. bubble rise velocity in surfactant solution is time dependent.

Thus, it was thought desirable to study the effect of surfactant concentration as well as free stream turbulence on the rise velocity of individual bubbles as well as bubbles rising in chains. The nearly isotropic turbulence was generated by two oscillating grids. The bubble trajectories and 3-D liquid velocity field were recorded by using a high speed camera and stereo PIV. The shape oscillations of the bubbles were also quantified using image processing. Experiments reveal that the change induced in the bubble shape by the turbulence as well as the surfactant concentration is vital in determining the rise velocity.

4. LES Simulation of Rectangular Bubble Column

In the majority of reported literature on CFD of bubble column, the authors have used the k - ϵ turbulence model which provides only the time-average information of the flow. The bubble column can be operated in two regimes: at low superficial gas velocity bubbles rise in rectilinear way and the the flow is called to be in homogeneous regime; while at higher superficial gas velocity the circulations start developing and the flow is called to be in heterogeneous regime. Most of the bubble columns at industrial scale operate in heterogeneous regime where the flow is highly unstable. Hence the transient behavior of the flow is important while it has not received much attention yet.

Therefore, it was thought desirable to undertake CFD modeling using Large Eddy Simulation (LES) which predicts the transient phenomenon very well for single phase (Mathpati and Joshi, 2007, Mathpati et al., 2009) and bubbly two phase flows (Deen et al., 2001; Tabib et al., 2008).

Large eddy simulation (with CFX 11.0) has been carried out for rectangular bubble column. Along with the mean velocity and gas hold-up profiles, the instantaneous, three dimensional snapshots of velocity field obtained from LES were subjected to filter banks to quantify the flow structures of different sizes. A three dimensional Gaussian filter kernel was used with different lengths across different dimensions owing to lower depth and width of the column compared to its height. The filtered velocity and hold-up fields were subjected to a threshold and the resultant structures were analyzed to quantify their shape and size using a data processing program written in MATLAB.

Quantification of Turbulent flow in Bubble Column

The flow pattern in a narrow rectangular (2D) and cylindrical bubble column has been studied using experimental techniques like PIV, LDA, endoscope and Pressure sensors. The overall flow parameters like the profiles of liquid velocity, gas velocity and gas hold-up have been quantified and subjected to the criteria of liquid and gas phase material balance. The liquid velocity was captured over a plane using PIV along with bubble characteristics like bubble shape, size and velocity in rectangular bubble column. This information was used to quantify the instantaneous drag and lift forces on bubbles. The point velocity data obtained from LDA was subjected to the multiresolution analysis following the procedure described by Kulkarni and Joshi (2001). The resultant data was subjected to same constraints of material balance as mentioned earlier. The liquid velocity data obtained after subtracting the points corresponding to the bubbles was

DEVELOPMENT OF EXPERIMENTAL TECHNIQUES AND CFD SIMULATIONS OF MULTIPHASE DISPERSIONS

subjected to fourier transform in order to observe the structure of the turbulent energy spectrum. As attempt is being made to capture separately characteristic features of bubble and shear generated turbulence.

References

- Sathe, M. J., Thaker, I. H., Strand, T. E. and Joshi, J. B., 2010. Advanced PIV/LIF and Shadowgraphy System to Visualize Flow Structure in Two-Phase Bubbly Flows. *Chemical Engineering Science*, 65 (8), 2431-2442.
- Sathe, M. J., Deshmukh, S. S., Joshi, J. B. and Koganti, S. B., 2010. Computational fluid dynamics simulation and experimental investigation: Study of two-phase liquid-liquid flow in a vertical Taylor-couette contactor. *Industrial and Engineering Chemistry Research*, 49 (1), 14-28.
- Mathpati, C. S., Joshi, J. B., 2007. Insight into theories of heat and mass transfer at the solid-fluid interface using direct numerical simulation and large eddy simulation. *Ind. Eng. Chem. Res.* 46, 8525-8557.
- Mathpati, C. S., Deshpande, S. S., Joshi, J. B., 2009. Computational and experimental Fluid dynamics of Jet loop reactor. *AIChEJ* 55, 2526-2544.
- Deen, N. G., Solberg, T., Hjertager, B. H., 2001. Large eddy simulation of the gas-liquid flow in a square cross-sectioned bubble column. *Chem. Eng. Sci.* 56, 6341-6349.
- Tabib, M. V., Roy, S. A., Joshi, J. B., 2008. CFD simulation of bubble column - An analysis of interphase forces and turbulence models. *Chem. Eng. J.* 139, 589-614.